

Technische Universität Kaiserslautern

Fachbereich Chemie

**Cryo Spectroscopy and Kinetics
of Isolated Transition Metal Clusters and Complexes**

Am Fachbereich Chemie der Technischen Universität Kaiserslautern zur Erlangung

des akademischen Grades "Doktor der Naturwissenschaften" genehmigte

Dissertation

(D386)

vorgelegt von

Dipl.-Chem. Sebastian Dillinger

Betreuer: Prof. Dr. G. Niedner-Schatteburg

Tag der wissenschaftliche Aussprache: 26.10.2017

Technische Universität Kaiserslautern 2017

Die vorliegende Arbeit wurde im Zeitraum von Januar 2015 bis August 2017 im Fachbereich Chemie der Technischen Universität Kaiserslautern unter Betreuung von Prof. Dr. G. Niedner-Schatteburg angefertigt.

Datum des Antrags der Eröffnung des Promotionsverfahrens: 21.08.2017

Promotionskommission:

Vorsitzender	Prof. Dr. H. Sitzmann
1. Berichterstatter	Prof. Dr. G. Niedner-Schatteburg
2. Berichterstatter	Prof. Dr. M. Gerhards

MEINEN GROßELTERN

„Da steh ich nun, ich armer Tor und bin so klug als wie zuvor.“

Johann Wolfgang von Goethe, Faust

Content

1	Introduction	1
1.1	References	3
2	Experimental and Computational Methods.....	9
2.1	Ion Sources.....	9
2.1.1	Laser Vaporization (LVAP) Source	9
2.1.2	ElectroSpray Ionization (ESI) Source	10
2.2	Fourier Transform Ion Cyclotron Resonance Mass Spectrometry (FT-ICR MS)	12
	FRITZ	15
2.3	Isothermal Cryo Kinetics	17
	Relative Rate Constants	17
	Absolute Rate Constants	18
2.4	InfraRed (Multiple) Photon Dissociation (IR-(M)PD)	19
	Optical Parametric Oscillator / Amplifier (OPO / OPA) IR Laser System.....	20
2.5	Density Functional Theory (DFT)	22
2.6	References	24
3	Infrared Spectroscopy of N₂ Adsorption on Size Selected Cobalt Cluster Cations in Isolation	29
3.1	Preamble.....	29
3.2	Reprint	30
4	Cryo Kinetics and Spectroscopy of Cationic Nickel Clusters: Rough and Smooth Surfaces	37
4.1	Preamble.....	37
4.2	Reprint	38
4.3	Supplementary Information	51
5	Probing Cluster Surface Morphology by Cryo Kinetics of N₂ on Cationic Nickel Clusters	71
5.1	Preamble.....	71

5.2	Abstract.....	73
5.3	Introduction	74
5.4	Experimental and Computational Methods	75
5.5	Results and Discussion.....	77
5.6	Conclusions	90
5.7	Acknowledgements	91
5.8	References	91
5.9	Supplementary Material.....	93
6	Probing Cluster Surface Morphology by Cryo Spectroscopy of N₂ on Cationic Nickel Clusters.....	105
6.1	Preamble.....	105
6.2	Abstract.....	107
6.3	Introduction	108
6.4	Experimental and Computational Methods	110
6.5	Results and Discussion.....	111
6.6	Conclusions	128
6.7	Acknowledgements	129
6.8	References	130
6.9	Supplementary Material.....	133
7	Cryo IR Spectroscopy and Cryo Kinetics of N₂ on Cationic Iron Clusters.....	147
7.1	Preamble.....	147
7.2	Abstract.....	149
7.3	Introduction	149
7.4	Experimental and Computational Methods	151
7.5	Results and Discussion.....	153
7.6	Conclusions	170
7.7	Acknowledgements	171
7.8	References	171
7.9	Supplementary Material.....	177

8	Cryo IR Spectroscopy of N₂ and H₂ on Ru₈⁺: The Effect of N₂ on the H-Migration	189
8.1	Preamble.....	189
8.2	Abstract.....	191
8.3	Introduction	192
8.4	Experimental and Computational Methods	193
8.5	Results and Discussion.....	194
8.6	Conclusions	200
8.7	Acknowledgments	200
8.8	References:	201
8.9	Supporting Information	203
9	Cryo IR Spectroscopy of [Hemin]⁺ Complexes in Isolation	229
9.1	Preamble.....	229
9.2	Reprint	230
9.3	Supporting Information	237
10	Summary and Outlook.....	269
11	Zusammenfassung und Ausblick	273
12	Appendix: Further Joint Publications	279
12.1	Vibrational fingerprints of a tetranuclear cobalt carbonyl cluster within a cryo tandem ion trap	281
12.1.1	Preamble	281
12.1.2	Reprint.....	282
12.2	Vibrational Blue Shift of coordinated N ₂ in [Fe ₃ O(OAc) ₆ (N ₂) _n] ⁺ : “Non Classical” Dinitrogen Complexes	289
12.2.1	Preamble	289
12.2.2	Reprint.....	290
12.3	Infrared Spectroscopic Investigations of Structures and N ₂ Adsorption Induced Relaxations of Isolated Rhodium Clusters	295
12.3.1	Preamble	295
	Lebenslauf.....	325

List of Publications.....	327
Contribution to Conferences	329
Danksagung.....	333
Eidesstattliche Erklärung.....	335

1 Introduction

Transition metals (TM) and TM containing compounds are inevitably linked with life. A large number of proteins contain a TM center as a cofactor. Most prominent representative of such metalloproteins are Vitamin B₁₂ and Hemoglobin.^[1] The latter one maintains the respirational process of vertebrates by the transportation of O₂ via a Fe center.^[2] The functionality of this metalloprotein is highly impacted by the electronic configuration of the Fe center.^[3-4] TM complexes with structural similarities to the prosthetic groups may serve as model systems for the otherwise very complex proteins.^[5]

Besides their outermost importance in living creatures, TM enable modern everyday life as we know it by facilitating the production of fertilizers^[6] or gasoline^[7]. Most industrial processes depend on TM based catalysts like the Haber-Bosch process (Fe)^[8] or the Fischer-Tropsch process (Co, Fe, Ni,...)^[9]. A fundamental/mechanistic understanding of such reactions is of great importance for the improvement of available catalysts or the design of new ones. Direct investigations of industrial processes is challenging due to their complexity. Therefore model systems are employed to elucidate the fundamental catalytic steps.^[10] Size-selected TM clusters with 2 – 30 atoms may serve as model systems for heterogeneous catalysis.^[11-12] They represent the transition from TM atoms to the bulk and exhibit remarkable size-dependent properties^[13-14] and exhibit a conceivable cluster-surface analogy^[15-17]. They may render the possible structure sensitivity of catalytic reactions.^[18]

Mass spectrometry^[19] in combination with ElectroSpray Ionization (ESI) sources^[20] or Laser VAPorization (LVAP) cluster ion sources^[21] serves for the generation and subsequent characterization of such model systems under isolated conditions. The possibility of gas phase investigations of reactions on TM clusters and TM compounds provide for the unique opportunity to gather fundamental insights into structures and reactivity omitting perturbing effects such as solvents or packing. Such studies bear the ability to unravel the fundamental interplay of model systems with biologically or catalytically relevant molecules. Numerous studies focused on the gas phase reactions of biomolecules^[22] and TM clusters with e.g. hydrogen,^[23-26] nitrogen,^[27-28] ammonia,^[26, 29-31] water,^[26, 32-33] and carbon monoxide^[34]. These studies provided for insight into the thermochemistry and bond energies. Furthermore such studies suggested various cluster structures as they utilized adsorbates as

chemical probes for their geometries.^[29, 35-37] The unknown cluster structures were as well subject to numerous density functional theory (DFT) studies.^[38-42] However, computations including adsorbates are rather scarce.^[43-45]

Furthermore, vibrational spectroscopy of isolated ions by either free electron lasers (FEL) or tunable table top lasers is commonly applied to obtain structural information.^[46-47] The InfaRed (Multiple) Photon Dissociation (IR(M)-PD) technique has proven to be a valuable tool for the structural elucidation of biomolecules^[48-49], TM complexes,^[50-52] and bare TM clusters^[53-55]. The investigations on TM atoms with adsorbates^[56-58] and TM cluster adsorbate complexes^[59-64] provide for fundamental insights into the coordination of the respective adsorbate and has the ability to reveal possible activations.

The introduction of cryogenically cooled ion traps has created new opportunities as it allows for the generation of previously inaccessible reaction products.^[65-66] In combination with IR spectroscopy it enables so-called tagging or messenger techniques.^[67-68] These techniques allow for a one photon dissociation omitting any spectral artefacts caused by multi photon absorption.

The research studies presented in this thesis combines the afore mentioned techniques. They include cryo IR-PD spectroscopy and cryo kinetics to isolated TM cluster and biomolecule adsorbate complexes in conjunction with DFT modelling to gain insight into their structure and reactivity. This thesis comprises of seven research studies of which each provides for an individual introduction, experimental, discussion and conclusion part. A general introduction to the utilized experimental and computational methods is given in chapter 2.

The chapter 3 elucidates the N₂ adsorption to size selected cationic Co clusters by cryo IR-PD spectroscopy in combination with preliminary DFT modelling. It identifies cluster size dependent effects and a favored μ_1 head-on adsorption of the N₂ to the Co clusters. This study can be seen as a starting point for the subsequent studies.

The chapters 4 – 6 focus on the adsorption of N₂ to cationic Ni clusters. These studies characterize the cluster morphologies by kinetic, spectroscopic and computational investigations and allow for a classification of the probed Ni clusters into four classes of structure related surface adsorption behavior.

The chapter 7 provides for kinetic and spectroscopic investigations on N₂ on cationic Fe clusters. It observes remarkable cluster size dependent features that in contrast to the Ni clusters do not allow for a structure related classification. Preliminary DFT modelling allows for a first interpretation of the unreactivity towards N₂ of the Fe₁₇⁺ and one isomer of the Fe₁₈⁺ cluster.

The chapter 8 investigates the coadsorption of N₂ and H₂ to a Ru₈⁺ cluster by cryo IR-PD spectroscopy and DFT modelling. It identifies remarkable effects of the reaction gas sequence on the migration possibility of the hydrides on the cluster.

The chapter 9 characterizes various [Hemin]⁺ adducts by IR-PD spectroscopy in conjunction with DFT modelling. It reports the effect of different adsorbates (N₂, CO, O₂) on the biomolecule and it observes the transition from a non-classical to a classical CO complex.

1.1 References

- (1) Waldron, K. J.; Rutherford, J. C.; Ford, D.; Robinson, N. J., Metalloproteins and metal sensing, *Nature* **2009**, *460*, 823.
- (2) Kepp, K. P., Heme: From quantum spin crossover to oxygen manager of life, *Coord. Chem. Rev.* **2017**, *344*, 363-374.
- (3) Chen, H.; Ikeda-Saito, M.; Shaik, S., Nature of the Fe–O₂ Bonding in Oxy-Myoglobin: Effect of the Protein, *J. Am. Chem. Soc.* **2008**, *130*, 14778-14790.
- (4) Pauling, L.; Weiss, J. J., NATURE OF IRON-OXYGEN BOND IN OXYHAEMOGLOBIN, *Nature* **1964**, *203*, 182-&.
- (5) Karlin, K. D., Metalloenzymes, structural motifs, and inorganic models, *SCIENCE-NEW YORK THEN WASHINGTON-* **1993**, *261*, 701-701.
- (6) Erisman, J. W.; Sutton, M. A.; Galloway, J.; Klimont, Z.; Winiwarter, W., How a century of ammonia synthesis changed the world, *Nature Geosci* **2008**, *1*, 636-639.
- (7) Dry, M. E., High quality diesel via the Fischer–Tropsch process – a review, *J. Chem. Technol. Biotechnol.* **2002**, *77*, 43-50.
- (8) Schlögl, R., Ammonia Synthesis. In *Handbook of Heterogeneous Catalysis*, Wiley-VCH Verlag GmbH & Co. KGaA: 2008.
- (9) Dry, M. E., The Fischer–Tropsch process: 1950–2000, *Catal. Today* **2002**, *71*, 227-241.
- (10) Somorjai, G. A.; Contreras, A. M.; Montano, M.; Rioux, R. M., Clusters, surfaces, and catalysis, *Proc. Natl. Acad. Sci.* **2006**, *103*, 10577-10583.
- (11) Lang, S. M.; Bernhardt, T. M., Gas phase metal cluster model systems for heterogeneous catalysis, *Phys. Chem. Chem. Phys.* **2012**, *14*, 9255-9269.

- (12) Johnson, G. E.; Mitric, R.; Bonacic-Koutecky, V.; Castleman, A. W., Jr., Clusters as model systems for investigating nanoscale oxidation catalysis, *Chem. Phys. Lett.* **2009**, *475*, 1-9.
- (13) Knickelbein, M. B., Reactions of transition metal clusters with small molecules, *Annu. Rev. Phys. Chem.* **1999**, *50*, 79-115.
- (14) Luo, Z.; Castleman, A. W.; Khanna, S. N., Reactivity of Metal Clusters, *Chem. Rev.* **2016**, *116*, 14456-14492.
- (15) Muetterties, E. L.; Rhodin, T. N.; Band, E.; Brucker, C. F.; Pretzer, W. R., Clusters and Surfaces, *Chem. Rev.* **1979**, *79*, 91-137.
- (16) Muetterties, E. L., Molecular metal clusters, *Science* **1977**, *196*, 839-848.
- (17) Muetterties, E. L., Metal Clusters in Catalysis .3. Clusters as Models for Chemisorption Processes and Heterogeneous Catalysis, *Bull. Soc. Chim. Belg.* **1975**, *84*, 959-986.
- (18) Jacobsen, C. J. H.; Dahl, S.; Hansen, P. L.; Törnqvist, E.; Jensen, L.; Topsøe, H.; Prip, D. V.; Møenshaug, P. B.; Chorkendorff, I., Structure sensitivity of supported ruthenium catalysts for ammonia synthesis, *J. Mol. Catal. A: Chem.* **2000**, *163*, 19-26.
- (19) Gross, J. H., *Mass spectrometry: a textbook*. Springer Science & Business Media: 2006.
- (20) Fenn, J. B.; Mann, M.; Meng, C. K.; Wong, S. F.; Whitehouse, C. M., Electrospray ionization for mass spectrometry of large biomolecules, *Science* **1989**, *246*, 64-71.
- (21) Duncan, M. A., Invited Review Article: Laser vaporization cluster sources, *Rev. Sci. Instrum.* **2012**, *83*, 041101.
- (22) Green, M. K.; Lebrilla, C. B., Ion-molecule reactions as probes of gas-phase structures of peptides and proteins, *Mass Spectrom. Rev.* **1997**, *16*, 53-71.
- (23) Richtsmeier, S.; Parks, E.; Liu, K.; Pobo, L.; Riley, S., Gas phase reactions of iron clusters with hydrogen. I. Kinetics, *J. Chem. Phys.* **1985**, *82*, 3659-3665.
- (24) Parks, E.; Liu, K.; Richtsmeier, S.; Pobo, L.; Riley, S., Reactions of iron clusters with hydrogen. II. Composition of the fully hydrogenated products, *J. Chem. Phys.* **1985**, *82*, 5470-5474.
- (25) Jones, N.; Beltran, M.; Khanna, S. N.; Baruah, T.; Pederson, M., Hydrogen adsorption and magnetic behavior of Fe_n and Co_n clusters: Controlling the magnetic moment and anisotropy one atom at a time, *Phys. Rev. B* **2004**, *70*, 165406.
- (26) Parks, E.; Weiller, B.; Bechthold, P.; Hoffman, W.; Nieman, G.; Pobo, L.; Riley, S., Chemical probes of metal cluster structure: reactions of iron clusters with hydrogen, ammonia, and water, *J. Chem. Phys.* **1988**, *88*, 1622-1632.
- (27) Tan, L.; Liu, F. Y.; Armentrout, P. B., Thermochemistry of the activation of N₂ on iron cluster cations: Guided ion beam studies of the reactions of Fe-n(+) (n=1-19) with N₂, *J. Chem. Phys.* **2006**, *124*, 084302.
- (28) Liu, F.; Li, M.; Tan, L.; Armentrout, P. B., Guided ion beam studies of the reactions of Co(n)(+) (n=1-18) with N(2): Cobalt cluster mononitride and dinitride bond energies, *J. Chem. Phys.* **2008**, *128*, 194313.
- (29) Parks, E. K.; Nieman, G. C.; Pobo, L. G.; Riley, S. J., The Reaction of Iron Clusters with Ammonia .1. Compositions of the Ammoniated Products and Their Implications for Cluster Structure, *J. Chem. Phys.* **1988**, *88*, 6260-6272.
- (30) Fossan, K. O.; Uggerud, E., Reactions of cationic iron clusters with ammonia, models of nitrogen hydrogenation and dehydrogenation, *Dalton Trans.* **2004**, 892-897.

-
- (31) Irion, M. P.; Schnabel, P., FT-ICR studies of sputtered metal cluster ions. 5. The chemistry of iron cluster cations with ammonia and hydrazine, *J. Phys. Chem.* **1991**, *95*, 10596-10599.
- (32) Gutsev, G.; Mochena, M.; Bauschlicher, C., Interaction of water with small Fe *n* clusters, *Chem. Phys.* **2005**, *314*, 291-298.
- (33) Weiller, B. H.; Bechthold, P. S.; Parks, E. K.; Pobo, L. G.; Riley, S. J., The Reactions of Iron Clusters with Water, *J. Chem. Phys.* **1989**, *91*, 4714-4727.
- (34) McNary, C. P.; Armentrout, P. B., Iron cluster-CO bond energies from the kinetic energy dependence of the Fe-*n*(+) (*n*=4-17) + CO association reactions, *Phys. Chem. Chem. Phys.* **2014**, *16*, 26467-26477.
- (35) Parks, E. K.; Zhu, L.; Ho, J.; Riley, S. J., The Structure of Small Nickel Clusters .1. Ni-3-Ni-15, *J. Chem. Phys.* **1994**, *100*, 7206-7222.
- (36) Parks, E. K.; Zhu, L.; Ho, J.; Riley, S. J., The Structure of Small Nickel Clusters .2. Ni-16-Ni-28, *J. Chem. Phys.* **1995**, *102*, 7377-7389.
- (37) Ho, J.; Parks, E. K.; Zhu, L.; Riley, S. J., Reactions of Small Cobalt Clusters with N-2 - Implications for Cluster Structure, *Chem. Phys.* **1995**, *201*, 245-261.
- (38) Calaminici, P.; Beltran, M. R., A density functional study of structure and stability of Ni8, Ni8+ and Ni8- cluster, *Comput. Lett.* **2005**, *1*, 172-182.
- (39) Ma, Q.-M.; Xie, Z.; Wang, J.; Liu, Y.; Li, Y.-C., Structures, binding energies and magnetic moments of small iron clusters: A study based on all-electron DFT, *Solid State Commun.* **2007**, *142*, 114-119.
- (40) Gutsev, G. L.; Weatherford, C. A.; Jena, P.; Johnson, E.; Ramachandran, B. R., Structure and Properties of Fe_n, Fe_n⁻, and Fe_n⁺ Clusters, *n* = 7–20, *J. Phys. Chem. A* **2012**, *116*, 10218-10228.
- (41) Gutsev, G. L.; Weatherford, C. W.; Belay, K. G.; Ramachandran, B. R.; Jena, P., An all-electron density functional theory study of the structure and properties of the neutral and singly charged M-12 and M-13 clusters: M = Sc-Zn, *J. Chem. Phys.* **2013**, *138*.
- (42) Chaves, A. S.; Piotrowski, M. J.; Da Silva, J. L. F., Evolution of the structural, energetic, and electronic properties of the 3d, 4d, and 5d transition-metal clusters (30 TM_n systems for *n* = 2-15): a density functional theory investigation, *Phys. Chem. Chem. Phys.* **2017**, *19*, 15484-15502.
- (43) Curotto, E.; Matro, A.; Freeman, D. L.; Doll, J. D., A semi-empirical potential for simulations of transition metal clusters: Minima and isomers of Ni-*n* (*n* = 2-13) and their hydrides, *J. Chem. Phys.* **1998**, *108*, 729-742.
- (44) Boyukata, M.; Guvenc, Z. B.; Ozcelik, S.; Durmus, P.; Jellinek, J., Structure and reactivity of Ni(*n*) (*n*=7-14, 19) clusters, *Int. J. Quantum Chem.* **2001**, *84*, 208-215.
- (45) Takahashi, K.; Isobe, S.; Ohnuki, S., The stabilization of Fe, Ru, and Os clusters upon hydrogenation, *RSC Advances* **2013**, *3*, 21841-21847.
- (46) Oomens, J.; Sartakov, B. G.; Meijer, G.; von Helden, G., Gas-phase infrared multiple photon dissociation spectroscopy of mass-selected molecular ions, *Int. J. Mass Spectrom.* **2006**, *254*, 1-19.
- (47) Schöllkopf, W.; Gewinner, S.; Junkes, H.; Paarmann, A.; von Helden, G.; Bluem, H.; Todd, A. M. M. In *The new IR and THz FEL facility at the Fritz Haber Institute in Berlin*, 2015; pp 95121L-95121L-13.
- (48) Polfer, N. C.; Oomens, J., Vibrational spectroscopy of bare and solvated ionic complexes of biological relevance, *Mass Spectrom. Rev.* **2009**, *28*, 468-494.
-

- (49) Little, D. P.; Speir, J. P.; Senko, M. W.; O'Connor, P. B.; McLafferty, F. W., Infrared multiphoton dissociation of large multiply charged ions for biomolecule sequencing, *Anal. Chem.* **1994**, *66*, 2809-2815.
- (50) Gaffga, M.; Munstein, I.; Mueller, P.; Lang, J.; Thiel, W. R.; Niedner-Schatteburg, G., Multistate-Mediated Rearrangements and FeCl₂ Elimination in Dinuclear FePd Complexes, *J. Phys. Chem. A* **2015**, *119*, 12587-12598.
- (51) Lanucara, F.; Scuderi, D.; Chiavarino, B.; Fornarini, S.; Maitre, P.; Crestoni, M. E., IR Signature of NO Binding to a Ferrous Heme Center, *J. Phys. Chem. Lett.* **2013**, *4*, 2414-2417.
- (52) MacAleese, L.; Maitre, P., Infrared spectroscopy of organometallic ions in the gas phase: From model to real world complexes, *Mass Spectrom. Rev.* **2007**, *26*, 583-605.
- (53) Kerpal, C.; Harding, D. J.; Rayner, D. M.; Lyon, J. T.; Fielicke, A., Far-IR Spectra and Structures of Small Cationic Ruthenium Clusters: Evidence for Cubic Motifs, *J. Phys. Chem. C* **2015**, *119*, 10869-10875.
- (54) Gruene, P.; Butschke, B.; Lyon, J. T.; Rayner, D. M.; Fielicke, A., Far-IR Spectra of Small Neutral Gold Clusters in the Gas Phase, *Zeitschrift Fur Physikalische Chemie-International Journal of Research in Physical Chemistry & Chemical Physics* **2014**, *228*, 337-350.
- (55) Harding, D. J.; Walsh, T. R.; Hamilton, S. M.; Hopkins, W. S.; Mackenzie, S. R.; Gruene, P.; Haertelt, M.; Meijer, G.; Fielicke, A., Communications: The structure of Rh-8(+) in the gas phase, *J. Chem. Phys.* **2010**, *132*, 011101.
- (56) Brathwaite, A. D.; Abbott-Lyon, H. L.; Duncan, M. A., Distinctive Coordination of CO vs N₂ to Rhodium Cations: An Infrared and Computational Study, *J. Phys. Chem. A* **2016**, *120*, 7659-7670.
- (57) Pillai, E. D.; Jaeger, T. D.; Duncan, M. A., IR spectroscopy and density functional theory of small V+(N₂)(n) complexes, *J. Phys. Chem. A* **2005**, *109*, 3521-3526.
- (58) Pillai, E. D.; Jaeger, T. D.; Duncan, M. A., IR spectroscopy of Nb+(N₂)(n) complexes: Coordination, structures, and spin states, *J. Am. Chem. Soc.* **2007**, *129*, 2297-2307.
- (59) Kerpal, C.; Harding, D. J.; Lyon, J. T.; Meijer, G.; Fielicke, A., N₂ Activation by Neutral Ruthenium Clusters, *J. Phys. Chem. C* **2013**, *117*, 12153-12158.
- (60) Harding, D. J.; Kerpal, C.; Meijer, G.; Fielicke, A., Activated Methane on Small Cationic Platinum Clusters, *Angewandte Chemie-International Edition* **2012**, *51*, 817-819.
- (61) Fielicke, A.; Gruene, P.; Meijer, G.; Rayner, D. M., The adsorption of CO on transition metal clusters: A case study of cluster surface chemistry, *Surf. Sci.* **2009**, *603*, 1427-1433.
- (62) Lyon, J. T.; Gruene, P.; Fielicke, A.; Meijer, G.; Rayner, D. M., Probing C-O bond activation on gas-phase transition metal clusters: Infrared multiple photon dissociation spectroscopy of Fe, Ru, Re, and W cluster CO complexes, *J. Chem. Phys.* **2009**, *131*, 184706.
- (63) Gruene, P.; Fielicke, A.; Meijer, G.; Rayner, D. M., The adsorption of CO on group 10 (Ni, Pd, Pt) transition-metal clusters, *Phys. Chem. Chem. Phys.* **2008**, *10*, 6144-6149.
- (64) Swart, I.; de Groot, F. M. F.; Weckhuysen, B. M.; Gruene, P.; Meijer, G.; Fielicke, A., H₂ adsorption on 3d transition metal clusters: A combined infrared spectroscopy and density functional study, *J. Phys. Chem. A* **2008**, *112*, 1139-1149.

- (65) Ferrand, L.; Soorkia, S.; Gregoire, G.; Broquier, M.; Soep, B.; Shafizadeh, N., Bonding of heme Fe-III with dioxygen: observation and characterization of an incipient bond, *Phys. Chem. Chem. Phys.* **2015**, *17*, 25693-25699.
- (66) Gerlich, D.; Jašík, J.; Andris, E.; Navrátil, R.; Roithová, J., Collisions of FeO⁺ with H₂ and He in a Cryogenic Ion Trap, *ChemPhysChem* **2016**, *17*, 3723-3739.
- (67) Wolk, A. B.; Leavitt, C. M.; Garand, E.; Johnson, M. A., Cryogenic ion chemistry and spectroscopy, *Acc. Chem. Res.* **2013**, *47*, 202-210.
- (68) Rizzo, T. R.; Boyarkin, O. V., Cryogenic Methods for the Spectroscopy of Large, Biomolecular Ions. In *Gas-Phase IR Spectroscopy and Structure of Biological Molecules*, Rijs, A. M.; Oomens, J., Eds. Springer International Publishing: Cham, 2015; pp 43-97.

2 Experimental and Computational Methods

2.1 Ion Sources

Ion sources are inevitably linked with mass spectrometry. The diversity of available ion sources provides for manifold possibilities for the characterization and analyzation of gaseous ions.^[1-2] In the following chapters two selected ion sources are presented as they were used in the research studies of this thesis.

2.1.1 Laser Vaporization (LVAP) Source

The investigated metal clusters are produced by a home built Laser VAPorization (LVAP) cluster ion source. The LVAP cluster ion source was first described by Bondybey and English^[3-4], and Smalley^[5-6]. Our source mainly comprises a home built piezoelectric valve^[7], an expansion / interaction block, and an expansion channel (**Figure 2.1**).

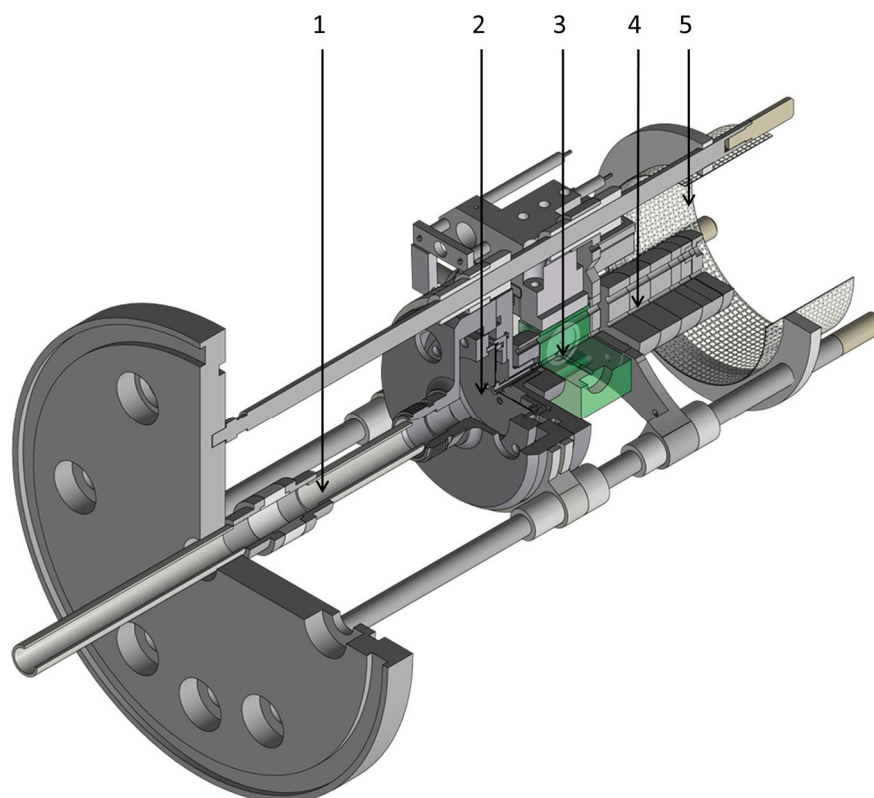


Figure 2.1 Schematic drawing of a LVAP source: gas line (1), piezoelectric valve (2), expansion / interaction block (3), expansion channel (4), mesh (5).

The second harmonic of a Nd:YAG laser (Innolas, Spitlight 300; 20 Hz) is focused on a rotating metal foil (thickness: 0.1 – 0.5 mm) composed of the metal or alloy of interest. The resulting plasma consists of neutral atoms, cationic and anionic species. The plasma is captured by a short transversal He gas pulse generated by the home built piezoelectric valve. This valve operates with a backing pressure of 12 – 20 bar, an opening time of approximately 40 μ s, and a repetition rate of 20 Hz. The gas pulse expands into the source vacuum chamber, raising the chamber pressure from 2×10^{-7} mbar up to 2×10^{-4} mbar. The metal plasma is cooled within the supersonic expansion of the He gas and metal cluster ions are formed in the expansion channel. No further ionization step is needed. Clusters in the size range of 2 to 40 atoms are generated. The intensity maximum of the produced cluster distribution can be influenced by variation of the backing pressure, the valve opening time, the laser-valve-delay, and the applied source voltages. The charge state of the produced clusters can be selected by the polarity of the source voltages and of the subsequent ion optics.

The cobalt foil was purchased from Alfa Aesar (purity: 99.95 %). The nickel, iron, and ruthenium foils were purchased as mono isotopic materials from Oak Ridge National Laboratory (^{58}Ni purity: 99.61 %, ^{56}Fe purity: 99.93 %, ^{102}Ru : 99.38 %).

2.1.2 ElectroSpray Ionization (ESI) Source

ElectroSpray Ionization (ESI) is a method to gently transfer ions from solution into the gas phase. The basis for the development of ESI has been described by Zeleny in 1917^[8] and was first realized by Dole in 1968^[9]. In 2002 Fenn was awarded with the Nobel Prize for the combination of the ESI source with a quadrupole mass spectrometer and its application.^[10-11] Since then ESI mass spectrometry has been proven to be a valuable tool with wide range applications. Inter alia, it enables the analysis of biomolecules^[12], non-covalent complexes^[13], catalytic intermediates^[14-15] or transition metal complexes^[16].

To start the ESI process (**Figure 2.2**) an analyte solution is pushed through an electroconductive capillary (ESI capillary) by a syringe pump. A strong electrostatic field is applied between the capillary and the orifice of the mass spectrometer. This leads to a charge separation within the solution and the formation of a Taylor Cone^[17-18]. Charged droplets are released from the Taylor Cone when the coulomb repulsion exceeds the surface

tension of the solvent. The generated droplets shrink by solvent evaporation until they reach the Rayleigh limit^[19] and undergo Coulomb explosions. This process is repeated until the droplets are in the nanometer size region^[20]. The final release of the ions into the gas phase is discussed in three different models^[21]: the ion evaporation model^[22-23], the charge residue model^[24-25], and the chain ejection model^[26-27].

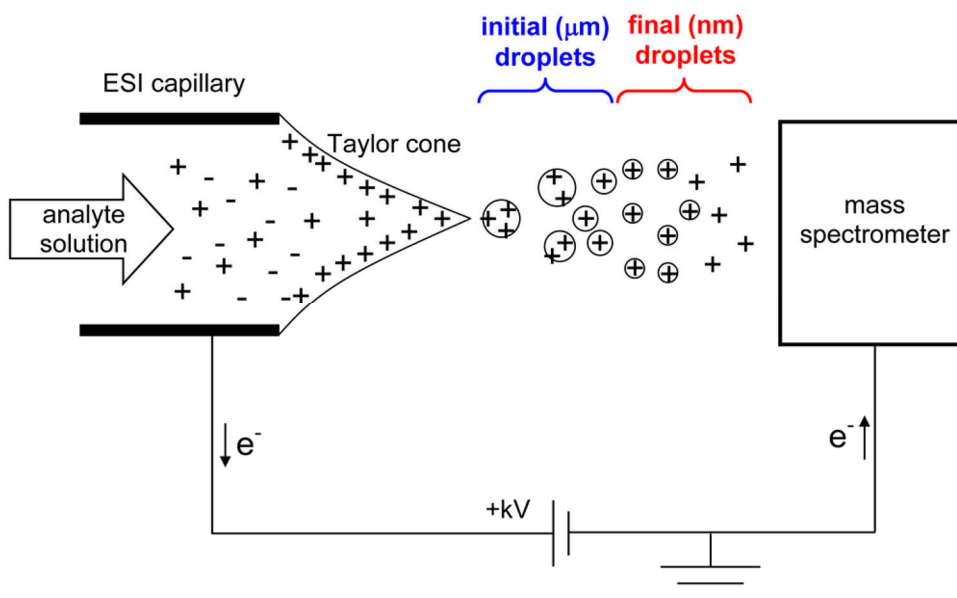


Figure 2.2^[20] Schematic drawing of an ESI source visualizing the release of charged droplets during the ESI process.

We use a commercially available Apollo II ESI source (Bruker, **Figure 2.3**). The sample solution (10^{-4} mol/l) is placed in a HamiltonTM gas tight syringe (0.5 ml). The sample solution is continuously injected into the electrospray needle through a peek capillary. The syringe pump provides for a constant flow rate of 120 $\mu\text{L/h}$. A nebulizer gas (N_2 , 3.0 L/min) facilitates the nebulization of the analyte solution and a heated dry gas (N_2 , 220 $^\circ\text{C}$, 6.0 L/min) supports the solvent evaporation. The electrospray needle is grounded and a high voltage is applied to the spray shield in order to generate an electrostatic field. An additional electrostatic potential between the spray shield and the glass capillary focuses the ions into the capillary. This glass capillary is platinum coated at both ends which allows to apply an electrostatic gradient that guides the ions into the subsequent vacuum stage. After the glass capillary the ions are deflected into an ion funnel. A skimmer is located at the end of this first ion funnel. By adjusting the voltage of the skimmer in-source collision induced dissociation (in-source CID) can be performed. Then the ions enter the second ion funnel that leads to the source

hexapole. This hexapole can be used to accumulate the ions and generate ion packages before entering the next vacuum stage (*cf.* FRITZ).

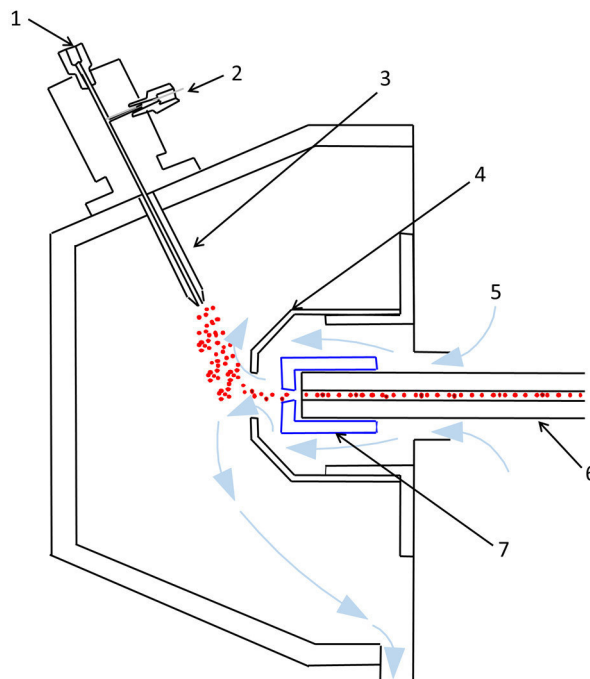


Figure 2.3^[28] Schematic drawing of the Bruker Apollo II ESI source with the sample inlet (1), the nebulizer gas inlet (2), the electrospray needle (3), the spray shield (4), the heated dry gas (5), the glass capillary (6), and the capillary cap (7).

2.2 Fourier Transform Ion Cyclotron Resonance Mass Spectrometry (FT-ICR MS)

The principles of cyclotron was first described by Lawrence in 1930.^[29-31] On the basis of this effect the first ion cyclotron resonance (ICR) mass spectrometers were constructed in the early 1950.^[32] The first Fourier Transform Ion Cyclotron (FT-ICR) mass spectrometers were introduced by Comisarow and Marshall.^[33-34] The performances of these mass spectrometers were further increased with the combination with superconducting magnets.^[35-36]

In an ICR mass spectrometer the ions of interest are stored in an ion trap (ICR cell or Penning trap) that is located in a strong homogeneous magnetic field. The magnetic field forces the ions on a circular trajectory inside the ion trap. The radius of this motion is dictated by two opposing forces: the Lorentz and the Centrifugal force.

$$F_L = qv_{xy}B \quad 2-1$$

$$F_{Cf} = \frac{mv_{xy}^2}{r} \quad 2-2$$

- F_L Lorentz force
 F_{Cf} Centrifugal force
 q charge of the ion ($q = z \cdot e$)
 z number of charges
 e elementary charge
 v_{xy} velocity of the ion in the xy plane
 B magnetic field
 m ion mass
 r radius of the ions orbit

The velocity in the xy plane is substituted by the angular velocity and the cyclotron frequency can be inserted into the equation:

$$v_{xy} = r\omega_c \quad 2-3$$

$$\omega_c = 2\pi f_c = \frac{qB}{m} \quad 2-4$$

$$f_c = \frac{qB}{2\pi m} \quad 2-5$$

The cyclotron frequency is independent from the initial velocity in the xy plane and proportional to the mass to charge ration (m/z).

An ICR cell consists of at least six plates (**Figure 2.4**). The front and the back trapping plate serve to trap the ions in the cell along the z-axis by an electrostatic field. This trapping results in an oscillatory motion along the z-axis - the trapping motion. The two excitation plates facing each other provide for the alternating electric field. By applying a frequency sweep to the excitation plates, the ions are accelerated and their orbits increase. The oscillating ions induce an image current in the two detection plates. The spectrum is recorded by measuring this image current.

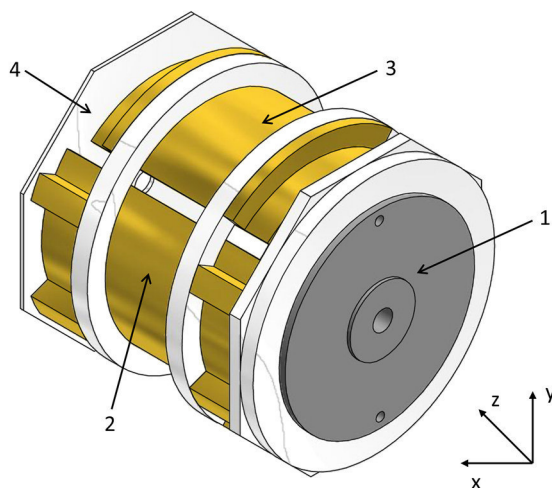


Figure 2.4 Schematic Drawing of an ICR cell (Bruker Infinity CellTM^[37]) with the front trapping plate (1), an excitation plate (2), a detection plate (3), and the back trapping plate (4).

The ion movement inside the ICR cell consists of several components(**Figure 2.5**). Besides the already mentioned cyclotron motion and the trapping motion, the ions move along an electrostatic potential. This motion is called magnetron motion and is mass independent. All motions are superimposed.

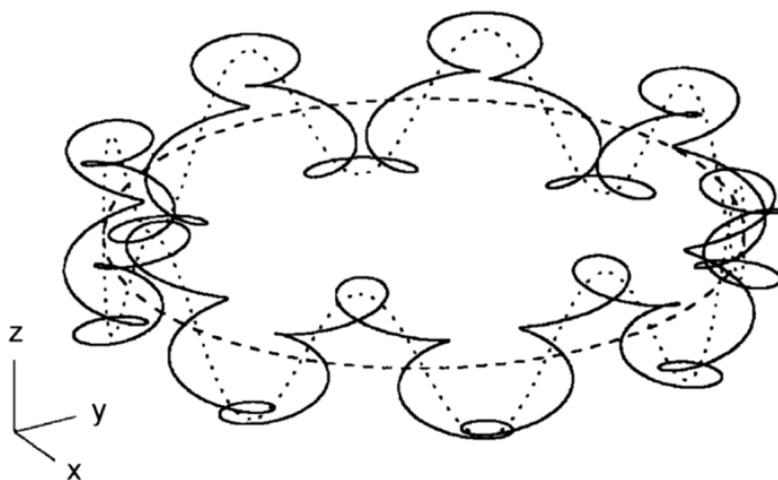


Figure 2.5^[38] Ion motion within an ICR cell consisting of the magnetron motion (dashed line), the magnetron motion plus the trapping motion (dotted line), and the overall motion including the cyclotron motion (solid line).

The ICR cell can also be used as a mass selector. A specific m/z ratio can be isolated by applying a frequency sweep excluding the resonance frequency of the m/z ratio of interest. The other ions are ejected from the ICR cell as they are excited on much higher and unstable

orbits than for detection. By applying this high excitation only to one specific resonance frequency, the respective m/z ratio can be ejected from the ICR cell.

FRITZ

The experimental setup FRITZ (Fouriertransform Reactive Investigation Test Zoo) is a modified FT-ICR mass spectrometer (Bruker, Apex Ultra) that is equipped with two different ion sources and two cryogenically cooled ion traps (**Figure 2.6**).

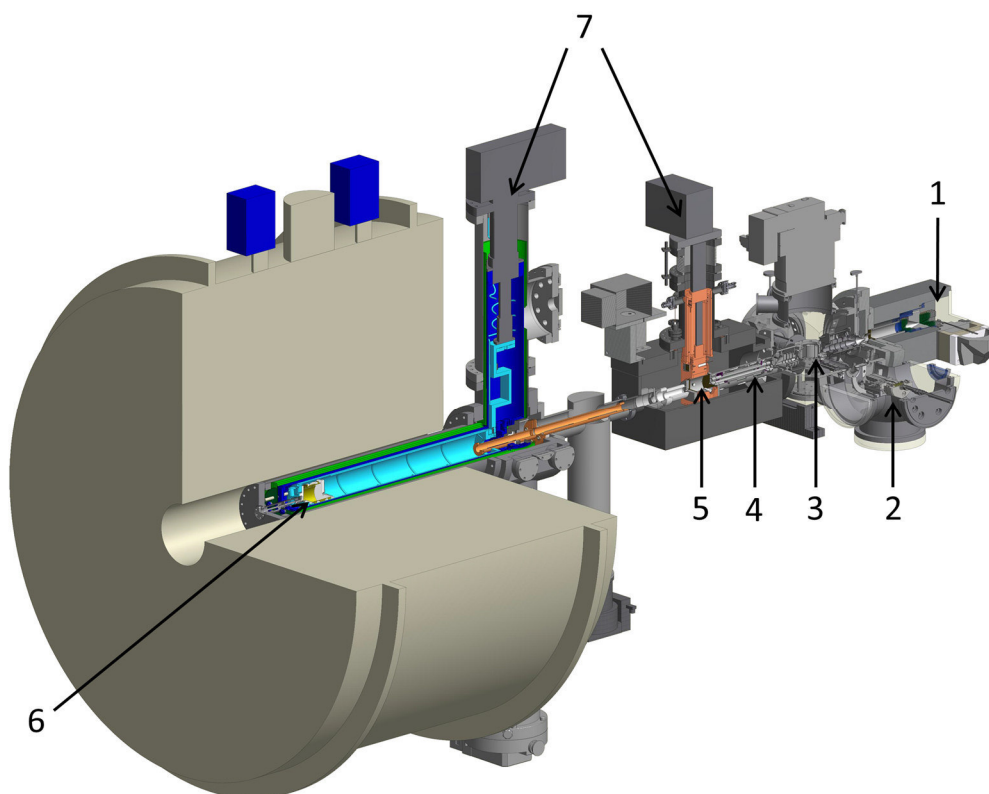


Figure 2.6 Schematic drawing of the FRITZ setup with the ESI source (1) that is located opposing the LVAP source but is shown here on the magnetic field axis for clarity, the LVAP source (2), the quadrupole ion beam bender (3), the quadrupole mass filter (4), the cryogenically cooled hexapole ion trap (5), the cryogenically cooled ICR cell (6), and the two two-stage closed cycle He cryostats (7).

The ions are generated by either the LVAP source or the commercially available Apollo II ESI source. Both ion sources are coupled to the mass spectrometer by home built gate valves to ensure the possibility of individual operation of the source vacuum systems. Home built ion optics guide the ions to a home built electrostatic quadrupole ion beam bender. This ion beam bender bends the ion beam by 90° onto the magnetic field axis. The beam is guided

into a quadrupole mass filter by another stack of home built ion optics. This mass filter provides for the possibility of a first mass selection. After the mass filter the ions enter the cryogenically cooled hexapole ion trap. This ion trap is connected to the second stage of a 4 K two-stage closed cycle He cryostat (Sumitomo SRDK-101E with a HC-4E compressing unit). The temperature of both cooling stages is monitored with two temperature sensors (LakeShore, Cernox™ CX-1060-CO-HT-P-1.4M) that are calibrated from 1.4 to 420 K. The temperature can be adjusted by heating resistors (Cartridge Heater, Janis Research, $R = 50 \Omega$) that are controlled by a temperature controller (LakeShore, Model 336). There are two gas lines attached to the hexapole ion trap for the injection of buffer and/or reaction gas. The gases can be introduced by either pulsed or leak valves. After a variable storage time (0 – 30 s), the ions are transferred to the ICR cell. This ICR cell is located in the high field region of a superconducting solenoid ($B = 7 \text{ T}$) within the ultra high vacuum region of this setup. The ICR cell is connected to the second stage of a 10 K two-stage closed cycle He cryostat (Sumitomo SRDK-408S2 with a W-71D compressing unit) and shielded by two actively cooled and three passively cooled shielding tubes. The temperature is monitored by three temperature sensors (LakeShore, Cernox™ CX-1050-CO-HT-P) calibrated from 4 to 325 K that are located directly on the second stage of the cold head, on a shield connected to first stage, and on the backside of the ICR cell. Again the temperature can be adjusted and is controlled by a temperature controller (LakeShore, Model 340). There is again the possibility to introduce gas either pulsed or continuously into the ICR cell. Furthermore the ions can be irradiated with an IR laser in this cell. Thus, the ICR cell serves as reaction cell, mass selector and mass analyzer altogether.

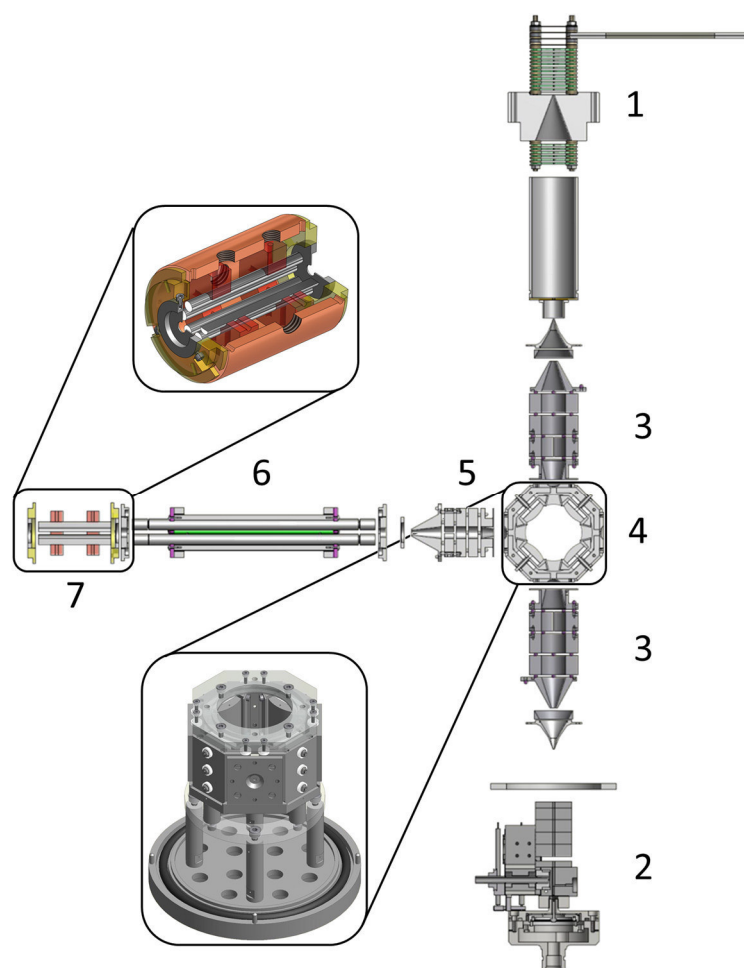


Figure 2.7 Scheme of the ion sources and optics leading to the hexapole ion trap: ESI source (1), LVAP source (2), ion optics (3) and (5), quadrupole ion beam bender (4), quadrupole mass filter (6), and hexapole ion trap (7).

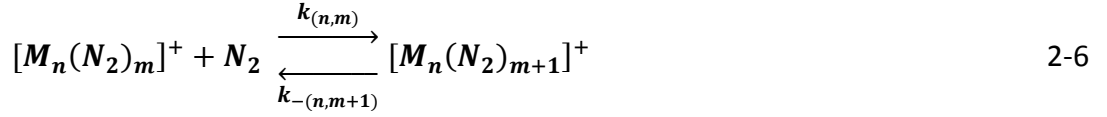
2.3 Isothermal Cryo Kinetics

Isothermal Cryo Kinetics are recorded by storing specific mass selected ions in the hexapole at a well-defined temperature and a well-defined amount of reaction gas. After storing the ions for variable reaction times in the hexapole, mass spectra are recorded. Reaction products appear as additional masses in the respective mass spectrum in dependence of the reaction time, while the intensity of the parent ions decrease.

Relative Rate Constants

The relative rate constants are determined by fitting the normalized reaction time dependent intensities of the parent and product ions derived from the mass spectra. The fits to pseudo-first-order-kinetics are performed with the *evofit* program.^[39] Fitting the

experimental kinetics allows for the quantitative determination of the relative rate constants like in the case of the stepwise N₂ adsorption:



Absolute Rate Constants

The average dipole orientation theory (ADO)^[40-41] describes the collision rate of polar molecules and is an extension of the classical Langevin collision rate^[42]. The ADO theory provides for the theoretical limit of the absolute rate:

$$k_{ADO} = \frac{q}{2\epsilon_0\sqrt{\mu}} \left(\sqrt{\alpha} + c\mu_D \sqrt{\frac{2}{\pi k_B T}} \right) \quad 2-7$$

μ reduced mass

α polarizability

μ_D dipole moment

c parameter between 0 and 1, expressed by polarizability volume and μ_D

This theory is often used to calculate the reaction rates of charged clusters with small molecules but it underestimates the reaction rates.^[43-44] Therefore two other models were introduced by Kummerlöwe and Beyer – the hard sphere average dipole orientation model (HAS) and the surface charge capture model (SCC).^[45]

The absolute rate constants $k_{(n,m)}^{abs}$ can be derived from the relative rate constants $k_{(n,m)}$ and the absolute collision gas number density $\rho_{N_2}(T)$:

$$k_{(n,m)}^{abs} = \frac{k_{(n,m)}}{\rho_{N_2}(T)} \quad 2-8$$

The collision gas number is calculated from the pressure in the chamber $p_c^{300 K}$ and an effective geometry factor c_{app} :

$$\rho_{N_2} = \frac{c_{app} p_c^{300 K}}{k_B T_{300 K}} \quad 2-9$$

The geometry factor we estimated the geometry factor by the virtue of numerous kinetic studies to be 1.8 ± 0.4 at 26 K with a net uncertainty of $\pm 50\%$. The absolute reaction

efficiency γ is calculated from the absolute rate constant and collision rate. It can be seen as reaction probability after a collision or as sticking probability as know from surface science.

$$\gamma = \frac{k_{abs}}{k_{coll}} \quad 2-10$$

2.4 InfraRed (Multiple) Photon Dissociation (IR-(M)PD)

Infrared (IR) (absorption) spectroscopy is a valuable tool to provide for vibrational/structural information and reactivity of various substances. The application of IR spectroscopy to isolated gaseous ions would enable investigations omitting any solvent or crystal effects. However, direct measurements of light absorption are not possible due to the low particle density in the ion traps. Therefore, more elaborated schemes are needed to obtain the IR spectra of gaseous ions. The InfraRed (Multiple) Photon Dissociation (IR-(M)PD) spectroscopy is an action spectroscopy approach record the vibrational spectra.^[46] Here the isolated gaseous ion is irradiated with tunable IR laser radiation. If the laser radiation frequency is in resonance with a vibrational transition of the ion, a photon is absorbed. The absorbed energy is rapidly distributed into other molecular vibrational degrees of freedom by internal vibrational redistribution (IVR).^[47] The original adsorbing mode is now able to adsorb another IR photon. This process is repeated until enough energy is available in the ion to break a weak bond^[46] (**Figure 2.8**).

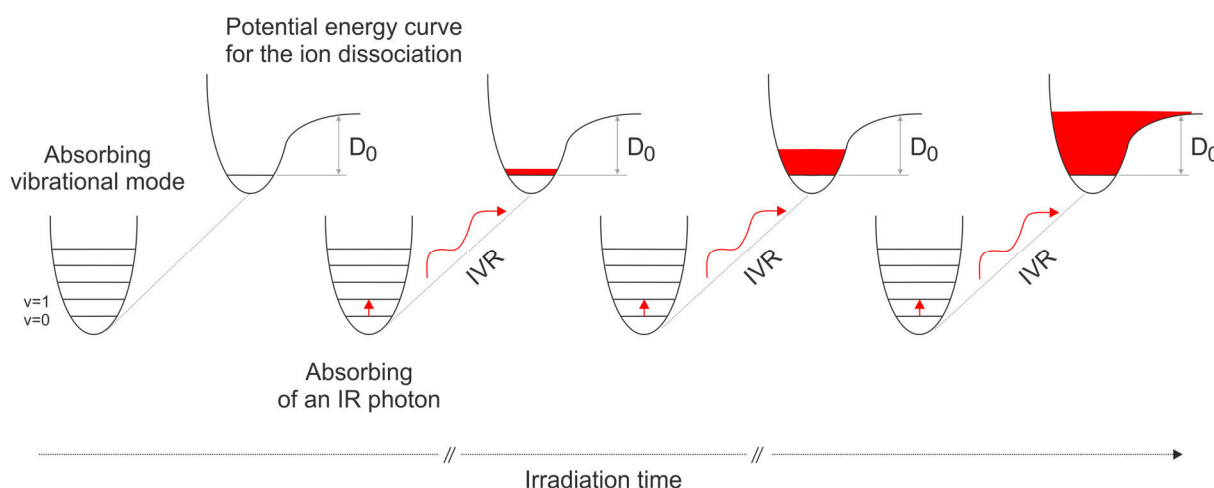


Figure 2.8^[48] Schematic representation of the IR-MPD process. A resonant IR photon is adsorbed by the ion and the energy is redistributed by IVR. This process is repeated until the dissociation threshold is reached and the ion fragmentizes.

The resulting fragments can be detected by mass spectrometry and the IR-(M)PD spectrum is obtained by plotting the fragmentation efficiency (frag. eff.) vs. the laser frequency.

$$\text{frag. eff.} = \frac{\sum_i I_i^{fr}}{\sum_i I_i^{fr} + \sum_i I_i^p} \quad 2-11$$

I_i^{fr} intensity of the fragment ions

I_i^p intensity of the parent ions

Note that if multiple photons are required to dissociate the ion, the fragmentation efficiency is not linearly correlated to laser intensity and the adsorption cross section of the respective ion. Therefore IR-MPD spectra may differ in intensity to solid state spectra or calculated linear adsorption spectra.

For the cleavage of covalent bonds multiple IR photons are required as one IR photon in the region from 800 cm^{-1} to 4000 cm^{-1} does not provide the sufficient energy (10 – 50 kJ/mol).^[49-50] To enable a single photon dissociation messenger or tagging techniques can be applied.^[51] In this techniques a weakly bound unreactive atom or molecule (He, Ar, H₂, N₂,...) is attached to the species of interest. Low temperatures are needed for the attachment that can be achieved by the use of supersonic expansion jets or cryogenically cooled ion traps.^[51-53]

Optical Parametric Oscillator / Amplifier (OPO / OPA) IR Laser System

For the recording of IR-(M)PD spectra over a wide frequency range an intense tunable light source is needed. Optical Parametric Oscillator^[54] (OPO) / Optical Parametric Amplifier^[55] (OPA) laser systems provide for such radiation. Our OPO / OPA laser system (LaserVision) (**Figure 2.9**) is pumped by a pulsed injection seeded Nd:YAG (Continuum Powerlite DLS 8000) that provides for intense laser radiation at 1064 nm, a pulse length of about 7 ns, and a pulse energy in the range of 530 – 600 mJ/pulse.

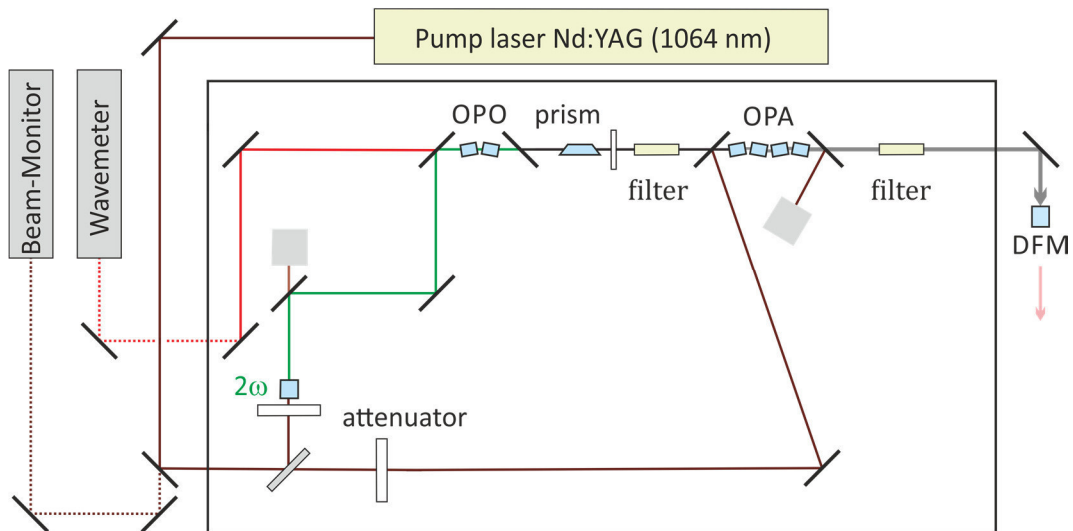


Figure 2.9 Scheme of the beam path in the OPO / OPA laser system (LaserVision).

This fundamental beam is divided by a beam splitter into two beams with one third and two thirds of the original intensity. Two thirds of the intensity are directed to the OPA stage and the one third is frequency doubled (second harmonic generation, SHG) to 532 nm by a potassium titanyl phosphate crystal (KTP). The residual fundamental beam is dumped and the 532 nm beam is guided into to the OPO resonator. This resonator consists of two KTP crystals that split the 532 nm into the signal 1 and the idler 1 waves. The signal wave has a higher frequency than the idler wave, per definition. The frequency can be tuned by varying the angle between the KTP crystals and the incident 532 nm beam. Note that the photon energy of 532 nm is identical to the sum of the photon energy of the signal and idler due to energy conservation. The signal 1 radiation is dumped by a silicon filter and the idler 1 radiation is guided into the OPA stage. The OPA stage consists of four potassium titanyl arsenate (KTA) crystals. Within this stage the remaining two thirds of the fundamental beam is combined with the idler 1 beam. This process yields signal 2 and idler 2 radiation in which the signal 2 beam corresponds to the amplified idler 1. Now either the signal 2 beam is dumped and the idler 2 is guided towards the mass spectrometer, or both beams are mixed in an additional difference frequency generation (DFM) stage. This stage consists of a silver gallium diselenide (AgGaSe_2) crystal^[56] and a zinc selenide (ZnSe) filter to dump the residual signal 2 and idler 2 radiation.

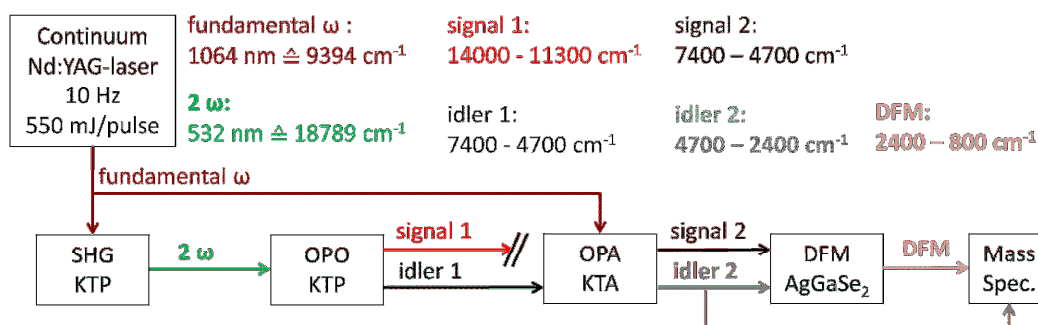


Figure 2.10 Scheme of the nonlinear optical processes and frequency conversions within the OPO / OPA laser system, yielding the respective IR photons.

The idler 2 wave provides for radiation in the region from 4700 – 2400 cm⁻¹ that is suitable to probe OH, NH or CH stretching modes. The signal 2 wave may also be used to observe low lying electronic transition. The DFM crystal generates radiation in the region from 2400 – 800 cm⁻¹ that enables the measurement of CO stretching modes, CH bending modes or the stretching mode of adsorbed N₂.

Overall this OPO / OPA laser systems provides for intense tunable IR radiation in the region from 7400 to 800 cm⁻¹, a pulse energy between 0.1 – 20 mJ/pulse and a spectral resolution of approximately 0.9 cm⁻¹. The laser system is calibrated with a wave meter (Bristol Instruments, 821B-NIR) and the beam profile of the fundamental beam is constantly monitored with a beam profiler camera (DataRay Inc., WinCamD).

2.5 Density Functional Theory (DFT)

To provide for a more detailed interpretation of experimental results a comparison with calculations is indispensable. Density Functional Theory (DFT) is a widely used approach for the calculations of molecular properties, like structures or IR frequencies.^[57-59]

The basis for DFT is that all information required for the determination of the energy of a molecule is given by its electron density $\rho(\vec{r})$. This was first described by Thomas and Fermi.^[60-61] Hohenberg and Kohn proved the correctness of this statement by their 1st theorem^[62] and showed that the variational principle could be applied by their 2nd theorem. The energy minimization by application of the variational principle was described by Kohn and Sham^[63], which defined the energy as function of the electron density as follows:

$$E(\rho) = T_0(\rho) + \int d\mathbf{r} \rho(\vec{r})(V_{eff}(\vec{r}) + \frac{1}{2}\varphi(\vec{r})) + E_{XC}(\rho) \quad 2-12$$

- $T_0(\rho)$ kinetic energy
 $V_{eff}(\vec{r})$ effective potential
 $\varphi(\vec{r})$ Coulomb potential
 $E_{XC}(\rho)$ exchange correlation energy

The corresponding Kohn-Sham wavefunction is a single Slater determinant and is constructed from a set of orbitals that are the lowest energy solution to:

$$\left(-\frac{\hbar^2}{2m}\nabla^2 + V_{eff}(\vec{r})\right)\Phi_i(r) = \varepsilon_i\Phi_i(r) \quad 2-13$$

- $\Phi_i(r)$ Kohn-Sham orbital i
 ε_i orbital energy

The electron density of the system can now be described as:

$$\rho(\vec{r}) = \sum_i^N |\Phi_i(r)|^2 \quad 2-14$$

The most crucial part in DFT is the approximation of the exchange correlation energy $E_{XC}(\rho)$. It includes all unknown factors and has a significant contribution. The exchange correlation energy is subject to the used functionals. The local density approximation (LDA)^[58] or the generalized gradient approximation (GGA) are common approaches to estimate the exchange correlation energy. The use of hybrid functionals has proven to provide for accurate results of many systems.^[64-65]

For the geometry optimization of the calculated system the potential energy surface has to be scanned for so called stationary points. Such stationary points occur if the first derivative equals zero, which happens at energetic minima (minimum structures) or energetic saddle points (transition states). To discriminate between these, the second derivative has to be inspected. If all values are positive a minimum structure is reached and if one value is negative a transition state. As this method only finds minimum structures with geometries similar to the starting geometry, several calculations with different starting

structures have to be performed. The global minimum can be found by comparing the calculated energies of the different structures. The comparison of calculated properties, like the linear absorption spectra, with experiments structural assignments can be made.

All calculations presented here were performed using the Gaussian 09 program package^[66]. The used functional and basis sets will be addressed in each chapter separately. The calculations were gratefully performed on the computing clusters of the Theoretical Chemistry department under the supervision of Prof. C. van Wüllen.

2.6 References

- (1) Gross, J. H., *Mass spectrometry: a textbook*. Springer Science & Business Media: 2006.
- (2) Duncan, M. A., Invited Review Article: Laser vaporization cluster sources, *Rev. Sci. Instrum.* **2012**, *83*, 041101.
- (3) Berg, C.; Schindler, T.; Niedner-Schatteburg, G.; Bondybey, V. E., Reactions of simple hydrocarbons with Nb+n: Chemisorption and physisorption on ionized niobium clusters, *J. Chem. Phys.* **1995**, *102*, 4870.
- (4) Bondybey, V. E.; English, J. H., LASER-INDUCED FLUORESCENCE OF METAL-CLUSTERS PRODUCED BY LASER VAPORIZATION - GAS-PHASE SPECTRUM OF PB-2, *J. Chem. Phys.* **1981**, *74*, 6978-6979.
- (5) Dietz, T. G.; Duncan, M. A.; Powers, D. E.; Smalley, R. E., Laser Production of Supersonic Metal Cluster Beams, *J. Chem. Phys.* **1981**, *74*, 6511-6512.
- (6) Maruyama, S.; Anderson, L. R.; Smalley, R. E., DIRECT INJECTION SUPERSONIC CLUSTER BEAM SOURCE FOR FT-ICR STUDIES OF CLUSTERS, *Rev. Sci. Instrum.* **1990**, *61*, 3686-3693.
- (7) Proch, D.; Trickl, T., A HIGH-INTENSITY MULTI-PURPOSE PIEZOELECTRIC PULSED MOLECULAR-BEAM SOURCE, *Rev. Sci. Instrum.* **1989**, *60*, 713-716.
- (8) Zeleny, J., Instability of Electrified Liquid Surfaces, *Phys. Rev.* **1917**, *10*, 1-6.
- (9) Dole, M.; Mack, L. L.; Hines, R. L.; Mobley, R. C.; Ferguson, L. D.; Alice, M. B., Molecular Beams of Macroions, *J. Chem. Phys.* **1968**, *49*, 2240-2249.
- (10) Fenn, J. B.; Mann, M.; Meng, C. K.; Wong, S. F.; Whitehouse, C. M., Electrospray ionization for mass spectrometry of large biomolecules, *Science* **1989**, *246*, 64-71.
- (11) Fenn, J. B., Electrospray wings for molecular elephants (Nobel lecture), *Angewandte Chemie-International Edition* **2003**, *42*, 3871-3894.
- (12) Aebersold, R.; Goodlett, D. R., Mass Spectrometry in Proteomics, *Chem. Rev.* **2001**, *101*, 269-296.
- (13) Pramanik, B. N.; Bartner, P. L.; Mirza, U. A.; Liu, Y.-H.; Ganguly, A. K., Electrospray ionization mass spectrometry for the study of non-covalent complexes: an emerging technology, *J. Mass Spectrom.* **1998**, *33*, 911-920.
- (14) Vikse, K. L.; Ahmadi, Z.; McIndoe, J. S., The application of electrospray ionization mass spectrometry to homogeneous catalysis, *Coord. Chem. Rev.* **2014**, *279*, 96-114.
- (15) Schröder, D., Applications of electrospray ionization mass spectrometry in mechanistic studies and catalysis research, *Acc. Chem. Res.* **2012**, *45*, 1521-1532.

-
- (16) Katta, V.; Chowdhury, S. K.; Chait, B. T., Electrospray ionization: a new tool for the analysis of ionic transition-metal complexes, *J. Am. Chem. Soc.* **1990**, *112*, 5348-5349.
- (17) Taylor, G., Disintegration of Water Drops in an Electric Field, *Proceedings of the Royal Society of London. Series A. Mathematical and Physical Sciences* **1964**, *280*, 383-397.
- (18) Wilm, M. S.; Mann, M., Electrospray and Taylor-Cone theory, Dole's beam of macromolecules at last?, *Int. J. Mass Spectrom. Ion Processes* **1994**, *136*, 167-180.
- (19) Rayleigh, L., XX. On the equilibrium of liquid conducting masses charged with electricity, *The London, Edinburgh, and Dublin Philosophical Magazine and Journal of Science* **1882**, *14*, 184-186.
- (20) Konermann, L.; Ahadi, E.; Rodriguez, A. D.; Vahidi, S., Unraveling the Mechanism of Electrospray Ionization, *Anal. Chem.* **2013**, *85*, 2-9.
- (21) Crotti, S.; Seraglia, R.; Traldi, P., Some thoughts on electrospray ionization mechanisms, *Eur. J. Mass Spectrom.* **2011**, *17*, 85-99.
- (22) Iribarne, J. V.; Thomson, B. A., On the evaporation of small ions from charged droplets, *J. Chem. Phys.* **1976**, *64*, 2287-2294.
- (23) Thomson, B. A.; Iribarne, J. V., Field induced ion evaporation from liquid surfaces at atmospheric pressure, *J. Chem. Phys.* **1979**, *71*, 4451-4463.
- (24) Schmelzeisen-Redeker, G.; Bütfering, L.; Röllgen, F. W., Desolvation of ions and molecules in thermospray mass spectrometry, *Int. J. Mass Spectrom. Ion Processes* **1989**, *90*, 139-150.
- (25) Iavarone, A. T.; Williams, E. R., Mechanism of charging and supercharging molecules in electrospray ionization, *J. Am. Chem. Soc.* **2003**, *125*, 2319-2327.
- (26) Ahadi, E.; Konermann, L., Modeling the behavior of coarse-grained polymer chains in charged water droplets: implications for the mechanism of electrospray ionization, *J. Phys. Chem. B* **2011**, *116*, 104-112.
- (27) Konermann, L.; Rodriguez, A. D.; Liu, J., On the formation of highly charged gaseous ions from unfolded proteins by electrospray ionization, *Anal. Chem.* **2012**, *84*, 6798-6804.
- (28) Apollo II – MTP Users Manual. Bruker Daltonics GmbH: 2006; p 11.
- (29) Lawrence, E. O.; Edlefsen, N. E., On the production of high speed protons, *Science* **1930**, *72*, 376-377.
- (30) Lawrence, E. O.; Livingston, M. S., The Production of High Speed Light Ions Without the Use of High Voltages, *Phys. Rev.* **1932**, *40*, 19-35.
- (31) Lawrence, E. O.; Cooksey, D., On the Apparatus for the Multiple Acceleration of Light Ions to High Speeds, *Phys. Rev.* **1936**, *50*, 1131-1140.
- (32) Sommer, H.; Thomas, H. A.; Hipple, J. A., The Measurement of e/M by Cyclotron Resonance, *Phys. Rev.* **1951**, *82*, 697-702.
- (33) Comisarow, M. B.; Marshall, A. G., Frequency-sweep fourier transform ion cyclotron resonance spectroscopy, *Chem. Phys. Lett.* **1974**, *26*, 489-490.
- (34) Comisarow, M. B.; Marshall, A. G., Fourier-Transform Ion-Cyclotron Resonance Spectroscopy, *Chem. Phys. Lett.* **1974**, *25*, 282-283.
- (35) Marshall, A. G.; Hendrickson, C. L.; Jackson, G. S., Fourier transform ion cyclotron resonance mass spectrometry: A primer, *Mass Spectrom. Rev.* **1998**, *17*, 1-35.
- (36) Marshall, A. G., Milestones in fourier transform ion cyclotron resonance mass spectrometry technique development, *Int. J. Mass Spectrom.* **2000**, *200*, 331-356.
-

- (37) Caravatti, P.; Allemann, M., The 'infinity cell': A new trapped-ion cell with radiofrequency covered trapping electrodes for fourier transform ion cyclotron resonance mass spectrometry, *Org. Mass Spectrom.* **1991**, *26*, 514-518.
- (38) Schweikhard, L.; Ziegler, J.; Bopp, H.; Lutzenkirchen, K., THE TRAPPING CONDITION AND A NEW INSTABILITY OF THE ION MOTION IN THE ION-CYCLOTRON RESONANCE TRAP, *Int. J. Mass Spectrom. Ion Processes* **1995**, *141*, 77-90.
- (39) Graf, M., Entwicklung eines auf Evolutionsstrategien basierenden Computerprogrammes zum optimierten Anpassen kinetischer Daten aus FT-ICRMassenspektrometrie-Messungen, *Diploma Thesis, TU Kaiserslautern* **2006**.
- (40) Su, T.; Bowers, M. T., Theory of ion-polar molecule collisions. Comparison with experimental charge transfer reactions of rare gas ions to geometric isomers of difluorobenzene and dichloroethylene, *J. Chem. Phys.* **1973**, *58*, 3027-3037.
- (41) Su, T.; Bowers, M. T., Ion-polar molecule collisions. Proton transfer reactions of H₃⁺ and CH₅⁺ to the geometric isomers of difluoroethylene, dichloroethylene, and difluorobenzene, *J. Am. Chem. Soc.* **1973**, *95*, 1370-1373.
- (42) Langevin, M. In *Une formule fondamentale de théorie cinétique*, Annales de chimie et de physique, Series, 1905; pp 245-288.
- (43) Balteanu, I.; Balaj, O. P.; Fox-Beyer, B. S.; Rodrigues, P.; Barros, M. T.; Moutinho, A. M.; Costa, M. L.; Beyer, M. K.; Bondybey, V. E., Size-and charge-state-dependent reactivity of azidoacetonitrile with anionic and cationic rhodium clusters Rh n[±], *Organometallics* **2004**, *23*, 1978-1985.
- (44) Anderson, M. L.; Ford, M. S.; Derrick, P. J.; Drewello, T.; Woodruff, D. P.; Mackenzie, S. R., Nitric Oxide Decomposition on Small Rhodium Clusters, Rh n⁺, *J. Phys. Chem. A* **2006**, *110*, 10992-11000.
- (45) Kummerlöwe, G.; Beyer, M. K., Rate estimates for collisions of ionic clusters with neutral reactant molecules, *Int. J. Mass Spectrom.* **2005**, *244*, 84-90.
- (46) Polfer, N. C., Infrared multiple photon dissociation spectroscopy of trapped ions, *Chem. Soc. Rev.* **2011**, *40*, 2211-2221.
- (47) Fung, Y.; Kjeldsen, F.; Silivra, O. A.; Chan, T.; Zubarev, R. A., Facile disulfide bond cleavage in gaseous peptide and protein cations by ultraviolet photodissociation at 157 nm, *Angew. Chem. Int. Ed.* **2005**, *44*, 6399-6403.
- (48) Roithova, J., Characterization of reaction intermediates by ion spectroscopy, *Chem. Soc. Rev.* **2012**, *41*, 547-559.
- (49) Grant, E. R.; Schulz, P. A.; Sudbo, A. S.; Shen, Y. R.; Lee, Y. T., Is Multiphoton Dissociation of Molecules a Statistical Thermal Process?, *Phys. Rev. Lett.* **1978**, *40*, 115-118.
- (50) Lupo, D. W.; Quack, M., IR-laser photochemistry, *Chem. Rev.* **1987**, *87*, 181-216.
- (51) Wolk, A. B.; Leavitt, C. M.; Garand, E.; Johnson, M. A., Cryogenic ion chemistry and spectroscopy, *Acc. Chem. Res.* **2013**, *47*, 202-210.
- (52) Walker, N.; Walters, R.; Tsai, M.-K.; Jordan, K. D.; Duncan, M., Infrared Photodissociation Spectroscopy of Mg⁺ (H₂O) Ar n Complexes: Isomers in Progressive Microsolvation, *J. Phys. Chem. A* **2005**, *109*, 7057-7067.
- (53) Kamrath, M. Z.; Garand, E.; Jordan, P. A.; Leavitt, C. M.; Wolk, A. B.; Van Stipdonk, M. J.; Miller, S. J.; Johnson, M. A., Vibrational Characterization of Simple Peptides Using Cryogenic Infrared Photodissociation of H-2-Tagged, Mass-Selected Ions, *J. Am. Chem. Soc.* **2011**, *133*, 6440-6448.

-
- (54) Eckardt, R. C.; Nabors, C.; Kozlovsky, W. J.; Byer, R. L., Optical parametric oscillator frequency tuning and control, *JOSA B* **1991**, *8*, 646-667.
- (55) Brida, D.; Manzoni, C.; Cirimi, G.; Marangoni, M.; De Silvestri, S.; Cerullo, G., Generation of broadband mid-infrared pulses from an optical parametric amplifier, *Optics express* **2007**, *15*, 15035-15040.
- (56) Gerhards, M., High energy and narrow bandwidth mid IR nanosecond laser system, *Opt. Commun.* **2004**, *241*, 493-497.
- (57) Szabo, A.; Ostlund, N. S., *Modern quantum chemistry: introduction to advanced electronic structure theory*. Courier Corporation: 2012.
- (58) Kohn, W.; Becke, A. D.; Parr, R. G., Density functional theory of electronic structure, *J. Phys. Chem.* **1996**, *100*, 12974-12980.
- (59) Parr, R. G.; Yang, W., Density-functional theory of the electronic structure of molecules, *Annu. Rev. Phys. Chem.* **1995**, *46*, 701-728.
- (60) Thomas, L. H. In *The calculation of atomic fields*, Mathematical Proceedings of the Cambridge Philosophical Society, Cambridge University Press: 1927; pp 542-548.
- (61) Fermi, E., Eine statistische Methode zur Bestimmung einiger Eigenschaften des Atoms und ihre Anwendung auf die Theorie des periodischen Systems der Elemente, *Zeitschrift für Physik* **1928**, *48*, 73-79.
- (62) Hohenberg, P.; Kohn, W., Inhomogeneous Electron Gas, *Phys. Rev.* **1964**, *136*, B864-B871.
- (63) Kohn, W.; Sham, L., Density function theory, *J. Phys. Rev* **1965**, *140*, A1133-A1138.
- (64) Becke, A. D., DENSITY-FUNCTIONAL THERMOCHEMISTRY .3. THE ROLE OF EXACT EXCHANGE, *J. Chem. Phys.* **1993**, *98*, 5648-5652.
- (65) Becke, A. D., A NEW MIXING OF HARTREE-FOCK AND LOCAL DENSITY-FUNCTIONAL THEORIES, *J. Chem. Phys.* **1993**, *98*, 1372-1377.
- (66) Frisch, M. J.; Trucks, G. W.; Schlegel, H. B.; Scuseria, G. E.; Robb, M. A.; Cheeseman, J. R.; Scalmani, G.; Barone, V.; Petersson, G. A.; Nakatsuji, H., et al., Gaussian 09, *Gaussian, Inc., Wallingford CT* **2013**, Revision D.01.

3 Infrared Spectroscopy of N₂ Adsorption on Size Selected Cobalt Cluster Cations in Isolation

Sebastian Dillinger, Jennifer Mohrbach, Joachim Hewer, Maximilian Gaffga,
and Gereon Niedner-Schatteburg

*Fachbereich Chemie und Forschungszentrum OPTIMAS
Technische Universität Kaiserslautern
67663 Kaiserslautern*

3.1 Preamble

The following chapter is a reprint of a publication in the journal “Physical Chemistry Chemical Physics”.

The experiments were performed by the experimental team consisting of J. Mohrbach, J. Hewer, M. Gaffga and myself. The data evaluation was done by J. Mohrbach and myself. G. Niedner-Schatteburg performed the computations. I wrote the initial manuscript and revised it with the help of G. Niedner-Schatteburg and J. Mohrbach.

Full Reference:

Infrared spectroscopy of N₂ adsorption on size selected cobalt cluster cations in isolation

S. Dillinger, J. Mohrbach, J. Hewer, M. Gaffga and G. Niedner-Schatteburg, *Physical Chemistry Chemical Physics*, **2015**, 17, 10358-10362.

<http://dx.doi.org/10.1039/C5CP00047E>

3.2 Reprint

Reprint License

Infrared spectroscopy of N₂ adsorption on size selected cobalt cluster cations in isolation

S. Dillinger, J. Mohrbach, J. Hower, M. Gaffga and G. Niedner-Schatteburg, *Phys. Chem. Chem. Phys.*, 2015, **17**, 10358

DOI: 10.1039/C5CP00047E

This article is licensed under a [Creative Commons Attribution 3.0 Unported Licence](#). Material from this article can be used in other publications provided that the correct acknowledgement is given with the reproduced material.

Reproduced material should be attributed as follows:

- For reproduction of material from NJC:
[Original citation] - Published by The Royal Society of Chemistry (RSC) on behalf of the Centre National de la Recherche Scientifique (CNRS) and the RSC.
- For reproduction of material from PCCP:
[Original citation] - Published by the PCCP Owner Societies.
- For reproduction of material from PPS:
[Original citation] - Published by The Royal Society of Chemistry (RSC) on behalf of the European Society for Photobiology, the European Photochemistry Association, and RSC.
- For reproduction of material from all other RSC journals:
[Original citation] - Published by The Royal Society of Chemistry.

Information about reproducing material from RSC articles with different licences is available on our [Permission Requests page](#).



PCCP

COMMUNICATION

View Article Online
View Journal | View IssueCite this: *Phys. Chem. Chem. Phys.*,
2015, 17, 10358Received 5th January 2015,
Accepted 18th March 2015

DOI: 10.1039/c5cp00047e

www.rsc.org/pccp

Infrared spectroscopy of N₂ adsorption on size selected cobalt cluster cations in isolation

Sebastian Dillinger, Jennifer Mohrbach, Joachim Hewer, Maximilian Gaffga and Gereon Niedner-Schatteburg

We report IR active N₂ stretching frequencies in isolated and size selected cobalt cluster nitrogen adsorbate complexes, [Co_n(N₂)₁]⁺ as recorded by virtue of InfraRed Photon Dissociation (IRPD) spectroscopy. The observed frequencies of the [Co_n(N₂)₁]⁺ complexes (*n* = 8–17) are significantly redshifted (2180 to 2290 cm⁻¹) with respect to the IR inactive vibrations of free N₂ (2359 cm⁻¹). These bands are assigned to a μ₁ head-on type of coordination of the N₂ to the cobalt cluster surface, revealing remarkable cluster size dependent features to interpret.

It is often difficult to investigate heterogeneously catalyzed reactions due to their complexity. Reactions of isolated transition metal clusters may serve to elucidate elementary processes in such reactions. The initial adsorption event is often the rate limiting step in multistep bond activation that precedes any further activation and the phenomenon of gas adsorption in layers became an early subject of research.^{1,2} Historically adsorption is classified into chemisorption and physisorption by phenomenological persistence of the adsorbate. Physisorbed species often serve as precursors for activation. The initial adsorption and activation of N₂ is the rate limiting step in the Haber-Bosch process. Therefore the characterization of the precursor state is of great importance for the mechanistic understanding of this catalytic conversion.³

CO adsorption on metal surfaces has been characterized by numerous kinetic^{4–7} and spectroscopic studies.^{8–10} The observed redshift of the CO stretching vibration is understood to indicate the CO coordination site – on top (μ₁), on bridge (μ₂) or on hollow (μ₃). It moreover reflects interaction strength and of course charge effects. Complementary insights arise from the IR based characterization of CO adsorbates on the surfaces of isolated metal clusters.^{11–13}

There is equally great interest in the kinetics of the N₂ adsorption on metal surfaces.^{14–16} Spectroscopic and kinetic studies of N₂ adsorbed on Fe(111) revealed that there are three

characteristic α-, δ- and γ-states, which refer to side-on, and head-on adsorption to highly and to less coordinated metal surface atoms.^{17–19} Many reaction studies have been performed for a better understanding of the N₂ adsorption kinetics with metal clusters.^{20–25} Two of these studies^{24,25} have drawn far reaching structural conclusions from so called uptake plots of average association numbers of multiple N₂ molecules under flow reactor conditions. They discuss icosahedral, hexagonal (hcp) and face centered cubic (fcc) packing speculating about pressure dependent inter conversion. Despite obvious need merely a single spectroscopic study elucidated the N₂ adsorption on isolated metal clusters, namely those of Ruthenium,²⁶ with no unambiguous assignment of the recorded spectral features.

Common interpretation of the head-on adsorption of CO and N₂ to surfaces of extended bulk metal samples and of size selected clusters arises in terms of a σ-donor π-acceptor synergistic bonding scheme according to the so called Blyholder model.²⁷ *Ab initio* DFT modelling reaches its limits when it comes to the appropriate choice of exchange correlation functionals.⁷

The present study probes the N–N stretching frequency of N₂ when adsorbed on size selected cobalt cluster cations at cryogenic temperatures. We aim to gain insight into the binding motifs of the adsorbates and towards the structure of the cobalt clusters themselves. Preliminary *ab initio* DFT calculations augment the current experiments, failing to provide unambiguous structural conclusions as of now.

A customized Fourier Transform-Ion Cyclotron Resonance (FT-ICR)-mass spectrometer (Apex Ultra Bruker Daltonics) served to perform the cluster production, isolation, N₂ condensation, InfraRed Photon Dissociation (IRPD) and mass analysis. The metal clusters were generated using a home-built laser vaporization cluster ion source as described before.^{28,29} In brief, cobalt atoms are evaporated from a rotating 1 mm thick cobalt foil by the second harmonic of a pulsed Nd:YAG laser. The hot plasma is captured by a He gas pulse (40 μs, 10–15 bar) created by a home-built piezoelectric valve.³⁰ The atoms and ions are cooled and aggregate to clusters in the subsequent jet expansion through a 60 mm long channel (2 mm diameter) into vacuum (10⁻⁶ mbar).

Fachbereich Chemie und Forschungszentrum OPTIMAS,
Technische Universität Kaiserslautern, 67663 Kaiserslautern, Germany

The clusters are skimmed and injected into a cryogenic hexapole ion trap passing different ion lenses, a 90 degrees ion beam bender and a quadrupole mass filter. The ion trap is cooled to 26 K by a closed cycle He cryostat. Buffer or reaction gas can be introduced both pulsed and continuously. In this work we used the continuous gas inlet. He or Ar ($\text{He: } [\text{Co}_{8-10}(\text{N}_2)_1]^+$, Ar: $[\text{Co}_{11-17}(\text{N}_2)_1]^+$) is used to increase the pressure in the ion trap from 1.7×10^{-7} mbar up to 1.0×10^{-6} mbar to accomplish the efficient trapping and cooling of the ions. The attachment of nitrogen is achieved due to impurities in the buffer gas and can only be observed at temperatures below 28 K. After storage of the ions for a variable time (0–10 s), the manipulated ions are guided by electrostatic lenses into the FT-ICR cell of the so-called “infinity” type.³¹ This cell is held at a temperature of 10 K with a closed cycle He cryostat to prevent heating of the clusters by black body radiation. The cell is also used for isolation and detection of the ions.

For the acquisition of the (IRPD) spectra the FT-ICR cell is coupled to a tunable IR laser ($\delta n = 0.9 \text{ cm}^{-1}$, $\delta t = 7 \text{ ns}$). This laser is a KTP/KTA optical parametric oscillator/amplifier (OPO/A, LaserVision) system pumped by a pulsed 10 Hz injection seeded Nd:YAG laser (PL8000, Continuum). The difference frequency (DF) between the OPA signal and idler waves is generated in a AgGaSe₂ crystal. This generates IR radiation in the range of 1400–2400 cm^{-1} . Each trapped and isolated package of ions is irradiated by 10–15 laser pulses (0.1–1.2 mJ per pulse) to yield a sufficient amount of fragment ions. The IR spectra were recorded as ion chromatograms while continuously scanning the IR wavelength. The IRPD signal was evaluated as $\sum_i F_i / (\sum_i F_i + \sum_i P_i)$, where F_i and P_i indicate fragment and the parent ion signals, respectively. An experimental IRPD spectrum arises from a plot of the fragmentation efficiency as a function of laser frequency. We employed the IRPD spectroscopy in the 2100–2350 cm^{-1} range on the $[\text{Co}_n(\text{N}_2)_1]^+$ species ($n = 8-17$). In this range we expected the N₂ stretching frequencies of the species. For all complexes the loss of the N₂ was the only observed fragmentation channel.

The cold IRPD spectra of the cryo cooled $[\text{Co}_n(\text{N}_2)_1]^+$ cluster adsorbate complexes reveal well resolved bands (cf. Fig. 1). All complexes show a single or multiple IR active bands within the range of 2180 to 2290 cm^{-1} (2110–2350 cm^{-1} probed). These bands are significantly redshifted with respect to the IR inactive stretching mode of free N₂ (at 2359 cm^{-1} ³²). Some clusters show multiple bands ($n = 14-17$), other clusters reveal single bands ($n = 8-13$). Dissociative $[\text{N-Co}_n\text{-N}]^+$ adsorption would inevitably lead to much lower Co–N stretching frequencies which may become as low as 600 cm^{-1} when interstitial nitrides form. Therefore we confirm molecular (intact) adsorption (physisorption) of N₂ on naked cobalt cluster surfaces. While we cannot exclude some (at present invisible) dissociation of N₂ we do not find forcing evidence. Such an activation would, if any, occur in competition to intact adsorption.

The observed cluster size dependence reveals continuous variations and “jumps”/discontinuities alike. The dotted red line serves to guide the eye. It is slightly tilted towards the red with cluster size. A plain charge dilution effect would lead to an opposite effect namely to a blue shifting by increasing cluster size.

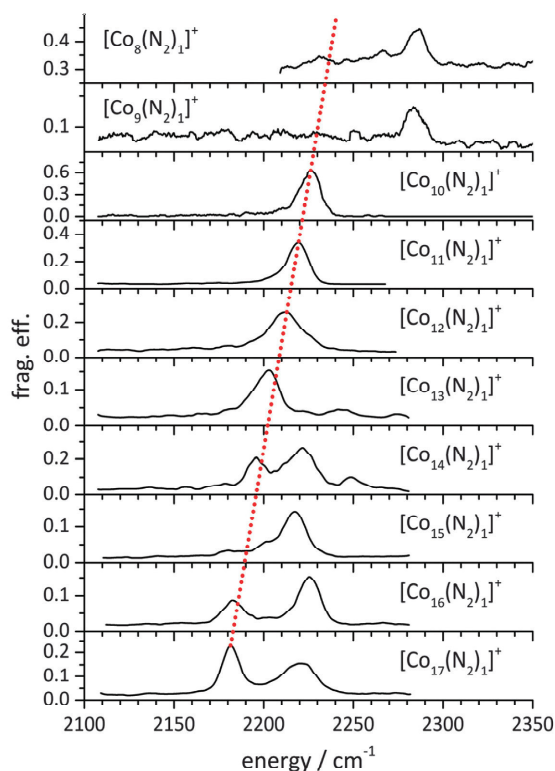


Fig. 1 IRPD spectra of $[\text{Co}_n(\text{N}_2)_1]^+$ for $n = 8-17$. The dotted red line serves to guide the eye. Its slight tilt with cluster size indicates a conceivable cooperative polarization effect. Note the variation in the observed peak positions and splittings. Multiple major peaks likely indicate cluster core isomers, spin isomers or N₂ bonding isomers while weak sidebands to the blue may arise from combination bands (N₂ stretching and wagging modes, cf. Table 1). Note the “jump” of the major peak from $n = 9$ to $n = 10$.

Instead one might recall the (likely) metallic nature of the cobalt cluster allowing for electron density shifts in response to external perturbation. Such polarization may couple back to the perturbing adsorbate and enhance electron donation into empty antibonding orbitals – the more the larger the cluster. Hence this would lead to a weakening of the N–N binding strength and an increasing redshift of the stretching frequency with cluster size.

Looking at the bands in detail it is obvious that $[\text{Co}_8(\text{N}_2)_1]^+$ and $[\text{Co}_9(\text{N}_2)_1]^+$ do not follow the trend illustrated by the red line. The absorption of $[\text{Co}_8(\text{N}_2)_1]^+$ and $[\text{Co}_9(\text{N}_2)_1]^+$ (both at 2285 cm^{-1}) are significantly less redshifted than those of all other cluster complexes studied. The clusters with $n = 10-13$ show merely one strong band that aligns well to the mentioned polarization effect (2226, 2219, 2212, 2203 cm^{-1}). In the case of $[\text{Co}_{13}(\text{N}_2)_1]^+$ this main absorption band is accompanied by weak sidebands to the blue. These may arise from combination bands (N₂ stretching and wagging modes, cf. Table 1, as supported by calculations). Besides these sidebands of $[\text{Co}_{13}(\text{N}_2)_1]^+$, the main band is in line with a possible icosahedral structure (I_h). A major difference arises

Table 1 Computed vibrations in [Co₁₃(N₂)₁]⁺ (*I_h*, 2*S* + 1 = 15). Explicitly listed values document all those modes that involve significant motion of either of the two N-atoms

Mode	Type	Freq./ cm ⁻¹	Scaled freq./ cm ⁻¹	IR intensity/ km mol ⁻¹
ν_1	N ₂ wagging	33.8	32.1	0.04
ν_2	N ₂ wagging	46.7	44.4	0.08
ν_3	N \uparrow -N-Co \downarrow bending	78	74	0.17
$\nu_{3\cdots\nu_{37}}$	Co ₁₃ ⁺ skeleton modes	78...306		<2.7
ν_{38}	N \uparrow -N \downarrow -Co \uparrow bending	354	336	37
ν_{39}	N-N stretching	2338	2221	605

for even larger clusters, which reveal multiple bands. These are possibly due to cobalt cluster isomers, to spin state isomers or to N₂ bonding isomers or to combinations of all three effects. [Co₁₄(N₂)₁]⁺ is most prominent in revealing three major bands (at 2195, 2222, 2248 cm⁻¹). A possible explanation is the presence of spin isomers. The Co₁₄⁺ cluster core structure is conceivable, yet speculative. Our preliminary calculations reveal a possible adatom to a icosahedral core (little overall relaxation), alternatively: significant reorganization (from Co₁₃⁺ to Co₁₄⁺) through incorporation of the extra Co atom into prior Co₁₃⁺ cluster surface, *e.g.* by opening the prior five membered rings to a six membered ring. This would provide for a higher (sixfold) coordinated Co surface atom in the center of the six membered ring. This working hypothesis might serve to explain the new band at 2222 cm⁻¹ in [Co₁₄(N₂)₁]⁺.

A similar picture can be found in [Co₁₅(N₂)₁]⁺, except for the vanishing “red” peak (which was strong for [Co₁₀₋₁₄(N₂)₁]⁺), indicative of a major change in structural binding motif. Possibly explained by a change from icosahedral to hexagonal close-packed (hcp) as found in larger cobalt clusters by Trapped Ion Electron Diffraction (TIED) experiments (Co bulk: hcp; Co cluster: icosahedral).³³

DFT calculations of [Co₁₃(N₂)₁]⁺ (at PBE0/ECP(Co); cc-pVTZ(N) level of theory) reveal full icosahedral *I_h* geometry of the Co₁₃⁺ core with little relaxation by the N₂ attachment. SCF convergence is tedious and can be achieved only by tolerating relaxed SCF convergence criteria of 10⁻⁵ (as compared to 10⁻⁸ in “standard” DFT calculations). Choice of an appropriate spin multiplicity is crucial. Our previous XMCD investigations yielded a spin magnetic moment of 2.30(15) μ_B per atom for the Co₁₄⁺ cluster.³⁴ That implies 32(2) unpaired electrons and a multiplicity of 2*S* + 1 = 33(2). Our present DFT calculations have revealed stable high spin state structures of a [Co₁₄(N₂)₁]⁺ complex with multiplicities 30(+47), 32(0) and 34(+29), relative stabilities in kJ mol⁻¹ indicated in parentheses. Both findings are in good agreement – assuming that N₂ adsorption does not alter spin states in Co₁₄⁺.

On the basis of this agreement we utilized our DFT approach to undertake an extended search of minimum structures of [Co₈(N₂)₁]⁺, [Co₉(N₂)₁]⁺, [Co₁₀(N₂)₁]⁺ (*cf.* Fig. 3), [Co₁₃(N₂)₁]⁺, [Co₁₄(N₂)₁]⁺ and [Co₁₇(N₂)₁]⁺. The calculations reveal head-on N₂ binding in μ_1 N-Co coordination, irrespective of chosen cobalt cluster geometry – allowing for full relaxation without constraints – and irrespective of chosen N₂ coordination site,

and irrespective of particular spin multiplicity. Other assumed coordinations (μ_2 or μ_3) relax towards μ_1 coordination. This finding is the more important as μ_2 or μ_3 coordinated N₂ would be weak or inactive in the IR. Any activation towards dinitride species was found vastly endothermic. The computed zero Kelvin adsorption enthalpies of N₂ to Co₁₃⁺ were found to range around 80 kJ mol⁻¹ in case of all likely spin states (2*S* + 1 = 25, 27, 29 and 31), the Co-N distances round 1.890(2) Å. It thus takes two to three IR photons to induce the observed IRPD processes.

Standard *ab initio* calculations reveal force constants and subsequent normal mode analysis reveal harmonic vibrational frequencies. After appropriate lump sum scaling for anharmonicities (empirical factor 0.95) the thus obtained values compare to experimental data. We chose to document the case of [Co₁₃(N₂)₁]⁺ in more detail (*cf.* Table 1) assuming an icosahedral *I_h* geometry of Co₁₃⁺ (*cf.* Fig. 2). The IR inactive N-N stretching mode of free N₂ at 2359 cm⁻¹ redshifts through coordination with Co₁₃⁺ to 2203 cm⁻¹ (expt.) and 2221 cm⁻¹ (calc. ν_{39}) in [Co₁₃(N₂)₁]⁺. The concomitant N-N-Co bending mode within [Co₁₃(N₂)₁]⁺ is predicted to occur at 336 cm⁻¹ which is outside of our experimental probing range. However, the experimental spectrum reveals weak sidebands to the N₂ stretching mode which locate at $\nu_s(\text{N}_2) + 15$ cm⁻¹, 35 cm⁻¹ and (maybe) 68 cm⁻¹. We assign these sidebands to combination modes ($\nu_{39} + \nu_1$), ($\nu_{39} + \nu_2$) and ($\nu_{39} + \nu_3$), which is in qualitative agreement with the DFT computed ν_1 , ν_2 and ν_3 values of +32 cm⁻¹, +44 cm⁻¹ and +78 cm⁻¹.

Despite all current effort the accordingly computed vibrational spectra of other clusters (as listed above) do not recover the subtle changes in the recorded experimental spectra. Obtained N₂ stretching frequencies do indeed fall into the range of experimental values. There is, however, no further insight from calculations into the origin of the three experimental observations: general and steady increase of N₂ redshift, sudden increase of N₂ redshift when going from [Co_{8,9}(N₂)₁]⁺ to [Co₁₀(N₂)₁]⁺, and multiple strong vibrational peaks in the spectra of cluster [Co₁₄(N₂)₁]⁺ and beyond.

It remains to be seen whether further calculations achieve more insight. Four improvements come to our minds. Broken symmetry

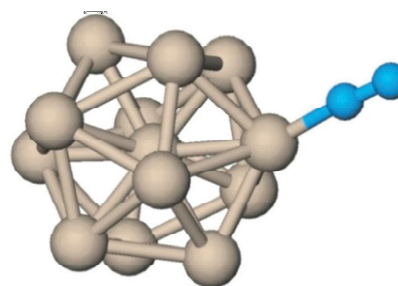


Fig. 2 Computed geometry of [Co₁₃(N₂)₁]⁺. The assumed icosahedral Co₁₃⁺ core is a low lying stable geometry, and it only physisorbs N₂ in μ_1 head-on coordination. Note, that all cobalt surface atoms are equivalent, thus giving rise to a single IR active N-N stretching vibration at about 2230 cm⁻¹ (scaled by 0.95) with variations by spin multiplicity of the cobalt cluster core (likely 2*S* + 1 = 25, 27, 29, 31) (see text for discussion).

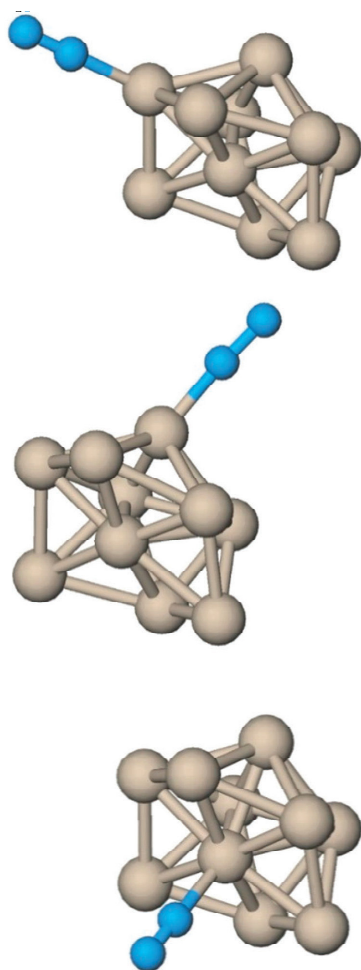


Fig. 3 Three computed geometries of $[\text{Co}_{10}(\text{N}_2)_1]^+$. The calculated species show the different binding sites of N_2 to the Co_{10}^+ core. N_2 only coordinates μ_1 head-on. The structures differ in the binding motif of the coordination site (Co atom). The structures illustrate an adsorption of N_2 on a Co atom which in turn coordinates to four- (top), five- (middle) or six- (bottom) membered cobalt atom rings. It comes somewhat as a surprise that the present DFT calculations find little variation of N_2 stretching frequencies in response to this change of coordination (e.g. shifts by less than 10 cm^{-1}).

DFT would allow to check for conceivable antiferromagnetic coupling.^{35–38} Variation of the DFT functional is mandatory and tedious. Dispersion interaction needs to be considered. Dynamic basin hopping/annealing calculations might retrieve otherwise overlooked geometries.

Conclusions

The N_2 adsorption on cationic Co_n^+ clusters in the size range of $n = 8$ – 17 has been investigated *via* IRPD spectroscopy. The recorded spectra revealed remarkable cluster size dependent features.

All species show bands within the range of 2180 to 2290 cm^{-1} , suggesting a head-on μ_1 coordination of the N_2 on the cluster surface. Current DFT calculations reveal a possible icosahedral Co_{13}^+ core. Nevertheless the calculations do not allow for a final assignment of the observed spectral features (e.g. the “jump” from $n = 9$ to $n = 10$ or the presence of multiple bands). It is mandatory to spend further effort in *ab initio* calculations to gain invaluable insight into the binding motifs of the nitrogen and of conceivable activation routes.

Acknowledgements

This work was supported by the DFG founded transregional collaborative research center SFB/TRR 88 “3MET.de” and by the state research center OPTIMAS.

Notes and references

- 1 I. Langmuir, *J. Am. Chem. Soc.*, 1918, **40**, 1361–1403.
- 2 S. Brunauer, P. H. Emmett and E. Teller, *J. Am. Chem. Soc.*, 1938, **60**, 309–319.
- 3 G. Ertl, *Catal. Rev.*, 1980, **21**, 201–223.
- 4 D. M. Cox, K. C. Reichmann, D. J. Trevor and A. Kaldor, *J. Chem. Phys.*, 1988, **88**, 111–119.
- 5 G. A. Somorjai, *Introduction to Surface Chemistry and Catalysis*, John Wiley & Sons, 1994.
- 6 G. Ertl, M. Neumann and K. M. Streit, *Surf. Sci.*, 1977, **64**, 393–410.
- 7 A. Nilsson and L. G. M. Pettersson, in *Chemical Bonding at Surfaces and Interfaces*, ed. A. N. G. M. P. K. Nørskov, Elsevier, Amsterdam, 2008, pp. 57–142.
- 8 A. Crossley and D. A. King, *Surf. Sci.*, 1977, **68**, 528–538.
- 9 R. M. Hammaker, S. A. Francis and R. P. Eischens, *Spectrochim. Acta*, 1965, **21**, 1295–1309.
- 10 F. M. Hoffmann, *Surf. Sci. Rep.*, 1983, **3**, 107–192.
- 11 A. Fielicke, P. Gruene, G. Meijer and D. M. Rayner, *Surf. Sci.*, 2009, **603**, 1427–1433.
- 12 A. Fielicke, G. von Helden, G. Meijer, D. B. Pedersen, B. Simard and D. M. Rayner, *J. Chem. Phys.*, 2006, **124**, 194305.
- 13 J. T. Lyon, P. Gruene, A. Fielicke, G. Meijer and D. M. Rayner, *J. Chem. Phys.*, 2009, **131**, 184706.
- 14 D. A. King and M. G. Wells, *Proc. R. Soc. London, Ser. A*, 1974, **339**, 245–269.
- 15 D. A. King and M. G. Wells, *Surf. Sci.*, 1972, **29**, 454–482.
- 16 G. Ertl, S. B. Lee and M. Weiss, *Surf. Sci.*, 1982, **114**, 515–526.
- 17 C. N. R. Rao and G. R. Rao, *Surf. Sci. Rep.*, 1991, **13**, 221–263.
- 18 M. C. Tsai, U. Ship, I. C. Bassignana, J. Küppers and G. Ertl, *Surf. Sci.*, 1985, **155**, 387–399.
- 19 J. J. Mortensen, L. B. Hansen, B. Hammer and J. K. Nørskov, *J. Catal.*, 1999, **182**, 479–488.
- 20 M. B. Knickelbein, *Annu. Rev. Phys. Chem.*, 1999, **50**, 79–115.
- 21 M. D. Morse, M. E. Geusic, J. R. Heath and R. E. Smalley, *J. Chem. Phys.*, 1985, **83**, 2293–2304.
- 22 A. Berces, P. A. Hackett, L. Lian, S. A. Mitchell and D. M. Rayner, *J. Chem. Phys.*, 1998, **108**, 5476–5490.

- 23 L. Fuyi, L. Ming, T. Lin and P. B. Armentrout, *J. Chem. Phys.*, 2008, **128**, 194313.
- 24 J. Ho, E. K. Parks, L. Zhu and S. J. Riley, *Chem. Phys.*, 1995, **201**, 245–261.
- 25 S. J. Riley, *J. Non-Cryst. Solids*, 1996, **205–207**(Part 2), 781–787.
- 26 C. Kerpál, D. J. Harding, J. T. Lyon, G. Meijer and A. Fielicke, *J. Phys. Chem. C*, 2013, **117**, 12153–12158.
- 27 G. Blyholder, *J. Phys. Chem.*, 1964, **68**, 2772–2777.
- 28 S. Maruyama, L. R. Anderson and R. E. Smalley, *Rev. Sci. Instrum.*, 1990, **61**, 3686–3693.
- 29 C. Berg, T. Schindler, G. Niednerschatteburg and V. E. Bondybey, *J. Chem. Phys.*, 1995, **102**, 4870–4884.
- 30 D. Proch and T. Trickl, *Rev. Sci. Instrum.*, 1989, **60**, 713–716.
- 31 P. Caravatti and M. Allemann, *Org. Mass Spectrom.*, 1991, **26**, 514–518.
- 32 W. M. Haynes, *CRC Handbook of Chemistry and Physics*, Taylor & Francis, 93rd edn, 2012.
- 33 T. Rapps, R. Ahlrichs, E. Waladt, M. M. Kappes and D. Schooss, *Angew. Chem., Int. Ed.*, 2013, **52**, 6102–6105.
- 34 S. Peredkov, M. Neeb, W. Eberhardt, J. Meyer, M. Tombers, H. Kampschulte and G. Niedner-Schatteburg, *Phys. Rev. Lett.*, 2011, **107**, 233401.
- 35 E. M. V. Kessler, S. Schmitt and C. van Wullen, *J. Chem. Phys.*, 2013, **139**, 184110.
- 36 C. van Wullen, *J. Phys. Chem. A*, 2009, **113**, 11535–11540.
- 37 F. Neese, *J. Phys. Chem. Solids*, 2004, **65**, 781–785.
- 38 F. Neese, *Coord. Chem. Rev.*, 2009, **253**, 526–563.

4 Cryo Kinetics and Spectroscopy of Cationic Nickel Clusters: Rough and Smooth Surfaces

Jennifer Mohrbach, Sebastian Dillinger, and Gereon Niedner-Schatteburg

Fachbereich Chemie und Forschungszentrum OPTIMAS

Technische Universität Kaiserslautern

67663 Kaiserslautern

4.1 Preamble

The following chapter is a reprint of a publication in the journal “The Journal of Physical Chemistry C”.

The experiments were performed by the experimental team consisting of J. Mohrbach, and myself. The data evaluation was done by J. Mohrbach and myself. The computations were performed by myself. The initial manuscript was written by J. Mohrbach and revised with the help of G. Niedner-Schatteburg and myself.

Full Reference:

Cryo Kinetics and Spectroscopy of Cationic Nickel Clusters: Rough and Smooth Surfaces

J. Mohrbach, **S. Dillinger**, and G. Niedner-Schatteburg, *The Journal of Physical Chemistry C*, **2017**, 121, 20, 10907-10918.

<http://dx.doi.org/10.1021/acs.jpcc.6b12167>

4.2 Reprint

Reprint License



RightsLink®

Home

Create Account

Help



Title: Cryo Kinetics and Spectroscopy of Cationic Nickel Clusters: Rough and Smooth Surfaces

Author: Jennifer Mohrbach, Sebastian Dillinger, Gereon Niedner-Schatteburg

Publication: The Journal of Physical Chemistry C

Publisher: American Chemical Society

Date: May 1, 2017

Copyright © 2017, American Chemical Society

LOGIN

If you're a [copyright.com user](#), you can login to RightsLink using your [copyright.com credentials](#). Already a [RightsLink user](#) or want to [learn more?](#)

PERMISSION/LICENSE IS GRANTED FOR YOUR ORDER AT NO CHARGE

This type of permission/license, instead of the standard Terms & Conditions, is sent to you because no fee is being charged for your order. Please note the following:

- Permission is granted for your request in both print and electronic formats, and translations.
- If figures and/or tables were requested, they may be adapted or used in part.
- Please print this page for your records and send a copy of it to your publisher/graduate school.
- Appropriate credit for the requested material should be given as follows: "Reprinted (adapted) with permission from (COMPLETE REFERENCE CITATION). Copyright (YEAR) American Chemical Society." Insert appropriate information in place of the capitalized words.
- One-time permission is granted only for the use specified in your request. No additional uses are granted (such as derivative works or other editions). For any other uses, please submit a new request.

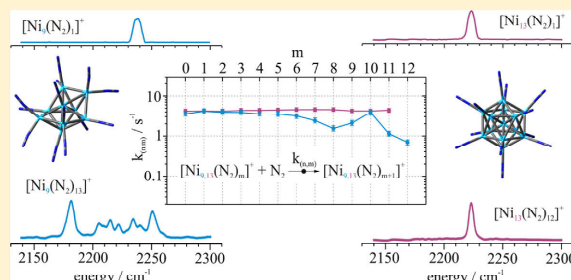
Cryo Kinetics and Spectroscopy of Cationic Nickel Clusters: Rough and Smooth Surfaces

Jennifer Mohrbach, Sebastian Dillinger, and Gereon Niedner-Schatteburg*

Fachbereich Chemie and Forschungszentrum OPTIMAS, Technische Universität Kaiserslautern, 67663 Kaiserslautern, Germany

Supporting Information

ABSTRACT: The stepwise N₂ adsorption on size selected Ni₉⁺ and Ni₁₃⁺ clusters at 26 K is studied in a hybrid tandem ion trap instrument. Adsorption kinetics of these clusters in conjunction with infrared photon dissociation (IR-PD) spectroscopy of their cluster adsorbate complexes allows for the elucidation of various N₂ coverage and cluster size dependent effects, which are related to the rough Ni₉⁺ and smooth Ni₁₃⁺ cluster surface morphologies. Pseudo-first-order kinetic fits confirm consecutive adsorption steps by single exponential decays exclusively. The recorded IR-PD spectra of all observed cluster adsorbate complexes reveal IR active vibrational bands at frequencies of 2170–2260 cm⁻¹, which coincides with the range of metal head-on coordinated N–N stretching modes. Density functional theory (DFT) calculations confirm the experiments and reinforce a possible isomerization with low N₂ coverage in the case of Ni₉⁺.



1. INTRODUCTION

Reactivity studies of naked metal clusters are an ongoing endeavor, providing new perspectives on the repetitively stated cluster-surface analogy.^{1–6} In the “non-scalable cluster size regime”,^{7–9} atom-by-atom dependent variation superimposes to the gradual, scalable change of cluster properties by size.^{7,10} Nonscalable jumps in molecular adsorption to size selected clusters have been interpreted in terms of structural changes at local binding sites on the cluster surfaces.^{11–15} In the context of CO adsorption to metal clusters and of related carbonyl complexes, it showed that adsorbates may well serve to titrate available surface sites up to saturation for the elucidation of underlying structural motifs.^{16,17} Beyond mere adsorption, it warrants to study and understand the activation of this and other diatomic molecules, e.g., NO, N₂, and H₂, driven by perspectives and challenges in heterogeneous catalysis.^{18–20}

It has proven helpful to study the vibrational modes of adsorbates on transition metal (TM) clusters and in TM coordination complexes as isolated ions by infrared multiple photon dissociation (IR-MPD).^{21–24} This method has further gained by the introduction of tunable free electron lasers (FEL).^{25–27} Cryo IR-action spectroscopy achieves significant advances by so-called tagging or messenger techniques where weakly bound species serve to provide for a preferred fragmentation channel, sometimes driven by single photon absorption.^{28,29} The study of in situ generated TM clusters helped to elucidate the influence of net charge and oxidation state onto the single molecule CO adsorption in terms of a charge dilution model.^{30–32}

1.1. N₂ Coordination. Isoelectronic to CO, the N₂ molecule—nonpolar when isolated—polarizes upon surface

adsorption through a σ donor π acceptor synergism in analogy to that of CO—some differences in size and shape of participating MOs notwithstanding. The resulting red shifts of CO vibrations are usually discussed in terms of the Dewar–Chatt–Duncanson model, which explains coordinative complexation to single TM centers,^{33,34} or in terms of the Blyholder model, when interpreting surface coordination.³⁵ The concept of both models applies to N₂ adsorption as well. The discovery of dinitrogen-pent-amine Ru(II) complexes in 1965³⁶ has initiated a fertile field of N₂ coordination chemistry^{37–40} in quest for its activation.

Early DFT revealed a strong preference of N₂ for end-on coordination to single Fe centers with some evidence for rather exceptional side-on η^2 coordination of at most two N₂ to otherwise naked Fe atoms.^{41,42} Other than in a Zr–N₂–Zr arrangement^{39,43} and to the best of our knowledge, there is no spectroscopic evidence for such side-on coordination to a transition metal center in a molecular coordination complex. In this respect, it pays to recognize a most recent study of N₂ adsorption to Ta clusters, which interprets their experimental findings in terms of a DFT computed N₂ side-on (η^2) coordination.⁴⁴ Recent IR-MPD studies of N₂ adsorption to Ru clusters have concluded in exclusive end-on (η^1) coordination.⁴⁵

Special Issue: ISSPIC XVIII: International Symposium on Small Particles and Inorganic Clusters 2016

Received: December 2, 2016

Revised: December 15, 2016

Published: December 16, 2016

1.2. Prior Studies of Nickel Clusters. Experiments on magnetism of neutral and cationic Ni clusters were recently reviewed in the context of XMCD gas phase studies.⁴⁶ In parallel to the experiments, an increasing interest arose to model the electronic and magnetic properties of these nickel clusters,^{47–49} and of nickel alloys.^{48,50–52} The particularly narrow PES spectrum of Ni₁₃ was interpreted in terms of a highly symmetric structure, likely of icosahedral *T_d* symmetry.^{53,54} CO adsorption up to saturation to small nickel clusters Ni_{*n*} (*n* = 2–20) revealed the limits of electron counting rules and the stability of larger clusters with internal metal atoms, while small clusters (*n* ≤ 13) undergo adsorption induced structural changes in favor of enhanced adsorption to achieve coverages close to the electron counting rule predictions for the bare cluster geometries.⁵⁵ D₂ was found to adsorb readily to Ni_{*n*}⁺ (*n* = 2–16), while the formation of Ni_{*n*}D⁺ exhibits thresholds.⁵⁶ A simulation of Ni_{*n*} (*n* = 2–150) by a dedicated *Aufbau/Abbau* method predicted structures, symmetries, and stabilities of most stable isomers and found a particularly high stability of Ni₁₃.⁵⁷ Studies of activated CH₄ reactions with Ni_{*n*}⁺ (*n* = 2–16) found a rich chemistry that is consistent with simple bond order considerations.⁵⁸ IR-MPD studies of H₂ adsorbed onto Ni_{4–6}⁺ revealed propensities for activation and hydride formation.^{59,60} IR-MPD spectroscopy helped to characterize vibrational patterns of hydrated and complexed Ni⁺.^{61,62} First adsorption studies of N₂ on nickel were carried out in the 1950s on evaporated nickel films⁶³ and on nickel powders.⁶⁴ N₂ uptake studies with nickel clusters Ni_{*n*} (*n* = 3–28) were interpreted in terms of head-on N₂ coordination.^{65,66}

1.3. Kinetic Models. The classical Langevin collision rate of ions with neutrals⁶⁷ is conveniently extended toward polar molecules by the average dipole orientation (ADO) theory.^{68,69} This ADO theory is frequently used to calculate the reaction rates of charged clusters with small molecules, knowingly underestimating the reaction rates for charged metal clusters significantly.^{70–72} Another model to estimate the collision rates of ionic clusters with neutral molecules is the surface charge capture model (SCC), which leads to significantly increased collision rate constants, in comparison with Langevin or ADO rates.⁷³

1.4. Prior Nickel - N₂ Spectroscopy. IR spectra of nitrogen adsorbed on silica-supported Ni films⁷⁴ revealed a strong infrared absorption band at 2202 cm⁻¹, attributed to the N–N stretching vibration of head-on bound N₂. A combined IR spectroscopy and electron-microscopic study of N₂ adsorbed on silica supported nickel samples (at –80 to –20 °C) revealed that this IR active N₂ only occurs on nickel particles with diameters between 15 and 70 Å.⁷⁵ Matrix infrared spectra of, e.g., Ni(N₂)_{*n*} (*n* = 1–4) in argon⁷⁶ reinforce interpretation in terms of an end-on coordination. Several strong dinitrogen frequencies in the range 2100–2230 cm⁻¹ were identified in these matrix infrared spectra. More recently, there was a report on N₂ stretching frequencies at 2223/2234 cm⁻¹ by an end-on coordinated N₂ in cationic Ni(II) complexes,⁷⁷ well in line with those observed for N₂ adducts of molecular Ni(II) halides.⁷⁸ The N₂ interaction with an open coordination site on a Ni(I) macrocycle revealed head-on coordination with a dinitrogen frequency at 2170 cm⁻¹.⁷⁹

1.5. Our Approach. We have been preparing ionic TM clusters within ion traps, e.g., for kinetic studies of hydrocarbon activation,⁶ and we have introduced X-ray studies by cryo ion trapping for the investigation of spin and orbital contributions to the magnetic moments of TM clusters.^{46,80} In parallel, we

have utilized table top IR lasers for the identification of dark IR-MPD bands in oligonuclear TM complexes,⁸¹ torsional isomerizations,⁸² and multistate-mediated rearrangements.⁸³ Recently, we have upgraded our instrumentation toward tandem cryo ion trapping,⁸⁴ and we have started a long-term quest for the vibrational spectroscopy of N₂ adsorbates on size selected TM clusters under isothermal cryo conditions, first results on [Co_{*n*}(N₂)₁]⁺ clusters and on Fe based “non-classical” dinitrogen complexes being published.^{85,86} This study aims to elucidate N₂ adsorption onto cationic nickel clusters, [Ni_{*n*}(N₂)_{*m*}]⁺, by a combination of kinetic investigations, IR-PD spectroscopy, and DFT based modeling of structures and vibrations. We aim to gain insight into the metal–adsorbate bonding and to unravel structure–reactivity relationships. Within this work, we have chosen to discuss the archetypical cases of Ni₉⁺ and Ni₁₃⁺ in more detail and up to the prevailing adsorption limits of saturation.

2. EXPERIMENTAL AND COMPUTATIONAL METHODS

A customized Fourier transform ion cyclotron resonance (FT-ICR) mass spectrometer (Apex Ultra Bruker Daltonics) served to perform the cluster production, isolation, N₂ condensation, infrared photon dissociation (IR-PD), and mass analysis. The nickel clusters were generated using a home-built laser vaporization cluster ion source as described before.^{70,87} In brief, nickel atoms are evaporated from a rotating 0.4 mm thick isotopically enriched ⁵⁸Ni foil (99.61%, Oak Ridge National Laboratories) by the second harmonic of a pulsed Nd:YAG laser (Innolas *Spotlight 300*, 20 Hz). The hot plasma is captured by a He gas pulse (40 μs, 15 bar) created by a home-built piezoelectric valve.⁸⁸ The atoms and ions are cooled and aggregate to clusters in the subsequent jet expansion through a 50 mm long channel (Ø 2 mm) into a vacuum (10⁻⁷ mbar). The clusters are skimmed and injected into a cryogenic hexapole ion trap passing a 90° ion beam bender and a quadrupole mass filter. The ion trap is cooled to 26 K by a closed cycle He cryostat. Buffer and reaction gas are introduced continuously. Sufficient nitrogen attachment is achieved by increasing the pressure in the ion trap from 1.1 × 10⁻⁷ mbar up to 3.0 × 10⁻⁷ mbar. Additional He is introduced to increase the pressure up to 3.0 × 10⁻⁶ mbar to accomplish an efficient trapping and cooling of the ions. After storing the mass-selected ions for a variable time (0–5 s), the manipulated ions of the form [Ni_{*n*}(N₂)_{*m*}]⁺ = (*n*,*m*) are guided by electrostatic lenses into the FT-ICR cell of the so-called “infinity” type.⁸⁹ The ICR cell is held at temperatures below 10 K with a closed cycle He cryostat to prevent heating of the clusters by blackbody radiation prior to ion detection.

For kinetic investigations, the ICR cell serves for the detection of the formed [Ni_{*n*}(N₂)_{*m*}]⁺ = (*n*,*m*) cluster adsorbate complexes. The kinetic curves of cationic nickel clusters and their nitrogen adducts originate from reaction delay scans and subsequent evaluation of the recorded mass spectra. Fits to pseudo-first-order kinetics occur through the “evoFit” program.⁹⁰ Our thus determined rate constants for the (*9*,*m*) species (recorded at *p*(N₂) = 3.0 × 10⁻⁷ mbar) are normalized to the experimental conditions for the (*13*,*m*) species (recorded at *p*(N₂) = 1.3 × 10⁻⁷ mbar). The relative rate constants *k*_(*n*,*m*) determine the absolute rate constants *k*_(*n*,*m*)^{abs}, the absolute collision gas number densities ρ_{N₂}(*T*) serving as the conversion factor:

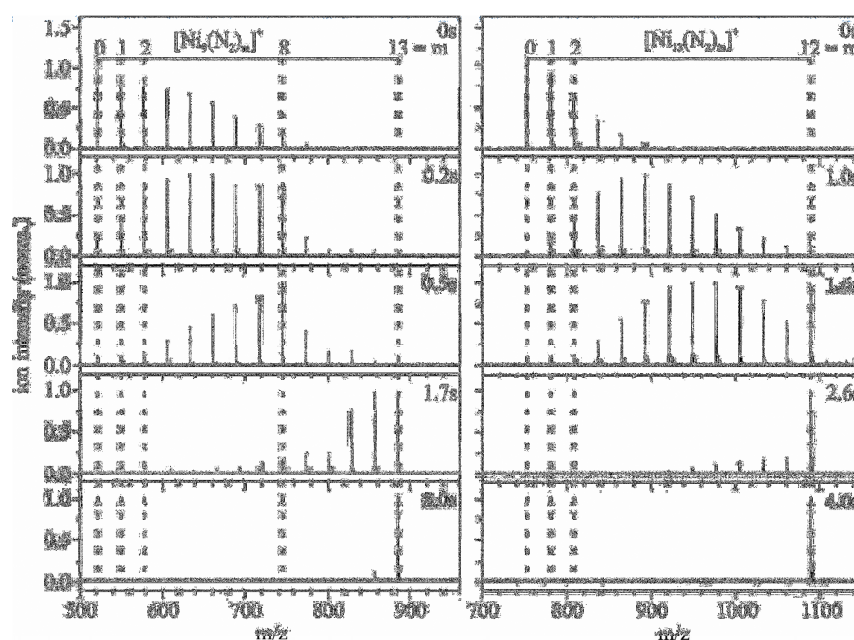


Figure 1. Temporal evolution of the mass spectra of mass-selected Ni_9^+ ($(9,0)$) clusters exposed to 3.0×10^{-7} mbar of N_2 in 3.0×10^{-6} mbar of He at 26 K for up to 5 s (left) and of mass-selected Ni_{13}^+ ($(13,0)$) clusters exposed to 1.3×10^{-7} mbar of N_2 in 3.0×10^{-6} mbar of He at 26 K for up to 4 s (right).

$$k_{(n,m)}^{\text{abs}} = k_{(n,m)}/\rho_{\text{N}_2}(T)$$

We obtain approximate values for $\rho_{\text{N}_2}(T)$ indirectly from the pressure in the surrounding chamber $p_c^{(300\text{K})}$ and an effective geometry factor c_{app} :

$$\rho_{\text{N}_2}(26\text{K}) = \frac{c_{\text{app}} p_c^{300\text{K}}}{k_{\text{B}} T_{300\text{K}}}$$

The geometry factor c_{app} bears a significant dependence on the temperature of the hexapole ion trap. By numerous kinetic studies of transition metal cluster cations with neutral reactants at cryogenic temperatures, we evaluated this factor c_{app} to 1.8 ± 0.4 at 26 K with a net uncertainty of $\pm 50\%$. The quotient of the absolute rate constants and the collision rate enables us to calculate the absolute reaction efficiency γ for the adsorption of N_2 by cationic Ni clusters. This absolute reaction efficiency indicates the probability of a reaction occurring after a collision between a metal cluster ion and its reaction partner.

To record IR-PD spectra, the ICR cell is used for the isolation of each observed (n,m) species, subsequent storage for ion irradiation, and the detection of the resulting ions. It is coupled to a tunable IR laser ($\delta n = 0.9\text{ cm}^{-1}$, $\delta t = 7\text{ ns}$). The laser is comprised of a KTP/KTA optical parametric oscillator/amplifier (OPO/A, LaserVision) system pumped by a pulsed 10 Hz injection seeded Nd:YAG laser (PL8000, Continuum). In this work, we used the difference frequency (DF) between the OPA signal and idler waves generated in a AgGaSe₂ crystal. This generates IR radiation in the range 1000–2400 cm^{-1} . Each trapped and isolated package of ions is irradiated by 5–10 laser pulses (0.1–1.2 mJ per pulse) to yield a sufficient amount of fragment ions. The IR spectra were recorded as mass chromatograms while continuously scanning the IR wavelength. The IR-PD signal was evaluated as $\Sigma F_i / (\Sigma_i F_i + \Sigma P_i)$, where F_i

and P_i indicate the fragment and the parent ion signals, respectively. An experimental IR PD spectrum arises from a plot of the fragmentation efficiency as a function of laser frequency. We employed the IR-PD spectroscopy in the 2140–2300 cm^{-1} range on the isolated (n,m) species. In this range, we expected the N_2 stretching frequencies of these species. For all complexes, the loss of N_2 was the only observed fragmentation channel.

Linear IR absorption spectra were calculated at the PBE0⁹¹ level of theory using the cc-pVTZ basis sets⁹² (N) and the Stuttgart RSC 1997⁹³ effective core potential (Ni), respectively, as implemented in the Gaussian 09 program package.⁹⁴ All calculated spectra were scaled to account for prevalent anharmonicities (empirical factor 0.93). Full geometry optimization yielded multiple local minimum structures for spin multiplicities $2S + 1 = 6–18$ (e.g., Table S4 in the Supporting Information). The lowest energy structure is assumed to represent the most stable isomer. All local minimum structures were confirmed by the absence of imaginary frequencies. SCF convergence is tedious and can be achieved only at the expense of relaxed SCF convergence criteria of 10^{-5} (as compared to 10^{-8} in DFT calculations on light main group elements). Zero point energy effects are small if any (see Table S1).

3. RESULTS AND DISCUSSION

3.1. Molecular Nitrogen Adsorption on Nickel Cluster Cations: Trends and Limits of Adsorption. We stored the generated $[\text{Ni}_n(\text{N}_2)_m]^+$ ((n,m)) cluster adsorbate complexes in the cryogenic hexapole under isothermal conditions at 26 K. In all investigated cases ($n = 5, \dots, 20$), stepwise N_2 uptake reaches a strict adsorption limit m_{max} . Here (Figure 1) and in the following, we elucidate the two cases of $(n,m) = (9,m)$ and $(13,m)$.

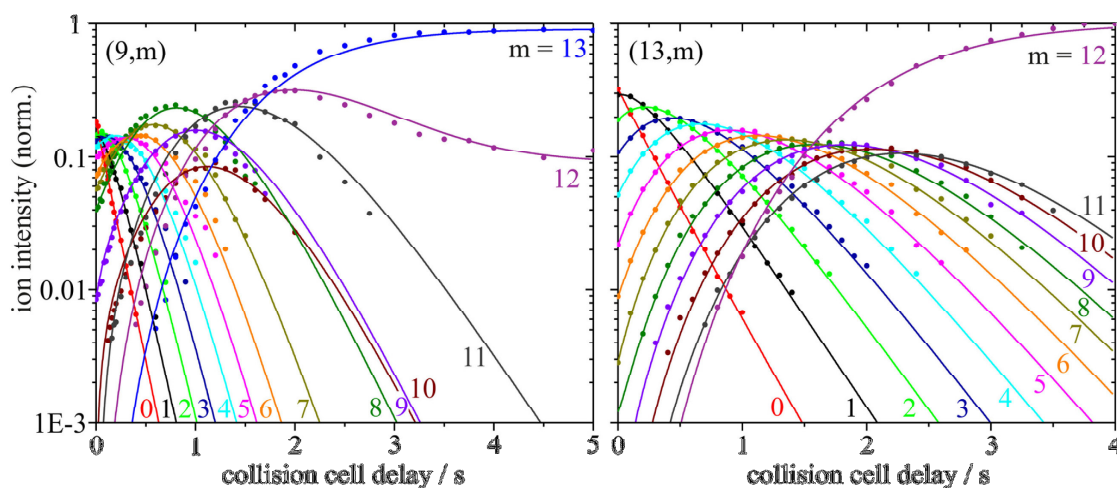


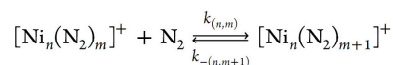
Figure 2. Isothermal kinetics of the stepwise N_2 adsorption by isolated Ni_9^+ clusters (left) and Ni_{13}^+ clusters (right) at 26 K. The fits (shown as lines) assume pseudo-first-order kinetics in a reaction chain of up to 13 consecutive steps for Ni_9^+ clusters and up to 12 for Ni_{13}^+ clusters.

Starting from the bare nickel clusters, the temporal evolution of the detected species reveals a successive gain of $28 m/z$, which does indicate the adsorption of molecular nitrogen. This temporal evolution indicates subtle details: In the case of $(9,m)$, we observe the N_2 adsorption limit at $(9,13)$ preceded by an additional intermittent adsorption limit at $(9,8)$, which does not suppress further adsorption but causes some retardation. In the case of $(13,m)$, we observe a sole N_2 adsorption limit at $(13,12)$ without any intermittent adsorption limit or retardation. Note that neither an increase of N_2 pressure nor of storage times up to 30 s would drive the N_2 adsorption beyond these limits at $(9,13)$ and $(13,12)$.

3.2. Isothermal Kinetics under Cryogenic Conditions.

We further investigated the stepwise N_2 adsorption on Ni_9^+ and Ni_{13}^+ clusters at 26 K by recording their reaction kinetics in more detail, and we performed pseudo-first-order kinetic fits by our genetic algorithm routine, which confirms consecutive adsorption steps (Figure 2). Both Ni_9^+ and Ni_{13}^+ clusters decay mono exponentially without any indication of a second component. This, and the overall superior quality of all fits, entitles us to fit each consecutive step by a single rate constant throughout. The fit of the very last adsorption step of $(9,12) \rightarrow (9,13)$ requires a significant backward reaction in parallel, which indicates swift N_2 desorption $(9,13) \rightarrow (9,12)$. It is noteworthy at this point to emphasize the obvious and manifest differences in the reaction kinetics of Ni_9^+ and Ni_{13}^+ : N_2 adsorption to Ni_9^+ takes place step by step at individual rates. Each step is different. N_2 adsorption to Ni_{13}^+ takes place step by step at equal rates. Each step is the same.

Fitting the experimental kinetics implies the quantitative determination of relative rate constants for N_2 adsorption $k_{(9,m)}$ and $k_{(13,m)}$ for each step $m \rightarrow m+1$ and for N_2 desorption $k_{-(9,m+1)}$ and $k_{-(13,m+1)}$ for each step $m+1 \rightarrow m$ alike:



The consecutive relative rate constants of the $(9,m)$ species (cf. Figure 3, Table 1) $k_{(9,m)}$ are constant up to $k_{(9,4)}$ within the uncertainties of the fits. Relative rate constants start to decline at $k_{(9,5)}$ and reach a minimum at $k_{(9,8)} = 1.5 \text{ s}^{-1}$. The rate

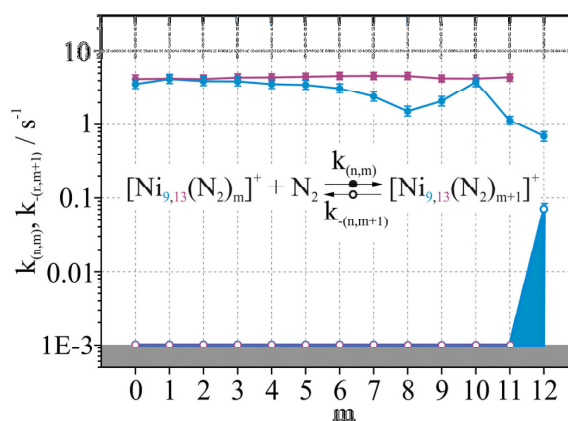


Figure 3. Observed rate constants of the $(9,m)$ species (blue) and the $(13,m)$ species (red) as a function of N_2 coverage. Filled circles show the rate of adsorption, and open circles indicate single N_2 desorption.

Table 1. Pseudo-First-Order Rate Constants for the N_2 Adsorption on Ni_9^+ Clusters $k_{(9,m)}$ for Each Step $m \rightarrow m+1$, Related Absolute Rate Constants $k_{(9,m)}^{abs}$ and Calculated Absolute Reaction Efficiencies $\gamma_{L(9,m)}$ and $\gamma_{SCC(9,m)}$

m	$k_{(9,m)}$ (s^{-1})	$k_{(9,m)}^{abs}$ ($10^{-10} \text{ cm}^3 \text{ s}^{-1}$)	$\gamma_{L(9,m)}$	$\gamma_{SCC(9,m)}$
0	3.6(3)	6.37	1.05	0.50
1	4.2(3)	7.43	1.23	0.58
2	3.9(3)	6.90	1.14	0.53
3	3.9(3)	6.90	1.15	0.53
4	3.6(3)	6.37	1.06	0.49
5	3.5(3)	6.19	1.03	0.47
6	3.1(3)	5.48	0.91	0.41
7	2.4(2)	4.25	0.71	0.32
8	1.5(2)	2.65	0.44	0.20
9	2.1(2)	3.72	0.62	0.27
10	3.8(4)	6.72	1.12	0.49
11	1.1(1)	1.94	0.33	0.14
12	0.7(1)	1.24	0.21	0.09

constants of the two subsequent adsorption steps $k_{(9,9)}$ and $k_{(9,10)}$ increase with further adsorption declining to a total minimum of $k_{(9,12)} = 0.7 \text{ s}^{-1}$ (Table 2). Please note the sole

Table 2. Pseudo-First-Order Rate Constants for the N_2 Adsorption on Ni_{13}^+ Clusters $k_{(13,m)}$ for Each Step $m \rightarrow m + 1$, Related Absolute Rate Constants $k_{(13,m)}^{\text{abs}}$ and Calculated Absolute Reaction Efficiencies $\gamma_{\text{L}(13,m)}$ and $\gamma_{\text{SCC}(13,m)}$

m	$k_{(13,m)}$ (s^{-1})	$k_{(13,m)}^{\text{abs}}$ ($10^{-10} \text{ cm}^3 \text{ s}^{-1}$)	$\gamma_{\text{L}(13,m)}$	$\gamma_{\text{SCC}(13,m)}$
0	4.2(2)	7.38	1.23	0.54
1	4.2(2)	7.38	1.23	0.54
2	4.2(2)	7.38	1.23	0.53
3	4.4(2)	7.74	1.29	0.56
4	4.4(2)	7.74	1.29	0.55
5	4.5(2)	7.91	1.32	0.56
6	4.6(3)	8.09	1.35	0.57
7	4.6(3)	8.09	1.35	0.57
8	4.6(3)	8.09	1.36	0.56
9	4.3(2)	7.56	1.27	0.52
10	4.2(2)	7.38	1.24	0.51
11	4.4(2)	7.74	1.30	0.53

significant backward reaction of N_2 desorption from (9,13) of $k_{-(9,13)} = 0.07$. In all other cases, any desorption/back reaction is insignificant up to our experimental detection limits. The determined relative rate constants of the (13, m) species are

constant without variation within uncertainties of the fits up to the adsorption limit ($k_{(13,m)} \sim 4.4 \text{ s}^{-1}$; cf. Figure 3, Table 2).

Collision rate constants are calculated as Langevin rates and on the basis of the SCC model. The ratios of the determined absolute rate constants $k_{(n,m)}^{\text{abs}}$ and either of the two collision rates k_{L} or k_{SCC} provide for absolute reaction efficiencies $\gamma_{\text{L}(n,m)}$ or $\gamma_{\text{SCC}(n,m)}$, respectively (see Tables S2 and S3 for all values). Note that the current case of N_2 adsorption makes reaction efficiencies equivalent to sticking probabilities as defined in conjunction with surface science.

We obtain absolute rate constants in the range of $10^{-10} \text{ cm}^3 \text{ s}^{-1}$ for all adsorption steps. In the case of (9, m), the absolute rate constants for the N_2 adsorption attain their minimum of $1.24 \times 10^{-10} \text{ cm}^3 \text{ s}^{-1}$ when reaching the adsorption limit. The absolute reaction efficiency for this last adsorption step is as low as 21% ($\gamma_{\text{L}(9,12)}$) or 9% ($\gamma_{\text{SCC}(9,12)}$), respectively (cf. Table 1). In contrast, the absolute rate constant for the observed N_2 desorption from (9,13) is an order of magnitude smaller (cf. Table S2).

The absolute rate constants for the N_2 adsorption on Ni_{13}^+ clusters $k_{(13,m)}^{\text{abs}}$ stay constant up to the N_2 adsorption limit. They exceed the predicted Langevin rates ($\sim 6.0 \times 10^{-10} \text{ cm}^3 \text{ s}^{-1}$) by 30%, and they are 40% below the collision rates ($\sim 13.5 \times 10^{-10} \text{ cm}^3 \text{ s}^{-1}$) by the SCC model (cf. Table 2).

There is a significant change in the reaction rates for $m \geq 9$ in (9, m), and there is an undisputable absence of $m \geq 13$ species in (13, m). These two eminent findings may indicate various N_2 coverage and cluster size dependent effects: a

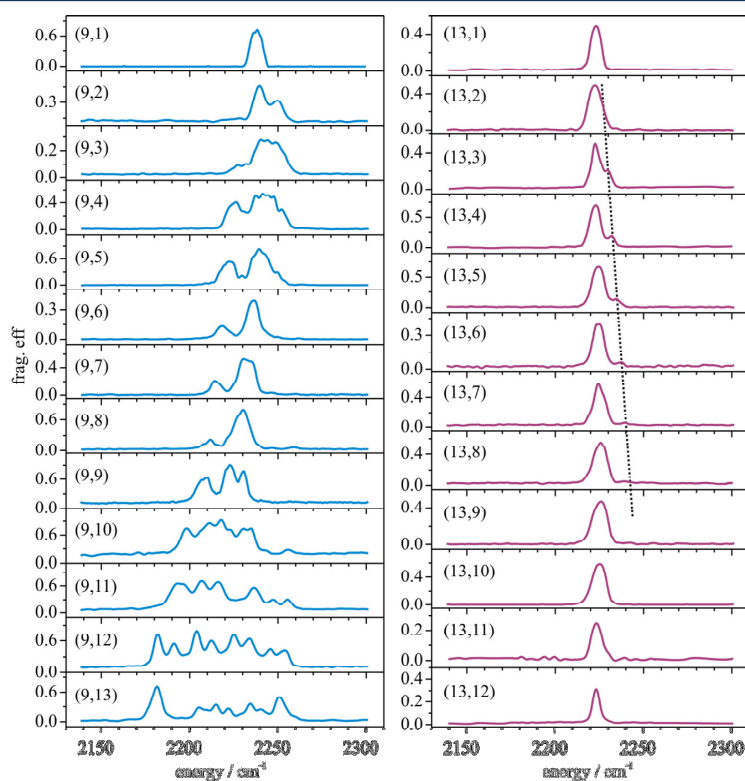


Figure 4. IR-PD spectra of the (9, m) species (blue curves/left) and (13, m) species (red curves/right) at 26 K. Note the variation in the observed band positions and splittings with further adsorption for the (9, m) species in contrast to the single dominant band for all (13, m) species. The black dotted line highlights the minor peak, that progressively shifts to the blue and decreases with further N_2 adsorption. See text for details.

change in the adsorption type (e.g., end-on, side-on, head-on/atop (μ_1), bridging (μ_2), face bound (μ_3), etc.), a change in the N_2 adsorption number per site (vicinal vs geminal binding motifs), a change of the cluster geometry (reorganization/isomerization), N_2 adsorption shell closing, first monolayer formation, saturation of all coordination sites, differences in the morphology of the respective cluster surfaces.

A change in the N_2 adsorption type with coverage is rather unlikely on Ni compounds. Investigations of N_2 adsorbed on Ni(100) and Ni(110) surfaces have suggest end-on coordination.^{95,96} N_2 adsorption studies on neutral Ni clusters^{65,66} reinforce head-on coordination.

A change in the N_2 adsorption number per site on neutral Ni clusters has been suggested from so-called uptake plots of average association numbers of multiple N_2 molecules under flow reactor conditions.^{65,66} It is found that atoms that are 4 or less coordinated can bind two nitrogen molecules. In some cases, nitrogen adsorption causes a change in the cluster structure, usually to one that can accommodate more N_2 molecules.

It is an ongoing issue whether the prevalence of conceiving cluster isomers would have consequences on kinetic studies and how they would emerge. Two cases may prevail. If isomers undergo reactive processes at comparable rates, it would show as kinetics of a single species. It would not make a difference. If isomers react with different rates, it would show in the form of bi- or multiexponential kinetics. In the present cases of N_2 adsorption on nickel clusters, we have found no evidence for multiexponential kinetics. All fits are by single exponentials, and we conclude that there is no evidence for distinctly different isomers. If prevailing, they do need to take very similar structures and react with equal rates.

The closing of a first adsorption shell would imply occupation of all available adsorption sites, which is first monolayer formation in surface science language. Once achieved, a change in kinetic efficiency of subsequent adsorption steps would be inevitable.

Any discussion in terms of cluster surfaces requires prior knowledge—or at least sincere estimates—of cluster geometries. Icosahedral shapes and according trigonal binding motifs seem likely, given the ground breaking electron diffraction experiments of Schooß, Kappes et al.,⁹⁷ which unambiguously unraveled a double closed shell icosahedral shape of Ni_{55}^- ions when trapped in an ion trap. From this and other work, it is known that icosahedral motifs minimize surface energy in disfavor of bulk cohesion. It seems justified to assume such icosahedral motifs prevailing in smaller clusters as well—as confirmed by our DFT calculations (cf. section 3.4). A perfect icosahedron of Ni_{13}^+ provides for a single bulk atom and for 12 surface atoms of equal coordination to 6 nearest neighbors. It shows a *smooth* surface.

The Ni_9^+ cluster arranges its atoms in remarkable contrast, likely in the form of a tricapped octahedron or in the form of a bicapped pentagonal bipyramid—which upon further cluster growth would easily isomerize into pure icosahedral shape. These cluster geometries provide various coordinated Ni atoms ranging from 3-fold coordination up to 8-fold coordination to nearest neighbors. Both types show a *rough* surface.

The origin of the found variation in relative rate constants in Ni_9^+ and its absence in Ni_{13}^+ seem to relate to the cluster surface morphologies. However, we address this issue by recording IR-PD spectra of the (n,m) species of interest.

3.3. Experimental IR-PD Spectra of the (n,m) Species ($n = 9, 13; m = 1, \dots, 13$). We have recorded IR-PD spectra of a large range of $[Ni_n(N_2)_m]^+$ cluster adsorbate complexes. Here we want to present and discuss the two cases $(n,m) = (9,m)$ and $(13,m)$ up to $m = m_{\max}$. The IR-PD spectra reveal several vibrational bands at frequencies from 2170 to 2260 cm^{-1} (Figure 4). The range of these bands coincides with the range of metal head-on coordinated N–N stretching modes in $[Co_n(N_2)_m]^+$ cluster adsorbate complexes of our previous study.⁸⁵ All bands are significantly red-shifted with respect to the IR inactive stretching mode of free N_2 at 2330 cm^{-1} .

The recorded IR-PD spectra of $(9,m)$ show remarkable shifts of peak positions and onset of splittings by increase of the N_2 coverage (cf. Figure 4, left). This is indicative of a *rough* surface—as suggested by our kinetic results. In more detail: The IR-PD spectrum of the singly adsorbed species $(9,1)$ shows a single band at 2238 cm^{-1} . The $(9,2)$ species shows a second blue-shifted band at 2250 cm^{-1} . Going to higher N_2 coverages for the $(9,m)$ clusters ($m > 2$), an additional red-shifted weaker band occurs in the IR-PD spectra. The spectra in the range from $m = 3$ to $m = 8$ stand out by successive shifting of the stretching frequencies from 2220–2260 to 2200–2240 cm^{-1} , resulting in a major band at 2230 cm^{-1} and a minor band at 2210 cm^{-1} for the $(9,8)$ species. The spectrum of the $(9,9)$ species shows three resolved bands induced by a 10 cm^{-1} splitting of the major band. Further adsorption up to $m = 13$ leads to complicated vibrational patterns comprising multiple bands within a range of 70 cm^{-1} . The spectrum of the $(9,13)$ species shows two strong bands at 2181 and 2252 cm^{-1} and several less intense bands in between. Note the overall asymmetrical broadening of the vibrational pattern to the red with N_2 coverage.

We also recorded the IR-PD spectrum of the $(9,13)$ species in an extended frequency range of 1010–2340 cm^{-1} (cf. Figure S1 of the Supporting Information)—with no further recordable features arising. Thus, there is no evidence for the presence of adsorption types other than the head-on bound N_2 , as evident in the presented spectra.

Each $(13,m)$ IR-PD spectrum (Figure 4, right) shows a single dominant band around 2222 cm^{-1} which does not shift upon increasing N_2 adsorption up to saturation. This encourages the proposition of a *smooth* Ni_{13}^+ cluster surface, where all 12 surface atoms are equivalent. Note the minor peak at 2230 cm^{-1} for $(13,3)$ that progressively shifts to the blue and decreases with further N_2 adsorption (black dotted line in Figure 4). We tentatively attribute this feature to combination bands with N_2 wagging modes. Interestingly, this would imply a gradual stiffening of the wagging coordinate with increasing N_2 coverage of the adsorbing, curved cluster surface. This allows us to deduce a self-organized proximity of as little as three to four N_2 adsorbates on the Ni_{13}^+ cluster surface and, in consequence, an attraction among these adsorbates—albeit a weak one. Note that a coupling between the adsorbed N_2 molecules could cause symmetric and antisymmetric N_2 stretching modes. These modes would occur in the IR-PD spectra with about equal intensities.

3.4. Comparison of the Experimental IR-PD Spectra with Simulations. Geometry optimizations yielded multiple local minimum structures for the naked Ni_9^+ cluster, likely in an octet or dactet spin state. A bicapped pentagonal bipyramidal cluster core is favored. The three most stable structures (0–21 kJ/mol) found are of this motif and differ in positions of the capping two atoms. There is another stable structure (+30 kJ/mol) that consists of a tricapped octahedral geometry. Both

structural motifs, the pentagonal and octahedral ones, prefer neighboring capping atoms in order to reach high coordination of their Ni atoms (computed geometries and their relative stabilities are shown in Figure S2 of the **Supporting Information**). We treated the Ni_{13}^+ cluster core in an assumed icosahedral structure only. Geometry optimization for multiple spin multiplicities resulted in a clearly preferred $2S + 1 = 16$ spin state (relative stabilities for $2S + 1 = 10-18$ are listed in Table S4 of the **Supporting Information**).

In the case of Ni_9^+ , the observed N_2 adsorption limit at (9,13) is consistent with a tricapped octahedral as well as a bicapped pentagonal bipyramidal structure (both with neighboring capping atoms). In the case of Ni_{13}^+ , the observed N_2 adsorption limit at (13,12) is consistent with the icosahedral structure (cf. Figure 5).

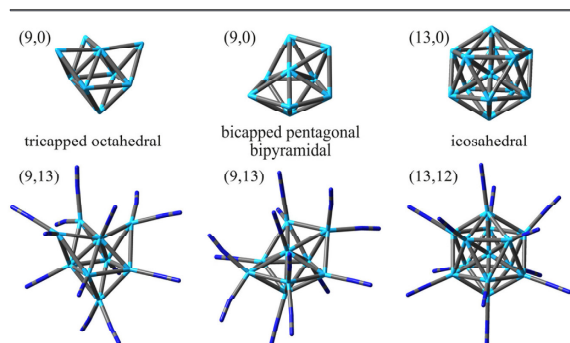


Figure 5. Computed geometries of different possible (n,m) ($m = 0, m_{\text{max}}$) species. The displayed tricapped octahedral and bicapped pentagonal bipyramidal Ni_9^+ clusters and the icosahedral Ni_{13}^+ cluster are low lying stable geometries. Sole head-on coordination results in (9,13) from geminal N_2 binding to the 3- and 4-coordinate atoms and single N_2 binding to the 5-, 6-, 7-, and 8-coordinate atoms. (13,12) results from single N_2 binding to all 12 surface atoms.

The tricapped octahedron of Ni_9^+ provides for three atoms of 3-fold coordination to nearest neighbors, one atom of 4-fold coordination, two atoms of 5-fold coordination, two atoms of 6-fold coordination, and one atom with 7-fold coordination. The bicapped pentagonal bipyramid provides for four atoms of 4-fold coordination, two atoms of 5-fold coordination, two atoms of 6-fold coordination, and one atom with 8-fold coordination. These geometries corroborate the observed adsorption limit (9,13) as well as the intermittent adsorption limit (9,8). The (9,8) case would result from all but the 7- or 8-fold coordinated Ni atoms binding one N_2 molecule, and (9,13) from geminal binding of N_2 to the 3- and 4-fold coordinated Ni atoms and single N_2 binding to the 7- or 8-fold coordinated Ni atoms.

The icosahedral Ni_{13}^+ provides for a single bulk atom and for 12 Ni surface atoms of equal coordination to 6 nearest Ni neighbors. This geometry corroborates the observed adsorption limit (13,12), which results from binding of a single N_2 to each of the 12 Ni surface atoms—a motif that may be called a monolayer or a first solvation shell at will.

We have conducted further DFT simulations to obtain linear IR absorption spectra for numerous relevant complex structures, and with variation of the spin multiplicity of the Ni cluster cores. The obtained IR spectra for the (n,m) species are sensitive to the binding position of the adsorbed N_2 , to its adsorption angle, and to geminal N_2 adsorption (two N_2 adsorbates to one Ni atom). We have considered a variation

of spin multiplicities in the range of $2S + 1 = 6-18$. Note that the spin contamination is insignificantly small (e.g., in the case of dectets: $S^2 - 24.75 < 10^{-2}$). In the case of the Ni_9^+ cluster, we find the highest stability in octet and dectet spin states, and this persists upon N_2 adsorption up to the adsorption limit (9,13). In the case of the Ni_{13}^+ cluster, we find a clear preference of high spin states in the naked cluster ($2S + 1 = 16$), that diminishes gradually upon stepwise N_2 adsorption up to the adsorption limit (13,12) which is preferentially a dectet. In the following, we restrict ourselves to the elucidation of the cases $(n,m) = (9,2), (9,5), (9,8), (9,9),$ and (13,12).

The best fit of the experimental IR-PD spectrum of $[\text{Ni}_9(\text{N}_2)_2]^+$ is obtained by a DFT simulation of the tricapped octahedron (9,2) species, where the two N_2 adsorbates locate at two (out of three) capping atoms (cf. Figure 6). The calculated

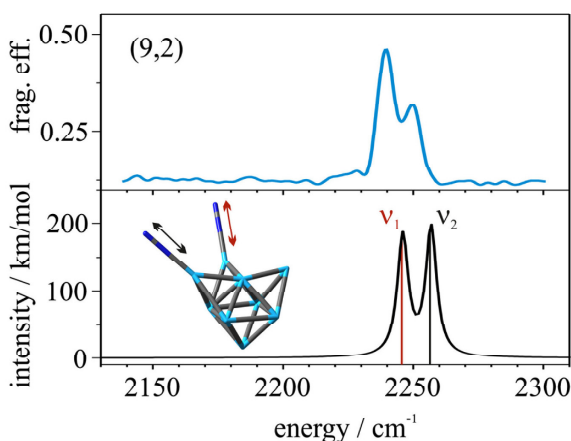


Figure 6. IR-PD spectrum of (9,2) (blue) and the calculated IR absorption spectrum for the tricapped octahedral motif where the N_2 molecules are adsorbed by different Ni capping atoms (black; PBE0/ECP(Ni), cc-pVTZ(N), $2S + 1 = 10$). The calculated spectrum is scaled by 0.93 and simulated using the Gaussian profile of fwhm = 5 cm^{-1} .

two N–N stretching frequencies split by 10 cm^{-1} , the N_2 adsorbates locating on the inner and one of the two outer Ni capping atoms, which make for two similar but inequivalent adsorption sites. The N_2 adsorbate at the outer capping Ni atom reveals a Ni–N bond distance (1.92 Å) which is 0.02 Å greater than that at the inner capping Ni atom (1.90 Å). The former case corresponds to a weaker π back-bonding, resulting in a blue shift of the N_2 stretching frequency.⁹⁸ Note that the second band cannot be explained by the assumption of a bicapped pentagonal bipyramidal cluster core, where a double N_2 adsorption to the lowest coordinated Ni atoms would lead to degenerate vibrational bands with a vanishing splitting—other than observed.

When further increasing the N_2 coverage ($m = 3$), the simulated spectra are in line with the experimental spectra when sticking with the assumption of a tricapped octahedral structure. Note that it is not feasible to achieve a definite assignment of the experimental spectrum, which is not fully resolved. It is conceivable that there are multiple N_2 adsorption isomers. For even higher adsorption numbers ($m \geq 4$), we find the best agreement of calculated and measured IR spectra when assuming a bicapped pentagonal bipyramidal motif. However,

there may be a bicapped pentagonal bipyramid and a tricapped octahedron in coexistence.

In particular, when reckoning the $m = 5$ case, the adsorption angles of the N_2 molecules appear to influence the absorption spectra significantly (Figure 7). This comes in parallel to the

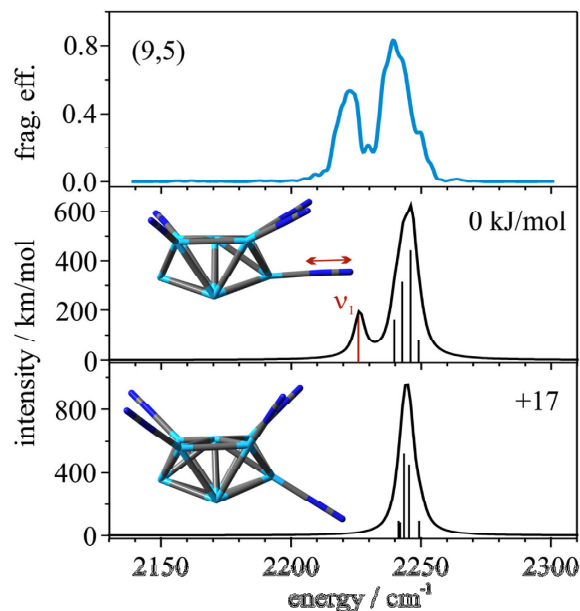


Figure 7. IR-PD spectrum of (9,5) (blue) and calculated IR absorption spectra for the bicapped pentagonal bipyramidal motif with different N_2 adsorption angles (black; PBE0/ECP(Ni), cc-pVTZ(N), $2S + 1 = 10$) scaled by 0.93 and simulated using the Gaussian profile of $fwhm = 5 \text{ cm}^{-1}$. Note that the viewpoint of the Ni_9^+ cluster is rotated with respect to that of Figure 5.

theoretical prediction of an isomerization of the Ni_9^+ cluster by the increased N_2 coverage: Naked and $m \leq 4$ tricapped octahedra seem to become a bicapped pentagonal bipyramid, and the dodec spin state persists. It would be a valid point of further investigation to check for the N_2 bending coordinate by parametric variation in a series of explicit DFT calculations, and to check for possible fingerprints by even colder high resolution IR spectra.

The N_2 uptake studies of small neutral Ni clusters⁶⁵ emphasize two cases, Ni_8 and Ni_9 , with evidence for two (or more) bare cluster structures at very low N_2 coverages. The mass spectra show clear bimodal distributions which hint for an isomerization at low N_2 coverages. They suggest that these two clusters, each, have two isomers of comparable energy. We are in line with these early findings.⁹⁹

Another issue of great interest is the onset of major splittings of the main N_2 stretching band for $m > 8$ (Figure 8). We interpret these splittings in terms of a geminal N_2 adsorption—two N_2 adsorbates to a single Ni atom—in the (9,9) case. The resulting symmetric and antisymmetric N_2 stretching frequencies would split by $\sim 10 \text{ cm}^{-1}$. DFT modeling reveals: The higher an adsorbing Ni atom is coordinated within the cluster, the more red-shifted is the stretching frequency of the adsorbed N_2 . It is unlikely that the origin of the observed vibrational splittings of (9,9) originates from an N_2 coordination to the

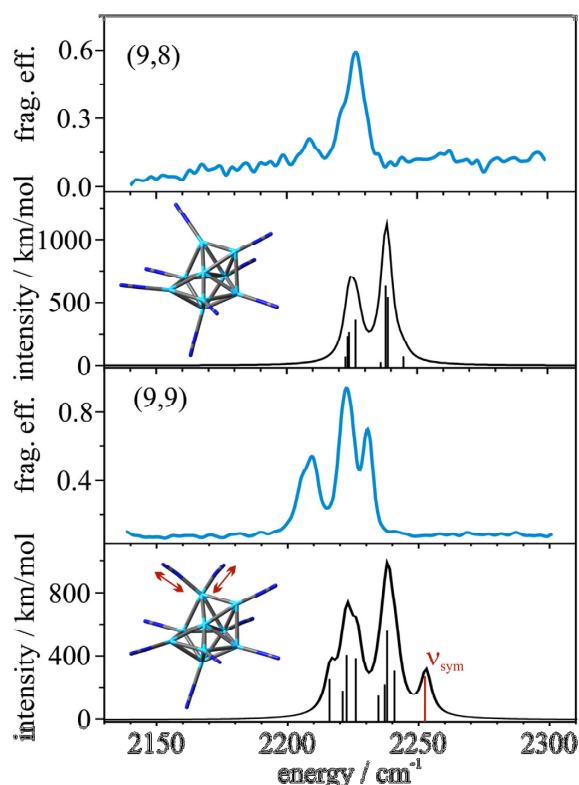


Figure 8. IR-PD spectra of (9,8) and (9,9) (blue) and calculated IR absorption spectra for the bicapped pentagonal bipyramidal motif with and without geminal binding (black; PBE0/ECP(Ni), cc-pVTZ(N), $2S + 1 = 10$) scaled by 0.93 and simulated using the Gaussian profile of $fwhm = 5 \text{ cm}^{-1}$.

highest coordinated Ni atom—which stays vacant in favor of the geminal N_2 adsorption at a low coordinated Ni atom.

Trends in the calculated N_2 binding energies of Ni_9^+ are in line with the kinetic and spectroscopic findings of this study (Table 3). The first N_2 binds stronger, $\Delta_{ads}H^{0K}(9,1) = 76 \text{ kJ/mol}$ (0.79 eV), than all subsequent adsorbates, namely, all other (9, m) cases. Further N_2 adsorption up to the (9,8) species takes place with $\Delta_{ads}H^{0K}(9,m \leq 8) \sim 50 \text{ kJ/mol}$. It is the ninth N_2 molecule which binds significantly weaker, $\Delta_{ads}H^{0K}(9,9) \sim 20 \text{ kJ/mol}$ —a finding which nicely matches the occurrence of an observed intermittent limit at (9,8). Notice that the case of (9,9) favors by $\sim 5 \text{ kJ/mol}$ one instance of geminal N_2 adsorption over one N_2 adsorption to the highest (8-fold) coordinated Ni site.

Further N_2 adsorption up to the adsorption limit at (9,13) leads to complicated vibrational patterns comprising multiple bands, most likely by further splittings as a result of geminal N_2 adsorption on the remaining three lowest coordinated Ni atoms and by adsorption on the highest coordinated Ni atom. The observed vibrational bands spread out over more than 70 cm^{-1} for $m > 9$, and this finding is well reproduced by our calculated IR spectra, but they fail in reflecting the absolute vibrational patterns (cf. Figures S5–S12 in the Supporting Information for more details on the (9, m) species).

In the case of $[Ni_{13}(N_2)_{12}]^+$, which is the (13,12) species, we find good agreement of the experimental IR-PD spectra and the

Table 3. Calculated N₂ Binding Energies of the Last Adsorbed N₂ (Highlighted in Magenta) to Various (9,*m*) Species in Dectet Spin States

(<i>n,m</i>)	calculated N ₂ binding energy / kJ/mol	
(9,1)	-75.9	
(9,2)	-53.6	
(9,8)	-46.5	
(9,9)	-20.4	
(9,9)	-15.8	

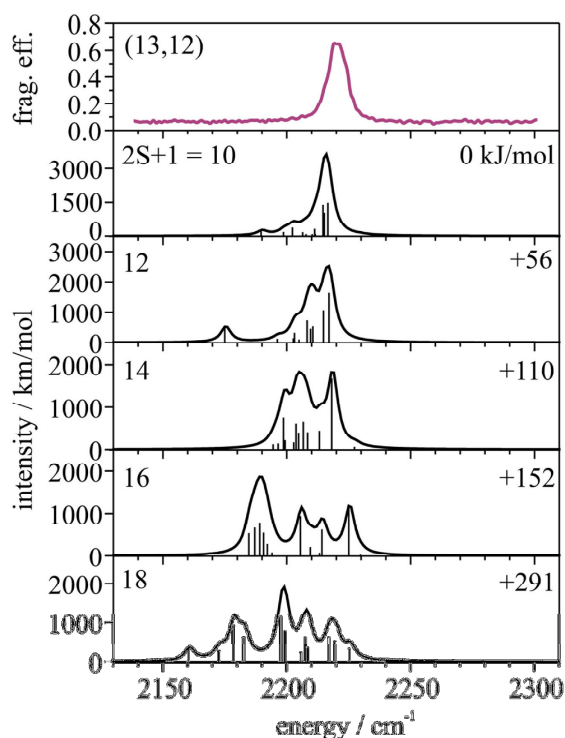
calculated IR absorption spectra, when assuming a spin quenching from $2S + 1 = 16 \rightarrow 10$ when $m = 0 \rightarrow 12$. Each experimental (13,*m*) IR-PD spectrum shows a single dominant band around 2222 cm^{-1} which does not shift upon increasing N₂ adsorption up to its limit. Assuming a perfect icosahedral Ni₁₃⁺ core, all 12 surface atoms would be equivalent and the N₂ stretching frequencies would degenerate—as observed. Note that such degeneracy is indeed predicted from DFT calculations of (13,*m*) when assuming the gradual spin quenching discussed above. Otherwise, there would be clearly discernible band splittings (cf. Figure 9)—other than observed.

Linear IR absorption spectra of several (9,*m*) species were calculated including the Grimme correction for dispersion with the original D3 damping function (GD3).¹⁰⁰ There is no significant change in band positions or intensities (cf. Figures S13 and S14 in the Supporting Information for the comparison of calculated spectra for (9,8) and (9,9) including GD3).

There is no clear correlation between N₂ vibrational frequencies and individual adsorption enthalpies, in particular when multiple N₂'s adsorb. Their vibrational modes are coupled, and the adsorption/desorption likely implies reorganization of the adsorbate layer.

Our DFT level of theory would not cover antiferromagnetic coupling within the Ni cluster core. As of now, we conclude that there is no evidence by our IR-PD spectra of either ferro- or antiferromagnetic coupling in Ni₁₃⁺. Other than in the case of Fe₁₃⁺,^{46,101} the XMCD investigation of Ni₁₃⁺ did not reveal any evidence for a reduction of magnetic moments by antiferromagnetic coupling.⁴⁶

Finally, our nonrelativistic DFT level of theory does not cover relativistic effects such as—most notably—spin orbit couplings. These, however, likely alter the orbital occupations within the Ni cluster core, which in turn might influence the coupling to and force constants with N₂ adsorbates. Thus, the calculated adsorbate vibrations may depend significantly on the spin multiplicity and in the case of otherwise equivalent adsorbate motifs.

**Figure 9.** IR-PD spectrum of (13,12) (red) and calculated IR absorption spectra (black; PBE0/ECP(Ni),cc-pVTZ(N)) scaled by 0.93 with variation by the spin multiplicity of the icosahedral nickel cluster core (likely $2S + 1 = 10, 12, 14, 16, 18$) and simulated using the Gaussian profile of $\text{fwhm} = 5 \text{ cm}^{-1}$.

4. CONCLUSIONS

We have investigated the stepwise N₂ adsorption on size selected Ni_{*n*}⁺ ($n = 5-20$) clusters by recording their reaction kinetics at 26 K in a hexapole ion trap. We performed pseudo-first-order kinetic fits, which confirm consecutive adsorption steps by single exponential decays exclusively, and we have chosen to discuss the archetypical cases of Ni₉⁺ and Ni₁₃⁺ in more detail. These two clusters show remarkable differences in the N₂ adsorption trends and in the adsorption limits of saturation: N₂ adsorption on Ni₉⁺ takes place at individual rates up to the adsorption limit at [Ni₉(N₂)₁₃]⁺ and retards at an additional intermittent adsorption limit at [Ni₉(N₂)₈]⁺. The fit of the very last adsorption step reveals a significant backward reaction, which indicates swift N₂ desorption. N₂ adsorption on Ni₁₃⁺ takes place at equal rates up to the adsorption limit at [Ni₁₃(N₂)₁₂]⁺. Our findings indicate a rough cluster surface of Ni₉⁺ with inequivalent adsorption sites and a smooth cluster surface of Ni₁₃⁺ with equivalent adsorption sites.

We have further investigated the origin of the found variation in relative rate constants in Ni₉⁺ and its absence in Ni₁₃⁺ via IR-PD spectroscopy. The recorded spectra of all observed cluster adsorbate complexes reveal IR active vibrational bands at frequencies from 2170 to 2260 cm⁻¹. The recorded range of these bands is compatible with the range of published head-on coordinated N–N stretching modes on TM metals. The IR-PD spectra of [Ni₉(N₂)_{*m*}]⁺ show significant shifts of peak positions and onset of splittings by increase of the N₂ coverage, as

suggested by our kinetic results. In contrast, all IR-PD spectra of $[\text{Ni}_{13}(\text{N}_2)_m]^+$ show a single dominant band around 2222 cm^{-1} which does not shift upon increasing N_2 adsorption up to saturation. This further encourages the proposition of a smooth Ni_{13}^+ cluster surface, where all surface atoms are equivalent.

Current DFT calculations reinforce a possible isomerization with low N_2 coverage in the case of Ni_9^+ , most likely from a tricapped octahedron to a bicapped pentagonal bipyramid, and geminal binding of N_2 setting in at $m = 9$. In the case of Ni_{13}^+ , we assume an icosahedral structure which coincides with all experimental findings and theory.

Our present study unravels subtle details of N_2 adsorption to individual sites on cluster surfaces of high (Ni_9^+) and low curvatures (Ni_{13}^+). High curvature enables low coordinated sites and surface roughness. Low curvature implies a higher regularity, equal coordinated sites, and surface smoothness. The rough surface of Ni_9^+ provides for a large variation of N_2 adsorption in terms of enthalpy and N_2 bond softening, while the smooth surface of Ni_{13}^+ merely provides one such case at all levels of N_2 coverage. It seems likely that a variation of adsorption conditions is more efficient for catalytic needs than a single situation. Rough likely beats smooth. The current study paves the way for subsequent N_2 activation studies with more active transition metals and their alloys. Such studies are underway.

■ ASSOCIATED CONTENT

Supporting Information

The Supporting Information is available free of charge on the ACS Publications website at DOI: 10.1021/acs.jpcc.6b12167.

Additional information on experiments and DFT calculations (PDF)

■ AUTHOR INFORMATION

Corresponding Author

*E-mail: gns@chemie.uni-kl.de.

ORCID

Gereon Niedner-Schatteburg: 0000-0001-7240-6673

Notes

The authors declare no competing financial interest.

■ ACKNOWLEDGMENTS

The ^{58}Ni isotopic sample used in this research was supplied by the United States Department of Energy Office of Science by the Isotope Program in the Office of Nuclear Physics. This work was supported by the German research foundation DFG within the transregional collaborative research center SFB/TRR 88 "Cooperative effects in homo and heterometallic complexes" (3MET.de) and by the state research center OPTIMAS.

■ REFERENCES

- Muetterties, E. L. Metal Clusters in Catalysis 0.3. Clusters as Models for Chemisorption Processes and Heterogeneous Catalysis. *Bull. Soc. Chim. Belg.* **1975**, *84*, 959–986.
- Muetterties, E. L. Molecular Metal Clusters. *Science* **1977**, *196*, 839–848.
- Muetterties, E. L.; Rhodin, T. N.; Band, E.; Brucker, C. F.; Pretzer, W. R. Clusters and Surfaces. *Chem. Rev.* **1979**, *79*, 91–137.
- Shustorovich, E. Cluster-Surface Analogy: New Developments. In *Quantum Chemistry: The Challenge of Transition Metals and Coordination Chemistry*; Veillard, A., Ed.; Springer: Dordrecht, The Netherlands, 1986; Vol. 176, pp 445–464.

- Ertl, G. Reactions at Surfaces: From Atoms to Complexity (Nobel Lecture). *Angew. Chem., Int. Ed.* **2008**, *47*, 3524–3535.
- Pfeffer, B.; Jaberg, S.; Niedner-Schatteburg, G. Reactions of Simple Aromatic Heterocycles with Niobium Cluster Ions ($n < 30$). *J. Chem. Phys.* **2009**, *131*, 194305.
- Haberland, H.; Kleinermanns, K.; Träger, F. Cluster. In *Lehrbuch Der Experimentalphysik Band 5 - Gase, Nanosysteme, Flüssigkeiten*, 2nd ed.; Walter de Gruyter: Berlin, 2006.
- Heiz, U.; Landman, U. *Nanocatalysis*; Springer: Berlin, 2007.
- Landman, U.; Yoon, B.; Zhang, C.; Heiz, U.; Arenz, M. Factors in Gold Nanocatalysis: Oxidation of Co in the non-Scalable Size Regime. *Top. Catal.* **2007**, *44*, 145–158.
- Rips, I.; Jortner, J. Ion Solvation in Clusters. *J. Chem. Phys.* **1992**, *97*, 536–546.
- Knickelbein, M. B.; Menezes, W. J. Metal Cluster-Rare Gas Van Der Waals Complexes: Physisorption on a Microscopic Scale. *J. Phys. Chem.* **1992**, *96*, 6611–6616.
- De Heer, W. A. The Physics of Simple Metal Clusters: Experimental Aspects and Simple Models. *Rev. Mod. Phys.* **1993**, *65*, 611.
- Ho, J.; Zhu, L.; Parks, E.; Riley, S. Temperature Dependence of the Reactions of Small Cobalt Clusters with Deuterium. *J. Chem. Phys.* **1993**, *99*, 140–147.
- Knickelbein, M. B. Reactions of Transition Metal Clusters with Small Molecules 1. *Annu. Rev. Phys. Chem.* **1999**, *50*, 79–115.
- Häkkinen, H.; Abbet, S.; Sanchez, A.; Heiz, U.; Landman, U. Structural, Electronic, and Impurity-Doping Effects in Nanoscale Chemistry: Supported Gold Nanoclusters. *Angew. Chem., Int. Ed.* **2003**, *42*, 1297–1300.
- Ervin, K. M. Metal-Ligand Interactions: Gas-Phase Transition Metal Cluster Carbonyls. *Int. Rev. Phys. Chem.* **2001**, *20*, 127–164.
- Ganteför, G.; Icking-Konert, G. S.; Handschuh, H.; Eberhardt, W. CO Chemisorption on Ni_n , Pd_n and Pt_n Clusters. *Int. J. Mass Spectrom. Ion Processes* **1996**, *159*, 81–109.
- Zambelli, T.; Wintterlin, J.; Trost, J.; Ertl, G. Identification of the "Active Sites" of a Surface-Catalyzed Reaction. *Science* **1996**, *273*, 1688.
- Nørskov, J. K.; Bligaard, T.; Logadottir, A.; Bahn, S.; Hansen, L. B.; Bollinger, M.; Bengaard, H.; Hammer, B.; Slijivancanin, Z.; Mavrikakis, M. Universality in Heterogeneous Catalysis. *J. Catal.* **2002**, *209*, 275–278.
- Honkala, K.; Hellman, A.; Remedakis, I.; Logadottir, A.; Carlsson, A.; Dahl, S.; Christensen, C. H.; Nørskov, J. K. Ammonia Synthesis from First-Principles Calculations. *Science* **2005**, *307*, 555–558.
- Duncan, M. A. Spectroscopy of Metal Ion Complexes: Gas-Phase Models for Solvation. *Annu. Rev. Phys. Chem.* **1997**, *48*, 69–93.
- Duncan, M. A. Infrared Spectroscopy to Probe Structure and Dynamics in Metal Ion–Molecule Complexes. *Int. Rev. Phys. Chem.* **2003**, *22*, 407–435.
- Walker, N. R.; Walters, R. S.; Duncan, M. A. Frontiers in the Infrared Spectroscopy of Gas Phase Metal Ion Complexes. *New J. Chem.* **2005**, *29*, 1495–1503.
- Roithova, J. Characterization of Reaction Intermediates by Ion Spectroscopy. *Chem. Soc. Rev.* **2012**, *41*, 547–559.
- Oomens, J.; Sartakov, B. G.; Meijer, G.; von Helden, G. Gas-Phase Infrared Multiple Photon Dissociation Spectroscopy of Mass-Selected Molecular Ions. *Int. J. Mass Spectrom.* **2006**, *254*, 1–19.
- MacAleese, L.; Maitre, P. Infrared Spectroscopy of Organometallic Ions in the Gas Phase: From Model to Real World Complexes. *Mass Spectrom. Rev.* **2007**, *26*, 583–605.
- Schöllkopf, W.; Gewinner, S.; Junkes, H.; Paarmann, A.; von Helden, G.; Bluem, H.; Todd, A. M. M. *Proc. SPIE* **2015**, 95121L–95121L-13.
- Kamrath, M. Z.; Garand, E.; Jordan, P. A.; Leavitt, C. M.; Wolk, A. B.; Van Stipdonk, M. J.; Miller, S. J.; Johnson, M. A. Vibrational Characterization of Simple Peptides Using Cryogenic Infrared Photodissociation of H_2 -Tagged, Mass-Selected Ions. *J. Am. Chem. Soc.* **2011**, *133*, 6440–6448.

- (29) Wolk, A. B.; Leavitt, C. M.; Garand, E.; Johnson, M. A. Cryogenic Ion Chemistry and Spectroscopy. *Acc. Chem. Res.* **2014**, *47*, 202–210.
- (30) Gruene, P.; Fielicke, A.; Meijer, G.; Rayner, D. M. The Adsorption of Co on Group 10 (Ni, Pd, Pt) Transition-Metal Clusters. *Phys. Chem. Chem. Phys.* **2008**, *10*, 6144–6149.
- (31) Fielicke, A.; von Helden, G.; Meijer, G.; Pedersen, D. B.; Simard, B.; Rayner, D. M. Size and Charge Effects on the Binding of CO to Late Transition Metal Clusters. *J. Chem. Phys.* **2006**, *124*, 194305–194305.
- (32) Harding, D. J.; Fielicke, A. Platinum Group Metal Clusters: From Gas-Phase Structures and Reactivities Towards Model Catalysts. *Chem. - Eur. J.* **2014**, *20*, 3258–3267.
- (33) Chatt, J.; Duncanson, L. 586. Olefin Co-Ordination Compounds. Part Iii. Infra-Red Spectra and Structure: Attempted Preparation of Acetylene Complexes. *J. Chem. Soc.* **1953**, 2939–2947.
- (34) Dewar, J. A Review of the Pi-Complex Theory. *Bull. Soc. Chim. Fr.* **1951**, *18*, C71–C79.
- (35) Blyholder, G. Molecular Orbital View of Chemisorbed Carbon Monoxide. *J. Phys. Chem.* **1964**, *68*, 2772–2777.
- (36) Allen, A.; Senoff, C. Nitrogenopentammineruthenium (II) Complexes. *Chem. Commun.* **1965**, 621–622.
- (37) Corfield, P. W.; Doedens, R. J.; Ibers, J. A. Studies of Metal-Nitrogen Multiple Bonds. I. Crystal and Molecular Structure of Nitridodichlorotris(Diethylphenyl-phosphine)Rhenium(V) $\text{ReCl}_2\text{P}(\text{C}_2\text{H}_5)_2\text{C}_6\text{H}_5$ 3. *Inorg. Chem.* **1967**, *6*, 197.
- (38) Collman, J. P. Patterns of Organometallic Reactions Related to Homogeneous Catalysis. *Acc. Chem. Res.* **1968**, *1*, 136–143.
- (39) Cohen, J. D.; Mylvaganam, M.; Fryzuk, M. D.; Loehr, T. M. Resonance Raman Studies of Dinuclear Zirconium Complexes with a Bridging Dinitrogen Ligand - Possible N_2 -Coordination Models for Nitrogenase. *J. Am. Chem. Soc.* **1994**, *116*, 9529–9534.
- (40) MacKay, B. A.; Fryzuk, M. D. Dinitrogen Coordination Chemistry: On the Biomimetic Borderlands. *Chem. Rev.* **2004**, *104*, 385–401.
- (41) Duarte, H. A.; Salahub, D. R.; Haslett, T.; Moskovits, M. $\text{Fe}(\text{N}_2)_n$ ($n = 1-5$): Structure, Bonding, and Vibrations from Density Functional Theory. *Inorg. Chem.* **1999**, *38*, 3895–3903.
- (42) Haslett, T.; Fedrigo, S.; Bosnick, K.; Moskovits, M.; Duarte, H.; Salahub, D. Binary Iron-Dinitrogen Compounds Synthesized by Co-Deposition of Mass-Selected Fe, Fe_2 , and Fe_3 with N_2 . *J. Am. Chem. Soc.* **2000**, *122*, 6039–6044.
- (43) Cohen, J. D.; Fryzuk, M. D.; Loehr, T. M.; Mylvaganam, M.; Rettig, S. J. Synthesis and Structure of a Zirconium Dinitrogen Complex with a Side-on Bridging N_2 Unit. *Inorg. Chem.* **1998**, *37*, 112–119.
- (44) Mafin , F.; Tawaraya, Y.; Kudoh, S. Nitrogen Molecule Adsorption on Cationic Tantalum Clusters and Rhodium Clusters and Desorption from Their Nitride Clusters Studied by Thermal Desorption Spectrometry. *J. Phys. Chem. A* **2016**, *120*, 4089–4095.
- (45) Kerpal, C.; Harding, D. J.; Lyon, J. T.; Meijer, G.; Fielicke, A. N_2 Activation by Neutral Ruthenium Clusters. *J. Phys. Chem. C* **2013**, *117*, 12153–12158.
- (46) Meyer, J.; Tombers, M.; van Wullen, C.; Niedner-Schatteburg, G.; Peredkov, S.; Eberhardt, W.; Neeb, M.; Palutke, S.; Martins, M.; Wurth, W. The Spin and Orbital Contributions to the Total Magnetic Moments of Free Fe, Co, and Ni Clusters. *J. Chem. Phys.* **2015**, *143*, 104302/1–104302/12.
- (47) Petkov, P. S.; Vayssilov, G. N.; Krueger, S.; Roesch, N. Density Functional Study of Ni_8 Clusters Containing Impurity Atoms. *Chem. Phys.* **2008**, *348*, 61–68.
- (48) Guzman-Ramirez, G.; Robles, J.; Vega, A.; Aguilera-Granja, F. Stability, Structural, and Magnetic Phase Diagrams of Ternary Ferromagnetic 3d-Transition-Metal Clusters with Five and Six Atoms. *J. Chem. Phys.* **2011**, *134*, 054101/1–054101/9.
- (49) Song, W.; Lu, W.-C.; Wang, C. Z.; Ho, K. M. Magnetic and Electronic Properties of the Nickel Clusters Ni_n ($n \leq 30$). *Comput. Theor. Chem.* **2011**, *978*, 41–46.
- (50) Sahoo, S.; Rollmann, G.; Entel, P. First-Principles Calculation of Cluster Geometries and Magnetization of Pure Ni and Fe-Ni Clusters. *Phase Transitions* **2005**, *78*, 723–731.
- (51) Gao, C.; Zhang, X. Geometries and Physical Properties of W_nNi_m ($n + m \leq 7$) Clusters. *J. Comput. Theor. Nanosci.* **2010**, *7*, 612–618.
- (52) Das, N. K.; Shoji, T. Geometry, Orbital Interaction, and Oxygen Chemisorption Properties of Chromium-Doped Nickel Clusters. *J. Phys. Chem. C* **2012**, *116*, 13353–13367.
- (53) Wang, L. S.; Wu, H. Photoelectron Spectroscopy of Transition Metal Clusters. *Z. Phys. Chem. (Muenchen, Ger.)* **1998**, *203*, 45–55.
- (54) Morenzin, J.; Kietzmann, H.; Bechthold, P. S.; Gantefor, G.; Eberhardt, W. Localization and Bandwidth of the 3d-Orbitals in Magnetic Ni and Co Clusters. *Pure Appl. Chem.* **2000**, *72*, 2149–2157.
- (55) Kerns, K. P.; Parks, E. K.; Riley, S. J. The Binding of CO to Nickel Clusters. II. Structural Implications and Comparisons with Electron Counting Rules. *J. Chem. Phys.* **2000**, *112*, 3394–3407.
- (56) Liu, F.; Liyanage, R.; Armentrout, P. B. Guided Ion Beam Studies of the Reaction of Ni_n^+ ($n = 2-16$) with D_2 : Nickel Cluster-Deuteride Bond Energies. *J. Chem. Phys.* **2002**, *117*, 132–141.
- (57) Grigoryan, V. G.; Springborg, M. Structural and Energetic Properties of Nickel Clusters: $2 \leq n \leq 150$. *Phys. Rev. B: Condens. Matter Mater. Phys.* **2004**, *70*, 205415/1–205415/15.
- (58) Liu, F.; Zhang, X. G.; Liyanage, R.; Armentrout, P. B. Methane Activation by Nickel Cluster Cations, Ni_n^+ ($n = 2-16$): Reaction Mechanisms and Thermochemistry of Cluster- CH_x ($x = 0-3$) Complexes. *J. Chem. Phys.* **2004**, *121*, 10976–10990.
- (59) Swart, L.; de Groot, F. M. F.; Weckhuysen, B. M.; Gruene, P.; Meijer, G.; Fielicke, A. H_2 Adsorption on 3d Transition Metal Clusters: A Combined Infrared Spectroscopy and Density Functional Study. *J. Phys. Chem. A* **2008**, *112*, 1139–1149.
- (60) Swart, L.; Gruene, P.; Fielicke, A.; Meijer, G.; Weckhuysen, B. M.; de Groot, F. M. F. Molecular Adsorption of H_2 on Small Cationic Nickel Clusters. *Phys. Chem. Chem. Phys.* **2008**, *10*, 5743–5745.
- (61) Walters, R. S.; Jaeger, T. D.; Duncan, M. A. Infrared Spectroscopy of $\text{Ni}^+(\text{C}_2\text{H}_2)_n$ Complexes: Evidence for Intracuster Cyclization Reactions. *J. Phys. Chem. A* **2002**, *106*, 10482–10487.
- (62) Walters, R. S.; Pillai, E. D.; Duncan, M. A. Solvation Dynamics in $\text{Ni}^+(\text{H}_2\text{O})_n$ Clusters Probed with Infrared Spectroscopy. *J. Am. Chem. Soc.* **2005**, *127*, 16599–16610.
- (63) Beeck, O. *Adv. Catal.* **1950**, *2*, 155.
- (64) Kokes, R.; Emmett, P. Chemisorption of Nitrogen on Nickel Catalysts. *J. Am. Chem. Soc.* **1958**, *80*, 2082–2086.
- (65) Parks, E.; Zhu, L.; Ho, J.; Riley, S. The Structure of Small Nickel Clusters. I. Ni_3 – Ni_{15} . *J. Chem. Phys.* **1994**, *100*, 7206–7222.
- (66) Parks, E.; Zhu, L.; Ho, J.; Riley, S. The Structure of Small Nickel Clusters. II. Ni_{16} – Ni_{28} . *J. Chem. Phys.* **1995**, *102*, 7377–7389.
- (67) Langevin, M. *Une Formule Fondamentale De Th orie Cin tique*; Annales de chimie et de physique, Series, 1905; 245–288.
- (68) Su, T.; Bowers, M. T. Theory of Ion-Polar Molecule Collisions. Comparison with Experimental Charge Transfer Reactions of Rare Gas Ions to Geometric Isomers of Difluorobenzene and Dichloroethylene. *J. Chem. Phys.* **1973**, *58*, 3027–3037.
- (69) Su, T.; Bowers, M. T. Ion-Polar Molecule Collisions. Proton Transfer Reactions of H_3^+ and CH_3^+ to the Geometric Isomers of Difluoroethylene, Dichloroethylene, and Difluorobenzene. *J. Am. Chem. Soc.* **1973**, *95*, 1370–1373.
- (70) Berg, C.; Schindler, T.; Niedner-Schatteburg, G.; Bondybey, V. E. Reactions of Simple Hydrocarbons with Nb_n^+ : Chemisorption and Physisorption on Ionized Niobium Clusters. *J. Chem. Phys.* **1995**, *102*, 4870–4884.
- (71) Balteanu, I.; Balaj, O. P.; Fox-Beyer, B. S.; Rodrigues, P.; Barros, M. T.; Moutinho, A. M. C.; Costa, M. L.; Beyer, M. K.; Bondybey, V. E. Size- and Charge-State-Dependent Reactivity of Azidoacetonitrile with Anionic and Cationic Rhodium Clusters Rh_n^\pm . *Organometallics* **2004**, *23*, 1978–1985.
- (72) Anderson, M. L.; Ford, M. S.; Derrick, P. J.; Drewello, T.; Woodruff, D. P.; Mackenzie, S. R. Nitric Oxide Decomposition on

- Small Rhodium Clusters, Rh_n^+ . *J. Phys. Chem. A* **2006**, *110*, 10992–11000.
- (73) Kummerlöwe, G.; Beyer, M. K. Rate Estimates for Collisions of Ionic Clusters with Neutral Reactant Molecules. *Int. J. Mass Spectrom.* **2005**, *244*, 84–90.
- (74) Fischens, R. P.; Jacknow, J. *Proc. 3rd Int. Congress on Catalysis (NorthHolland, Amsterdam)* **1965**, 627–643.
- (75) van Hardeveld, R.; van Montfoort, A. The Influence of Crystallite Size on the Adsorption of Molecular Nitrogen on Nickel, Palladium and Platinum. *Surf. Sci.* **1966**, *4*, 396–430.
- (76) Huber, H.; Kuendig, E. P.; Moskovits, M.; Ozin, G. A. Binary Transition Metal Dinitrogen Complexes. I. Matrix Infrared and Raman Spectra, Structure and Bonding of $\text{Ni}(\text{N}_2)_n$ and $\text{Pd}(\text{N}_2)_m$ ($n = 1-4$ and $m = 1-3$). *J. Am. Chem. Soc.* **1973**, *95*, 332–344.
- (77) Tsay, C.; Peters, J. C. Thermally Stable N_2 and H_2 Adducts of Cationic Nickel (II). *Chemical Science* **2012**, *3*, 1313–1318.
- (78) Bridgeman, A. J.; Wilkin, O. M.; Young, N. A. Dinitrogen Bonding Modes to Molecular Nickel(II) Halides: A Matrix Isolation IR and Dft Study. *Inorg. Chem. Commun.* **2000**, *3*, 681–684.
- (79) Craig, S. M.; Menges, F. S.; Johnson, M. A. Application of Gas Phase Cryogenic Vibrational Spectroscopy to Characterize the CO_2 , CO , N_2 and N_2O Interactions with the Open Coordination Site on a Ni(I) Macrocyclic Using Dual Cryogenic Ion Traps. *J. Mol. Spectrosc.* **2016**, in press, DOI: [10.1016/j.jms.2016.11.015](https://doi.org/10.1016/j.jms.2016.11.015).
- (80) Peredkov, S.; Noeb, M.; Eberhardt, W.; Meyer, J.; Tombers, M.; Kampschulte, H.; Niedner-Schatteburg, G. Spin and Orbital Magnetic Moments of Free Nanoparticles. *Phys. Rev. Lett.* **2011**, *107*, 233401/1–233401/5.
- (81) Nosenko, Y.; Menges, F.; Riehn, C.; Niedner-Schatteburg, G. Investigation by Two-Color IR Dissociation Spectroscopy of Hoogsteen-Type Binding in a Metalated Nucleobase Pair Mimic. *Phys. Chem. Chem. Phys.* **2013**, *15*, 8171–8178.
- (82) Lang, J.; Gaffga, M.; Menges, F.; Niedner-Schatteburg, G. Two-Color Delay Dependent IR Probing of Torsional Isomerization in a $[\text{AgL}_2\text{L}_2]^+$ Complex. *Phys. Chem. Chem. Phys.* **2014**, *16*, 17417–17421.
- (83) Gaffga, M.; Munstein, I.; Muller, P.; Lang, J.; Thiel, W. R.; Niedner-Schatteburg, G. Multistate-Mediated Rearrangements and FeCl_2 Elimination in Dinuclear FePd Complexes. *J. Phys. Chem. A* **2015**, *119*, 12587–12598.
- (84) Mohrbach, J.; Lang, J.; Dillinger, S.; Prosenč, M. A.; Braunstein, P.; Niedner-Schatteburg, G. Vibrational Fingerprints of a Tetranuclear Cobalt Carbonyl Cluster within an Ion Trap. *J. Mol. Spectrosc.* **2016**, in press, DOI: [10.1016/j.jms.2016.11.008](https://doi.org/10.1016/j.jms.2016.11.008).
- (85) Dillinger, S.; Mohrbach, J.; Hewer, J.; Gaffga, M.; Niedner-Schatteburg, G. Infrared Spectroscopy of N_2 Adsorption on Size Selected Cobalt Cluster Cations in Isolation. *Phys. Chem. Chem. Phys.* **2015**, *17*, 10358–10362.
- (86) Lang, J.; Mohrbach, J.; Dillinger, S.; Hewer, J. M.; Niedner-Schatteburg, G. Vibrational Blue Shift of Coordinated N_2 in $[\text{Fe}_3\text{O}(\text{OAc})_6(\text{N}_2)_n]^+$: “non-classical” Dinitrogen Complexes. *Chem. Commun.* **2017**, in press, DOI: [10.1039/C6CC07481B](https://doi.org/10.1039/C6CC07481B).
- (87) Maruyama, S.; Anderson, L. R.; Smalley, R. E. Direct Injection Supersonic Cluster Beam Source for Ft-Icr Studies of Clusters. *Rev. Sci. Instrum.* **1990**, *61*, 3686–3693.
- (88) Proch, D.; Trickl, T. A High-Intensity Multi-Purpose Piezo-electric Pulsed Molecular Beam Source. *Rev. Sci. Instrum.* **1989**, *60*, 713–716.
- (89) Caravatti, P.; Allemann, M. The ‘Infinity Cell’: A New Trapped-Ion Cell with Radiofrequency Covered Trapping Electrodes for Fourier Transform Ion Cyclotron Resonance Mass Spectrometry. *Org. Mass Spectrom.* **1991**, *26*, 514–518.
- (90) Graf, M. Entwicklung eines auf Evolutionsstrategien basierenden Computerprogrammes zum optimierten Anpassen kinetischer Daten aus FT-ICR-Massenspektrometrie-Messungen. Diploma Thesis, TU Kaiserslautern, September 2006.
- (91) Adamo, C.; Barone, V. Toward Reliable Density Functional Methods without Adjustable Parameters: The PBE0Model. *J. Chem. Phys.* **1999**, *110*, 6158–6170.
- (92) Dunning, T. H., Jr Gaussian Basis Sets for Use in Correlated Molecular Calculations. I. The Atoms Boron through Neon and Hydrogen. *J. Chem. Phys.* **1989**, *90*, 1007–1023.
- (93) Dolg, M.; Stoll, H.; Preuss, H.; Pitzer, R. M. Relativistic and Correlation Effects for Element 105 (Hahnium, Ha): A Comparative Study of M and Mo (M= Nb, Ta, Ha) Using Energy-Adjusted Ab Initio Pseudopotentials. *J. Phys. Chem.* **1993**, *97*, 5852–5859.
- (94) Frisch, M. J.; Trucks, G.; Schlegel, H.; Scuseria, G.; Robb, M.; Cheeseman, J.; Scalmani, G.; Barone, V.; Mennucci, B.; Petersson, G.; et al. *Gaussian 09*, revision A.1; Gaussian, Inc.: Wallingford, CT, 2009.
- (95) Grunze, M. J.; Fühler, J.; Neumann, M.; Brundle, C. R.; Auerbach, D. J.; Behm, J. A Search for Precursor States to Molecular Nitrogen Chemisorption on Ni(100), Re(0001) and W(100) Surfaces at ~ 20 K. *Surf. Sci.* **1984**, *139*, 109–120.
- (96) Grunze, M.; Driscoll, R. K.; Burland, G. N.; Cornish, J. C. L.; Pritchard, J. Molecular and Dissociative Chemisorption of N_2 on Ni(110). *Surf. Sci.* **1979**, *89*, 381–390.
- (97) Rapps, T.; Ahlrichs, R.; Waldt, E.; Kappes, M. M.; Schoof, D. On the Structures of 55-Atom Transition-Metal Clusters and Their Relationship to the Crystalline Bulk. *Angew. Chem., Int. Ed.* **2013**, *52*, 6102–6105.
- (98) For low adsorption numbers, DFT modeling suggests the first N_2 coordination to a 3-fold coordinated Ni atom, most likely to the inner capping Ni atom. This is in conjunction with the observed single absorption band for (9,1) at 2238 cm^{-1} , whereas the (9,2) species shows an additional band at 2250 cm^{-1} . For more information, please see the Supporting Information.
- (99) Parks and Riley argue that the metal cluster stability is enhanced by minimizing the number of atoms with low metal coordination, which would make the tricapped octahedron less stable than the bicapped pentagonal bipyramid. It is conceivable that nitrogen adsorption on the three-coordinate atoms might reverse the relative stabilities, in particular when the adsorption reaches saturation. Our findings agree in principle. However, we propose opposite stabilities: A tricapped octahedron is more stable when covered by a few N_2 adsorbates, and it becomes a bicapped pentagonal bipyramid when covered with nitrogen up to saturation.
- (100) Grimme, S.; Antony, J.; Ehrlich, S.; Krieg, H. A Consistent and Accurate Ab Initio Parametrization of Density Functional Dispersion Correction (DFT-D) for the 94 Elements H-Pu. *J. Chem. Phys.* **2010**, *132*, 154104/1–154104/19.
- (101) Niemeyer, M.; Hirsch, K.; Zamudio-Bayer, V.; Langenberg, A.; Vogel, M.; Kossick, M.; Ebrecht, C.; Egashira, K.; Terasaki, A.; Möller, T.; et al. Spin Coupling and Orbital Angular Momentum Quenching in Free Iron Clusters. *Phys. Rev. Lett.* **2012**, *108*, 057201/1–057201/5.

4.3 Supplementary Information

Table of Content:

Energy differences including zero-point-energy corrections for several $[\text{Ni}_9(\text{N}_2)_1]^+$ isomers

Table S1. Relative stabilities including zero-point-correction (in kJ/mol) for the computed tricapped octahedral Ni_9^+ cluster core upon the first N_2 adsorption for decet spin states at several adsorption positions.

Detailed information on all observed reaction steps of the N_2 adsorption/desorption

Table S2. Pseudo-first-order rate constants for the N_2 adsorption/desorption on Ni_9^+ clusters ($k_{(9,m)}$ and $k_{-(9,m+1)}$), related absolute rate constants ($k_{(9,m)\text{abs}}$ and $k_{-(9,m+1)\text{abs}}$) calculated collision rates (k_L and k_{SCC}).

Table S3. Pseudo-first-order rate constants for the N_2 adsorption/desorption on Ni_{13}^+ clusters ($k_{(13,m)}$ and $k_{-(13,m+1)}$), related absolute rate constants ($k_{(13,m)\text{abs}}$ and $k_{-(13,m+1)\text{abs}}$) and calculated collision rates (k_L and k_{SCC}).

Spectrum of the (9,13) species in an extended frequency range

Figure S1. IR-MPD spectrum of the (9,13) species in an extended frequency range of 1010 - 2340 cm^{-1} . Note, that this spectrum has been recorded with increased laser power.

Computed geometries and relative energies for multiple local minimum structures for the naked Ni_9^+ cluster and relative stabilities for icosahedral Ni_{13}^+ clusters considering several spin states.

Figure S2: Computed geometries for Ni_9^+ and their relative stabilities. Note, that the stated values are given for the favoured spin multiplicity, respectively.

Table S4. Relative stabilities for computed icosahedral Ni_{13}^+ with variation of the spin multiplicity, $2S + 1 = 10-18$.

Possible adsorption positions on the tricapped octahedral Ni_9^+ cluster core and relative stabilities with variation of the spin multiplicity

Figure S3: Tricapped octahedron with numbered adsorption positions. Note, that each number reflects the Ni-Ni coordination, respectively.

Table S5. Relative stabilities for the computed tricapped octahedral Ni_9^+ cluster core upon the first N_2 adsorption with variation of the spin multiplicity and adsorption position.

Comparison of the experimental IR-PD spectrum of (9,2) and calculated IR absorption spectra for the assumed tricapped octahedral and bicapped pentagonal bipyramidal Ni_9^+ motifs

Figure S4. IR-PD spectrum of (9,2) (blue) and the calculated IR absorption spectra for the tricapped octahedral and bicapped pentagonal bipyramidal motifs with variation in the adsorbing Ni atoms (black; PBE0/ECP(Ni), cc-pVTZ(N), $2S + 1 = 10$). The calculated spectra are scaled by 0.93 and simulated using the gaussian profile of $\text{fwhm} = 5 \text{ cm}^{-1}$.

Comparison of the experimental IR-PD spectra of (9,m) (m = 3,4,6,7, and 10-13) and calculated IR absorption spectra for the assumed tricapped octahedral and bicapped pentagonal bipyramidal Ni_9^+ motifs

Figure S5. IR-PD spectrum of (9,3) (blue) and the calculated IR absorption spectra for the tricapped octahedral and bicapped pentagonal bipyramidal motifs with variation in the adsorbing Ni atoms (black; PBE0/ECP(Ni), cc-pVTZ(N), $2S + 1 = 10$). The calculated spectra are scaled by 0.93 and simulated using the gaussian profile of $\text{fwhm} = 5 \text{ cm}^{-1}$.

Figure S6. IR-PD spectrum of (9,4) (blue) and the calculated IR absorption spectra for the tricapped octahedral and bicapped pentagonal bipyramidal motifs with variation in the adsorbing Ni atoms (black; PBE0/ECP(Ni), cc-pVTZ(N), $2S + 1 = 10$). The calculated spectra are scaled by 0.93 and simulated using the gaussian profile of $\text{fwhm} = 5 \text{ cm}^{-1}$.

Figure S7. IR-PD spectrum of (9,6) (blue) and the calculated IR absorption spectra for the tricapped octahedral and bicapped pentagonal bipyramidal motifs with variation in the adsorbing Ni atoms (black; PBE0/ECP(Ni), cc-pVTZ(N), $2S + 1 = 10$). The calculated spectra are scaled by 0.93 and simulated using the gaussian profile of $\text{fwhm} = 5 \text{ cm}^{-1}$.

Figure S8. IR-PD spectrum of (9,7) (blue) and the calculated IR absorption spectra for the tricapped octahedral and bicapped pentagonal bipyramidal motifs with variation in the adsorbing Ni atoms (black; PBE0/ECP(Ni), cc-pVTZ(N), $2S + 1 = 10$). The calculated spectra are scaled by 0.93 and simulated using the gaussian profile of $\text{fwhm} = 5 \text{ cm}^{-1}$.

Figure S9. IR-PD spectrum of (9,10) (blue) and the calculated IR absorption spectra for the tricapped octahedral and bicapped pentagonal bipyramidal motifs with variation in the adsorbing Ni atoms and in spin multiplicities (black; PBE0/ECP(Ni), cc-pVTZ(N)). The calculated spectra are scaled by 0.93 and simulated using the gaussian profile of $\text{fwhm} = 5 \text{ cm}^{-1}$.

Figure S10. IR-PD spectrum of (9,11) (blue) and the calculated IR absorption spectra for the tricapped octahedral and bicapped pentagonal bipyramidal motifs with variation in the adsorbing Ni atoms and in spin multiplicities (black; PBE0/ECP(Ni), cc-pVTZ(N)). The calculated spectra are scaled by 0.93 and simulated using the gaussian profile of $\text{fwhm} = 5 \text{ cm}^{-1}$.

Figure S11. IR-PD spectrum of (9,12) (blue) and the calculated IR absorption spectra for the tricapped octahedral and bicapped pentagonal bipyramidal motifs with variation in the sole vacant Ni atom and in spin multiplicities (black; PBE0/ECP(Ni), cc-pVTZ(N)). The calculated spectra are scaled by 0.93 and simulated using the gaussian profile of $\text{fwhm} = 5 \text{ cm}^{-1}$.

Figure S12. IR-PD spectrum of (9,13) (blue) and the calculated IR absorption spectra for the tricapped octahedral and bicapped pentagonal bipyramidal motifs with maximum N_2 adsorption as shown in Fig. 5 (black; PBE0/ECP(Ni), cc-pVTZ(N)). The calculated spectra are scaled by 0.93 and simulated using the gaussian profile of $\text{fwhm} = 5 \text{ cm}^{-1}$.

Calculated IR absorption spectra including the Grimme correction for dispersion with the original D3 damping function (GD3)

Figure S13. Calculated IR absorption spectra for the tricapped octahedral motif (top lanes) in comparison with calculated IR absorption spectra including the Grimme correction for dispersion with the original D3 damping function (bottom lanes) for (9,8) for the octet spin state (left) and the decet spin state (right). The calculated spectra are scaled by 0.93 and simulated using the gaussian profile of $\text{fwhm} = 5 \text{ cm}^{-1}$.

Figure S14. Calculated IR absorption spectra for the tricapped octahedral motif (top lanes) in comparison with calculated IR absorption spectra including the Grimme correction for dispersion with the original D3 damping function (bottom lanes) for (9,9) for the octet spin state (left) and the decet spin state (right). The calculated spectra are scaled by 0.93 and simulated using the gaussian profile of $\text{fwhm} = 5 \text{ cm}^{-1}$.

Energy differences including zero-point-energy corrections for several $[\text{Ni}_9(\text{N}_2)_1]^+$ isomers**Table S1.** Relative stabilities including zero-point-correction (in kJ/mol) for the computed tricapped octahedral Ni_9^+ cluster core upon the first N_2 adsorption for decet spin states at several adsorption positions.

position	$\Delta_f U_{0K}$	$\Delta_f U_{0K}^{ZPE}$	$\Delta_f U_{300K}$	$\Delta_f H_{300K}$	$\Delta_f G_{300K}$
3,1	4.5	5.5	9.5	9.5	0
3,2	0	0	0	0	0.8
4	15.9	16.1	18.3	18.3	13.7
5	10.8	10.8	12.8	12.8	9.2

Detailed information on all observed reaction steps of the N₂ adsorption/desorption**Table S2.** Pseudo-first-order rate constants for the N₂ adsorption/desorption on Ni₉⁺ clusters ($k_{(9,m)}$ and $k_{-(9,m+1)}$), related absolute rate constants ($k_{(9,m)}^{\text{abs}}$ and $k_{-(9,m+1)}^{\text{abs}}$) calculated collision rates (k_L and k_{SCC}).

m	$k_{(9,m)}$ s ⁻¹	$k_{-(9,m+1)}$ s ⁻¹	$k_{(9,m)}^{\text{abs}}$ 10 ⁻¹⁰ cm ³ s ⁻¹	$k_{-(9,m+1)}^{\text{abs}}$ 10 ⁻¹³ cm ³ s ⁻¹	k_L 10 ⁻¹⁰ cm ³ s ⁻¹	k_{SCC} 10 ⁻¹⁰ cm ³ s ⁻¹
0	3.6(3)	<0.001	6.37	<1.77	6.05	12.66
1	4.2(3)	<0.001	7.43	<1.77	6.04	12.78
2	3.9(3)	<0.001	6.90	<1.77	6.03	12.91
3	3.9(3)	<0.001	6.90	<1.77	6.02	13.02
4	3.6(4)	<0.001	6.37	<1.77	6.02	13.13
5	3.5(4)	<0.001	6.19	<1.77	6.01	13.24
6	3.1(3)	<0.001	5.48	<1.77	6.01	13.36
7	2.4(2)	<0.001	4.25	<1.77	6.00	13.46
8	1.5(2)	<0.001	2.65	<1.77	6.00	13.57
9	2.1(2)	<0.001	3.72	<1.77	5.99	13.68
10	3.8(4)	<0.001	6.72	<1.77	5.99	13.78
11	1.1(1)	<0.001	1.94	<1.77	5.99	13.88
12	0.7(1)	0.07(1)	1.24	123	5.98	13.98

Table S3. Pseudo-first-order rate constants for the N₂ adsorption/desorption on Ni₁₃⁺ clusters ($k_{(13,m)}$ and $k_{-(13,m+1)}$), related absolute rate constants ($k_{(13,m)}^{\text{abs}}$ and $k_{-(13,m+1)}^{\text{abs}}$) and calculated collision rates (k_L and k_{SCC}).

m	$k_{(13,m)}$ s ⁻¹	$k_{-(13,m+1)}$ s ⁻¹	$k_{(13,m)}^{\text{abs}}$ 10 ⁻¹⁰ cm ³ s ⁻¹	$k_{-(13,m+1)}^{\text{abs}}$ 10 ⁻¹³ cm ³ s ⁻¹	k_L 10 ⁻¹⁰ cm ³ s ⁻¹	k_{SCC} 10 ⁻¹⁰ cm ³ s ⁻¹
0	4.2(2)	<0.001	7.43	<1.77	6.00	13.60
1	4.2(2)	<0.001	7.43	<1.77	5.99	13.71
2	4.2(2)	<0.001	7.43	<1.77	5.99	13.81
3	4.4(2)	<0.001	7.78	<1.77	5.99	13.91
4	4.4(2)	<0.001	7.78	<1.77	5.98	14.01
5	4.5(2)	<0.001	7.96	<1.77	5.98	14.11
6	4.6(3)	<0.001	8.14	<1.77	5.98	14.20
7	4.6(3)	<0.001	8.14	<1.77	5.97	14.30
8	4.6(3)	<0.001	8.14	<1.77	5.97	14.39
9	4.3(2)	<0.001	7.61	<1.77	5.97	14.48
10	4.2(2)	<0.001	7.43	<1.77	5.97	14.57
11	4.4(2)	<0.001	7.78	<1.77	5.96	14.66

Spectrum of the (9,13) species in an extended frequency range

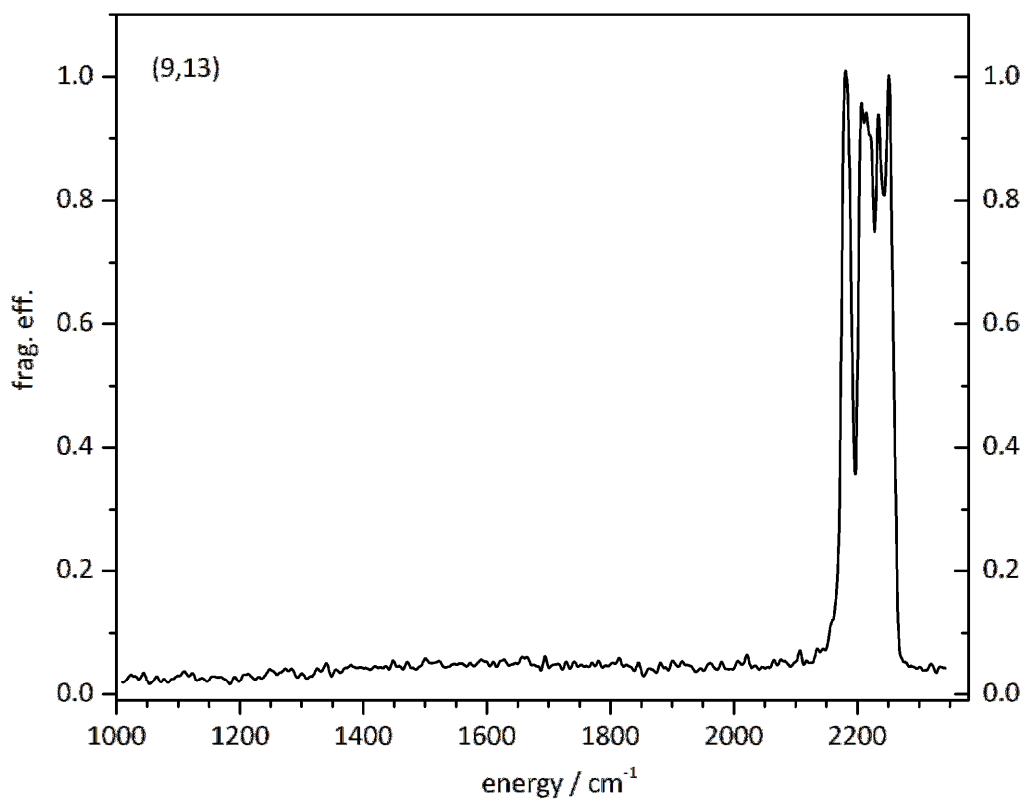


Figure S1. IR-MPD spectrum of the (9,13) species in an extended frequency range of 1010 - 2340 cm⁻¹. Note, that this spectrum has been recorded with increased laser power.

Computed geometries and relative energies for multiple local minimum structures for the naked Ni_9^+ cluster and relative stabilities for icosahedral Ni_{13}^+ clusters considering several spin states.

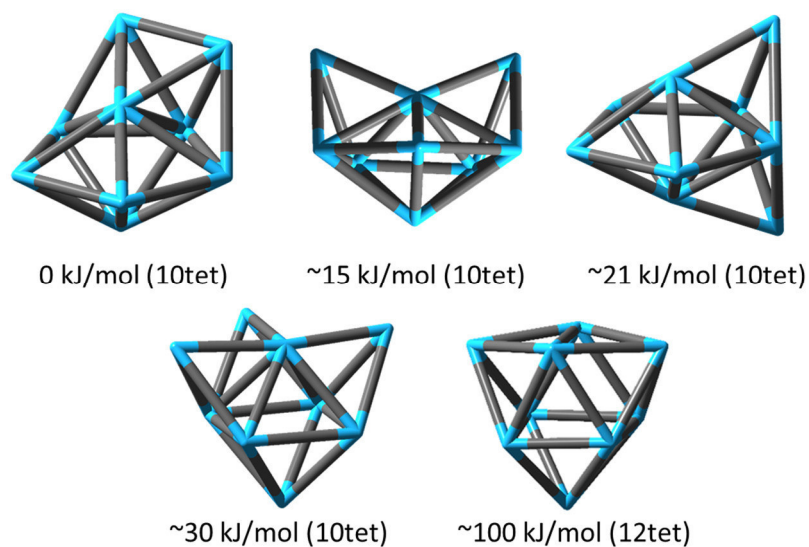


Figure S2: Computed geometries for Ni_9^+ and their relative stabilities. Note, that the stated values are given for the favoured spin multiplicity, respectively.

Table S4. Relative stabilities for computed icosahedral Ni_{13}^+ with variation of the spin multiplicity, $2S + 1 = 10-18$.

$2S+1$	rel. energy / kJ/mol
10	56
12	50
14	31
16	0
18	89

Possible adsorption positions on the tricapped octahedral Ni₉⁺ cluster core and relative stabilities with variation of the spin multiplicity

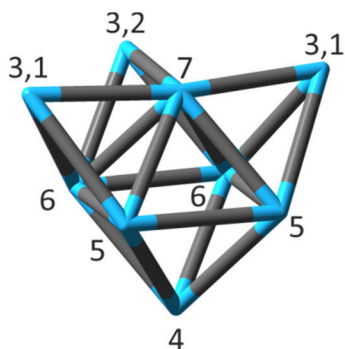


Figure S3: Tricapped octahedron with numbered adsorption positions. Note, that each number reflects the Ni-Ni coordination, respectively.

Table S5. Relative stabilities for the computed tricapped octahedral Ni₉⁺ cluster core upon the first N₂ adsorption with variation of the spin multiplicity and adsorption position.

position	2S+1	rel. energy / kJ/mol
3,1	6	23
	8	67
	10	5
	12	103
	14	168
3,2	6	75
	8	82
	10	0
	12	97
	14	139
4	6	22
	8	74
	10	16
	12	94
	14	205
5	6	22
	8	17
	10	10
	14	154
	6	6
8		57
10		15
12		74
14		189
7	6	138
	8	33
	10	22
	12	111
	14	187

Comparison of the experimental IR-PD spectrum of (9,2) and calculated IR absorption spectra for the assumed tricapped octahedral and bicapped pentagonal bipyramidal Ni₉⁺ motifs

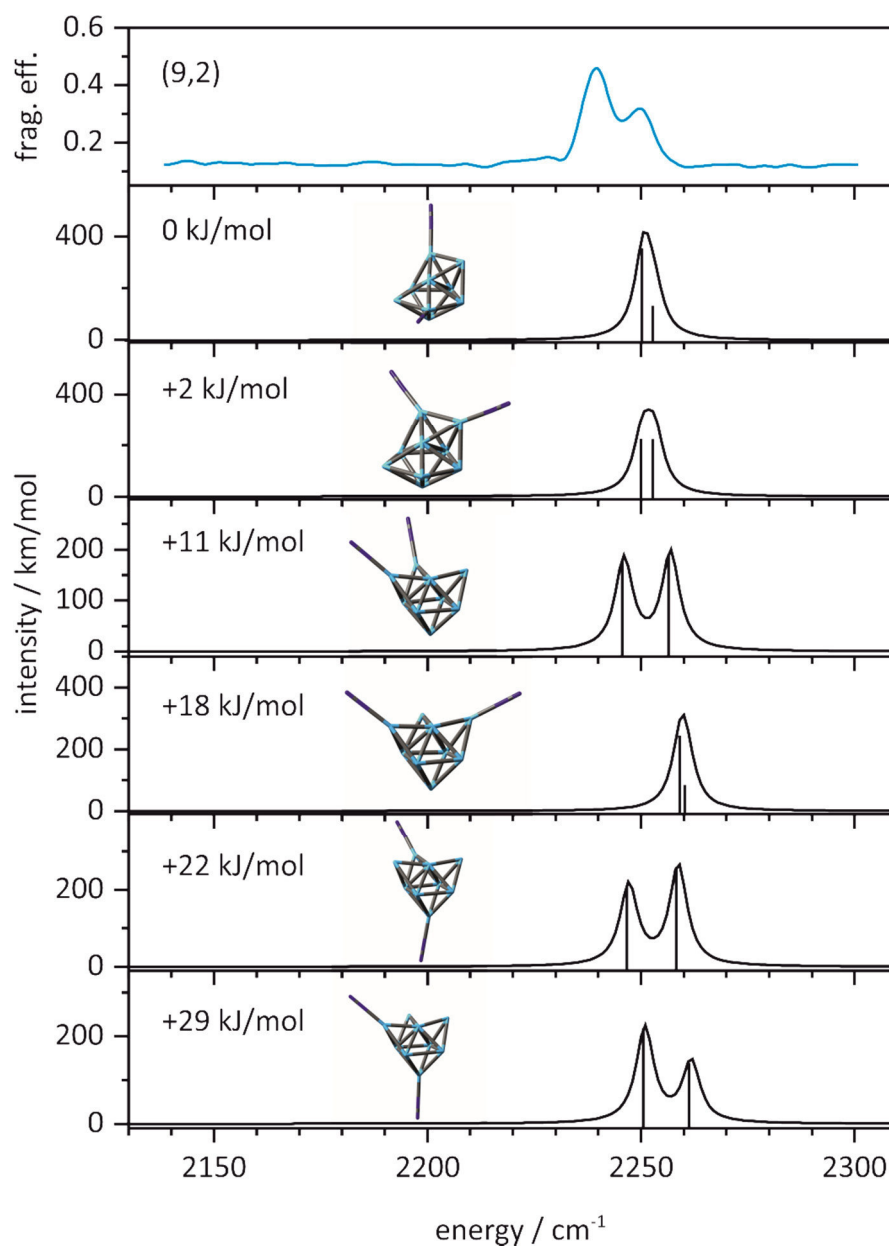


Figure S4. IR-PD spectrum of (9,2) (blue) and the calculated IR absorption spectra for the tricapped octahedral and bicapped pentagonal bipyramidal motifs with variation in the adsorbing Ni atoms (black; PBE0/ECP(Ni), cc-pVTZ(N), $2S + 1 = 10$). The calculated spectra are scaled by 0.93 and simulated using the gaussian profile of $\text{fwhm} = 5 \text{ cm}^{-1}$.

Comparison of the experimental IR-PD spectra of (9,m) ($m = 3,4,6,7$, and 10-13) and calculated IR absorption spectra for the assumed tricapped octahedral and bicapped pentagonal bipyramidal Ni_9^+ motifs

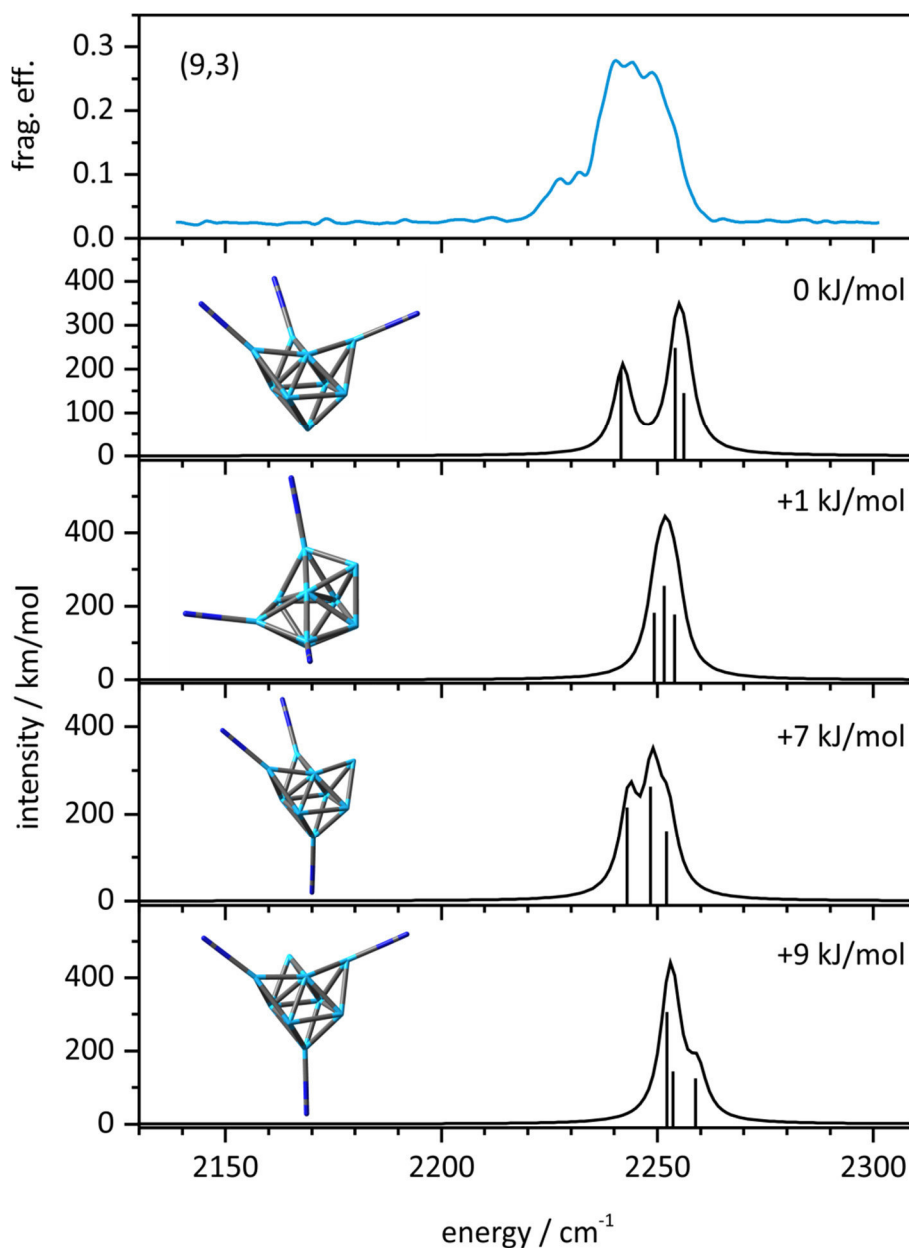


Figure S5. IR-PD spectrum of (9,3) (blue) and the calculated IR absorption spectra for the tricapped octahedral and bicapped pentagonal bipyramidal motifs with variation in the adsorbing Ni atoms (black; PBE0/ECP(Ni), cc-pVTZ(N), $2S + 1 = 10$). The calculated spectra are scaled by 0.93 and simulated using the gaussian profile of $fwhm = 5 \text{ cm}^{-1}$.

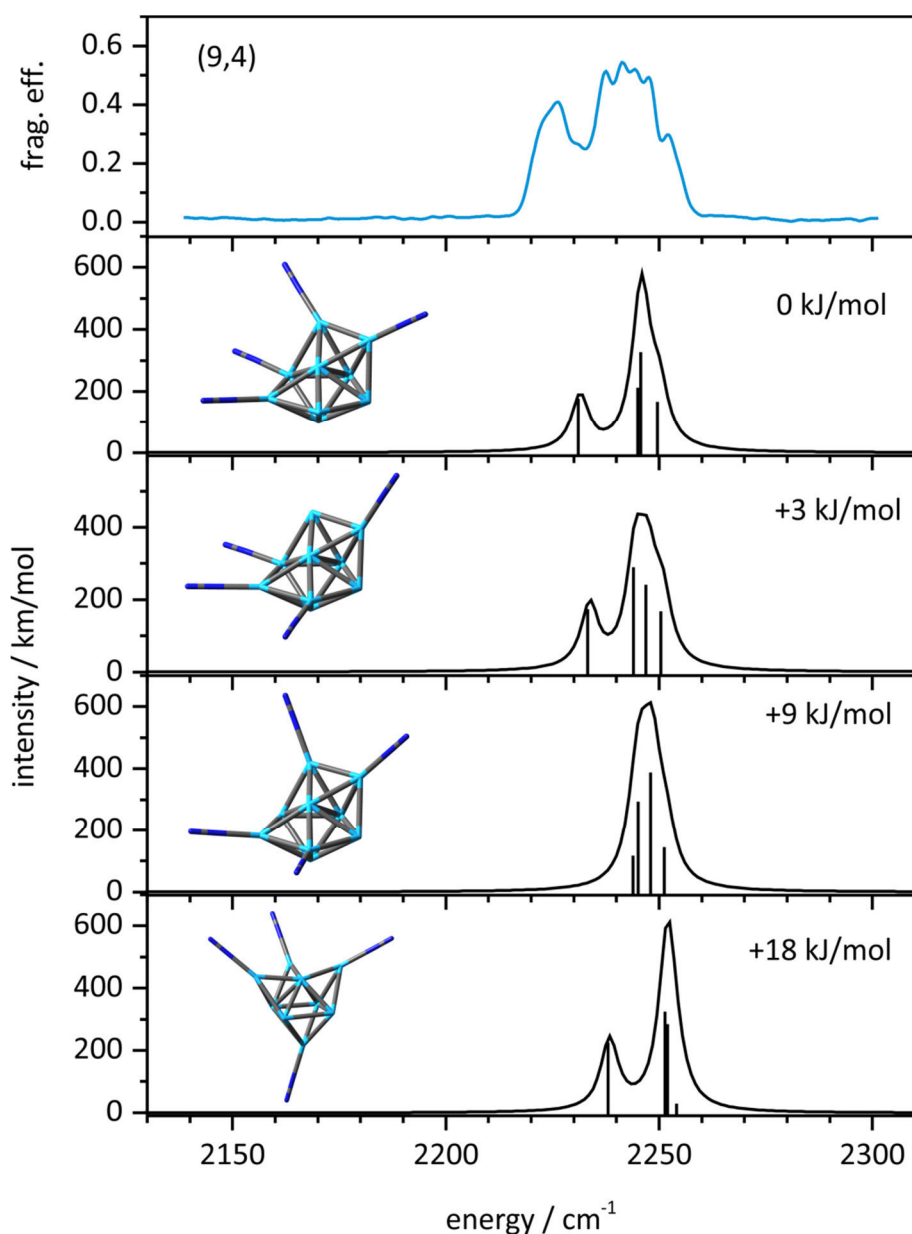


Figure S6. IR-PD spectrum of (9,4) (blue) and the calculated IR absorption spectra for the tricapped octahedral and bicapped pentagonal bipyramidal motifs with variation in the adsorbing Ni atoms (black; PBE0/ECP(Ni), cc-pVTZ(N), $2S + 1 = 10$). The calculated spectra are scaled by 0.93 and simulated using the gaussian profile of $\text{fwhm} = 5 \text{ cm}^{-1}$.

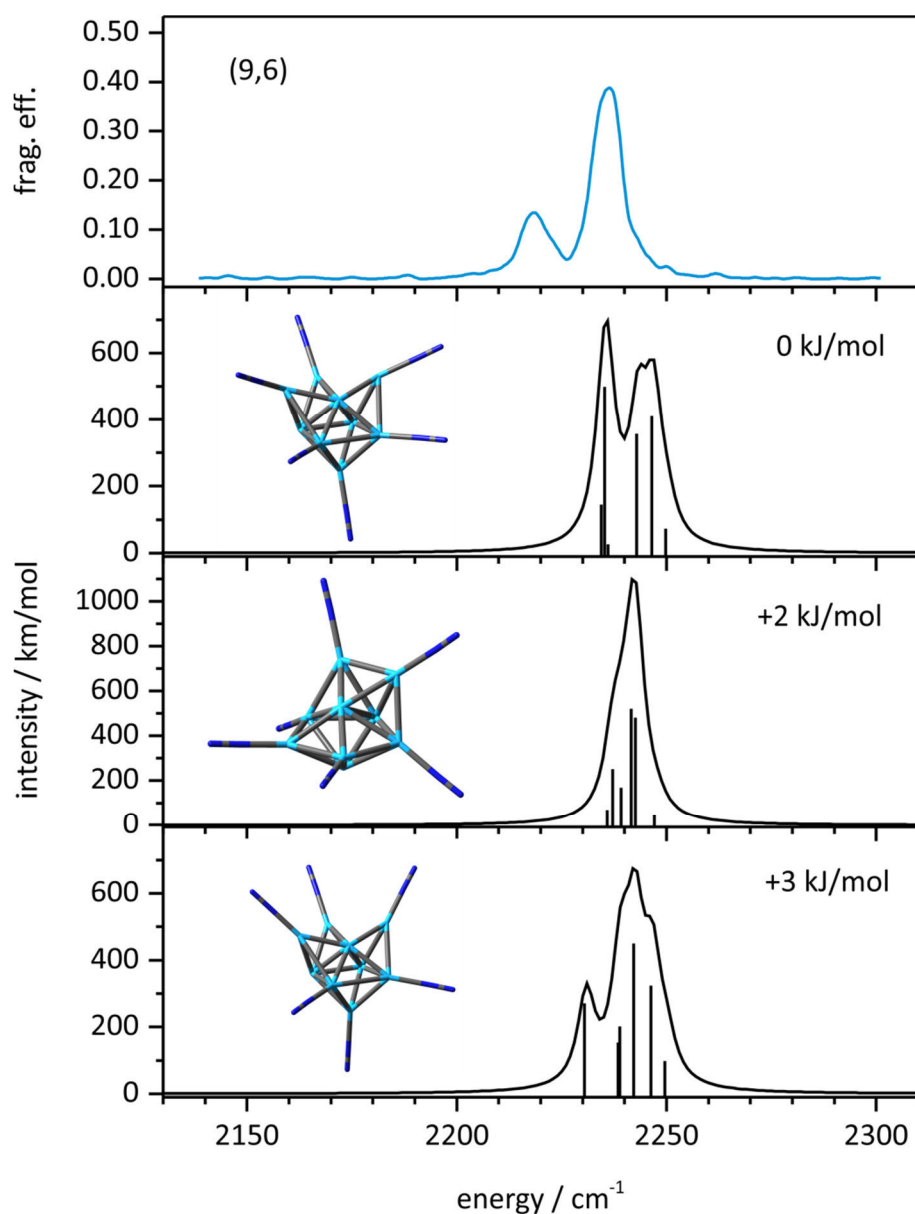


Figure S7. IR-PD spectrum of (9,6) (blue) and the calculated IR absorption spectra for the tricapped octahedral and bicapped pentagonal bipyramidal motifs with variation in the adsorbing Ni atoms (black; PBE0/ECP(Ni), cc-pVTZ(N), $2S + 1 = 10$). The calculated spectra are scaled by 0.93 and simulated using the gaussian profile of $\text{fwhm} = 5 \text{ cm}^{-1}$.

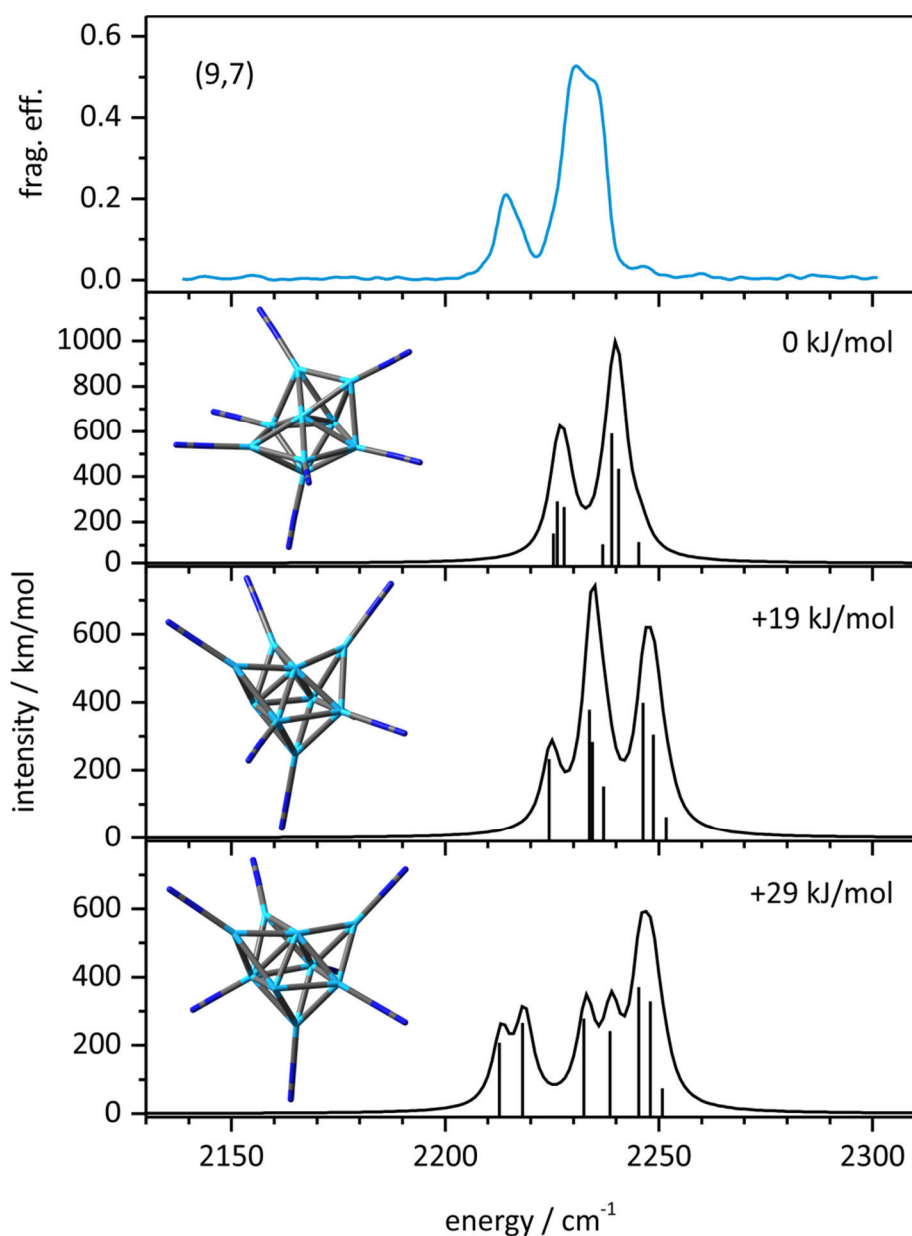


Figure S8. IR-PD spectrum of (9,7) (blue) and the calculated IR absorption spectra for the tricapped octahedral and bicapped pentagonal bipyramidal motifs with variation in the adsorbing Ni atoms (black; PBE0/ECP(Ni), cc-pVTZ(N), $2S + 1 = 10$). The calculated spectra are scaled by 0.93 and simulated using the gaussian profile of $\text{fwhm} = 5 \text{ cm}^{-1}$.

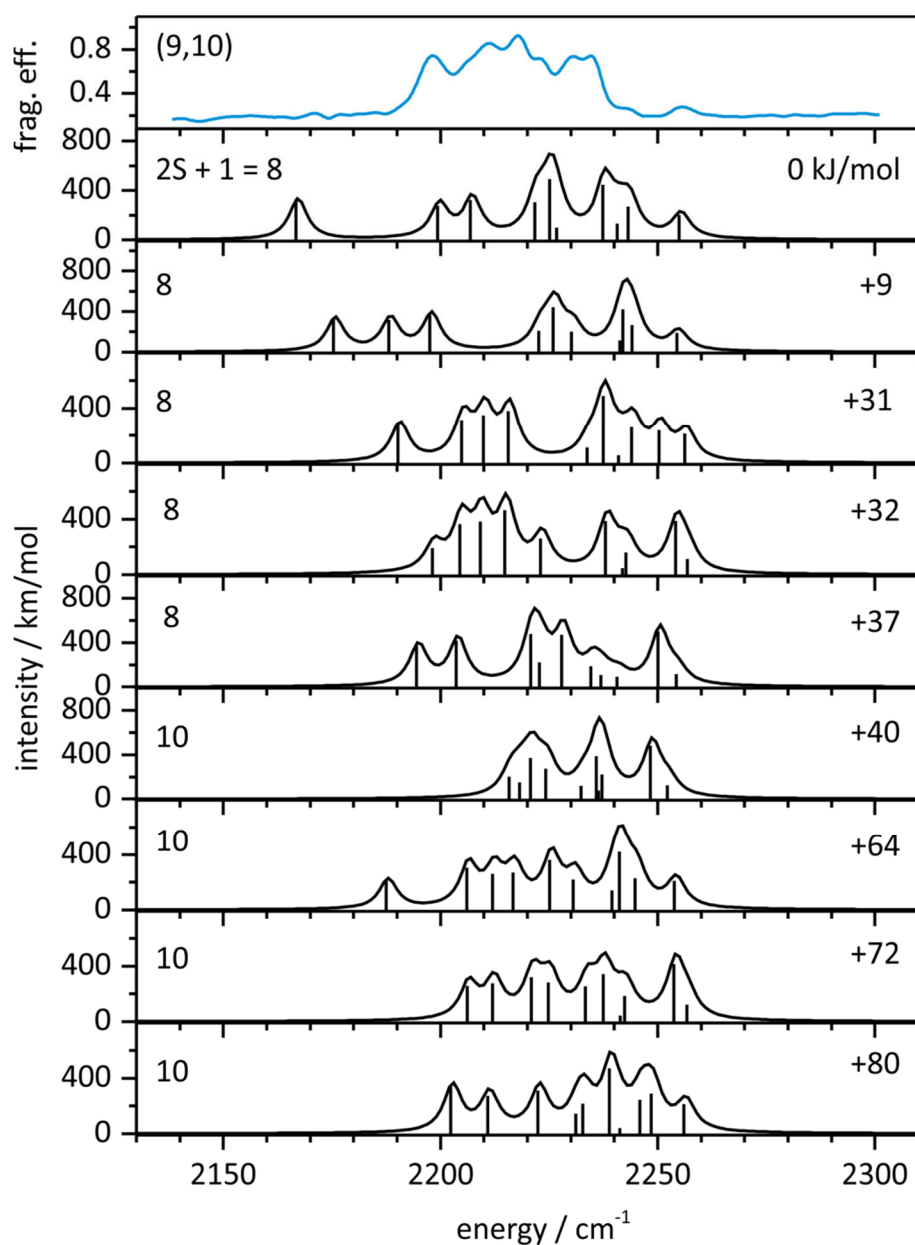


Figure S9. IR-PD spectrum of (9,10) (blue) and the calculated IR absorption spectra for the tricapped octahedral and bicapped pentagonal bipyramidal motifs with variation in the adsorbing Ni atoms and in spin multiplicities (black; PBE0/ECP(Ni), cc-pVTZ(N)). The calculated spectra are scaled by 0.93 and simulated using the gaussian profile of $\text{fwhm} = 5 \text{ cm}^{-1}$.

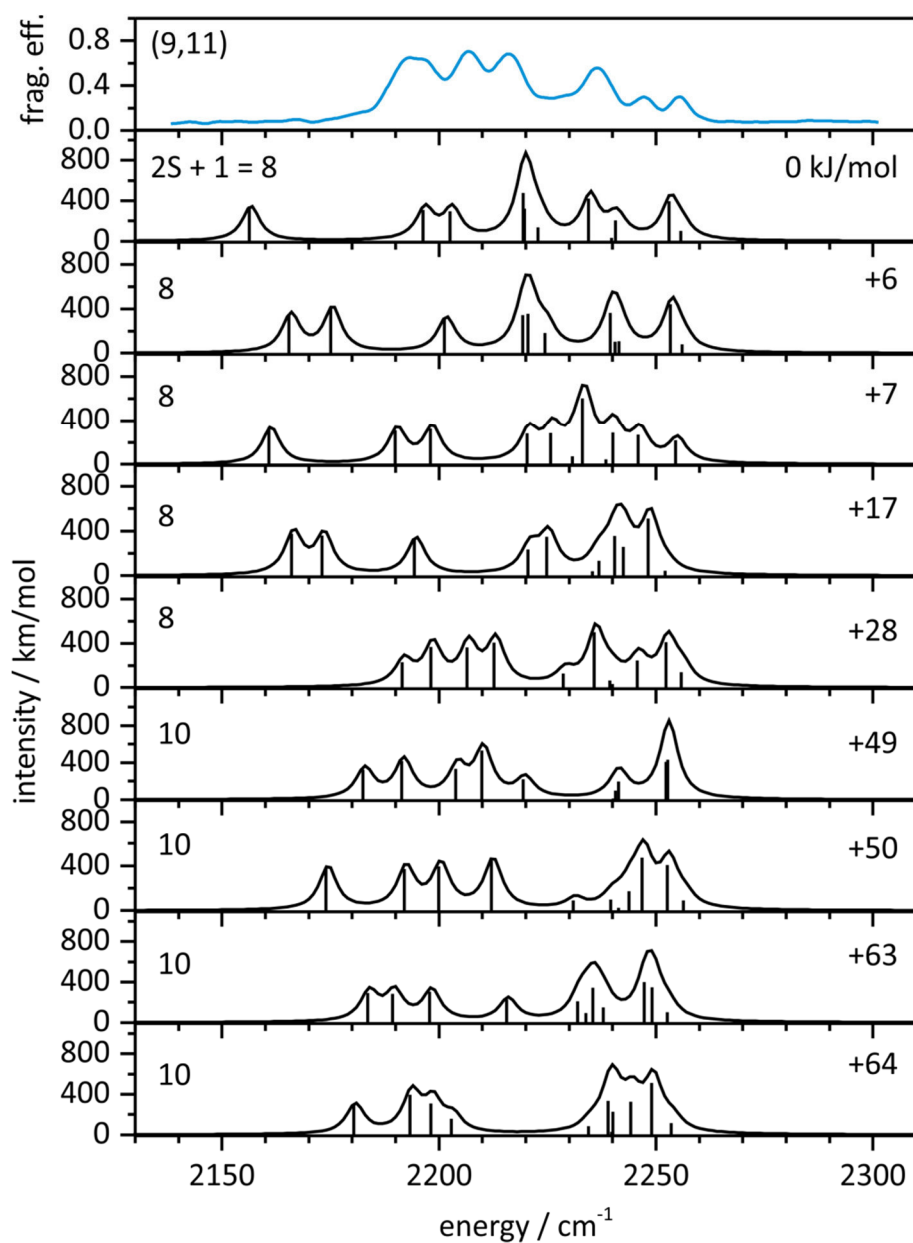


Figure S10. IR-PD spectrum of (9,11) (blue) and the calculated IR absorption spectra for the tricapped octahedral and bicapped pentagonal bipyramidal motifs with variation in the adsorbing Ni atoms and in spin multiplicities (black; PBE0/ECP(Ni), cc-pVTZ(N)). The calculated spectra are scaled by 0.93 and simulated using the gaussian profile of $\text{fwhm} = 5 \text{ cm}^{-1}$.

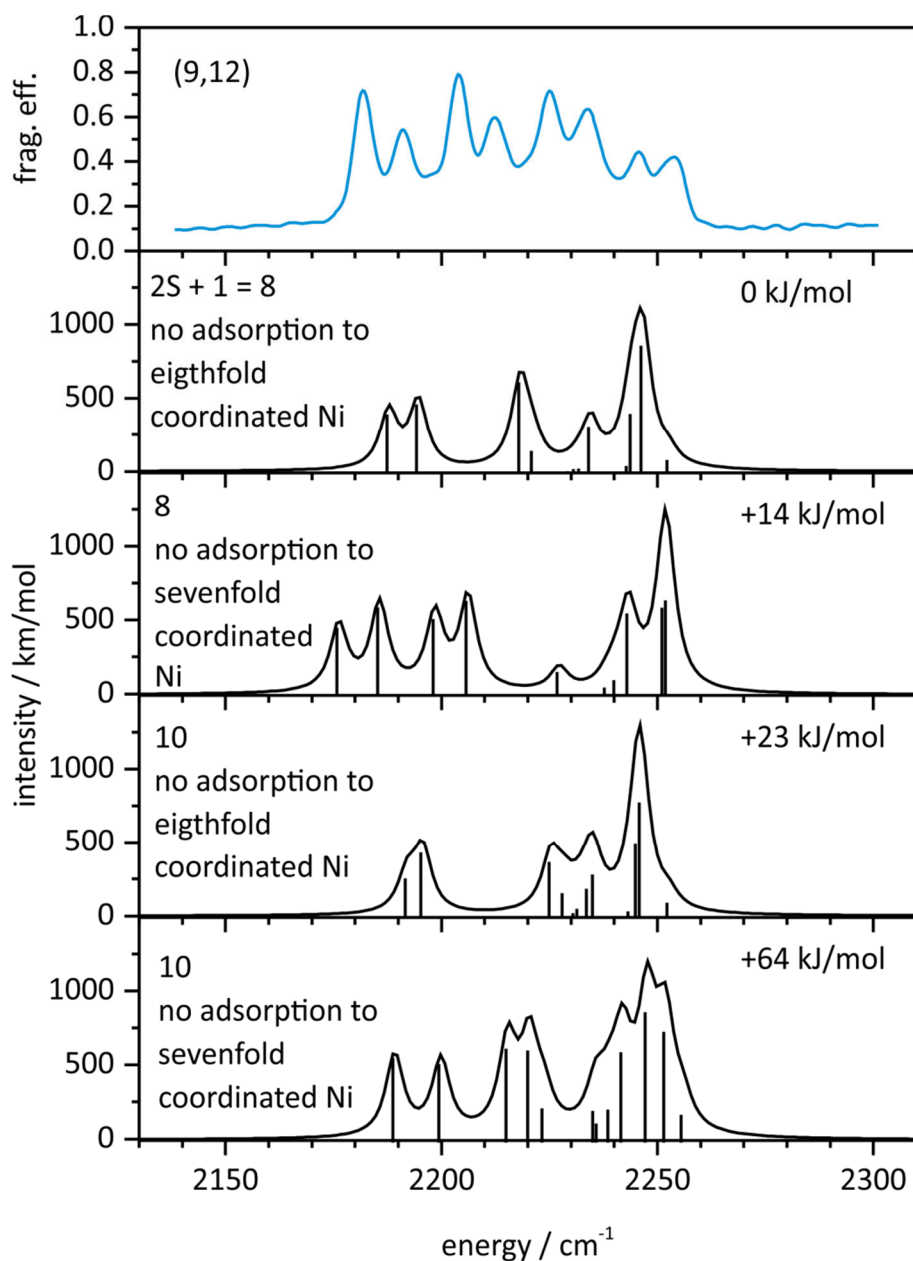


Figure S11. IR-PD spectrum of (9,12) (blue) and the calculated IR absorption spectra for the tricapped octahedral and bicapped pentagonal bipyramidal motifs with variation in the sole vacant Ni atom and in spin multiplicities (black; PBE0/ECP(Ni), cc-pVTZ(N)). The calculated spectra are scaled by 0.93 and simulated using the gaussian profile of $\text{fwhm} = 5 \text{ cm}^{-1}$.

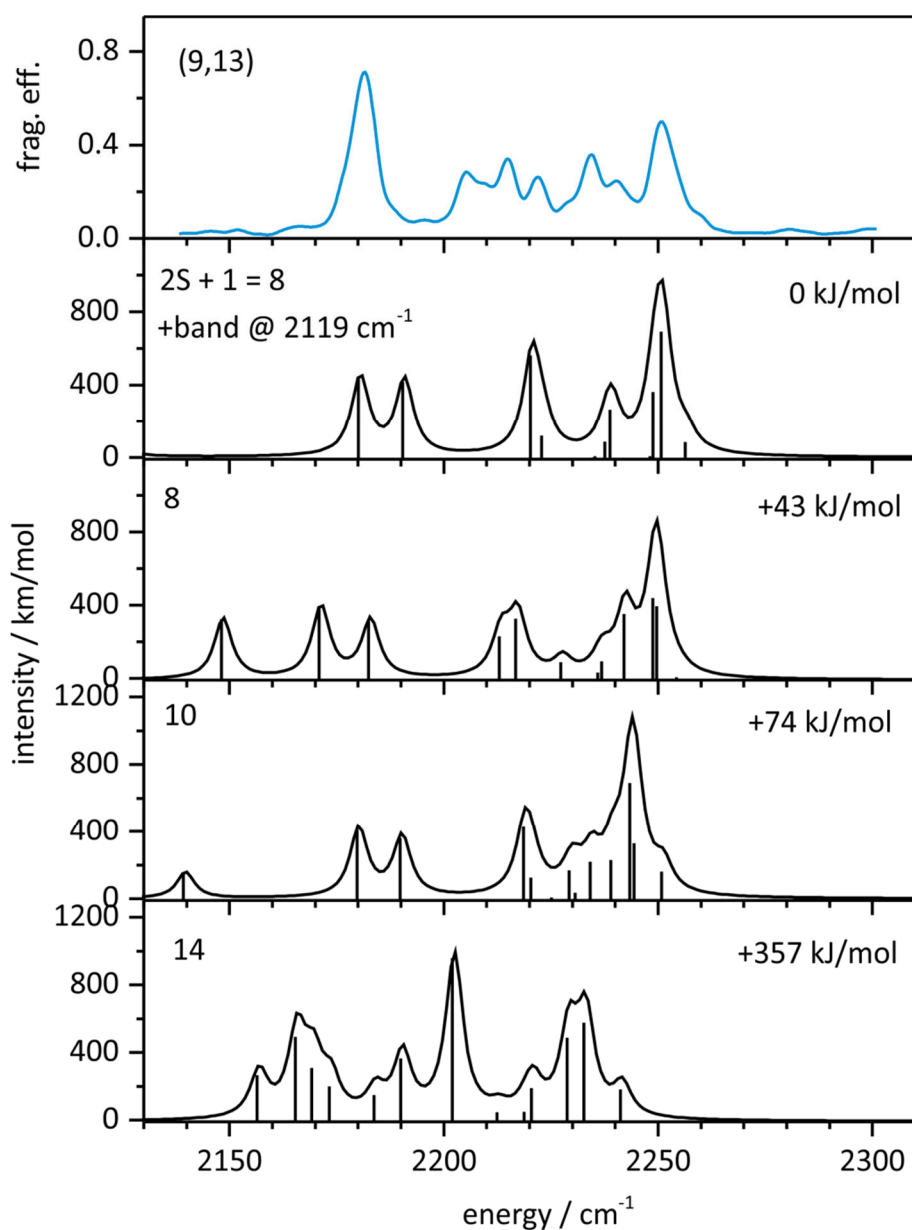


Figure S12. IR-PD spectrum of (9,13) (blue) and the calculated IR absorption spectra for the tricapped octahedral and bicapped pentagonal bipyramidal motifs with maximum N₂ adsorption as shown in Fig. 5 (black; PBE0/ECP(Ni), cc-pVTZ(N)). The calculated spectra are scaled by 0.93 and simulated using the gaussian profile of fwhm = 5 cm⁻¹.

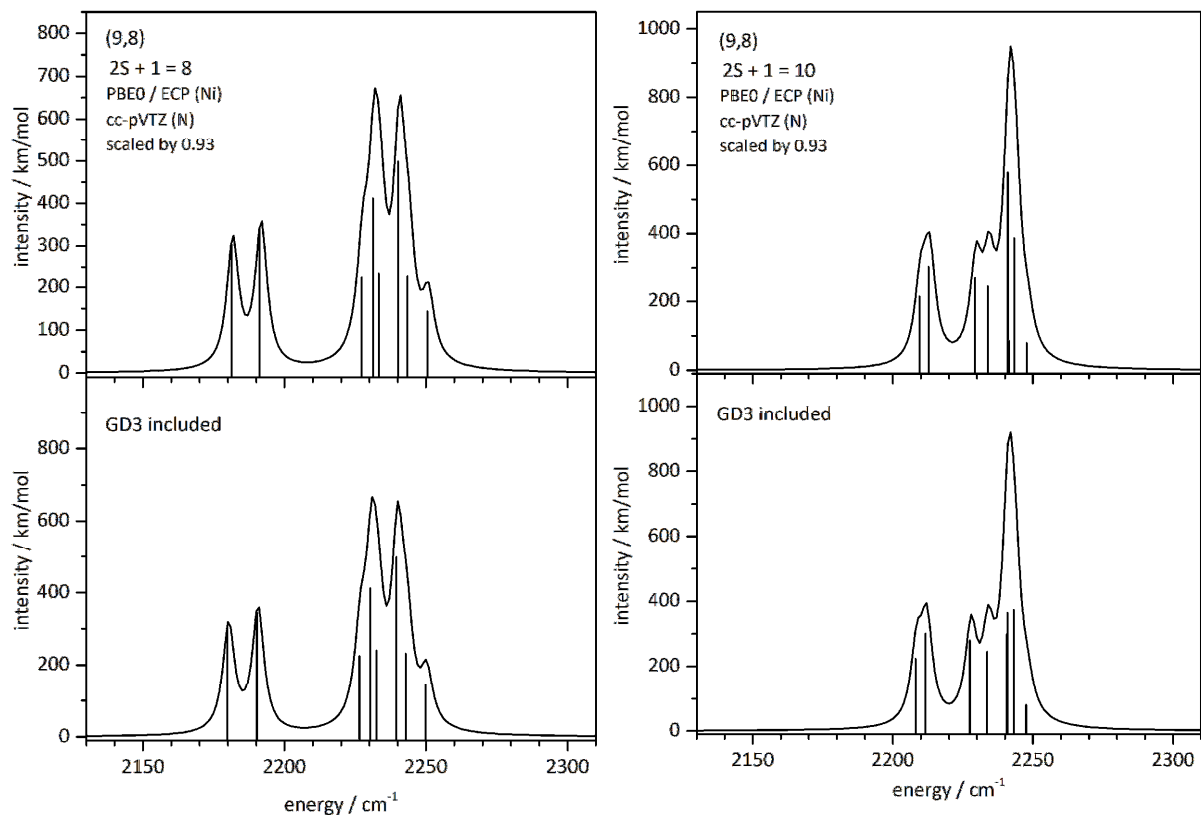
Calculated IR absorption spectra including the Grimme correction for dispersion with the original D3 damping function (GD3)

Figure S13. Calculated IR absorption spectra for the tricapped octahedral motif (top lanes) in comparison with calculated IR absorption spectra including the Grimme correction for dispersion with the original D3 damping function (bottom lanes) for (9,8) for the octet spin state (left) and the decet spin state (right). The calculated spectra are scaled by 0.93 and simulated using the gaussian profile of $fwhm = 5 \text{ cm}^{-1}$.

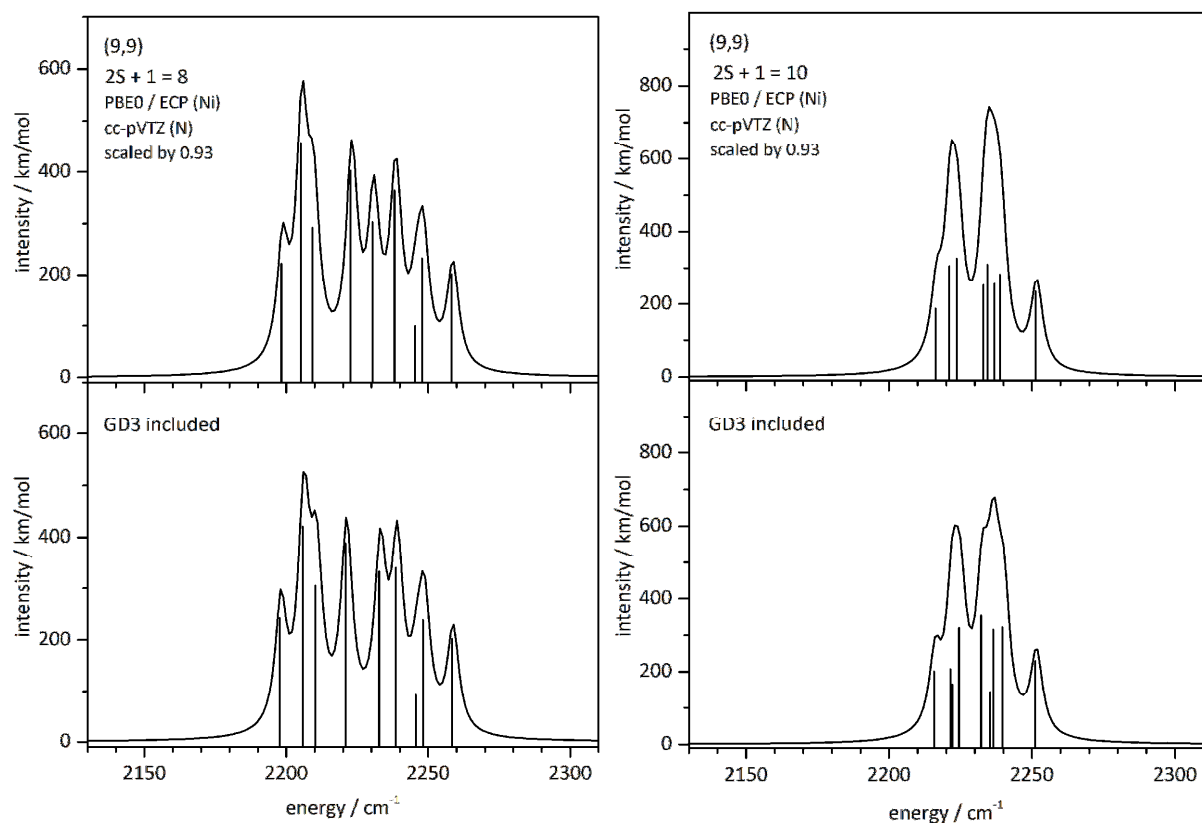


Figure S14. Calculated IR absorption spectra for the tricapped octahedral motif (top lanes) in comparison with calculated IR absorption spectra including the Grimme correction for dispersion with the original D3 damping function (bottom lanes) for (9,9) for the octet spin state (left) and the decet spin state (right). The calculated spectra are scaled by 0.93 and simulated using the gaussian profile of $\text{fwhm} = 5 \text{ cm}^{-1}$.

5 Probing Cluster Surface Morphology by Cryo Kinetics of N₂ on Cationic Nickel Clusters

Jennifer Mohrbach, Sebastian Dillinger, and Gereon Niedner-Schatteburg

Fachbereich Chemie und Forschungszentrum OPTIMAS

Technische Universität Kaiserslautern

67663 Kaiserslautern

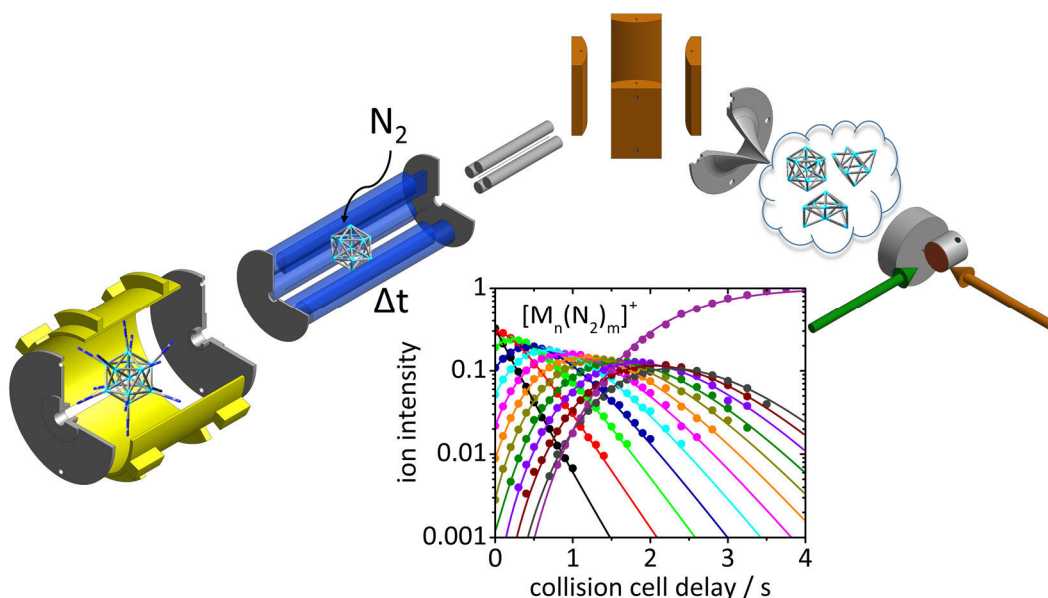
5.1 Preamble

The experiments were performed by the experimental team consisting of J. Mohrbach, and myself. The data evaluation was done by J. Mohrbach and myself. The initial manuscript was written by J. Mohrbach and revised by G. Niedner-Schatteburg and myself.

This manuscript has been **accepted** for publication in The Journal of Chemical Physics as part 1 of 2 of a back to back submission (for part 2 see chapter 6).

5.2 Abstract

We present the stepwise N₂ adsorption kinetics of size selected Ni_n⁺ (n =5-20) clusters at 26 K as obtained by a hybrid tandem ion trap instrument. Pseudo-first-order kinetic fits confirm consecutive adsorption steps without evidence of cluster isomers and up to adsorption limits, which scale with cluster size. The reaction rates for the initial N₂ adsorption increase smoothly with cluster size and similar to hard sphere cluster modelling. The isothermal kinetics allow for the tentative elucidation of cluster surface morphologies and for their classification into highly symmetrical clusters with all smooth surfaces, small clusters with rough surfaces, and large clusters with partially rough and smooth surface areas. The parallel characterization of the vibrational spectroscopy of some cluster adsorbate complexes supports and refines the achieved conclusions and is published back to back to this contribution. These two studies elucidate the adsorbate to cluster interaction, and they confirm and specify the sometimes considerable structural fluxionality of finite and curved metal surfaces in high detail. This work precedes further studies along the present lines of thought.



5.3 Introduction

Structure and adsorption dynamics of transition metal (TM) clusters have been subject of considerable research by experiments and computations alike. Such research is very involved. Reactivity studies of naked metal clusters provide a powerful approach towards cluster structure determination. The adsorption of weakly bound molecules to clusters is influenced by the coordination of the surface atoms, which in turn puts boundaries on conceivable overall cluster structures. In the context of CO adsorption on some transition metal clusters and of related carbonyl complexes it showed that adsorbates may well serve to titrate available surface sites up to saturation for the elucidation of underlying structural motifs.[1-5] Beyond mere adsorption to clusters and nanostructures, it is worthwhile to study and understand the relation of this and other diatomic molecules such as e.g. NO, N₂, and H₂ to corresponding bulk surfaces in general, driven by perspectives and challenges in heterogeneous catalysis.[6-8]

In particular the N₂ adsorption to Fe surfaces has been elucidated by angle resolved LEED studies in conjunction with potential surface modelling, pointing to α -N₂ and γ -N₂ motifs[9] which resemble η^2 side-on and η^1 end-on coordination of N₂ to multiple and single metal centers, respectively. Early adsorption studies of CO on Ni_n⁻ (n=3-10) clusters determined saturation limits,[10] and the results from those cluster reactions with N₂, O₂, CO₂ and N₂O were interpreted in terms of cluster structures by empirical many-body potential and by subsequent mol. dynamics (MD) simulations.[11] Collision induced dissociation (CID) studies of Ni_n⁺ (n=2-18) determined bond strengths and cohesion energies.[12] Butadiene dehydrogenation by Ni_n⁺ (n≤10) was found to be less efficient than by Pd_n⁺ or Pt_n⁺. [13] Kinetic studies of nickel cluster reactions with NO₂ revealed complex reaction mechanisms.[14] Hot kinetics of C₆₀ adsorption to Ni_n (n=2-72) revealed a size dependence consistent with C₆₀ adsorption on essentially spherical Ni_n clusters without any evidence for C₆₀ decomposition.[15] Methanol undergoes chemisorption, demethanation, and carbide formation by Ni_n⁺ (n=3-11), which was found to change dramatically with cluster size,[16] and the total reactivity to anti-correlate to the HOMO-LUMO gap.[17] Exposure of isolated Ni_n⁺ (n=3-11) cluster cations to benzene revealed vivid acetylene formation.[16] Multistep reactions of Ni_n⁺ (n=2-29) with O₂ revealed a selective formation of the nickel suboxides Ni₁₃O₈⁺ and Ni₁₆O₁₀⁺. [18] Structural, magnetic and adsorption properties of Ni_n (n=2-

16, 21, 55) by DFT calculations with the Perdew-Burke-Ernzerhof (PBE) functional elucidated the most stable isomers and their CH₄ adsorption into "on top" sites to be understood in terms of the electronic stability and localization of the frontier MO's.[19] Chemical probe experiments helped to elucidate structural motifs of Ni_n and Co_n clusters (n = 50-200), using ammonia and water as chemical probe molecules.[20, 21] The uptake of molecular nitrogen to small Ni_n clusters (n = 3-28, 49-71) helped to propose structures for bare clusters as well as for fully nitrogenated clusters.[22-24]

We have performed kinetic studies of hydrocarbon activation on charged TM clusters,[25] and we have introduced X-ray studies by cryo ion trapping for the investigation of spin and orbital contributions to the magnetic moments of TM clusters.[26, 27] Our tandem cryo ion trap instrument[28] enabled us to focus on the vibrational spectroscopy of N₂ adsorbates on size selected TM clusters under isothermal cryo conditions, first results on [Co_n(N₂)₁]⁺ (n = 8 – 17) clusters, and on [Ni_n(N₂)_m]⁺ (n = 9, 13; m = 0 - 13) clusters being published.[29, 30]

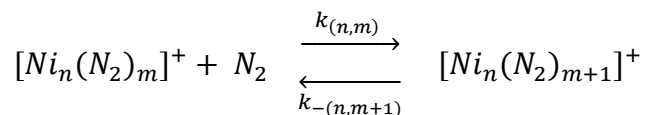
This study aims to elucidate N₂ adsorption onto cationic nickel clusters [Ni_n(N₂)_m]⁺ (n = 5-20) by kinetics investigation, and it obtains strong support of its findings through our adjoined infrared cryo spectroscopic study[31], which we will reference in the following as [SD], while we refer to the present kinetic study as [JM]. We aim to gain insight into the metal-adsorbate bonding and to unravel structure-reactivity relationships.

5.4 Experimental and Computational Methods

A customized Fourier Transform-Ion Cyclotron Resonance (FT-ICR) mass spectrometer (Apex Ultra Bruker Daltonics) served to perform the cluster production, isolation, N₂ condensation and mass analysis. A detailed description has been given before.[30] In brief: The nickel clusters were generated using a home-built laser vaporization cluster ion source as described before.[32, 33] Nickel atoms are evaporated from a rotating 0.4 mm thick isotopically enriched Ni foil (99,61%, Oak Ridge National Laboratories) by the second harmonic of a pulsed Nd:YAG laser (Innolas *Spotlight 300*, 20 Hz). The hot plasma is captured by a He gas pulse (40 μs, 15 bar) created by a homebuilt piezoelectric valve[34] and expanded into vacuum (10⁻⁷ mbar). The mass selected clusters are injected into a cryogenic hexapole ion trap. The ion trap is cooled to 26 K by a closed cycle He cryostat. Buffer and

reaction gas are introduced continuously. Sufficient nitrogen attachment is achieved by increasing the pressure in the ion trap from 1×10^{-7} mbar up to 4.5×10^{-7} mbar. Additional He is introduced to accomplish an efficient trapping and cooling of the ions ($\sim 5 \times 10^{-6}$ mbar). After storing the mass-selected ions for a variable time (0-30 s), the manipulated ions of the form $[\text{Ni}_n(\text{N}_2)_m]^+ = (n,m)$ are guided by electrostatic lenses into the FT-ICR cell of the so-called “infinity” type.[35] The ICR cell is held at temperatures below 10 K with a closed cycle He cryostat to prevent heating of the clusters by black body radiation prior to ion detection.

The ICR cell serves for the detection of the formed $[\text{Ni}_n(\text{N}_2)_m]^+ = (n,m)$ cluster adsorbate complexes. The kinetic curves of cationic nickel clusters and their nitrogen adducts originate from reaction delay scans and subsequent evaluation of the recorded mass spectra. Fits to pseudo-first-order-kinetics occur through the “evofit” program.[36] Our thus determined rate constants for the (n,m) species (recorded at various pressures $p(\text{N}_2) = 1.1 - 3.5 \times 10^{-7}$ mbar) are normalized to the experimental conditions for the $(13,m)$ species (recorded at $p(\text{N}_2) = 1.3 \times 10^{-7}$ mbar). Fitting the experimental kinetics implies the quantitative determination of relative rate constants for N₂ adsorption $k_{(n,m)}$ for each step $m \rightarrow m+1$, and for N₂ desorption $k_{-(n,m+1)}$ for each step $m+1 \rightarrow m$ alike:



The relative rate constants $k_{(n,m)}$ determine the absolute rate constants $k_{(n,m)}^{abs}$, the absolute collision gas number densities $\rho_{\text{N}_2}(T)$ serving as the conversion factor:

$$k_{(n,m)}^{abs} = k_{(n,m)} / \rho_{\text{N}_2}(T)$$

We obtain approximate values for $\rho_{\text{N}_2}(T)$ indirectly from the pressure in the surrounding chamber $p_c^{(300\text{ K})}$ and an effective geometry factor c_{app} :

$$\rho_{\text{N}_2}(26\text{ K}) = \frac{c_{app} p_c^{300\text{ K}}}{k_B T_{300\text{ K}}}$$

The geometry factor c_{app} shows to bear a significant dependence on the temperature of the hexapole ion trap. By numerous kinetic studies of transition metal cluster cations with neutral reactants at cryogenic temperatures we evaluated this factor c_{app} to 1.8 ± 0.4 at 26 K with a net uncertainty of $\pm 50\%$.

The classical Langevin collision rate of ions with neutrals[37] is conveniently extended towards polar molecules by the average dipole orientation theory (ADO).[38, 39] The ADO theory gives the theoretical limit of the absolute rate constants, the collision rate k^{ADO} , based on a classical trajectory of a linear dipole in the field of a point charge:

$$k^{ADO} = \frac{q}{2\varepsilon_0\sqrt{\mu}} \left(\sqrt{\alpha} + c\mu_D \sqrt{\frac{2}{\pi k_B T}} \right)$$

μ is the reduced mass (of the cluster adsorbate complex), α is the polarizability and μ_D is the dipole moment (in Debye). The parameter c lies between 0 and 1, and can be expressed by the polarizability volume α' and the molecular dipole moment μ_D – the latter vanishing in the present case of N₂. [40]

This ADO theory is frequently utilized to estimate the reaction rates of charged clusters with small molecules, knowingly underestimating the reaction rates for charged metal clusters significantly.[41, 42] Kummerlöwe and Beyer introduced two more models for the collision rates of ionic clusters with neutral molecules, the HSA model (hard sphere average dipole orientation) and the surface charge capture (SCC) model.[43] In both models, the cluster and the neutral reaction partner are treated as hard spheres, and the charge is treated as either fixed or mobile point charge. For the HSA collision rate k^{HSA} , the charge is located fixed in the center of the cluster, while in the SCC model (k^{SCC}), the mobile charge is drawn to the cluster surface by the attractive interaction with the neutral collision partner.

5.5 Results and Discussion

We investigated the stored $[\text{Ni}_n(\text{N}_2)_m]^+ = (n,m)$ clusters for their N₂ adsorption in the cryogenic hexapole under isothermal conditions at 26 K. In general, we observe two different adsorption behaviors – reminiscent of the two show-cases Ni₉⁺ and Ni₁₃⁺ that we have discussed before.[30] The mass spectra of all detected Ni_n⁺ clusters reveal a successive gain of 28 m/z, which does indicate the stepwise adsorption of molecular nitrogen in consecutive chains of individual adsorption processes (see Fig. S1 in the supplementary material). In all investigated cases ($n = 5 - 20$) stepwise N₂ uptake reaches a strict adsorption limit m_{max} within $t < 12$ sec, and this does not increase further up to $t < 30$ sec. In some cases we observe the N₂ adsorption limit preceded by one or more additional intermittent

adsorption limits, which do not suppress further adsorption but cause some retardation. In the other cases we observe a sole N₂ adsorption limit without any intermittent adsorption limit or retardation. This behavior is representative for rough and smooth cluster surfaces, respectively.

Adsorption limits at 26 Kelvin

Visual inspection of recorded mass spectra suffices to identify adsorption limits (filled circles in Fig. 1) and intermittent adsorption limits (green stars in Fig. 1) as well.

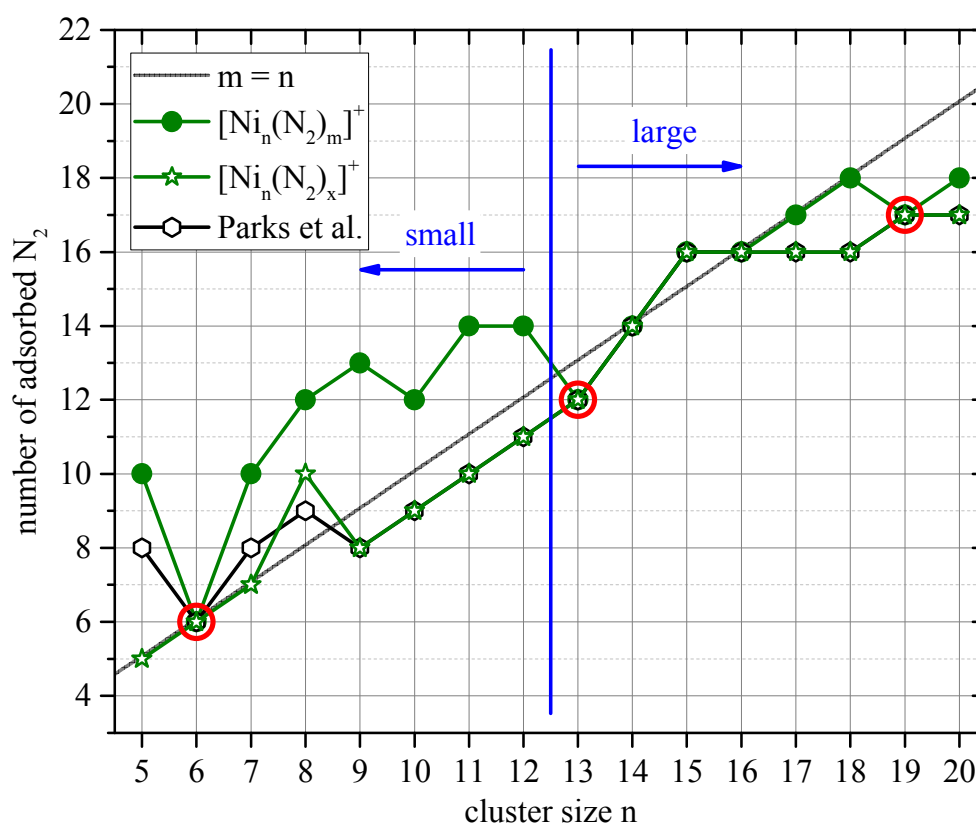


Figure 1 Recorded adsorption limits m_{\max} (filled circles) and most intense intermittent adsorption limits m_x (stars) of N₂ adsorption to cationic nickel clusters Ni_n⁺, $n = 5 - 20$ in comparison to N₂ uptake “plateaus” of neutral nickel clusters¹⁹⁻²⁰ (black hexagons). Each mass-selected Ni_n⁺ cluster was stored for up to 30 s – saturation typically reached much before. Highly symmetrical clusters are marked in red, size ranges indicated in blue.

They may serve as initial guidelines for some elucidation of cluster surface morphology that receive subsequent verification by our kinetic studies (chapter 3.2) and our IR spectroscopic studies (see [SD]). The mass spectra reveal stoichiometries which show, that

Ni_n⁺ clusters tend to adsorb N₂ close to an equal atom-N₂-ratio ($n = m$), which correlates with single N₂ head-on adsorption to each cluster surface atom. In this regard, we identify two size ranges of small clusters ($n < 13$) and large clusters ($n \geq 13$) as indicated in Fig. 1. Small clusters exceed the 1:1 ratio, likely by geminal adsorption to low coordinated surface atoms, yielding a 1:2 ratio for such fourfold or less coordinated Ni atoms - the $n = 6$ cluster being exceptional by smoothly adsorbing six N₂ molecules up to a mere 1:1 ratio. Large clusters of the size $13 \leq n \leq 16$ and $n = 19$ do not form pronounced intermittent adsorption limits either, indicative for smooth cluster surfaces. An intermittent adsorption limit close to the adsorption limit is observed for $n = 17, 18$ and 20 - likely due to one or two exposed surface atoms, e.g. capping atoms, which accept a second N₂ adsorbate, but reluctantly. The clusters $n = 6, 13,$ and 19 stick out by low and smooth N₂ uptake without intermittent delay. Such double (geminal) occupation of low coordinated Ni surface sites was proposed before[44, 45] for N₂ adsorption on neutral Ni clusters at flow reactor conditions (according adsorption limits indicated as open hexagon symbols in Fig. 1).

Kinetics of small Nickel clusters: Ni₅⁺ – Ni₁₂⁺

We further investigated in more detail the stepwise N₂ adsorption on Ni_n⁺ clusters by explicitly recording their reaction kinetics when trapped under isothermal cryo buffer gas conditions, and we performed pseudo-first-order kinetic fits to the experimental data by our genetic algorithm routine. The obtained fits confirm consecutive adsorption steps (Fig.s 2-5). All Ni_n⁺ clusters decay mono exponentially without any indication of a second component. This, and the overall superior quality of all fits, entitles us to fit each consecutive step by a single rate constant throughout. Some fits require significant backward reaction in cases of high N₂ coverages, which indicates swift N₂ desorption (see the supplementary information for details on the corresponding rate constants $k_{(n,m)}$).

Small nickel clusters Ni_n⁺ in the range of $n = 5 - 12$ exhibit a large variety with respect to the values of their stepwise rate constants $k_{(n,m)}$, their adsorption limits m_{max} , and their intermittent adsorption limits m_x . These findings are characteristic for rough cluster morphologies. Such clusters provide a variety of unique surface atoms, likely by low Ni-Ni coordination. There is no significant backward reaction for the adsorption steps of $n = 5 - 8$. All clusters reveal a strict adsorption limit at $m \geq n$ (*cf.* Fig. 2).

5. Probing Cluster Surface Morphology by Cryo Kinetics of N₂ on Cationic Nickel Clusters

In the case of (5,m) the recorded kinetic curves clearly reveal the intermittent adsorption limit at (5,5) and the adsorption limit at (5,10) (see Fig. 2, top left). A structure with only fourfold or less coordinated Ni atoms would explain the intermittent adsorption limit by single N₂ adsorption on each Ni atom as well as the adsorption limit (of $m = 2n$) by the adsorption of a second N₂ molecule, respectively. The trigonal bipyramid or a square pyramid—exclusively possessing three- and fourfold coordinated Ni atoms—would represent the most likely structures for Ni₅⁺.

Inspection of the detailed kinetic curves of (6,m) confirm the exceptional status of $n = 6$ as deduced from the adsorption limits (*cf.* Fig. 2 top right). The smooth N₂ adsorption kinetics on (6,m) clusters is indicative for a highly symmetrical structure of six equally coordinated surface atoms. The Ni₆⁺ cluster has most likely an octahedral structure. By merely adsorbing a single N₂ molecule on each Ni atom, the cluster adsorbate complex would retain its symmetry. This finding is corroborated by our spectroscopic studies as documented in [SD].

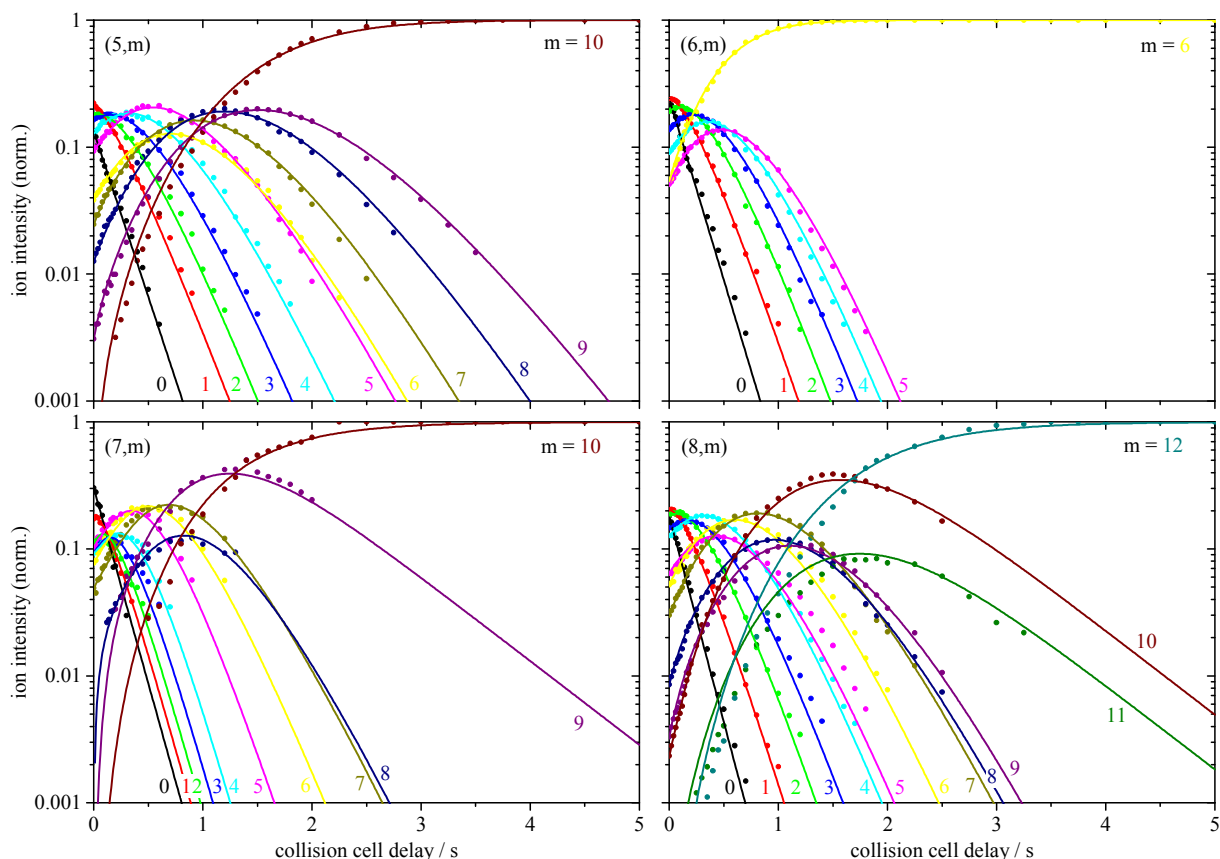


Figure 2. Isothermal kinetics of the stepwise N₂ adsorption by isolated Ni_n⁺ clusters ($n = 5-8$) within 26 Kelvin He buffer gas and 3.0×10^{-7} mbar of N₂ (solid points). The pseudo-first-order kinetic fits (solid lines) reveal reaction chains of up to 12 consecutive steps.

In the case of (7,m) the kinetics confirm the intermittent adsorption limits at (7,7), and the adsorption limit at (7,10). Single binding to all Ni atoms and the adsorption of a second N₂ molecule by three Ni atoms would result in dominant (7,7) and (7,10) species. The capped octahedron would be the most likely structure for Ni₇⁺, having a single threefold coordinated Ni capping atom. At this point we cannot exclude, however, a structural change of the cluster geometry upon N₂ adsorptions substantiated by the spectroscopic studies of [SD].

In the case of (8,m) the pattern of recorded kinetic curves is much involved. Each step seems unique, and the extracted rate constants vary (cf. Fig. S3 bottom right and Table S1 in the supplementary material) such that $k_{(8,4)}$, $k_{(8,7)}$, and $k_{(8,10)}$ are somewhat smaller than others which nicely corresponds to the intermittent maxima of the corresponding kinetic curves (Fig. 2, bottom right). In this case, we thus observe several intermittent adsorption limits at (8,4), (8,7) and (8,10), and the adsorption limit at (8,12). A structure with four atoms of low coordination could cause a first intermittent limit at (8,4). Note, that this cluster is the smallest one to reveal an intermittent limit at $m = n-1$. This indicates the presence of a highly coordinated Ni atom which adsorbs N₂ less swiftly than a low coordinated Ni site able to accept a second N₂ adsorbate. Single binding to all Ni atoms but the highest coordinated Ni atom and the adsorption of a second N₂ molecule by four Ni atoms would result in dominant (8,7) and (8,12) species. Reflecting all of these details we suggest likely structures of Ni₈⁺: Either a bicapped octahedron (providing for two threefold, two fourfold, two fivefold and two sixfold coordinated Ni atoms) or a capped pentagonal bipyramid (providing for one threefold, three fourfold, three fivefold and one sixfold coordinated Ni atoms) or isomeric mixtures of both. Both structures would explain the intermittent limit at (8,4) by adsorption of one N₂ to the three- and fourfold coordinated Ni atoms. Only the capped pentagonal bipyramid would explain the intermittent limit at (8,7) by adsorption of one N₂ to all Ni atoms except the sixfold coordinated one, and only the capped octahedron would explain the intermittent limit at (8,10) by adsorption of one N₂ to every Ni atom except the highest coordinated one and a second N₂ to the three- and fourfold coordinated ones. Therefore we do not make a final assignment based only on the kinetic data. Note that an octahedral structure is clearly supported by the kinetics of (6,6), and a monocapped octahedron structure in (7,10) by the spectroscopic data of [SD]. As the exceptional behavior of Ni₁₃⁺ suggests icosahedral motifs, a transition towards pentagonal motifs likely sets in at some

5. Probing Cluster Surface Morphology by Cryo Kinetics of N₂ on Cationic Nickel Clusters

cluster size, which might well be the Ni₈⁺ case. It is well possible that an adsorbate induced reorganization takes place upon N₂ saturation – in any case turning a rough cluster surface into another rough one.

The kinetics of clusters with more than eight Ni atoms ($n = 9 - 12$) require fits which include significant backward reactions for the last adsorption steps. This finding reveals the presence of one or more weakly bound N₂ adsorbate upon saturation (*cf.* Fig. 3).

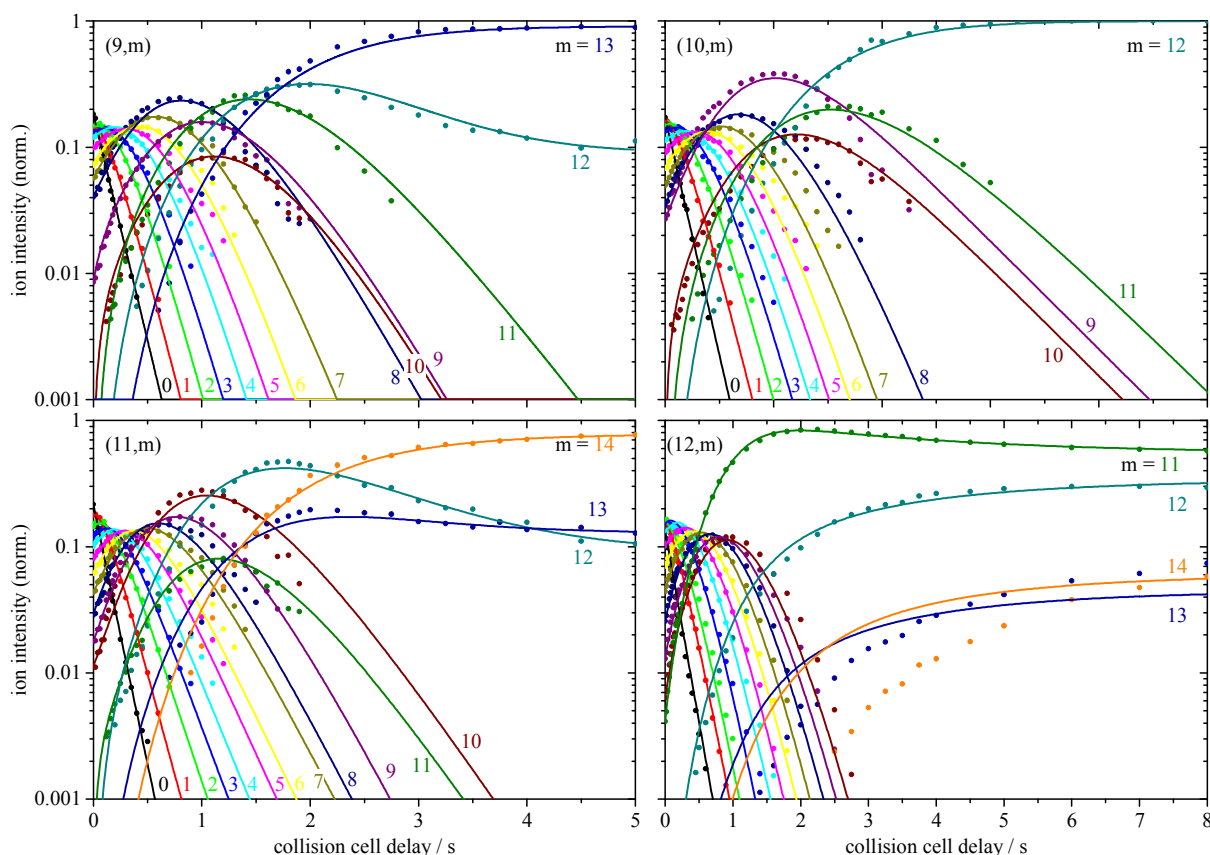


Figure 3. Isothermal kinetics of the stepwise N₂ adsorption by isolated Ni_n⁺ clusters ($n = 9-12$) within 26 Kelvin He buffer gas and 3.0×10^{-7} mbar of N₂ ($n = 12$: $p(\text{N}_2) = 3.2 \times 10^{-7}$ mbar) (solid points). The pseudo-first-order kinetic fits (solid lines) reveal reaction chains of up to 14 consecutive steps.

We have discussed the cases of rough surfaces of (9,m) and all smooth surfaces of (13,m) *in extenso* in a previous publication,[30] and we have observed an intermittent adsorption limit at (9,8) and the adsorption limit at (9,13). In conjunction with our spectroscopic investigation and DFT computations, we have concluded in a possible isomerization upon low N₂ coverage, likely from a tricapped octahedron to a bicapped pentagonal bipyramid, and in geminal binding of N₂ setting in at $m = 9$. In the case of smooth Ni₁₃⁺ we have

concluded in an icosahedral structure which coincides with all experimental findings and theory.

In the cases of (10,m), (11,m) we observe dominant intermittent adsorption limits at $m = n-1$. This indicates once more the structural motif of one semi internal, highly coordinated Ni atom that is initially reluctant to accept an N₂ adsorbate. Conceivable structures might base on the successive packing of additional Ni capping atoms to a pentagonal bipyramid – a building scheme that would eventually lead to an icosahedral Ni₁₃⁺ cluster. Of course, the rough surface morphologies of the (10,m) and (11,m) species are less stable and susceptible to adsorbate induced relaxation, in particular upon an increasing N₂ coverage. The observed adsorption limits at (10,12) and (11,14) are well in line with such suggestions. For further insights refer to the spectroscopic findings in [SD].

The cases of the (12,m) species are somewhat special as compared to the previous ones. We find strong evidence for a smooth surface by the kinetic curves (Fig. 3, bottom right) and the obtained rate constants $k_{(12,m)}$ (Fig. S4 and Table S2 in the supplementary material) up to (12,11). This behaviour is reminiscent of the cases (6,m) in the present study and of (13,m) before. In a clear demarcation, however, (12,11) slowly reacts on by significantly slower stepwise uptake of further N₂ adsorbates up to (12,14) which indicates $m_{\max} = 14$. Note that the deviations between the experimental data and the kinetic fits of the final products most likely originate from the low ion intensities of (12,13) and (12,14). The saturation stoichiometry of $n : m = 12 : 14$ is significantly beyond a 1 : 1 ratio. This is only conceivable through a rough surface morphology that would provide for some – likely two - low coordinated Ni sites which serve to accept N₂ adsorbates in a geminal fashion. In summary, we conclude in evidence for smooth surface up to (12,11) and in rough surface up to (12,14). This change of adsorption behaviour likely indicates an adsorbate induced Ni cluster core relaxation. It is most gratifying to find according evidence by our spectroscopic study, cf. [SD], where we discuss structural motifs explicitly.

Micro kinetics of small nickel clusters

Initial N₂ collisions hit naked Ni cluster surfaces at arbitrary locations, and subsequent sticking occurs either at the same, or at some other location. Our N₂ adsorption studies with small clusters (rough surfaces) likely imply reduced mobility and stable localization of N₂

adsorbate on site or nearby. The more the surface fills by stepwise adsorption the more likely the next N₂ collision hits occupied or unfavorable adsorption sites missing the next most favorable location. Initially trapped into a metastable situation the cluster adsorbate complex may relax either by N₂ migration or by cluster core reorganization. Either case may evidence by spectroscopic fingerprints as subject of the accompanying paper, see [SD].

Kinetics of large Nickel clusters: Ni₁₃⁺ – Ni₂₀⁺

The N₂ adsorption kinetics of Ni_n⁺ clusters of sizes 13 ≤ n ≤ 16 do not reveal pronounced intermittent adsorption limits (*cf.* Fig. 4). The Ni₁₃⁺ cluster is known to persist as a perfect icosahedron of a single interior Ni atom and 12 surface atoms of equal coordination to six nearest neighbors - irrespective of the level of N₂ adsorbate load and without any observable structure relaxation. It possesses a smooth surface, coinciding with the finding of constant reaction rates up to the adsorption limit at (13,12).

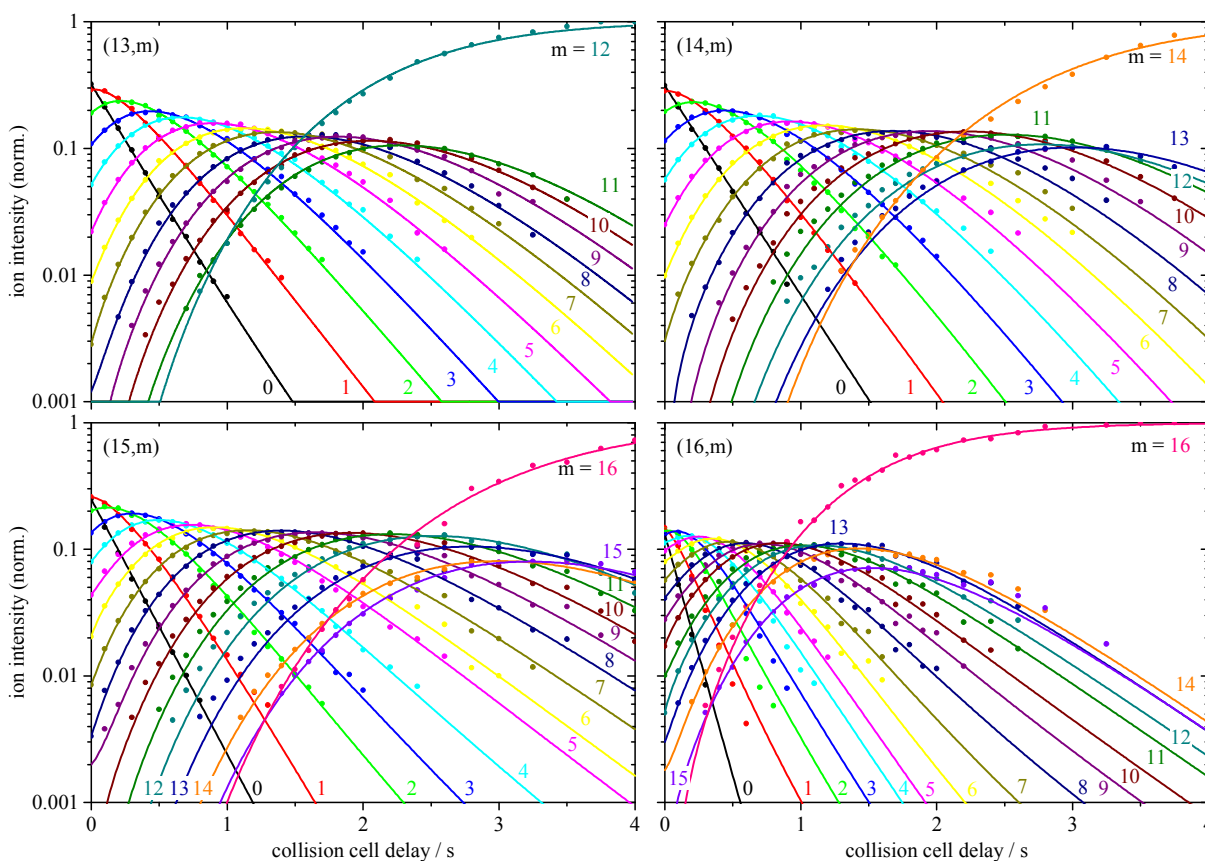


Figure 4. Isothermal kinetics of the stepwise N₂ adsorption by isolated Ni_n⁺ clusters (n = 13-16) within 26 Kelvin He buffer gas and 1.3 × 10⁻⁷ mbar of N₂ (solid points). The pseudo-first-order kinetic fits (solid lines) reveal a reaction chain of up to 16 consecutive steps.

In the case of (14,m) we observe smooth reaction kinetics up to an adsorption limit at (14,14) and without any intermittent retardation. Reminiscent of the highly symmetrical icosahedral (13,12) case, we find an explanation when assuming a capped icosahedron, where the capping Ni atom might accept two N₂ adsorbates (geminal occupation). It is a noteworthy finding that the last, 14th N₂ adsorbate attaches with equal rate as all previous ones.

In the case of (15,m) we observe smooth stepwise N₂ adsorption up to an adsorption limit at (15,16). All steps are equally fast up to (15,13) where a minor decline of rates sets in. This finding supports a bicapped icosahedron with two non-neighboring low coordinated capping Ni atoms. Such a structural conclusion is somewhat far reaching on its own. It is in line with the spectroscopic findings of [SD]. We might conceive at this point the alternative of a truncated octahedron, which is, however, ruled out by [SD].

In the case of (16,m) we observe the adsorption limit at (16,16). All adsorption steps are equally fast with some minor decline to the end. Such largely smooth surface behavior would be in line with e.g. a tricapped icosahedral structure, where the three extra Ni atoms neighbour each other.

Our studies of cluster adsorbate complexes $n = 17 - 20$ (Fig. 5) revealed large similarities to those of $n = 13 - 16$ (Fig. 4) and minor differences which is why we will present and discuss these clusters together. We identify five findings as follows:

Finding F0: $n = 13$ and 19 reveal all even kinetics by all smooth surfaces of high symmetry

It is only the (13,m) and (19,m) species which reveal exclusively steady kinetics up to saturation such that each adsorption step proceeds by the same rate constant k_m within our experimental uncertainties. Subtle details on the final reaction steps k_m and k_{-m} , where $m = m_{\max-1}$, are to find in the separate chapter on our micro kinetic model. It seems sound to conclude in icosahedral and bi-icosahedral structures with smooth surfaces of evenly high coordinated surface Ni atoms and void of any defects and low coordinated extra adsorption site Ni atoms. The found $m_{\max} = 12, 17$ saturation values support this conclusion in terms of a pure Ni : N₂ 1 : 1 coordination.

Finding F1: n = 14, 15, 16, 17, 18, and 20 reveal initially even kinetics

All other large clusters (n = 14, 15, 16, 17, 18, and 20) reveal stepwise N₂ adsorption where the initial steps are equally fast.

Finding F2: n = 14 – 17 reveal slower kinetics at pre-saturation

A minor retardation of N₂ adsorption sets in at two to three steps before saturation (*cf.* Fig.s S5, S6 and Tables S3, S4 in the supplementary material). This finding is also vaguely recognizable in the intensity maxima of consecutive adsorption products (n,m-3), (n,m-2), and (n,m-1), where m = m_{max} in the cases of n = 14, 15, 16 and m = m_x where n = 17, 18, *cf.* Fig.s 4 and 5.

Finding F3: n = 17, 18, 20 reveal intermittent limits

Note, that it is among all large clusters only n = 17 and 18 which reveal intermittent adsorption limits in our 26 Kelvin kinetics up to 10 sec reaction delay.

Finding F4: n = 18 and 20 have additional long time kinetics

However, through further collisions on longer time scales or by increased pressure there are further slow N₂ adsorption steps taking place which lead up to (18,18) and (20,18) (*cf.* Figs. S1 and S2 in the supplementary material).

The findings *F0* through *F4* all together allow for further interpretation in terms of tentative structural conclusions: The clusters n = 13 and 19 provide for an all smooth surface (*F0*) which can be interpreted in terms of highly symmetric cluster core structures: icosahedron for n = 13 and bi-icosahedron for n = 19. All other large clusters show similar even kinetics in the first steps (*F1*) which indicates partly smooth cluster cores. The appearance of some retardation in the final steps (*F2*), intermittent limits (*F3*) and longtime kinetics (*F4*) point towards some low coordinated Ni surface atoms or a possible cluster core reorganization. Altogether we conclude that these cluster have rough and smooth surface areas which is in line with an icosahedral cluster growth from an icosahedron (n = 13) to a bi-icosahedron (n = 19). This growth leaves one hemisphere of an icosahedron unaffected (smooth part) and provides for some low coordinated capping Ni atoms on the other part (single defects). Verification and further insights arise from the IR studies of adsorbate

complexes in conjunction with some DFT modelling as far as possible, which is subject of the accompanying [SD] publication.

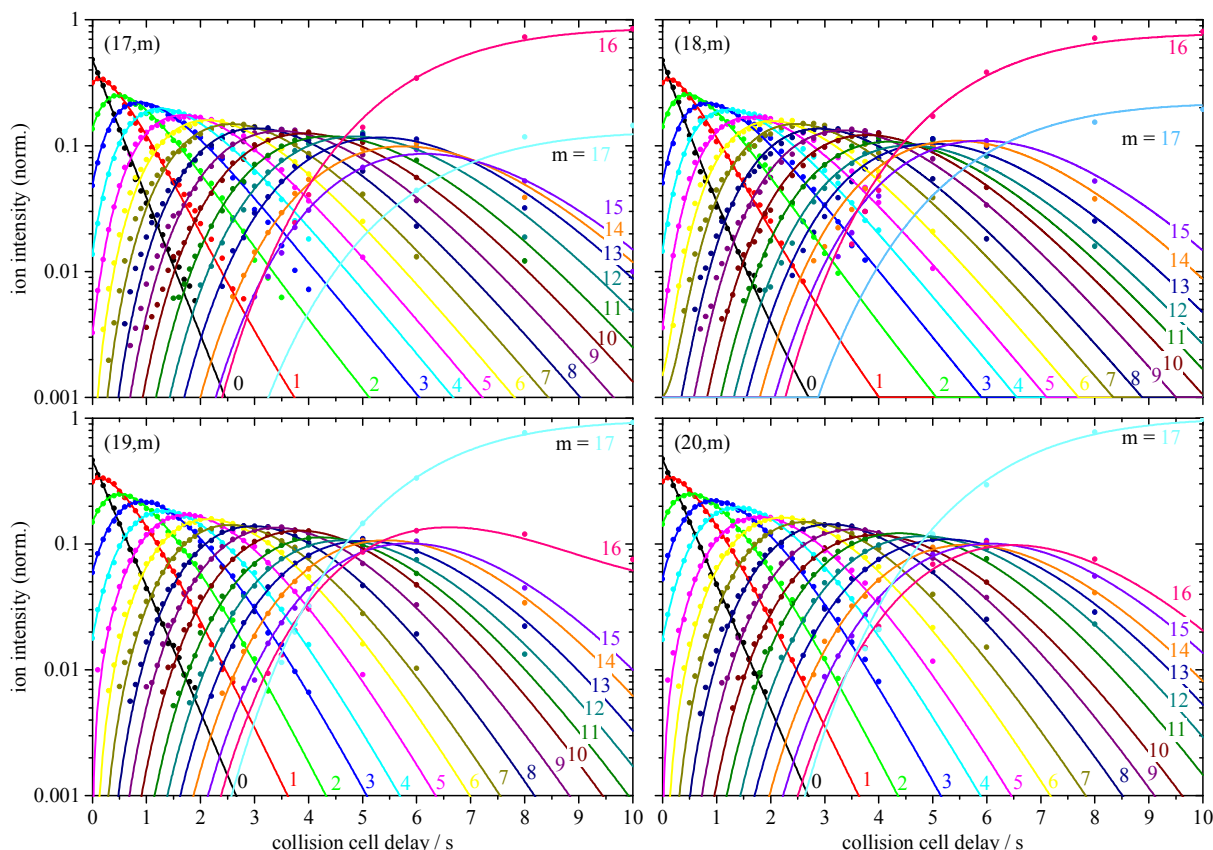


Figure 5. Isothermal kinetics of the stepwise N₂ adsorption by isolated Ni_n⁺ clusters ($n = 17-20$) within 26 Kelvin He buffer gas and 1.1×10^{-7} mbar of N₂ (solid points). The pseudo-first-order kinetic fits (solid lines) reveal reaction chains of up to 17 consecutive steps. Note, that Ni₁₈⁺ and Ni₂₀⁺ reveal long time kinetics up to $m_{\max} = 18$, cf. Fig.s S1 and S2 in the supplementary material.

Micro kinetics of highly symmetrical clusters and of large clusters

In case of the highly symmetrical clusters ($n = 6, 13$ & 19) with all smooth surfaces and void of defects we conclude in initially high mobility of N₂ adsorbates and in considerable probabilities for site hopping after first N₂ cluster encounter. As the first shell of N₂ adsorbates starts to fill this turns into a pseudo-diffusion-like migration of the remaining adsorbate vacancies. Shell filling up to saturation certainly comes with significant adsorbate loss when looking at larger surfaces as in the case of $n = 19$ – as fitted by assumed back reactions (adsorbate evaporation, cf. Table S4 and Fig. S6 in the supplementary material). In cases of large clusters $n > 13$ (but $n = 19$) the found kinetics point to high N₂ adsorbate mobility in conjunction with effective sticking largely as for the highly symmetrical clusters

$n = 6, 13,$ and 19 . Such stochastic, precursor mediated migration may eventually lead to N₂ stabilization at low coordinated Ni surface atoms which are inevitably present in large clusters other than the exceptional, highly symmetrical ones. Second solvation shell N₂ adsorption may act as precursor - albeit highly facile and largely back dissociating. Instead it seems likely that pairwise surface 1Ni : 1N₂ adsorption morphology reorganizes in favor of geminal 1Ni : 2N₂ stoichiometry at low coordinated Ni sites and as early as required. In no case we see as large stepwise variations as with the small clusters with rough surfaces. We thus tentatively assume large clusters of mainly smooth surfaces with some single surface defects.

Absolute rate constants of the initial N₂ adsorption

So far we have presented and discussed relative pseudo-first-order rate constants. These convert to absolute rate constants $k_{(n,m)}^{abs}$ as described (see exptl. part). In our previous study we have focused on the consecutive adsorption steps $k_{(9,m)}^{abs}$ and $k_{(13,m)}^{abs}$ with N₉⁺ and Ni₁₃⁺. We found that ADO/Langevin would underestimate the true adsorption rate, implying a sticking probability larger unity. The SCC model would overestimates the adsorption rate implying a sticking probability much below unity. Neither of both cases seems likely.

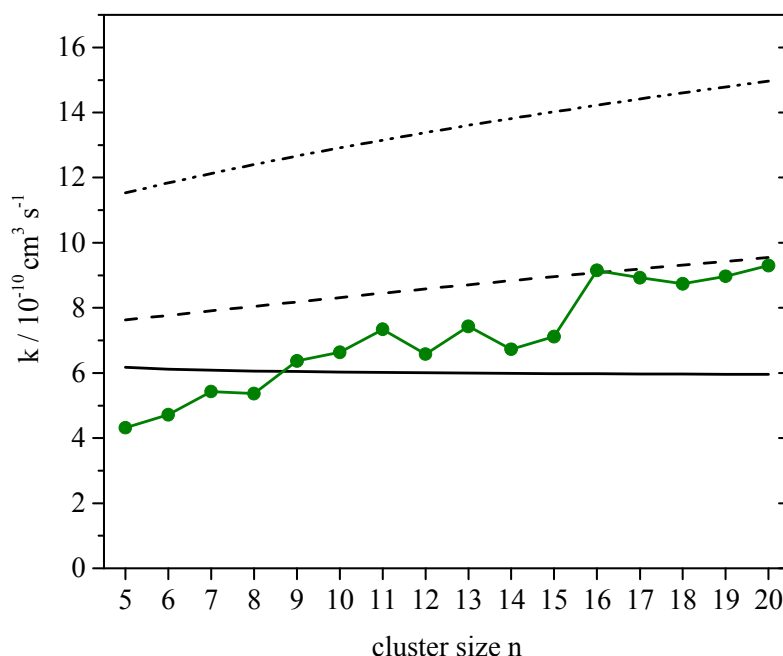


Figure 6. Experimental absolute rate constants $k_{(n,0)}^{abs}$ of the initial N₂ adsorption to naked Ni_n⁺ clusters (solid green dots), and modelled collision rate constants according to the ADO theory (black line), to the HSA model (dashed line), and to the SCC model (dot-dashed line). See text for details on the models.

In the present case, we consider the initial N₂ adsorption step, $k_{(n,0)}^{abs}$ as a function of cluster size n (green circles in Fig. 6), and in comparison to collision rate constants by models as above, and by the HSA model in addition. None of these models describes all of the recorded absolute values in a quantitative way. This renders it likely that the sticking probabilities of small clusters $n < 9$ fall below unity. This is conceivable in view of their finite size. Moreover, we find evidence for collision rates and the according adsorption rates beyond the ADO values for clusters $n > 10$, where the HSA seems to describe the recorded rates sufficiently. The sheer size of the large clusters thus enhances adsorption cross sections and rate constants. We find, however, no evidence for the surface charge localization effect by the SCC model through our present studies. The minor, particular variations of $k_{(n,0)}^{abs}$ in cases of individual n values certainly relate to structures and shapes of these Ni_n⁺ clusters. The determined rate constants are rendered by the individual geometries of the Ni_n⁺ clusters which are not sufficiently described by the presented models.

Table 1. Pseudo-first-order rate constants $k_{(n,0)}$, absolute rate constants $k_{(n,0)}^{abs}$ for the initial N₂ adsorption on Ni_n⁺ ($n = 5-20$) clusters (both by experiment), and modelled collision rate constants as obtained by ADO theory, by the HSA model and by the SCC model.

n	$k_{(n,0)}$ s ⁻¹	$k_{(n,0)}^{abs}$ 10 ⁻¹⁰ cm ³ s ⁻¹	$k_{(n,0)}^{ADO}$ 10 ⁻¹⁰ cm ³ s ⁻¹	$k_{(n,0)}^{HSA}$ 10 ⁻¹⁰ cm ³ s ⁻¹	$k_{(n,0)}^{SCC}$ 10 ⁻¹⁰ cm ³ s ⁻¹
5	2.4	4.32	6.17	7.63	11.53
6	2.7	4.72	6.12	7.77	11.84
7	3.1	5.43	6.09	7.91	12.13
8	3.0	5.37	6.06	8.05	12.40
9	3.6	6.37	6.05	8.18	12.66
10	3.8	6.64	6.03	8.32	12.91
11	4.2	7.34	6.02	8.45	13.15
12	3.7	6.58	6.01	8.58	13.38
13	4.2	7.43	6.00	8.71	13.60
14	3.8	6.73	5.99	8.84	13.82
15	4.0	7.12	5.98	8.96	14.02
16	5.2	9.15	5.98	9.08	14.22
17	5.1	8.93	5.97	9.20	14.42
18	4.9	8.74	5.97	9.32	14.60
19	5.1	8.97	5.96	9.43	14.79
20	5.3	9.30	5.96	9.54	14.97

5.6 Conclusions

We have investigated the stepwise N₂ adsorption on size selected Ni_n⁺ (n = 5 – 20) clusters by recording their reaction kinetics at 26 K in a hexapole ion trap. We performed pseudo-first-order kinetic fits, which confirm consecutive adsorption steps by single exponent decays exclusively. N₂ desorption, if any, only occurs at high levels of N₂ coverage. In all investigated cases the stepwise N₂ uptake reaches a strict adsorption limit m_{max}, which does not increase further, and scales with cluster size.

By the recorded N₂ adsorption kinetics and their limits we are able to identify three classes of structure related surface adsorption behavior of cationic Ni clusters: The clusters Ni₆⁺, Ni₁₃⁺, and Ni₁₉⁺ are highly symmetrical clusters with all smooth surfaces. They reveal all even reaction kinetics up to their adsorption limits, which is strong evidence for all equally coordinated Ni atoms. We conclude in most likely high symmetry structures such as octahedron (n = 6), icosahedron (n = 13), and bi-icosahedron (n = 19). The clusters Ni₅⁺, and Ni₇₋₁₂⁺ are small clusters with rough surfaces. They possess a large variety of stepwise adsorption kinetics and limits which are characteristic for rough cluster morphologies with a variety of unique surface atoms. We likely see a transition from octahedral to icosahedral cluster structures. The clusters Ni₁₄₋₁₈⁺, and Ni₂₀⁺ are large clusters with rough and smooth surface areas. They provide for initially even kinetics, for intermittent limits and for some retarded longtime kinetics which indicate partly smooth cluster surfaces with some low coordinated Ni surface atoms, in line with stepwise Ni cluster growth from icosahedron (n = 13) to bi-icosahedron (n = 19).

We observe an overall increase in the absolute rate constants with cluster size in line with a hard sphere average dipole orientation model (HSA). The observed stoichiometries of intermittent and ultimate adsorbate shell closures at m_x and m_{max}, respectively, are understood in terms of initial single adsorbate occupation of available binding sites, followed by further adsorption through solvent shell re-organization towards double (geminal) occupation of low coordinated Ni surface sites. We devise a micro kinetic model with some level of speculation. It would be beneficial to obtain a future verification of our envisaged Ni cluster surface morphology and adsorption dynamics by conceivable molecular dynamics simulations, and we find full support of our cryo kinetic interpretations by the adjoined cryo spectroscopic study [SD].

5.7 Acknowledgements

We dedicate this work to the memory of the late Tamotsu Kondow in recognition of his seminal contributions to the field of cluster science. This work was supported by the German research foundation DFG within the transregional collaborative research center SFB/TRR 88 “Cooperative effects in homo and heterometallic complexes” (3MET.de) and by the state research center OPTIMAS. The ⁵⁸Ni isotopic sample used in this research was supplied by the United States Department of Energy Office of Science by the Isotope Program in the Office of Nuclear Physics. We thank Thomas Kolling for technical assistance and valuable discussions.

5.8 References

- [1] K. M. Ervin, *Int. Rev. Phys. Chem.*, **20**, 127, (2001).
- [2] G. Ganteför, G. S. Icking-Konert, H. Handschuh, and W. Eberhardt, *Int. J. Mass Spectrom. Ion Processes*, **159**, 81, (1996).
- [3] E. K. Parks, K. P. Kerns, and S. J. Riley, *J. Chem. Phys.*, **112**, 3384, (2000).
- [4] K. P. Kerns, E. K. Parks, and S. J. Riley, *J. Chem. Phys.*, **112**, 3394, (2000).
- [5] Z. Luo, A. W. Castleman, and S. N. Khanna, *Chem. Rev.*, **116**, 14456, (2016).
- [6] T. Zambelli, J. Wintterlin, J. Trost, and G. Ertl, *Science*, **273**, 1688, (1996).
- [7] J. K. Nørskov, T. Bligaard, A. Logadottir, S. Bahn, L. B. Hansen, M. Bollinger, H. Bengaard, B. Hammer, Z. Sljivancanin, and M. Mavrikakis, *J. Catal.*, **209**, 275, (2002).
- [8] K. Honkala, A. Hellman, I. Remediakis, A. Logadottir, A. Carlsson, S. Dahl, C. H. Christensen, and J. K. Nørskov, *Science*, **307**, 555, (2005).
- [9] H. J. Freund, B. Bartos, R. P. Messmer, M. Grunze, H. Kühlenbeck, and M. Neumann, *Surf. Sci.*, **185**, 187, (1987).
- [10] P. A. Hintz, and K. M. Ervin, *J. Chem. Phys.*, **103**, 7897, (1995).
- [11] S. K. Nayak, S. N. Khanna, B. K. Rao, and P. Jena, *J. Phys. Chem. A*, **101**, 1072, (1997).
- [12] L. Lian, C. X. Su, and P. B. Armentrout, *J. Chem. Phys.*, **96**, 7542, (1992).
- [13] T. F. Magnera, D. E. David, and J. Michl, *J. Am. Chem. Soc.*, **109**, 936, (1987).
- [14] W. D. Vann, R. C. Bell, and A. W. Castleman, Jr., *J. Phys. Chem. A*, **103**, 10846, (1999).
- [15] E. K. Parks, K. P. Kerns, S. J. Riley, and B. J. Winter, *Phys. Rev. B: Condens. Matter Mater. Phys.*, **59**, 13431, (1999).
- [16] T. Hanmura, M. Ichihashi, and T. Kondow, *J. Phys. Chem. A*, **106**, 4525, (2002).
- [17] R. T. Yadav, M. Ichihashi, and T. Kondow, *J. Phys. Chem. A*, **108**, 7188, (2004).
- [18] K.-i. Sugawara, and K. Koga, *Chem. Phys. Lett.*, **409**, 197, (2005).
- [19] P. L. Rodriguez-Kessler, and A. R. Rodriguez-Dominguez, *J. Phys. Chem. C*, **119**, 12378, (2015).
- [20] T. Klots, B. Winter, E. Parks, and S. t. J. Riley, *J. Chem. Phys.*, **95**, 8919, (1991).
- [21] E. Parks, B. Winter, T. Klots, and S. Riley, *J. Chem. Phys.*, **94**, 1882, (1991).
- [22] E. Parks, L. Zhu, J. Ho, and S. Riley, *J. Chem. Phys.*, **100**, 7206, (1994).
- [23] E. Parks, L. Zhu, J. Ho, and S. Riley, *J. Chem. Phys.*, **102**, 7377, (1995).

- [24] E. Parks, and S. Riley, *Zeitschrift für Physik D Atoms, Molecules and Clusters*, **33**, 59, (1995).
- [25] B. Pfeffer, S. Jaberg, and G. Niedner-Schatteburg, *J. Chem. Phys.*, **131**, 194305, (2009).
- [26] S. Peredkov, M. Neeb, W. Eberhardt, J. Meyer, M. Tombers, H. Kampschulte, and G. Niedner-Schatteburg, *Phys. Rev. Lett.*, **107**, (2011).
- [27] J. Meyer, M. Tombers, C. van Wüllen, G. Niedner-Schatteburg, S. Peredkov, W. Eberhardt, M. Neeb, S. Palutke, M. Martins, and W. Wurth, *J. Chem. Phys.*, **143**, 104302, (2015).
- [28] J. Mohrbach, J. Lang, S. Dillinger, M. A. Prosenc, P. Braunstein, and G. Niedner-Schatteburg, *J. Mol. Spectrosc.*, accepted 21.11.2016, (2017).
- [29] S. Dillinger, J. Mohrbach, J. Hewer, M. Gaffga, and G. Niedner-Schatteburg, *Phys. Chem. Chem. Phys.*, **17**, 10358, (2015).
- [30] J. Mohrbach, S. Dillinger, and G. Niedner-Schatteburg, *J. Phys. Chem. C*, **121**, 10907, (2017).
- [31] S. Dillinger, J. Mohrbach, and G. Niedner-Schatteburg, *J. Chem. Phys.*, submitted, (2017).
- [32] C. Berg, T. Schindler, G. Niedner-Schatteburg, and V. E. Bondybey, *J. Chem. Phys.*, **102**, 4870, (1995).
- [33] S. Maruyama, L. R. Anderson, and R. E. Smalley, *Rev. Sci. Instrum.*, **61**, 3686, (1990).
- [34] D. Proch, and T. Trickl, *Rev. Sci. Instrum.*, **60**, 713, (1989).
- [35] P. Caravatti, and M. Allemann, *Org. Mass Spectrom.*, **26**, 514, (1991).
- [36] M. Graf, Diploma Thesis, TU Kaiserslautern, (**unpublished**), (2006).
- [37] M. Langevin, in *Annales de chimie et de physique, Series 1905*, pp. 245.
- [38] T. Su, and M. T. Bowers, *J. Chem. Phys.*, **58**, 3027, (1973).
- [39] T. Su, and M. T. Bowers, *J. Am. Chem. Soc.*, **95**, 1370, (1973).
- [40] T. Su, and M. T. Bowers, *International Journal of Mass Spectrometry and Ion Physics*, **12**, 347, (1973).
- [41] M. L. Anderson, M. S. Ford, P. J. Derrick, T. Drewello, D. P. Woodruff, and S. R. Mackenzie, *J. Phys. Chem. A*, **110**, 10992, (2006).
- [42] I. Balteanu, O. P. Balaj, B. S. Fox-Beyer, P. Rodrigues, M. T. Barros, A. M. C. Moutinho, M. L. Costa, M. K. Beyer, and V. E. Bondybey, *Organometallics*, **23**, 1978, (2004).
- [43] G. Kummerlöwe, and M. K. Beyer, *Int. J. Mass Spectrom.*, **244**, 84, (2005).
- [44] E. K. Parks, L. Zhu, J. Ho, and S. J. Riley, *J. Chem. Phys.*, **100**, 7206, (1994).
- [45] E. K. Parks, L. Zhu, J. Ho, and S. J. Riley, *J. Chem. Phys.*, **102**, 7377, (1995).

5.9 Supplementary Material

Table of Content:

Figure S1. Temporal evolution of the mass spectra of mass-selected Ni₆⁺, Ni₁₈⁺ clusters at 26 K.

Figure S2. Isothermal kinetics of the stepwise N₂ adsorption by isolated Ni₁₈⁺ clusters at p(N₂) = 1.1 × 10⁻⁷ mbar (top) and p(N₂) = 3.2 × 10⁻⁷ mbar (bottom) within 26 Kelvin He buffer gas. The fits (shown as lines) assume pseudo-first-order kinetics in a reaction chain of up to 18 consecutive steps.

Figure S3. Observed rate constants of the (n,m) species n = 5-8 as a function of N₂ coverage. Filled circles show the rate of adsorption and open circles indicate single N₂ desorption.

Table S1. Pseudo-first-order rate constants for the N₂ adsorption/desorption $k_{(n,m)} / k_{-(n,m+1)}$ on Ni_n⁺ (n = 5-8) clusters.

Figure S4. Observed rate constants of the (n,m) species n = 9-12 as a function of N₂ coverage. Filled circles show the rate of adsorption and open circles indicate single N₂ desorption.

Table S2. Pseudo-first-order rate constants for the N₂ adsorption/desorption $k_{(n,m)} / k_{-(n,m+1)}$ on Ni_n⁺ (n = 9-12) clusters.

Figure S5. Observed rate constants of the (n,m) species n = 13-16 as a function of N₂ coverage. Filled circles show the rate of adsorption and open circles indicate single N₂ desorption.

Table S3. Pseudo-first-order rate constants for the N₂ adsorption/desorption $k_{(n,m)} / k_{-(n,m+1)}$ on Ni_n⁺ (n = 13-16) clusters.

Figure S6. Observed rate constants of the (n,m) species n = 17-20 as a function of N₂ coverage. Filled circles show the rate of adsorption and open circles indicate single N₂ desorption.

Table S4. Pseudo-first-order rate constants for the N₂ adsorption/desorption $k_{(n,m)} / k_{-(n,m+1)}$ on Ni_n⁺ (n = 17-20) clusters.

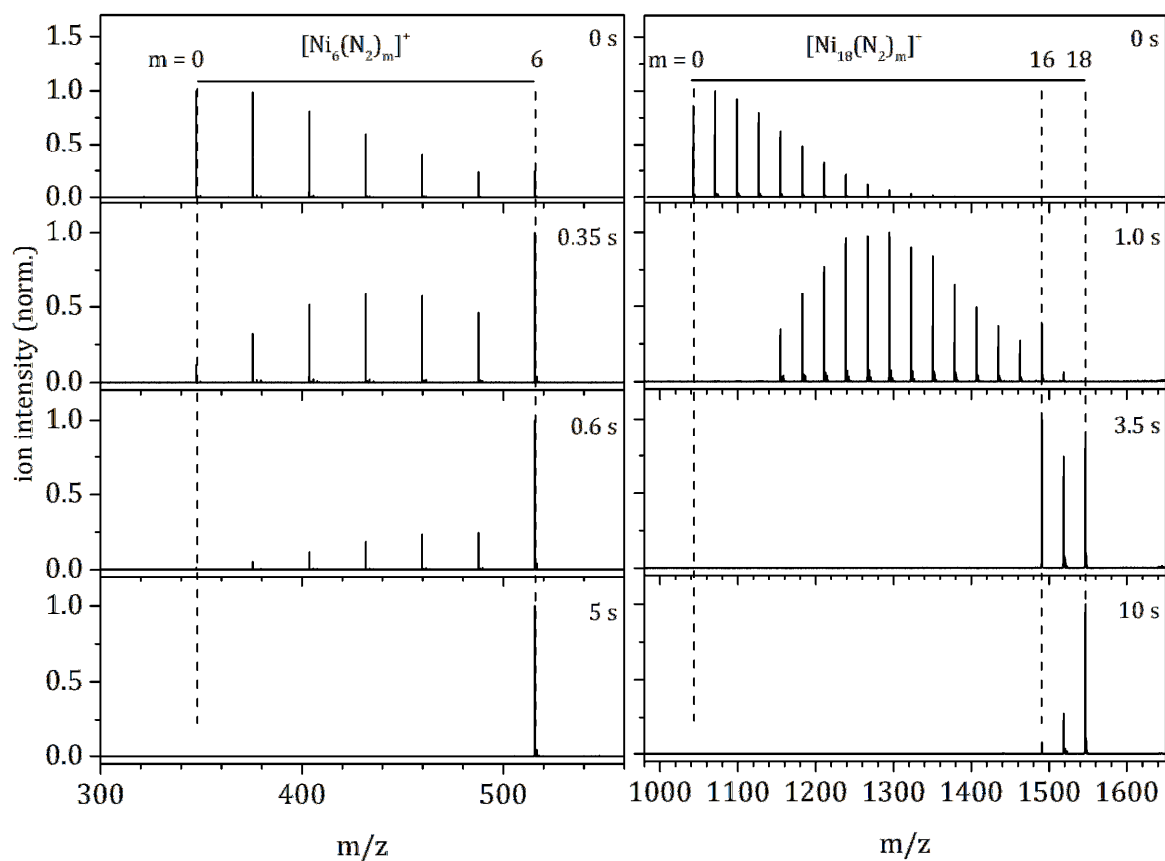


Figure S1. Temporal evolution of the mass spectra of mass-selected Ni_6^+ , Ni_{18}^+ clusters at 26 K.

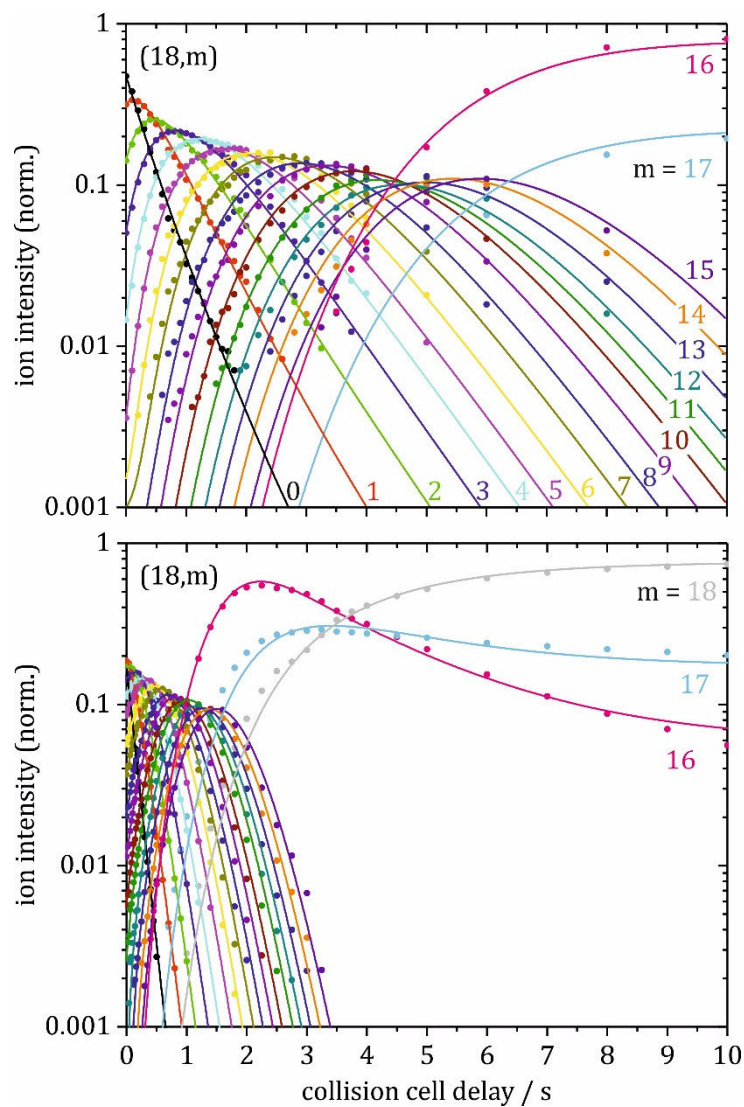


Figure S2. Isothermal kinetics of the stepwise N₂ adsorption by isolated Ni₁₈⁺ clusters at $p(\text{N}_2) = 1.1 \times 10^{-7}$ mbar (top) and $p(\text{N}_2) = 3.2 \times 10^{-7}$ mbar (bottom) within 26 Kelvin He buffer gas. The fits (shown as lines) assume pseudo-first-order kinetics in a reaction chain of up to 18 consecutive steps.

5. Probing Cluster Surface Morphology by Cryo Kinetics of N₂ on Cationic Nickel Clusters

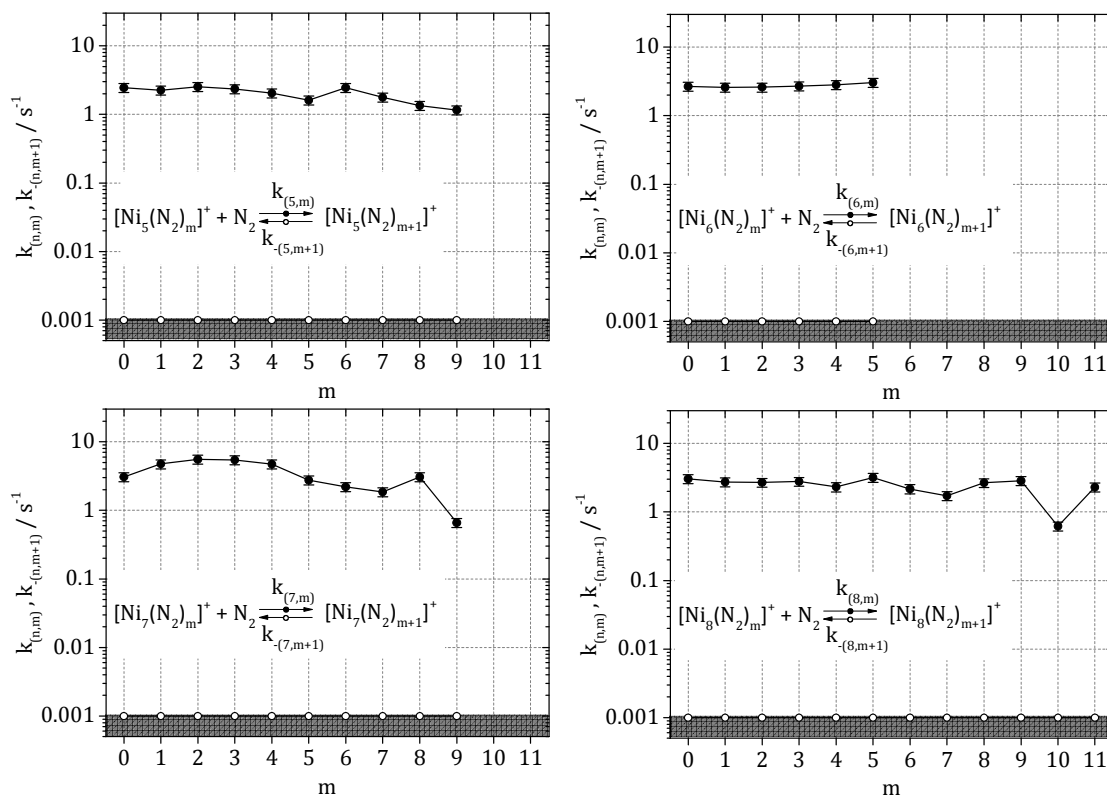


Figure S3. Observed rate constants of the (n,m) species $n = 5-8$ as a function of N_2 coverage. Filled circles show the rate of adsorption and open circles indicate single N_2 desorption.

Table S1. Pseudo-first-order rate constants for the N₂ adsorption/desorption $k_{(n,m)} / k_{-(n,m+1)}$ on Ni_n⁺ (n = 5-8) clusters.

m	$k_{(5,m)}$ s ⁻¹	$k_{-(5,m+1)}$ s ⁻¹	$k_{(6,m)}$ s ⁻¹	$k_{-(6,m+1)}$ s ⁻¹	$k_{(7,m)}$ s ⁻¹	$k_{-(7,m+1)}$ s ⁻¹	$k_{(8,m)}$ s ⁻¹	$k_{-(8,m+1)}$ s ⁻¹
0	2.4	<0.001	2.7	<0.001	3.1	<0.001	3.0	<0.001
1	2.2	<0.001	2.6	<0.001	4.7	<0.001	2.7	<0.001
2	2.5	<0.001	2.6	<0.001	5.5	<0.001	2.7	<0.001
3	2.3	<0.001	2.7	<0.001	5.4	<0.001	2.8	<0.001
4	2.0	<0.001	2.8	<0.001	4.7	<0.001	2.3	<0.001
5	1.6	<0.001	3.0	<0.001	2.8	<0.001	3.2	<0.001
6	2.5	<0.001			2.2	<0.001	2.2	<0.001
7	1.8	<0.001			1.9	<0.001	1.7	<0.001
8	1.3	<0.001			3.1	<0.001	2.7	<0.001
9	1.2	<0.001			0.7	<0.001	2.8	<0.001
10							0.6	<0.001
11							2.3	<0.001

5. Probing Cluster Surface Morphology by Cryo Kinetics of N₂ on Cationic Nickel Clusters

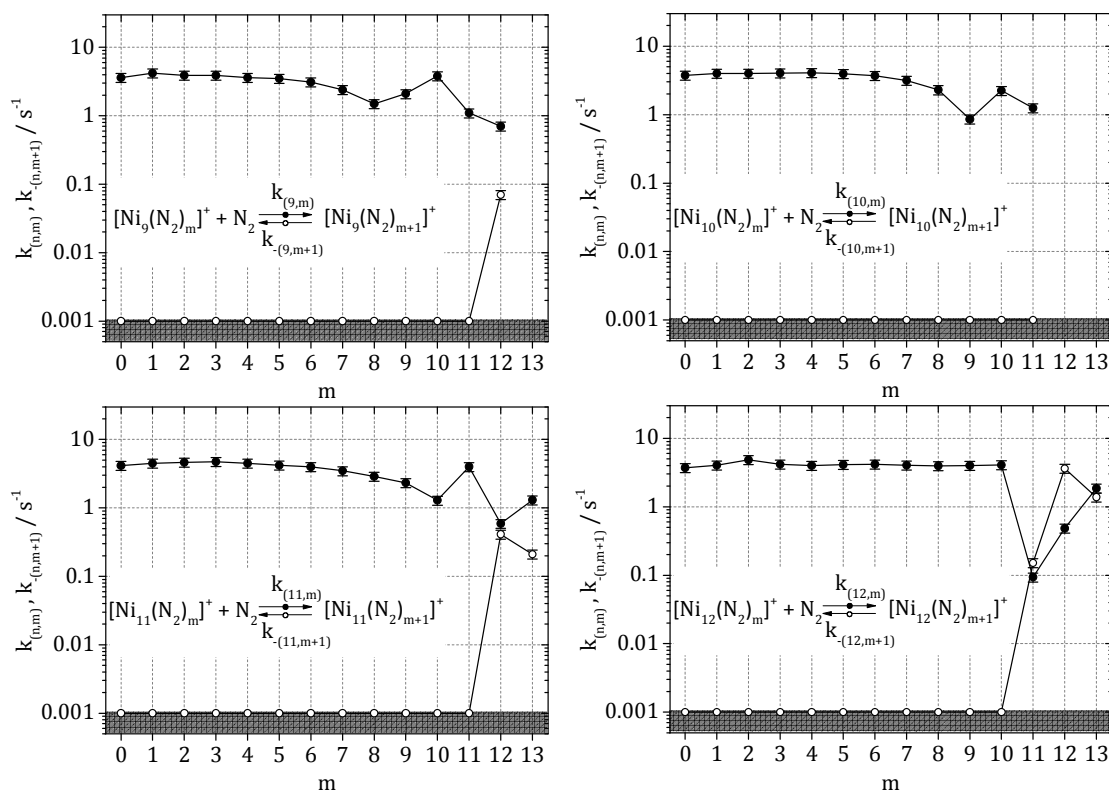


Figure S4. Observed rate constants of the (n,m) species $n = 9-12$ as a function of N_2 coverage. Filled circles show the rate of adsorption and open circles indicate single N_2 desorption.

Table S2. Pseudo-first-order rate constants for the N₂ adsorption/desorption $k_{(n,m)} / k_{-(n,m+1)}$ on Ni_n⁺ (n = 9-12) clusters.

m	$k_{(9,m)}$ s ⁻¹	$k_{-(9,m+1)}$ s ⁻¹	$k_{(10,m)}$ s ⁻¹	$k_{-(10,m+1)}$ s ⁻¹	$k_{(11,m)}$ s ⁻¹	$k_{-(11,m+1)}$ s ⁻¹	$k_{(12,m)}$ s ⁻¹	$k_{-(12,m+1)}$ s ⁻¹
0	3.6	<0.001	3.8	<0.001	4.2	<0.001	3.7	<0.001
1	4.2	<0.001	4.0	<0.001	4.5	<0.001	4.0	<0.001
2	3.9	<0.001	4.0	<0.001	4.6	<0.001	4.8	<0.001
3	3.9	<0.001	4.1	<0.001	4.7	<0.001	4.2	<0.001
4	3.6	<0.001	4.1	<0.001	4.5	<0.001	4.0	<0.001
5	3.5	<0.001	3.9	<0.001	4.2	<0.001	4.1	<0.001
6	3.1	<0.001	3.7	<0.001	4.0	<0.001	4.2	<0.001
7	2.4	<0.001	3.2	<0.001	3.5	<0.001	4.0	<0.001
8	1.5	<0.001	2.3	<0.001	2.9	<0.001	4.0	<0.001
9	2.1	<0.001	0.9	<0.001	2.3	<0.001	4.0	<0.001
10	3.8	<0.001	2.2	<0.001	1.3	<0.001	4.1	<0.001
11	1.1	<0.001	1.3	<0.001	4.0	<0.001	0.1	0.15
12	0.7	0.07			0.6	0.41	0.5	3.62
13					1.3	0.21	1.9	1.38

5. Probing Cluster Surface Morphology by Cryo Kinetics of N₂ on Cationic Nickel Clusters

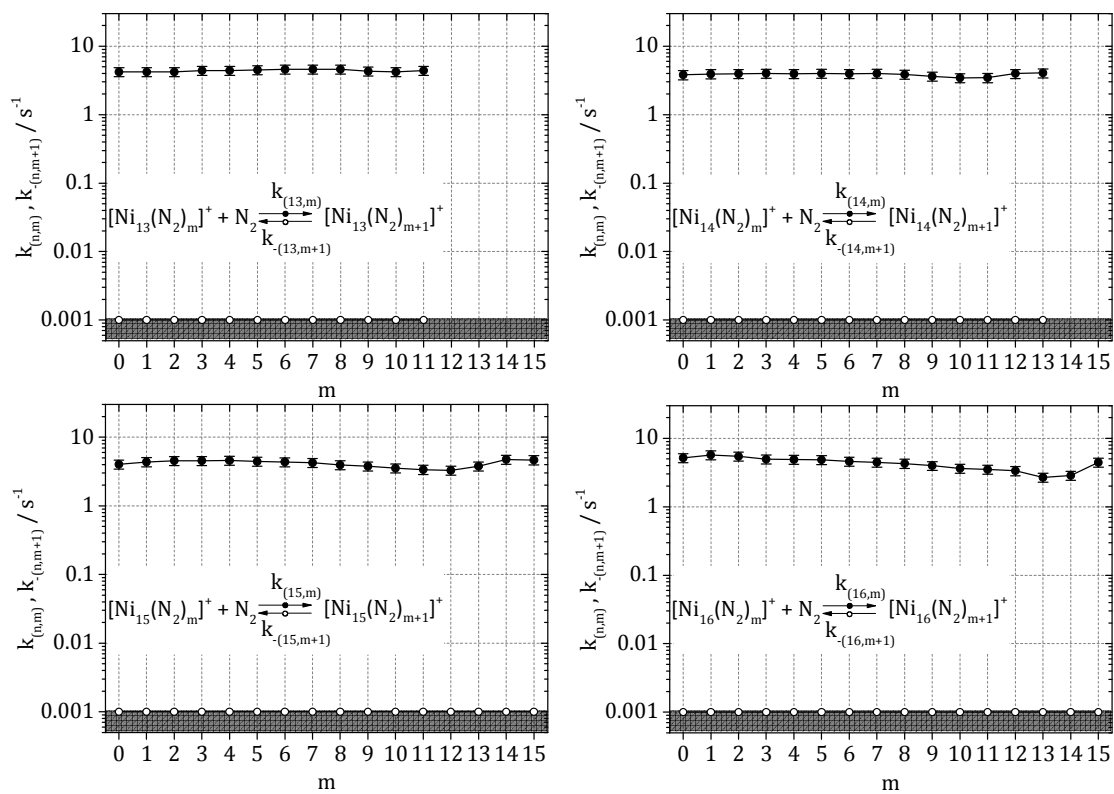


Figure S5. Observed rate constants of the (n,m) species n = 13-16 as a function of N₂ coverage. Filled circles show the rate of adsorption and open circles indicate single N₂ desorption.

Table S3. Pseudo-first-order rate constants for the N₂ adsorption/desorption $k_{(n,m)} / k_{-(n,m+1)}$ on Ni_n⁺ (n = 13-16) clusters.

m	$k_{(13,m)}$ s ⁻¹	$k_{-(13,m+1)}$ s ⁻¹	$k_{(14,m)}$ s ⁻¹	$k_{-(14,m+1)}$ s ⁻¹	$k_{(15,m)}$ s ⁻¹	$k_{-(15,m+1)}$ s ⁻¹	$k_{(16,m)}$ s ⁻¹	$k_{-(16,m+1)}$ s ⁻¹
0	4.2	<0.001	3.8	<0.001	4.0	<0.001	5.2	<0.001
1	4.2	<0.001	3.9	<0.001	4.4	<0.001	5.7	<0.001
2	4.2	<0.001	4.0	<0.001	4.6	<0.001	5.4	<0.001
3	4.4	<0.001	4.0	<0.001	4.6	<0.001	5.0	<0.001
4	4.4	<0.001	3.9	<0.001	4.6	<0.001	4.9	<0.001
5	4.5	<0.001	4.0	<0.001	4.4	<0.001	4.8	<0.001
6	4.6	<0.001	4.0	<0.001	4.4	<0.001	4.6	<0.001
7	4.6	<0.001	4.0	<0.001	4.2	<0.001	4.5	<0.001
8	4.6	<0.001	3.9	<0.001	3.9	<0.001	4.3	<0.001
9	4.3	<0.001	3.6	<0.001	3.8	<0.001	4.0	<0.001
10	4.2	<0.001	3.4	<0.001	3.5	<0.001	3.6	<0.001
11	4.4	<0.001	3.5	<0.001	3.4	<0.001	3.5	<0.001
12			4.0	<0.001	3.3	<0.001	3.3	<0.001
13			4.1	<0.001	3.8	<0.001	2.7	<0.001
14					4.8	<0.001	2.9	<0.001
15					4.7	<0.001	4.4	<0.001

5. Probing Cluster Surface Morphology by Cryo Kinetics of N₂ on Cationic Nickel Clusters

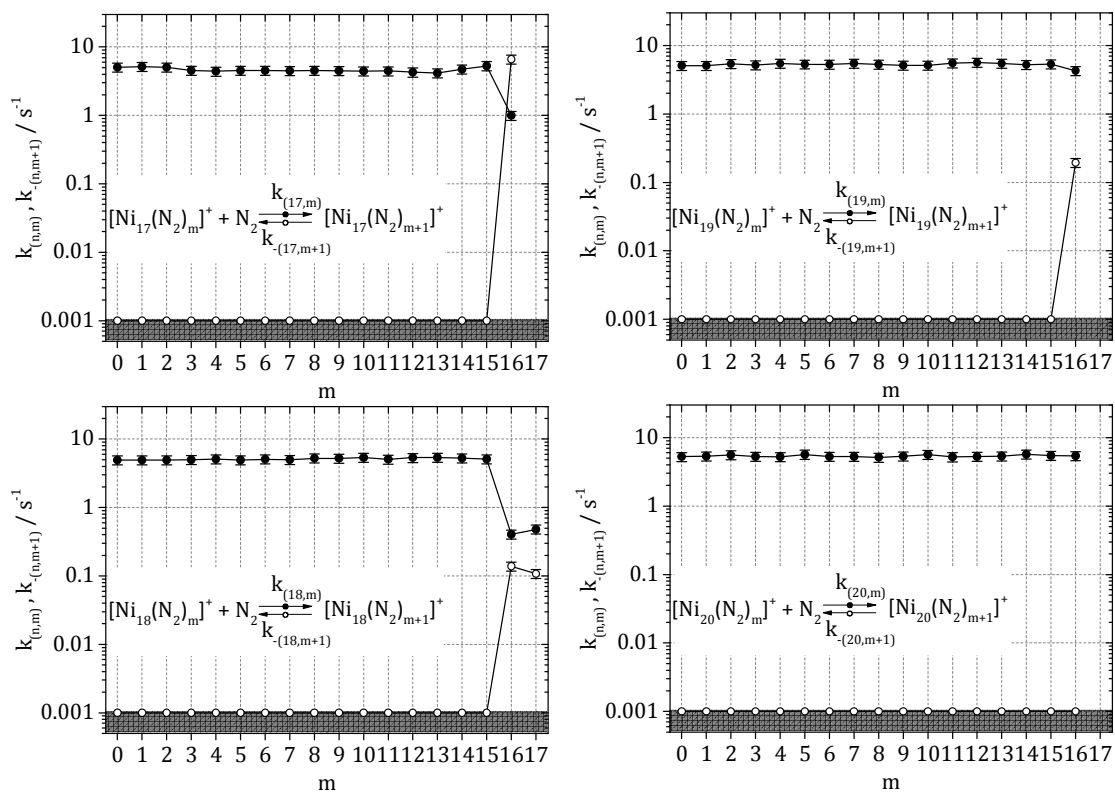


Figure S6. Observed rate constants of the (n,m) species $n = 17-20$ as a function of N_2 coverage. Filled circles show the rate of adsorption and open circles indicate single N_2 desorption.

Table S4. Pseudo-first-order rate constants for the N₂ adsorption/desorption $k_{(n,m)} / k_{-(n,m+1)}$ on Ni_n⁺ (n = 17-20) clusters.

m	$k_{(17,m)}$ s ⁻¹	$k_{-(17,m+1)}$ s ⁻¹	$k_{(18,m)}$ s ⁻¹	$k_{-(18,m+1)}$ s ⁻¹	$k_{(19,m)}$ s ⁻¹	$k_{-(19,m+1)}$ s ⁻¹	$k_{(20,m)}$ s ⁻¹	$k_{-(20,m+1)}$ s ⁻¹
0	5.1	<0.001	4.9	<0.001	5.1	<0.001	5.3	<0.001
1	5.2	<0.001	4.9	<0.001	5.1	<0.001	5.3	<0.001
2	5.0	<0.001	4.9	<0.001	5.4	<0.001	5.6	<0.001
3	4.5	<0.001	5.0	<0.001	5.2	<0.001	5.3	<0.001
4	4.4	<0.001	5.1	<0.001	5.5	<0.001	5.2	<0.001
5	4.5	<0.001	4.9	<0.001	5.3	<0.001	5.7	<0.001
6	4.5	<0.001	5.1	<0.001	5.3	<0.001	5.3	<0.001
7	4.5	<0.001	5.0	<0.001	5.5	<0.001	5.3	<0.001
8	4.5	<0.001	5.2	<0.001	5.3	<0.001	5.1	<0.001
9	4.5	<0.001	5.2	<0.001	5.1	<0.001	5.3	<0.001
10	4.4	<0.001	5.4	<0.001	5.1	<0.001	5.7	<0.001
11	4.5	<0.001	5.1	<0.001	5.5	<0.001	5.2	<0.001
12	4.3	<0.001	5.4	<0.001	5.6	<0.001	5.3	<0.001
13	4.2	<0.001	5.4	<0.001	5.5	<0.001	5.4	<0.001
14	4.7	<0.001	5.3	<0.001	5.2	<0.001	5.7	<0.001
15	5.3	<0.001	5.1	<0.001	5.3	<0.001	5.4	<0.001
16	1.0	6.63	0.4	0.14	4.3	0.19	5.4	<0.001
17			0.5	0.11				

6 Probing Cluster Surface Morphology by Cryo Spectroscopy of N₂ on Cationic Nickel Clusters

Jennifer Mohrbach, Sebastian Dillinger, and Gereon Niedner-Schatteburg

Fachbereich Chemie und Forschungszentrum OPTIMAS

Technische Universität Kaiserslautern

67663 Kaiserslautern

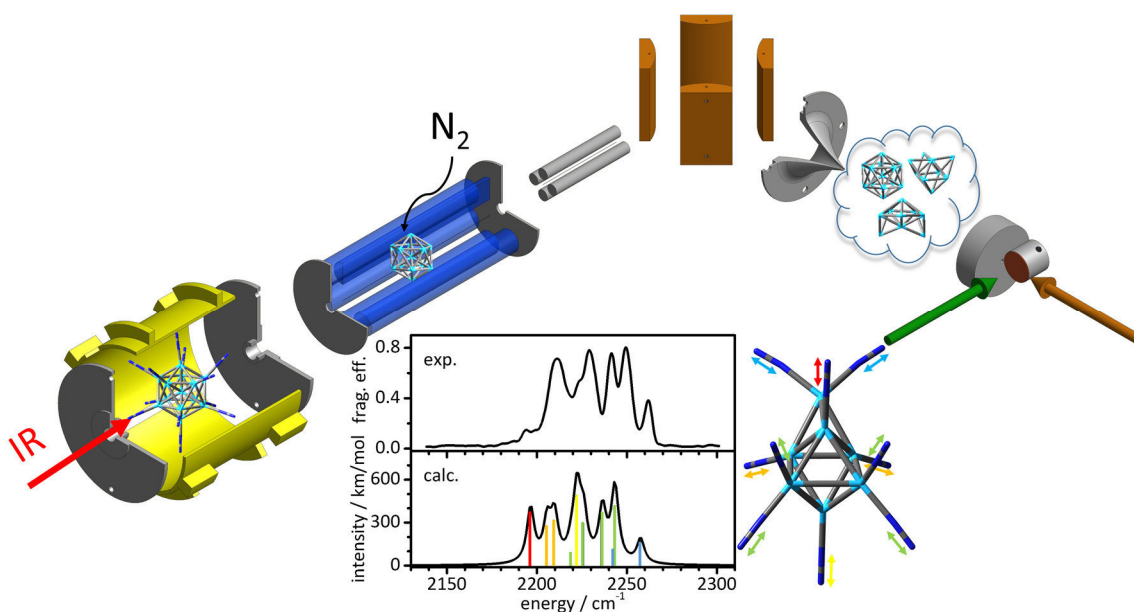
6.1 Preamble

The experiments were performed by the experimental team consisting of J. Mohrbach, and myself. The data evaluation was done by J. Mohrbach and myself. The computations were done by myself. The initial manuscript was written by myself and revised with the help of G. Niedner-Schatteburg and J. Mohrbach.

This manuscript has been **accepted** for publication in The Journal of Chemical Physics as part 2 of 2 of a back to back submission (for part 1 see chapter 5).

6.2 Abstract

We present the cryogenic (26 Kelvin) IR spectra of selected $[\text{Ni}_n(\text{N}_2)_m]^+$ ($n = 5 - 20$, $m = 1 - m_{\text{max}}$), which reveal strongly n - and m -dependent features in the N₂ stretching region, in conjunction with density functional theory (DFT) modelling of some of these findings. The observed spectral features allows to refine the kinetic classification (cf. accompanying paper) and to define four classes of structure related surface adsorption behavior: Class (1) of Ni₆⁺, Ni₁₃⁺, and Ni₁₉⁺, are highly symmetrical clusters with all smooth surface of equally coordinated Ni atoms, that entertain stepwise N₂ adsorption up to stoichiometric N₂ : Ni_{surface} saturation. Class (2) of Ni₁₂⁺, and Ni₁₈⁺ are highly symmetrical clusters minus one. Their relaxed smooth surfaces reorganize by enhanced N₂ uptake towards some low coordinated Ni surface atoms with double N₂ occupation. Class (3) of Ni₅⁺, and Ni₇⁺ through Ni₁₁⁺ are small clusters of rough surfaces with low coordinated Ni surface atoms, some reveal semi internal Ni atoms of high next neighbor coordination. Surface reorganization upon N₂ uptake turns rough into rough surface by Ni atom migration and turns octahedral based structures into pentagonal bipyramidal structures. Class (4) of Ni₁₄⁺ through Ni₁₇⁺, and Ni₂₀⁺ are large clusters with rough and smooth surface areas. They possess smooth icosahedral surfaces with some proximate capping atom(s) on one hemisphere of the icosahedron with the other one largely unaffected.



6.3 Introduction

In practice, much of heterogeneous catalysis is based on transition metals(TM) [1-4], and we are in desperate need for a better understanding at the level of participating elementary steps[2, 5]. Metal clusters are conceivable model system for heterogeneous catalysis [6-9]. Smaller than nanostructured catalysts, isolated clusters offer unique opportunities to study highly corrugated and highly curved surfaces, albeit at the expense of indirect access to their structural features. Elaborate studies of clusters may reveal their stabilities and instabilities alike. On the basis of such knowledge cluster studies provide insight into TM – adsorbate interactions which are complementary to TM bulk surface science studies, this analogy being recognized before and repeatedly. [10-13]

N₂ activation is crucial in ammonia synthesis, the corresponding Haber Bosch process being based on Fe, Ni, Ru, and other TMs .[14] Several surface science studies characterized the Fe N₂ interactions [15-20] and angle resolved photoemission studies in conjunction with potential surface modelling, concluded in α -N₂ and γ -N₂ motifs[21] which resemble η^2 side-on and η^1 end-on coordination of N₂ to multiple and single metal centers. Some studies recognized the resemblance of such topics to the N₂ interaction with the surfaces of Fe clusters.[22, 23] Numerous studies elucidated N₂ adsorbates on other first row transition metal surfaces, undertaken by a variety of experimental and theoretical methods, such as in the case of N₂ on Ni surfaces [24-27].

Armentrout and coworkers elucidated the thermochemistry of several small molecules (D₂, O₂ and CH₄) on Ni clusters, and they determined bond energies of adsorbates and products with considerable precision.[28-30] The dissociation of ions and mass detection of the resulting fragments helps in gathering structural information about molecules. In complement, the study of the vibrational modes of adsorbates on TM clusters and in TM coordination complexes as isolated ions by Infrared Multiple Photon Dissociation (IR-MPD) is prevalent.[31-34] The IR-MPD method has been extended by the introduction of tunable free electron lasers (FEL).[35-37] In this context IR spectroscopic studies of different adsorbates on Ni clusters are already published including the interaction of size selected Ni clusters with H₂ and CO. [38, 39] The latter one proposed a charge dilution model for the observed redshifts of the adsorbed CO on metal clusters. This model is in line with earlier proposed models for metal adsorbate/ligand interactions: the Dewar-Chatt Duncanson

6. Probing Cluster Surface Morphology by Cryo Spectroscopy of N₂ on Cationic Nickel Clusters

model for the coordination of alkenes with atomic metal centers [40] and the Blyholder model for the adsorption of CO on metal surfaces[41]. These findings may be helpful regarding N₂ adsorbate complexes as CO is isoelectronic to N₂. The fundamental interplay of N₂ with atomic transition metal cations (V, Nb, Rh) have been studied by the Duncan group by utilizing table top IR lasers.[42-44]

IR spectroscopy is inseparably linked to computational modelling of the investigated systems. Most theoretical studies focus on the modelling of the structures and energetics of bare Ni clusters [45-48]. Such studies are doubtlessly of high significance. The most rewarding modelling of cluster adsorbate complexes has received much less attention in the past, and there are merely a few studies on the modelling of Ni cluster adsorbate complexes[49, 50].

Two publications recently opened the research field of IR spectroscopy of N₂ on transition metal cluster: N₂ on neutral Ru clusters by Felicke et al. [51], and N₂ on cationic Co clusters under isothermal cryo conditions by ourselves[52].

There are merely a few experimental studies of N₂ on size selected Ni clusters, however. Early studies investigated the N₂ adsorption of neutral nickel clusters under flow reactor conditions by Parks et al, which have been published over two decades ago. They proposed several cluster structures.[53, 54] Yet there is no definite assignment. In this regard we must mention our recent publication on the $[\text{Ni}_n(\text{N}_2)_m]^+$ ($n = 9, 13$; $m = 1 - 13$) systems, which elucidated the cluster surface morphologies in terms of rough and smooth surfaces.[55] Knowing the possibly relaxing cluster structures throughout their participation in catalytic cycles, and unravelling the structural effects onto their reactivity would be a great leap in understanding catalysis and might assist the design of new catalysts.

This study aims to elucidate the vibrational spectroscopy of N₂ adsorbates onto cationic nickel clusters $[\text{Ni}_n(\text{N}_2)_m]^+$ ($n = 5 - 20$), and it obtains strong support of its findings through our preceding kinetic study[56], which we will reference in the following as **[JM]**, while we refer to the present spectroscopic study as **[SD]**.

6.4 Experimental and Computational Methods

The experiments were carried out in a customized Fourier Transform - Ion Cyclotron Resonance (FT-ICR) – mass spectrometer (Apex Ultra Bruker Daltonics). It served to perform the cluster production, isolation, N₂ condensation, InfraRed (Multi) Photon Dissociation (IR(M)PD) spectroscopy and mass analysis. For a detailed description of the formation of the cluster adsorbate complexes refer to [JM].

For the acquisition of the IR-PD spectra the FT-ICR cell is coupled to a tunable IR laser (spectral resolution: $\delta\nu = 0.9 \text{ cm}^{-1}$, pulse length: $\delta t = 7 \text{ ns}$). This laser is a KTP/KTA optical parametric oscillator/amplifier (OPO/A, LaserVision) system pumped by a pulsed 10 Hz injection seeded Nd:YAG laser (PL8000, Continuum). The difference frequency (DF) between the OPA signal and idler waves is generated in a AgGaSe₂ crystal. This generates IR radiation in the range of 1000 – 2400 cm^{-1} . Each trapped and isolated package of ions is irradiated by 7 – 10 laser pulses (0.1 – 1.5 mJ/pulse) to yield a sufficient amount of fragment ions. The IR spectra were recorded as ion chromatograms while continuously scanning the IR wavelength. The IR-PD signal was evaluated as $\sum_i F_i / (\sum_i F_i + \sum_i P_i)$, where F_i and P_i indicate fragment and the parent ion signals, respectively. An experimental IR-PD spectrum arises from a plot of the fragmentation efficiency as a function of laser frequency. We employed the IR-PD spectroscopy in the 2140 – 2300 cm^{-1} range on the $[\text{Ni}_n(\text{N}_2)_m]^+ = (n,m)$ species ($n = 5 - 20$). In this range we expected the N₂ stretching frequencies of the species. For all complexes the loss of one or two N₂ was the only observed fragmentation channel. Note, that IR-PD spectra of (n,m) species with high m likely originate from single photon absorption, whereas those of low m likely originate from two or even multiple photon absorption – rendering the latter IRMPD spectra.

Linear IR absorption spectra were calculated at the PBE0[57] level of theory using the cc-pVTZ basis sets[58] (N), and the Stuttgart RSC 1997[59] effective core potential (Ni), respectively, as implemented in the Gaussian 09 program package[60]. SCF convergence is tedious and can be achieved only at the expense of relaxed SCF convergence criteria of 10^{-5} (as compared to 10^{-8} in DFT calculations on light main group elements). The calculated spectra are scaled by 0.93 to account for prevailing anharmonicities and simulated using the Lorentz profile of $\text{fwhm} = 5 \text{ cm}^{-1}$. We regard our obtained results as starting points for future

and more elaborate treatments - as far as possible. In this regard, our current DFT results are “preliminary”.

6.5 Results and Discussion

Low N₂ coverages

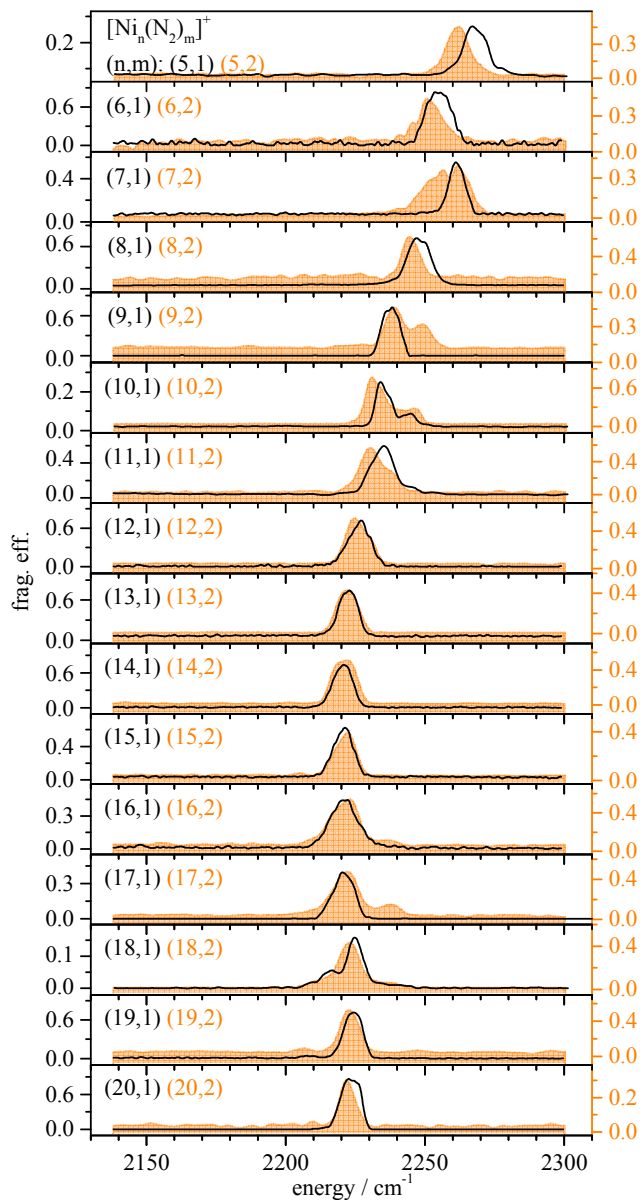


Fig. 1 IR-PD spectra of (n,1) (solid lines) and (n,2) (orange shaded areas) species for $n = 5 - 20$. There are subtle differences in the IR-PD spectra induced by the adsorption of a second N₂ molecule. Refer to the supplementary material for figures that show spectra of (n,1) and (n,2) separately.

We employed our cryo IR-PD spectroscopy scheme in the 2140 – 2300 cm⁻¹ range on the [Ni_n(N₂)_m]⁺ = (n,m) adsorbate cluster species ($n = 5 - 20$). In the cases of single and double N₂

adsorption, (n,1) and (n,2), we found IR active bands in the region of 2210 cm⁻¹ to 2280 cm⁻¹ (Fig. 1).

First N₂ adsorbate

The recorded IR-PD bands of (n,1) and (n,2) fall into a region (above 2000 cm⁻¹) which likely corresponds to a head on / end on adsorption of N₂ on top of single Ni atoms of the cluster, as we have shown before in the cases of (9,m) and (13,m).[55] Most (n,1) species – those with a single N₂ – reveal a single IR band in the N-N stretching region; with the exceptions of the n = 10 and n = 18 species, both of which provide for spectra that reveal a weaker second band. Such additional bands are possible indicators for the presence either of spin states isomers, or of cluster structural isomers, or of N₂ binding site isomers. We will discuss these possibilities in the light of further results below.

Aside from these specific exceptions, there is a clear and dominating trend throughout the recorded IR spectra: The larger the clusters the larger the observed red shifts. At (5,1) we find a redshift of 65 cm⁻¹ with respect to the IR inactive (yet well known) stretching frequency of free N₂ (2330 cm⁻¹), and in (20,1) we find a redshift of 107 cm⁻¹. The increase is nonlinear in cluster size n, and it becomes constant beyond n = 14 (at ~ 2221 cm⁻¹; cf. Figs. 1 and 2). It follows a trend observed before in the case of CO adsorption on cationic Rh_n⁺ [61] and Ni_n⁺ [38] clusters. There is an exception at n = 7 which reveals less red shift than expected from the general trend (by about 11 cm⁻¹). A similar exception was found in the IR spectra of CO on Ni₇⁺ [61] without receiving particular attention. Elucidation of conceivable structures arises in the light of our preliminary DFT structure modelling. At this point we want to emphasize that a reduced red shift likely points towards low coordinated Ni surface atoms. They carry localized cationic charge that suffices to hamper efficient π back donation – thus reducing observable N₂ bond weakening.

Second N₂ adsorbate

IR spectra of the (n,2) species almost coincide with those of (n,1) - some subtle differences prevailing. Most remarkably the small (n,2) species, n ≤ 11, seem to provide for additional, partially resolved contributions which are often slightly to the red of the single (n,1) peaks and rarely to the blue (as in the sole case of n = 9).

It was expected that the adsorption of a second N₂ adsorbate in the (n,2) species gives rise to additional spectral signatures. While the first N₂ adsorbate likely finds the most favorable adsorption site on the surface of the Ni clusters, the second N₂ may be forced to settle for another, possibly nonequivalent site. Either sort of sites originates from individual Ni atoms at the cluster surface. These Ni atoms may reside in various coordination environments that make up for a rough or smooth cluster surface as shown before[55]. It is likely the small clusters (n < 12) which provide for “rough” surfaces.

Our previous study of (9,m) and (13,m) [55] had revealed another mechanism of spectral complexity: Adjacent N₂ adsorbates may couple to symmetric or antisymmetric combinations of their stretching excitations. In the case of Ni clusters this leads to a largely constant splitting of $\sim 12 \text{ cm}^{-1}$. We observe such splittings in many IR spectra of (n,m); however, with $m \gg 2$. In the case of (9,2) our DFT calculations had revealed that a splitting of comparable magnitude arose from N₂ coordination to two Ni centers which were three- and fourfold coordinated within the Ni clusters, respectively. In all other cases, there is no indication for any such coupling. It is conceivable that first and second N₂ adsorbates initially stick to surface sites without relaxing into spatial proximity. The other minor, only partially resolved structures likely resolve such pinning to nonequivalent sites.

3.1.3 Charge dilution

When inspecting the recorded N₂ stretching bands for their values (Fig. 2) one finds a systematic increase of red shift with cluster size, running into a limiting value of about 2220 cm^{-1} which comes close to the N₂ stretching band position of N₂ molecules adsorbed on Ni surfaces [24, 62]. While the bands of n = 14 – 17 and of n = 18 – 20 merely shift, those of n = 17 to n = 18 are less red shifted by about 5 cm^{-1} with respect to the aforementioned ones. The red side bands of (18,1) and (18,2) fall within the range of the surface values. The observed trend can be explained by a charge dilution model as proposed by Fielicke before.[61] This model takes into account the cluster size dependent effect of net charge on the π back donation. It was first applied to transition metal clusters with CO. This rather simple model is well suited to describe analogous effects in the isoelectronic N₂ adsorption. We do observe indeed the same trend and magnitude ($\sim 50 \text{ cm}^{-1}$) in the present N₂ spectra as in the previous CO spectra. It is remarkable that we observe the same trend in the (n,2)

species, and it may be described by the same model, only minor differences prevailing with respect to the (n,1) cases.

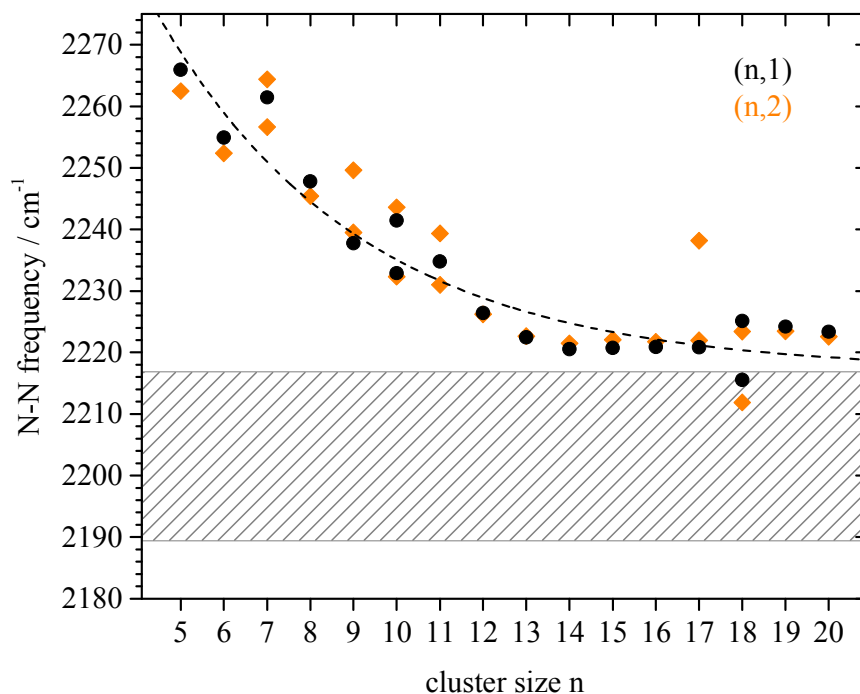


Fig. 2 N-N stretching frequencies of (n,1) (black dots) and (n,2) (orange diamonds) Ni cluster adsorbate complexes as function of cluster size $n = 5 - 20$. The dashed line is to guide the eye and corresponds to charge dilution model proposed before[65]. The shaded area indicates the range of the N-N stretching frequencies on various Ni surfaces.[24, 66] Note the slight increase in N₂ frequencies when $n > 15$.

High N₂ coverages

It is imperative to check for spectral N₂ features on Ni clusters at higher N₂ coverages. We chose to apply our cryo IR-PD spectroscopy scheme to N₂ loaded cluster complexes with (n,m) = (n,m_x) - the intermittent adsorption limit - and (n,m_{max}) - the adsorption limit. Note, that these well-defined limits arose from our own kinetic studies. For a detailed explanation refer to [JM]. We obtained spectra of $n = 5 - 20$, for (n,m_{max}) and (n,m_x) (Fig. 3). All of these spectra show IR active bands in the region between 2160 cm⁻¹ and 2270 cm⁻¹ which still corresponds to a head on adsorption of the N₂.

As expected the IR spectra for the adsorption limits provide for a significantly higher degree of complexity than those of the (n,1) and (n,2) species (cf. Fig. 3 right). This general statement holds true but for the exceptions of $n = 6, 13, 19$ - all of which are assumed to

provide for highly symmetric structures of all smooth surfaces (octahedron, icosahedron, and bi-icosahedron).

Other than these three highly symmetrical clusters, there are two distinct size ranges, namely $n_{\text{small}} = 5 - 12$ (without $n = 6$) and $n_{\text{large}} = 14 - 20$ (without $n = 19$) as defined by kinetic findings in [JM]. For ease of reading, we label these size ranges as “small” and “large” clusters. While the small clusters provide for rough surfaces and suffer from a somewhat ambiguous definition of the intermittent size limit, the large clusters are found to provide for smooth surfaces and well defined intermittent size limits if any (cf. [JM]). It is gratifying to see that these kinetic findings find some correspondence in the recorded IR-PD spectra. Both classes of clusters reveal an enhanced spectral complexity upon saturation of N₂ coverage at m_{max} – largely irrespective of their size. However, the small and large clusters proceed differently on their way towards m_{max} .

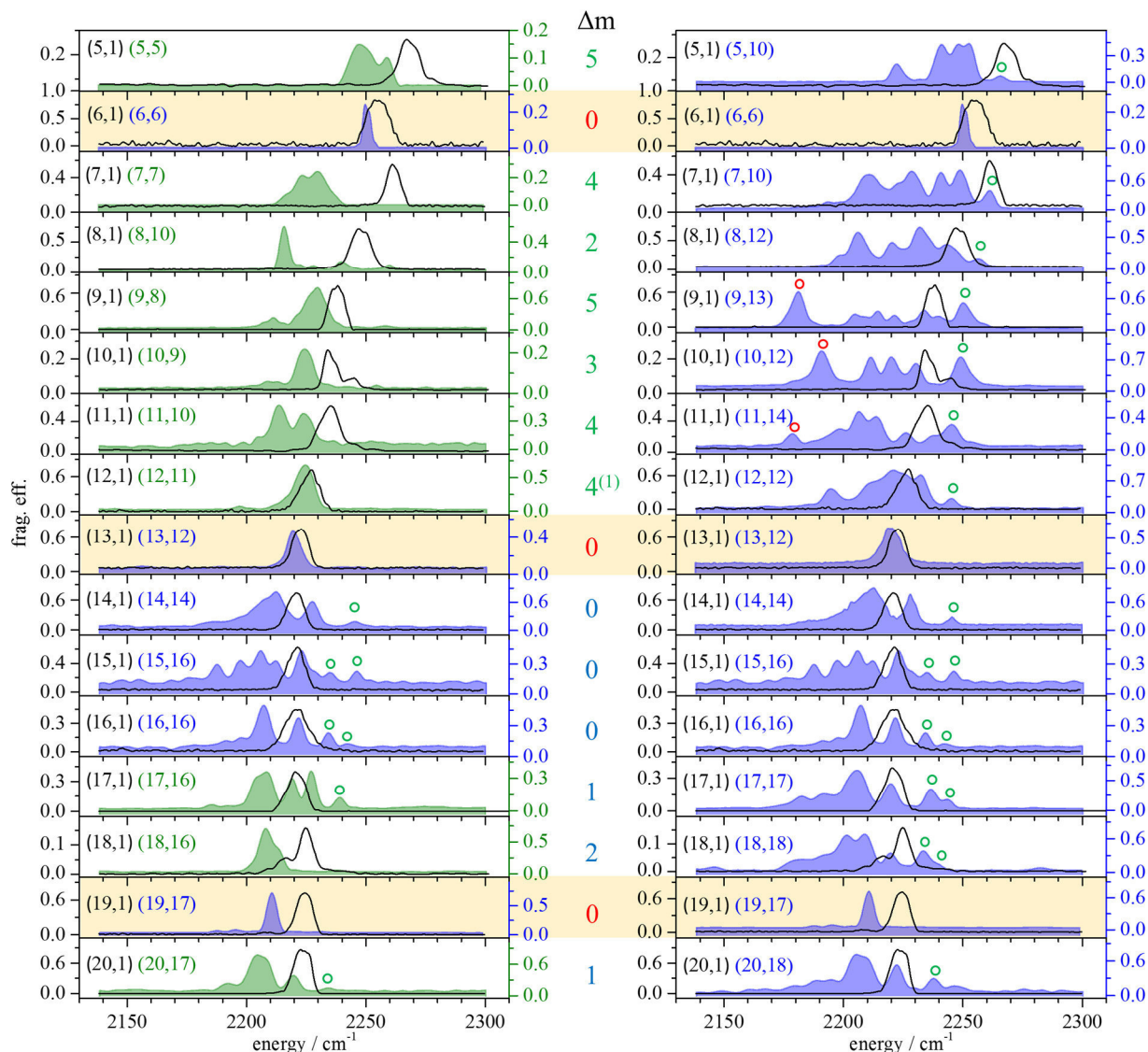
Small clusters

There is a constant redshift of the spectral window of observed features, *cf.* green boxes in Fig. S22, for all (n_{small}, m_x) with respect to the free N₂ stretching ($\Delta\nu \sim -105 \text{ cm}^{-1}$). This is in noteworthy contrast to the clear increase of redshift with n_{small} in the cases of $(n_{\text{small}}, 1)$ and $(n_{\text{small}}, 2)$ – indicative of a reduction of charge influence with n_{small} as discussed above.

Upon going from $m = 1$ to $m = m_x$ the spectral broadening is small/limited ($\Delta\Delta\nu \leq 35 \text{ cm}^{-1}$). Large spectral broadening, which is indicative of enhanced couplings, sets in only upon going from m_x to m_{max} where it reaches considerable amounts ($\Delta\Delta\nu \leq 85 \text{ cm}^{-1}$). Note that large spectral width/broadening implies large variety of Ni coordination environments, and some N₂ – N₂ sym/asym coupling on top.

The enhanced spectral broadening has three components: Enhanced couplings account for the major part of spectral complexity for all n_{small} ($\Delta\Delta\nu \sim 55 \text{ cm}^{-1}$). To the blue there are one or two distinct additional peaks ($\nu \sim 2260 - 2245 \text{ cm}^{-1}$, marked with green circles) which we attribute to symmetrically coupled N₂ stretching modes of pairs of N₂ adsorbates on top of low coordinated Ni atoms, supported by our DFT results in the following. It is noticeable that we do not observe such green circle bands in the spectra of (n_{small}, m_x) . This indicates a lack of double N₂ occupation on low coordinated Ni sites up to the intermittent limits m_x of small clusters n_{small} .

6. Probing Cluster Surface Morphology by Cryo Spectroscopy of N₂ on Cationic Nickel Clusters



⁽¹⁾ $\Delta m=4$ is the kinetic finding. Experimental limitations hampered spectroscopic data taking of $(12, m > 12)$. We include $(12, 12)$ instead, nicely documenting the adsorbate induced reorganization.

Fig. 3 IR-PD spectra of $[\text{Ni}_n(\text{N}_2)]^+$ cluster adsorbate complexes $n = 5 - 20$ at the intermittent adsorption limits (n, m_x) (green shaded areas, left) and at the adsorption limits (n, m_{max}) (blue shaded areas, right). The Δm numbers in between of both stacks indicate the difference of adsorption limit and intermittent adsorption limit, $\Delta m = m_{\text{max}} - m_x$, color coded in red for highly symmetrical clusters, in green for small clusters, and in blue for large clusters. Highly symmetrical cluster spectra are highlighted with a yellow background. The $(n, 1)$ spectra of Fig. 1 are indicated by solid lines. In some cases there is no intermittent adsorption limit ($\Delta m = 0$), and we plot the adsorption limit instead (blue spectra on the left). In the case of $(12, m)$ the complex at the adsorption limit $(12, m_{\text{max}}) = (12, 14)$ was too weak for interrogation. We chose to study the more intense $(12, 12)$ instead. The green and red circles are to highlight significant bands, which are discussed in the text.

There are red circle peaks only for $n_{\text{small}} = 9, 10, 11$ which are those sizes that might provide for semi internal Ni atoms of highest coordination (7 to 9 nearest Ni neighbors) yet accessible for adsorbates from the outside.

It is interesting to focus on the cases of (12,11) and (12,12) in particular. They seem to break the rules. (12,11) is narrow / single line and little redshift. Best conceivable explanation comes by structural assumption based on icosahedron minus one surface atom. All equivalent Ni surface atoms of the same or at least similar coordination numbers to next Ni neighbors. In remarkable contrast, there is significant red shift and spectral broadening in (12,12), together with some blue shifted bands. Indicative for an adsorbate induced surface reconstruction from smooth to rough yielding some low coordinated Ni surface atoms, which give rise to a “green circle” band in the blue. Note that we did not highlight the band at around 2195 cm^{-1} in the spectrum of (12,12) as a “red circle” band because we find it highly speculative to assign this band exclusively to a N₂ coordinated to a highly coordinated, semi internal Ni atom. Furthermore the spectrum of (12,11) reveals a small feature in this region as well and DFT does not suggest the binding of N₂ to a highly coordinated Ni atom (see 3.2.3). The adsorbates are possibly able to induce a Ni cluster reorganization and break the high symmetry of an unstable icosahedron-minus-one-structure.

Large clusters

There is a constant redshift of the spectral window of observed features, *cf.* green boxes in Fig. S22, for all (n_{large}, m_x) with respect to the free N₂ stretching ($\Delta\nu \sim -105 \text{ cm}^{-1}$) and of the same value as for (n_{small}, m_x) . Upon going from $m = 1$ to $m = m_x$ and to $m = m_{\text{max}}$ the spectral broadening is considerable ($\Delta\Delta\nu \leq 70 - 80 \text{ cm}^{-1}$). It is only the case of (18,16) – similar to (12,11) – which has a single band, and it seems to reorganize towards spectral complexity – evidenced by a broad spectral window – upon full coverage at (18,18). (18,16) is equally exempt with respect to “green circle” bands, which occur in all other large clusters. Some redshift and significant spectral broadening appear upon $m = 1$ to $m = m_x$. It is surprising to see the exception of (18,16) where the redshift comes without broadening. The single band at (18,16) may indicate a smooth surface of equivalent coordination of surface atoms with two interior/bulk Ni atoms. The spectral broadening of (18,18) indicates significant reorganization. The “green circle” band points to low coordinated Ni surface atom, which might be only in the case of adsorbate induced reorganization.

IR spectra and DFT modelling per cluster size

Putting everything together, we now look at the effect of N₂ adsorption level m per Ni _{n} core size in more detail:

[Ni₅(N₂) _{m}]⁺ = (5, m): The IR-PD spectrum of the intermittent adsorption limit (5, m_x) = (5,5) reveals two close lying bands which likely indicates two distinct adsorption sites (Fig. 3, top left). This would be in line with a cluster structure of a trigonal bipyramid: Three equatorial Ni atoms form a triangular ring, four next Ni neighbors each; two polar apex Ni atoms above and below the triangular plane are threefold coordinated each. All Ni atoms are in a low coordination environment, in particular as compared to close packed fcc Ni(111) surfaces where the next neighbor count is 9. The 1:1 adsorption of Ni : N₂ onto these two classes of adsorption sites renders the occurrence of two vibrational bands likely. We expect – and we find – these two bands in close proximity with a small splitting of merely 12cm⁻¹. Single N₂ adsorption to all of the three Ni atoms causes the band to the red; single adsorption to both polar Ni atoms causes the band to the blue.

The IR-PD spectrum of the saturated species (5, m_{max}) = (5,10) shows a broader absorption pattern of five bands (Fig. 3, top right) which spread out over ~ 52 cm⁻¹ – as compared to mere 22 cm⁻¹ in the case of (5,5). The increased complexity can be attributed to the enhanced couplings of N₂ adsorbates which share the same Ni adsorption site in the given 1 : 2 adsorption stoichiometry. Note that such a double occupation of adsorption sites is unlikely – if not impossible – on a planar dense packed bulk surface, while conceivable in conjunction with a curved cluster surface.

As of now we did not manage to reproduce the seemingly simple vibrational spectra of (5,5) and (5,10) by standard DFT methods (*cf.* Fig. S19 in the supplementary material). We speculate that prevailing symmetry reductions by Jahn-Teller and/or Renner-Teller effects would render dedicated treatments necessary.

[Ni₆(N₂) _{m}]⁺ = (6, m): This exceptional Ni cluster without an intermittent adsorption limit reveals an IR-PD spectrum of a single band in all three cases recorded: (6,1), (6,2), and (6, m_{max}) = (6,6). It is most noteworthy to point out that the width of the single band in (6,6) reduces by almost a factor of three with respect to that of (6,1) and (6,2): $\Delta v_{fwhm(6,6)} = 3.8 \text{ cm}^{-1}$ and $\Delta v_{fwhm(6,1)} = 10 \text{ cm}^{-1}$. These findings can be explained by a high symmetry of the cluster

itself. An octahedral structure should adsorb six N₂ onto six Ni atoms, one each. Retaining its symmetry upon adsorption the resulting IR spectrum should only show one single band. Seemingly, the 1:1 adsorption stoichiometry at saturation limit helps to stiffen the N₂ adsorption geometries and reduces angular tilts and/or conceivable adsorbate induced symmetry breaking. We have found and discussed similar effects in the cases of (13,m) before.[55] Here, we utilized DFT modelling to endorse our structural hypothesis on (6,1) and (6,6), see Fig. 4.

Our DFT modelling of the (6,1) complex in a quartet state reveals an N₂ stretching vibration at 2240 cm⁻¹ in reasonable agreement with the recorded IR-PD band at 2255 cm⁻¹. Other multiplicities would be less stable.

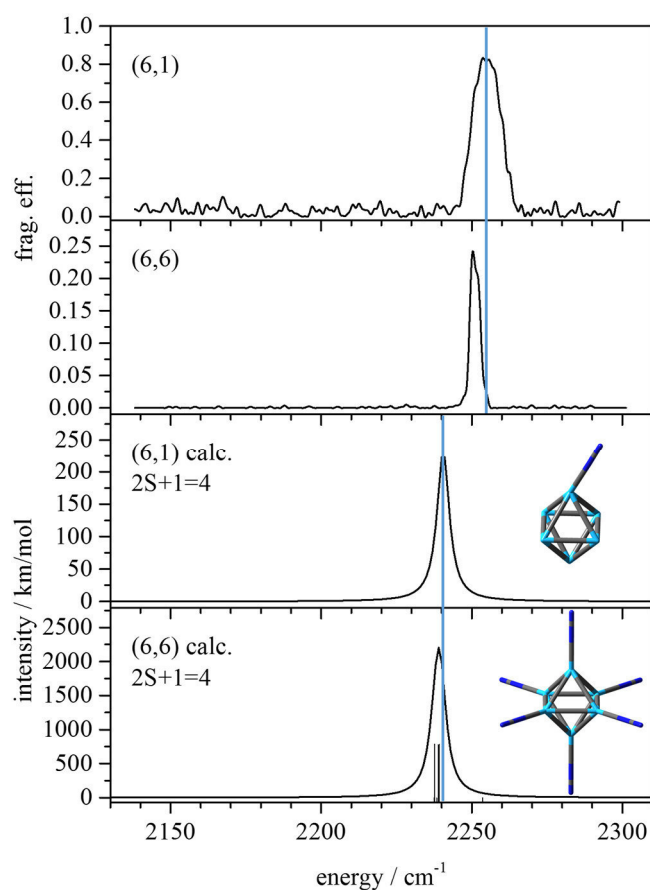


Fig. 4 Experimental IR-PD spectra and DFT modelling of (6,1) and (6,6). Both calculated clusters have a quartet spin state and an octahedral cluster core. For the (6,6) cluster we enforced a C_{2h} symmetry, a much larger splitting occurring otherwise (cf. Fig. S20). The (6,1) cluster was optimized without restrictions. The blue lines are to emphasize the slight redshift from (6,1) to (6,6) – in experiment and calculations alike.

In the (6,6) case we find that the quartet state is more stable than a doublet or a sextet – no matter which geometry. Full geometry relaxation would yield N₂ tilts off the Ni adsorption site symmetry axis (the “surface normal vector”) and a concomitant spread of N₂ vibrational frequencies of up to 40 cm⁻¹ which would be ten times beyond the experimental width (cf. Fig S20 in the supplementary material). Given the very sharp experimental band, we assume a high symmetry of the Ni cluster core and of the N₂ adsorption layer, and we have continued further modelling accordingly. Interestingly, we achieved converged DFT results only when enforcing a reduced C_{2h} symmetry – thus allowing for some Jahn-Teller relaxation of the Ni core while enforcing strictly linear Ni - N₂ on symmetry axis adsorption - and we failed when asking for full octahedral O_h symmetry. Under such symmetry restrictions we obtain a closely spaced bunch of N₂ adsorbate stretching vibrations in (6,6) the center of which is slightly red shifted with respect to the according value in (6,1), $\Delta v_{(6,6)-(6,1),\text{calc}} = -1.5 \text{ cm}^{-1}$. This corresponds to the experimental value, $\Delta v_{(6,6)-(6,1),\text{IR-PD}} = -3.9 \text{ cm}^{-1}$ (cf. Fig. 4 and blue lines, to guide the eye).

[Ni₇(N₂)_m]⁺ = (7,m): Three possible cluster structures have been proposed by Parks & Riley for the Ni₇⁺ cluster: a pentagonal bipyramid, a capped octahedron and a four capped trigonal prism. They conclude the capped octahedron to be most likely, even though they could not rule out a structural rearrangement upon coordination of the first N₂ adsorbate.[53] Our own search revealed that the calculated vibrational spectrum of a capped octahedral Ni₇ core with 10 N₂ adsorbates reproduces the experimental IR-PD spectrum of (7,10) well and in most details (Fig. 5), while the calculated spectra of complexes with other Ni₇ core structures do not.

This substantiates the theory of a capped octahedral cluster structure of the high coordinated species. The DFT calculations predict IR intensities, which are in very good agreement with the experiment – except for the lowest N₂ stretching frequency at 2196 cm⁻¹ that is significantly weaker in the IR-PD spectrum. Our modelling attributes this vibration to the N₂ adsorbate on top of the highest coordinated nickel atom (cf. Fig. 5 red arrow).

Nevertheless, we see a clear trend in the calculated IR spectrum of the (7,10) complex (cf. color code in Fig.5): The higher the coordination number of the Ni, the larger the redshift of the N₂ vibration. Stretching vibrations of N₂ adsorbates on the same Ni atom couple to symmetric and antisymmetric combinations, which typically split by ~ 10 cm⁻¹.

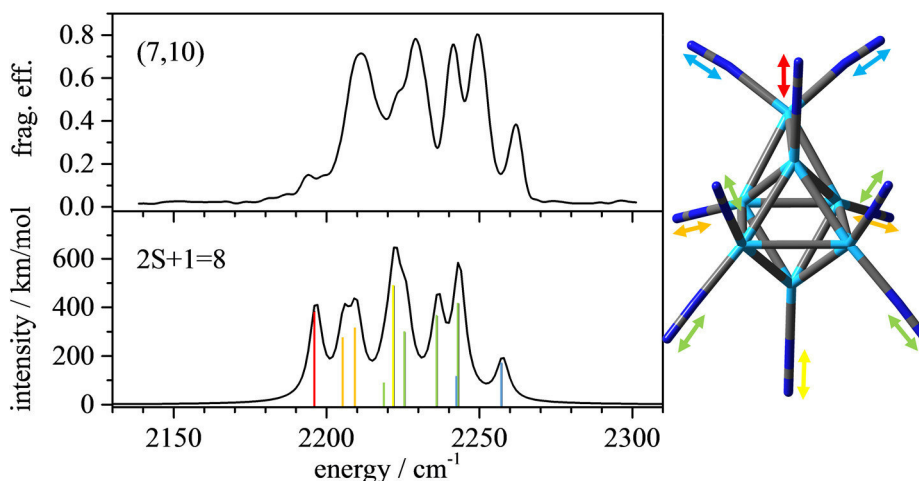


Fig. 5 Experimental IR-PD spectrum and DFT modelling of (7,10). The computed structure is a capped octahedron with a spin state of $2S+1 = 8$. Each Ni atom adsorbs a single N₂, and the three least coordinated Ni atoms another second N₂. The color-coding of the stick spectrum and of the vibrational double arrows relate these to each other. Note the vibrational splittings by symmetric and antisymmetric couplings of N₂ vibrations at doubly occupied Ni sites (green and blue) or at adjacent equivalent Ni sites (orange and green).

It is noteworthy to emphasize that the adsorbate layer of intermittent size, the (7,7) complex reveals a seemingly much simpler spectral pattern, but shifted with respect to the sole bands of the (7,1) complex. One may be tempted to speculate about a pentagonal bipyramid structure with a 1 : 1 adsorption scheme, all Ni sites similar, being four- or five-fold coordinated. Certainly, there is no low coordinated Ni site, as there is no “green circle” band. Unfortunately, there are no reliable structure calculations available as of now.

[Ni₈(N₂)_m]⁺ = (8,m): The IR spectrum of the (8,m_x) = (8,10) complex consists of one main band at 2216 cm⁻¹ (Fig. 3, left row, spectrum in green) which is redshifted by 32 cm⁻¹ with respect to (8,1), and accompanied by several weaker bands to the blue. The spectrum of the (8,m_{max}) = (8,12) complex reveals a broad vibrational pattern of at least six strong bands which partially overlap, and which has a strong similarity to the pattern of (7,10). One may speculate about a bicapped octahedron or a mono-capped pentagonal bipyramid, as suggested by our kinetic studies as well, see [JM]. Our DFT modelling has not led to a reasonable simulation of the observed vibrational spectrum yet.

[Ni₉(N₂)_m]⁺ = (9,m): We have studied and published these species before.[55] The adsorption limit at (9,13) and the intermittent adsorption limit (9,8) could be explained by both a tricapped octahedron and a bicapped pentagonal bipyramid. Utilizing DFT

calculations, we showed that there is a possible structural rearrangement upon adsorption of N₂. Starting from a tricapped octahedron the cluster relaxes to a bicapped pentagonal bipyramid. In any case, the n = 9 cluster complexes have shown strong evidence for a single highly coordinated Ni atom, that might be regarded as “semi-internal” or embryonic on the way to internal or bulk. It is this highly coordinated Ni atom which seems to receive an N₂ adsorbate only upon saturation, namely at the (9,12) and (9,13) complexes. Here, we conclude that the most red shifted band at 2181 cm⁻¹ (marked by red circle in Fig. 3) originates from such an N₂ adsorbate on the semi-internal Ni site.

[Ni₁₀(N₂)_m]⁺ = (10, m): The spectrum of (10, m_x) = (10,9) resembles that of (9, m_x) = (9,8), and that of (10, m_{max}) = (10,12) resembles that of (9, m_{max}) = (9,13). This finding suggests structural similarities. The (10, m_x) = (10,9) stoichiometry indicates a highly coordinated, semi-internal Ni atom, further substantiated by the “red circle” fingerprinting band at 2191 cm⁻¹ – subtle structural balances modulating the very band position slightly. Appearance of a “green circle” band to the blue once more indicates the occurrence of double N₂ occupation of a low coordinated Ni site. Taken altogether these spectral observations suggest a conceivable tricapped pentagonal bipyramid structure.

[Ni₁₁(N₂)_m]⁺ = (11, m): Once more spectral similarities to (9, m) and (10, m) suggest structural similarity. The (11, m_x) = (11,10) stoichiometry indicates a highly coordinated, semi-internal Ni atom, further substantiated by the “red circle” fingerprinting band at 2179 cm⁻¹ – once more shifted by some subtle structural balances. A “green circle” band indicates double N₂ on a low coordinated Ni site. We speculate on a conceivable tetra-capped pentagonal bipyramid structure – which would be isomorph to an icosahedron missing two neighboring atoms.

Our structural modelling by DFT suggests similar structures and reasonable spin states, 2S+1=10. It manages to simulate all but one spectral features: The observed “red circle” band is missing by simulation (Fig. 6). This might be due to slight overbinding of the Ni apex atoms. If the low coordinated Ni apex atoms next to the semi-internal Ni site were a little more to the outside, the otherwise shielded central Ni atom might become accessible for N₂ adsorbates. DFT modelling of the intermittent adsorption limit (11,10) is still in progress (Fig. S21 in the supplementary material). A superposition of two different spin states is conceivable.

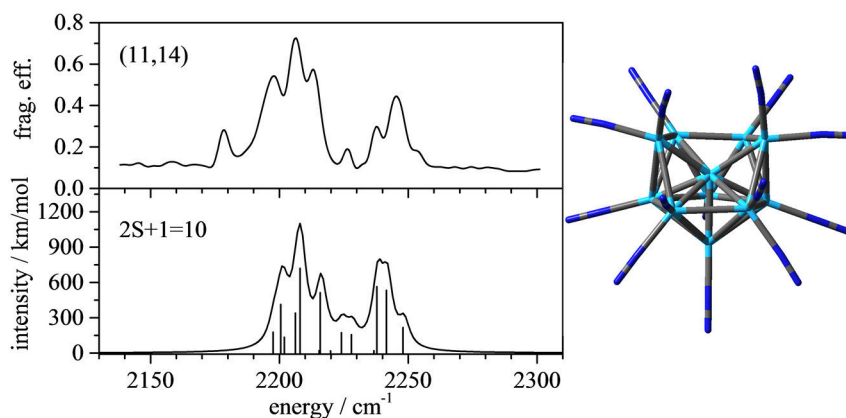


Fig. 6 Experimental IR-PD spectrum and DFT modelling of (11,14). The computed structure is an icosahedron missing two neighboring atoms with a spin state of $2S+1=10$. Every Ni atom adsorbs at least a single N₂, except for the Ni atom in the center of the cluster which stays vacant. The four least coordinated Ni atoms accept an additional N₂. The computed spectrum models the experimental measured spectrum closely, except for the experimental band at 2179 cm⁻¹.

[Ni₁₂(N₂)_m]⁺ = (12,m): The spectrum of the (12,m)_x = (12,11) species is dominated by a single band at 2222 cm⁻¹ which suggests a smooth surface of the Ni core. A weak sideband at 2196 cm⁻¹ asks for some explanation.

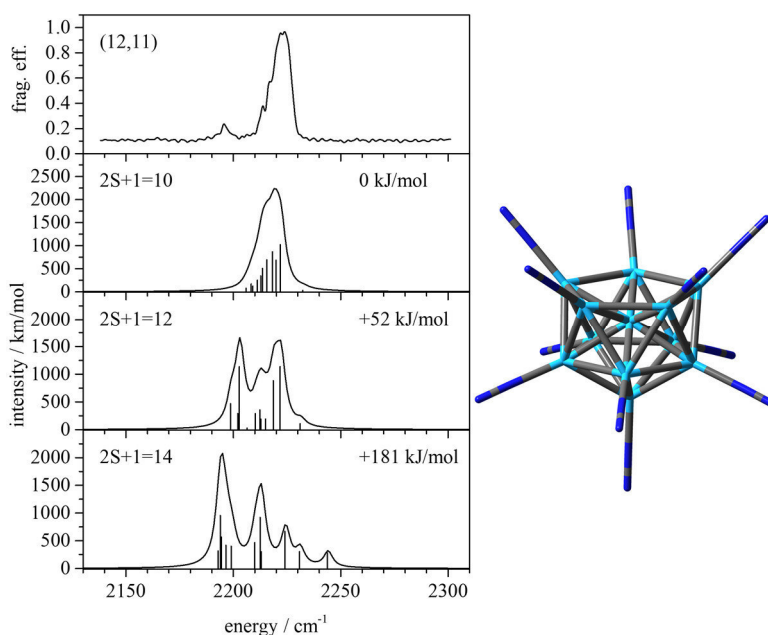


Fig. 7 Experimental IR-PD spectrum of (12,11) and DFT modelling by an icosahedral structure with one missing surface atom. Each Ni atom adsorbs a single N₂, except for the semi internal Ni atom. There are several conceivable spin states.

Our DFT modelling converges to an icosahedron minus one surface atom with a single N₂ occupation of each Ni site but the internal one. This structure stabilizes a spin state of

6. Probing Cluster Surface Morphology by Cryo Spectroscopy of N₂ on Cationic Nickel Clusters

$2S+1=10$, and its spectrum matches the experimental spectrum quite well (Fig. 7) – except for the weak sideband, which we attribute to possible contributions from the 12tet spin state.

The experimental IR-PD spectrum of the $(12, m_{\max}) = (12, 12)$ complex reveals a broad and more complex pattern. It gives rise to a green circle band, which indicates double N₂ adsorption to a low coordinated Ni atom. This cluster complex does not possess the rather smooth structure of the $(12, 11)$ complex. We thus observe a presumable reorganization of the Ni cluster core by an increase of the N₂ adsorption by one molecule, from 11 to 12. The Ni₁₂⁺ cluster most likely does not provide for the high stability of the highly symmetric Ni₁₃⁺ cluster. Thus, it is possible that adsorbates induce reorganization. A similar effect has been predicted for neutral Ni clusters before[45]: Highly symmetrical clusters of closed geometric shells ($n = 13, 19$) provide for large reorganization energies, while all others reveal low lying isomers close to the most stable minimum structure. The latter ones are subject of high probability for reorganization, e.g. upon adsorbate induced distortions.

[Ni₁₃(N₂)_m]⁺ = (13, m): The naked Ni₁₃⁺ cluster is assumed to be of icosahedral shape with an all smooth surface. Therefore, the experimental IR-PD spectrum of the $(13, m_{\max}) = (13, 12)$ complex consists of a single band. For a detailed discussion see our recent publication.[55]

[Ni₁₄(N₂)_m]⁺ = (14, m): The IR-PD spectrum of $(14, m_{\max}) = (14, 14)$ reveals two narrow bands at 2229 cm⁻¹ and 2246 cm⁻¹, and an asymmetric wide band at 2212 cm⁻¹ with a tail to the red. Our DFT modelling suggests a capped icosahedron, the capping Ni atom doubly occupied and all other Ni sites singly. Despite all effort, we only achieved a fair agreement of the modelled vibrational spectrum with the experimental IR-PD spectrum (cf. Fig. 8). A weak band to the blue nicely models the “green circle” band of the IR-PD. All the other modelling deviates significantly from the experiment. In particular, the strong experimental doublet at 2212 and 2229 cm⁻¹ finds no correspondence in modelling – which in turn finds significant IR intensities below 2180 cm⁻¹ void of correspondence in experiment. Obviously, DFT modelling reaches limits at this point – at least by our currently available methods. The found motifs of all but the green circle vibrations originate from various delocalized N₂ stretching modes remote of the capping Ni site. It may be this coupling, which ceases to be modelled accurately as of now. The experiment reveals a clear 17 cm⁻¹ splitting which comes close to

the previously observed symmetric to asymmetric combination mode differences by adjacent N₂ adsorbates [55].

The N₂ adsorption kinetics show no evidence for any reorganization and/or intermittent adsorption limits. We thus have no reason to speculate about those in the present case – similar to what follows.

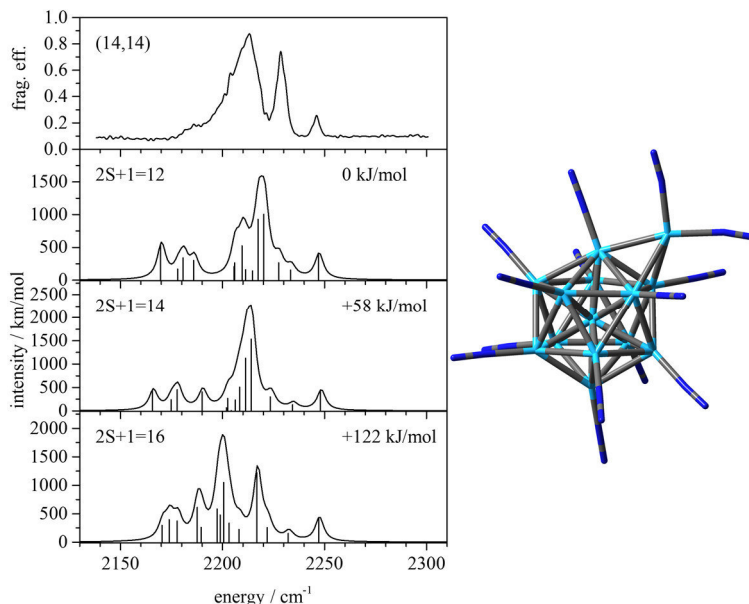


Fig. 8 Experimental IR-PD spectrum of (14,14) and DFT modelling by a capped icosahedral structure. Each Ni surface atom adsorbs a single N₂, except for the capping Ni atom which accepts another second N₂. There are several conceivable spin states.

Of course, we have checked for various spin states in the course of our DFT modelling, and we found less stable 14tet and 16tet states, the IR spectra of which do not agree with experiment either. While it was stated that standard DFT may underestimate spin magnetic moments [63] we find good agreement with our own previous determination of these by XMCD experiments on isolated cluster ions[64]. Finally, we have to consider the possibility of somewhat higher atomic moments – more unpaired d electrons – which might be in part antiferromagnetically coupled. It would take high effort to model such electronics by broken symmetry calculations, and this is clearly beyond the scope of our present study.

[Ni₁₅(N₂)_m]⁺ = (15,m): The spectrum of (15,m_{max}) = (15,16) is similar to that of (14,14) but for two changes: It provides for some additional bands. There are two “green circle” bands at 2247 cm⁻¹ and 2235 cm⁻¹, instead of merely one in (14,14). This indicates two low coordinated Ni sites which accept double occupation by N₂ adsorbates each - conceivably an

6. Probing Cluster Surface Morphology by Cryo Spectroscopy of N₂ on Cationic Nickel Clusters

icosahedral Ni core structure with two non-neighboring Ni capping atoms. Note, that thereby we rule out an otherwise conceivable truncated octahedron (cf. **[JM]**) which would be void of such low coordinated Ni atoms. Additional bands to the red make up for an increased spectral complexity. This might be explained by the superposition of multiple spin states and / or by the coexistence of multiple structural isomers, the latter arising from different positioning of the two capping Ni atom with respect to each other: adjacent or remote.

In the cases of this and larger complexes, we refrained from pursuing DFT modelling on our own. This challenging task is left to others and it would find our full support – once pursued.

[Ni₁₆(N₂)_m]⁺ = (16,m) and [Ni₁₇(N₂)_m]⁺ = (17,m): The spectra of (16,m_{max}) = (16,16) and (17,m_{max}) = (17,17) provide for a very large similarity. In both cases, there are two “green circle” bands around 2240 cm⁻¹, which we assign to the symmetric stretching vibrations of a pair of two N₂ adsorbates on top of low coordinated Ni capping atoms, much like in the (15,16) case discussed above. The central part of both spectra is dominated by a pair of strong bands close to what we found in (14,14) and in (15,16). Such close similarities suggest likely similar structural motifs. It is conceivable that the Ni cluster cores originate from a stepwise addition of single Ni atoms to the triangular faces of a Ni₁₃ icosahedron. This would eventually lead to a bi-icosahedral shape at Ni₁₉, and we will discuss this option latter. It is likely that the capping atoms preferentially accumulate on one side of the Ni₁₃ core and in mutual proximity in order to gain cohesion energy. Such a stepwise adding up process maintains the previously smooth icosahedral surface on one side while creating defect like rough surface parts on the other side. It is this Janus head like situation of all clusters n = 14 – 17 which renders the resulting IR spectra similar. There is an ubiquitous symmetric to asymmetric N₂ coupling splitting in all cases, and is accordingly seen in the spectra by the dominant 17 cm⁻¹ splitting of the two strongest bands.

[Ni₁₈(N₂)_m]⁺ = (18,m): The spectrum of the (18,m_x) = (18,16) species is dominated by a single band at 2209 cm⁻¹ which suggests a smooth surface of the Ni core. A weak shoulder to the blue might correspond somehow to the weak additional band to the red of the sole dominant peak in (18,1). In any case this simple spectrum is in remarkable contrast to the spectral complexity of the n = 14 – 17 clusters. The more noteworthy it is that the n = 18

cluster turns into spectral complexity once there are two more N₂ adsorbates, namely at (18, m_{max}) = (18, 18). This behavior is reminiscent of the (12, 11) and (12, 12) cases where we concluded in structural reorganization upon N₂ saturation. Dwelling on this analogy we postulate a rather smooth cluster structure at the intermittent adsorption limit (18, 16) (e.g. a bi-icosahedron missing one apex atom) which would provide for all equivalent Ni sites for N₂ adsorption but one semi internal, highly coordinated Ni atom that remains vacant in (18, 16). As such a structure does not provide for the stability of a high symmetry cluster (n = 19, bi-icosahedron) further N₂ adsorption might induce some structural reorganization. This inevitably leads to coordination loss of some Ni surface atoms and accordingly to surface roughening, or in other words to the emergence of some defect sites. The spectral consequence of such roughening is by now well known to us: The appearance of a “green circle” band would be inevitable and fingerprinting: Indeed, the IR-PD spectrum of (18, 18) clearly reveals two of these in partial coalescence at ~ 2234 and 2238 cm⁻¹.

[Ni₁₉(N₂)_m]⁺ = (19, m): The spectrum of (19, m_{max}) = (19, 17) is almost as simple as those of (6, 6) and (13, 12): All of these consist of a single strong band, which points towards high symmetry and all equivalent Ni surface sites. In the case of (19, 17) it is straightforward to assume bi-icosahedral Ni₁₉ core, the 17 Ni surface atoms of which are “titrated” by 17 N₂ adsorbates in 1:1 adsorption stoichiometry. Besides the main band of (19, 17) at 2211 cm⁻¹ a second glance reveals two very weak bands arise to the red, at 2196 cm⁻¹ and at 2188 cm⁻¹ (cf. Fig. S17 in the supplementary material). While we have no proof of any explanation we feel entitled to speculate about spin state isomers, which might stabilize by minute structural distortions. By our own DFT modelling of the small Ni clusters we would expect stretching vibrations of N₂ adsorbates to such high spin isomers (also refer to [55] Fig. 9) shifting to the red by amounts on the order of the observed weak bands in (19, 17).

[Ni₂₀(N₂)_m]⁺ = (20, m): The recorded IR-PD spectra of (20, m_x) = (20, 17) and (20, m_{max}) = (20, 18) show high similarities. Both consist of three strong bands, and both species give rise to “green circle” bands. Only minor differences prevail: There is a somewhat broader shoulder to the red of the 2205 cm⁻¹ band in (20, 18), and its “green circle” band is somewhat more distinct. The general spectral pattern is reminiscent of (14, 14). Dwelling once more on an analogy – here to (13, 12) - all of the spectral features in (20, 18) suggest a singly capped bi-icosahedral Ni₂₀⁺ core structure where the low coordinated Ni capping atom

6. Probing Cluster Surface Morphology by Cryo Spectroscopy of N₂ on Cationic Nickel Clusters

accepts a pair of N₂ adsorbates (see green circle band in the spectrum). This capping atom most likely goes to the waist of bi-icosahedron and thereby slightly bends it off linearity. The disfavored Ni counterpart on the opposite site acquires a locally convex surface environment, ceasing to accept an N₂ adsorbate. In total the number count of saturation comes to (20,18).

6.6 Conclusions

D The recorded IR-PD spectra of all (n,1) and (n,2) cluster adsorbate complexes show IR active bands by head-on bound N₂ adsorbates which shift from ~ 2270 cm⁻¹ at small (n,1) and (n,2) to ~ 2220 cm⁻¹ at large ones. These redshifts (~ 50 cm⁻¹) with increasing cluster size are in line with the established charge dilution model.

The many recorded IR-PD spectra of intermittent (n,m_x) and saturated (n,m_{max}) species – together with the few successfully modeled DFT spectra – allow to refine our initial separation by presumed structure and observed adsorption behavior (small, large, and highly symmetric) as stated on the basis of the recorded kinetic data [JM]. We now conclude that there are four classes of structure related surface adsorption behavior:

Class (1) of highly symmetrical clusters with all smooth surfaces comprises Ni₆⁺, Ni₁₃⁺, and Ni₁₉⁺, and their N₂ adsorbate complexes up to saturated (n,m_{max}). These clusters of exceptional high symmetry (octahedron, icosahedron, bi-icosahedron) provide for simple IR-PD spectra. Adsorption kinetics, IR-PD spectra, and DFT in line conclude in step wise and largely independent N₂ adsorption up to a 1:1 stoichiometry of Ni_{surface} : N_{2,adsorbate}.

Class (2) of some highly symmetrical clusters minus one Ni atom comprises Ni₁₂⁺, and Ni₁₈⁺, and their N₂ adsorbate complexes up to saturated (n,m_{max}). These two clusters are short of one Ni atom relative to the all smooth surface class (1) species. The IR-PD spectra strongly suggest that the naked clusters, and those with few N₂ adsorbates, have relaxed into some structure with a smooth surface and void of defects such as low coordinated Ni surface atoms. Upon enhanced N₂ load they reorganize into partially rough surface structures which allow for N₂ uptake beyond the 1:1 stoichiometry, in particular by providing low coordinated Ni surface atoms which stabilize by double N₂ adsorption.

Class (3) of small clusters with rough surfaces comprises Ni₅⁺, and Ni₇⁺ through Ni₁₁⁺, and their N₂ adsorbate complexes up to saturated (n_{small},m_{max}). The IR-PD spectra suggest rough

surfaces with one or multiple low coordinated Ni surface atoms by “green circle” bands, and they fingerprint semi internal Ni atoms of high next neighbor coordination by “red circle” bands in the cases of $n_{\text{small}} = 9, 10, \text{ and } 11$. We conceive surface reorganization upon N₂ uptake, namely from rough to rough surface by Ni atom migration. Such migration might induce the transition from octahedral based structures to pentagonal bipyramidal structures, which are representative for icosahedral cluster growth.

Class (4) of large clusters with rough and smooth surface areas comprises Ni₁₄⁺ through Ni₁₇⁺, and Ni₂₀⁺, and their N₂ adsorbate complexes up to saturated ($n_{\text{large}}, m_{\text{max}}$). We observe smooth surfaces with minor defects such as e.g. capping atom(s) on an icosahedral surface. From the IR-PD spectra we extract evidence for the Ni capping atoms to locate in proximity to each other – resulting from a stepwise cluster growth on one hemisphere of the initial icosahedron, leaving the other hemisphere largely unaffected. The N₂ saturation stoichiometry thus runs up to m_{max} values beyond the Ni cluster surface atom count $n_{\text{surface}} < n_{\text{total}}$ – once more invoking double N₂ occupation of low coordinated Ni surface atoms.

We provide a graphical summary of this classification, based on Fig. 3, in the supplement (Fig. S22 in the supplementary material).

This study and the accompanying kinetic study **[JM]** are understood as a basis for our subsequent studies on various other TM clusters (of Fe, Ru, and alike), and of some of their alloys. Such cluster adsorbate complexes shall help to elucidate crucial elementary steps in catalysis, and they shall benchmark current theoretical modelling and help in designing new approaches with predicting power.

6.7 Acknowledgements

We dedicate this work to the memory of the late A. W. “Will” Castleman, Jr. in recognition of his seminal contributions to the field of cluster science. This work was supported by the German research foundation DFG within the transregional collaborative research center SFB/TRR 88 “Cooperative effects in homo and heterometallic complexes” (3MET.de) and by the state research center OPTIMAS. The ⁵⁸Ni isotopic sample used in this research was supplied by the United States Department of Energy Office of Science by the Isotope Program in the Office of Nuclear Physics. We thank Thomas Kolling for technical assistance and valuable discussions. Finally, we thank the reviewers for valuable suggestions.

6.8 References

- [1] J. M. Thomas, and W. J. Thomas, *Principles and Practice of Heterogeneous Catalysis* (Wiley, 1997).
- [2] T. Bligaard, and J. K. Nørskov, in *Chemical Bonding at Surfaces and Interfaces*, edited by A. N. G. M. P. K. Nørskov (Elsevier, Amsterdam, 2008), pp. 255.
- [3] G. Ertl, H. Knözinger, and J. Weitkamp, (1997).
- [4] B. Cornils, W. A. Herrmann, and H.-W. Zanthoff, *Catalysis from A to Z* (Wiley-Vch New York, 2013).
- [5] R. Schlögl, and S. B. Abd Hamid, *Angew. Chem. Int. Ed.*, **43**, 1628, (2004).
- [6] P. B. Armentrout, *Catalysis Science & Technology*, **4**, 2741, (2014).
- [7] E. L. Muetterties, *Bull. Soc. Chim. Belg.*, **84**, 959, (1975).
- [8] C. Berg, G. NiednerSchatteburg, and V. E. Bondybey, in *Second International Conference on Low Temperature Chemistry*, edited by J. R. Durig, and K. J. Klabunde (BkMk Press, Kansas City, 1996), pp. 189.
- [9] S. M. Lang, and T. M. Bernhardt, *Phys. Chem. Chem. Phys.*, **14**, 9255, (2012).
- [10] E. L. Muetterties, *Science*, **196**, 839, (1977).
- [11] E. L. Muetterties, T. N. Rhodin, E. Band, C. F. Brucker, and W. R. Pretzer, *Chem. Rev.*, **79**, 91, (1979).
- [12] G. Ertl, *Angewandte Chemie-International Edition*, **47**, 3524, (2008).
- [13] E. Shustorovich, in *Quantum Chemistry: The Challenge of Transition Metals and Coordination Chemistry*, edited by A. Veillard (Springer Netherlands, 1986), pp. 445.
- [14] R. Schlögl, in *Handbook of Heterogeneous Catalysis* (Wiley-VCH Verlag GmbH & Co. KGaA, 2008).
- [15] F. Bozso, G. Ertl, M. Grunze, and M. Weiss, *J. Catal.*, **49**, 18, (1977).
- [16] F. Bozso, G. Ertl, and M. Weiss, *J. Catal.*, **50**, 519, (1977).
- [17] G. Ertl, *Catalysis Reviews*, **21**, 201, (1980).
- [18] G. Ertl, S. B. Lee, and M. Weiss, *Surf. Sci.*, **114**, 515, (1982).
- [19] M. Grunze, M. Golze, W. Hirschwald, H. J. Freund, H. Pulm, U. Seip, M. C. Tsai, G. Ertl, and J. Kuppers, *Phys. Rev. Lett.*, **53**, 850, (1984).
- [20] M. C. Tsai, U. Ship, I. C. Bassignana, J. Küppers, and G. Ertl, *Surf. Sci.*, **155**, 387, (1985).
- [21] H. J. Freund, B. Bartos, R. P. Messmer, M. Grunze, H. Kühlenbeck, and M. Neumann, *Surf. Sci.*, **185**, 187, (1987).
- [22] M. D. Morse, M. E. Geusic, J. R. Heath, and R. E. Smalley, *J. Chem. Phys.*, **83**, 2293, (1985).
- [23] L. Tan, F. Y. Liu, and P. B. Armentrout, *J. Chem. Phys.*, **124**, 084302, (2006).
- [24] M. Grunze, R. K. Driscoll, G. N. Burland, J. C. L. Cornish, and J. Pritchard, *Surf. Sci.*, **89**, 381, (1979).

- [25] M. E. Brubaker, and M. Trenary, *J. Chem. Phys.*, **85**, 6100, (1986).
- [26] M. E. Brubaker, and M. Trenary, *J. Electron Spectrosc. Relat. Phenom.*, **44**, 47, (1987).
- [27] K. Horn, J. Dinardo, W. Eberhardt, H. J. Freund, and E. W. Plummer, *Surf. Sci.*, **118**, 465, (1982).
- [28] F. Y. Liu, R. Liyanage, and P. B. Armentrout, *J. Chem. Phys.*, **117**, 132, (2002).
- [29] D. Vardhan, R. Liyanage, and P. B. Armentrout, *J. Chem. Phys.*, **119**, 4166, (2003).
- [30] F. Y. Liu, X. G. Zhang, R. Liyanage, and P. B. Armentrout, *J. Chem. Phys.*, **121**, 10976, (2004).
- [31] M. A. Duncan, *Annu. Rev. Phys. Chem.*, **48**, 69, (1997).
- [32] M. A. Duncan, *Int. Rev. Phys. Chem.*, **22**, 407, (2003).
- [33] N. R. Walker, R. S. Walters, and M. A. Duncan, *New J. Chem.*, **29**, 1495, (2005).
- [34] J. Roithova, *Chem. Soc. Rev.*, **41**, 547, (2012).
- [35] J. Oomens, B. G. Sartakov, G. Meijer, and G. von Helden, *Int. J. Mass Spectrom.*, **254**, 1, (2006).
- [36] L. MacAleese, and P. Maitre, *Mass Spectrom. Rev.*, **26**, 583, (2007).
- [37] W. Schöllkopf, S. Gewinner, H. Junkes, A. Paarmann, G. von Helden, H. Bluem, and A. M. M. Todd, (2015), pp. 95121L.
- [38] P. Gruene, A. Fielicke, G. Meijer, and D. M. Rayner, *Phys. Chem. Chem. Phys.*, **10**, 6144, (2008).
- [39] I. Swart, F. M. F. de Groot, B. M. Weckhuysen, P. Gruene, G. Meijer, and A. Fielicke, *J. Phys. Chem. A*, **112**, 1139, (2008).
- [40] J. S. Dewar, *Bull. Soc. Chim. Fr.*, **18**, C71, (1951).
- [41] G. Blyholder, *J. Phys. Chem.*, **68**, 2772, (1964).
- [42] A. D. Brathwaite, H. L. Abbott-Lyon, and M. A. Duncan, *J. Phys. Chem. A*, **120**, 7659, (2016).
- [43] E. D. Pillai, T. D. Jaeger, and M. A. Duncan, *J. Phys. Chem. A*, **109**, 3521, (2005).
- [44] E. D. Pillai, T. D. Jaeger, and M. A. Duncan, *J. Am. Chem. Soc.*, **129**, 2297, (2007).
- [45] V. G. Grigoryan, and M. Springborg, *Phys. Rev. B*, **70**, 205415, (2004).
- [46] C. L. Cleveland, and U. Landman, *J. Chem. Phys.*, **94**, 7376, (1991).
- [47] G. L. Gutsev, C. W. Weatherford, K. G. Belay, B. R. Ramachandran, and P. Jena, *J. Chem. Phys.*, **138**, (2013).
- [48] J. A. Alonso, *Chem. Rev.*, **100**, 637, (2000).
- [49] E. Curotto, A. Matro, D. L. Freeman, and J. D. Doll, *J. Chem. Phys.*, **108**, 729, (1998).
- [50] M. Boyukata, Z. B. Guvenc, S. Ozcelik, P. Durmus, and J. Jellinek, *Int. J. Quantum Chem.*, **84**, 208, (2001).
- [51] C. Kerpel, D. J. Harding, J. T. Lyon, G. Meijer, and A. Fielicke, *J. Phys. Chem. C*, **117**, 12153, (2013).
- [52] S. Dillinger, J. Mohrbach, J. Hewer, M. Gaffga, and G. Niedner-Schatteburg, *Phys. Chem. Chem. Phys.*, **17**, 10358, (2015).
- [53] E. K. Parks, L. Zhu, J. Ho, and S. J. Riley, *J. Chem. Phys.*, **100**, 7206, (1994).

- [54] E. K. Parks, L. Zhu, J. Ho, and S. J. Riley, *J. Chem. Phys.*, **102**, 7377, (1995).
- [55] J. Mohrbach, S. Dillinger, and G. Niedner-Schatteburg, *The Journal of Physical Chemistry C*, **121**, 10907, (2017).
- [56] S. Dillinger, J. Mohrbach, and G. Niedner-Schatteburg, *J. Chem. Phys.*, submitted, (2017).
- [57] C. Adamo, and V. Barone, *J. Chem. Phys.*, **110**, 6158, (1999).
- [58] T. H. Dunning, *J. Chem. Phys.*, **90**, 1007, (1989).
- [59] M. Dolg, U. Wedig, H. Stoll, and H. Preuss, *J. Chem. Phys.*, **86**, 866, (1987).
- [60] M. J. Frisch, G. W. Trucks, H. B. Schlegel, G. E. Scuseria, M. A. Robb, J. R. Cheeseman, G. Scalmani, V. Barone, G. A. Petersson, H. Nakatsuji, M. C. X. Li, A. Marenich, J. Bloino, B. G. Janesko, R. Gomperts, B. Mennucci, H. P. Hratchian, J. V. Ortiz, A. F. Izmaylov, J. L. Sonnenberg, D. Williams-Young, F. Ding, F. Lipparini, F. Egidi, J. Goings, B. Peng, A. Petrone, T. Henderson, D. Ranasinghe, V. G. Zakrzewski, J. Gao, N. Rega, G. Zheng, W. Liang, M. Hada, M. Ehara, K. Toyota, R. Fukuda, J. Hasegawa, M. Ishida, T. Nakajima, Y. Honda, O. Kitao, H. Nakai, T. Vreven, K. Throssell, J. A. Montgomery Jr., J. E. Peralta, F. Ogliaro, M. Bearpark, J. J. Heyd, E. Brothers, K. N. Kudin, V. N. Staroverov, R. K. T. Keith, J. Normand, K. Raghavachari, A. Rendell, J. C. Burant, S. S. Iyengar, J. Tomasi, M. Cossi, J. M. Millam, M. Klene, C. Adamo, R. Cammi, J. W. Ochterski, R. L. Martin, K. Morokuma, O. Farkas, J. B. Foresman, and D. J. Fox, Gaussian, Inc., Wallingford CT, **Revision D.01**, (2013).
- [61] A. Fielicke, G. von Helden, G. Meijer, D. B. Pedersen, B. Simard, and D. M. Rayner, *J. Chem. Phys.*, **124**, 194305, (2006).
- [62] J. Yoshinobu, R. Zenobi, J. Xu, Z. Xu, and J. T. Yates Jr, *J. Chem. Phys.*, **95**, 9393, (1991).
- [63] A. Langenberg, K. Hirsch, A. Lawicki, V. Zamudio-Bayer, M. Niemeyer, P. Chmiela, B. Langbehn, A. Terasaki, B. V. Issendorff, and J. T. Lau, *Phys. Rev. B*, **90**, 184420, (2014).
- [64] J. Meyer, M. Tombers, C. van Wullen, G. Niedner-Schatteburg, S. Peredkov, W. Eberhardt, M. Neeb, S. Palutke, M. Martins, and W. Wurth, *J. Chem. Phys.*, **143**, (2015).

6.9 Supplementary Material

Table of Content:

Fig. S1 Mass spectrum of a cationic nickel cluster distribution

Fig. S2 IR-PD spectra of $[\text{Ni}_n(\text{N}_2)_1]^+$ (n,1) and $[\text{Ni}_n(\text{N}_2)_2]^+$ (n,2) for n = 5 – 20.

Fig. S3 IR-PD spectra of (5,m)

Fig. S4 IR-PD spectra of (6,m)

Fig. S5 IR-PD spectra of (7,m)

Fig. S6 IR-PD spectra of (8,m)

Fig. S7 IR-PD spectra of (9,m)

Fig. S8 IR-PD spectra of (10,m)

Fig. S9 IR-PD spectra of (11,m)

Fig. S10 IR-PD spectra of (12,m)

Fig. S11 IR-PD spectra of (13,m)

Fig. S12 IR-PD spectra of (14,m)

Fig. S13 IR-PD spectra of (15,m)

Fig. S14 IR-PD spectra of (16,m)

Fig. S15 IR-PD spectra of (17,m)

Fig. S16 IR-PD spectra of (18,m)

Fig. S17 IR-PD spectra of (19,m)

Fig. S18 IR-PD spectra of (20,m)

Fig. S19 IR-PD spectra of (5,10) in comparison with computed spectra of the different spin states.

Fig. S20 IR-PD spectra of (6,6) in comparison with computed spectra of the different spin states.

Fig. S21 IR-PD spectra of (11,10) in comparison with computed spectra of the different spin states.

Fig. S22 IR-PD spectra of $[\text{Ni}_n(\text{N}_2)_m]^+$ cluster adsorbate complexes n = 5 – 20 at the intermittent adsorption limits (n,m_x) and at the adsorption limits (n,m_{max}).

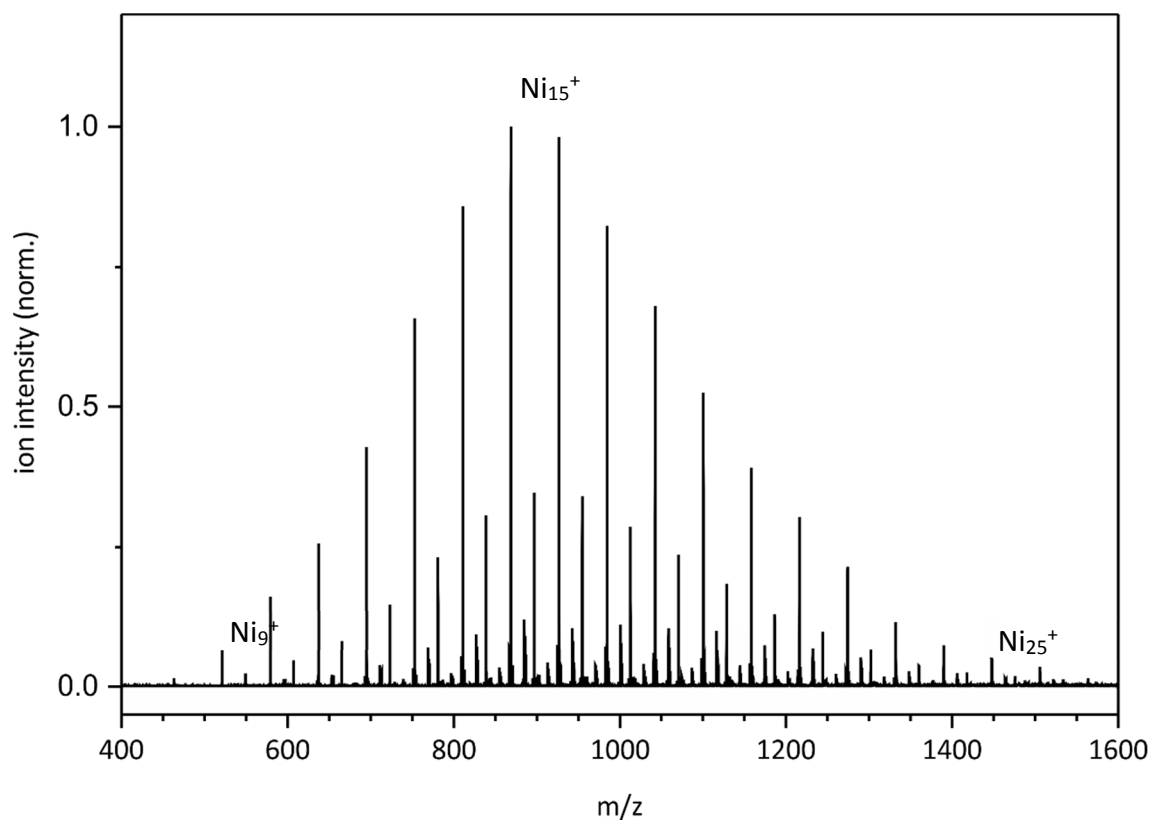


Fig. S1 Mass spectrum of a cationic nickel cluster distribution from about Ni₉⁺ (521 m/z) to about Ni₂₅⁺ (1448 m/z) with a maximum at Ni₁₅⁺ (869 m/z)..

6. Probing Cluster Surface Morphology by Cryo Spectroscopy of N₂ on Cationic Nickel Clusters

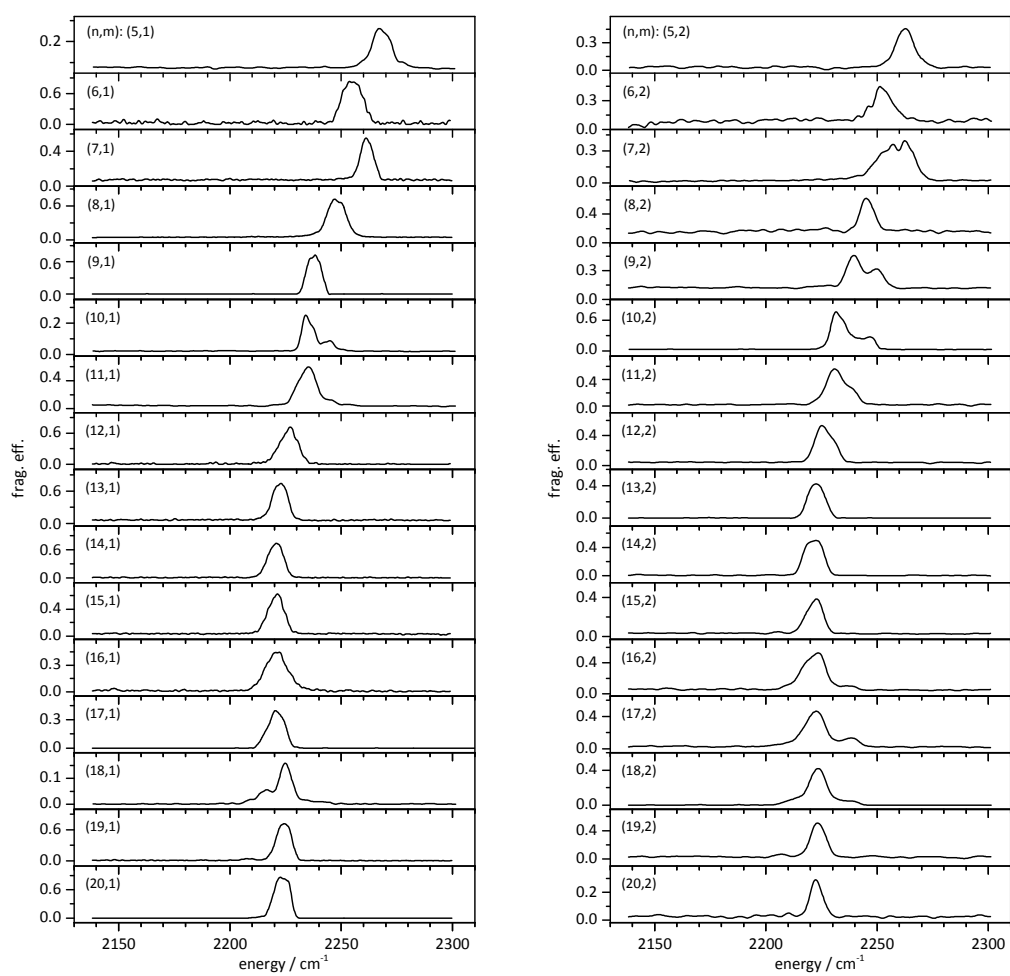


Fig. S2 IR-PD spectra of [Ni_n(N₂)₁]⁺ (n,1) (left) and [Ni_n(N₂)₂]⁺ (n,2) (right) for n = 5 – 20.

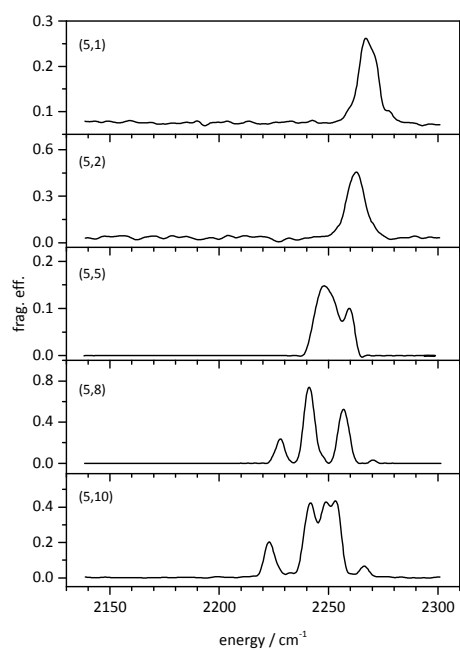


Fig. S3 IR-PD spectra of (5,m)

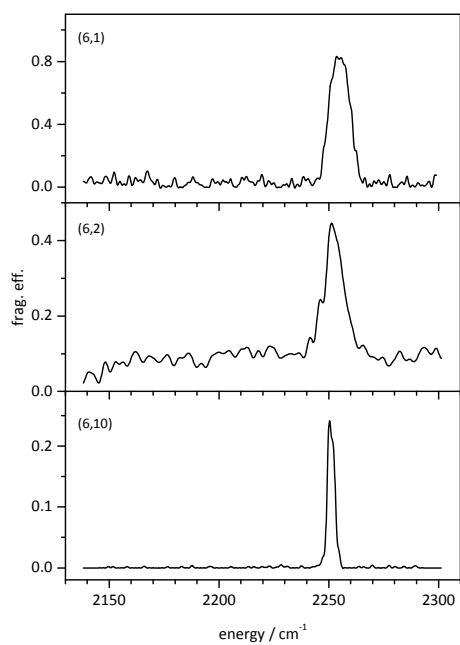


Fig. S4 IR-PD spectra of (6,m)

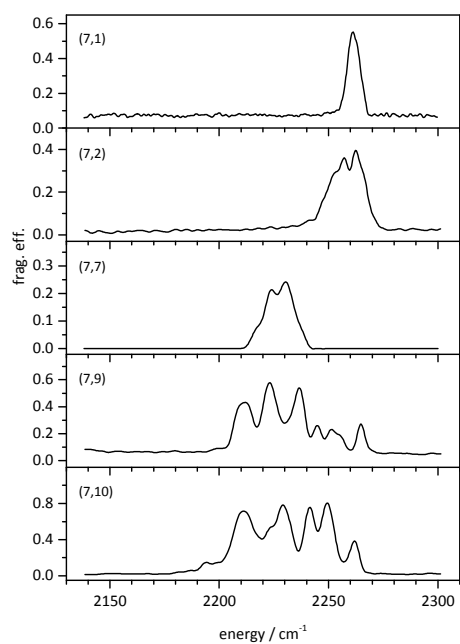


Fig. S5 IR-PD spectra of (7,m)

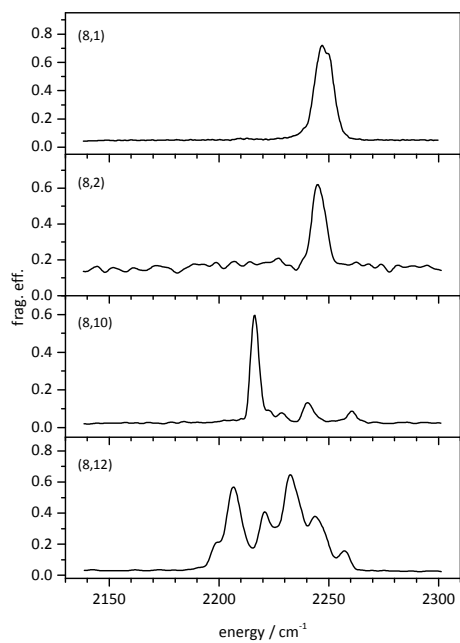


Fig. S6 IR-PD spectra of (8,m)

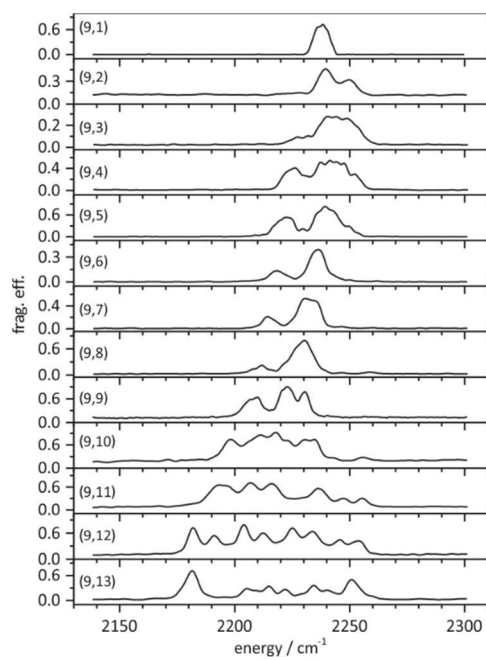


Fig. S7 IR-PD spectra of (9,m)

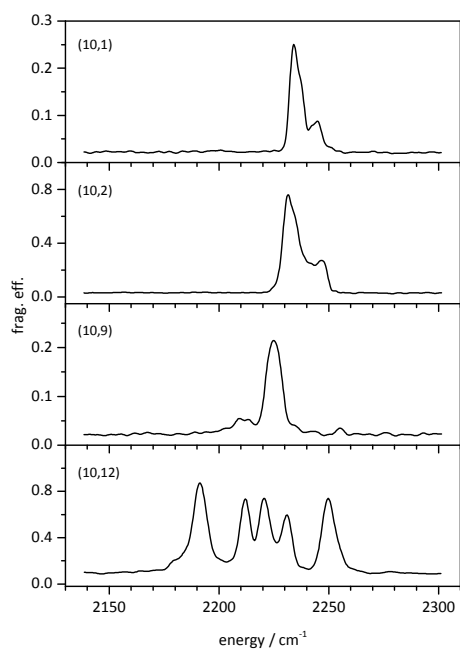


Fig. S8 IR-PD spectra of (10,m)

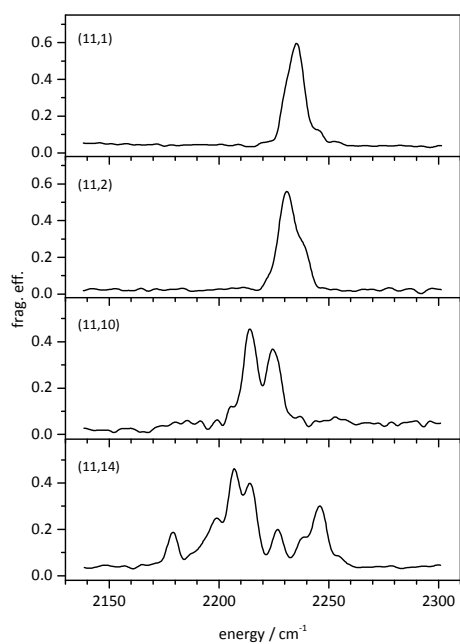


Fig. S9 IR-PD spectra of (11,m)

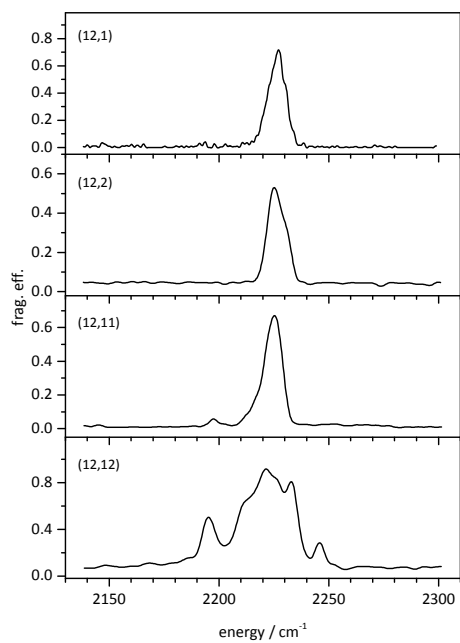


Fig. S10 IR-PD spectra of (12,m)

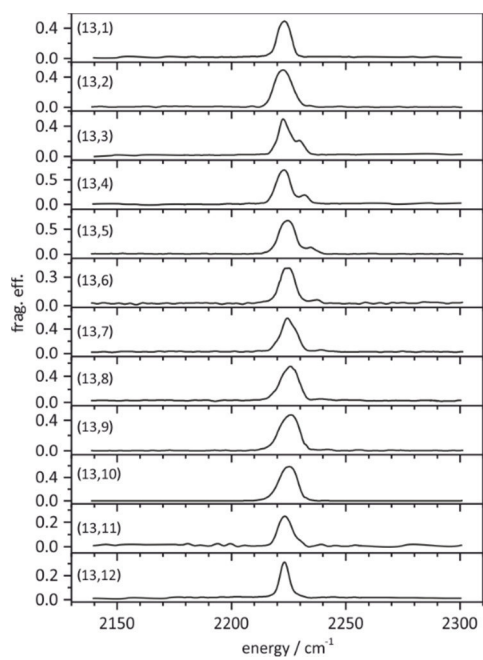


Fig. S11 IR-PD spectra of (13,m)

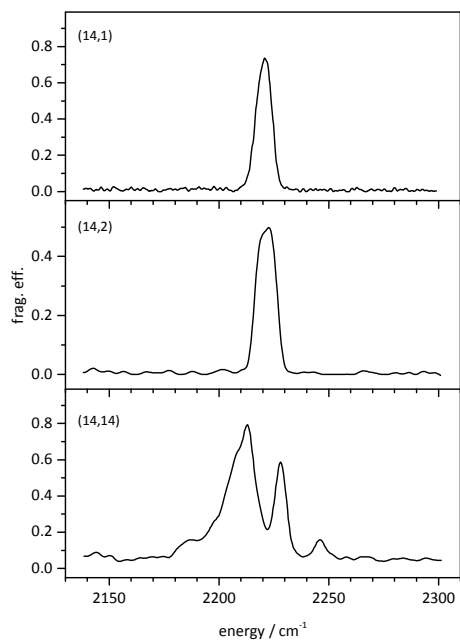


Fig. S12 IR-PD spectra of (14,m)

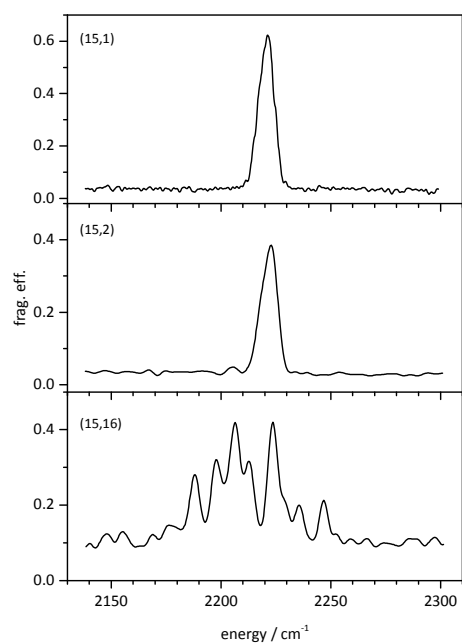


Fig. S13 IR-PD spectra of (15,m)

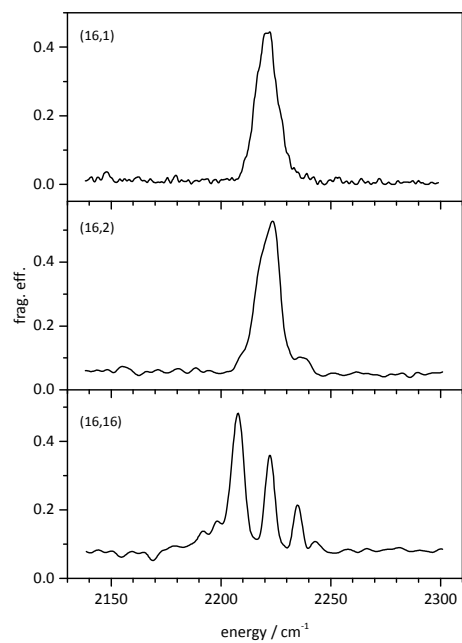


Fig. S14 IR-PD spectra of (16,m)

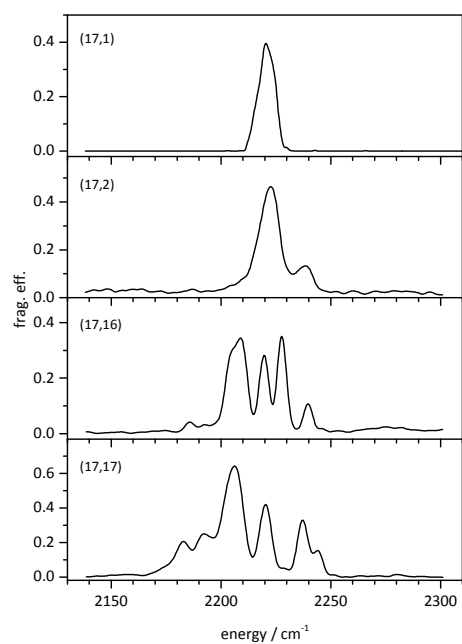


Fig. S15 IR-PD spectra of (17,m)

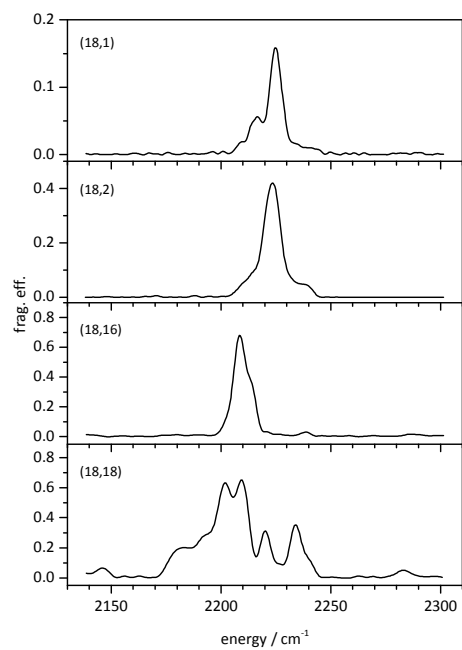


Fig. S16 IR-PD spectra of (18,m)

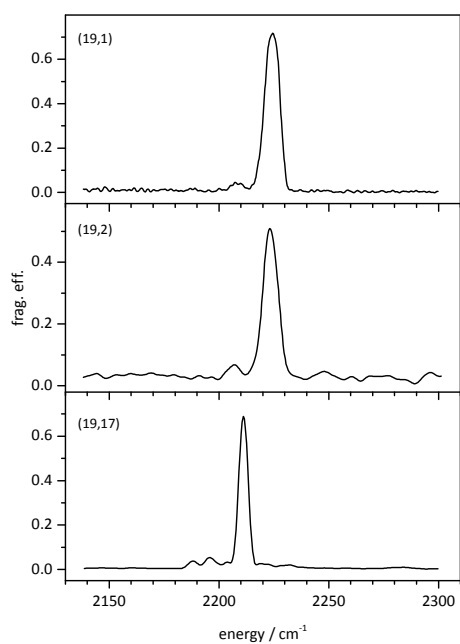


Fig. S17 IR-PD spectra of (19,m)

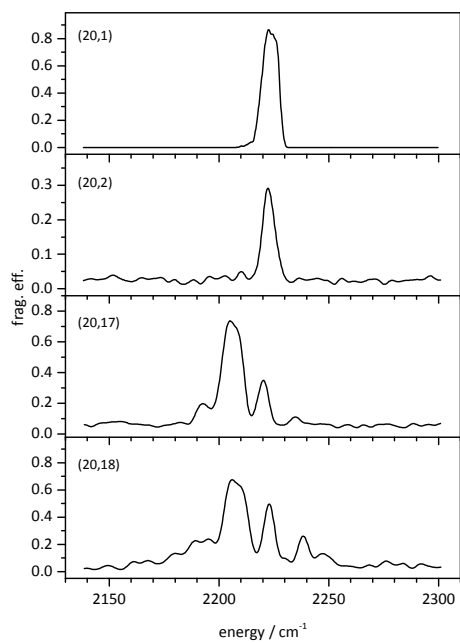


Fig. S18 IR-PD spectra of (20,m)

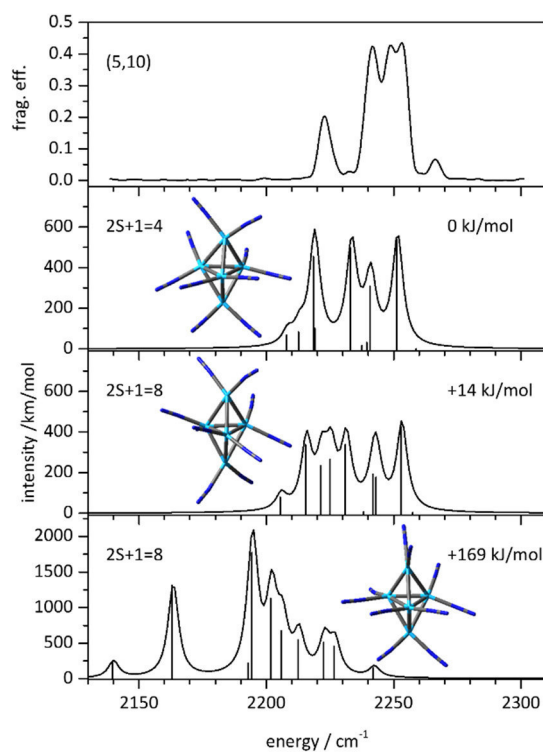


Fig. S19 Experimental IR-PD spectra of (5,10) in comparison with computed spectra (PBE0/ECP(Ni); cc-pVTZ(N) level of theory, scaled with 0.93) of the different spin states.

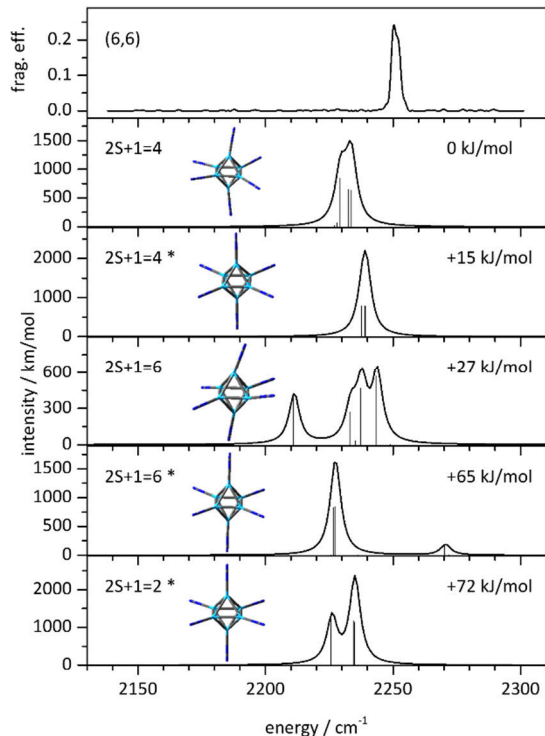


Fig. S20 Experimental IR-PD spectra of (6,6) in comparison with computed spectra (PBE0/ECP(Ni); cc-pVTZ(N) level of theory, scaled with 0.93) of the different spin states. The species marked with "*" have forced C_{2h} symmetry.

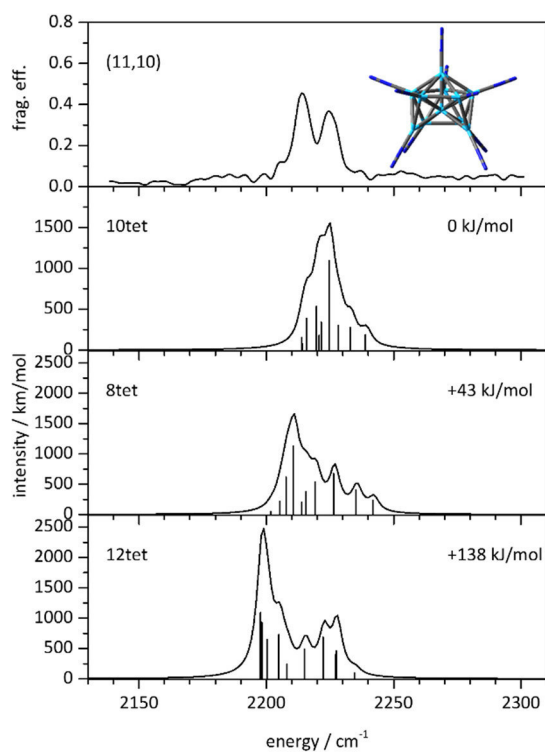


Fig. S21 Experimental IR-PD spectra of (11,10) in comparison with computed spectra (PBE0/ECP(Ni); cc-pVTZ(N) level of theory, scaled with 0.93) of the different spin states.

7 Cryo IR Spectroscopy and Cryo Kinetics of N₂ on Cationic Iron Clusters

Sebastian Dillinger, Jennifer Mohrbach, Marc H. Prosenc, and Gereon Niedner-Schatteburg

Fachbereich Chemie und Forschungszentrum OPTIMAS

Technische Universität Kaiserslautern

67663 Kaiserslautern

7.1 Preamble

The experiments were performed by the experimental team consisting of J. Mohrbach, and myself. The data evaluation was done by J. Mohrbach and myself. The computations were done by M. H. Prosenc. The kinetic part of the manuscript was written by J. Mohrbach and the spectroscopy part was written by myself.

7.2 Abstract

The stepwise N₂ adsorption on size selected Fe_n⁺ (n = 8 – 20) clusters at 26 K is studied in a hybrid tandem ion trap instrument. Infrared photon dissociation (IR-PD) spectroscopy helped to identify N₂ head-on adsorption in the first adsorption steps. We observed remarkable cluster size dependence of the adsorption limits. The exceptional Fe₁₇⁺ cluster does not show any reactivity towards N₂ at all. We identified two isomers of the Fe₁₈⁺ cluster of which one is unreactive. Preliminary density function theory (DFT) calculations provide for a first explanation for the size dependent inertness towards N₂.

7.3 Introduction

The ligation of transition metal (TM) clusters exhibits physical and chemical properties that are highly dependent on the geometrical cluster structure. Many studies of such metal-ligand clusters are largely motivated by their potential applications in catalysis.^[1-5] Early research on the chemical reactivity of transition metal clusters reveals a strong size effect.^[6-8] Iron clusters, in particular, show a strong variation in their reaction rates with small molecules as the cluster size increases. Several experimental and theoretical studies on the gas phase reactivity of Fe_n clusters with different ligands, such as the adsorption of hydrogen,^[7, 9-11] ammonia,^[7, 12-14] carbon^[15], water,^[7, 16-17] and benzene^[18-20] have been carried out. Guided ion beam studies elucidated the gas phase thermochemistry of cationic Fe clusters with N₂,^[21] O₂,^[22] and CO^[23]. These studies demonstrated the high reactivity exhibited especially for small iron clusters. Time-of-flight (TOF) mass spectra reveal an unusual sequence of magic numbers n = 7, 13, 15, 19 and 23 for Fe_n clusters,^[24] which can be explained neither by electronic shell closure^[25] nor by packing of hard spheres.^[26] Because of the unique ferromagnetic properties of bulk iron, studies on the magnetic properties of small iron clusters have drawn considerable interests. Iron clusters are found to be magnetic with higher moments than those found in the bulk.^[27-30] The intimate relationship between structure, magnetic properties and stability poses an uncommon challenge that motivated many theoretical studies of Fe_n clusters.^[31-40] The Fe₁₃⁺ cluster has drawn special attention with its proposed antiferromagnetic coupling.^[41-42] Still, important controversies remain unresolved among the reported results, including the ground-state atomic arrangements,

magnetic moments, noncollinear magnetism, and finally the stability spectrum of small Fe aggregates.

The physisorption and chemisorption of N₂ on metal surfaces have been studied extensively^[43] due to their importance in many catalytic processes. For example, the rate-determining step in the industrial synthesis of ammonia is the dissociation of N₂, using iron as a catalyst.^[44] The fixation of nitrogen by the nitrogenase enzyme is the equivalent process in biological systems.^[45] The behavior of N₂ reacting with iron clusters of different nuclearity is therefore particularly relevant to industrial and biological processes involving N-N bond breaking. Experimentally, it has been shown that N₂ adsorption to Fe(111) surfaces takes place in α -N₂ and γ -N₂ motifs, elucidated by angle resolved LEED studies in conjunction with potential surface modelling.^[46] This resembles η^2 side-on and η^1 end-on coordination of N₂ to multiple and single metal centers, respectively. Spectroscopic and kinetic studies of N₂ adsorbed on Fe(111) revealed that there are three characteristic α -, δ - and γ -states, which refer to side-on, and head-on adsorption to highly and to less coordinated metal surface atoms.^[43, 47-48] Early density functional theory (DFT) calculations revealed strong preference for end-on coordination of N₂ to single Fe centers with some evidence for rather exceptional η^2 side-on coordination of at most two N₂ to otherwise naked Fe atoms.^[49-50] However, there are merely gas phase IR studies on the interaction of adsorbates with Fe clusters irrespective of their charge state. Such studies provide for the unique opportunity to gather structural information of size dependent reactions as demonstrated by the observation of hydride formation on Fe clusters^[51] or the size dependent dissociation of water^[52].

Our tandem cryo ion trap instrument allows for the study of adsorption and reaction kinetics of clusters under single collision conditions at temperature as low as 11 K and for Infrared Photon Dissociation (IR-PD) spectroscopy –initially focusing on the one and two color investigations of metal organic complexes.^[53] We have started a systematic study of N₂ and H₂ cryo adsorption on size selected Fe, Co, and Ni clusters, first results being published.^[54-56] X-ray studies by cryo ion trapping help for the investigation of spin and orbital contributions to the magnetic moments of these TM clusters.^[57-58]

Here, we present detailed isothermal cryo kinetics and cryo IR spectroscopy of the N₂ adsorption onto cationic iron clusters Fe_n⁺ (n = 8 - 20) in conjunction with DFT modelling.

This study aims to enable insight into the metal-adsorbate bonding and into the reactivity of individual Fe clusters towards N₂ adsorption

7.4 Experimental and Computational Methods

A customized Fourier Transform Ion Cyclotron Resonance (FT-ICR) mass spectrometer (Apex Ultra Bruker Daltonics) served to perform the cluster production, isolation, N₂ condensation and mass analysis. The iron clusters were generated using a home-built laser vaporization cluster ion source as described before.^[59-60] In brief, iron atoms are evaporated from a rotating 0.4 mm thick isotopically enriched ⁵⁶Fe foil (99,93%, Oak Ridge National Laboratories) by the second harmonic of a pulsed Nd:YAG laser (Innolas *Spitlight 300*, 20 Hz). The hot plasma is captured by a He gas pulse (40 μs, 15 bar) created by a homebuilt piezoelectric valve.^[61] The atoms and ions are cooled and aggregate to clusters in the subsequent jet expansion through a 50 mm long channel (∅ 2 mm) into vacuum (10⁻⁷ mbar). The clusters are skimmed, mass selected and injected into a cryogenic hexapole ion trap. The ion trap is cooled to 26 K by a closed cycle He cryostat. Buffer and reaction gas are introduced continuously. Sufficient nitrogen attachment is achieved by increasing the pressure in the ion trap from 1.1 x 10⁻⁷ mbar to 1.6 x 10⁻⁷ mbar. Additional He is introduced to increase the pressure up to 3.5 x 10⁻⁶ mbar to accomplish an efficient trapping and cooling of the ions. After storing the ions for a variable time (0-10 s), the manipulated ions of the form [Fe_n(N₂)_m]⁺ = (n,m) are guided by electrostatic lenses into the FT-ICR cell of the so-called “infinity” type.^[62] The ICR cell is held at temperatures below 10 K with a closed cycle He cryostat to prevent heating of the clusters by black body radiation. The ICR cell serves for the detection and isolation of the formed [Fe_n(N₂)_m]⁺ = (n,m) cluster adsorbate complexes.

The kinetic curves of cationic iron clusters and their nitrogen adducts originate from reaction delay scans and subsequent evaluation of the recorded mass spectra. Each of these mass spectra originates from an average of 20 mass spectra for the fixed collision cell delay. Fits to pseudo-first-order-kinetics occur through the “evofit” program.^[63] The relative rate constants $k_{(n,m)}$ determine the absolute rate constants $k_{(n,m)}^{abs}$, the absolute collision gas number densities $\rho_{N_2}(T)$ serving as the conversion factor:

$$k_{(n,m)}^{abs} = k_{(n,m)} / \rho_{N_2}(T)$$

We obtain approximate values for $\rho_{N_2}(T)$ indirectly from the pressure in the surrounding chamber $p_c^{(300\text{ K})}$ and an effective geometry factor c_{app} :

$$\rho_{N_2}(26\text{ K}) = \frac{c_{app} p_c^{300\text{ K}}}{k_B T_{300\text{ K}}}$$

The geometry factor c_{app} shows to bear a significant dependence on the temperature of the hexapole ion trap. By numerous kinetic studies of transition metal cluster cations with neutral reactants at cryogenic temperatures we evaluated this factor c_{app} to 1.8 ± 0.4 at 26 K with a net uncertainty of $\pm 50\%$.

The classical Langevin collision rate of ions with neutrals^[64] is conveniently extended towards polar molecules by the average dipole orientation theory (ADO).^[65-66] The ADO theory gives the theoretical limit of the absolute rate constants, the collision rate k^{ADO} , based on a classical trajectory of a linear dipole in the field of a point charge:

$$k^{ADO} = \frac{q}{2\epsilon_0\sqrt{\mu}} \left(\sqrt{\alpha} + c\mu_D \sqrt{\frac{2}{\pi k_B T}} \right)$$

μ is the reduced mass (of the cluster adsorbate complex), α is the polarizability and μ_D is the dipole moment (in Debye). The parameter c lies between 0 and 1, and can be expressed by the polarizability volume α' and μ_D .^[67]

Kummerlöwe and Beyer introduced two models for calculating the collision rates of ionic clusters with neutral molecules, the HSA model (hard sphere average dipole orientation) and the surface charge capture (SCC) model.^[68] In both models, the cluster and the neutral reaction partner are treated as hard spheres, and the charge is treated as point charge. For the HSA collision rate k^{HSA} , the charge is located in the center of the cluster, while in the SCC model (k^{SCC}), the charge is drawn to the cluster surface by the attractive interaction with the neutral collision partner.

For the acquisition of the (IR-PD) spectra the FT-ICR cell is coupled to a tunable IR laser ($\delta n = 0.9\text{ cm}^{-1}$, $\delta t = 7\text{ ns}$). This laser is a KTP/KTA optical parametric oscillator/amplifier (OPO/A, LaserVision) system pumped by a pulsed 10 Hz injection seeded Nd:YAG laser (PL8000, Continuum). The difference frequency (DF) between the OPA signal and idler waves is generated in a AgGaSe₂ crystal. This generates IR radiation in the range of 1000 –

2400 cm⁻¹. Each trapped and isolated package of ions is irradiated by 7 – 10 laser pulses (0.1 – 1.5 mJ/pulse) to yield a sufficient amount of fragment ions. The IR spectra were recorded as ion chromatograms while continuously scanning the IR wavelength. The IR-PD signal was evaluated as $\sum_i F_i / (\sum_i F_i + \sum_i P_i)$, where F_i and P_i indicate fragment and the parent ion signals, respectively. An experimental IR-PD spectrum arises from a plot of the fragmentation efficiency as a function of laser frequency. We employed the IR-PD spectroscopy in the 2150 – 2340 cm⁻¹ range on the $[\text{Fe}_n(\text{N}_2)_m]^+$ species ($n = 8 - 20$). For all complexes the loss of N₂ was the only observed fragmentation channel.

All density functional theory calculations were performed using the Turbomole suit of programs [73-74]. For all atoms the def2-TZVP basis set was used [75]. For corrections of energies and gradients the PBE GGA functional has been employed [76]. Calculation of occupation numbers at a finite temperature located the lowest energy spin state.

Geometries were optimized and checked for stationary points by second derivative calculations revealing no imaginary frequencies for minima. Jahn-Teller distortions were resolved by initially optimization of the geometry at the highest symmetry followed by frequency calculations and by subsequent IRC calculations from the saddle point to reveal the optimal distorted geometry which was then fully optimized and checked again for possible further distortions.

7.5 Results and Discussion

Molecular nitrogen adsorption on iron cluster cations: Trends and limits of adsorption

We investigated the stored $[\text{Fe}_n(\text{N}_2)_m]^+ = (n,m)$ clusters for their N₂ adsorption in the cryogenic hexapole under isothermal conditions at 26 K. The mass spectra of all detected Fe_n⁺ clusters - except for Fe₁₇⁺ - reveal a successive gain of 28 m/z, which does indicate the stepwise adsorption of molecular nitrogen in consecutive chains of individual adsorption processes (*cf.* Fig. 1).

In all investigated cases ($n = 8 - 20$) stepwise N₂ uptake reaches a strict adsorption limit m_{max} within $t < 12$ s, and this does not increase further up to $t < 30$ s. In most cases we

observe the N₂ adsorption limit preceded by one or more additional intermittent adsorption limits, which do not suppress further adsorption but cause some retardation.

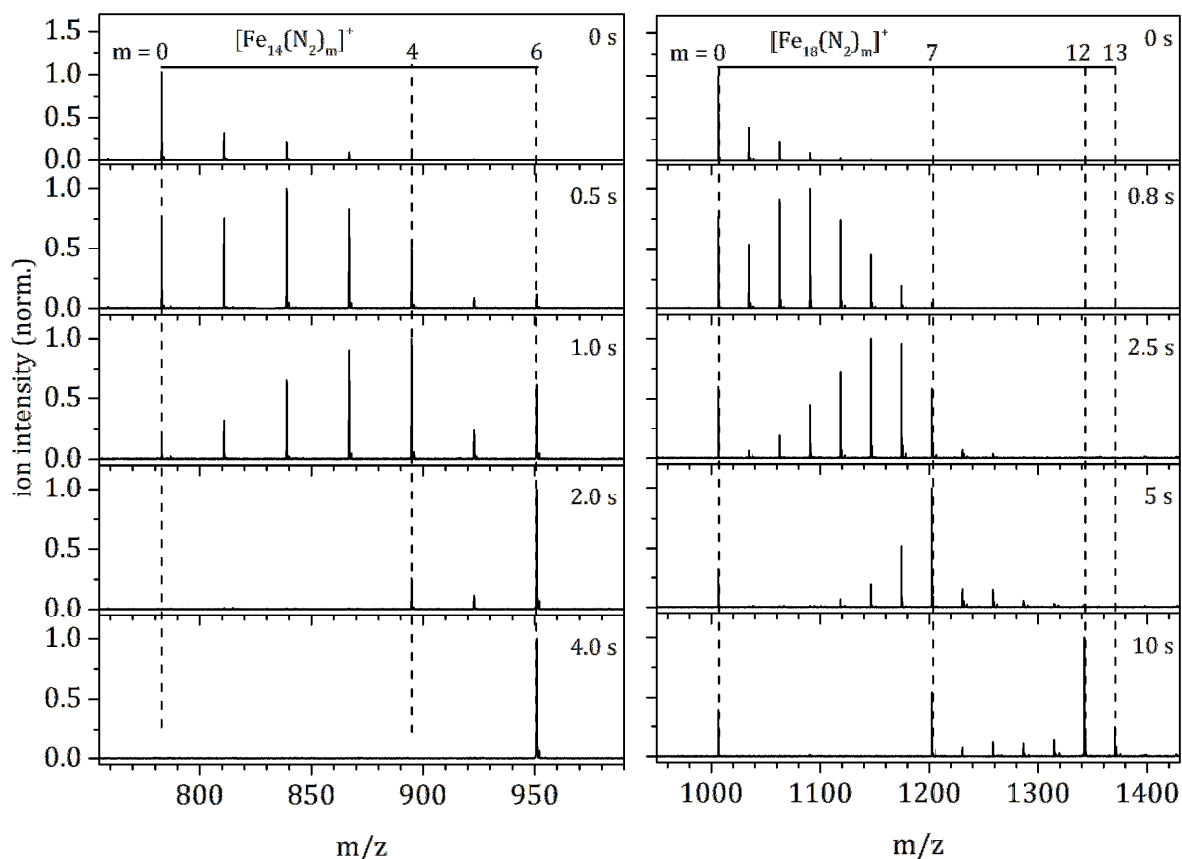


Fig. 1 Temporal evolution of the mass spectra of mass-selected Fe₁₄⁺ = (14,0) clusters up to 4 s (left) and of mass-selected Fe₁₈⁺ = (18,0) clusters up to 10 s (right), exposed to 1.6 × 10⁻⁷ mbar N₂ within 26 K He buffer gas (3.5 × 10⁻⁶ mbar).

The intermittent adsorption limits (blue stars in Fig. 2) and the adsorption limits (filled blue circles in Fig. 2) serve as guidelines for some elucidation of adsorbate bonding and cluster geometries. It shows, that the n:m stoichiometry is > 1 in all investigated cases n = 8 – 20, when reaching the respective N₂ adsorption limit. Yet, there is a trend in N₂ adsorption limits towards a molar ratio of n:m_{max} = 1:1 for small clusters (n ≤ 12). The overall adsorption behavior cannot be explained by single N₂ head-on adsorption to each cluster surface atom, as shown for Ni_n⁺ clusters.^[55] For clusters with less than 18 Fe atoms the observed intermittent adsorption limits are close to the recorded adsorption limits. Note the pronounced dip in the adsorption limits for 13 ≤ n ≤ 16 and the absence of N₂ adsorption to

the Fe₁₇⁺ clusters. Clusters with $n > 17$ exhibit an increase in reactivity towards N₂ adsorption. IR-PD experiments indicate μ_1 head-on adsorption of the initial adsorbed N₂ for all investigated (n,1) cluster adsorbate complexes.^[14]

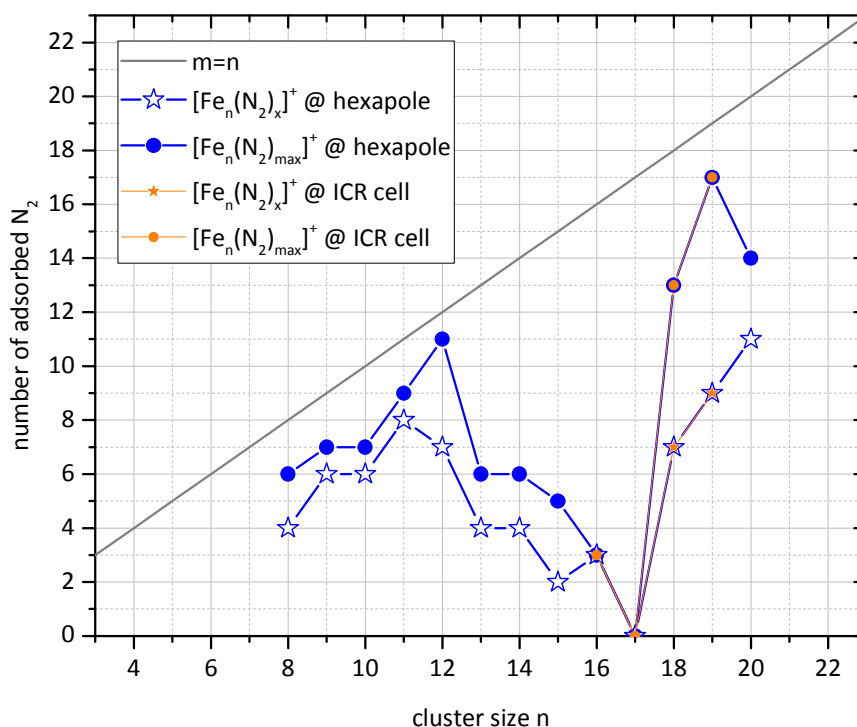


Fig. 2 Recorded adsorption limits (filled circles) and intermittent limits (stars) of nitrogen adsorbed on a cationic iron clusters. The limits are displayed as a function of cluster size for $n = 8 - 20$. The blue symbols indicate that the N₂ was adsorbed in the hexapole and the orange symbols indicate the adsorption in the ICR cell.

Preliminary results of N₂ adsorption kinetics recorded in the ICR cell yield (*cf.* Fig. 2, orange symbols) the same results as the kinetics recorded in the hexapole. We observe the same adsorption limits, the non-reactive Fe₁₇⁺, and a non-reactive isomer in the case of Fe₁₈⁺. Therefore the observed effects are confirmed by two individual experiments.

Kinetics:

We further investigated the stepwise N₂ adsorption on Fe_n⁺ clusters by recording their reaction kinetics in more detail, and we performed pseudo-first-order kinetic fits by our genetic algorithm routine. The obtained fits confirm consecutive adsorption steps (Fig.s 2-4).

All but one Fe_n⁺ clusters decay mono exponentially without any indication of a second component. This, and the overall superior quality of all fits, entitles us to fit each consecutive step by a single rate constant. Some fits require significant backward reaction in cases of high N₂ coverages, which indicates swift N₂ desorption (see the supplementary information for details on the corresponding rate constants $k_{(n,m)}$ for all cluster kinetics). There is one exception: The N₂ adsorption to Fe₁₈⁺ exhibits a biexponentially decay in the initial adsorption step.

Fe₈⁺ – Fe₁₁⁺:

Small iron clusters Fe_n⁺ in the range of $n = 8 - 11$ exhibit little deviation in the observed adsorption limits and the intermittent adsorption limits. All clusters reveal a strict adsorption limit at $n \geq m$. There are significant backward reactions for the last adsorption steps, suggesting one or more weakly bound N₂ molecules when reaching cluster saturation (*cf.* Fig. 3).

In the case of (8, m) we observe an intermittent adsorption limit at (8,4) and the adsorption limit at (8,6). The predicted most stable structures for Fe₈ clusters correspond to a capped pentagonal bipyramid,^[36-37, 69-70] or a bisdisphenoid structure.^[36-40] The capped pentagonal bipyramid consists of one threefold, three fourfold, two fivefold, one sixfold and one sevenfold coordinated Fe atom. Assuming the same N₂ adsorption ‘rules’ as stated for Ni_n⁺ clusters,^[55] the adsorption limits should be observed at (8,7) and (8,12). In contrast, initial binding to the three- and fourfold coordinated Fe sites and additional adsorption to the fivefold atoms would result in limits at (8,4) and (8,6), as observed. The bisdisphenoid structure consists of four fourfold and four fivefold coordinated Fe atoms, which would result in limits at (8,8) and (8,12) or at (8,4) and (8,8), other than observed.

In the cases of (9, m) and (10, m) we observe an intermittent adsorption limit at $n = 6$ and the adsorption limit at $n = 7$. The reported most stable structures for Fe₉ and Fe₁₀ clusters correspond to capped square antiprisms, capped pentagonal bipyramidal motifs, or capped trigonal bipyramidal motifs. These geometries are possible growth models leading to the icosahedral structure predicted for Fe₁₃.^[36-37, 69-70] The (11, m) cluster adsorbate complex exhibits an intermittent adsorption limit at (11,6) and the adsorption limit at (11,9), in

equilibrium with its precursor. The preferred structure for this cluster is found to be a tetra-capped pentagonal bipyramid.

Unfortunately, there is no universally applicable adsorption rule, which would explain the observed adsorption limits. Without further knowledge of the exact N₂ adsorption site, no comprehensive structural interpretation can be drawn out of the adsorption limits alone. We tentatively assume μ_1 head-on adsorption up to the adsorption limit, based on the shape of the kinetic curves in conjunction with those obtained for Ni_n⁺ clusters. In addition, IR-PD investigations of the (n,1) and (n,2) cluster adsorbate complexes point towards μ_1 head-on N₂ adsorption (see IR-PD part).

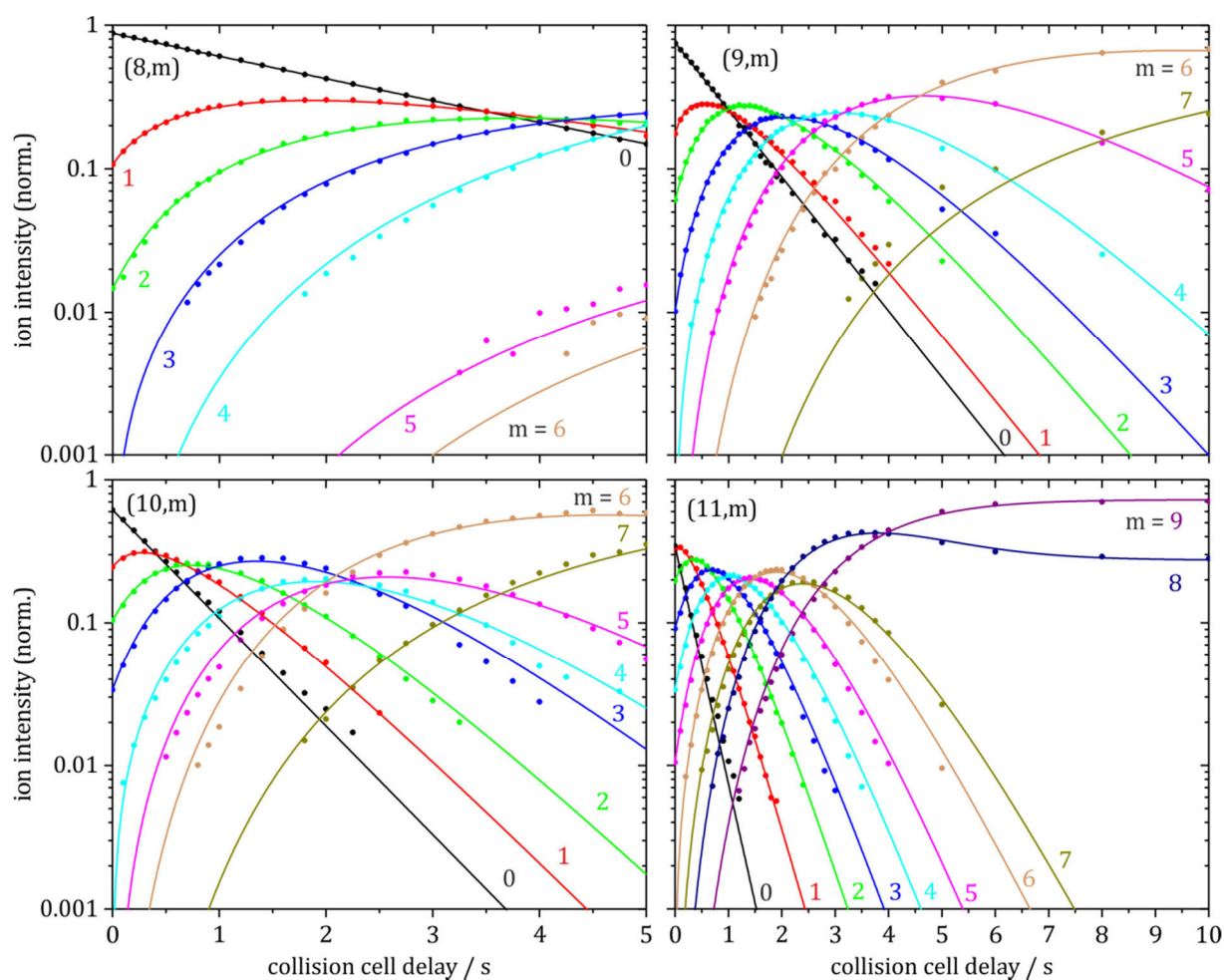


Fig. 3 Isothermal kinetics of the stepwise N₂ adsorption by isolated Fe_n⁺ clusters (n = 8 – 11). The fits (shown as lines) assume pseudo-first-order kinetics in a reaction chain of up to 9 consecutive steps.

Fe₁₂⁺ – Fe₁₅⁺:

In the range of $n = 12 - 15$ the N₂ adsorption behavior to Fe_n⁺ clusters changes dramatically (*cf.* Fig. 4). We observe a significant decrease in N₂ adsorption with cluster size for $n > 12$.

In the case of (12,m) we observe an intermittent adsorption limit at (12,7) and the adsorption limit at (12,11). In the cases of (13,m) and (14,m) we observe intermittent adsorption limits at $m = 4$ and the adsorption limit at $m = 6$. The (15,m) cluster adsorbate complex exhibits only five consecutive steps. The terminal four adsorbate species ($m = 2 - 5$) are in equilibrium in favor of $m = 2$. Note, that the intensities of the minor adsorption limits ($m = 3 - 5$) are close to our detection limit, resulting in a reduction of the fit quality.

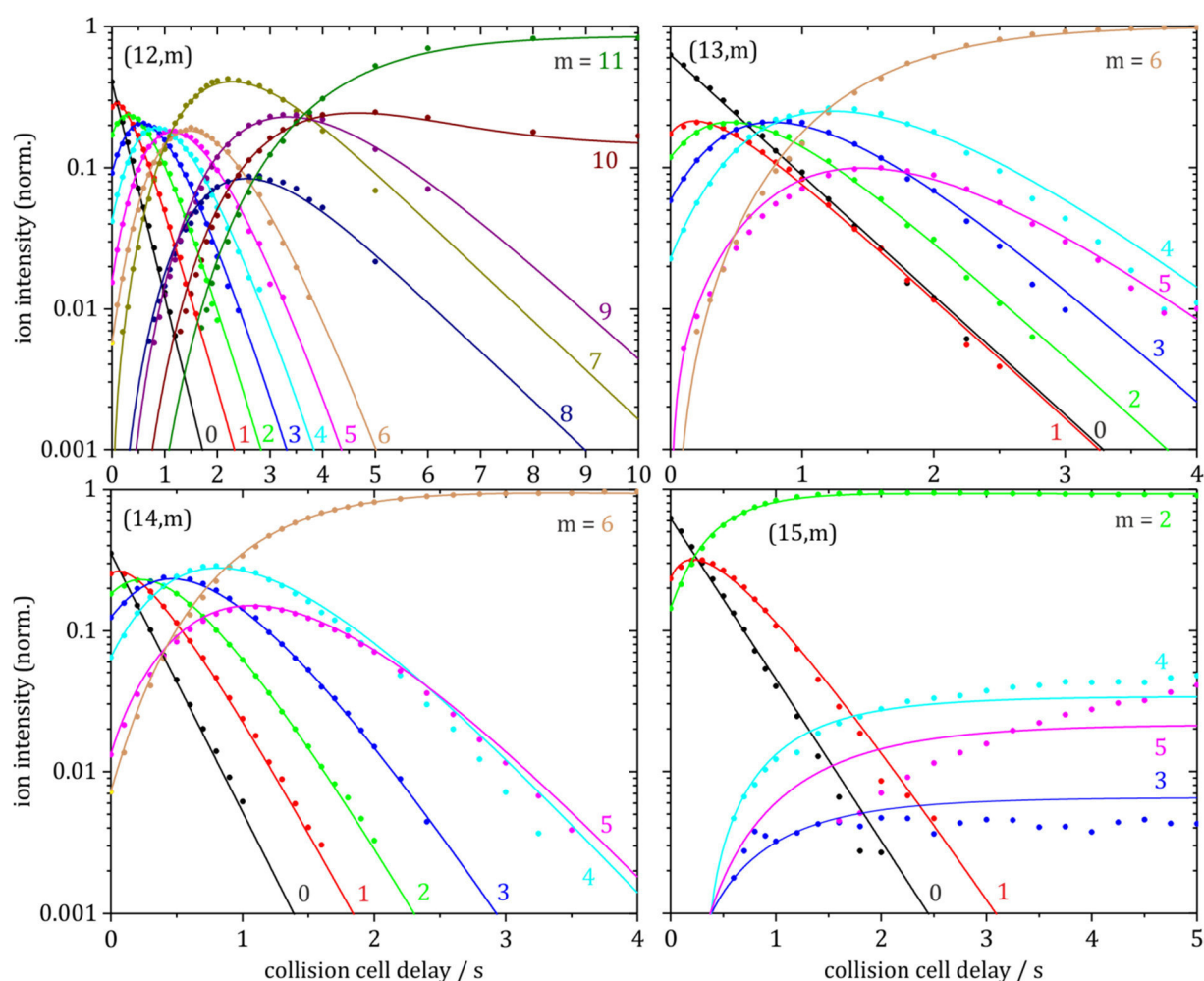


Fig. 4 Isothermal kinetics of the stepwise N₂ adsorption by isolated Fe_n⁺ clusters ($n = 12 - 15$). The fits (shown as lines) assume pseudo-first-order kinetics in a reaction chain of up to 11 consecutive steps.

Fe₁₆⁺ – Fe₂₀⁺:

In the range of $n = 16 - 20$ a significant change in reactivity towards N₂ adsorption is observed (*cf.* Fig. 4). Note, that in the case of Fe₁₇⁺ no N₂ adsorption could be detected within the described experimental conditions.

In the case of (16,m) we observe a sole adsorption limit at (16,3). Clusters of the sizes $n = 18, 19$ and 20 exhibit dominant intermittent adsorption limits. Note the observed irregularity in intensity with further N₂ adsorption beyond these limits, which can still be fitted as consecutive reaction steps with mono-exponentially decays in good quality. This finding might indicate a change in e.g. adsorption site, likely from head-on to side-on coordination by tilting the adsorbed N₂.

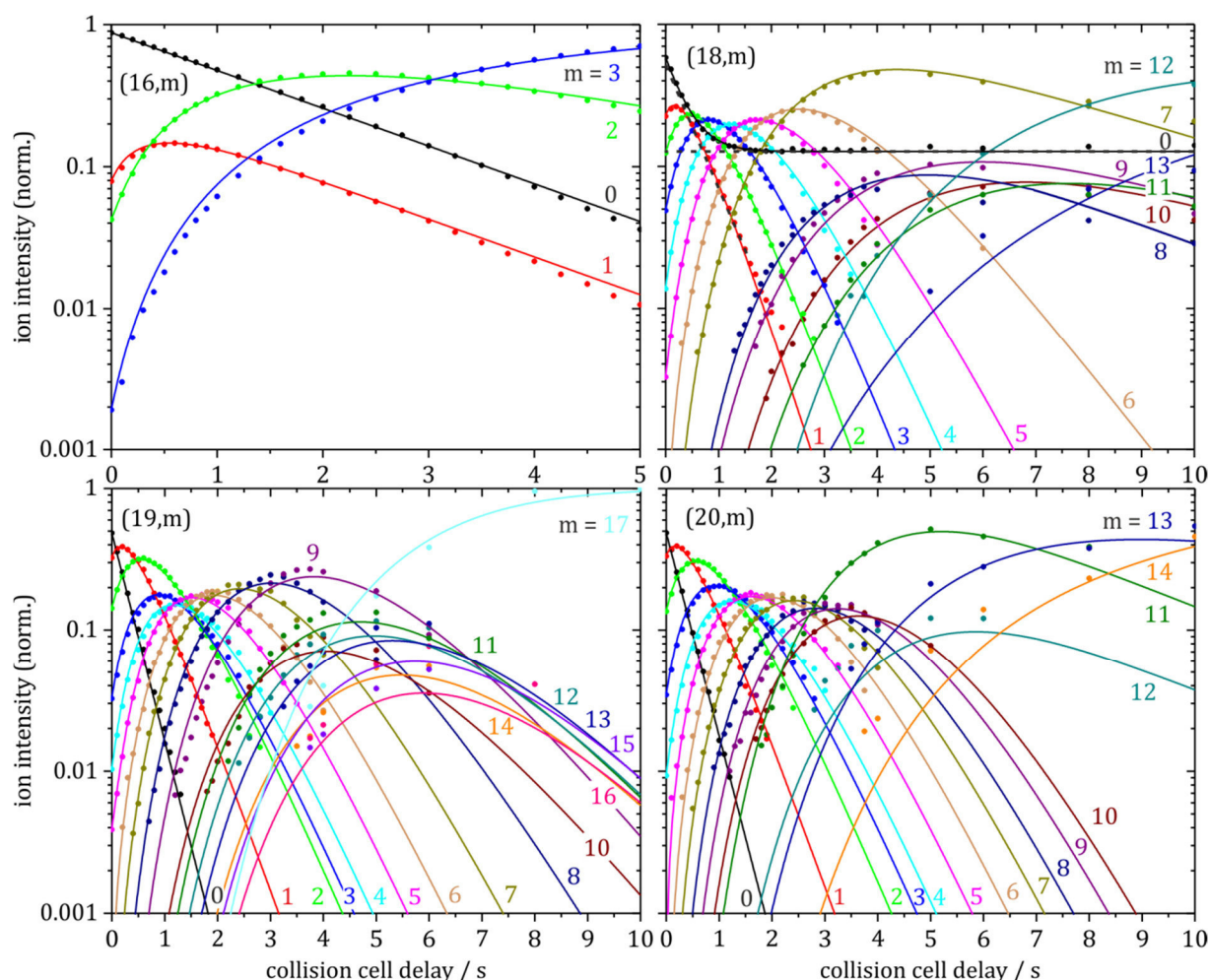


Fig. 5 Isothermal kinetics of the stepwise N₂ adsorption by isolated Fe_n⁺ clusters ($n = 16, 18 - 20$). The fits (shown as lines) assume pseudo-first-order kinetics in a reaction chain of up to 17 consecutive steps.

In the case of (18,m) we assume the presence of a second isomer which does not adsorb N₂ (~ 13 %, cf. Tab. 1) – presumably analogous to Fe₁₇⁺. A first explanation for the non-reactivity of the Fe₁₇⁺ cluster and the non-reactivity of one Fe₁₈⁺ isomer can be found in the DFT part. We observe a distinct intermittent adsorption limit at (18,7) and the adsorption limit at (18,13). In the cases of (19,m) and (20,m) we observe a first intermittent adsorption limit at m = 2 followed by intermittent adsorption limits at (19,9) and (20,11). The respective adsorption limits are observed at (19,17) and (20,14).

Table 1. Pseudo-first-order rate constants for the initial N₂ adsorption to Fe₁₈⁺ in 1.6 × 10⁻⁷ mbar of N₂ and 26 K He buffer gas.

	[Fe ₁₈ (N ₂) _m] ⁺	
	isomer I	isomer II
%	87	13
k _(18,0) / s ⁻¹	2.91	0.00

Absolute rate constants of the initial N₂ adsorption

The absolute rate constants $k_{(n,m)}^{abs}$ are obtained from the pseudo-first-order rate constants as a function of cluster size (Fig. 6, blue circles). Collision rate constants are calculated on the basis of classical ADO theory, as well as on the HSA and SCC models.

We observe an overall increase in the absolute rate constants with cluster size towards collision rates predicted by ADO theory. The absolute rate constants for clusters up to n = 11 increase rapidly. Clusters with n = 13 and 15 – 17 show a decrease in reactivity towards N₂ adsorption as compared to the stated increase with cluster size. Larger clusters with n ≥ 18 reveal equal rates for the initial N₂ adsorption (cf. Tab. 2).

We reach limits when trying to interpret the subtle details of the current kinetic findings on their own, as they do not correlate with the cluster structure like in the case of Ni clusters^[56]. Most noticeable, the seeming inertness of the Fe₁₇⁺ cluster bears elements of a miracle – that will be addressed later on.

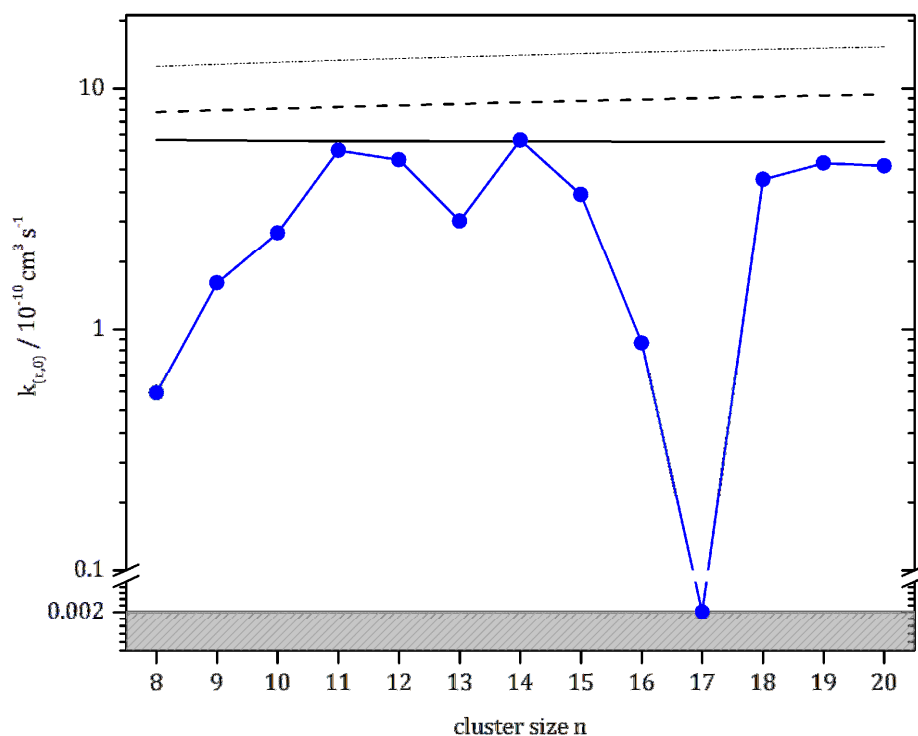


Fig. 6 Absolute rate constant $k_{(n,0)}^{abs}$ of the initial N₂ adsorption to Fe_n⁺ clusters by experiment (blue), according to classical average dipole orientation theory (black line), to the hard-sphere average dipole orientation model (dashed line), and to the surface charge capture model (dot-dashed line).

Table 2. Relative and calculated absolute rate constants for the initial N₂ adsorption to Fe_n⁺ clusters in comparison to the calculated rate constants assuming classical ADO theory, the HSA model, and the SCC model.

n	$k_{(n,0)}$ s^{-1}	$k_{(n,0)}^{abs}$ $10^{-10} \text{ cm}^3 \text{ s}^{-1}$	$k_{(n,0)}^{ADO}$ $10^{-10} \text{ cm}^3 \text{ s}^{-1}$	$k_{(n,0)}^{HSA}$ $10^{-10} \text{ cm}^3 \text{ s}^{-1}$	$k_{(n,0)}^{SCC}$ $10^{-10} \text{ cm}^3 \text{ s}^{-1}$
8	0.4	0.54	6.07	8.01	12.33
9	1.1	1.55	6.05	8.14	12.58
10	1.7	2.51	6.04	8.27	12.83
11	3.8	5.50	6.02	8.40	13.06
12	3.5	5.03	6.01	8.53	13.29
13	2.0	2.82	6.00	8.65	13.50
14	4.2	6.07	5.99	8.77	13.71
15	2.5	3.61	5.99	8.89	13.91
16	0.6	0.88	5.98	9.01	14.11
17	<0.001	<0.002	5.98	9.13	14.30
18	2.9	4.18	5.97	9.24	14.48
19	3.4	4.88	5.97	9.35	14.66
20	3.3	4.78	5.96	9.46	14.84

It is worth pointing out, however, that the drop in adsorption limit at $n = 13$ sets in at the very same cluster size that is confirmed for its antiferromagnetic coupling.^[41, 58] Inevitably, N₂ activation and nitride formation come to mind when dealing with the [Fe_nN] system. While this is conceivable, in general such processes would not explain an almost complete absence of any adsorption in the case of $n = 17$. Reaction products would be detected by MS. However, there are none. Fission or loss of charge when storing the clusters in the traps is negligible (see Fig. S5 in the supplementary information for more details).

IR-PD:

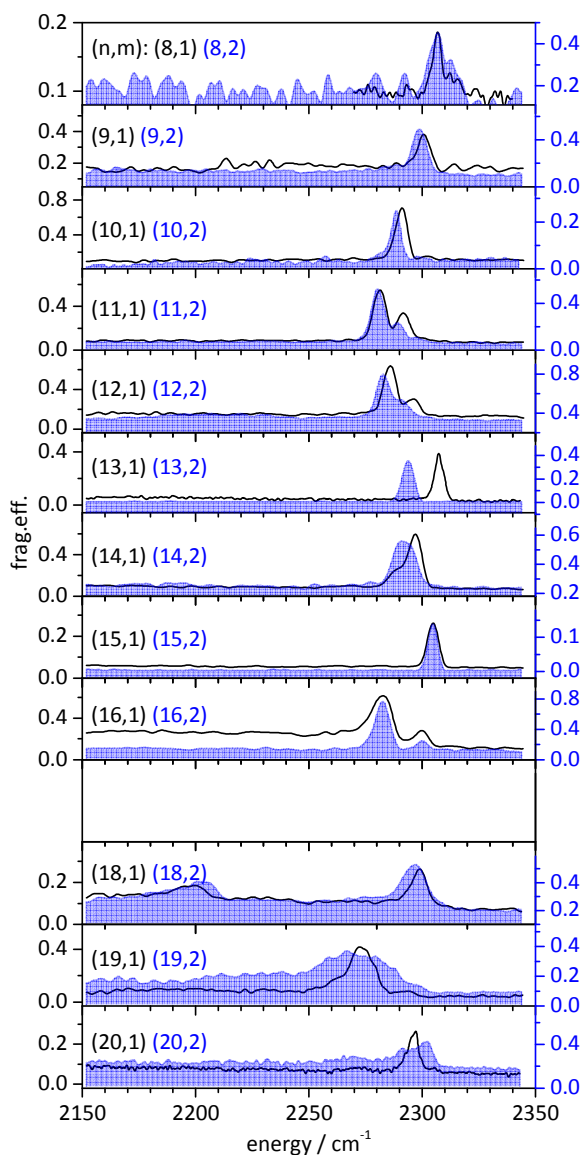


Fig. 7 IR-PD spectra of [Fe_n(N₂)₁]⁺ (solid lines) and [Fe_n(N₂)₂]⁺ (blue shaded areas) for $n = 8 - 20$. Note that for $n = 17$ no nitrogen attachment was observed.

To gain further insight into the Fe/N₂ systems, we applied our cryo IR-PD scheme to the [Fe_n(N₂)₁]⁺ (n,1) and the [Fe_n(N₂)₂]⁺ (n,2) for n = 8 – 20 species. We recorded the spectra in the region from 2150 to 2340 cm⁻¹ (Fig. 7). Furthermore, we recorded the spectra of (13,6) and (18,2) over the complete range of our IR laser to ensure that we do not miss any spectral features. No further bands were observed in the region below 2150 cm⁻¹ (cf. Fig. S6 and S7).

All species show one or two IR active bands in the probed region. The species with n = 11, 12, 16, and 18 exhibit a second band. The cluster with n = 14 shows a shoulder in the case of (14,1), that is no longer present in the (14,2) species. In general the bands are less redshifted with respect to the free N₂ stretching frequency (2330 cm⁻¹) compared to the nitrogen adsorption on cationic Co and Ni clusters [54-56].

Looking at the spectra in more detail, one can perceive several special features. Most conspicuous feature is the shift of the band from (13,1) to (13,2). The adsorption of a second N₂ leads to a redshift of over 10 cm⁻¹. Also noticeable are the missing spectra of (17,1) and (17,2), as under our experimental conditions no nitrogen attachment to the bare Fe₁₇⁺ cluster was observed, like already stated in the kinetics chapter. A first explanation of this inertness of Fe₁₇⁺ towards N₂ will be given in the DFT chapter. The spectra of the (18,1) and (18,2) species are the only ones which provide for a second far redshifted band. This second band is located at about 2200 cm⁻¹, representing an over 50 cm⁻¹ bigger redshift compared to any other species presented here. Note that the Fe₁₈⁺ cluster also reveals a special behavior in the kinetic studies in the form of a non-reactive isomer. The “far” redshift in the IR-PD spectra could be an indication for a tilting of a nitrogen molecule. A tilting could enable a larger interaction between cluster and nitrogen which would result in a larger redshift. This could be a precursor for a nitrogen activation. The IR-PD spectrum of (19,1) reveals a broad absorption (FWHM > 50 cm⁻¹) around 2270 cm⁻¹. Upon the adsorption of a second N₂ the narrows to FWHM = 13 cm⁻¹.

Nevertheless, we assign the observed spectral features to head-on bound N₂ on the Fe clusters. Other species, as known from surface studies, would provide for spectral features far below 2000 cm⁻¹.^[47, 71] The appearance of a second band could originate from cluster core isomers, different adsorption sites or different spin states of the cluster.

However, no overall trends were observed like increasing redshift with cluster size which could correspond to the charge dilution model as it was observed in cationic Ni clusters (*cf.* Fig. 8, dashed line)^[56]. Only the small clusters from $n = 8 - 11$ follow a similar trend. This simple model (charge dilution) cannot be applied for bigger clusters. Other effects prevail that are most likely from electronic origin and not mainly dominated by the cluster structure like in the case of cationic Ni clusters.^[56]

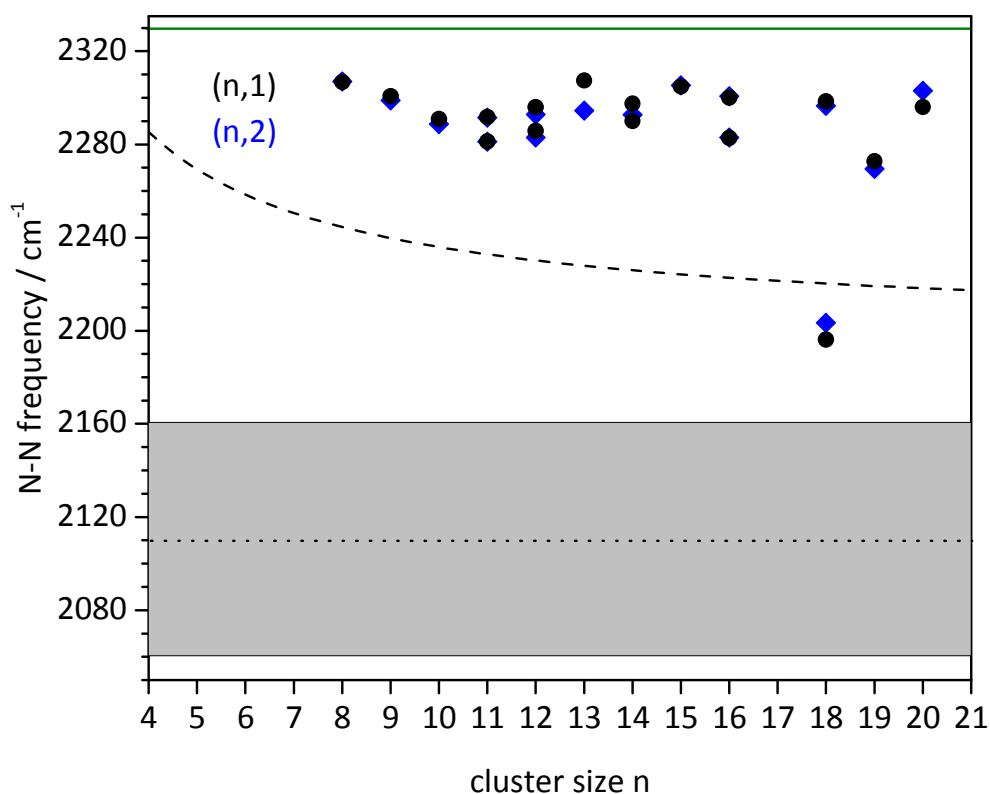


Fig. 8 N-N stretching frequency in $[\text{Fe}_n(\text{N}_2)_1]^+$ (black dots) and $[\text{Fe}_n(\text{N}_2)_2]^+$ (blue diamonds) for $n = 7 - 20$. The dashed line represents the trend of the N-N stretching frequency observed in cationic nickel clusters.^[56] The green line is the stretching frequency of free N₂. Also shown is the stretching frequency (black dotted line) with its FWHM (grey shaded area) of so called γ -N₂ on clean iron surfaces revealed via vibrational EELS.^[71]

Looking at the species with two N₂ adsorbed (n,2), nearly no change in peak position can be observed. This could hint at that the first and the second N₂ are equivalently bound to the cluster. As already mentioned, the only exception is Fe₁₃⁺ which shows a significant shift of over 10 cm⁻¹ upon adsorption of the second N₂. Comparing the spectral data with those of

N₂ on cationic Ni clusters (*cf.* Fig. 8), it is noticeable that Fe clusters reveal completely different behavior. No systematic overall trend can be observed. Furthermore the Fe clusters do not approach the value of N₂ on Fe surfaces with cluster size as it was observed in the case of N₂ on Ni cluster.

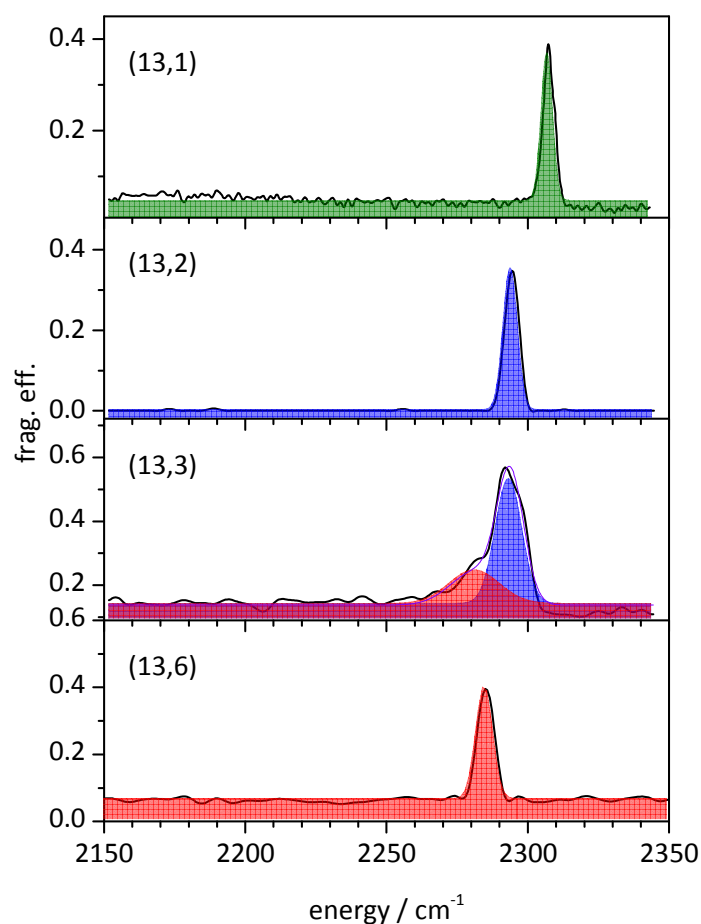


Fig. 9 IR-PD spectra of $[\text{Fe}_n(\text{N}_2)_m]^+$ (n,m) for $m = 1, 2, 3$ & 6 . Note the jump of the band from $m = 1$ to $m = 2$ of over 10 cm^{-1} . The color shaded areas are Gaussian profiles fitted to the spectra to illustrate the different peak positions. The spectra of the (13,3) species consists of a band (blue shaded area) with a shoulder (red shaded area) to lower energies. The main peak could correspond to the peak in the peak of (13,2) and the shoulder to the peak of (13,6). The spectra without the color shaded areas can be found in the supplement.

The spectra of (13, m) reveal several special features (see Fig. 9). The most outstanding one is the jump from 2307 cm^{-1} (13,1) to 2294 cm^{-1} (13,2) of 13 cm^{-1} . This cluster size is well known to provide for “special” features as already seen in XMCD and computational

studies.^[41-42] Those studies show a significant drop of the magnetic moment at $n = 13$. Therefore a possible explanation of this jump would be an adsorbate induced change of the spin state. As of now DFT failed to describe the observed jump. Perhaps we have to take antiferromagnetic coupling into account in the form of broken symmetry calculations to render the observed effect.^[72]

We still observe a single band in the IR-PD spectrum of (13,2), which lead to the conclusion that the N₂ are presumably equivalently bound. The cluster core has most likely an icosahedral structure^[42] and the two N₂ could be bound on two iron atoms facing each other. If you now assume a perfectly symmetric structure, this structure should show a symmetrically and an antisymmetrically coupled stretching vibration of the two N₂. The symmetrically coupled vibration should have no IR intensity due to no change in the dipole moment during this vibration. This should result in one single IR active band in N-N stretching region.

With the adsorption of one more N₂, resulting in the (13,3) species, the IR-PD spectrum reveals that the main band at 2193 cm⁻¹ does not change in position but a shoulder at lower energies (2282 cm⁻¹) arises. This is indicative for an adsorption site which is no longer equivalent to the previous ones. This results in a second band/shoulder. The Fe₁₃⁺ cluster adsorbs up to 6 N₂ under our experimental conditions. The IR-PD spectrum of the (13,6) shows only a single band at 2185 cm⁻¹. This band is located in the same region as the observed shoulder of the (13,3). One may speculate about the fact, that each N₂ blocks two Fe surface atoms. Yet there is no spectral evidence for a side-on adsorption of the N₂ on the Fe cluster or even the formation of nitrides that would provide for further red shifts than the observed.

DFT:

For geometry optimization of Fe₁₇⁺ we first optimized the total symmetric Cluster Fe₁₉⁺ and withdrew two distal iron atoms from the hyperoctahedron edges. Further geometry optimization revealed the nearly C_{2v}-symmetric cluster cation depicted in Fig. 10.

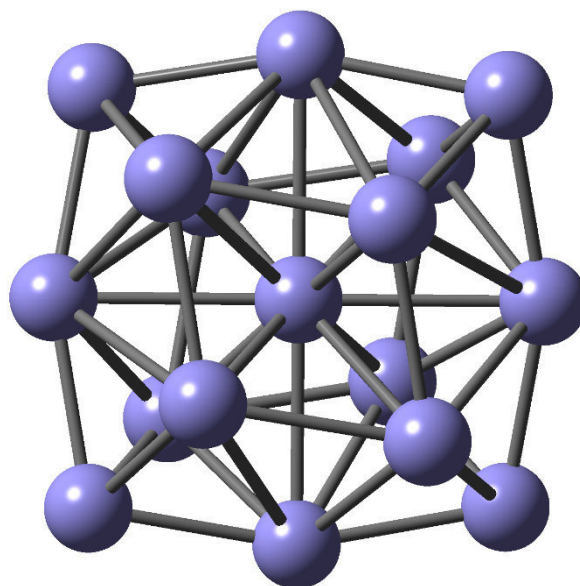


Fig. 10: Optimized structure of cluster Fe₁₇⁺.

The calculated electronic ground state includes 53 unpaired electrons which distribute nearly evenly by three unpaired electrons on the d-shells on each Fe-atom and two electrons also nearly distributed on the inner s and p-shells with slight preference to the inner iron atom and tip atoms of the polyhedron. Thus, all localized orbitals pointing outwards from the cluster are single occupied.

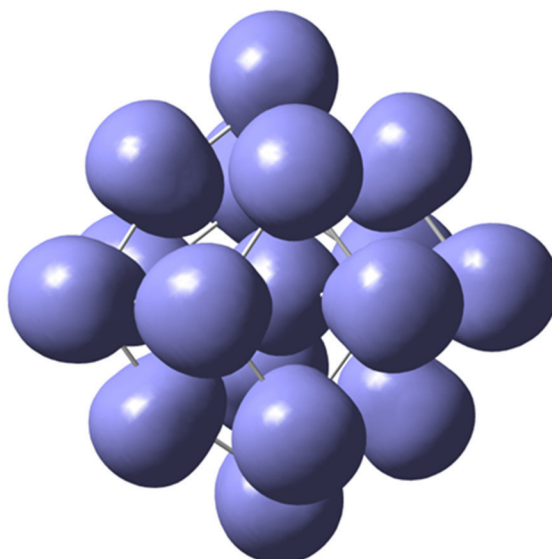


Fig. 11: Spin density calculated for the Fe₁₇⁺ Cluster.

Putative bonding of a N₂ molecule to an iron atom would be significantly reduced in strength by 2 center 3 electron interaction i.e. coulomb repulsion between the N₂-sigma orbital and the single occupied localized orbital on Fe (see Fig. 12).

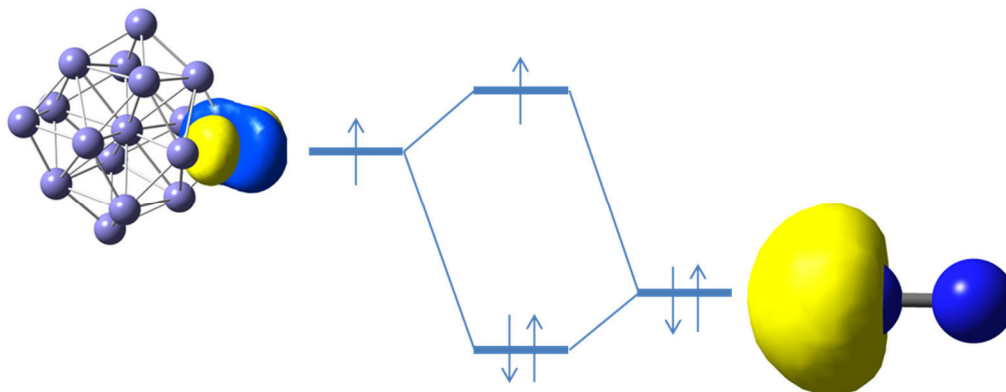


Figure 12: Interaction diagram of NLMOs (Natural Localized Molecular Orbitals) of Fe₁₇⁺(right) and N₂ (left). The interaction of the two electrons from the nitrogen molecule with the single occupied orbital of the iron cluster leads to a splitting of the molecular orbital levels with an occupied bonding and a single occupied antibonding orbital. This leads to a weakening of the N₂-Fe σ -bond.

From the calculations on the Cluster Fe₁₇⁺ it can be deduced that a spherical half-filled shell results in weak bonding from iron clusters to a N₂-molecule.

To probe this hypothesis we performed calculations on the Fe₁₈⁺ cluster which appear to appear in at least two isomeric forms; one which reacts with N₂ and one which does not.

The Initial geometry for optimization of the Fe₁₈⁺ cluster was again taken from the optimized Fe₁₉⁺ cluster from which one edge Fe-atom has been withdrawn. Geometry optimization revealed a geometry depicted in Fig. 13.

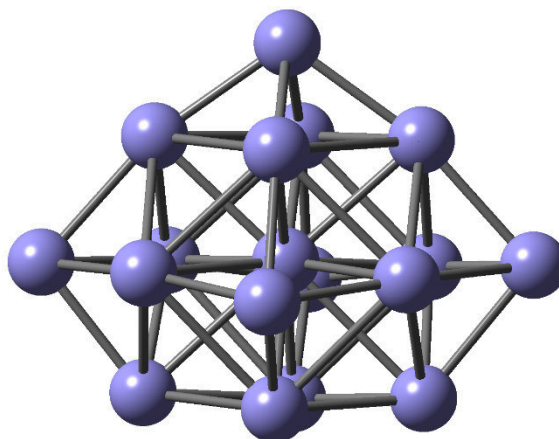


Fig. 13: Optimized geometry of the cluster Fe₁₈⁺

Calculation of the electronic ground state revealed 55 unpaired electrons and an electron distribution comparable to the cluster Fe₁₇⁺. The spin density is drawn in Fig. 14.

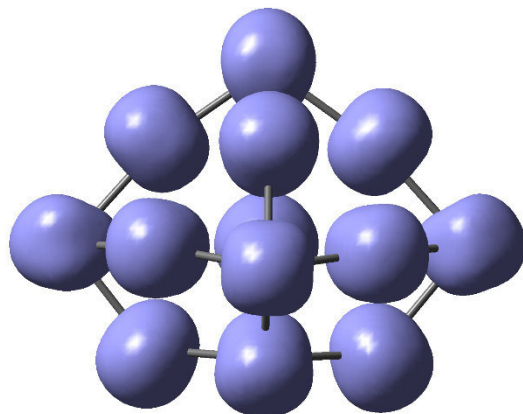


Fig. 14: Spin density of a Fe₁₈⁺ cluster isomer

Due to the outward polarized spin distribution a similar behavior towards N₂-molecules can be assumed. Thus, the Fe₁₈⁺ cluster isomer deduced from the Fe₁₉⁺ cluster has similar reactive properties. However, for Fe₁₈⁺ different isomers can be taken into account.

An isomer deduced from an icosahedron with nearly five-fold symmetry is depicted in Fig. 15.

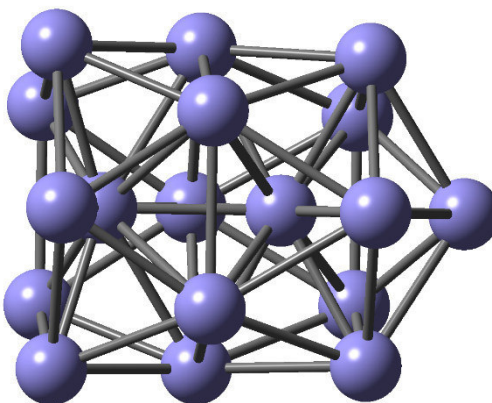


Fig. 15: Optimized geometry of the cluster Fe₁₈⁺ bearing a capped icosahedron.

In contrast to former structures for Fe₁₇⁺ and one isomer of Fe₁₈⁺ we calculated for the structure depicted in Figure 18 with 55 unpaired electrons a LUMO+1 to be unoccupied (Fig. 16). Thus, a *s*-bond of N₂ to the icosahedron based cluster Fe₁₈⁺ is feasible.

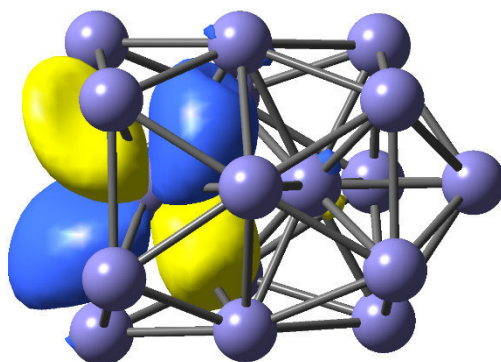


Fig. 16: LUMO+1 orbital of the cluster Fe₁₈⁺ bearing a capped icosahedron.

In conclusion, the cluster Fe₁₇⁺ derived from the hyperoctahedron Fe₁₉ was calculated to be less Lewis-acidic towards a dinitrogen molecule due to single occupied orbitals which causes coulomb repulsion with the nonbonding electron pair on nitrogen. Along this line, one isomer also derived from the hyperoctahedron exhibits the same electronic environment and thus, has less preferences for binding dinitrogen to one iron center. However, the isomer derived from an icosahedron exhibits on a central iron atom on one face of the cluster an unoccupied orbital which would facilitate dinitrogen bonding and thus, would be the main reason for the differences in reactivity.

7.6 Conclusions

We have investigated the stepwise N₂ adsorption on size selected Fe_n⁺ (n = 8 – 20) clusters by recording their reaction kinetics at 26 K in a hexapole ion trap. We performed pseudo-first-order kinetic fits, which confirm consecutive adsorption steps by single exponentially decays and by a biexponential decay in the case of Fe₁₈⁺. There is little N₂ adsorption to Fe₁₃⁺ - Fe₁₆⁺ and no N₂ adsorption to Fe₁₇⁺ clusters. The adsorption limits which stay below a molar ratio of n:m = 1:1 in all investigated cases n = 8-20. As of now, we cannot provide for an overall applicable adsorption rules for the N₂ adsorption on Fe clusters to explain the observed stoichiometries. These stoichiometries are not mainly dominated by the cluster structure itself like in the case of cationic Ni clusters. Other effects like the electronic configuration of the cluster prevail.

We further recorded the IR-PD spectra of the [Fe_n(N₂)₁]⁺ (n,1) and [Fe_n(N₂)₂]⁺ (n,2) species in the N-N stretching region and observe single or double bands. These bands are less

redshifted with respect to the free N₂ mode compared to N₂ on cationic Co or Ni cluster and we assign them to the μ_1 head-on adsorption of N₂ on the cluster. We do not observe a systematic variation of the band positions following a charge dilution model like previously observed for Ni clusters. We further identified a further redshifted band in the spectra of (18,1) and (18,2) that we tentatively assign to a slightly tilted N₂ on the cluster. This could be a precursor for the N₂ activation.

Preliminary DFT modelling provide for a first understanding of the miraculous unreactivity of Fe₁₇⁺ cluster towards N₂. The calculations found an electronic configuration that should not show a high reactivity towards N₂. Furthermore it identified two isomers for the Fe₁₈⁺ cluster one with a similar electronic configuration as the Fe₁₇⁺ cluster explaining the inertness and one reactive isomer.

7.7 Acknowledgements

This work was supported by the German research foundation DFG within the transregional collaborative research center SFB/TRR 88 "Cooperative effects in homo and heterometallic complexes" (3MET.de) and by the state research center OPTIMAS. The isotope used in this research were supplied by the United States Department of Energy Office of Science by the Isotope Program in the Office of Nuclear Physics.

7.8 References

- (1) Boissel, P., Organometallic chemistry and the interstellar medium: experimental evidence of coordination between metal cations and polycyclic hydrocarbons in the gas phase, *Astron. Astrophys.* **1994**, *285*.
- (2) Böhme, D. K.; Schwarz, H., Gas-Phase Catalysis by Atomic and Cluster Metal Ions: The Ultimate Single-Site Catalysts, *Angew. Chem. Int. Ed.* **2005**, *44*, 2336-2354.
- (3) Kubas, G. J., Fundamentals of H₂ binding and reactivity on transition metals underlying hydrogenase function and H₂ production and storage, *Chem. Rev.* **2007**, *107*, 4152-4205.
- (4) Armentrout, P. B., Gas-phase perspective on the thermodynamics and kinetics of heterogeneous catalysis, *Catalysis Science & Technology* **2014**, *4*, 2741-2755.
- (5) Russo, N.; Salahub, D. R., *Metal-ligand interactions: structure and reactivity*. Springer Science & Business Media: 2012; Vol. 474.
- (6) Morse, M. D.; Geusic, M.; Heath, J.; Smalley, R., Surface reactions of metal clusters. II. Reactivity surveys with D₂, N₂, and CO, *J. Chem. Phys.* **1985**, *83*, 2293-2304.

- (7) Parks, E.; Weiller, B.; Bechthold, P.; Hoffman, W.; Nieman, G.; Pobo, L.; Riley, S., Chemical probes of metal cluster structure: reactions of iron clusters with hydrogen, ammonia, and water, *J. Chem. Phys.* **1988**, *88*, 1622-1632.
- (8) Whetten, R.; Cox, D.; Trevor, D.; Kaldor, A., Correspondence between electron binding energy and chemisorption reactivity of iron clusters, *Phys. Rev. Lett.* **1985**, *54*, 1494.
- (9) Richtsmeier, S.; Parks, E.; Liu, K.; Pobo, L.; Riley, S., Gas phase reactions of iron clusters with hydrogen. I. Kinetics, *J. Chem. Phys.* **1985**, *82*, 3659-3665.
- (10) Parks, E.; Liu, K.; Richtsmeier, S.; Pobo, L.; Riley, S., Reactions of iron clusters with hydrogen. II. Composition of the fully hydrogenated products, *J. Chem. Phys.* **1985**, *82*, 5470-5474.
- (11) Jones, N.; Beltran, M.; Khanna, S. N.; Baruah, T.; Pederson, M., Hydrogen adsorption and magnetic behavior of Fe_n and Co_n clusters: Controlling the magnetic moment and anisotropy one atom at a time, *Phys. Rev. B* **2004**, *70*, 165406.
- (12) Parks, E. K.; Nieman, G. C.; Pobo, L. G.; Riley, S. J., The Reaction of Iron Clusters with Ammonia .1. Compositions of the Ammoniated Products and Their Implications for Cluster Structure, *J. Chem. Phys.* **1988**, *88*, 6260-6272.
- (13) Fossan, K. O.; Uggerud, E., Reactions of cationic iron clusters with ammonia, models of nitrogen hydrogenation and dehydrogenation, *Dalton Trans.* **2004**, 892-897.
- (14) Irion, M. P.; Schnabel, P., FT-ICR studies of sputtered metal cluster ions. 5. The chemistry of iron cluster cations with ammonia and hydrazine, *J. Phys. Chem.* **1991**, *95*, 10596-10599.
- (15) Gutsev, G. L.; Bauschlicher, C. W., Interaction of carbon atoms with Fe_n, Fe_n⁻, and Fe_n⁺ clusters (n= 1-6), *Chem. Phys.* **2003**, *291*, 27-40.
- (16) Gutsev, G.; Mochena, M.; Bauschlicher, C., Interaction of water with small Fe_n clusters, *Chem. Phys.* **2005**, *314*, 291-298.
- (17) Weiller, B. H.; Bechthold, P. S.; Parks, E. K.; Pobo, L. G.; Riley, S. J., The Reactions of Iron Clusters with Water, *J. Chem. Phys.* **1989**, *91*, 4714-4727.
- (18) Gehret, O.; Irion, M. P., Reactions of Fe_n⁺ clusters (n= 2-11) with C₆H₆ and C₆D₆. Ligand isomerization in the benzene precursor ion Fe₄(C₂H₂)₃⁺, *Chem. Phys. Lett.* **1996**, *254*, 379-383.
- (19) Valencia, I., On the structure and reactivity of small iron clusters with benzene, [Fe_n-C₆H₆]_{0,+,-}, n ≤ 7: A theoretical study, *Chem. Phys.* **2016**, *476*, 46-60.
- (20) Zheng, W.; Eustis, S. N.; Li, X.; Nilles, J. M.; Thomas, O. C.; Bowen, K. H.; Kandalam, A. K., Photoelectron spectroscopic study of iron-benzene cluster anions, *Chem. Phys. Lett.* **2008**, *462*, 35-39.
- (21) Tan, L.; Liu, F. Y.; Armentrout, P. B., Thermochemistry of the activation of N₂ on iron cluster cations: Guided ion beam studies of the reactions of Fe_n⁺ (n=1-19) with N₂, *J. Chem. Phys.* **2006**, *124*, 084302.

- (22) Li, M.; Liu, S.-R.; Armentrout, P. B., Collision-induced dissociation studies of Fe_mO_n⁺: Bond energies in small iron oxide cluster cations, Fe_mO_n⁺, (m=1-3, n=1-6), *J. Chem. Phys.* **2009**, *131*, 144310.
- (23) McNary, C. P.; Armentrout, P. B., Iron cluster-CO bond energies from the kinetic energy dependence of the Fe-*n*(+) (n=4-17) + CO association reactions, *Phys. Chem. Chem. Phys.* **2014**, *16*, 26467-26477.
- (24) Sakurai, M.; Watanabe, K.; Sumiyama, K.; Suzuki, K., Magic numbers in transition metal (Fe, Ti, Zr, Nb, and Ta) clusters observed by time-of-flight mass spectrometry, *J. Chem. Phys.* **1999**, *111*, 235-238.
- (25) Knight, W.-D.; Clemenger, K.; de Heer, W. A.; Saunders, W. A.; Chou, M.; Cohen, M. L., Electronic shell structure and abundances of sodium clusters, *Phys. Rev. Lett.* **1984**, *52*, 2141.
- (26) Miehle, W.; Kandler, O.; Leisner, T.; Echt, O., Mass spectrometric evidence for icosahedral structure in large rare gas clusters: Ar, Kr, Xe, *J. Chem. Phys.* **1989**, *91*, 5940-5952.
- (27) Billas, I. M.; Chatelain, A.; de Heer, W. A., Magnetism from the atom to the bulk in iron, cobalt, and nickel clusters, *Science* **1994**, *265*, 1682-1684.
- (28) Bucher, J.; Douglass, D.; Bloomfield, L., Magnetic properties of free cobalt clusters, *Phys. Rev. Lett.* **1991**, *66*, 3052.
- (29) Cox, D.; Trevor, D.; Whetten, R.; Rohlfing, E.; Kaldor, A., Magnetic behavior of free-iron and iron oxide clusters, *Phys. Rev. B* **1985**, *32*, 7290.
- (30) de Heer, W. A.; Milani, P.; Chatelain, A., Spin relaxation in small free iron clusters, *Phys. Rev. Lett.* **1990**, *65*, 488.
- (31) Chen, J.; Wang, C.; Jackson, K. A.; Pederson, M. R., Theory of magnetic and structural ordering in iron clusters, *Phys. Rev. B* **1991**, *44*, 6558.
- (32) Castro, M.; Salahub, D. R., Density-functional calculations for small iron clusters: Fe *n*, Fe *n*⁺, and Fe *n*⁻ for *n* ≤ 5, *Phys. Rev. B* **1994**, *49*, 11842.
- (33) Ballone, P.; Jones, R., Structure and spin in small iron clusters, *Chem. Phys. Lett.* **1995**, *233*, 632-638.
- (34) Oda, T.; Pasquarello, A.; Car, R., Fully unconstrained approach to noncollinear magnetism: application to small Fe clusters, *Phys. Rev. Lett.* **1998**, *80*, 3622.
- (35) Hobbs, D.; Kresse, G.; Hafner, J., Fully unconstrained noncollinear magnetism within the projector augmented-wave method, *Phys. Rev. B* **2000**, *62*, 11556.
- (36) Diéguez, O.; Alemany, M.; Rey, C.; Ordejón, P.; Gallego, L., Density-functional calculations of the structures, binding energies, and magnetic moments of Fe clusters with 2 to 17 atoms, *Phys. Rev. B* **2001**, *63*, 205407.
- (37) Rollmann, G.; Entel, P.; Sahoo, S., Competing structural and magnetic effects in small iron clusters, *Computational materials science* **2006**, *35*, 275-278.
- (38) Yu, S.; Chen, S.; Zhang, W.; Yu, L.; Yin, Y., Theoretical study of electronic structures and magnetic properties in iron clusters (*n* ≤ 8), *Chem. Phys. Lett.* **2007**, *446*, 217-222.

- (39) Ma, Q.-M.; Xie, Z.; Wang, J.; Liu, Y.; Li, Y.-C., Structures, binding energies and magnetic moments of small iron clusters: A study based on all-electron DFT, *Solid State Commun.* **2007**, *142*, 114-119.
- (40) Gutsev, G.; Weatherford, C.; Jena, P.; Johnson, E.; Ramachandran, B., Structure and Properties of Fe_n, Fe_n⁻, and Fe_n⁺ Clusters, n= 7–20, *J. Phys. Chem. A* **2012**, *116*, 10218-10228.
- (41) Niemeyer, M.; Hirsch, K.; Zamudio-Bayer, V.; Langenberg, A.; Vogel, M.; Kossick, M.; Ebrecht, C.; Egashira, K.; Terasaki, A.; Moeller, T., et al., Spin Coupling and Orbital Angular Momentum Quenching in Free Iron Clusters, *Phys. Rev. Lett.* **2012**, *108*, 057201.
- (42) Wu, M.; Kandalam, A. K.; Gutsev, G. L.; Jena, P., Origin of the anomalous magnetic behavior of the Fe₁₃⁺ cluster, *Phys. Rev. B* **2012**, *86*, 174410.
- (43) Rao, C. N. R.; Rao, G. R., NATURE OF NITROGEN ADSORBED ON TRANSITION-METAL SURFACES AS REVEALED BY ELECTRON-SPECTROSCOPY AND COGNATE TECHNIQUES, *Surf. Sci. Rep.* **1991**, *13*, 221-263.
- (44) Ertl, G., Reactions at surfaces: From atoms to complexity (Nobel lecture), *Angew. Chem. Int. Ed.* **2008**, *47*, 3524-3535.
- (45) Bottomley, F.; Burns, R., Treatise on Nitrogen Fixation. Wiley Interscience, New York: 1979.
- (46) Freund, H. J.; Bartos, B.; Messmer, R. P.; Grunze, M.; Kühlenbeck, H.; Neumann, M., THE ADSORPTION OF N₂ ON Fe(111) - ANGLE RESOLVED PHOTOEMISSION AND THEORETICAL-MODEL STUDIES, *Surf. Sci.* **1987**, *185*, 187-202.
- (47) Tsai, M. C.; Ship, U.; Bassignana, I. C.; Küppers, J.; Ertl, G., A vibrational spectroscopy study on the interaction of N₂ with clean and K-promoted Fe(111) surfaces: π-bonded dinitrogen as precursor for dissociation, *Surf. Sci.* **1985**, *155*, 387-399.
- (48) de Paola, R. A.; Hoffmann, F. M.; Heskett, D.; Plummer, E. W., Adsorption of molecular nitrogen on clean and modified Ru(001) surfaces: The role of σ-bonding, *Phys. Rev. B* **1987**, *35*, 4236-4249.
- (49) Duarte, H. A.; Salahub, D. R.; Haslett, T.; Moskovits, M., Fe (N₂)_n (n= 1-5): Structure, Bonding, and Vibrations from Density Functional Theory, *Inorg. Chem.* **1999**, *38*, 3895-3903.
- (50) Haslett, T.; Fedrigo, S.; Bosnick, K.; Moskovits, M.; Duarte, H.; Salahub, D., Binary Iron-Dinitrogen Compounds Synthesized by Co-deposition of Mass-Selected Fe, Fe₂, and Fe₃ with N₂, *J. Am. Chem. Soc.* **2000**, *122*, 6039-6044.
- (51) Swart, I.; de Groot, F. M. F.; Weckhuysen, B. M.; Gruene, P.; Meijer, G.; Fielicke, A., H-2 adsorption on 3d transition metal clusters: A combined infrared spectroscopy and density functional study, *J. Phys. Chem. A* **2008**, *112*, 1139-1149.
- (52) Kiawi, D. M.; Chernyy, V.; Oomens, J.; Buma, W. J.; Jamshidi, Z.; Visscher, L.; Waters, L. B.; Bakker, J. M., Water Dissociation upon Adsorption onto Free Iron Clusters Is Size Dependent, *J Phys Chem Lett* **2016**, *7*, 2381-7.

- (53) Lang, J.; Gaffga, M.; Menges, F.; Niedner-Schatteburg, G., Two-color delay dependent IR probing of torsional isomerization in a AgL₁L₂ (+) complex, *Phys. Chem. Chem. Phys.* **2014**, *16*, 17417-17421.
- (54) Dillinger, S.; Mohrbach, J.; Hewer, J.; Gaffga, M.; Niedner-Schatteburg, G., Infrared spectroscopy of N₂ adsorption on size selected cobalt cluster cations in isolation, *Phys. Chem. Chem. Phys.* **2015**, *17*, 10358-10362.
- (55) Mohrbach, J.; Dillinger, S.; Niedner-Schatteburg, G., Cryo Kinetics and Spectroscopy of Cationic Nickel Clusters: Rough and Smooth Surfaces, *The Journal of Physical Chemistry C* **2016**.
- (56) Dillinger, S.; Mohrbach, J.; Niedner-Schatteburg, G., Probing Cluster Surface Morphology by Cryo Spectroscopy of N₂ on Cationic Nickel Clusters, *J. Chem. Phys.* **2017**, submitted.
- (57) Peredkov, S.; Neeb, M.; Eberhardt, W.; Meyer, J.; Tombers, M.; Kampschulte, H.; Niedner-Schatteburg, G., Spin and Orbital Magnetic Moments of Free Nanoparticles, *Phys. Rev. Lett.* **2011**, *107*.
- (58) Meyer, J.; Tombers, M.; van Wüllen, C.; Niedner-Schatteburg, G.; Peredkov, S.; Eberhardt, W.; Neeb, M.; Palutke, S.; Martins, M.; Wurth, W., The spin and orbital contributions to the total magnetic moments of free Fe, Co, and Ni clusters, *J. Chem. Phys.* **2015**, *143*, 104302.
- (59) Berg, C.; Schindler, T.; Niedner-Schatteburg, G.; Bondybey, V. E., Reactions of simple hydrocarbons with Nb⁺ n: chemisorption and physisorption on ionized niobium clusters, *J. Chem. Phys.* **1995**, *102*, 4870-4884.
- (60) Maruyama, S.; Anderson, L. R.; Smalley, R. E., Direct injection supersonic cluster beam source for FT-ICR studies of clusters, *Rev. Sci. Instrum.* **1990**, *61*, 3686-3693.
- (61) Proch, D.; Trickl, T., A high-intensity multi-purpose piezoelectric pulsed molecular beam source, *Rev. Sci. Instrum.* **1989**, *60*, 713-716.
- (62) Caravatti, P.; Allemann, M., The 'infinity cell': A new trapped-ion cell with radiofrequency covered trapping electrodes for Fourier transform ion cyclotron resonance mass spectrometry, *Org. Mass Spectrom.* **1991**, *26*, 514-518.
- (63) Graf, M., *Diploma Thesis, TU Kaiserslautern* **2006**, (unpublished).
- (64) Langevin, M. In *Une formule fondamentale de théorie cinétique*, Annales de chimie et de physique, Series, 1905; pp 245-288.
- (65) Su, T.; Bowers, M. T., Theory of ion-polar molecule collisions. Comparison with experimental charge transfer reactions of rare gas ions to geometric isomers of difluorobenzene and dichloroethylene, *J. Chem. Phys.* **1973**, *58*, 3027-3037.
- (66) Su, T.; Bowers, M. T., Ion-polar molecule collisions. Proton transfer reactions of H₃⁺ and CH₅⁺ to the geometric isomers of difluoroethylene, dichloroethylene, and difluorobenzene, *J. Am. Chem. Soc.* **1973**, *95*, 1370-1373.
- (67) Su, T.; Bowers, M. T., Ion-polar molecule collisions: the effect of ion size on ion-polar molecule rate constants; the parameterization of the average-dipole-

- orientation theory, *International Journal of Mass Spectrometry and Ion Physics* **1973**, *12*, 347-356.
- (68) Kummerlöwe, G.; Beyer, M. K., Rate estimates for collisions of ionic clusters with neutral reactant molecules, *Int. J. Mass Spectrom.* **2005**, *244*, 84-90.
- (69) Jedidi, A.; Markovits, A.; Minot, C.; Abderrabba, M.; Van Hove, M. A., CO dissociation on magnetic Fe_n clusters, *Phys. Chem. Chem. Phys.* **2014**, *16*, 20703-20713.
- (70) Roy, D.; Robles, R.; Khanna, S., Magnetic moment and local moment alignment in anionic and/or oxidized Fe_n clusters, *J. Chem. Phys.* **2010**, *132*.
- (71) Rao, C. N. R.; Rao, G. R.; Ppabhakaran, K., A combined XPS-UPS-EELS study of nitrogen adsorbed on clean and barium-promoted iron surfaces: The nature of the precursor to dissociation, *Chem. Phys. Lett.* **1987**, *134*, 47-50.
- (72) van Wuelen, C., Broken Symmetry Approach to Density Functional Calculation of Magnetic Anisotropy or Zero Field Splittings for Multinuclear Complexes with Antiferromagnetic Coupling, *J. Phys. Chem. A* **2009**, *113*, 11535-11540.
- (73) Ahlrichs, R.; Bär, M.; Häser, M.; Horn, H.; Kölmel, C., Electronic structure calculations on workstation computers: The program system turbomole, *Chem. Phys. Lett.* **1989**, *162*, 165-169.
- (74) Eichkorn, K.; Weigend, F.; Treutler, O.; Ahlrichs, R., Auxiliary basis sets for main row atoms and transition metals and their use to approximate Coulomb potentials, *Theor. Chem. Acc.* **1997**, *97*, 119-124.
- (75) Weigend, F.; Ahlrichs, R., Balanced basis sets of split valence, triple zeta valence and quadruple zeta valence quality for H to Rn: Design and assessment of accuracy, *Phys. Chem. Chem. Phys.* **2005**, *7*, 3297-3305.
- (76) Perdew, J. P.; Burke, K.; Ernzerhof, M., Generalized gradient approximation made simple, *Phys. Rev. Lett.* **1996**, *77*, 3865.

7.9 Supplementary Material

Tabel of Content:

Figure S1 Observed rate constants of the (n,m) species n = 8-11 as a function of N₂ coverage. Filled circles show the rate of adsorption and open circles indicate single N₂ desorption.

Table S1 Relative rate constants for the N₂ adsorption $k_{(n,m)}$ to Fe_n⁺ clusters (n = 8-11) and for the respective N₂ desorption $k_{-(n,m+1)}$ from [Fe_n(N₂)_m]⁺ clusters.

Figure S2 Observed rate constants of the (n,m) species n = 12-15 as a function of N₂ coverage. Filled circles show the rate of adsorption and open circles indicate single N₂ desorption.

Table S2 Relative rate constants for the N₂ adsorption $k_{(n,m)}$ to Fe_n⁺ clusters (n = 12-15) and for the respective N₂ desorption $k_{-(n,m+1)}$ from [Fe_n(N₂)_m]⁺ clusters.

Figure S3 Observed rate constants of the (n,m) species n = 16, 18-20 as a function of N₂ coverage. Filled circles show the rate of adsorption and open circles indicate single N₂ desorption.

Table S3 Relative rate constants for the N₂ adsorption $k_{(n,m)}$ to Fe_n⁺ clusters (n = 16, 18-20) and for the respective N₂ desorption $k_{-(n,m+1)}$ from [Fe_n(N₂)_m]⁺ clusters.

Figure S4 Relative rate constant $k_{(n,0)}$ of the initial N₂ adsorption to Fe_n⁺ clusters recorded at 26 K (filled circles), and recorded at 25 K (open circles). Note, that the measurements at 25 K have been performed at a lower N₂ pressure, which causes the offset in relative rate constants.

Figure S5 Temporal intensity decrease of isolated Fe_n⁺ (n = 17 - 19) clusters at 26 K in the presence of 1.6 x 10⁻⁷ mbar of N₂. The grey shaded area indicates the loss of trapped ions.

Figure S6 IR-PD spectra of [Fe₁₃(N₂)₆]⁺ from 1000 cm⁻¹ to 2400 cm⁻¹. The grey line shows the powercurve of the IR laser in this spectral region.

Figure S7 IR-PD spectra of [Fe₁₈(N₂)₁]⁺ from 1000 cm⁻¹ to 2400 cm⁻¹. The grey line shows the powercurve of the IR laser in this spectral region.

Figure S8 IR-PD spectra of [Fe_n(N₂)_m]⁺ for m = 1, 2, 3 & 6. Note the jump of the band from m = 1 to m = 2 of over 10 cm⁻¹.

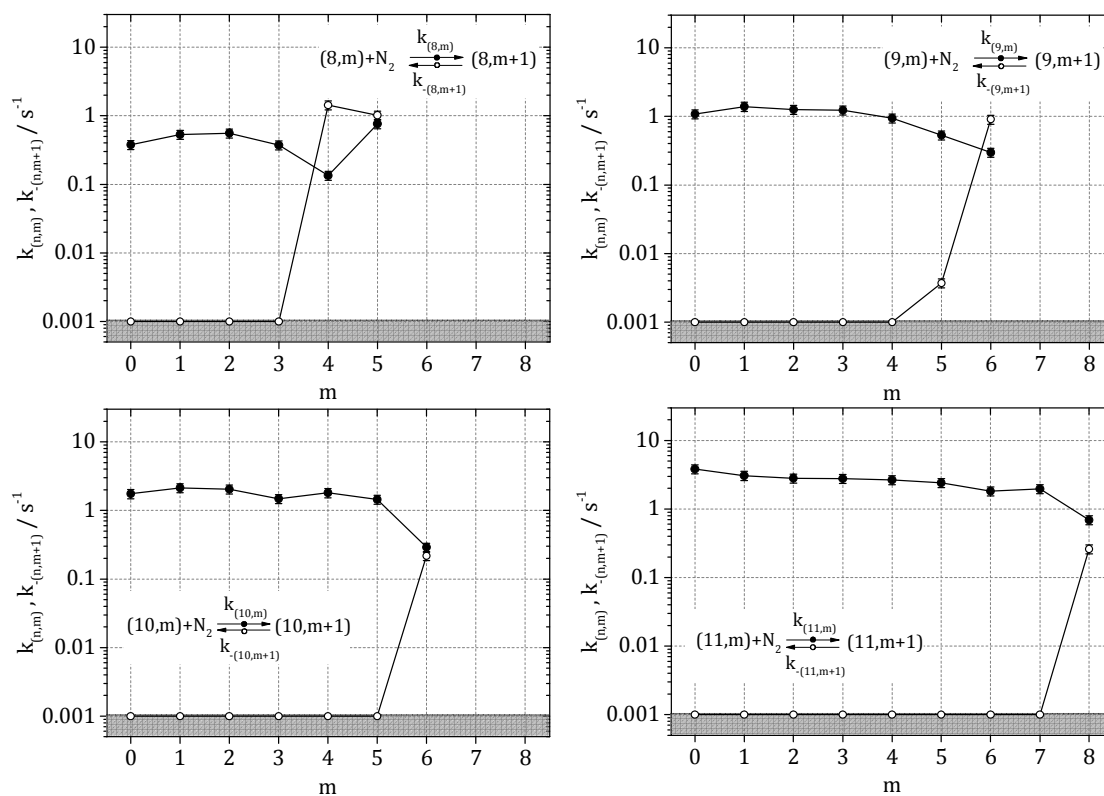


Figure S1. Observed rate constants of the (n,m) species $n = 8-11$ as a function of N₂ coverage. Filled circles show the rate of adsorption and open circles indicate single N₂ desorption.

Table S1. Relative rate constants for the N₂ adsorption $k_{(n,m)}$ to Fe_n⁺ clusters (n = 8-11) and for the respective N₂ desorption $k_{-(n,m+1)}$ from [Fe_n(N₂)_m]⁺ clusters.

m	$k_{(8,m)}$ s ⁻¹	$k_{-(8,m+1)}$ s ⁻¹	$k_{(9,m)}$ s ⁻¹	$k_{-(9,m+1)}$ s ⁻¹	$k_{(10,m)}$ s ⁻¹	$k_{-(10,m+1)}$ s ⁻¹	$k_{(11,m)}$ s ⁻¹	$k_{-(11,m+1)}$ s ⁻¹
0	0.4	<0.001	1.1	<0.001	1.7	<0.001	3.8	<0.001
1	0.5	<0.001	1.4	<0.001	2.1	<0.001	3.1	<0.001
2	0.6	<0.001	1.3	<0.001	2.0	<0.001	2.8	<0.001
3	0.4	<0.001	1.2	<0.001	1.5	<0.001	2.8	<0.001
4	0.1	1.43	0.9	<0.001	1.8	<0.001	2.7	<0.001
5	0.8	1.02	0.5	0.004	1.4	<0.001	2.4	<0.001
6			0.3	0.907	0.3	0.218	1.8	<0.001
7							2.0	<0.001
8							0.7	0.261

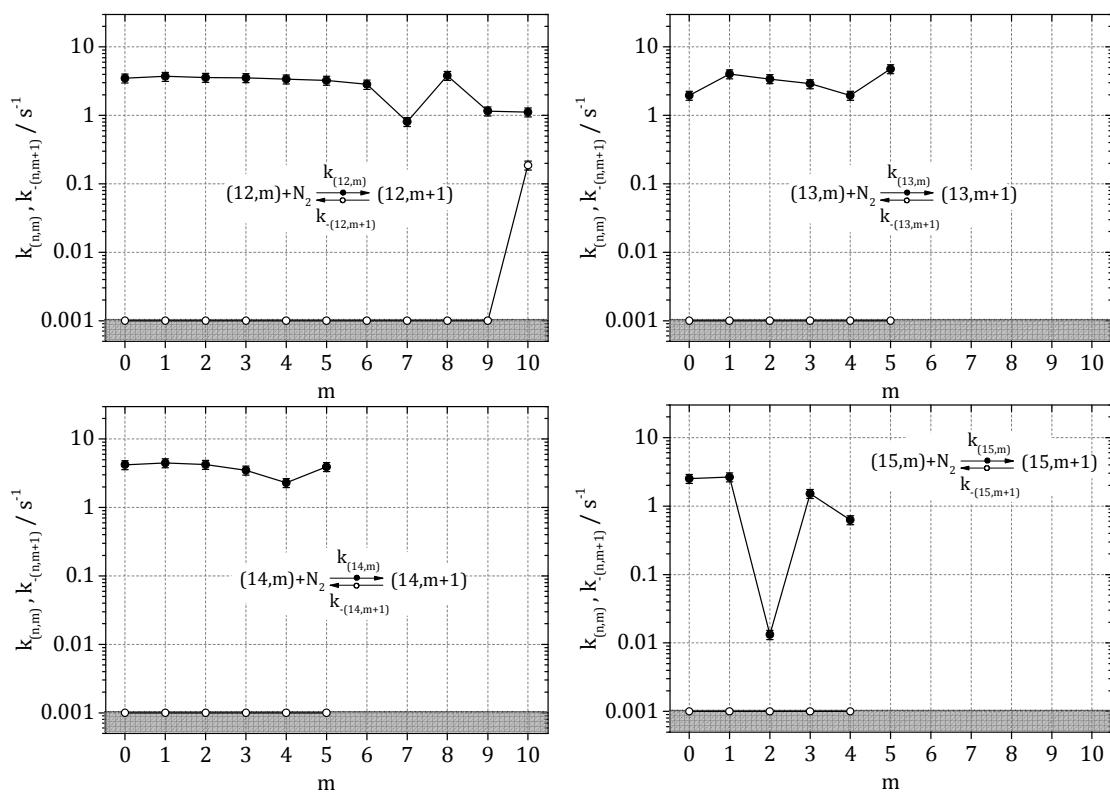


Figure S2. Observed rate constants of the (n,m) species $n = 12-15$ as a function of N_2 coverage. Filled circles show the rate of adsorption and open circles indicate single N_2 desorption.

Table S2. Relative rate constants for the N₂ adsorption $k_{(n,m)}$ to Fe_n⁺ clusters (n = 12-15) and for the respective N₂ desorption $k_{-(n,m+1)}$ from [Fe_n(N₂)_m]⁺ clusters.

m	$k_{(12,m)}$ s ⁻¹	$k_{-(12,m+1)}$ s ⁻¹	$k_{(13,m)}$ s ⁻¹	$k_{-(13,m+1)}$ s ⁻¹	$k_{(14,m)}$ s ⁻¹	$k_{-(14,m+1)}$ s ⁻¹	$k_{(15,m)}$ s ⁻¹	$k_{-(15,m+1)}$ s ⁻¹
0	3.5	<0.001	2.0	<0.001	4.2	<0.001	2.5	<0.001
1	3.7	<0.001	4.0	<0.001	4.5	<0.001	2.6	<0.001
2	3.6	<0.001	3.4	<0.001	4.2	<0.001	0.0	<0.001
3	3.5	<0.001	2.9	<0.001	3.5	<0.001	1.5	<0.001
4	3.4	<0.001	2.0	<0.001	2.3	<0.001	0.6	<0.001
5	3.2	<0.001	4.8	<0.001	3.9	<0.001		
6	2.8	<0.001						
7	0.8	<0.001						
8	3.8	<0.001						
9	1.2	<0.001						
10	1.1	0.186						

7. Cryo IR Spectroscopy and Cryo Kinetics of N₂ on Cationic Iron Clusters

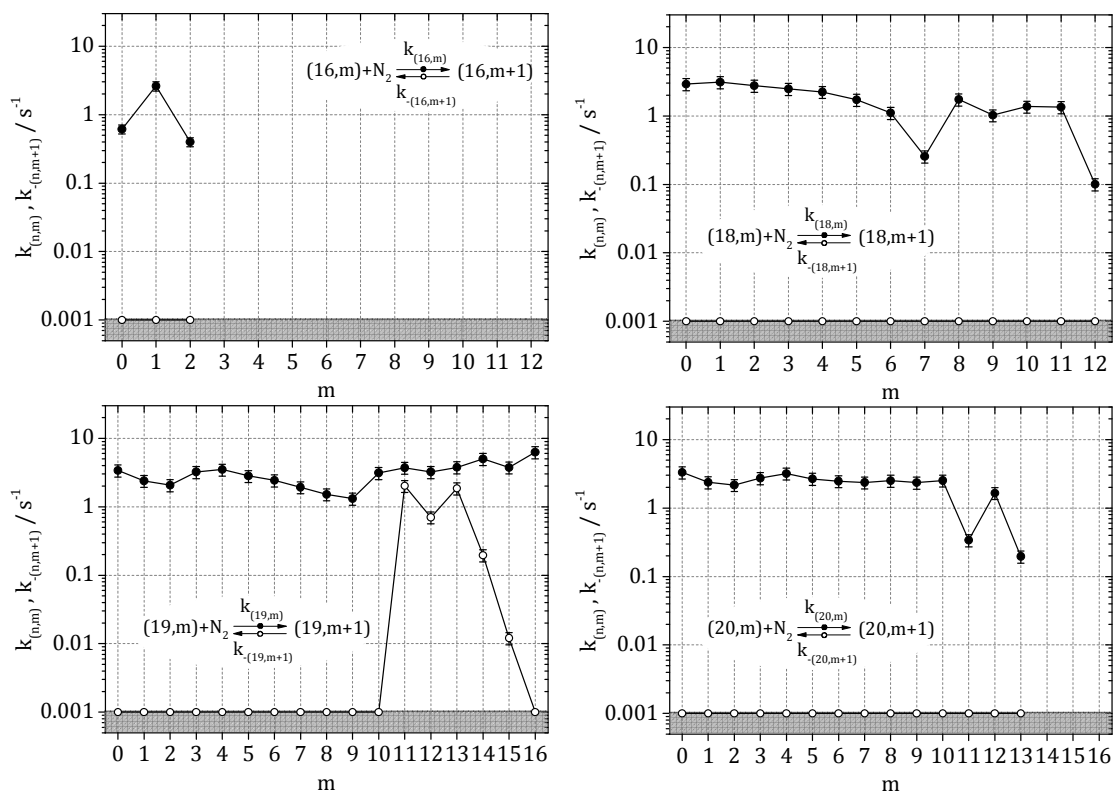


Figure S3. Observed rate constants of the (n,m) species $n = 16, 18-20$ as a function of N_2 coverage. Filled circles show the rate of adsorption and open circles indicate single N_2 desorption.

Table S3. Relative rate constants for the N₂ adsorption $k_{(n,m)}$ to Fe_n⁺ clusters (n = 16, 18-12) and for the respective N₂ desorption $k_{-(n,m+1)}$ from [Fe_n(N₂)_m]⁺ clusters.

m	$k_{(16,m)}$ s ⁻¹	$k_{-(16,m+1)}$ s ⁻¹	$k_{(18,m)}$ s ⁻¹	$k_{-(18,m+1)}$ s ⁻¹	$k_{(19,m)}$ s ⁻¹	$k_{-(19,m+1)}$ s ⁻¹	$k_{(20,m)}$ s ⁻¹	$k_{-(20,m+1)}$ s ⁻¹
0	0.6	<0.001	2.9	<0.001	3.40	<0.001	3.31	<0.001
1	2.6	<0.001	3.1	<0.001	2.39	<0.001	2.39	<0.001
2	0.4	<0.001	2.8	<0.001	2.06	<0.001	2.17	<0.001
3			2.5	<0.001	3.23	<0.001	2.73	<0.001
4			2.2	<0.001	3.49	<0.001	3.20	<0.001
5			1.7	<0.001	2.81	<0.001	2.67	<0.001
6			1.1	<0.001	2.43	<0.001	2.47	<0.001
7			0.3	<0.001	1.93	<0.001	2.37	<0.001
8			1.7	<0.001	1.52	<0.001	2.50	<0.001
9			1.0	<0.001	1.31	<0.001	2.36	<0.001
10			1.4	<0.001	3.13	<0.001	2.52	<0.001
11			1.3	<0.001	3.71	2.019	0.34	<0.001
12			0.1	<0.001	3.23	0.702	1.66	<0.001
13					3.77	1.859	0.20	<0.001
14					5.00	0.196		
15					3.76	0.012		
16					6.28	0.001		

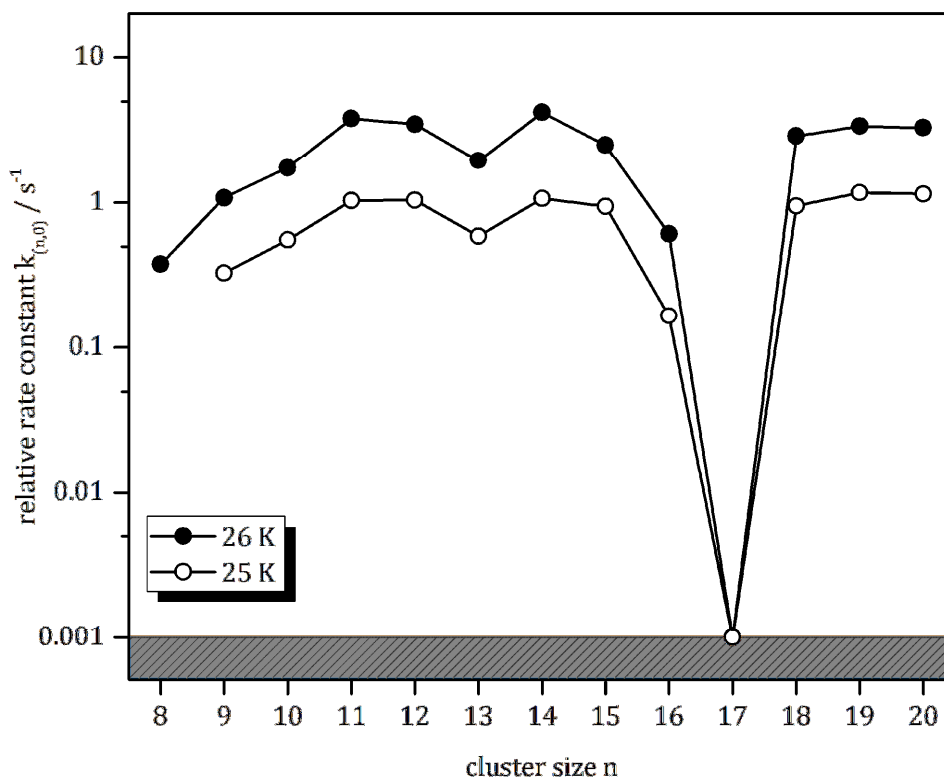


Figure S4. Relative rate constant $k_{(n,0)}$ of the initial N₂ adsorption to Fe_{*n*}⁺ clusters recorded at 26 K (filled circles), and recorded at 25 K (open circles). Note, that the measurements at 25 K have been performed at a lower N₂ pressure, which causes the offset in relative rate constants.

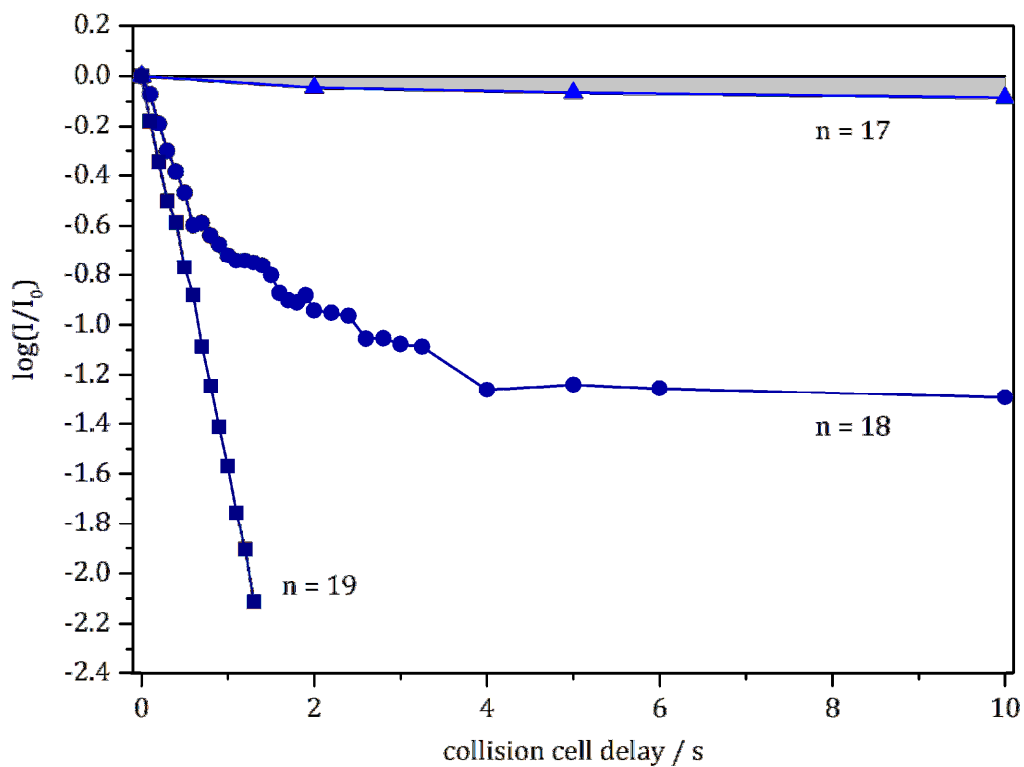


Figure S5. Temporal intensity decrease of isolated Fe_n⁺ (n = 17 - 19) clusters at 26 K in the presence of 1.6 × 10⁻⁷ mbar of N₂. The grey shaded area indicates the loss of trapped ions.

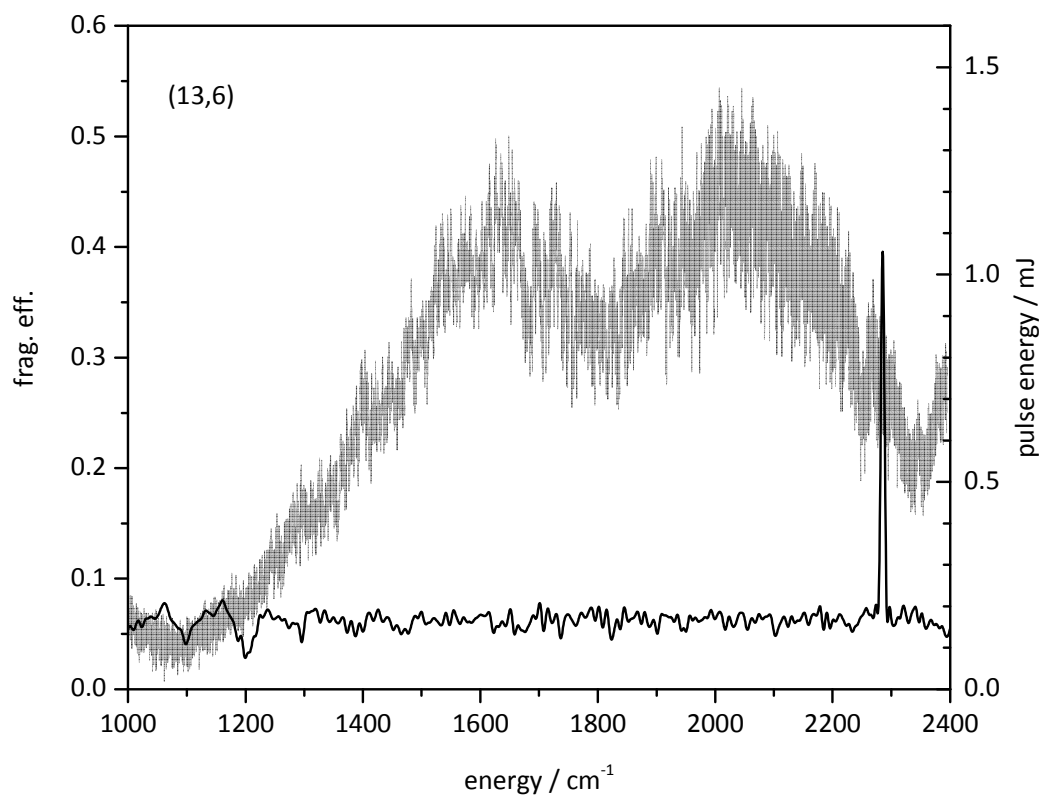


Figure S6 IR-PD spectra of $[\text{Fe}_{13}(\text{N}_2)_6]^+$ from 1000 cm^{-1} to 2400 cm^{-1} . The grey line shows the powercurve of the IR laser in this spectral region. Only a single absorption band at 2285 cm^{-1} can be observed.

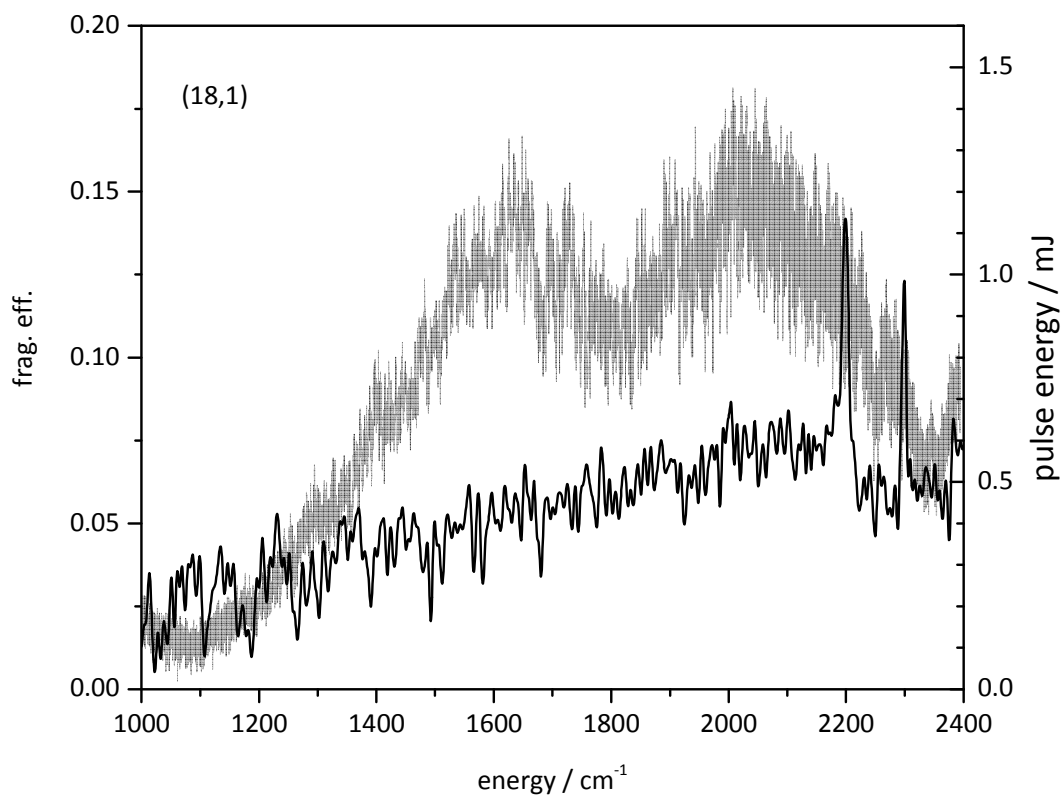


Figure S7 IR-PD spectra of $[\text{Fe}_{18}(\text{N}_2)_1]^+$ from 1000 cm^{-1} to 2400 cm^{-1} . The grey line shows the powercurve of the IR laser in this spectral region. Two absorption bands can be observed.

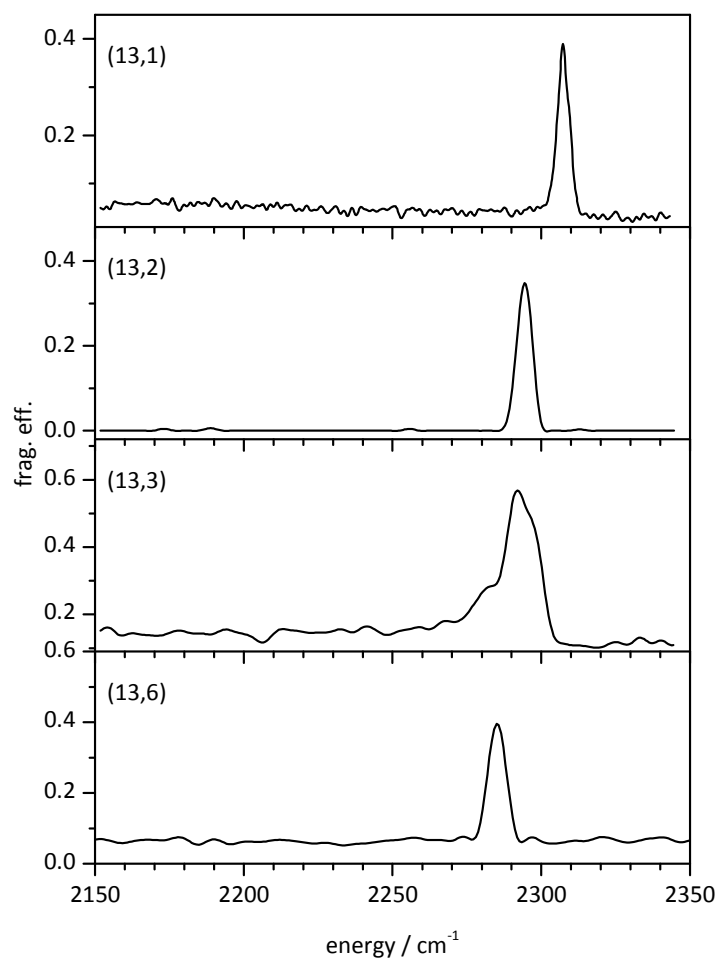


Figure S8 IR-PD spectra of $[\text{Fe}_n(\text{N}_2)_m]^+$ for $m = 1, 2, 3$ & 6 . Note the jump of the band from $m = 1$ to $m = 2$ of over 10 cm^{-1} .

8 Cryo IR Spectroscopy of N₂ and H₂ on Ru₈⁺: The Effect of N₂ on the H-Migration

Sebastian Dillinger¹, Matthias P. Klein¹, Annika Steiner¹, David C. McDonald II², Michael A. Duncan², Manfred M. Kappes^{3,4}, and Gereon Niedner-Schatteburg¹

¹*Fachbereich Chemie and Forschungszentrum OPTIMAS, Technische Universität Kaiserslautern, 67663 Kaiserslautern, Germany*

²*Department of Chemistry, University of Georgia, Athens, Georgia 30602, USA*

³*Institute of Physical Chemistry, Karlsruhe Institute of Technology (KIT), Fritz-Haber-Weg 2, 76131 Karlsruhe, Germany*

⁴*Institute of Nanotechnology, Karlsruhe Institute of Technology (KIT), Hermann-von-Helmholtz-Platz 1, 76344 Eggenstein-Leopoldshafen, Germany*

8.1 Preamble

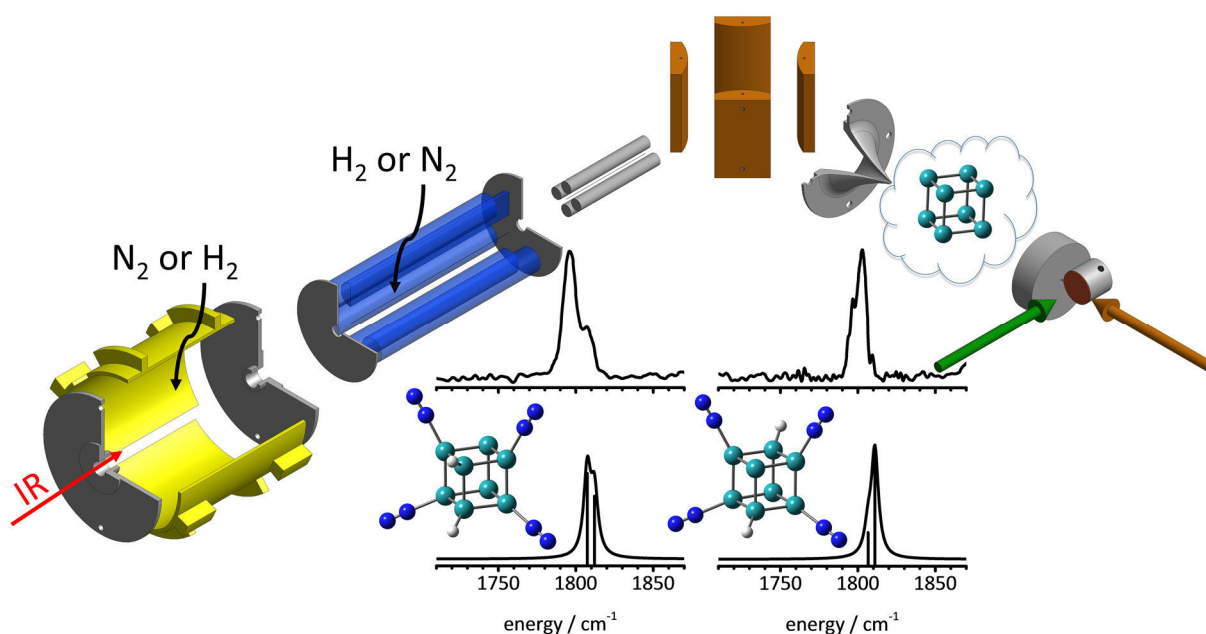
The experiments were performed by the experimental team consisting of M. P. Klein, A. Steiner, D. C. McDonald II, and myself. The data evaluation was done by myself. The computations were done by myself. The initial manuscript was written by myself and revised with the help of G. Niedner-Schatteburg, M. M. Kappes, and M. A. Duncan.

This manuscript is prepared for a submission to *Angewandte Chemie*.

8.2 Abstract

We present the cryo IR-PD spectra of $[\text{Ru}_8(\text{H}_2)_k]^+$, $k = 1 - 8$, of $[\text{Ru}_8(\text{N}_2)_m]^+$, $m = 1 - 8$, and of $[\text{Ru}_8(\text{H}_2)_1(\text{N}_2)_4]^+$ and $[\text{Ru}_8(\text{N}_2)_4(\text{H}_2)_1]^+$ species, which we record via application of tandem cryo ion trapping. The $[\text{Ru}_8(\text{H}_2)_{k>1}]^+$ spectra reveal strong evidence for dissociative H₂ adsorption, and the $[\text{Ru}_8(\text{N}_2)_m]^+$ spectra indicate N₂ head-on adsorption. The spectra of $[\text{Ru}_8(\text{H}_2)_1(\text{N}_2)_4]^+$ and $[\text{Ru}_8(\text{N}_2)_4(\text{H}_2)_1]^+$ species reveal differences in the Ru-H stretching region, which we assign to distal and proximal H atom locations on the Ru₈⁺ cluster, their migration likely hindered by preloaded N₂s, and unaffected by subsequent N₂ adsorption.

Table of Content Graphic:



8.3 Introduction

Ru based catalysts make it possible to run the Haber-Bosch process under milder conditions than with widespread Fe based catalysts.^[1] This is underlined by the industrial Kellogg Advanced Ammonia Process which uses supported Ru nanoparticles as catalyst and works at lower pressures and temperatures.^[2] Ammonia synthesis on Ru catalysts is highly structure sensitive.^[3] Highly reactive “B5 sites” (5 Ru atoms interact with N₂) are thought to mediate the rate limiting step in ammonia synthesis – the N₂ activation.^[4] Studies on isolated clusters can provide valuable information to elucidate such structure-sensitive reactions. Yet, mass spectrometric investigations of reactions of Ru clusters with small molecules like H₂ are very challenging due in part to the broad isotopic distribution of Ru.

Various spectroscopic studies of the N₂/Ru(001) surface-adsorbate system indicate that at low temperatures N₂ absorbs in a head-on position.^[5] High-resolution electron energy loss spectroscopy (HREELS) has identified the same type of adsorption on Ru(1010)^[6]. Dissociative adsorption of N₂ on Ru(0001) only sets in at higher surface temperatures.^[7] In contrast H₂ dissociatively chemisorbs on Ru(001) at temperatures as low as 50K.^[8] The corresponding change in work function has been associated with two different adsorption states as also observed in thermal desorption studies.^[9] HREELS measurements of hydride monolayers have allowed the determination of the Ru-H stretch and bend vibrations (around 820 and 1137 cm⁻¹).^[10] More recently, fast quantum tunneling effects of H on Ru (0001) have been observed at low temperatures.^[11] These may also play a role in the formation of NH on a Ru(001) surface.^[12]

The magnetic properties of isolated neutral Ru clusters in the size range between 10 and 100 atoms have been investigated by cluster beam deflection experiments which showed no evidence for significant ferromagnetism.^[13] Several computational studies predict that small Ru clusters favor cubic structures.^[14] This prediction was further substantiated by far IR spectroscopy of small cationic Ru clusters which provided evidence for cubic structures.^[15] Furthermore, trapped-ion electron diffraction (TIED) found a cubic motif for the Ru₈⁻ cluster.^[16] There are several reaction studies with Ru clusters, although these are complicated by the mentioned difficulties with the isotopic distribution. Mass spectrometry in conjunction with density functional calculations has revealed water activation by cationic Ru oxide clusters.^[17] TIED experiments have shown that Ru₁₉⁻ undergoes a structural

transition upon H₂ adsorption.^[18] H₂ on neutral Ru clusters has also been the subject of extensive theoretical investigations.^[19] IR spectroscopy has yielded fundamental insights into the binding of CO to cationic and anionic Ru^[20] clusters as well as into the adsorption of N₂ on neutral Ru clusters^[21]. Primarily head-on μ_1 adsorption of CO and N₂ have been inferred.

To our knowledge, there have been no experiments aimed at elucidating the coadsorption of H₂ and N₂ on isolated Ru clusters (in order to explore precursor states leading to catalytic activation). Our tandem cryo trap instrument provides the unique opportunity to conduct these experiments as shown by our previous work on N₂ on Co^[22] and Ni clusters^[23].

This study reports IR spectra of the [Ru₈(H₂)_k]⁺ k = 1 – 8, [Ru₈(N₂)_m]⁺ m = 1 – 8 and the coadsorbed [Ru₈(H₂)₁(N₂)₄]⁺ and [Ru₈(N₂)₄(H₂)₁]⁺ species (differing in adsorption sequence) under isolated conditions. It elucidates the interplay of H₂-N₂ coadsorption in unprecedented detail. In particular it provides clear evidence for dissociative chemisorption of H₂ and demonstrates that subsequent mobility of H atoms can be constrained by N₂ adsorption.

8.4 Experimental and Computational Methods

We performed all experiments in a customized Fourier Transform - Ion Cyclotron Resonance (FT-ICR) – mass spectrometer (Apex Ultra Bruker Daltonics) – in particular the cluster production, isolation, N₂/H₂ adsorption, InfraRed - Photodissociation (IR-PD) spectroscopy and mass analysis. The metal cluster ions were generated from a monoisotopic ¹⁰²Ru (99.38%, Oak Ridge National Laboratories; Fig. S1) foil using a home-built laser vaporization source^[24]. After mass selection the Ru clusters were stored in a cryogenic hexapole ion trap (17 K for H₂ and 26 K for N₂). Reaction gas (H₂ or N₂) was continuously introduced up to a pressure of 5.0×10^{-7} mbar to yield sufficient reaction products. Helium was used to increase the pressure up to 5.0×10^{-6} mbar to accomplish efficient trapping and cooling (*cf.* extended experimental description in the supplement). After a variable storage time (0 – 10 s), the ions were guided into the FT-ICR cell that was held at a temperature below 10 K for the spectroscopy of the [Ru₈(H₂)_k]⁺ and [Ru₈(N₂)_m]⁺ species. The cell was used for isolation and detection of the ions. For the coadsorption experiments the ICR cell served as second reaction cell that was heated to 19 K for reactions with H₂ or to 49 K for N₂ to avoid condensation. The pressure was increased from 2.0×10^{-9} mbar up to 1.0×10^{-8} mbar and the ions were stored up to 2 s.

For the acquisition of the IR-PD spectra the FT-ICR cell is coupled to a tunable IR laser that generates radiation in the range of 1000 – 2400 cm⁻¹. Each trapped and isolated packet of ions is irradiated by 7 – 10 laser pulses (0.1 – 1.5 mJ/pulse).

Linear (harmonic) IR absorption spectra were calculated at the PBE0^[25] level of theory using the cc-pVTZ basis sets^[26] (H, N), and the Stuttgart RSC 1997^[27] effective core potential (Ru), respectively, as implemented in the Gaussian 09 program package^[28] – appropriately gauged scaling factors correcting for the vibrational anharmonicities.

8.5 Results and Discussion

The IR-PD spectra for [Ru₈(H₂)_k]⁺ k = 1 – 8 (Fig. 1, left) were recorded in the region from 1700 to 2200 cm⁻¹ and for [Ru₈(N₂)_m]⁺ m = 1 – 8 (Fig. 1, right) from 2140 to 2300 cm⁻¹.

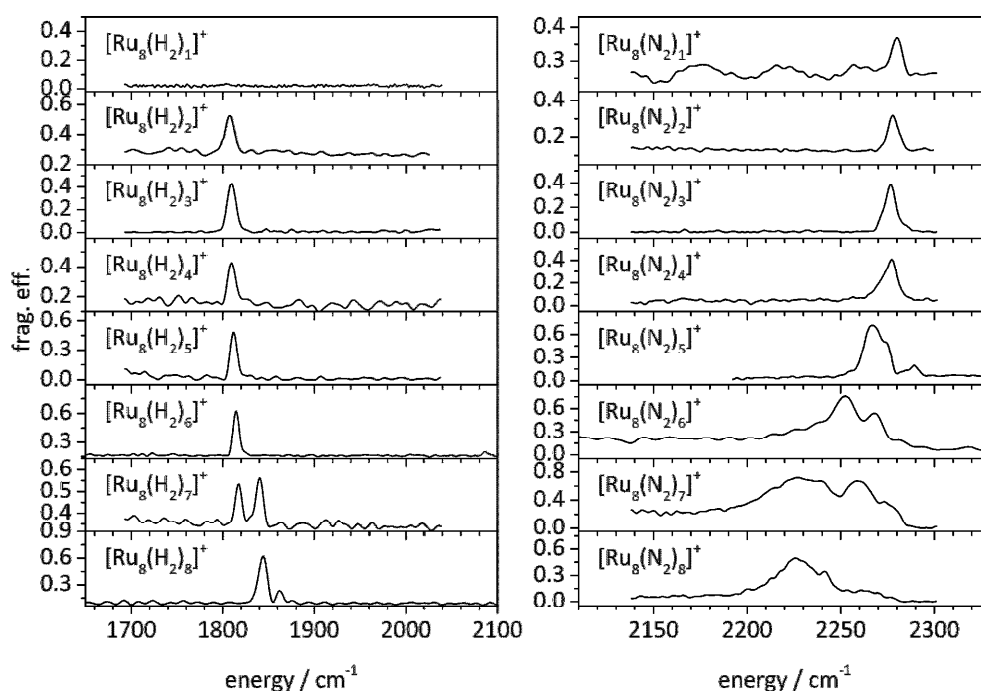


Fig. 1 IR-PD spectra of the [Ru₈(H₂)_k]⁺ k = 1 – 8 (left) and the [Ru₈(N₂)_m]⁺ m = 1 – 8 (right) species. The lack of spectral features for [Ru₈(H₂)₁]⁺ is likely caused by a low fragmentation efficiency.

IR-PD spectra of [Ru₈(H₂)_k]⁺

The spectra of the [Ru₈(H₂)_k]⁺ species reveal no (in the case of k = 1), one (k = 2 – 6), and two bands (k = 7 and 8), all of which occur in the region of 1800 to 1880 cm⁻¹, and with no further spectral features throughout the extended range of 750 to 2375 cm⁻¹ (Fig. S2). The sole vibrational band in [Ru₈(D₂)₆]⁺ (Fig. S3), which is isotopically shifted by 508 cm⁻¹ to

1307 cm⁻¹, helped us to assign the [Ru₈(H₂)_k]⁺ spectral features to a Ru-H stretching mode – indicating dissociative chemisorption of H₂.

IR absorption leads to H₂ elimination as the only fragmentation channel, except for k = 1 which shows no fragmentation (possibly reflecting a higher kinetic barrier for recombination of distal hydrogens on opposing Ru atoms, *cf.* Fig. S14 and below). We find a slight blue shift of 8 cm⁻¹ with increasing H₂ coverage from k = 2 to k = 6 (1807 to 1815 cm⁻¹). Exceeding the intermediate adsorption limit at k = 6 (for a kinetic reasoning of the term “intermediate adsorption limit”, also known as “intermittent adsorption limit”, refer to [23]), the spectra of k = 7 and 8 consist of two bands. The k = 7 species reveals a band at 1817 cm⁻¹, still in line with the aforementioned slight blue shift, and a new spectral feature at 1840 cm⁻¹. The spectrum of H₂ saturated species at k = 8 consists of two bands, the main one at 1843 cm⁻¹ and a less intense side band at 1862 cm⁻¹. Overall one may speculate about an adsorbate-induced reorganization of the core upon exceeding the intermediate adsorption limit at k = 6. Other possible explanations would be spin state changes, or a structural reorganization of the adsorbate layer.

IR-PD spectra of [Ru₈(N₂)_m]⁺

The spectra of [Ru₈(N₂)_m]⁺, m = 1 – 8, reveal features in the region between 2190 and 2300 cm⁻¹. N₂ loss is the only fragmentation channel observed. All bands are redshifted with respect to the free N₂ vibration (2330 cm⁻¹ [29]) and fall in the range previously observed for head-on coordinated N₂ on (other) cationic transition metal clusters^[22-23, 30].

Note, that the feature observed for [Ru₈(N₂)_m]⁺, m = 1, is about 80 cm⁻¹ less red shifted compared to neutral [Ru₈(N₂)₁], which has a band at 2201 cm⁻¹ [22]. This less pronounced red shift can be attributed to charge effects. In the cationic cluster less electron density is available to be transferred into the antibonding orbitals of the N₂.

The spectra of the m = 1 – 4 species reveal a single band which shows a slight red shift with increasing N₂ coverage (2280 cm⁻¹ to 2276 cm⁻¹) similar to the trend observed on Ru(001) surfaces. This has been tentatively rationalized in terms of two opposing coverage-dependent contributions to the shift: dipole-dipole coupling and “chemical (repulsive) effects” associated with N₂ surface bonding^[5a, 31].

In DFT simulations of [Ru₈(N₂)₄]⁺, we have focused on a cubic Ru₈⁺ cluster core predicted to be the lowest energy form of the naked cluster in previous computational studies - as also supported by experiment.^[14-16] We conclude, that the spin state is a quartet and that there is a diagonal N₂ arrangement (close to C_{2v} that Jahn-Teller relaxes into C_s symmetry by pairwise N₂ twists). A force constant analysis reveals four almost degenerate N₂ stretch modes, which convolute into a single, red-shaded band with a shape very similar to that recorded in the IR-PD measurement (*cf.* Fig. S7).

The spectrum of the m = 5 species is the first to show two bands - at 2268 and 2289 cm⁻¹. Beyond the intermediate adsorption limit at m = 5, the spectra are no longer well resolved. The spectrum of m = 6 consists of at least two bands at 2229 and 2258 cm⁻¹ and in the cases of m = 7 and 8 only a broad adsorption between 2200 and 2290 cm⁻¹ is observed.

Again one may speculate about adsorbate induced reorganization when exceeding the intermediate adsorption limit at m = 5. In fact, the cluster core geometry may already be slightly distorted at the intermediate adsorption limit given that its vibrational pattern consists of at least two bands (in contrast to the spectra of the m = 1 – 4 species).

Interestingly, in the case of H₂ the intermediate limit is seen at k = 6 whereas for N₂ it occurs at m = 5. If adsorbate induced reorganization is indeed responsible, it sets in with fewer N₂ than H₂ adsorbates, which may reflect the different steric requirements of H vs. N₂.

IR-PD spectra of [Ru₈(H₂)₁(N₂)₄]⁺ and [Ru₈(N₂)₄(H₂)₁]⁺

Using our tandem cryo trapping technique we were able to produce H₂-N₂-coadsorbates by sequential addition **in either order**. We find that the IR-PD spectra of the “mixed” adsorbates can depend on this order. To demonstrate this, we have selected the two species [Ru₈(H₂)₁(N₂)₄]⁺ and [Ru₈(N₂)₄(H₂)₁]⁺, where the notation signifies the order of attachment: the [Ru₈(H₂)₁(N₂)₄]⁺ species is assembled by first adsorbing a single H₂ in the cryo hexapole trap followed by four N₂ adsorbates in the cryo FT-ICR trap. Conversely, the [Ru₈(N₂)₄(H₂)₁]⁺ species is formed by adding four N₂ adsorbates in the cryo hexapole trap and one H₂ adsorbate in the subsequent cryo FT-ICR trap.

At first sight, the IR-PD spectra of both species reveal similar Ru-H and N₂ stretching features (Fig. 2) much like those seen with separate adsorbates; the supporting information

provides extended spectra (Fig. S4 and S5) – void of additional features – which document the excellent reproducibility of individual features over multiple measurements (Fig. S18).

Upon closer inspection, the Ru-H bands differ in the $[\text{Ru}_8(\text{H}_2)_1(\text{N}_2)_4]^+$ and $[\text{Ru}_8(\text{N}_2)_4(\text{H}_2)_1]^+$ spectra: the former reveals a resolved side peak 10 cm^{-1} to the blue from the main peak at 1796 cm^{-1} , which is not present in the latter. The latter has an asymmetric peak shape with some red shading, which is absent in the former. The dominant Ru-H stretch blue shifts by 6 cm^{-1} from the former to the latter.

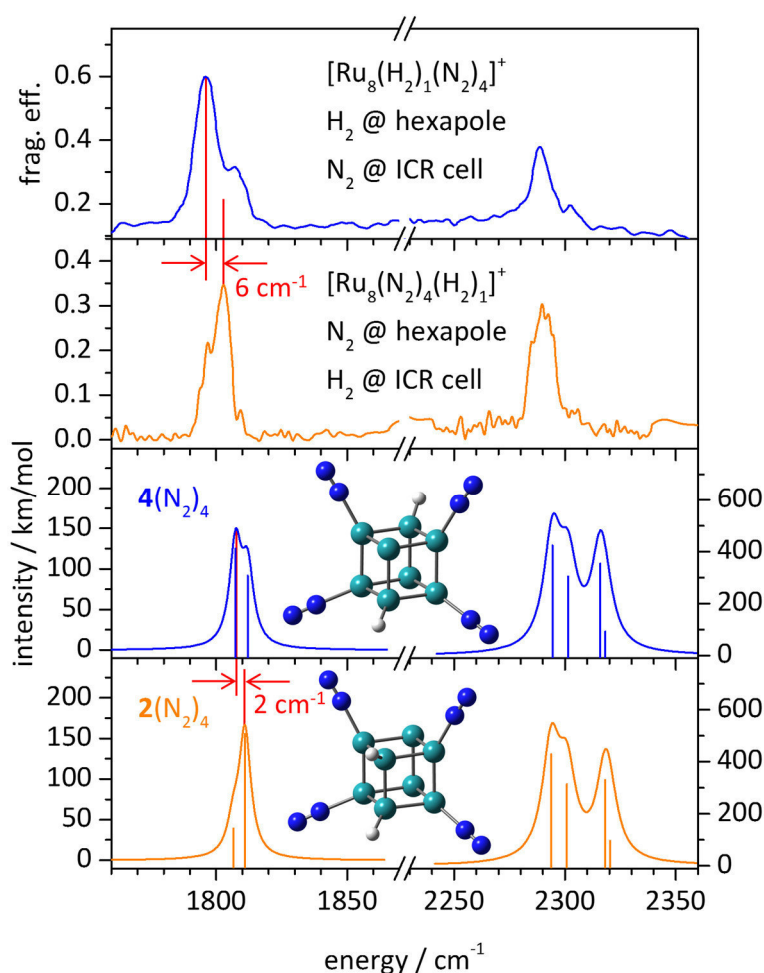


Fig. 2 IR-PD spectra of $[\text{Ru}_8(\text{H}_2)_1(\text{N}_2)_4]^+$ (blue) and $[\text{Ru}_8(\text{N}_2)_4(\text{H}_2)_1]^+$ (orange) compared to the predictions of theory. The red lines serve to highlight the shifts induced by varying the sequence of N₂/H₂ addition. For a discussion of the predicted bands (including * features) refer to the text and the supplement.

In the N₂ stretch region both the $[\text{Ru}_8(\text{H}_2)_1(\text{N}_2)_4]^+$ and the $[\text{Ru}_8(\text{N}_2)_4(\text{H}_2)_1]^+$ species reveal a strong main peak at about 2290 cm^{-1} with a weak feature about 13 cm^{-1} to the blue; this is well resolved in the former and somewhat blurry in the latter.

We refer the reader to supporting information (Fig. S6) for a figure contrasting the spectra of the coadsorbed species with those of [Ru₈(H₂)_k]⁺ and [Ru₈(N₂)_m]⁺, respectively.

DFT modelling of IR-PD spectra of [Ru₈(H₂)₁(N₂)₄]⁺ and [Ru₈(N₂)₄(H₂)₁]⁺

We extended our DFT calculations to model H₂-N₂-coadsorption. In particular we checked relative energies and predicted IR allowed vibrational transitions for numerous plausible structural variants of [cubic Ru₈, 4N₂, 2H]⁺ (for structures and corresponding spectra see Fig. S7 – S14; for structural labels see Fig. 3). Note that the spin quenches from a quartet in the case of cubic Ru₈^{+/1} and [Ru₈(N₂)₄]^{+/1}(N₂)₄ to a doublet upon further addition of 2H. On the basis of energetics and spectral features we conclude that the two most likely structures of [cubic Ru₈, 4N₂, 2H]⁺ have doublet spin states (see insets to Fig. 2). We present their predicted IR absorption spectra in the lower traces of Fig. 2.

The assigned calculated spectra show features which are quite similar to the experimental IR-PD spectra, except for the predicted * bands which occur significantly weaker in the experiment. This deviation is likely due to a lack of efficient internal vibrational redistribution (IVR) in these cases (*cf.* the supplement), which limits the dissociation yield.

In the Ru-H band region we find a close resemblance of the IR absorption spectra predicted by DFT for isomers **4**(N₂)₄ and **2**(N₂)₄ with the IR-PD spectra recorded for the two distinct species [Ru₈(H₂)₁(N₂)₄]⁺ and [Ru₈(N₂)₄(H₂)₁]⁺: DFT modelling reveals a shoulder to the blue of the RuH stretching band in **4**(N₂)₄, and asymmetric red shading in case of **2**(N₂)₄. The predicted blue shift of the RuH band of **4**(N₂)₄ with respect to that of **2**(N₂)₄ (about 2 cm⁻¹) closely corresponds to the IR-PD bands of [Ru₈(H₂)₁(N₂)₄]⁺ and [Ru₈(N₂)₄(H₂)₁]⁺, which differ by a blue shift of about 6 cm⁻¹.

Based on all of the above findings we are confident to assign the **4**(N₂)₄ structure to the [Ru₈(H₂)₁(N₂)₄]⁺ species, and the **2**(N₂)₄ structure to the [Ru₈(N₂)₄(H₂)₁]⁺ species. Both have the same arrangement of N₂ on the cubic Ru₈⁺ cluster as in **1**(N₂)₄. They merely differ in their RuH positions: in the case of [Ru₈(H₂)₁(N₂)₄]^{+/4}(N₂)₄ the hydrogens are located on two opposing Ru atoms (distal “trans” HH arrangement) and in the case of [Ru₈(N₂)₄(H₂)₁]^{+/2}(N₂)₄ on two neighboring Ru atoms (proximal “cis” HH arrangement).

Our vibrational band assignments lead to the tentative conclusion that H atom migration is hindered on N₂ preloaded Ru₈⁺ clusters, whereas on naked Ru₈⁺ H atoms can apparently

swiftly migrate to the most favorable Ru binding sites in a cooperative manner (see Fig. S14). These lie on two (space) diagonally opposing Ru atoms (distal “trans” HH arrangement). Once formed, this arrangement apparently persists upon subsequent N₂ adsorption. When H₂ adsorbs to an N₂ preloaded Ru₈⁺ cluster (**1**(N₂)₄), it dissociates as well – but the adsorbed N₂s likely hinder H migration. The H atoms are forced to stay on two neighboring Ru atoms (proximal “cis” HH arrangement).

In order to further support the above interpretation, we calculated a range of possible reaction paths for H-migration on a cubic Ru₈⁺ cluster, thereby confirming the effect of coadsorbed N₂ (Fig. 3). We predict facile H atom hopping among adjacent (unloaded) Ru atoms, whereas H migration across a face of the Ru₈⁺ cube is energetically precluded (Fig. S15). In the case of H₂ adsorption on a naked Ru₈⁺ (blue reaction path in Fig. 3), the migration from two neighboring Ru-H (**2**) occurs via an intermediate with the Hs on two (face) diagonal Ru atoms (**3**) (and via two low lying Ru-H-Ru “on bridge” transition states (**23**[‡] and **32**[‡])), ultimately to two opposing Ru-H (**4**) (distal “trans” HH arrangement), which convert without a barrier by stepwise N₂ adsorption into **4**(N₂)₄.

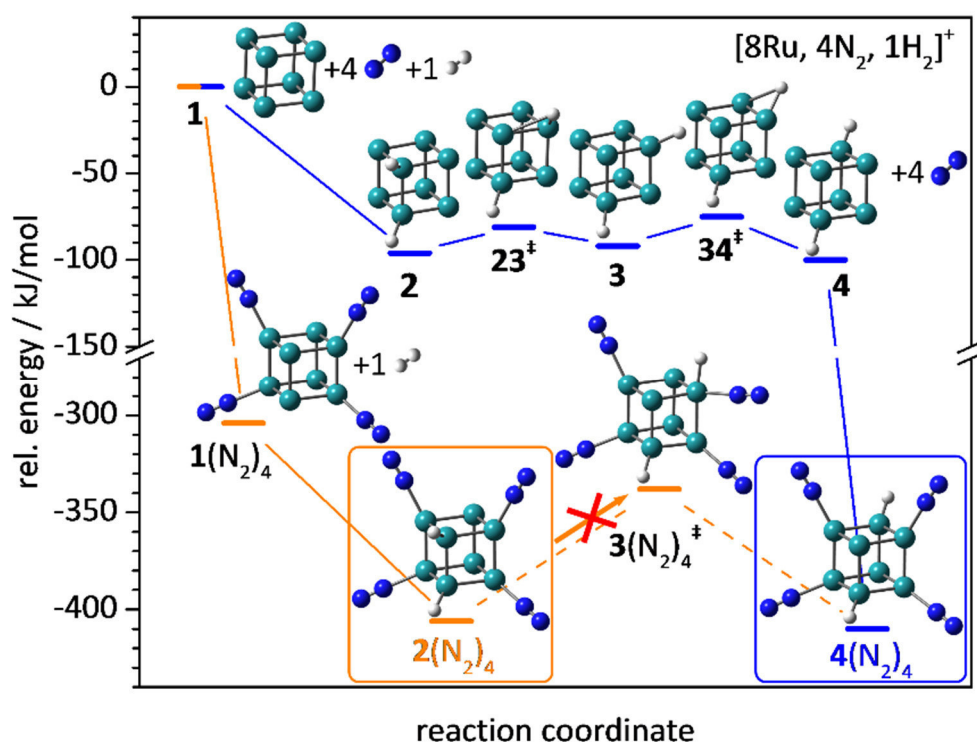


Fig. 3 Predicted reaction paths for the formation of [Ru₈(H₂)₁(N₂)₄]⁺/4(N₂)₄ and [Ru₈(N₂)₄(H₂)₁]⁺/2(N₂)₄.

The H₂ adsorption on a preloaded [Ru₈(N₂)₄]⁺/1(N₂)₄ species (orange reaction path in Fig. 3) results in the 2(N₂)₄ species with the Hs on two neighboring Ru atoms (proximal “cis” HH arrangement). It is essentially impossible to reach the 4(N₂)₄ species by further hydrogen hopping, which would involve a high energy transition state where the H atom would be located on an N₂ loaded Ru site (3(N₂)₄[‡]). Thus, the 2(N₂)₄ species is the final product upon N₂ preloading.

8.6 Conclusions

We have presented the cryo IR-PD spectra of [Ru₈(H₂)_k]⁺ k = 1 – 8 and [Ru₈(N₂)_m]⁺ m = 1 – 8. We find dissociative chemisorption of H₂ in all [Ru₈(H₂)_k]⁺ with k > 1, and we postulate an adsorbate induced reorganization of the cluster core and/or the adsorbate layer after exceeding the intermediate adsorption limit at k = 6. In the case of [Ru₈(N₂)_m]⁺ we identify a head-on adsorption of N₂ and an intermediate adsorption limit at m = 5 beyond which a structural reorganization may occur. The cryo IR-PD spectra of the [Ru₈(H₂)₁(N₂)₄]⁺ and [Ru₈(N₂)₄(H₂)₁]⁺ species, where the listed order signifies the order of adsorption, show tantalizing differences - in particular in the Ru-H bands. We interpret this in terms of distal or proximal hydrogen locations on the Ru₈⁺ cluster as well as by differences in hydrogen migration kinetics. This is likely hindered by preloading with N₂s but unaffected by subsequent N₂ adsorption. We elucidate the interplay of low temperature H₂-N₂ coadsorption in unprecedented detail. It will be important to extend such studies towards further adsorbate species such as HD and NH₃, and towards photo activation and product identification.

8.7 Acknowledgments

This work was supported by the German research foundation DFG within the transregional collaborative research center SFB/TRR 88 “Cooperative effects in homo and heterometallic complexes” (3MET.de) and by the state research center OPTIMAS. We gratefully acknowledge the generous support for D.C.M. from the Air Force Office of Scientific Research through grant no. FA9550-15-1-0088. The isotopes used in this research were supplied by the United States Department of Energy Office of Science by the Isotope Program in the Office of Nuclear Physics.

8.8 References:

- [1] R. Schlögl, in *Handbook of Heterogeneous Catalysis*, Wiley-VCH Verlag GmbH & Co. KGaA, **2008**.
- [2] H. Bielawa, O. Hinrichsen, A. Birkner, M. Muhler, *Angew. Chem. Int. Ed.* **2001**, *40*, 1061-1063.
- [3] C. J. H. Jacobsen, S. Dahl, P. L. Hansen, E. Törnqvist, L. Jensen, H. Topsøe, D. V. Prip, P. B. Møenshaug, I. Chorkendorff, *J. Mol. Catal. A: Chem.* **2000**, *163*, 19-26.
- [4] a)R. van Hardeveld, A. van Montfoort, *Surf. Sci.* **1966**, *4*, 396-430; b)S. Shetty, A. P. J. Jansen, R. A. van Santen, *J. Phys. Chem. C* **2008**, *112*, 17768-17771.
- [5] a)R. A. de Paola, F. M. Hoffmann, D. Heskett, E. W. Plummer, *Phys. Rev. B* **1987**, *35*, 4236-4249; b)H. Shi, K. Jacobi, *Surf. Sci.* **1992**, *278*, 281-285.
- [6] M. Gruyters, K. Jacobi, *Surf. Sci.* **1995**, *336*, 314-320.
- [7] H. Shi, K. Jacobi, G. Ertl, *J. Chem. Phys.* **1993**, *99*, 9248-9254.
- [8] M. Tatarkhanov, F. Rose, E. Fomin, D. F. Ogletree, M. Salmeron, *Surf. Sci.* **2008**, *602*, 487-492.
- [9] P. Feulner, D. Menzel, *Surf. Sci.* **1985**, *154*, 465-488.
- [10] K. L. Kostov, W. Widdra, D. Menzel, *Surf. Sci.* **2004**, *560*, 130-144.
- [11] E. M. McIntosh, K. T. Wikfeldt, J. Ellis, A. Michaelides, W. Allison, *J. Phys. Chem. Lett.* **2013**, *4*, 1565-1569.
- [12] I. Waluyo, Y. Ren, M. Trenary, *J. Phys. Chem. Lett.* **2013**, *4*, 3779-3786.
- [13] A. J. Cox, J. G. Louderback, S. E. Apse, L. A. Bloomfield, *Phys. Rev. B* **1994**, *49*, 12295-12298.
- [14] a)S. F. Li, H. S. Li, J. Liu, X. L. Xue, Y. T. Tian, H. He, Y. Jia, *Phys. Rev. B* **2007**, *76*; b)F. Aguilera-Granja, L. C. Balbás, A. Vega, *J. Phys. Chem. A* **2009**, *113*, 13483-13491; c)W. Q. Zhang, H. T. Zhao, L. C. Wang, *J. Phys. Chem. B* **2004**, *108*, 2140-2147.
- [14] C. Kerpál, D. J. Harding, D. M. Rayner, J. T. Lyon, A. Fielicke, *J. Phys. Chem. C* **2015**, *119*, 10869-10875.
- [16] E. Waldt, A.-S. Hehn, R. Ahlrichs, M. M. Kappes, D. Schooss, *J. Chem. Phys.* **2015**, *142*, 024319.
- [17] S. M. Lang, T. M. Bernhardt, M. Krstic, V. Bonacic-Koutecky, *Phys. Chem. Chem. Phys.* **2014**, *16*, 26578-26583.
- [18] D. Bumüller, A.-S. Hehn, E. Waldt, R. Ahlrichs, M. M. Kappes, D. Schooss, *J. Phys. Chem. C* **2017**, *121*, 10645-10652.
- [19] a)G.-X. Ge, H.-X. Yan, Q. Jing, Y.-H. Luo, *J. Cluster Sci.* **2011**, *22*, 473; b)K. Takahashi, S. Isobe, S. Ohnuki, *RSC Advances* **2013**, *3*, 21841-21847; c) Cusinato, L.; Martínez-Prieto, L. M.; Chaudret, B.; Del Rosal, I.; Poteau, R., *Nanoscale* **2016**, *8*, 10974-10992.
- [20] J. T. Lyon, P. Gruene, A. Fielicke, G. Meijer, D. M. Rayner, *J. Chem. Phys.* **2009**, *131*, 184706.
- [21] C. Kerpál, D. J. Harding, J. T. Lyon, G. Meijer, A. Fielicke, *J. Phys. Chem. C* **2013**, *117*, 12153-12158.
- [22] S. Dillinger, J. Mohrbach, J. Hower, M. Gaffga, G. Niedner-Schatteburg, *Phys. Chem. Chem. Phys.* **2015**, *17*, 10358-10362.
- [23] J. Mohrbach, S. Dillinger, G. Niedner-Schatteburg, *J. Phys. Chem. C* **2016**.
- [24] a)S. Maruyama, L. R. Anderson, R. E. Smalley, *Rev. Sci. Instrum.* **1990**, *61*, 3686-3693; b)C. Berg, T. Schindler, G. Niednerschatteburg, V. E. Bondybey, *J. Chem. Phys.* **1995**, *102*, 4870-4884.

- [25] C. Adamo, V. Barone, *J. Chem. Phys.* **1999**, *110*, 6158-6170.
- [26] T. H. Dunning, *J. Chem. Phys.* **1989**, *90*, 1007-1023.
- [27] D. Andrae, U. Haeussermann, M. Dolg, H. Stoll, H. Preuss, *Theor. Chem. Acc.* **1990**, *77*, 123-141.
- [28] M. J. Frisch, G. W. Trucks, H. B. Schlegel, G. E. Scuseria, M. A. Robb, J. R. Cheeseman, G. Scalmani, V. Barone, G. A. Petersson, H. Nakatsuji, M. C. X. Li, A. Marenich, J. Bloino, B. G. Janesko, R. Gomperts, B. Mennucci, H. P. Hratchian, J. V. Ortiz, A. F. Izmaylov, J. L. Sonnenberg, D. Williams-Young, F. Ding, F. Lipparini, F. Egidi, J. Goings, B. Peng, A. Petrone, T. Henderson, D. Ranasinghe, V. G. Zakrzewski, J. Gao, N. Rega, G. Zheng, W. Liang, M. Hada, M. Ehara, K. Toyota, R. Fukuda, J. Hasegawa, M. Ishida, T. Nakajima, Y. Honda, O. Kitao, H. Nakai, T. Vreven, K. Throssell, J. A. Montgomery Jr., J. E. Peralta, F. Ogliaro, M. Bearpark, J. J. Heyd, E. Brothers, K. N. Kudin, V. N. Staroverov, R. K. T. Keith, J. Normand, K. Raghavachari, A. Rendell, J. C. Burant, S. S. Iyengar, J. Tomasi, M. Cossi, J. M. Millam, M. Klene, C. Adamo, R. Cammi, J. W. Ochterski, R. L. Martin, K. Morokuma, O. Farkas, J. B. Foresman, D. J. Fox, *Gaussian, Inc., Wallingford CT* **2013**, Revision D.01.
- [29] W. M. Haynes, *CRC Handbook of Chemistry and Physics, 93rd Edition*, CRC Press/Taylor & Francis, Boca Raton, Florida, USA, **2012**.
- [30] S. Dillinger, J. Mohrbach, G. Niedner-Schatteburg, *J. Chem. Phys.* **2017**, submitted.
- [31] A. B. Anton, N. R. Avery, B. H. Toby, W. H. Weinberg, *J. Electron Spectrosc. Relat. Phenom.* **1983**, *29*, 181-186.

8.9 Supporting Information

Table of Content:

Detailed Experimental and Computational Methods

Fig. S1. Mass spectra recorded in the Ru₈⁺ cluster mass range using a Ru laser vaporization target with natural isotope ratio (top) and a monoisotopic ¹⁰²Ru foil (bottom).

Fig. S2 IR-PD spectra of the [Ru₈(H₂)₆]⁺ and [Ru₈(H₂)₈]⁺ species from 750 cm⁻¹ to 2375 cm⁻¹.

Fig. S3 IR-PD spectrum of [Ru₈(D₂)₆]⁺.

Fig. S4 IR-PD spectra of the [Ru₈(H₂)₁(N₂)₄]⁺ and [Ru₈(N₂)₄(H₂)₁]⁺ species from 1700 cm⁻¹ to 2375 cm⁻¹ including the laser power (gray).

Fig. S5 IR-PD spectra of the [Ru₈(H₂)₁(N₂)₄]⁺ and [Ru₈(N₂)₄(H₂)₁]⁺ species from 2650 cm⁻¹ to 4200 cm⁻¹ including the laser power (gray).

Fig. S6 IR-PD spectra of [Ru₈(H₂)_k]⁺ k = 1 – 8 (left) and [Ru₈(N₂)_m]⁺ m = 1 – 8 (right). Both stacks include the spectra of the [Ru₈(H₂)₁(N₂)₄]⁺ and [Ru₈(N₂)₄(H₂)₁]⁺ species for comparison.

Fig. S7. IR-PD spectrum of [Ru₈(N₂)₄]⁺ in comparison with DFT predictions for various structural models based on a cubic Ru₈⁺ core with different N₂ adsorption sites.

Fig. S8. IR-PD spectra of [Ru₈(H₂)₁(N₂)₄]⁺ and [Ru₈(N₂)₄(H₂)₁]⁺ in comparison with DFT calculations of different N₂ adsorption sites on a cubic Ru₈⁺ with the H atoms on two (face) diagonal Ru atoms in doublet spin states.

Fig. S9. IR-PD spectra of [Ru₈(H₂)₁(N₂)₄]⁺ and [Ru₈(N₂)₄(H₂)₁]⁺ in comparison with DFT calculations of different N₂ adsorption sites on a cubic Ru₈⁺ with the H atoms on two (face) diagonal Ru atoms in quartet spin states.

Fig. S10. IR-PD spectra of [Ru₈(H₂)₁(N₂)₄]⁺ and [Ru₈(N₂)₄(H₂)₁]⁺ in comparison with DFT calculations of different N₂ adsorption sites on a cubic Ru₈⁺ with the H atoms on two neighboring Ru atoms in doublet spin states.

Fig. S11. IR-PD spectra of [Ru₈(H₂)₁(N₂)₄]⁺ and [Ru₈(N₂)₄(H₂)₁]⁺ in comparison with DFT calculations of different N₂ adsorption sites on a cubic Ru₈⁺ with the H atoms on two neighboring Ru atoms in quartet spin states.

Fig. S12. IR-PD spectra of [Ru₈(H₂)₁(N₂)₄]⁺ and [Ru₈(N₂)₄(H₂)₁]⁺ in comparison with DFT calculations of different N₂ adsorption sites on a cubic Ru₈⁺ with the H atoms on two opposing Ru atoms (space diagonal/distal) in doublet spin states.

Fig. S13. IR-PD spectra of [Ru₈(H₂)₁(N₂)₄]⁺ and [Ru₈(N₂)₄(H₂)₁]⁺ in comparison with DFT calculations of different N₂ adsorption sites on a cubic Ru₈⁺ with the H atoms on two opposing Ru atoms in quartet spin states.

Fig. S14. IR-PD spectrum of [Ru₈(H₂)₁]⁺ in comparison with DFT calculations of different H adsorption sites on cubic Ru₈⁺ clusters in doublet and quartet spin states.

Fig. S15. Alternative calculated reaction paths for the formation of **4** from **2** (left) and for the formation of **4**(N₂)₄ from **2**(N₂)₄ (right).

Fig. S16. IR-PD spectra of [Ru₈(N₂)₄]⁺, [Ru₈(H₂)₁(N₂)₄]⁺ and [Ru₈(N₂)₄(H₂)₁]⁺ in comparison with DFT calculations.

Discussion of DFT Predicted Splittings and Intensities of N₂ Stretching Bands in Comparison to the Experimental IR-PD Spectra

Fig. S17. Calculated spectra of **4**(N₂)₄ and **2**(N₂)₄ and their respective structure.

Table S1. Calculated IR frequencies and assignment of **4**(N₂)₄.

Table S2. Calculated IR frequencies and assignment of **2**(N₂)₄.

Fig. S18. IR-PD spectra of [Ru₈(H₂)₁(N₂)₄]⁺ and [Ru₈(N₂)₄(H₂)₁]⁺ recorded on two separate measurement days.

Fig. S19. IR-PD spectra of [Ru₈(H₂)₁(N₂)₄]⁺ and [Ru₈(N₂)₄(H₂)₁]⁺ in comparison with DFT calculations using a range of different density functionals.

Fig. S20. IR-PD spectra of [Ru₈(H₂)₁(N₂)₄]⁺ and [Ru₈(N₂)₄(H₂)₁]⁺ in comparison with DFT calculations using a range of different density functionals.

Detailed Experimental and Computational Methods

All experiments were carried out in a customized Fourier Transform - Ion Cyclotron Resonance (FT-ICR) – mass spectrometer (Apex Ultra Bruker Daltonics). The specific apparatus configuration allowed for cluster production, isolation, N₂/H₂ adsorption, InfraRed (Multi) Photon Dissociation (IR(M)PD) spectroscopy and mass analysis. The metal cluster ions were generated using a home-built laser vaporization source as described previously.^[1] For this ruthenium atoms are evaporated from a rotating 0.4 mm thick monoisotopic ¹⁰²Ru (99.38%, Oak Ridge National Laboratories; Fig. S1) foil by the second harmonic of a pulsed Nd:YAG laser. The hot plasma is captured by a He gas pulse (40 μs, 15 bar) created by a home-built piezoelectric valve.^[2] The atoms and ions are cooled and aggregate to clusters in the subsequent jet expansion through a 60 mm long channel (2 mm diameter) into vacuum (10⁻⁷ mbar) yielding a continuous cluster size distribution. The cluster beam is skimmed and steered using different electrostatic lenses and a 90 degrees ion beam bender. After this the bare metal cluster cations can be mass selected in a quadrupole mass filter. Subsequently the ions are injected into a cryogenic hexapole ion trap cooled to 17 K for reactions with H₂ and to 26 K for reactions with N₂ by a closed cycle He cryostat. Buffer or reaction gas can be introduced either continuously or in pulses. For this work we used the continuous gas inlets. Sufficient amounts of reaction products were obtained by flowing enough H₂ or N₂ into the vacuum chamber to raise its base pressure 1.1×10^{-7} mbar up to 5.0×10^{-7} mbar. Additionally, He was added to improve trapping and cooling of ions thus increasing the total pressure up to 5.0×10^{-6} mbar. Due to the large mass differences between the buffer gas He and the adsorbate gases H₂/ N₂ and Ru₈, only a minor part of the residual kinetic energy of Ru₈ (acquired by prior electrostatic accelerations) transforms into the center of mass frame. In the case of H₂ it is safe to state that an $E_{\text{kin}}(\text{Ru}_8)$ of up to 1 eV do not lead to raised effective temperatures beyond 30 K. In the case of N₂ some hyperthermal collisions may initially occur. By virtue of the excess of Helium (more than 100:1) in the hexapole cell the kinetic thermalization of Ru₈ occurs within few milli seconds, whereas the observed reactions take place on a multiple second time scale.

After storage of the ions for a variable time (0 – 10 s), the reaction products (with either N₂ or H₂ attached) were guided by electrostatic lenses into the FT-ICR cell which is of the so-called “infinity” type.^[3] This cell was held at a temperature below 10 K with a closed cycle He

cryostat for the spectroscopy of the [Ru₈(H₂)_k]⁺ and the [Ru₈(N₂)_m]⁺ species. The cell is normally used for isolation, laser irradiation and detection of the ions. For the coadsorption experiments the ICR cell also served as a second reaction cell. In this case the ICR cell was heated to 19 K for additional reactions with H₂ or to 49 K for N₂ to avoid condensation of the respective reaction gas. The pressure was correspondingly increased from 2.0 × 10⁻⁹ mbar (base pressure) up to 1.0 × 10⁻⁸ mbar and the ions were stored up to 2 s in the ICR cell.

For the acquisition of IR-PD spectra the FT-ICR cell is coupled to a tunable IR laser ($\delta n = 0.9 \text{ cm}^{-1}$, $\delta t = 7 \text{ ns}$). This laser is a KTP/KTA optical parametric oscillator/amplifier (OPO/A, LaserVision) system pumped by a pulsed 10 Hz injection seeded Nd:YAG laser (PL8000, Continuum). The difference frequency (DF) between the OPA signal and idler waves is generated in a AgGaSe₂ crystal. This generates IR radiation in the range of 1000 – 2400 cm⁻¹. Each trapped and isolated package of ions is irradiated by 7 – 10 laser pulses (0.1 – 1.5 mJ/pulse) to yield a sufficient amount of fragment ions. The IR spectra were recorded by acquiring fragmentation mass spectra while continuously scanning the IR wavelength. The IR-PD signal was evaluated as $\sum_i F_i / (\sum_i F_i + \sum_i P_i)$, where F_i and P_i indicate fragment and the parent ion signals, respectively. An experimental IR-PD spectrum is then obtained from a plot of the fragmentation efficiency as a function of laser frequency.

Linear (harmonic) IR absorption spectra were calculated at the PBE0^[4] level of theory using the cc-pVTZ basis sets^[5] (H, N), and the Stuttgart RSC 1997^[6] effective core potential (Ru), respectively, as implemented in the Gaussian 09 program package^[7]. SCF convergence is tedious and can be achieved only at the expense of relaxed SCF convergence criteria of 10⁻⁵ (as compared to 10⁻⁸ in DFT calculations on light main group elements). The calculated spectra were scaled for anharmonicities by 0.9656 above 2150 cm⁻¹ (N₂ stretching region, scaling factor obtained by scaling the matching calculated spectrum of [Ru₈(N₂)₄]⁺ to the experiment) and by 0.923 below 2150 cm⁻¹ (Ru-H stretching region, scaling factor obtained by scaling the band of the calculated energetic minimum of [Ru₈(H₂)₁]⁺ to the experimental band of [Ru₈(H₂)₂]⁺) and simulated using Lorentz profiles with fwhm = 5 cm⁻¹ above 2150 cm⁻¹ and of fwhm = 3 cm⁻¹ below 2150 cm⁻¹.

References:

- [1] a) S. Maruyama, L. R. Anderson, R. E. Smalley, *Rev. Sci. Instrum.* **1990**, *61*, 3686-3693;
b) C. Berg, T. Schindler, G. Niedner-Schatteburg, V. E. Bondybey, *J. Chem. Phys.* **1995**, *102*, 4870-4884.
- [2] D. Proch, T. Trickl, *Rev. Sci. Instrum.* **1989**, *60*, 713-716.
- [3] P. Caravatti, M. Allemann, *Org. Mass Spectrom.* **1991**, *26*, 514-518.
- [4] C. Adamo, V. Barone, *J. Chem. Phys.* **1999**, *110*, 6158-6170.
- [5] T. H. Dunning, *J. Chem. Phys.* **1989**, *90*, 1007-1023.
- [6] D. Andrae, U. Haeussermann, M. Dolg, H. Stoll, H. Preuss, *Theor. Chem. Acc.* **1990**, *77*, 123-141.
- [7] M. J. Frisch, G. W. Trucks, H. B. Schlegel, G. E. Scuseria, M. A. Robb, J. R. Cheeseman, G. Scalmani, V. Barone, G. A. Petersson, H. Nakatsuji, M. C. X. Li, A. Marenich, J. Bloino, B. G. Janesko, R. Gomperts, B. Mennucci, H. P. Hratchian, J. V. Ortiz, A. F. Izmaylov, J. L. Sonnenberg, D. Williams-Young, F. Ding, F. Lipparini, F. Egidi, J. Goings, B. Peng, A. Petrone, T. Henderson, D. Ranasinghe, V. G. Zakrzewski, J. Gao, N. Rega, G. Zheng, W. Liang, M. Hada, M. Ehara, K. Toyota, R. Fukuda, J. Hasegawa, M. Ishida, T. Nakajima, Y. Honda, O. Kitao, H. Nakai, T. Vreven, K. Throssell, J. A. Montgomery Jr., J. E. Peralta, F. Ogliaro, M. Bearpark, J. J. Heyd, E. Brothers, K. N. Kudin, V. N. Staroverov, R. K. T. Keith, J. Normand, K. Raghavachari, A. Rendell, J. C. Burant, S. S. Iyengar, J. Tomasi, M. Cossi, J. M. Millam, M. Klene, C. Adamo, R. Cammi, J. W. Ochterski, R. L. Martin, K. Morokuma, O. Farkas, J. B. Foresman, D. J. Fox, *Gaussian, Inc., Wallingford CT* **2013**, *Revision D.01*.

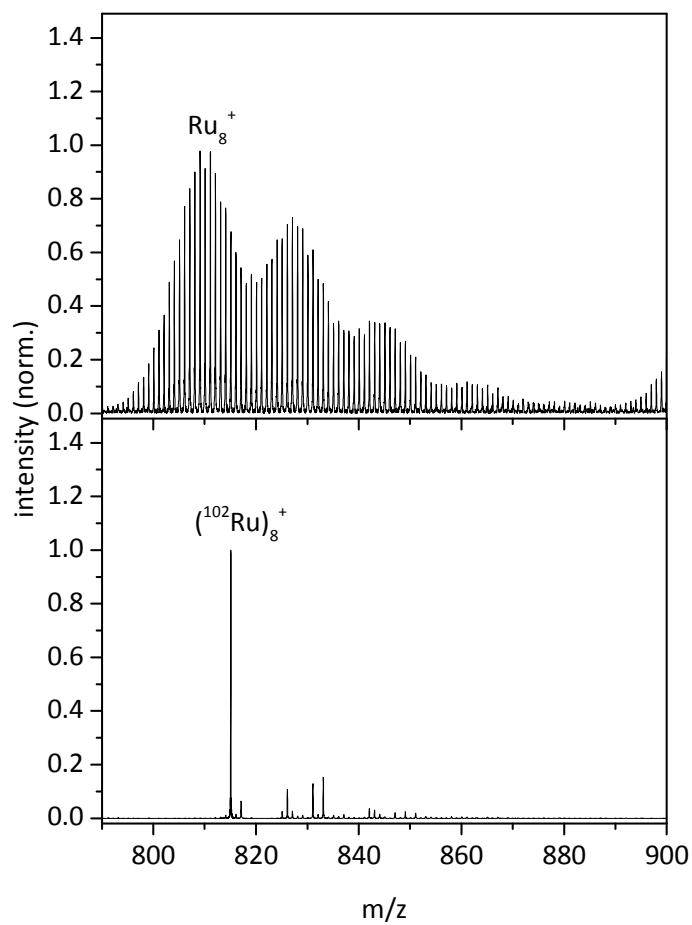


Fig. S1 Mass spectra recorded in the Ru₈⁺ cluster mass range using a Ru laser vaporization target with natural isotope ratio (top) and a monoisotopic ¹⁰²Ru foil (bottom).

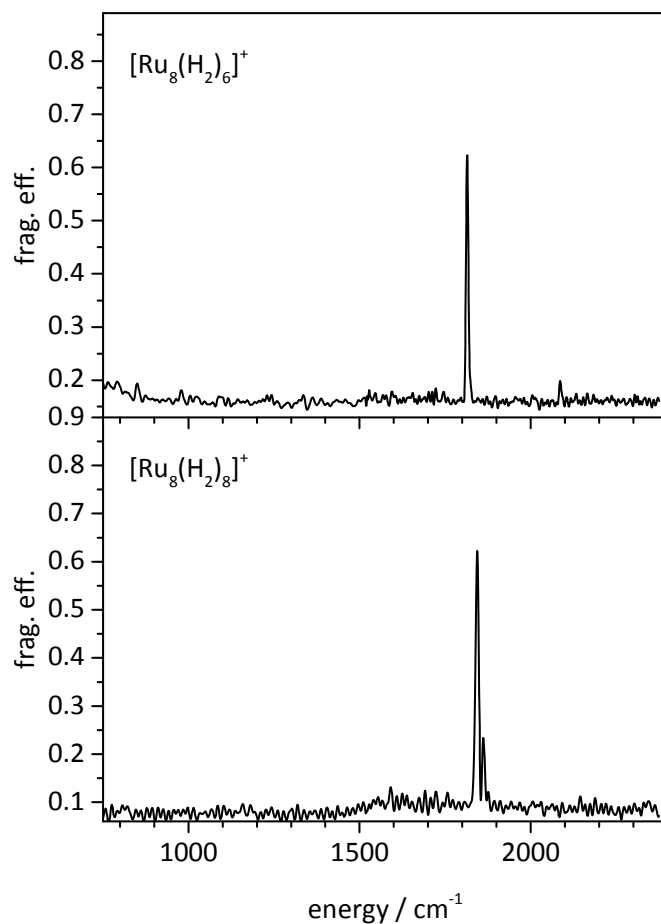


Fig. S2 IR-PD spectra of the $[\text{Ru}_8(\text{H}_2)_6]^+$ and $[\text{Ru}_8(\text{H}_2)_8]^+$ species from 750 cm^{-1} to 2375 cm^{-1} . These extended range overview spectra verify that no further spectral features are present in this region.

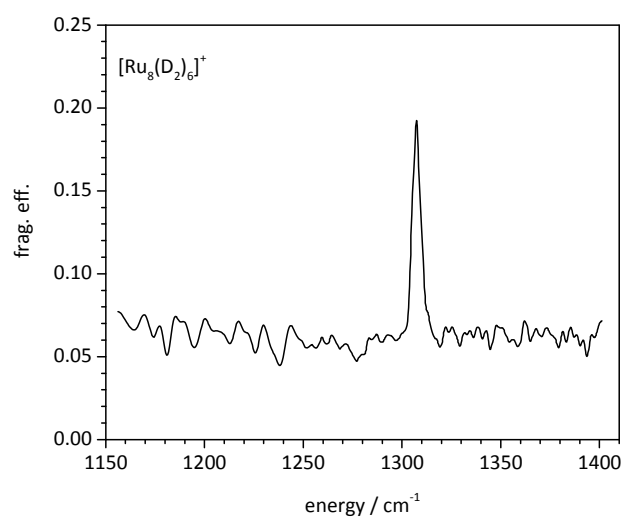


Fig. S3 IR-PD spectrum of $[\text{Ru}_8(\text{D}_2)_6]^+$.

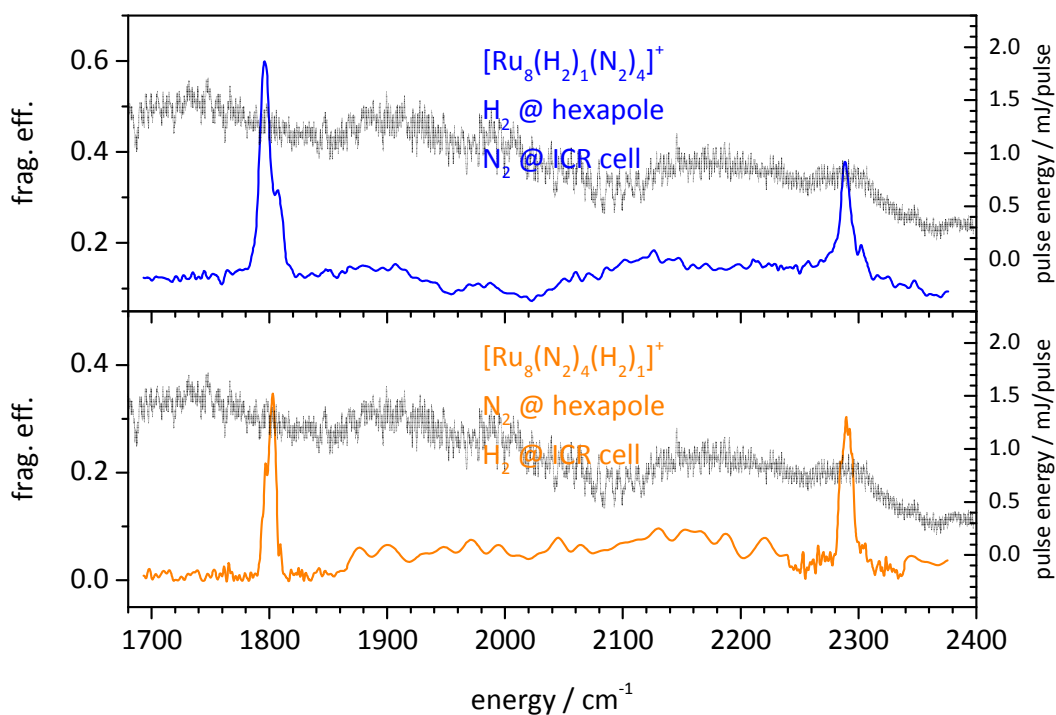


Fig. S4 IR-PD spectra of the $[\text{Ru}_8(\text{H}_2)_1(\text{N}_2)_4]^+$ and $[\text{Ru}_8(\text{N}_2)_4(\text{H}_2)_1]^+$ species from 1700 cm⁻¹ to 2375 cm⁻¹ including the laser power (gray).

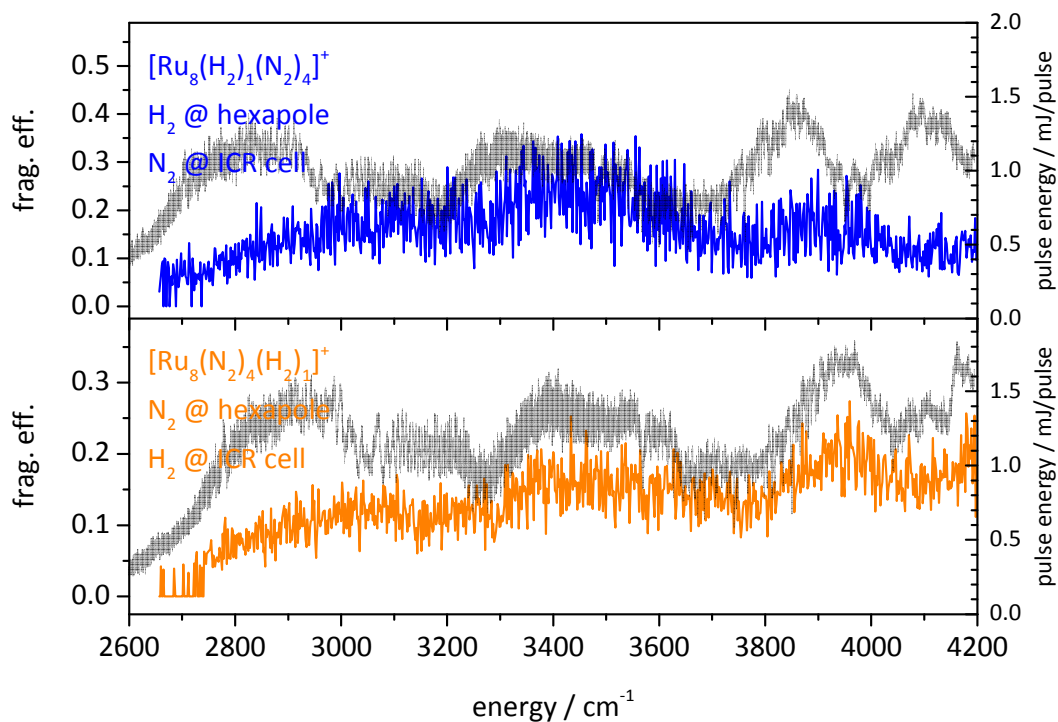


Fig. S5 IR-PD spectra of the $[\text{Ru}_8(\text{H}_2)_1(\text{N}_2)_4]^+$ and $[\text{Ru}_8(\text{N}_2)_4(\text{H}_2)_1]^+$ species from 2650 cm⁻¹ to 4200 cm⁻¹ including the laser power (gray).

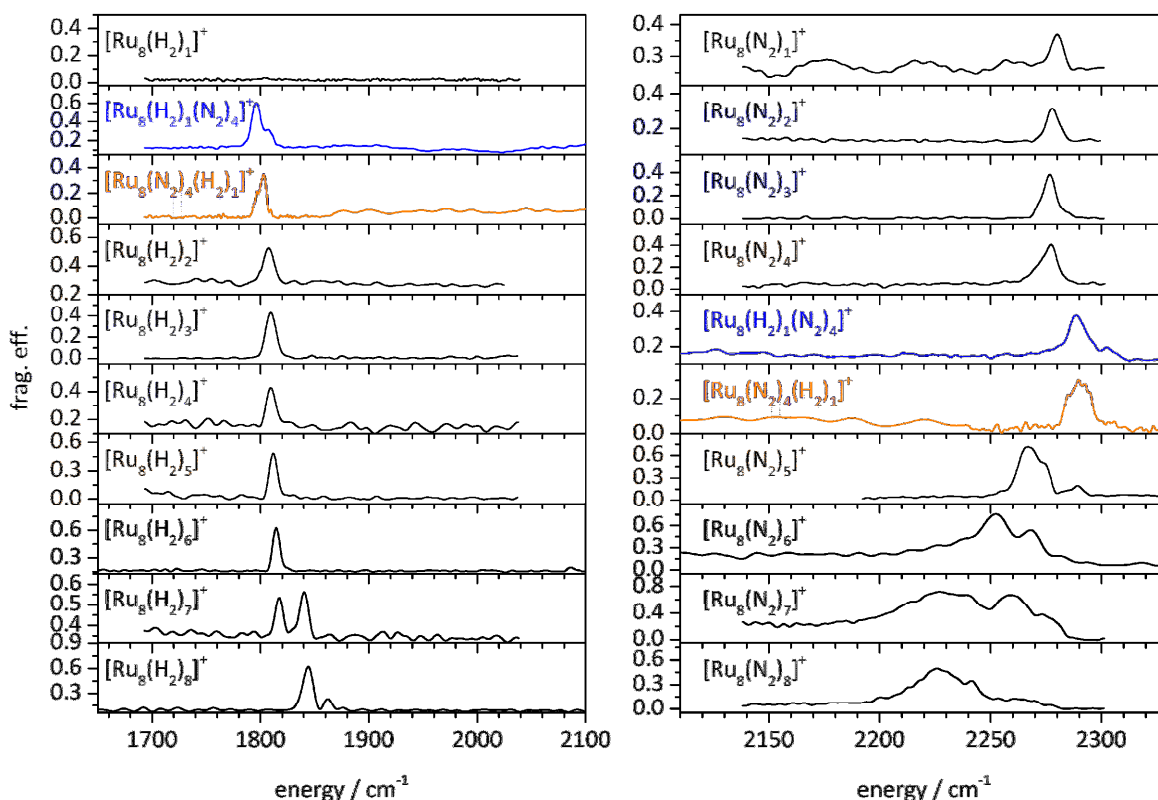


Fig. S6 IR-PD spectra of $[\text{Ru}_8(\text{H}_2)_k]^+$ $k = 1 - 8$ (left) and $[\text{Ru}_8(\text{N}_2)_m]^+$ $m = 1 - 8$ (right). Both stacks include the spectra of the $[\text{Ru}_8(\text{H}_2)_1(\text{N}_2)_4]^+$ (blue) and $[\text{Ru}_8(\text{N}_2)_4(\text{H}_2)_1]^+$ (orange) species for comparison.

Comparison of the spectra of coadsorbed species with those of $[\text{Ru}_8(\text{H}_2)_k]$ (Fig. S6, left): Both coadsorbed species are in line with the blue shift observed with increasing l . Therefore, N₂s has a minor influence on the overall position of the bands compared to the other $[\text{Ru}_8(\text{H}_2)_k]^+$ species. Yet, there are subtle differences between both coadsorbed species, which we have addressed in the main text.

Comparison of the spectra of coadsorbed species with those of $[\text{Ru}_8(\text{N}_2)_m]^+$ (Fig. S6, right): Note that the overall number of coadsorbates is equal to the intermediate adsorption limit of Ru_8^+ with N_2 ($m = m_{\text{coad}} + k_{\text{coad}} = 5$). The vibrational pattern of both coadsorbed species show similarities to $[\text{Ru}_8(\text{N}_2)_5]^+$. Yet the pattern of both coadsorbed species is blue shifted. These findings could indicate that the adsorbed H_2 has a similar (steric) effect to that of an additional N_2 / i.e. adsorption requires a similar spatial reorganization of the other N_2 's resulting in a similar pattern. Furthermore, the H_2 alters the electronic properties of the cluster, causing a blue shift. The Ru-H bond needs electron density and therefore there is less electron density available on the cluster core. The less electron density available the less

can be shifted into the anti-bonding orbitals of the adsorbed N₂s resulting in a less pronounced red shift with respect to the free N₂ vibration.

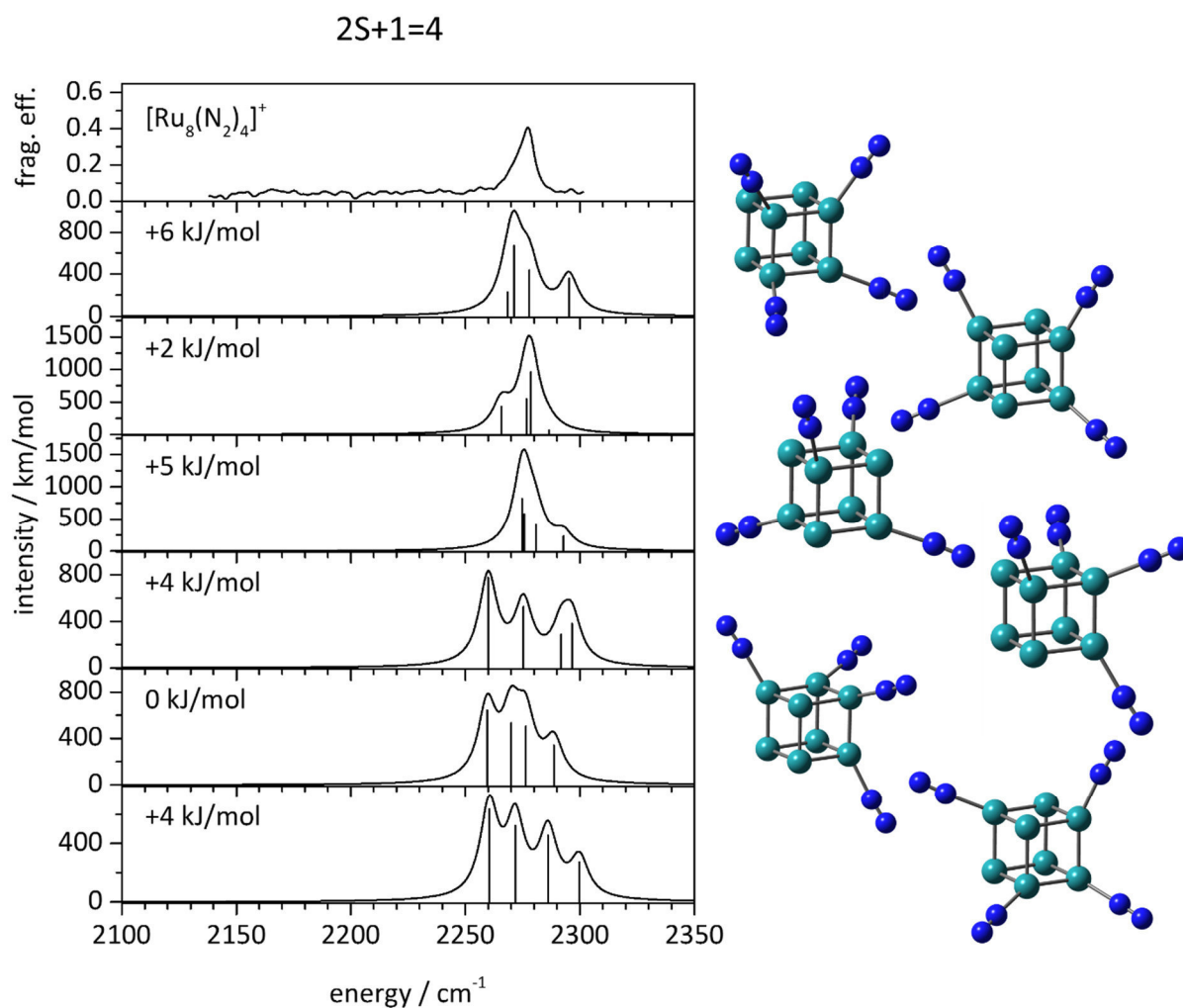


Fig. S7. IR-PD spectrum of $[\text{Ru}_8(\text{N}_2)_4]^+$ in comparison with DFT calculations of different N_2 adsorption sites on a cubic Ru_8^+ core. Only the quartet spin states are shown as the doublet spin states converged to a quartet during geometry optimization. Calculations were performed at the PBE0 level of theory using cc-pVTZ (N) and Stuttgart RSC 1997 effective core potential (Ru) basis sets. The calculated harmonic vibrations were scaled by 0.9656.

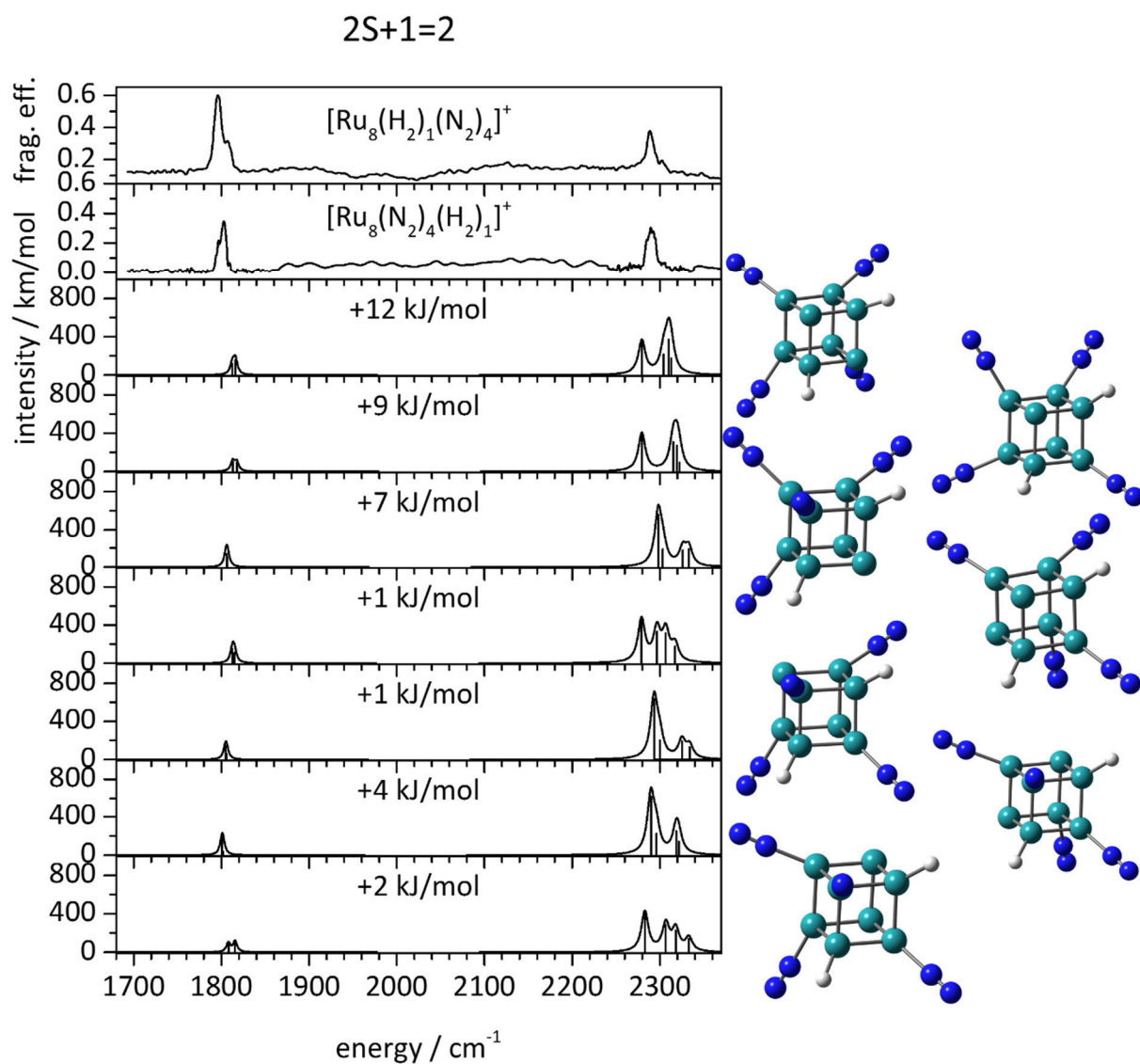


Fig. S8. IR-PD spectra of [Ru₈(H₂)₁(N₂)₄]⁺ and [Ru₈(N₂)₄(H₂)₁]⁺ in comparison with DFT calculations of spectra for different N₂ adsorption sites on a cubic Ru₈⁺ with the H atoms on two (face) diagonal Ru atoms in doublet spin states. Calculations were performed at the PBE0 level of theory using cc-pVTZ (N) and Stuttgart RSC 1997 effective core potential (Ru) basis sets. The calculated harmonic vibrations were scaled by 0.9656 above 2150 cm⁻¹ and by 0.923 below 2150 cm⁻¹.

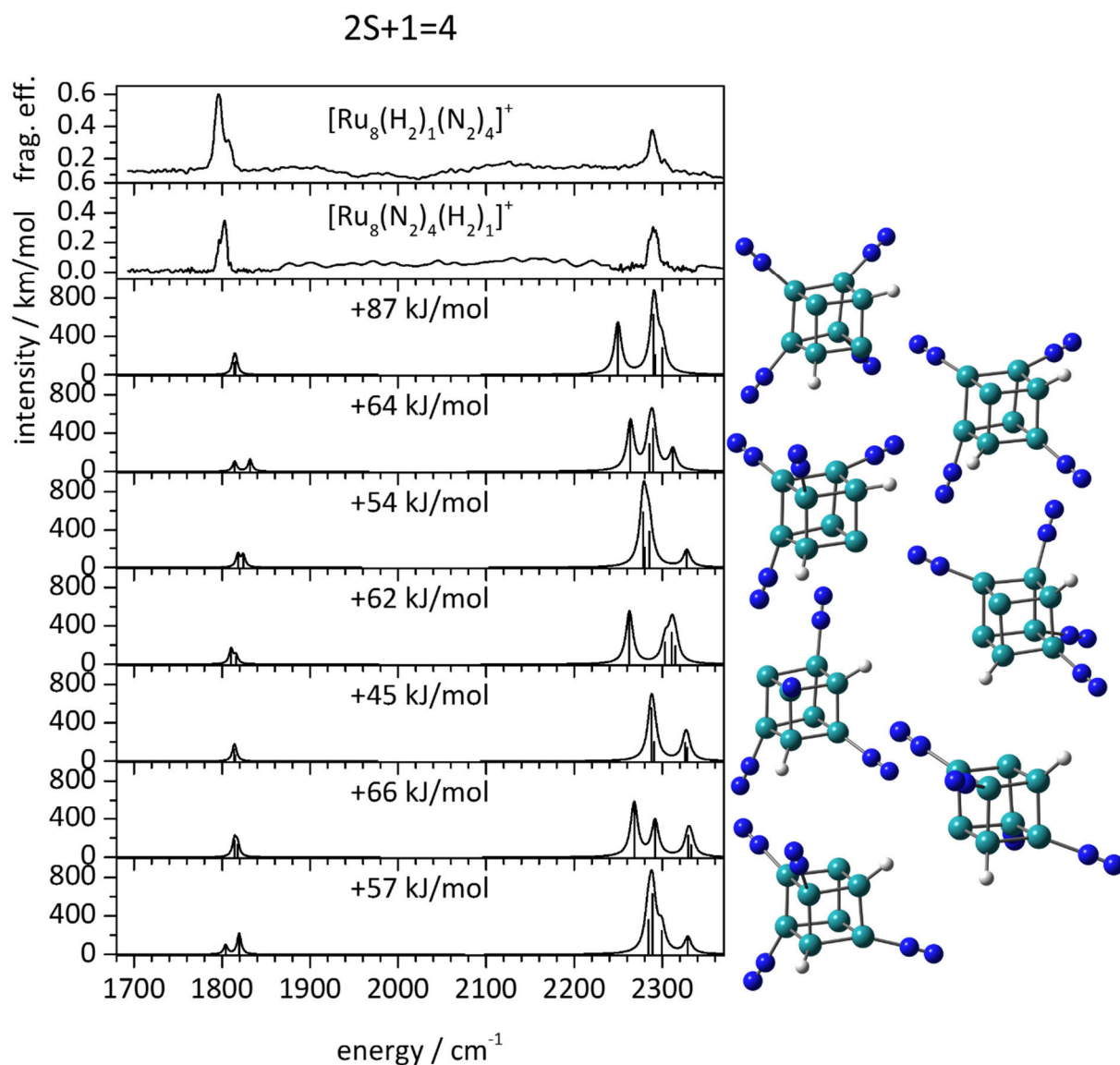


Fig. S9. IR-PD spectra of $[\text{Ru}_8(\text{H}_2)_1(\text{N}_2)_4]^+$ and $[\text{Ru}_8(\text{N}_2)_4(\text{H}_2)_1]^+$ in comparison with DFT calculations of different N₂ adsorption sites on a cubic Ru₈⁺ with the H atoms on two (face) diagonal Ru atoms in quartet spin states. Calculations were performed at the PBE0 level of theory using cc-pVTZ (N) and Stuttgart RSC 1997 effective core potential (Ru) basis sets. The calculated harmonic vibrations were scaled by 0.9656 above 2150 cm⁻¹ and by 0.923 below 2150 cm⁻¹.

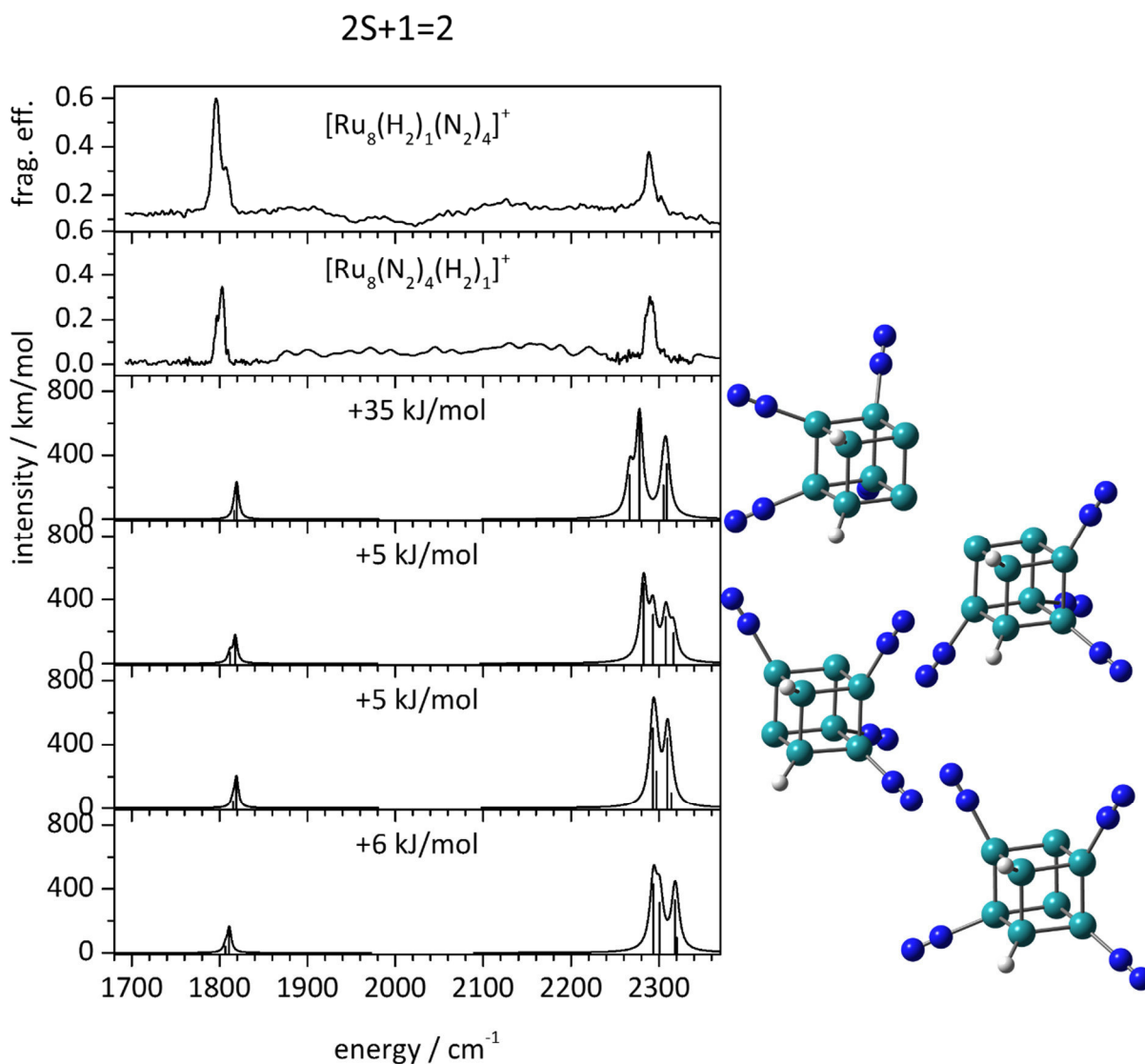


Fig. S10. IR-PD spectra of $[\text{Ru}_8(\text{H}_2)_1(\text{N}_2)_4]^+$ and $[\text{Ru}_8(\text{N}_2)_4(\text{H}_2)_1]^+$ in comparison with DFT calculations of different N₂ adsorption sites on a cubic Ru₈⁺ with the H atoms on two neighboring Ru atoms in doublet spin states. Calculations were performed at the PBE0 level of theory using cc-pVTZ (N) and Stuttgart RSC 1997 effective core potential (Ru) basis sets. The calculated harmonic vibrations were scaled by 0.9656 above 2150 cm⁻¹ and by 0.923 below 2150 cm⁻¹.

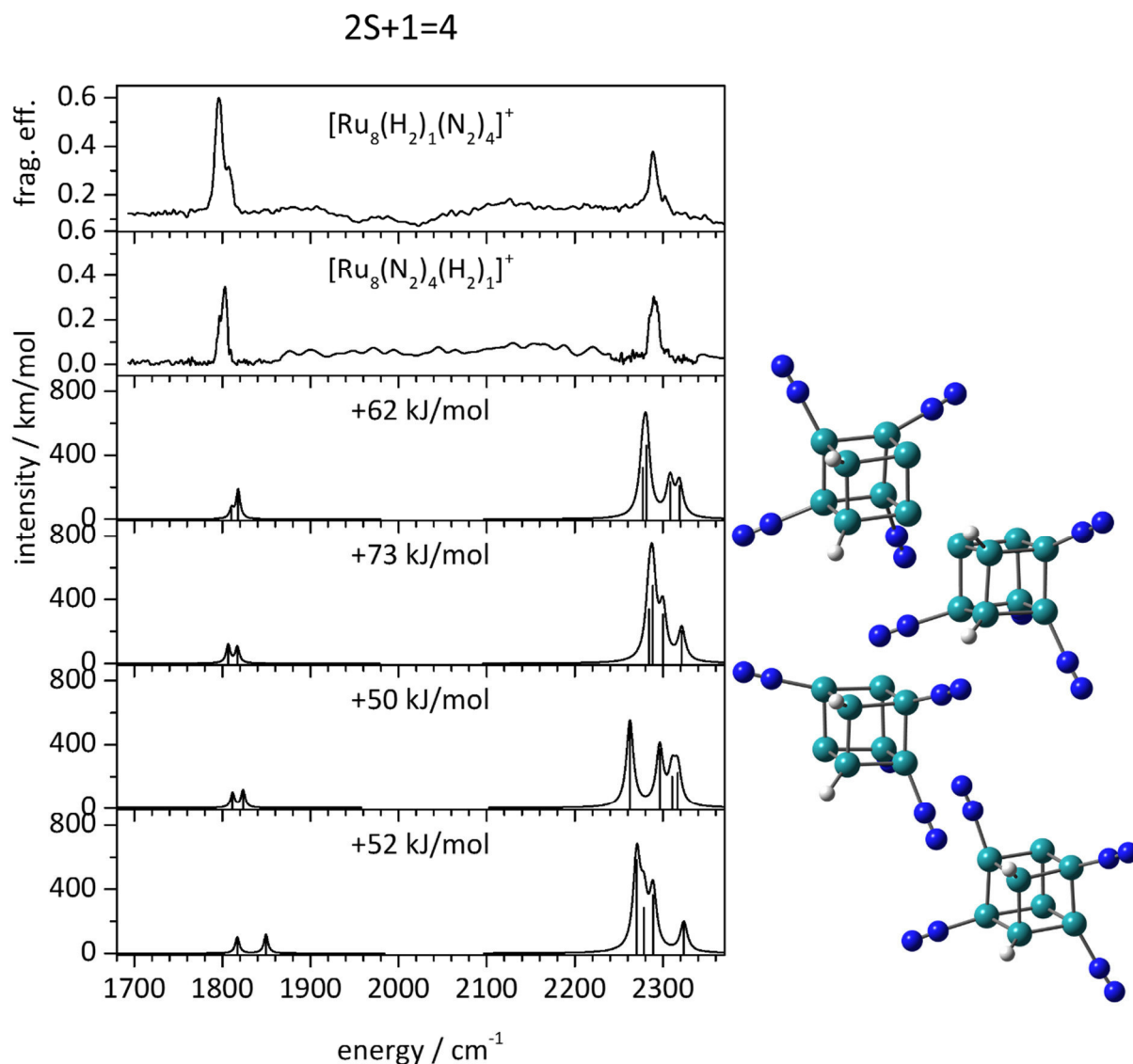


Fig. S11. IR-PD spectra of $[\text{Ru}_8(\text{H}_2)_1(\text{N}_2)_4]^+$ and $[\text{Ru}_8(\text{N}_2)_4(\text{H}_2)_1]^+$ in comparison with DFT calculations of different N₂ adsorption sites on a cubic Ru₈⁺ with the H atoms on two neighboring Ru atoms in quartet spin states. Calculations were performed at the PBE0 level of theory using cc-pVTZ (N) and Stuttgart RSC 1997 effective core potential (Ru) basis sets. The calculated harmonic vibrations were scaled by 0.9656 above 2150 cm^{-1} and by 0.923 below 2150 cm^{-1} .

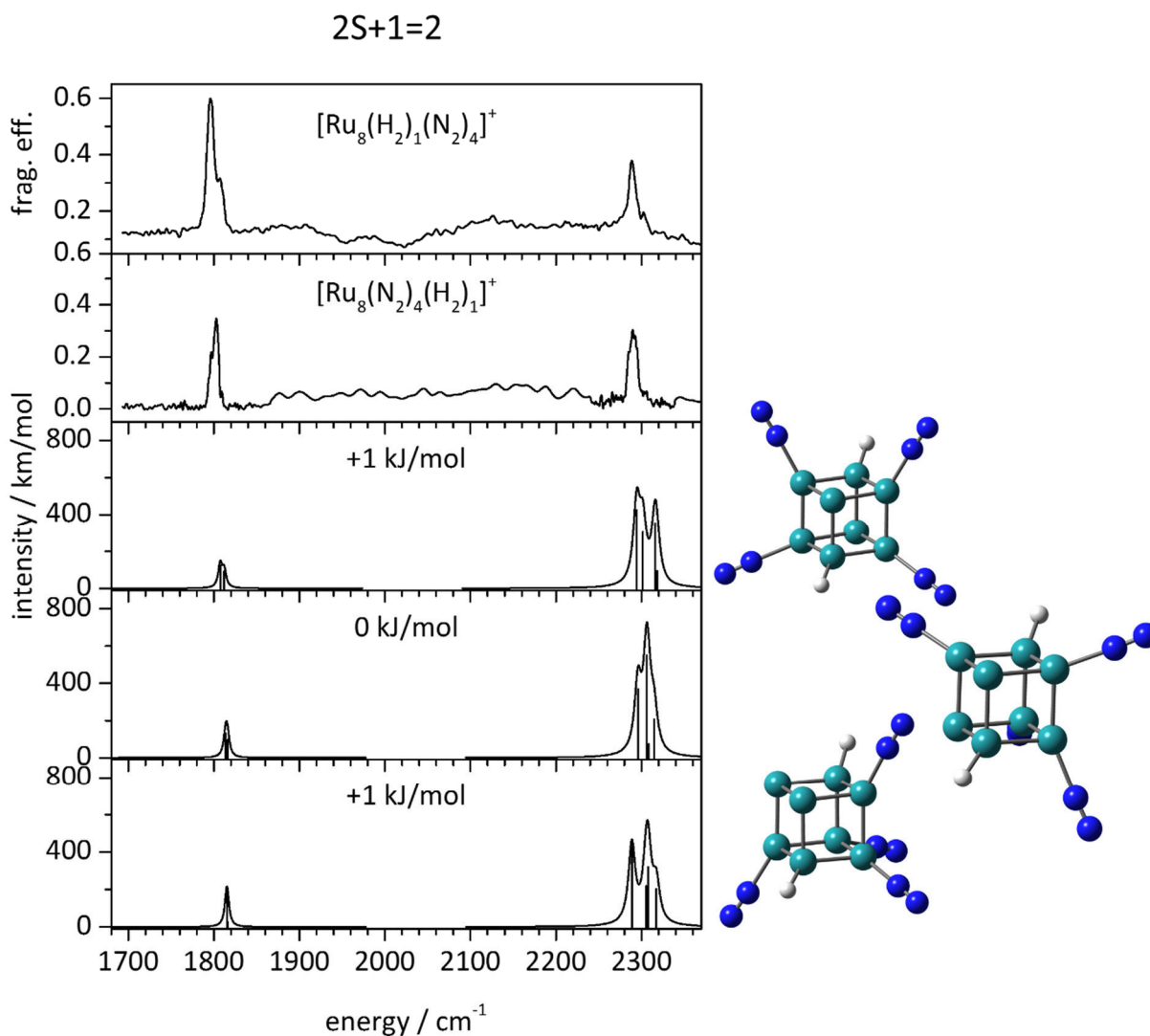


Fig. S12. IR-PD spectra of $[\text{Ru}_8(\text{H}_2)_1(\text{N}_2)_4]^+$ and $[\text{Ru}_8(\text{N}_2)_4(\text{H}_2)_1]^+$ in comparison with DFT calculations of different N₂ adsorption sites on a cubic Ru₈⁺ with the H atoms on two opposing Ru atoms (space diagonal/distal) in doublet spin states. Calculations were performed at the PBE0 level of theory using cc-pVTZ (N) and Stuttgart RSC 1997 effective core potential (Ru) basis sets. The calculated harmonic vibrations were scaled by 0.9656 above 2150 cm^{-1} and by 0.923 below 2150 cm^{-1} .

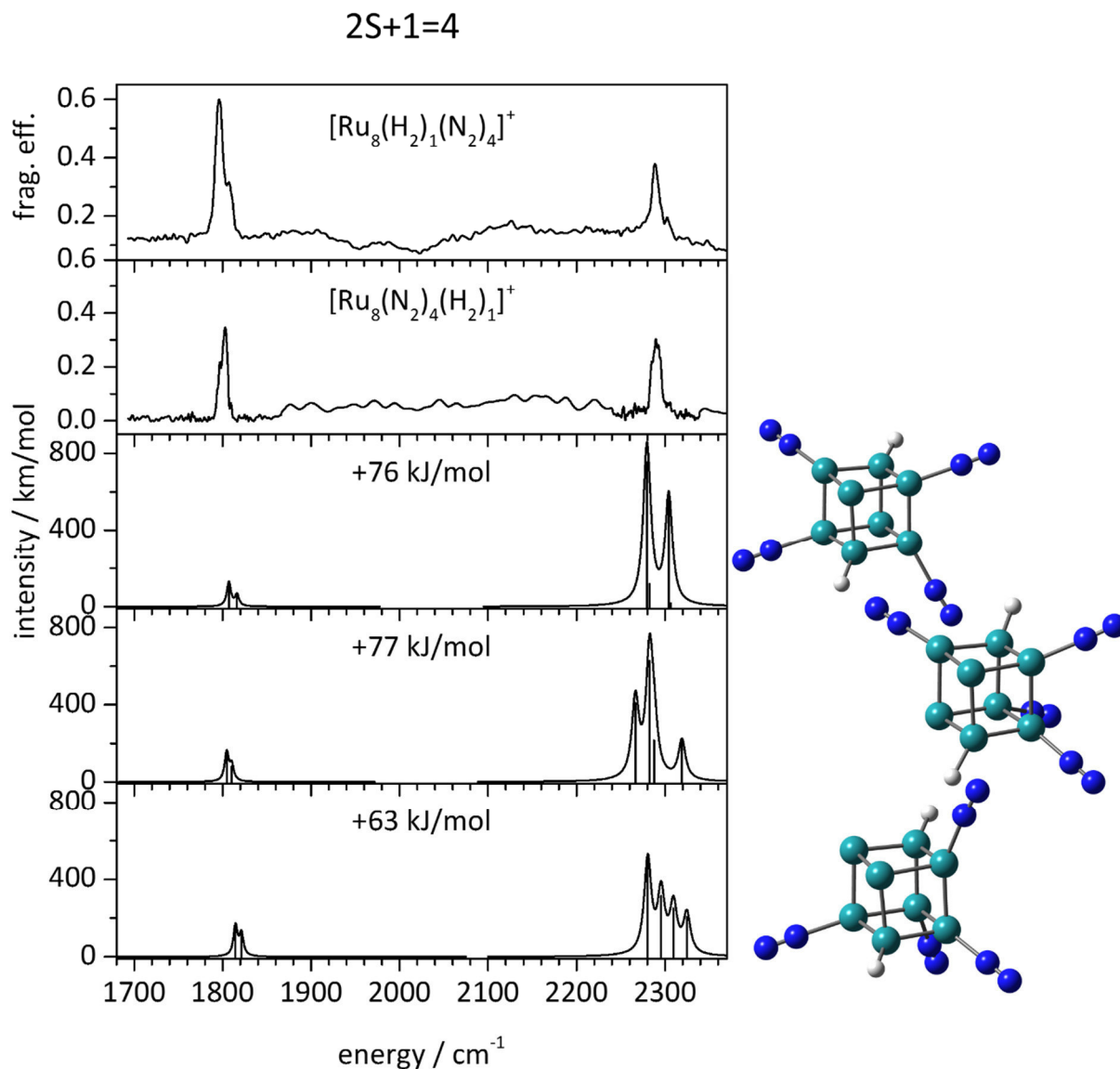


Fig. S13. IR-PD spectra of $[\text{Ru}_8(\text{H}_2)_1(\text{N}_2)_4]^+$ and $[\text{Ru}_8(\text{N}_2)_4(\text{H}_2)_1]^+$ in comparison with DFT calculations of different N₂ adsorption sites on a cubic Ru₈⁺ with the H atoms on two opposing Ru atoms (space diagonal/distal) in quartet spin states. Calculations were performed at the PBE0 level of theory using cc-pVTZ (N) and Stuttgart RSC 1997 effective core potential (Ru) basis sets. The calculated harmonic vibrations were scaled by 0.9656 above 2150 cm⁻¹ and by 0.923 below 2150 cm⁻¹.

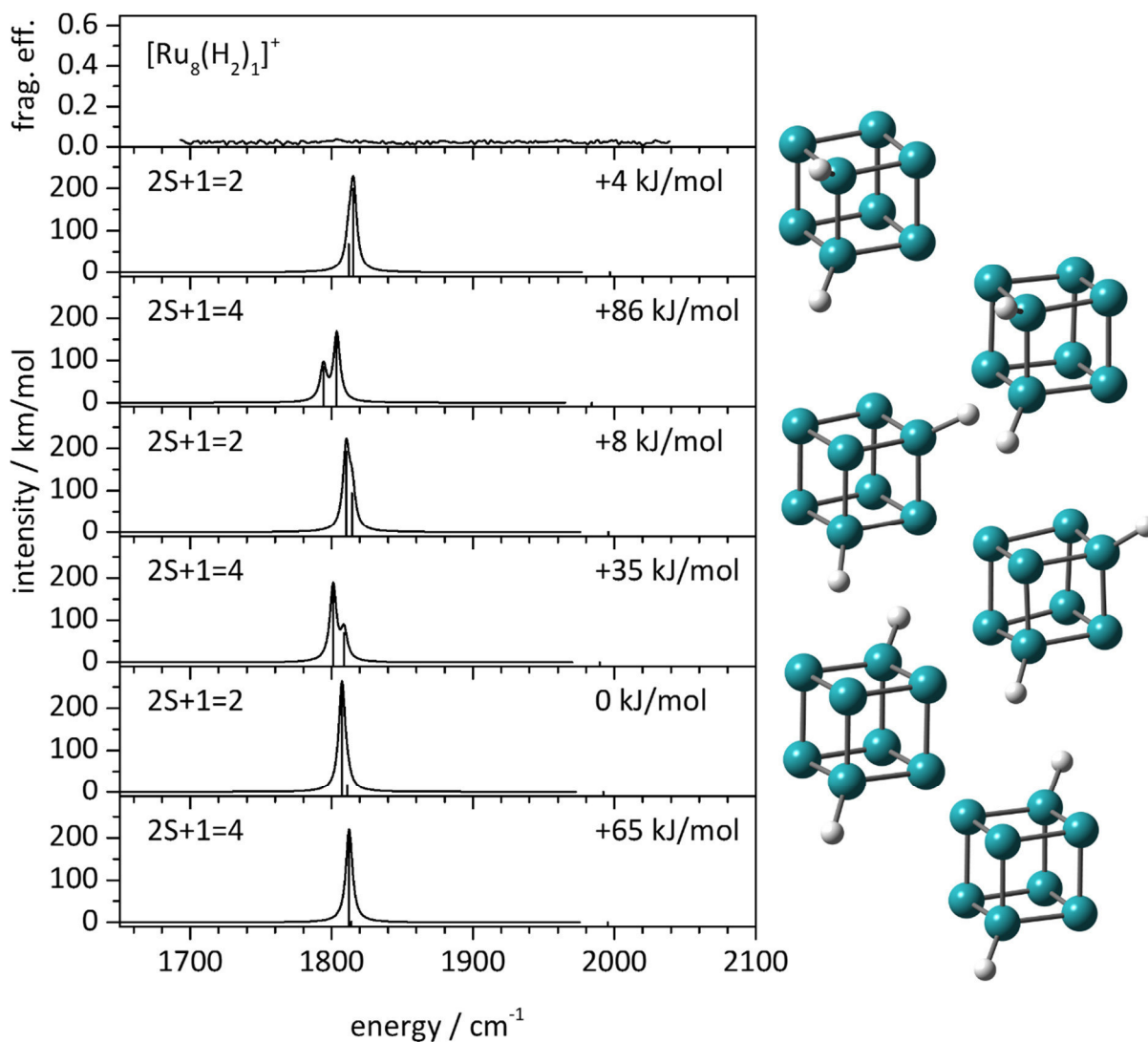


Fig. S14. IR-PD spectrum of [Ru₈(H₂)₁]⁺ in comparison with DFT calculations of different H adsorption sites on cubic Ru₈⁺ cluster in doublet and quartet spin states. Calculations were performed at the PBE0 level of theory using cc-pVTZ (N) and Stuttgart RSC 1997 effective core potential (Ru) basis sets. The calculated harmonic vibrations were scaled by 0.923.

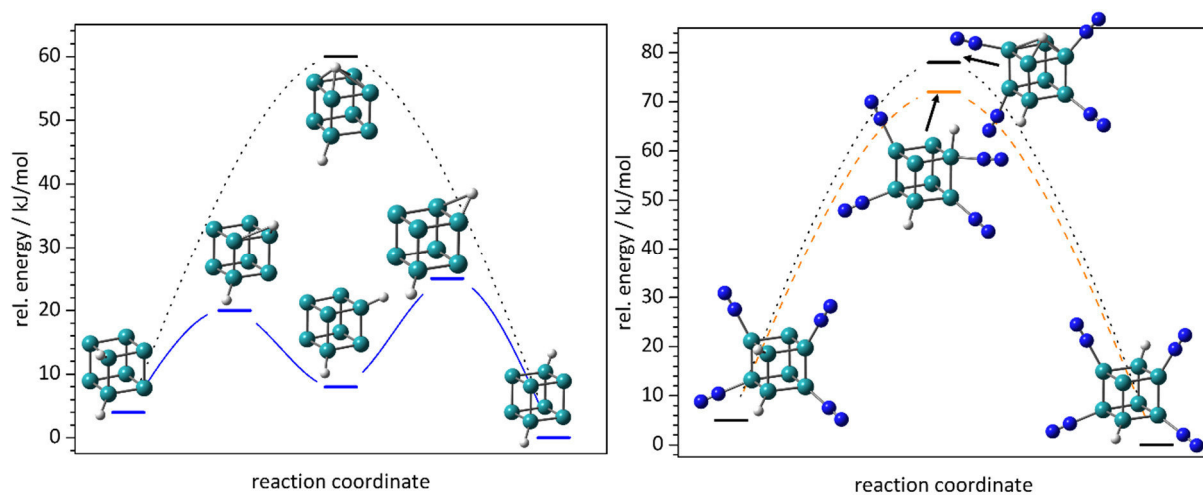


Fig. S15. Alternative calculated reaction paths for the formation of 4 from 2 (left) and for the formation of 4(N₂)₄ from 2(N₂)₄ (right). All displayed structures are either fully optimized local minimum structures or transition states with either none or exactly one imaginary frequency, respectively.

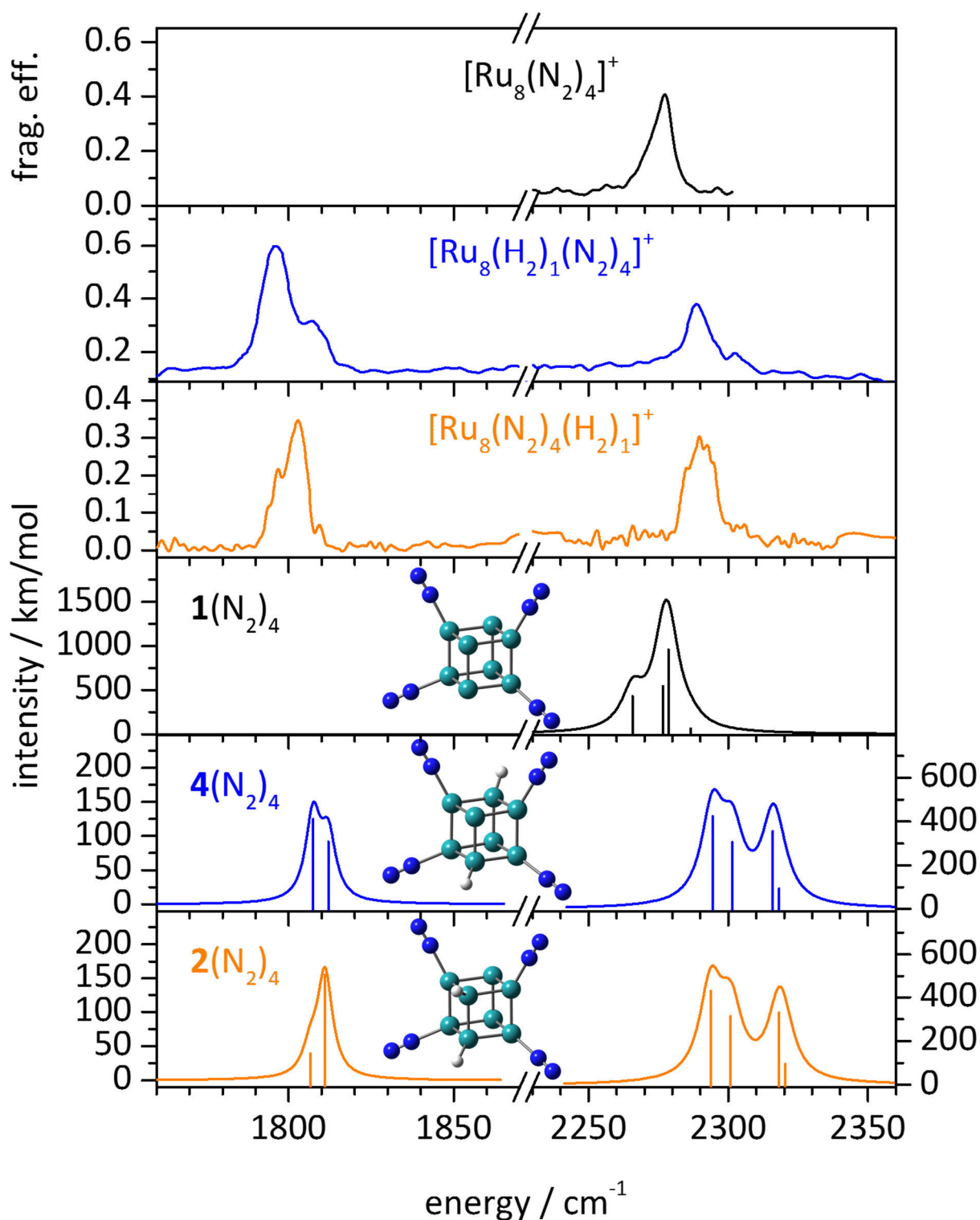


Fig. S16. IR-PD spectra of $[\text{Ru}_8(\text{N}_2)_4]^+$, $[\text{Ru}_8(\text{H}_2)_1(\text{N}_2)_4]^+$ and $[\text{Ru}_8(\text{N}_2)_4(\text{H}_2)_1]^+$ in comparison with DFT calculations. Calculations were performed at the PBE0 level of theory using cc-pVTZ (N) and Stuttgart RSC 1997 effective core potential (Ru) basis sets. The calculated harmonic vibrations were scaled by 0.9656 above 2150 cm⁻¹ and by 0.923 below 2150 cm⁻¹.

Discussion of DFT Predicted Splittings and Intensities of N₂ Stretching Bands as Compared to the Experimental IR-PD Spectra:

DFT predictions reveal four N₂ stretching bands which originate from combined motions of the four N₂ chromophores t1, t2, b1, and b2 as labeled in Fig. S17 and as assigned in Table S1 and S2. Within the experimental band width of about 5 cm⁻¹ the asymmetric/symmetric combination of the (t1,t2) couple is degenerate, and the according combination of the (b1,b2) couple as well. The experimental splitting of 13 cm⁻¹ between (t1,t2) and (b1,b2) bands comes close to the splitting of 18 cm⁻¹ predicted by DFT.

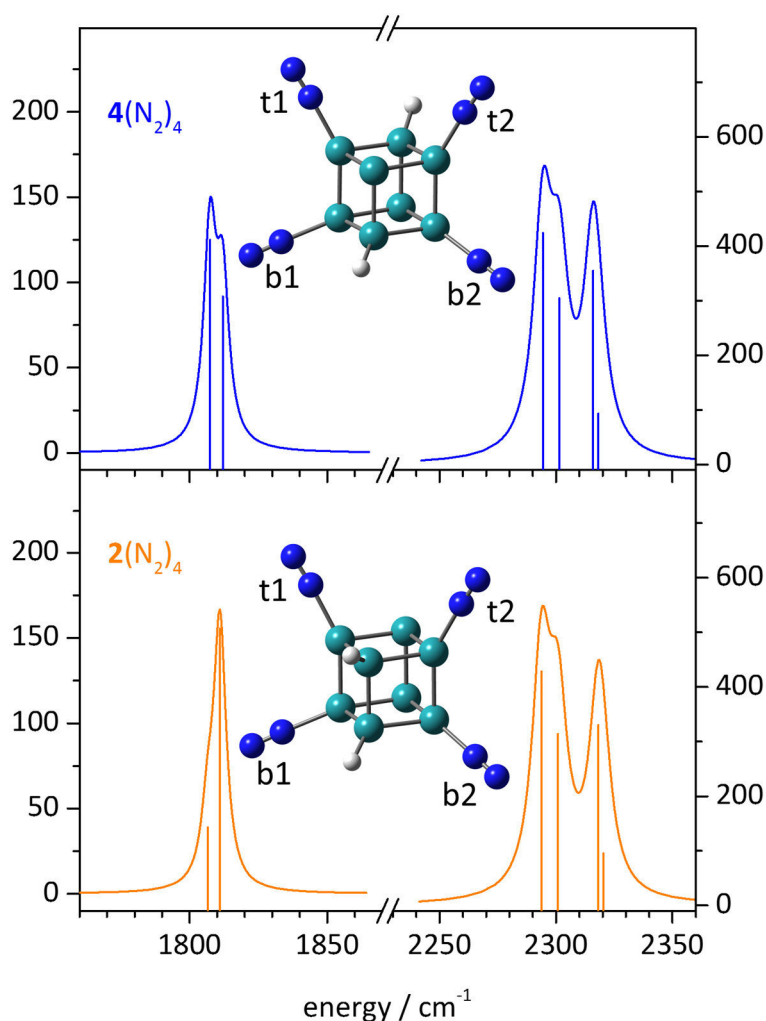


Fig. S17. Calculated spectra of $4(N_2)_4$ and $2(N_2)_4$ and their respective structure. The structures include the naming of the adsorbed N₂s.

Table S1. Calculated IR frequencies and assignment of the **4(N₂)₄**.

freq. unscaled / cm ⁻¹	freq. scaled / cm ⁻¹	intensity / km/mol	assignment
2376	2294	424	(t1,t2) asymmetric combination
2383	2301	305	(t1,t2) symmetric combination
2398	2316	355	(b1,b2) asymmetric combination
2401	2318	94	(b1,b2) symmetric combination

Table S2. Calculated IR frequencies and assignment of the **2(N₂)₄**.

freq. unscaled / cm ⁻¹	freq. scaled / cm ⁻¹	intensity / km/mol	assignment
2375	2294	429	(t1,t2) asymmetric combination
2383	2301	314	(t1,t2) symmetric combination
2401	2318	330	(b1,b2) asymmetric combination
2403	2320	96	(b1,b2) symmetric combination

As often discussed before^[1] IR-PD intensities may deviate from DFT predicted IR absorption intensities particularly when vibrational state densities are sparse – leading to “dark bands” in IR-PD spectra. In the present case these state densities seem high at first glance. Note however, that given the mass mismatch of Ru and N₂, distant N₂ oscillators may be decoupled from motions of the Ru₈ core, from the RuH oscillators, and possibly also from each other. The stability of all of the predicted N₂ band positions against H-migration (**2N₂**

versus 4N₂ isomers) proves decoupling from the RuH oscillators. The 7 cm⁻¹ splitting within the asymmetric/symmetric N₂ stretching combinations of the (t1,t2)-pairs in both isomers strongly suggests the coupling of these N₂ oscillators into global modes, while the negligible splitting of (b1,b2) bands (2 cm⁻¹) suggests the decoupling of these N₂ oscillators towards local modes. The differences in the coupling of (t1,t2) pairs versus (b1,b2) pairs likely originate from the small versus large tilt and/or the concomitant proximity versus distance amongst these N₂ pairs, respectively.

It is thus likely possible to excite the b1 and b2 chromophores independently, and their excitation may sustain long enough such that their vibrational ground states stay depleted and another $|0\rangle \rightarrow |1\rangle$ excitation of each chromophore cannot occur within the limited duration of the IR photon pulse (6 ns) in the experiment. In such a case only one IR absorption takes place – fragmentation likely not: the considerable heat of fragmentation $\Delta_{\text{frag}}H(\text{Ru-N}_2)$ of ~50 kJ/mol would require at least a two photon excitation and an effective coupling of excited oscillators to the heat bath of the entire complex, and thereby to the Ru-N₂ fragmentation coordinate. In effect, the * labelled strong IR absorption bands (by DFT) correspond to significantly diminished experimental IR-PD bands, this difference originating from a lack of efficient internal vibrational redistribution (IVR).

A 2c-IR2PD scheme with two independent IR colors in the same spectral range in combination with cryo tandem ion trapping would allow us to better explore these intensity issues. The corresponding large scale instrumental modification is in progress.

References:

- [1] a) T. Pankewitz, A. Lagutschenkov, G. Niedner-Schatteburg, S. S. Xantheas, Y. T. Lee, *J. Chem. Phys.* **2007**, *126*, 074307; b) Y. Nosenko, F. Menges, C. Riehn, G. Niedner-Schatteburg, V. E. Bondybey, *Phys. Chem. Chem. Phys.* **2013**, *15*, 8171-8178.

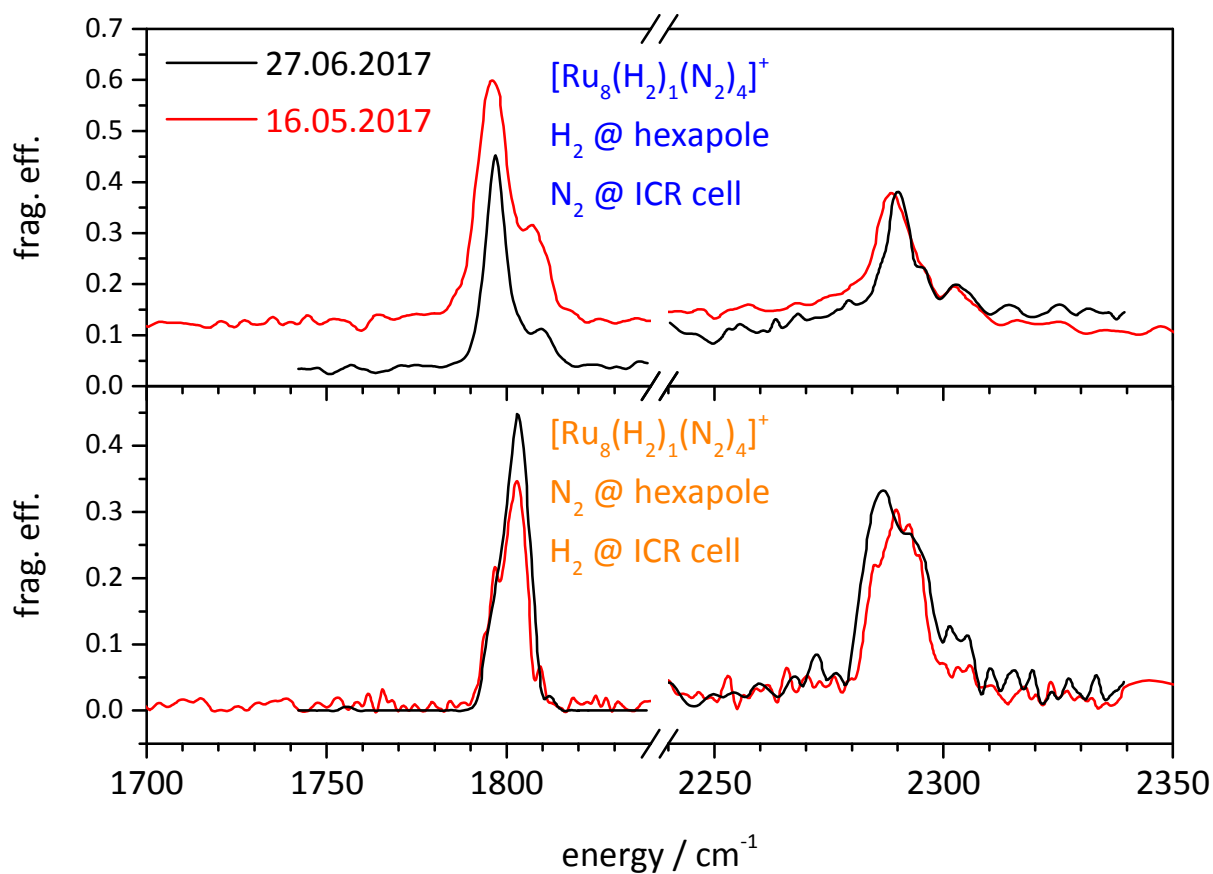


Fig. S18. IR-PD spectra of [Ru₈(H₂)₁(N₂)₄]⁺ and [Ru₈(N₂)₄(H₂)₁]⁺ recorded on two separate measurement days. Note the reproducibility even of minor features.

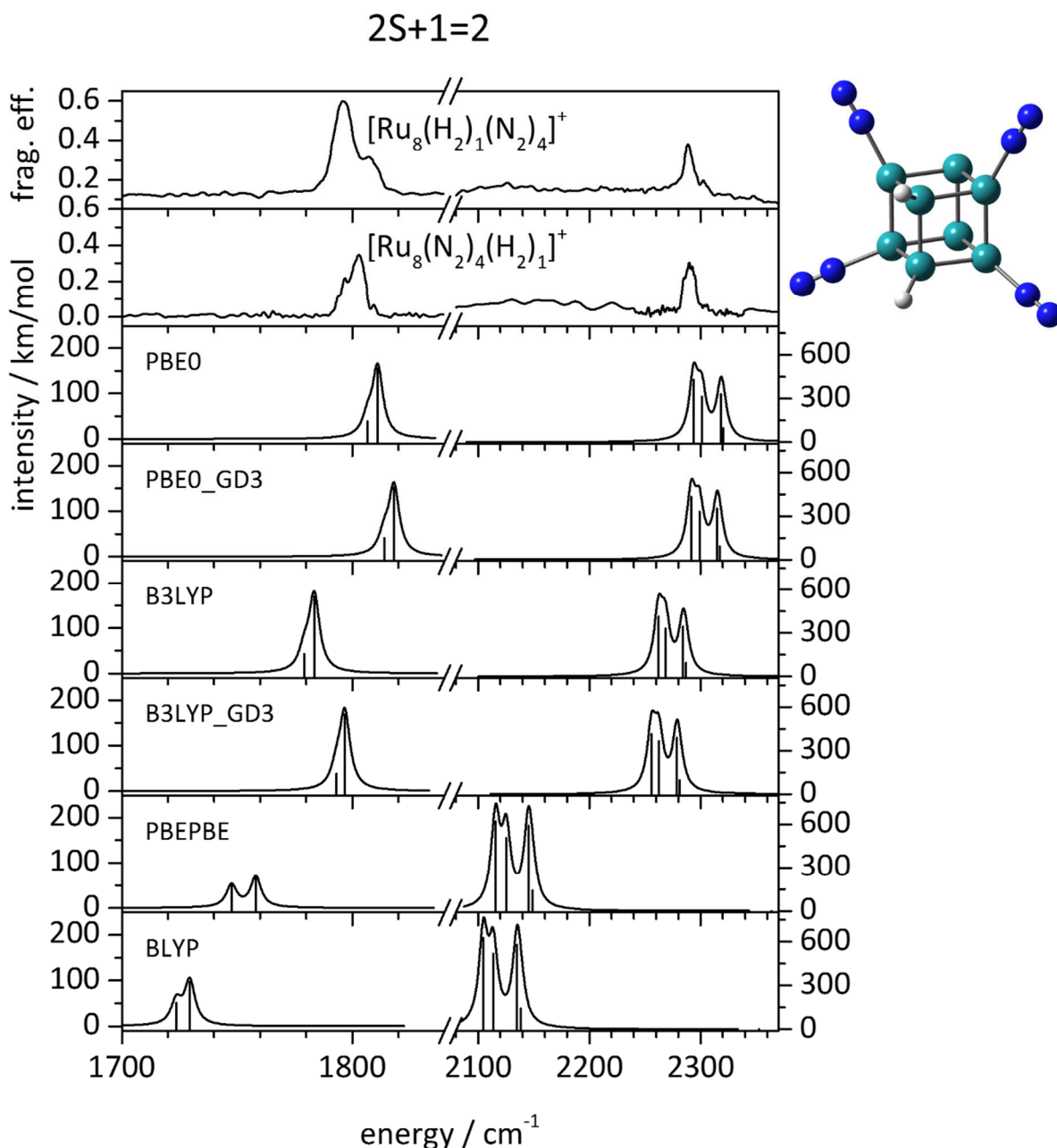


Fig. S19. IR-PD spectra of $[\text{Ru}_8(\text{H}_2)_1(\text{N}_2)_4]^+$ and $[\text{Ru}_8(\text{N}_2)_4(\text{H}_2)_1]^+$ in comparison with DFT calculations with different functionals (PBE0, PBE0 including the Grimme correction for dispersion (GD3), B3LYP, B3LYP including the Grimme correction for dispersion (GD3), PBEPBE, and BLYP). Calculations were performed using cc-pVTZ (N) and Stuttgart RSC 1997 effective core potential (Ru) basis sets. The calculated harmonic vibrations were scaled by 0.9656 above 2150 cm⁻¹ and by 0.923 below 2150 cm⁻¹.

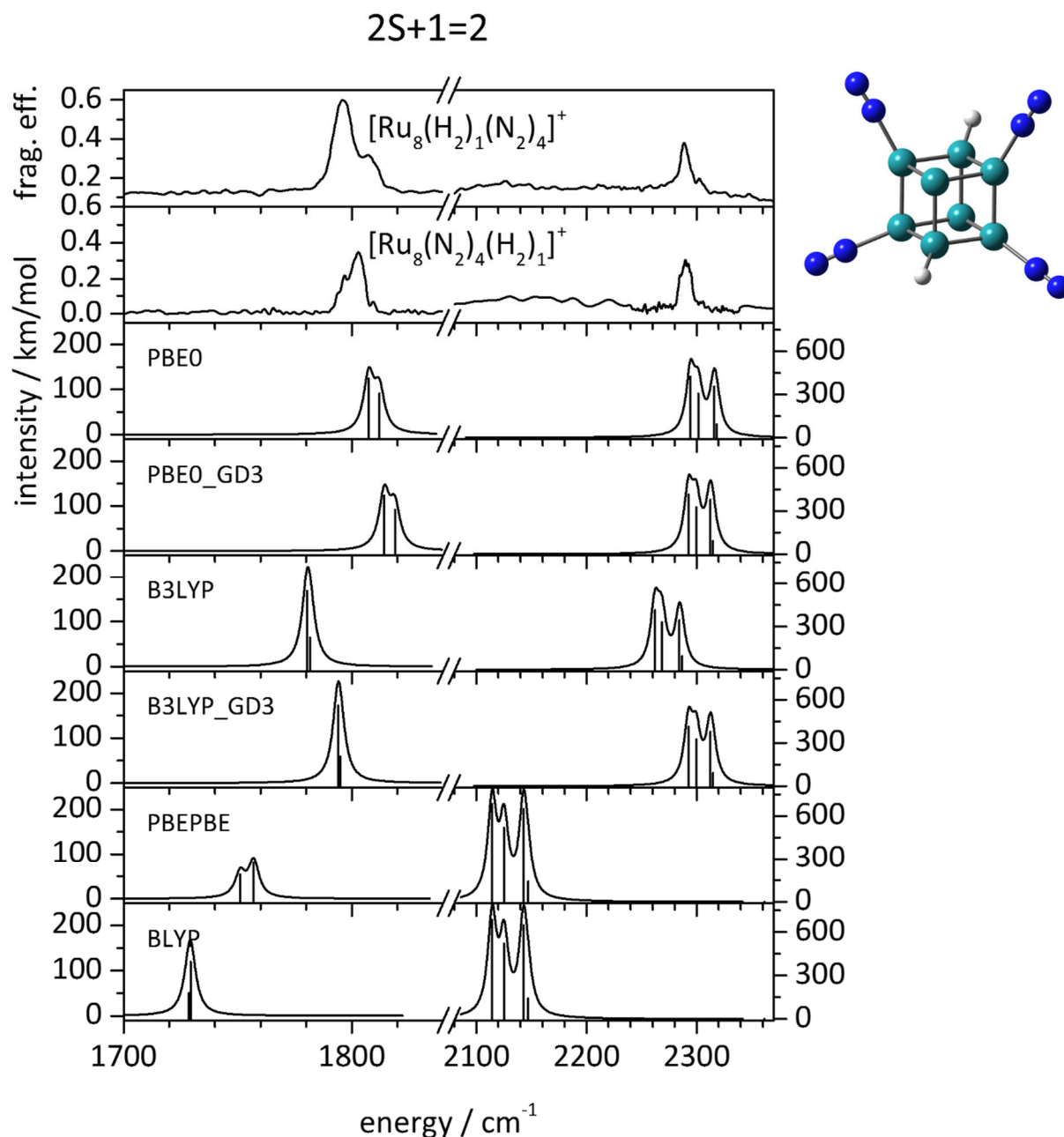


Fig. S20. IR-PD spectra of $[\text{Ru}_8(\text{H}_2)_1(\text{N}_2)_4]^+$ and $[\text{Ru}_8(\text{N}_2)_4(\text{H}_2)_1]^+$ in comparison with DFT calculations with different functionals (PBE0, PBE0 including the Grimme correction for dispersion (GD3), B3LYP, B3LYP including the Grimme correction for dispersion (GD3), PBEPBE, and BLYP). Calculations were performed using cc-pVTZ (N) and Stuttgart RSC 1997 effective core potential (Ru) basis sets. The calculated harmonic vibrations were scaled by 0.9656 above 2150 cm⁻¹ and by 0.923 below 2150 cm⁻¹.

9 Cryo IR Spectroscopy of [Hemin]⁺ Complexes in Isolation

Sebastian Dillinger, Johannes Lang, and Gereon Niedner-Schatteburg

Fachbereich Chemie und Forschungszentrum OPTIMAS

Technische Universität Kaiserslautern

67663 Kaiserslautern

9.1 Preamble

The following chapter is a reprint of a publication in the journal “The Journal of Physical Chemistry A”.

The experiments were performed by myself. The data evaluation was done by myself. The computations were done by myself. The initial manuscript was written by myself and revised with the help of G. Niedner-Schatteburg and J. Lang.

Full Reference:

Cryo IR Spectroscopy of [Hemin]⁺ Complexes in Isolation

S. Dillinger, J. Lang, and G. Niedner-Schatteburg, *The Journal of Physical Chemistry A*, **2017**, 121, 38, 7191-7196.

<http://dx.doi.org/10.1021/acs.jpca.7b08604>

9.2 Reprint

Reprint License



RightsLink®

Home

Create Account

Help



ACS Publications
Most Trusted. Most Cited. Most Read.

Title: Cryo IR Spectroscopy of [Hemin]+ Complexes in Isolation
Author: Sebastian Dillinger, Johannes Lang, Gereon Niedner-Schatteburg
Publication: The Journal of Physical Chemistry A
Publisher: American Chemical Society
Date: Sep 1, 2017
Copyright © 2017, American Chemical Society

[LOGIN](#)

If you're a copyright.com user, you can login to RightsLink using your copyright.com credentials. Already a RightsLink user or want to [learn more?](#)

PERMISSION/LICENSE IS GRANTED FOR YOUR ORDER AT NO CHARGE

This type of permission/license, instead of the standard Terms & Conditions, is sent to you because no fee is being charged for your order. Please note the following:

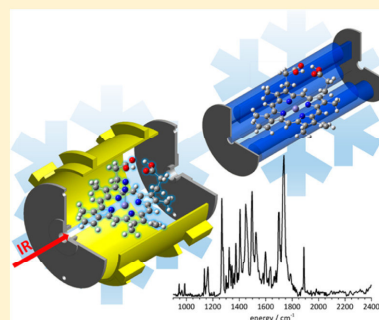
- Permission is granted for your request in both print and electronic formats, and translations.
- If figures and/or tables were requested, they may be adapted or used in part.
- Please print this page for your records and send a copy of it to your publisher/graduate school.
- Appropriate credit for the requested material should be given as follows: "Reprinted (adapted) with permission from (COMPLETE REFERENCE CITATION). Copyright (YEAR) American Chemical Society." Insert appropriate information in place of the capitalized words.
- One-time permission is granted only for the use specified in your request. No additional uses are granted (such as derivative works or other editions). For any other uses, please submit a new request.

Cryo IR Spectroscopy of [Hemin]⁺ Complexes in IsolationSebastian Dillinger, Johannes Lang, and Gereon Niedner-Schatteburg*[✉]

Fachbereich Chemie and Forschungszentrum OPTIMAS, TU Kaiserslautern, 67663 Kaiserslautern, Germany

S Supporting Information

ABSTRACT: We present cryo IR spectra of isolated [Hemin]⁺ adducts with CO, N₂, and O₂ ([Hemin(CO)₁]⁺, [Hemin(CO)₂]⁺, [Hemin(¹⁴N₂)]⁺, [Hemin(¹⁵N₂)]⁺, and [Hemin(O₂)]⁺). Well resolved bands allow for the elucidation of structure and spin multiplicity in conjunction with density functional (DFT) calculations. There is a quartet spin state for the N₂ and CO adducts and a sextet spin state for the O₂ adduct, where the O₂ retains its triplet state. The double CO adsorption induces significant changes in the vibrational patterns of the IR spectra, which we take as strong evidence for a spin quenching into a doublet. Our study characterizes [Hemin]⁺, which is the Fe³⁺ oxidation product of heme that is of ubiquitous presence in hemeproteins.



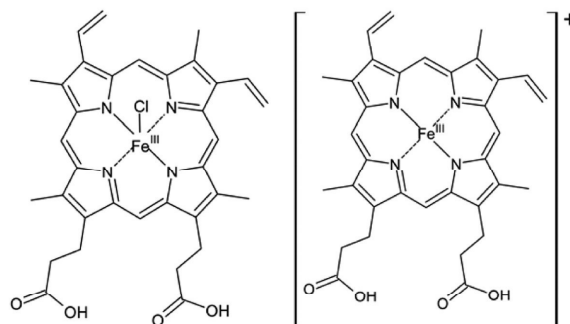
■ INTRODUCTION

Porphyrins and porphyrin iron complexes, such as heme, are of utmost importance in biochemistry.^{1,2} Hemeproteins maintain the respiratory O₂ transport of vertebrates^{3,4} and many other redox catalytic processes.^{5,6} Since the first discovery and interpretation of the binding of O₂ and CO to hemoglobin,⁷ it is well-known that the active center in heme is a Fe²⁺ ion.⁸ There are remarkable changes in the magnetic susceptibilities upon the coordination of O₂ to hemoglobin, resulting in a diamagnetic species.⁷ This has been interpreted in terms of a Fe²⁺ (high spin quintet) and an isolated O₂⁻ (triplet), which change upon coordination to an antiferromagnetically coupled Fe³⁺ (low spin doublet) and an O₂⁻ (doublet).^{8,9} Thus, the oxidation state of this metal atom is critical for the formation of this bond, as O₂ does not bind to the complex under physiological conditions if iron is initially in the Fe³⁺ state.¹⁰ Nevertheless, it is of interest to elucidate the coordination of Fe³⁺-heme ([Hemin]⁺, Scheme 1 right) with biorelevant molecules, as e.g. the reduction of denatured Fe³⁺ cytochrome has proven instrumental in the investigation of hemeprotein folding.¹¹

Hence, there are not only reaction studies of isolated Fe²⁺ porphyrins¹² but also several studies of the interactions of [Hemin]⁺ with different molecules under isolated conditions which elucidated the kinetics and thermodynamics of these reactions.^{13–19} Ion mobility studies of [Hemin]⁺ elucidated structural features in the gas phase in combination with DFT calculations²⁰ and its solution phase behavior by FTIR spectroscopy.²¹ Void of solvent effects [Hemin]⁺ was the subject of spectroscopic characterization in the Soret band and Q-band region.^{22,23} The interaction of [Hemin]⁺ with NO has been extensively studied, using both visible²⁴ and IR^{25,26} spectroscopy in the gas phase.

As already mentioned [Hemin]⁺ does not bind O₂ at room temperature due to its oxidation state (III) of the central iron

Scheme 1. Molecular Structure of Hemin (Fe^{III}C₃₄H₃₂N₄O₄Cl, Left) and [Hemin]⁺ ([Fe^{III}C₃₄H₃₂N₄O₄]⁺, Right)



atom. However, Ferrand et al. recently described the first ever observation of [Hemin]⁺-N₂ and [Hemin]⁺-O₂ complexes in a cryogenic ion trap and characterized them using electronic spectroscopy and determined the bond formation enthalpy of [Hemin]⁺-O₂ by means of temperature dependent measurements.^{27,28}

Our approach aims at the creation of [Hemin]⁺ adducts with various biorelevant molecules in a cryogenic ion trap and characterization of structures and spin states by InfraRed Photon Dissociation (IR-PD) spectroscopy in conjunction with DFT modeling.

Received: August 29, 2017

Revised: August 31, 2017

Published: September 6, 2017

EXPERIMENTAL AND COMPUTATIONAL METHODS

We utilized a customized Fourier Transform Ion Cyclotron Resonance (FT-ICR) mass spectrometer (Apex Ultra, Bruker Daltonics)²⁹ for generation of the species of interest and the subsequent InfraRed Photon Dissociation (IR-PD) spectroscopy using a laser-driven OPO/OPA system. This mass spectrometer is equipped with an Electrospray Ionization (ESI) source (Apollo 2, Bruker) and a home-built laser vaporization cluster ion source (Figure 1).

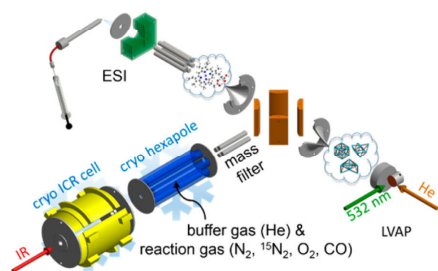


Figure 1. Schematic drawing of our tandem cryo trap FT-ICR MS. The ions are generated via Electro Spray Ionization (ESI) or Laser Vaporization (LVAP). The ions enter the cryo hexapole after passing a mass filter. The hexapole is held at a constant temperature between 11 and 300 K. Reaction gas and buffer gas can be introduced into this ion trap. The ions are transferred into the cryo ICR cell after a variable reaction time. In the cryo ICR cell the ions are isolated, irradiated with an IR laser, and detected.

Hemin (Scheme 1 left) was purchased from Sigma-Aldrich and used without further purification. Sample solutions of the Hemin complex in methanol at the concentration of 1×10^{-4} mol/L were used. We detect the [Hemin]⁺ ($[\text{FeC}_{34}\text{H}_{32}\text{N}_4\text{O}_4]^+$, Scheme 1 right). We mass selected the [Hemin]⁺ and guided it into the cryo hexapole. Reaction gas (CO, ¹⁴N₂, ¹⁵N₂, and O₂) was continuously introduced in the ion trap. The temperature was adjusted to the respective reaction gas (30 K for CO, 28 K for ¹⁴N₂ and ¹⁵N₂, 45 K for O₂). The ions are guided into the FT-ICR cell.³⁰ This cell is cooled to a temperature of about 10 K. The ICR cell is used for trapping, isolation, and detection of the ions. It is coupled to a tunable pulsed IR laser ($\Delta\nu = 0.9 \text{ cm}^{-1}$, $\Delta t = 7 \text{ ns}$).

Optimized minimum energy structures and linear IR absorption spectra were calculated at the B3LYP^{31,32} level of theory using 6-31+G* basis sets (C, H, N, O)³³ and Stuttgart RSC 1997³⁴ effective core potential (Fe) basis sets, respectively, as implemented in the Gaussian 09 program package.³⁵ We included the Grimme correction for dispersion (GD3).³⁶ We ran the calculations with several different basis sets and a different functional which did not provide for a significant improvement agreement (cf. Figures S13–S15). We scaled the calculated harmonic vibrational frequencies by a factor of 0.97 and broadened using the Lorentz profile (fwhm = 5 cm^{-1}). For a more detailed description of the experimental and computational methods refer to the Supporting Information.

RESULTS AND DISCUSSION

We stored the generated [Hemin]⁺ ions in our cryogenically cooled hexapole ion trap. Addition of reaction gas results in the formation of [Hemin]⁺ adsorbate complexes (cf. Figure 2). The temperature was individually adjusted for each reaction gas to

prevent condensation of the respective molecules (CO = 30 K, N₂ = 28 K, O₂ = 45 K).

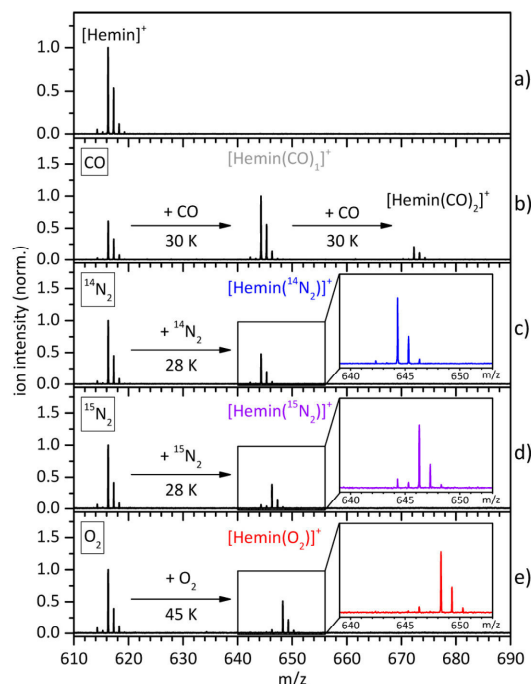


Figure 2. Mass spectra of [Hemin]⁺ in isolation (a) and with various reaction gases (b–e). The temperature of the ion trap was adjusted to yield a sufficient amount of reaction product. Insets illustrate mass shifts due to adsorption.

Without any reaction gas, a single species arises in the mass spectrum at 616 m/z (most abundant isotope peak, cf. Figure 2a), which is assigned to the [Hemin]⁺ species. We safely exclude the observation of dicationic dimers as the isotopic pattern shows a 1 m/z spacing exclusively. Reaction with CO yields two additional mass peaks which are shifted by 28 m/z and 56 m/z . (cf. Figure 2b). We assign these peaks to the singly adsorbed CO species ($[\text{Hemin}(\text{CO})_1]^+$) and the doubly adsorbed CO species ($[\text{Hemin}(\text{CO})_2]^+$). Nitrogen reaction gases, ¹⁴N₂ and ¹⁵N₂, lead to mass peaks at 644 m/z and 646 m/z (cf. Figure 2b and 2c) corresponding to $[\text{Hemin}(\text{}^{14}\text{N}_2)]^+$ and $[\text{Hemin}(\text{}^{15}\text{N}_2)]^+$, respectively. The reaction gas O₂ gives rise to a new peak in the mass spectrum shifted by 32 m/z , which is assigned to the $[\text{Hemin}(\text{O}_2)]^+$ complex.

We applied our IR-PD scheme in the range of 900 to 2400 cm^{-1} to the generated [Hemin]⁺ adducts to gather further insights into structure, binding motifs, and/or spin states supported by DFT calculations. We recorded numerous well resolved bands in this region (Figure 3). In addition, we checked the region from 2800 to 3800 cm^{-1} where we found extremely broad bands (cf. Figure S2) which we tentatively assign to low lying electronic transitions. Free OH oscillators seem absent; the cold complexes likely involve double hydrogen bonding of the twin carboxylic residues which yields broad and structureless spectral features to the red of the free OH stretches.

There are remarkable similarities between the singly adsorbed species of CO, N₂, and O₂ ($[\text{Hemin}(\text{CO})_1]^+$,

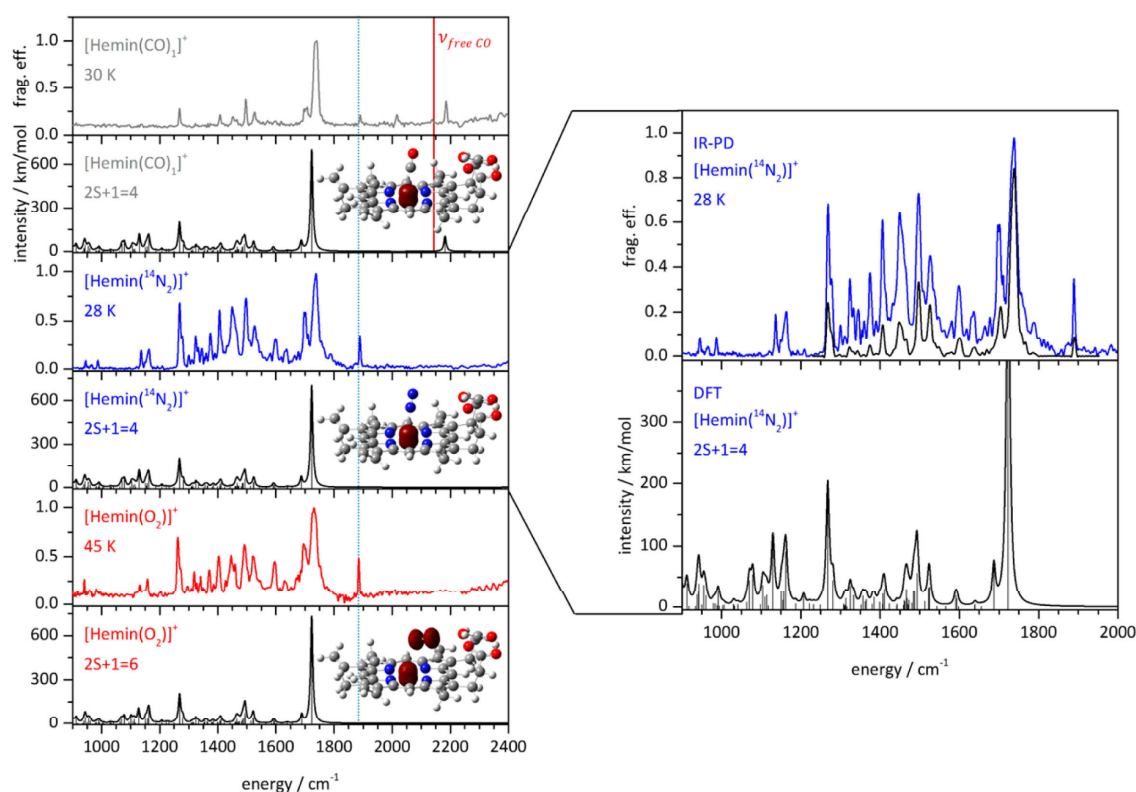


Figure 3. IR-PD spectra of the singly adsorbed species ($[\text{Hemin}(\text{CO})_1]^+$, $[\text{Hemin}({}^{14}\text{N}_2)]^+$, and $[\text{Hemin}(\text{O}_2)]^+$) and of the computed absorption spectra of the most stable isomers. The presented structures include the isosurfaces of the spin density. The red line is to indicate the stretching frequency of free CO (2143 cm^{-1}). The blue dotted line is to highlight the well resolved band which is not present in the solid state and which is only visible in the gas phase (cf. Figure S3). The zoom in on the right includes the experimental spectrum measured with attenuated laser power in black (cf. Figure S4).

$[\text{Hemin}({}^{14}\text{N}_2)]^+$, $[\text{Hemin}({}^{15}\text{N}_2)]^+$, and $[\text{Hemin}(\text{O}_2)]^+$. All spectra show two strong bands around 1740 and 1700 cm^{-1} , which correspond to the symmetric and asymmetric stretching modes of the carboxyl groups, and all spectra show almost identical vibrational patterns. This leads us to the conclusion that in all these cases the adsorbed molecules induce identical changes in the complex or do not alter the structure of the $[\text{Hemin}]^+$ at all.

All single adsorbate species show a narrow band at around 1890 cm^{-1} (cf. Figure 3, blue dotted line). This band is neither observed in the solid state spectrum of Hemin (Figure S3)³⁷ nor reproduced by the calculations. Its stability against ligand variation (CO, N₂, O₂) and against isotopic variation (${}^{14}\text{N}_2$ vs ${}^{15}\text{N}_2$) proves that the vibrations of this band are located entirely on the $[\text{Hemin}]^+$. We further exclude that this band originates from another isomer as we did not find any structures with vibrations in this spectral region. We further exclude the observation of any hot band as we investigate cryo cooled species which diminishes the probability of hot bands.³⁸ Overtones in this spectral region are also unlikely as the calculations do not predict vibrational transitions of high IR intensity around 950 cm^{-1} . Hence, we assign this band to a combination mode similar to what has been observed before above 1800 cm^{-1} .³⁹ Our tentative assignment is a combination of the asymmetric carboxyl stretch ($[\text{Hemin}({}^{14}\text{N}_2)]^+$: IR-PD: 1736 cm^{-1} , DFT scaled: 1723 cm^{-1}) with an alkyl carboxyl arm

twist ($[\text{Hemin}({}^{14}\text{N}_2)]^+$: DFT scaled: 160 cm^{-1}). In view of the prevailing double H-bond such a coupling is self-evident when in isolation. Stacking of the hemin units and competing intermolecular H-bonds may have significant effects on vibrational modes in solid state.^{40,41} Therefore, such a combination band is expected to vanish in an according solid state IR spectrum, and normal-mode analysis derived DFT predictions merely report its components.

To gain further insight we performed DFT calculations of different H-bonding isomers, of cis and trans binding sites, and of low, medium, and high spin states ($2S+1 = 2$ (doublet), $2S+1 = 4$ (quartet), and $2S+1 = 6$ (sextet)) for all complexes (Figures S6–S8, S16). In all cases the most stable isomer forms two H-bonds with its two carboxyl groups, and the adsorbate arranges itself on the iron center and in cis configuration to the adjacent alkyl carboxyl moieties, which is both on the same side of the porphyrin plane (Figure S5). The calculations predict a stabilization of the cis isomer by about 3 kJ/mol (cf. Figure S9), and we will focus on this cis adsorption in the following.

First we will discuss the DFT modeling of the $[\text{Hemin}({}^{14}\text{N}_2)]^+$ complex as representative for the singly adsorbed species (Figure 3), and all singly adsorbed species exhibit similar features. Minor differences in the spectra of the other adsorbates will be discussed later when appropriate. The DFT calculations of $[\text{Hemin}({}^{14}\text{N}_2)]^+$ predict that the most stable isomers are in the quartet spin state, and the other possible spin

states are less stable. We exclude the other spin states which do not correlate well with our recorded IR-PD spectrum (doublets in Figure S6) or which are more than 30 kJ/mol less stable (sextets in Figure S6). An intermediate (quartet) spin state has been predicted for the naked [Hemin]⁺ before.⁴²

The close-up of the calculated quartet spectrum (Figure 3 right) shows the excellent agreement with the experimental spectrum. The vibrational pattern is adequately reproduced with minor exceptions. We observe no IR-PD bands in the region from 1020 to 1120 cm⁻¹ which is due to the decrease of laser power in this region (cf. Figure S4), which then fails to induce fragmentation. Note that the calculations do not predict any combination bands in principle, while we have discussed a tentative assignment of the 1890 cm⁻¹ IR-PD band to a combination of calculated normal modes above.

The N–N stretching mode of the adsorbed ¹⁴N₂ is not visible in the recorded spectrum. The calculations predict the N–N stretching frequency around 2390 cm⁻¹ (unscaled: 2463.48 cm⁻¹) and by a meager IR intensity of only 2.3 km/mol. The predicted low IR intensity (cf. Table S1) makes it nearly impossible to detect this stretching mode. Note that the calculated IR frequency corresponds to a blue shift of 60 cm⁻¹ with respect to the (IR inactive) mode of the free ¹⁴N₂ (2330 cm⁻¹).⁴³ This finding is in line with the observed blue shift of the CO mode in the [Hemin(CO)₁]⁺ complex and with our previous results of a blue shift of the N₂ mode upon the adsorption on Fe³⁺ in a “nonclassical” N₂–Fe complex.⁴⁴ The IR-PD spectra of the isotopologue complexes, [Hemin(¹⁴N₂)]⁺ and [Hemin(¹⁵N₂)]⁺, reveal no isotopic shifts of any observed band (cf. Figure S10), all of which thus locate at the [Hemin]⁺ itself.

The experimental IR-PD spectrum of the [Hemin(CO)₁]⁺ complex is significantly weaker than that of [Hemin(N₂)]⁺ apart from the carboxyl band at 1740 cm⁻¹, the applied laser intensities kept identical. The calculated IR intensities of these species are similar (cf. Figure 3). The observed intensity differences thus relate to a higher fragmentation enthalpy in the CO complex. A CO ligand at an Fe³⁺ ion, as well established by coordination chemistry, allows for optimal σ donor and π^* acceptor overlap with appropriate d orbitals at Fe³⁺, whereas an N₂ ligand provides for lower lying σ orbitals and higher π^* orbitals which results in a weaker overlap with the Fe³⁺ d orbitals.⁴⁵ The DFT modeling of [Hemin(CO)₁]⁺ predicts a quartet spin state (cf. Figure 3 and Figure S7 for other spin states) as well. Again, we exclude the other spin states, which do not correlate well with our recorded IR-PD spectrum (doublets in Figure S7) or which are about 30 kJ/mol less stable (doublets and sextets in Figure S7). The calculated spectrum looks very similar to the one of [Hemin(N₂)]⁺ - in line with the recorded IR-PD spectra - except for subtle differences. The experimental IR-PD spectrum of [Hemin(CO)₁]⁺ reveals two additional bands: One band is located at 2016 cm⁻¹ below the free CO stretch (2143 cm⁻¹, Figure 3 red line);⁴³ the other band is located at 2185 cm⁻¹ above. We assign the 2185 cm⁻¹ band to the bound CO stretch mode and 42 cm⁻¹ to the blue of the free CO mode. Similar observations were made in nonclassical Ag⁺–CO complexes^{46,47} and in recently characterized Fe³⁺–N₂ complexes⁴⁴ - our current DFT modeling lending further support (cf. Figure 3). In contrast, the 2016 cm⁻¹ band is not reproduced by DFT. Once more excluding a hot band, we deduce another combination band which needs to involve the CO ligand. Close inspection of the normal modes as predicted by our DFT modeling allows us to

suggest a tentative assignment in terms of a combination of the asymmetric carboxyl stretch ([Hemin(CO)₁]⁺: IR-PD: 1737 cm⁻¹, DFT scaled: 1723 cm⁻¹) with the ν_{40} and/or ν_{41} modes (DFT scaled: 276 and 275 cm⁻¹) that describe a combined porphyrin ring bending and CO wagging. The corresponding modes of the [Hemin(¹⁴N₂)]⁺ complex reveal significantly less motion of the adsorbed N₂. This would explain why such a combination band only contributes to the IR-PD spectrum of the [Hemin(CO)₁]⁺ complex.

The experimental IR-PD spectrum of [Hemin(O₂)]⁺ is almost identical to that of [Hemin(N₂)]⁺. Our DFT modeling reveals a most stable sextet spin state, and the according linear IR spectrum agrees well with experiment (cf. Figure S8). The [Hemin(O₂)]⁺ comprises 3 unpaired e⁻ at the Fe³⁺ and 2 unpaired e⁻ on the O₂, yielding in total a sextet spin state of 5 unpaired e⁻. The isosurfaces of the spin densities on the iron center of the [Hemin(O₂)]⁺ (sextet), the [Hemin(¹⁴N₂)]⁺ (quartet), and the [Hemin(CO)₁]⁺ (quartet) are almost identical (cf. insets to Figure 3). In contrast the less stable [Hemin(¹⁴N₂)]⁺ sextet state would provide for more Fe spin density. Merely the [Hemin(O₂)]⁺ (sextet) provides spin density on the adsorbed molecule.

The recorded IR-PD spectrum of [Hemin(CO)₂]⁺ deviates significantly from all spectra of complexes with a single adsorbate molecule, and it reveals an astonishing loss of complexity (Figure 4) that could hint at strongly bound adsorbates resulting in nonlinear multiple photon fragmentation. The spectrum reveals only four bands. Two of these (at 1704 and 1739 cm⁻¹) are observed in the previously discussed

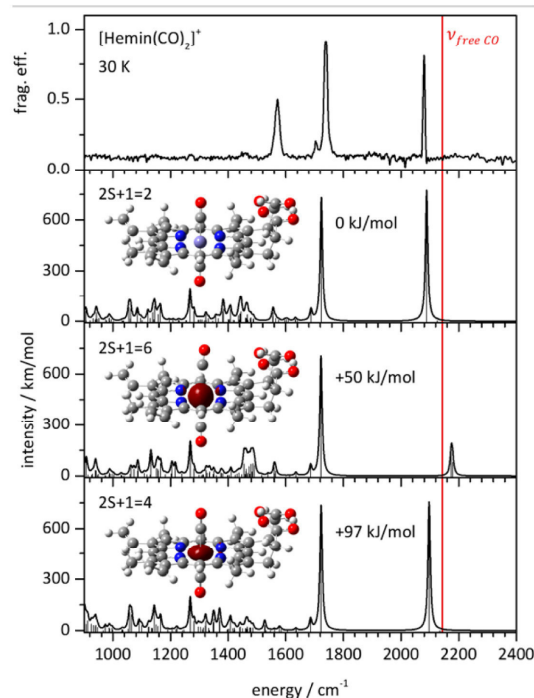


Figure 4. IR-PD spectrum of the [Hemin(CO)₂]⁺ complex (top) and calculated spectra of doublet, quartet, and sextet spin states (below). The presented structures (insets) include isosurface plots of the spin density. The red line is to indicate the stretching frequency of free CO (2143 cm⁻¹).

spectra as well; the other two (at 1570 and 2080 cm⁻¹) are new. The 2080 cm⁻¹ band corresponds to the asymmetric stretching mode of both coupled CO ligands, the symmetric combination lacking IR intensity. In contrast to the [Hemin(CO)₁]⁺ complex, this CO mode is red-shifted by more than 60 cm⁻¹. We thus observe the transition from a nonclassical CO complex ([Hemin(CO)₁]⁺, blue shift of the CO mode) to a classical CO complex ([Hemin(CO)₂]⁺, red shift of the CO mode) upon adsorption of the second CO. This finding is corroborated by our DFT calculations. The nonclassical blue shift is mainly caused by electrostatic interactions⁴⁸ between the positive Fe center (+2.02 by natural population analysis⁴⁹) and the adsorbed CO. The Fe-CO interaction in the [Hemin(CO)₂]⁺ doublet state (+0.18 at the Fe center) bears much less electrostatic character, and it is dominated by the classical π back-donation, which induces the observed red shift of the CO stretch. Note the Fe coordination in the porphyrin plane of the [Hemin(CO)₂]⁺ doublet and the slightly out of plane coordination in the [Hemin(CO)₁]⁺ quartet species (cf. structural data in the supplement). Albeit with too low an intensity, DFT predicts correctly the position of the experimental 1570 cm⁻¹ band in [Hemin(CO)₂]⁺ - a band which is highly delocalized over several porphyrin C-C bonds.

We are confident to predict a spin quenching into a doublet upon the adsorption of a second CO. This quenching is endorsed by the enhanced stability of the doublet - by at least 50 kJ/mol as of our DFT modeling. Crystal field theory would also predict a low spin ground state, as this theory classifies CO as one of the strongest ligands in the spectrochemical series, and it induces a large crystal field splitting in favor of low spin complexes.⁴⁵

CONCLUSIONS

We present the well-resolved gas phase IR spectra of [Hemin]⁺ complexes in isolation. We have identified a negligible spectral effect of single adsorbed molecules - all of these complexes containing a Fe³⁺ in the quartet spin state. The [Hemin(O₂)]⁺ complex is in an overall sextet spin state as the O₂ retains its triplet state upon adsorption. We identify multiple combination bands. We find a nonclassical ([Hemin(CO)₁]⁺) and a classical ([Hemin(CO)₂]⁺) carbonyl complex, which we assign to quartet and to quenched doublet spin states. This study provides for spectroscopic characterization Fe³⁺ heme oxidation products and complexes which are ubiquitously present in hemeproteins and which are in use for the experimental quantification of hemeprotein folding dynamics.

ASSOCIATED CONTENT

Supporting Information

The Supporting Information is available free of charge on the ACS Publications website at DOI: 10.1021/acs.jpca.7b08604.

Detailed experimental and computational methods; gas phase IR spectrum of [Hemin(¹⁴N₂)]⁺ with an extended spectral range; comparison of gas phase and solid state IR spectra; IR PD spectra and structures by additional DFT calculations; xyz files of geometry optimized [Hemin]⁺ complexes (PDF)

AUTHOR INFORMATION

Corresponding Author

*E-mail: gns@chemie.uni-kl.de.

ORCID

Gereon Niedner-Schatteburg: 0000-0001-7240-6673

Notes

The authors declare no competing financial interest.

ACKNOWLEDGMENTS

This work was supported by the DFG founded transregional collaborative research center SFB/TRR 88 "3MET.de" and by the state research center OPTIMAS. We thank the reviewers for valuable comments.

DEDICATION

This work is dedicated to Manfred Kappes in recognition of his seminal contributions to the field of porphyrin chemistry.

REFERENCES

- (1) Drabkin, D. L. In *The Porphyrins*; Dolphin, D., Ed.; Academic Press: New York, USA, 1978; pp 29–83.
- (2) Kepp, K. P. Heme: From Quantum Spin Crossover to Oxygen Manager of Life. *Coord. Chem. Rev.* **2017**, *344*, 363–374.
- (3) Perutz, M. F.; Fermi, G.; Luisi, B.; Shaanan, B.; Liddington, R. C. Stereochemistry of Cooperative Mechanisms in Hemoglobin. *Acc. Chem. Res.* **1987**, *20*, 309–321.
- (4) Springer, B. A.; Sligar, S. G.; Olson, J. S.; Phillips, G. N., Jr Mechanisms of Ligand Recognition in Myoglobin. *Chem. Rev.* **1994**, *94*, 699–714.
- (5) Poulos, T. L. Heme Enzyme Structure and Function. *Chem. Rev.* **2014**, *114*, 3919–3962.
- (6) Meunier, B. Metalloporphyrins as Versatile Catalysts for Oxidation Reactions and Oxidative DNA Cleavage. *Chem. Rev.* **1992**, *92*, 1411–1456.
- (7) Pauling, L.; Coryell, C. D. The Magnetic Properties and Structure of Hemoglobin, Oxyhemoglobin and Carbonmonoxyhemoglobin. *Proc. Natl. Acad. Sci. U. S. A.* **1936**, *22*, 210–216.
- (8) Pauling, L.; Weiss, J. J. Nature of Iron-Oxygen Bond in Oxyhaemoglobin. *Nature* **1964**, *203*, 182–183.
- (9) Chen, H.; Ikeda-Saito, M.; Shaik, S. Nature of the Fe–O₂ Bonding in Oxy-Myoglobin: Effect of the Protein. *J. Am. Chem. Soc.* **2008**, *130*, 14778–14790.
- (10) Linberg, R.; Conover, C. D.; Shum, K. L. Hemoglobin Based Oxygen Carriers: How Much Methemoglobin Is Too Much?, *Artificial Cells. Blood Substitutes, and Biotechnology* **1998**, *26*, 133–148.
- (11) Faraone-Mennella, J.; Gray, H. B.; Winkler, J. R. Early Events in the Folding of Four-Helix-Bundle Heme Proteins. *Proc. Natl. Acad. Sci. U. S. A.* **2005**, *102*, 6315–6319.
- (12) Karpuschkin, T.; Kappes, M. M.; Hampe, O. Binding of O₂ and CO to Metal Porphyrin Anions in the Gas Phase. *Angew. Chem., Int. Ed.* **2013**, *52*, 10374–10377.
- (13) Chiavarino, B.; Crestoni, M. E.; Fornarini, S.; Rovira, C. Unravelling the Intrinsic Features of NO Binding to Iron(II)- and Iron(III)-Hemes. *Inorg. Chem.* **2008**, *47*, 7792–7801.
- (14) De Petris, A.; Chiavarino, B.; Crestoni, M. E.; Coletti, C.; Re, N.; Fornarini, S. Exploring the Conformational Variability in the Heme b Propionic Acid Side Chains Through the Effect of a Biological Probe: A Study of the Isolated Ions. *J. Phys. Chem. B* **2015**, *119*, 1919–1929.
- (15) Chiavarino, B.; Crestoni, M. E.; Fornarini, S. Intrinsic Properties of Nitric Oxide Binding to Ferrous and Ferric Hemes. *Croat. Chem. Acta* **2014**, *87*, 307–314.
- (16) Crestoni, M. E.; Fornarini, S. Compound I of Naked Heme (Iron Protoporphyrin IX). *Inorg. Chem.* **2007**, *46*, 9018–9020.
- (17) Angelelli, F.; Chiavarino, B.; Crestoni, M. E.; Fornarini, S. Binding of Gaseous Fe(III)-Heme Cation to Model Biological Molecules: Direct Association and Ligand Transfer Reactions. *J. Am. Soc. Mass Spectrom.* **2005**, *16*, 589–598.
- (18) De Petris, A.; Crestoni, M. E.; Pirolli, A.; Rovira, C.; Iglesias-Fernández, J.; Chiavarino, B.; Ragno, R.; Fornarini, S. Binding of Azole

Drugs to Heme: A Combined MS/MS and Computational Approach, *Polyhedron* **2015**, *90*, 245–251.

(19) Lanucara, F.; Chiavarino, B.; Crestoni, M. E.; Scuderi, D.; Sinha, R. K.; Maitre, P.; Fornarini, S. Naked Five-Coordinate Fe(III) (NO) Porphyrin Complexes: Vibrational and Reactivity Features. *Inorg. Chem.* **2011**, *50*, 4445–4452.

(20) Siu, C. K.; Guo, Y. Z.; Hopkinson, A. C.; Siu, K. W. M. How Large Is the Fe-III(Protoporphyrin IX)⁺ Ion (Hemin⁺) in the Gas Phase? *J. Phys. Chem. B* **2006**, *110*, 24207–24211.

(21) Dörr, S.; Schade, U.; Hellwig, P. Far Infrared Spectroscopy on Hemoproteins: A Model Compound Study From 1800–100 cm⁻¹. *Vib. Spectrosc.* **2008**, *47*, 59–65.

(22) Lykkegaard, M. K.; Ehlerding, A.; Hvelplund, P.; Kadhane, U.; Kirketerp, M.-B. S.; Nielsen, S. B.; Panja, S.; Wyer, J. A.; Zettergren, H. A Soret Marker Band for Four-Coordinate Ferric Heme Proteins from Absorption Spectra of Isolated Fe(III)-Heme⁺ and Fe(III)-Heme⁺(His) Ions in Vacuo. *J. Am. Chem. Soc.* **2008**, *130*, 11856–11857.

(23) Wyer, J. A.; Nielsen, S. B. Absorption in the Q-Band Region by Isolated Ferric Heme⁺ and Heme⁺(Histidine) In Vacuo. *J. Chem. Phys.* **2010**, *133*, 084306.

(24) Wyer, J. A.; Brøndsted Nielsen, S. Absorption by Isolated Ferric Heme Nitrosyl Cations In Vacuo. *Angew. Chem., Int. Ed.* **2012**, *51*, 10256–10260.

(25) Lanucara, F.; Scuderi, D.; Chiavarino, B.; Fornarini, S.; Maitre, P.; Crestoni, M. E. IR Signature of NO Binding to a Ferrous Heme Center. *J. Phys. Chem. Lett.* **2013**, *4*, 2414–2417.

(26) Chiavarino, B.; Crestoni, M. E.; Fornarini, S.; Lanucara, F.; Lemaire, J.; Maitre, P.; Scuderi, D. Direct Probe of NO Vibration in the Naked Ferric Heme Nitrosyl Complex. *ChemPhysChem* **2008**, *9*, 826–828.

(27) Ferrand, L.; Soorkia, S.; Gregoire, G.; Broquier, M.; Soep, B.; Shafizadeh, N. Bonding of Heme Fe-III with Dioxygen: Observation and Characterization of an Incipient Bond. *Phys. Chem. Chem. Phys.* **2015**, *17*, 25693–25699.

(28) Shafizadeh, N.; Soorkia, S.; Gregoire, G.; Broquier, M.; Crestoni, M.-E.; Soep, B. Dioxygen Binding to Protonated Heme in the Gas Phase, an Intermediate Between Ferric and Ferrous Heme. *Chem. - Eur. J.* **2017**, DOI: 10.1002/chem.201702615.

(29) Mohrbach, J.; Lang, J.; Dillinger, S.; Proscenc, M.; Braunstein, P.; Niedner-Schatteburg, G. Vibrational Fingerprints of a Tetranuclear Cobalt Carbonyl Cluster Within a Cryo Tandem Ion Trap. *J. Mol. Spectrosc.* **2017**, *332*, 103–108.

(30) Caravatti, P.; Allemann, M. The 'Infinity Cell': A New Trapped-Ion Cell with Radiofrequency Covered Trapping Electrodes for Fourier Transform Ion Cyclotron Resonance Mass Spectrometry. *Org. Mass Spectrom.* **1991**, *26*, 514–518.

(31) Dunning, T., Jr. H., Gaussian Basis Sets for Use in Correlated Molecular Calculations. I. The Atoms Boron Through Neon and Hydrogen. *J. Chem. Phys.* **1989**, *90*, 1007–1023.

(32) Woon, D. E.; Dunning, T. H., Jr. Gaussian Basis Sets for Use in Correlated Molecular Calculations. III. The Atoms Aluminum Through Argon. *J. Chem. Phys.* **1993**, *98*, 1358–1371.

(33) Hariharan, P. C.; Pople, J. A. Influence of Polarization Functions on Molecular-Orbital Hydrogenation Energies. *Theor. Chim. Acta* **1973**, *28*, 213–222.

(34) Dolg, M.; Stoll, H.; Preuss, H.; Pitzer, R. M. Relativistic and Correlation Effects for Element 105 (Hahnium, Ha): a Comparative Study of M and MO (M = Nb, Ta, Ha) Using Energy-Adjusted Ab Initio Pseudopotentials. *J. Phys. Chem.* **1993**, *97*, 5852–5859.

(35) Frisch, M. J.; Trucks, G. W.; Schlegel, H. B.; Scuseria, G. E.; Robb, M. A.; Cheeseman, J. R.; Scalmani, G.; Barone, V.; Mennucci, B.; Petersson, G. A., et al. *Gaussian 09*, Revision D.01; Gaussian, Inc.: Wallingford, CT, 2013.

(36) Grimme, S.; Antony, J.; Ehrlich, S.; Krieg, H. A Consistent and Accurate Ab Initio Parametrization of Density Functional Dispersion Correction (DFT-D) for the 94 Elements H-Pu. *J. Chem. Phys.* **2010**, *132*, 154104.

(37) Owens, J. W.; O'Connor, C. J. Comparison of the Electronic and Vibrational-Spectra of Complexes of Protoporphyrin-IX, Hemioctapeptid, and Heme-Proteins. *Coord. Chem. Rev.* **1988**, *84*, 1–45.

(38) Rizzo, T. R.; Boyarkin, O. V. In *Gas-Phase IR Spectroscopy and Structure of Biological Molecules*; Rijs, A. M., Oomens, J., Eds.; Springer International Publishing: Cham, Switzerland, 2015; pp 43–97, DOI: 10.1007/128_2014_579.

(39) Stamm, A.; Bernhard, D.; Gerhards, M. Structural Investigations on a Linear Isolated Depsipeptide: The Importance of Dispersion Interactions. *Phys. Chem. Chem. Phys.* **2016**, *18*, 15327–15336.

(40) Golnak, R.; Xiao, J.; Atak, K.; Stevens, J. S.; Gainar, A.; Schroeder, S. L. M.; Aziz, E. F. Intermolecular Bonding of Hemin in Solution and in Solid State Probed by N K-Edge X-Ray Spectroscopies. *Phys. Chem. Chem. Phys.* **2015**, *17*, 29000–29006.

(41) Kaduk, J. A.; Wong-Ng, W.; Cook, L. P.; Chakraborty, B.; Lapidus, S. H.; Ribaud, L.; Brewer, G. Synchrotron X-ray Investigation of α -Chlorohemin, C₃₄H₃₂ClFeN₄O₄, an Fe-Porphyrin. *Solid State Sci.* **2016**, *53*, 63–70.

(42) Charkin, O. P.; Klimenko, N. M.; Charkin, D. O.; Chang, H. C.; Lin, S. H. Theoretical DFT Study of Fragmentation and Association of Heme and Hemin. *J. Phys. Chem. A* **2007**, *111*, 9207–9217.

(43) Haynes, W. M. *CRC Handbook of Chemistry and Physics*, 93rd Edition; Taylor & Francis: Boca Raton, USA, 2012.

(44) Lang, J.; Mohrbach, J.; Dillinger, S.; Hewer, J. M.; Niedner-Schatteburg, G. Vibrational Blue Shift of Coordinated N₂ in [Fe₃O(OAc)₆(N₂)_n]⁺: "Non-Classical" Dinitrogen Complexes. *Chem. Commun.* **2017**, *53*, 420–423.

(45) Janiak, C.; Meyer, H. J.; Riedel, E.; Alsfasser, R.; Gudat, D. *Moderne Anorganische Chemie*; De Gruyter: Berlin, Germany, 2012.

(46) Hurlburt, P. K.; Rack, J. J.; Luck, J. S.; Dec, S. F.; Webb, J. D.; Anderson, O. P.; Strauss, S. H. Nonclassical Metal Carbonyls: [Ag(CO)]⁺ and [Ag(CO)₂]⁺. *J. Am. Chem. Soc.* **1994**, *116*, 10003–10014.

(47) Willner, H.; Aubke, F. Homoleptic Metal Carbonyl Cations of the Electron-Rich Metals: Their Generation in Superacid Media Together with Their Spectroscopic and Structural Characterization. *Angew. Chem., Int. Ed. Engl.* **1997**, *36*, 2402–2425.

(48) Goldman, A. S.; Krogh-Jespersen, K. Why Do Cationic Carbon Monoxide Complexes Have High C–O Stretching Force Constants and Short C–O Bonds? Electrostatic Effects, Not σ -Bonding. *J. Am. Chem. Soc.* **1996**, *118*, 12159–12166.

(49) Reed, A. E.; Weinstock, R. B.; Weinhold, F. Natural Population Analysis. *J. Chem. Phys.* **1985**, *83*, 735–746.

9.3 Supporting Information

Table of Content:

Detailed Experimental and Computational Methods

Figure S1. Schematic drawing of our tandem cryo trap FT-ICR MS.

Scheme S1. Molecular structure of Hemin ($\text{Fe}^{\text{III}}\text{C}_{34}\text{H}_{32}\text{N}_4\text{O}_4\text{Cl}$) and $[\text{Hemin}]^+$ ($[\text{Fe}^{\text{III}}\text{C}_{34}\text{H}_{32}\text{N}_4\text{O}_4]^+$).

Figure S2. IR-PD spectrum of $[\text{Hemin}({}^{14}\text{N}_2)]^+$ in the region from 2800 to 3800 cm^{-1} .

Figure S3. Comparison of the gas phase IR-PD spectrum of $[\text{Hemin}({}^{14}\text{N}_2)]^+$ and a solid state IR spectrum of Hemin recorded via attenuated total reflection FTIR spectroscopy.

Figure S4. IR-PD spectra of $[\text{Hemin}({}^{14}\text{N}_2)]^+$ recorded with different laser powers.

Figure S5. Illustration of different possible adsorption sites for the reaction gases.

Figure S6. IR-PD spectrum of $[\text{Hemin}({}^{14}\text{N}_2)]^+$ in comparison with DFT calculations of different adsorption sites (trans and cis) and spin states (doublet, quartet and sextet).

Figure S7. IR-PD spectrum of $[\text{Hemin}(\text{CO})_1]^+$ in comparison with DFT calculations of different adsorption sites (trans and cis) and spin states (doublet, quartet and sextet).

Figure S8. IR-PD spectrum of $[\text{Hemin}(\text{O}_2)]^+$ in comparison with DFT calculations of different adsorption sites (trans and cis) and spin states (quartet and sextet).

Table S1. Calculated IR frequencies and intensities of the ${}^{14}\text{N}_2$ in $[\text{Hemin}({}^{14}\text{N}_2)]^+$.

Figure S9. IR-PD spectrum of $[\text{Hemin}({}^{14}\text{N}_2)]^+$ in comparison with DFT calculations of the energetically most favored isomers (cis quartet and trans quartet).

Figure S10. IR-PD spectra of the $[\text{Hemin}]^+$ adsorbate complexes.

Figure S11. Isosurfaces of the spin density of the $[\text{Hemin}(\text{O}_2)]^+$ cis quartet isomer with the $[\text{Hemin}({}^{14}\text{N}_2)]^+$ cis quartet and sextet.

Figure S12. Isosurfaces of the spin density of the $[\text{Hemin}(\text{CO})_2]^+$ doublet with a isovalue of the spin density of 0.02 (default) and an decreased value of 0.002 in comparison with the spin densities of the $[\text{Hemin}(\text{CO})_1]^+$ doublet and $[\text{Hemin}({}^{14}\text{N}_2)]^+$ doublet, both default isovalues.

Figure S13. IR-PD spectrum of $[\text{Hemin}({}^{14}\text{N}_2)]^+$ in comparison with DFT calculations with different basis sets (6-311++G** and 6-31+G*) of the cis quartet isomer.

Figure S14. IR-PD spectrum of $[\text{Hemin}({}^{14}\text{N}_2)]^+$ in comparison with DFT calculations with different basis sets (cc-pVDZ and 6-31+G*) of the cis quartet isomer.

Figure S15. IR-PD spectrum of [Hemin(¹⁴N₂)]⁺ in comparison with DFT calculations with different functionals (PBE0 and B3LYP) of the cis quartet isomer.

Figure S16. IR-PD spectrum of [Hemin(¹⁴N₂)]⁺ in comparison with DFT calculations of different isomers containing two, one or no hydrogen bonds (HBB).

XYZ-Files of Geometry Optimized [Hemin]⁺ Complexes

Detailed Experimental and Computational Methods:

We utilized a customized Fourier Transform Ion Cyclotron Resonance (FT-ICR) mass spectrometer (Apex Ultra, Bruker Daltonics)¹ for generation of the species of interest and the subsequent InfraRed Photon Dissociation (IR-PD) spectroscopy. This mass spectrometer is equipped with an Electrospray Ionization (ESI) source (Apollo 2, Bruker) and a home-built laser vaporization cluster ion source^{2 3} (Figure S1).

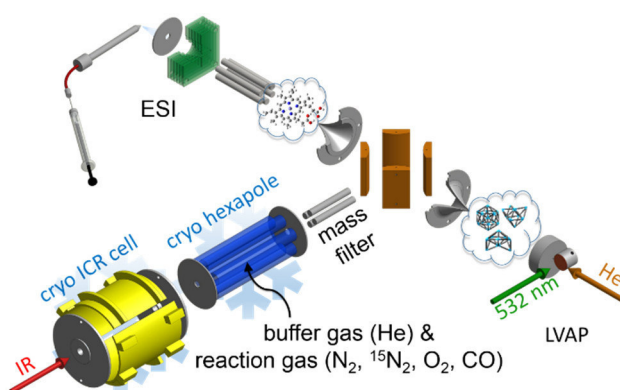
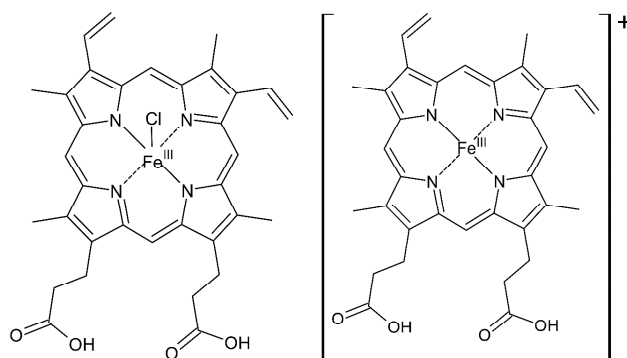


Figure S1. Schematic drawing of our tandem cryo trap FT-ICR MS. The ions can be generated via Electro Spray Ionization (ESI) or Laser VAPorization (LVAP). The ions enter the cryo hexapole after passing several ion optics and a quadrupole mass filter. The hexapole is held at a constant temperature between 11 and 300 K. Reaction gas and buffer gas can be introduced in this ion trap. The manipulated ions are transferred into the cryo ICR cell after a variable reaction time. In the cryo ICR cell the ions are isolated, irradiated with an IR laser and detected.

Hemin ($\text{FeC}_{34}\text{H}_{32}\text{N}_4\text{O}_4\text{Cl}$, Scheme S1 left) was purchased from Sigma Aldrich and used without further purification. Sample solutions of the Hemin complex in methanol at the concentration of 1×10^{-4} mol/l were continuously infused into the ESI source by a syringe pump at a flow rate of $2 \mu\text{L min}^{-1}$. The ion source was set to positive electrospray ionization mode. Nitrogen was used as drying gas with a flow rate of 3.0 L min^{-1} at 200°C . The solutions were electro-sprayed at a nebulizer flow of 1.5 L min^{-1} and the spray shield was held at 3.6 kV. We detect the $[\text{Hemin}]^+$ ($\text{FeC}_{34}\text{H}_{32}\text{N}_4\text{O}_4$, Scheme S1 right).



Scheme S1 Molecular structure of Hemin ($\text{Fe}^{\text{III}}\text{C}_{34}\text{H}_{32}\text{N}_4\text{O}_4\text{Cl}$, left) and $[\text{Hemin}]^+$ ($[\text{Fe}^{\text{III}}\text{C}_{34}\text{H}_{32}\text{N}_4\text{O}_4]^+$) generated via electro spray ionization (right).

We mass selected the $[\text{Hemin}]^+$ by our quadrupole mass filter and guided it into the hexapole ion trap which was held at a constant temperature. The ion trap is cooled by a closed cycle Helium cryostat. Reaction gas (CO , $^{14}\text{N}_2$, $^{15}\text{N}_2$ and O_2) was continuously introduced in the ion trap. The pressure of about 1.7×10^{-7} mbar is increased up to 5.0×10^{-7} mbar to yield sufficient amounts of adsorbate complexes. The temperature was adjusted to the respective reaction gas (30 K for CO , 28 K for $^{14}\text{N}_2$ and $^{15}\text{N}_2$, 45 K for O_2). The pressure is further increased up to 3.0×10^{-6} mbar to accomplish efficient trapping and cooling of the ions. Both gases were introduced continuously. The manipulated ions are guided by electrostatic lenses into the FT-ICR cell of the so-called “infinity” type.⁴ This cell is cooled to a temperature of about 10 K with a closed cycle Helium cryostat to prevent heating of the clusters by black body radiation. The ICR cell is used for trapping, isolation and detection of the ions. It is coupled to a tunable pulsed IR laser ($\Delta\tilde{\nu} = 0.9 \text{ cm}^{-1}$, $\Delta t = 7 \text{ ns}$. Note, that the modest mass difference between CO and N_2 of about 0.01 amu can be accurately resolved with our experimental setup.

The IR laser is a KTP/KTA optical parametric oscillator/amplifier (OPO/OPA, LaserVision) system pumped by a pulsed 10 Hz injection seeded Nd^{3+} :YAG laser (Continuum, Powerlite DLS 8000). In this work we used the difference frequency (DF) between the OPA signal and idler waves generated in a AgGaSe_2 crystal (0.1 – 1.2 mJ per pulse). We recorded IR-PD spectra in the range of $900 - 2400 \text{ cm}^{-1}$. Each trapped and isolated package of ions is irradiated by 10 laser pulses to yield a sufficient amount of fragment ions. The IR-PD spectra were recorded as ion chromatograms while continuously scanning the IR frequency (typically $< 0.2 \text{ cm}^{-1}/\text{s}$). The IR-PD signal was evaluated as $\Sigma F_i / (\Sigma_i F_i + \Sigma P_i)$, where F_i and P_i indicate the

fragment and the parent ion signals, respectively. An experimental IR-PD spectrum arises from a plot of the fragmentation efficiency as a function of laser frequency.

Optimized minimum energy structures and linear IR absorption spectra were calculated at the B3LYP^{5,6} level of theory using 6-31+G* basis sets (C, H, N, O)⁷, and Stuttgart RSC 1997⁸ effective core potential (Fe) basis sets, respectively, as implemented in the Gaussian 09 program package.⁹ We included the Grimme correction for dispersion (GD3).¹⁰ Standard convergence criteria were applied. We checked several spin states (doublet, quartet, sextet). We checked different basis sets and a different functional which did not provide for a significant improvement/better agreements (*cf.* Figure S12 – S14). Full geometry optimization of all nuclear coordinates yields multiple local minimum structures. The lowest energy structure is assumed to represent the most stable isomer. We scaled the calculated harmonic vibrational frequencies by a factor of 0.97 and broadened using the Lorentz profile (FWHM = 5 cm⁻¹).

References:

- (1) Mohrbach, J.; Lang, J.; Dillinger, S.; Prosenc, M.; Braunstein, P.; Niedner-Schatteburg, G., Vibrational Fingerprints of a Tetranuclear Cobalt Carbonyl Cluster within a Cryo Tandem Ion Trap, *J. Mol. Spectrosc.* **2017**, *332*, 103-108.
- (2) Maruyama, S.; Anderson, L. R.; Smalley, R. E., Direct Injection Supersonic Cluster Beam Source for FT-ICR Studies of Clusters, *Rev. Sci. Instrum.* **1990**, *61*, 3686-3693.
- (3) Berg, C.; Schindler, T.; Niedner-Schatteburg, G.; Bondybey, V. E., Reactions of Simple Hydrocarbons with Nb⁺: Chemisorption and Physisorption on Ionized Niobium Clusters, *J. Chem. Phys.* **1995**, *102*, 4870-4884.
- (4) Caravatti, P.; Allemann, M., The 'Infinity Cell': A New Trapped-Ion Cell with Radiofrequency Covered Trapping Electrodes for Fourier Transform Ion Cyclotron Resonance Mass Spectrometry, *Org. Mass Spectrom.* **1991**, *26*, 514-518.
- (5) Dunning Jr, T. H., Gaussian Basis Sets for Use in Correlated Molecular Calculations. I. The Atoms Boron Through Neon and Hydrogen, *J. Chem. Phys.* **1989**, *90*, 1007-1023.
- (6) Woon, D. E.; Dunning Jr, T. H., Gaussian Basis Sets for Use in Correlated Molecular Calculations. III. The Atoms Aluminum Through Argon, *J. Chem. Phys.* **1993**, *98*, 1358-1371.
- (7) Hariharan, P.; Pople, J. A., Influence of Polarization Functions on Molecular-Orbital Hydrogenation Energies, *Theor. Chim. Acta* **1973**, *28*, 213-222.

- (8) Dolg, M.; Stoll, H.; Preuss, H.; Pitzer, R. M., Relativistic and Correlation Effects for Element 105 (Hahnium, Ha): a Comparative Study of M and MO (M= Nb, Ta, Ha) Using Energy-Adjusted Ab Initio Pseudopotentials, *J. Phys. Chem.* **1993**, *97*, 5852-5859.
- (9) Frisch, M. J.; Trucks, G. W.; Schlegel, H. B.; Scuseria, G. E.; Robb, M. A.; Cheeseman, J. R.; Scalmani, G.; Barone, V.; Mennucci, B.; Petersson, G. A.; Nakatsuji, H.; Caricato, M.; Li, X.; Hratchian, H. P.; Izmaylov, A. F.; Bloino, J.; Zheng, G.; Sonnenberg, J. L.; Hada, M.; Ehara, M.; Toyota, K.; Fukuda, R.; Hasegawa, J.; Ishida, M.; Nakajima, T.; Honda, Y.; Kitao, O.; Nakai, H.; Vreven, T.; Montgomery, J. A., Jr.; Peralta, J. E.; Ogliaro, F.; Bearpark, M.; Heyd, J. J.; Brothers, E.; Kudin, K. N.; Staroverov, V. N.; Kobayashi, R.; Normand, J.; Raghavachari, K.; Rendell, A.; Burant, J. C.; Iyengar, S. S.; Tomasi, J.; Cossi, M.; Rega, N.; Millam, J. M.; Klene, M.; Knox, J. E.; Cross, J. B.; Bakken, V.; Adamo, C.; Jaramillo, J.; Gomperts, R.; Stratmann, R. E.; Yazyev, O.; Austin, A. J.; Cammi, R.; Pomelli, C.; Ochterski, J. W.; Martin, R. L.; Morokuma, K.; Zakrzewski, V. G.; Voth, G. A.; Salvador, P.; Dannenberg, J. J.; Dapprich, S.; Daniels, A. D.; Farkas, Ö.; Foresman, J. B.; Ortiz, J. V.; Cioslowski, J.; Fox, D. J., *Gaussian 09*, Revision D.01; Gaussian, Inc.: Wallingford, CT 2013.
- (10) Grimme, S.; Antony, J.; Ehrlich, S.; Krieg, H., A Consistent and Accurate Ab Initio Parametrization of Density Functional Dispersion Correction (DFT-D) for the 94 Elements H-Pu, *J. Chem. Phys.* **2010**, *132*, 154104-1 - 154104-19.

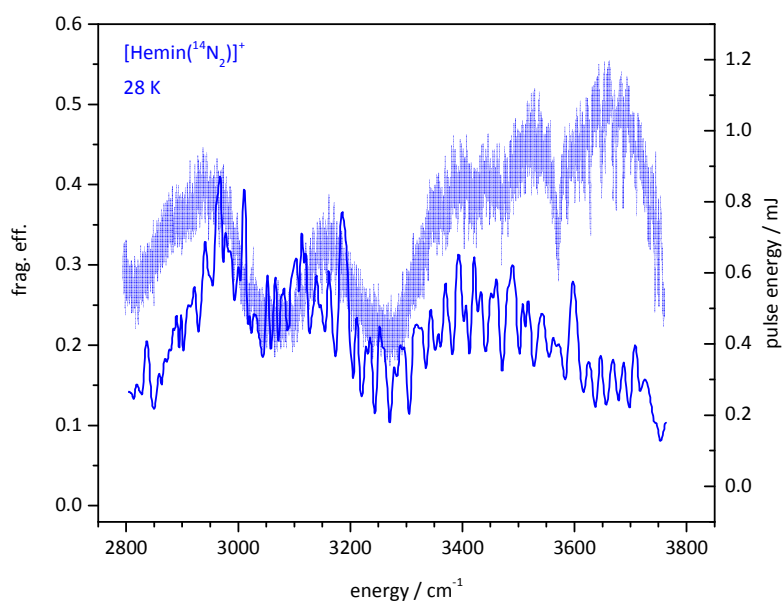


Figure S2. IR-PD spectrum of [Hemin(¹⁴N₂)]⁺ in the region from 2800 to 3800 cm⁻¹ including the power curve of the laser.

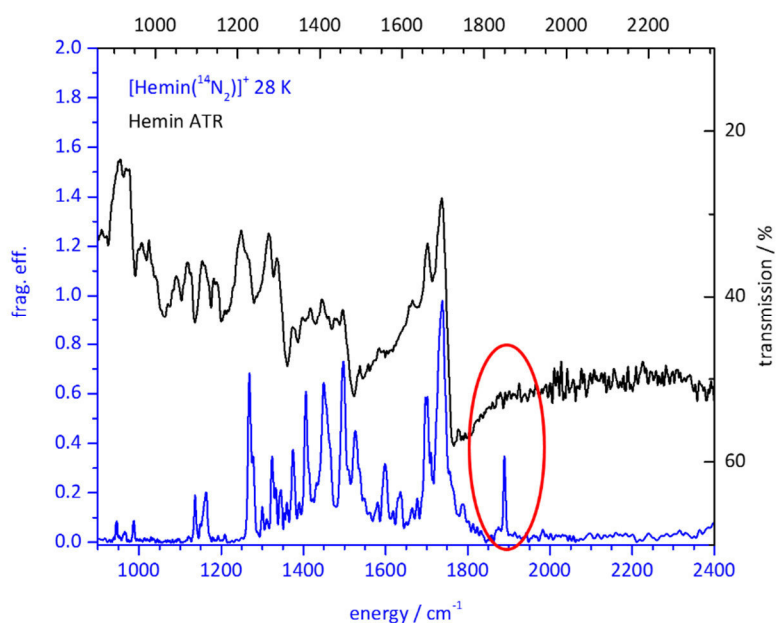


Figure S3. Comparison of the gas phase IR-PD spectrum of [Hemin(¹⁴N₂)]⁺ and a solid state IR spectrum of Hemin recorded via attenuated total reflection IR spectroscopy. Note that the solid state spectrum is shifted by 40 cm⁻¹ to align the most abundant bands. In general many similarities between both spectra are observed. Yet the gas phase spectrum shows much better resolved bands. The red circle is to highlight the band at about 1890 cm⁻¹ which is present in the gas phase but not in solid state.

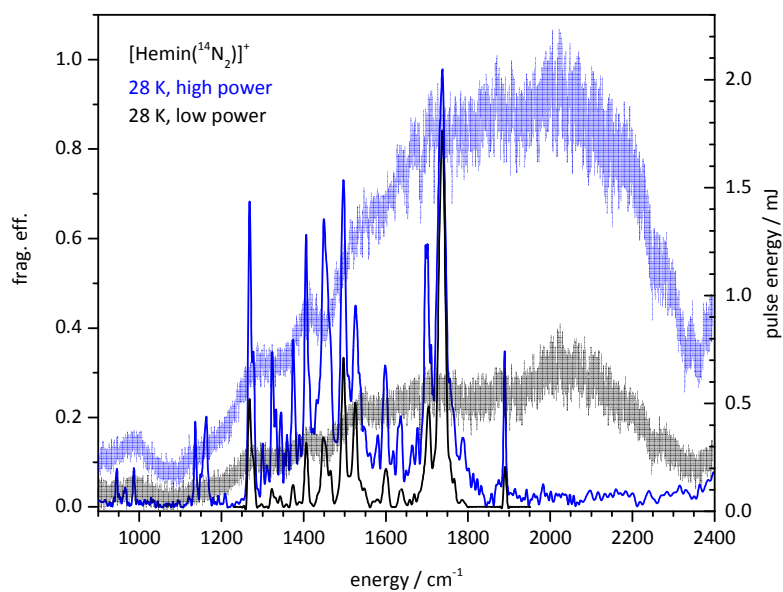


Figure S4. IR-PD spectra of [Hemin(¹⁴N₂)]⁺ recorded with different laser powers.

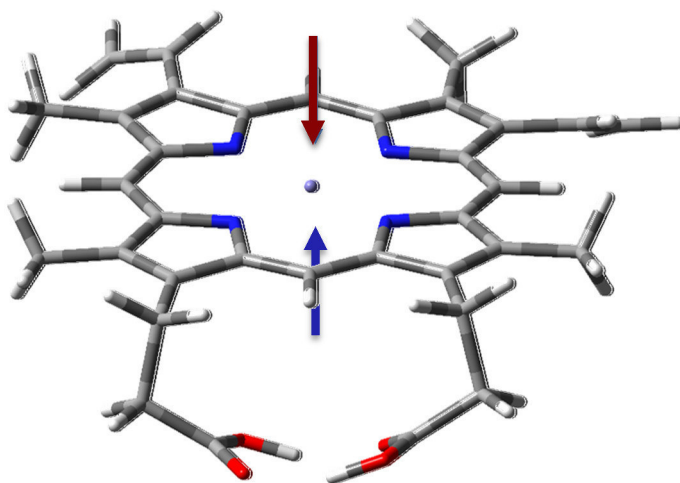


Figure S5. Illustration of different possible adsorption sites for the reaction gases. The molecules can attach either on the trans (red arrow) or on the cis (blue arrow) of the [Hemin]⁺. We will apply this nomenclature in the following calculated spectra.

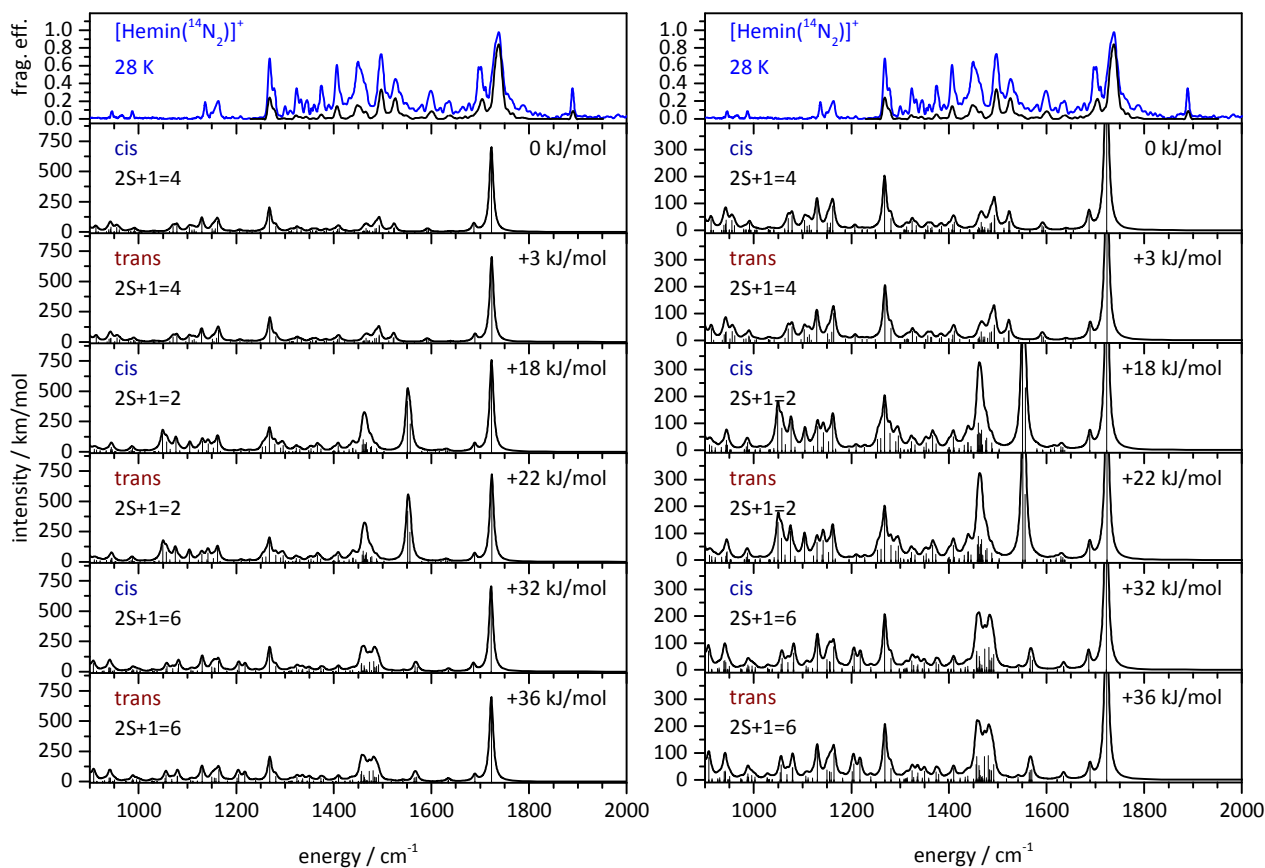


Figure S6. IR-PD spectrum of [Hemin(¹⁴N₂)]⁺ in comparison with DFT calculations of different adsorption sites (trans and cis, cf. Figure 4) and spin states (doublet, quartet and sextet). The black IR-PD spectrum was measured with attenuated laser power (cf. Figure S3). Calculations were performed at the B3LYP level of theory including the Grimme dispersion correction (GD3) using 6-31+G* (C, H, N, O) and Stuttgart RSC 1997 effective core potential (Fe) basis sets. The calculated harmonic vibrations were scaled by a factor of 0.97.

9. Cryo IR Spectroscopy of [Hemin]⁺ Complexes in Isolation

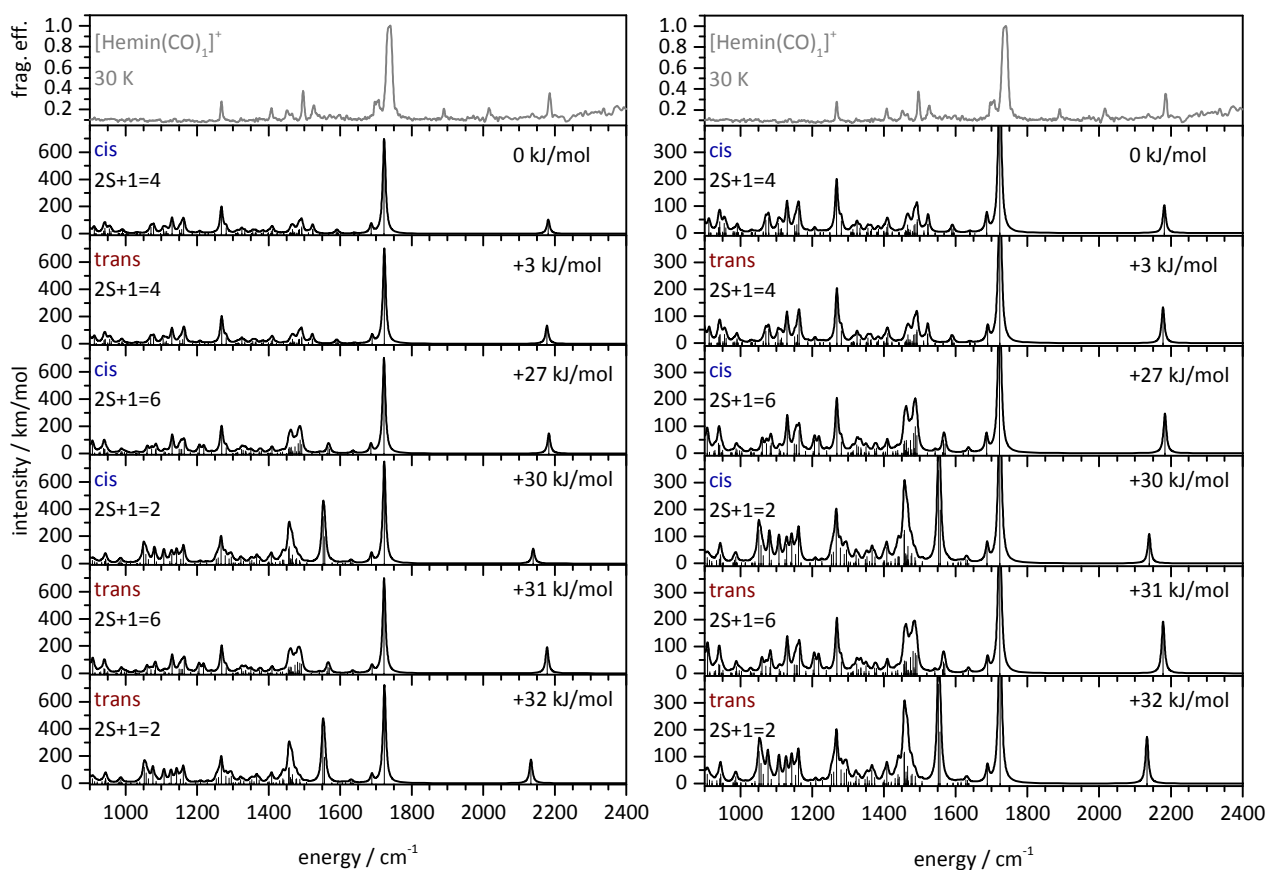


Figure S7. IR-PD spectrum of [Hemin(CO)₁]⁺ in comparison with DFT calculations of different adsorption sites (trans and cis) and spin states (doublet, quartet and sextet). Calculations were performed at the B3LYP level of theory including the Grimme dispersion correction (GD3) using 6-31+G* (C, H, N, O) and Stuttgart RSC 1997 effective core potential (Fe) basis sets. The calculated harmonic vibrations were scaled by a factor of 0.97.

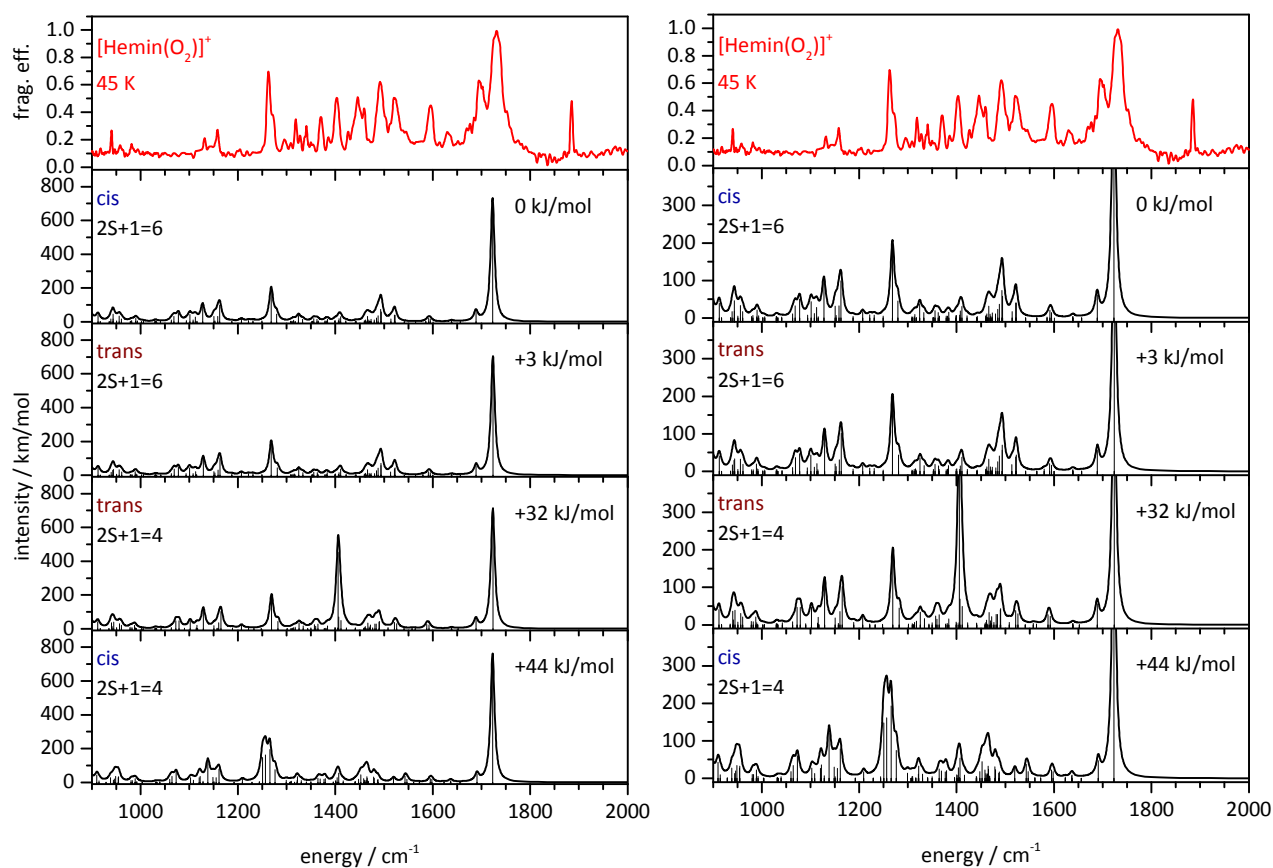


Figure S8. IR-PD spectrum of [Hemin(O₂)]⁺ in comparison with DFT calculations of different adsorption sites (trans and cis) and spin states (quartet and sextet). Calculations were performed at the B3LYP level of theory including the Grimme dispersion correction (GD3) using 6-31+G* (C, H, N, O) and Stuttgart RSC 1997 effective core potential (Fe) basis sets. The calculated harmonic vibrations were scaled by a factor of 0.97. The calculated spectra with a doublet spin state are not shown as they converged to a quartet spin state during the optimization process.

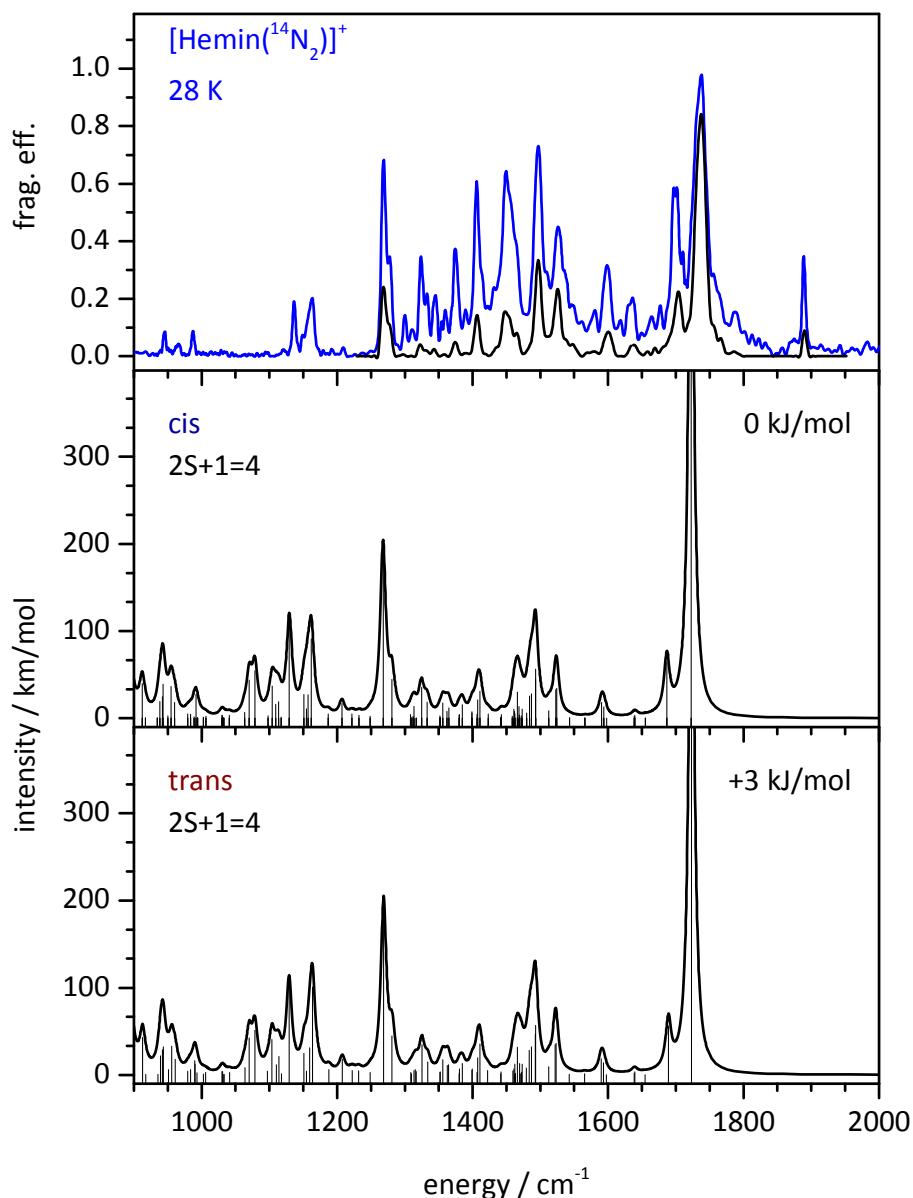


Figure S9. IR-PD spectrum of [Hemin(¹⁴N₂)]⁺ in comparison with DFT calculations of the energetically most favored isomers (cis quartet and trans quartet). The black IR-PD spectrum was measured with attenuated laser power (cf. Figure S3). Both calculated spectra look almost identical. However, the cis isomer is 3 kJ/mol lower in energy. Calculations were performed at the B3LYP level of theory including the Grimme dispersion correction (GD3) using 6-31+G* (C, H, N, O) and Stuttgart RSC 1997 effective core potential (Fe) basis sets. The calculated harmonic vibrations were scaled by a factor of 0.97. The calculated spectra with a doublet spin state are not shown as they converged to a quartet spin state during the optimization process.

Table S1. Calculated IR frequencies and intensities of the ¹⁴N₂ in [Hemin(¹⁴N₂)]⁺.

[Hemin(¹⁴ N ₂)] ⁺ isomer	IR frequency (unscaled) / cm ⁻¹	IR frequency (scaled by 0.97) / cm ⁻¹	IR intensity / km/mol
cis quartet	2463.48	2389.57	2.3
trans quartet	2462.78	2388.89	1.7
cis doublet	2453.69	2380.08	0.9
trans doublet	2449.93	2376.43	0.4
cis sextet	2461.52	2387.68	0.9
trans sextet	2460.41	2386.59	0.5

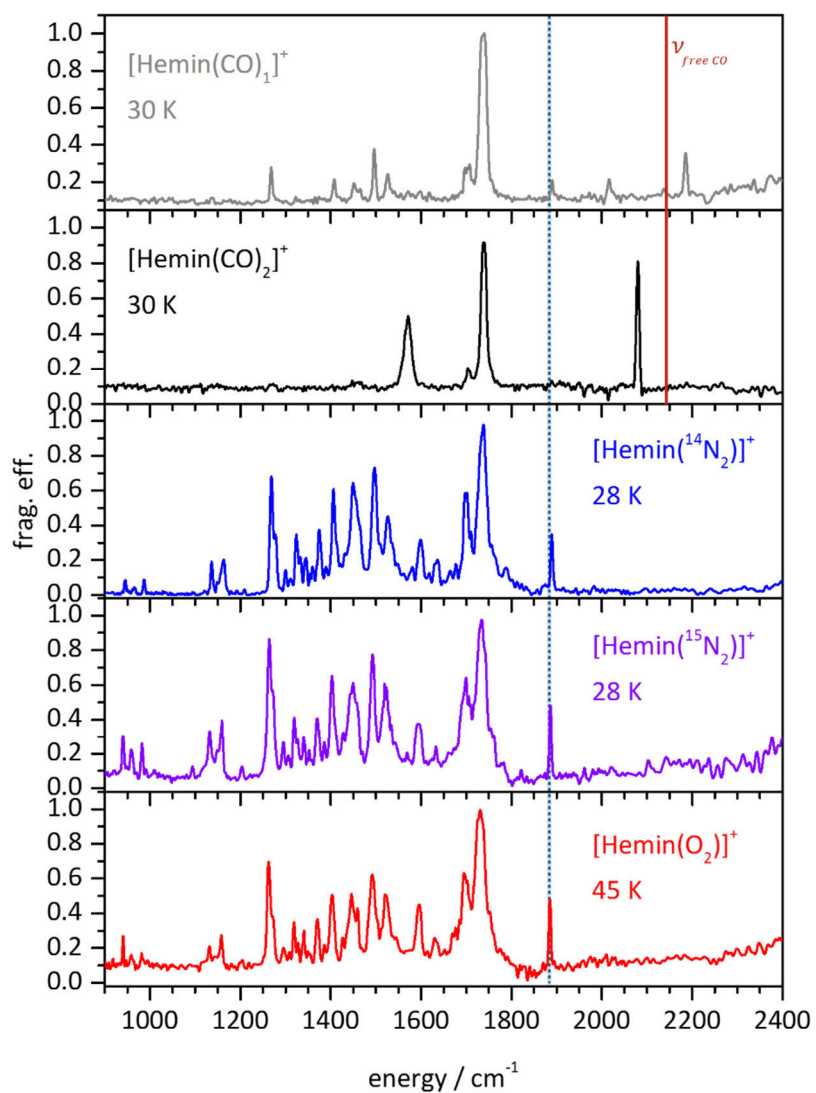


Figure S10. IR-PD spectra of the [Hemin]⁺ adsorbate complexes. The red line is to indicate the stretching frequency of free CO (2143 cm⁻¹). The blue dotted line is to highlight the well resolved band which is not present in the solid state / is only visible in the gas phase (*cf.* Figure S3).

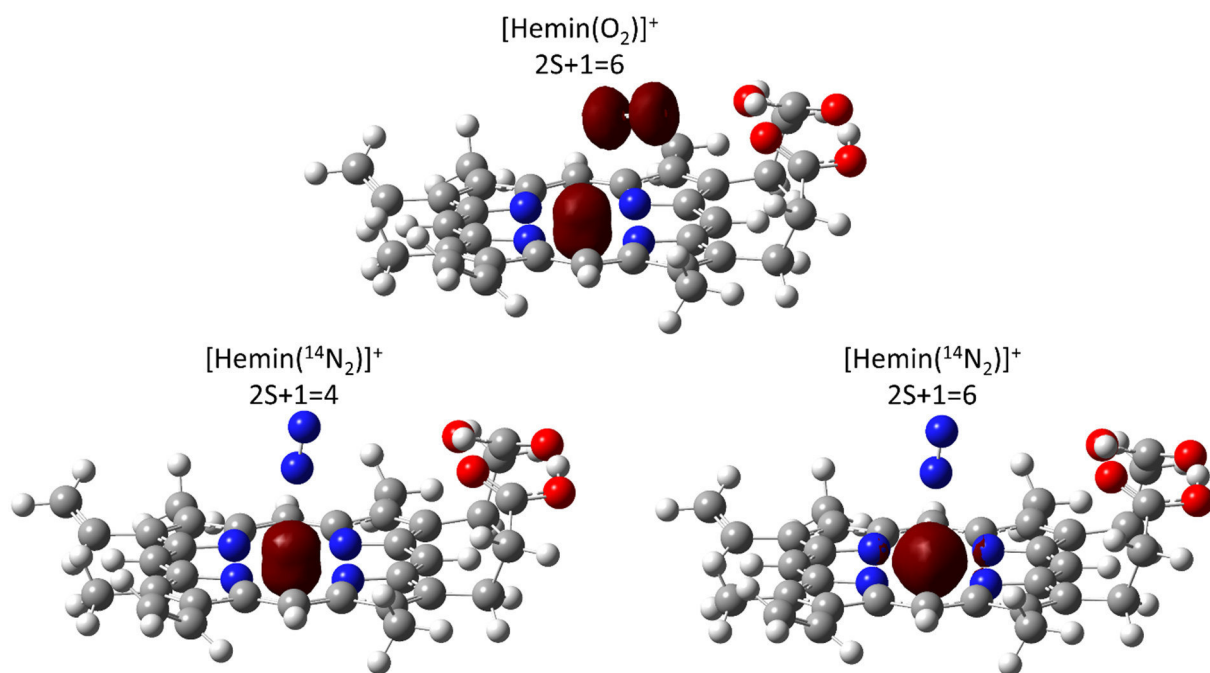


Figure S11. Isosurfaces of the spin density of the [Hemin(O₂)]⁺ cis quartet isomer (top) with the [Hemin(¹⁴N₂)]⁺ cis quartet (bottom left) and sextet.

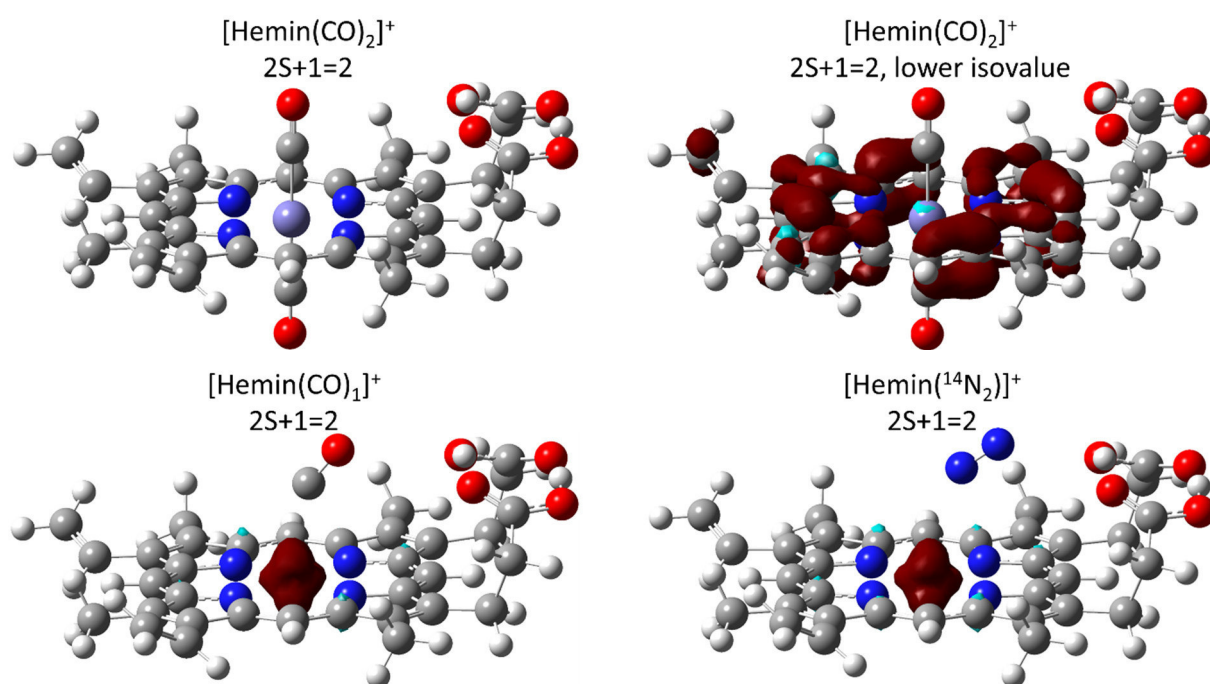


Figure S12. Isosurfaces of the spin density of the [Hemin(CO)₂]⁺ doublet with a isovalue of the spin density of 0.02 (default) (top left) and an decreased value of 0.002 (top right) in comparison with the spin densities of the [Hemin(CO)₁]⁺ doublet (bottom left) and [Hemin(¹⁴N₂)]⁺ doublet (bottom right), both default isovalues.

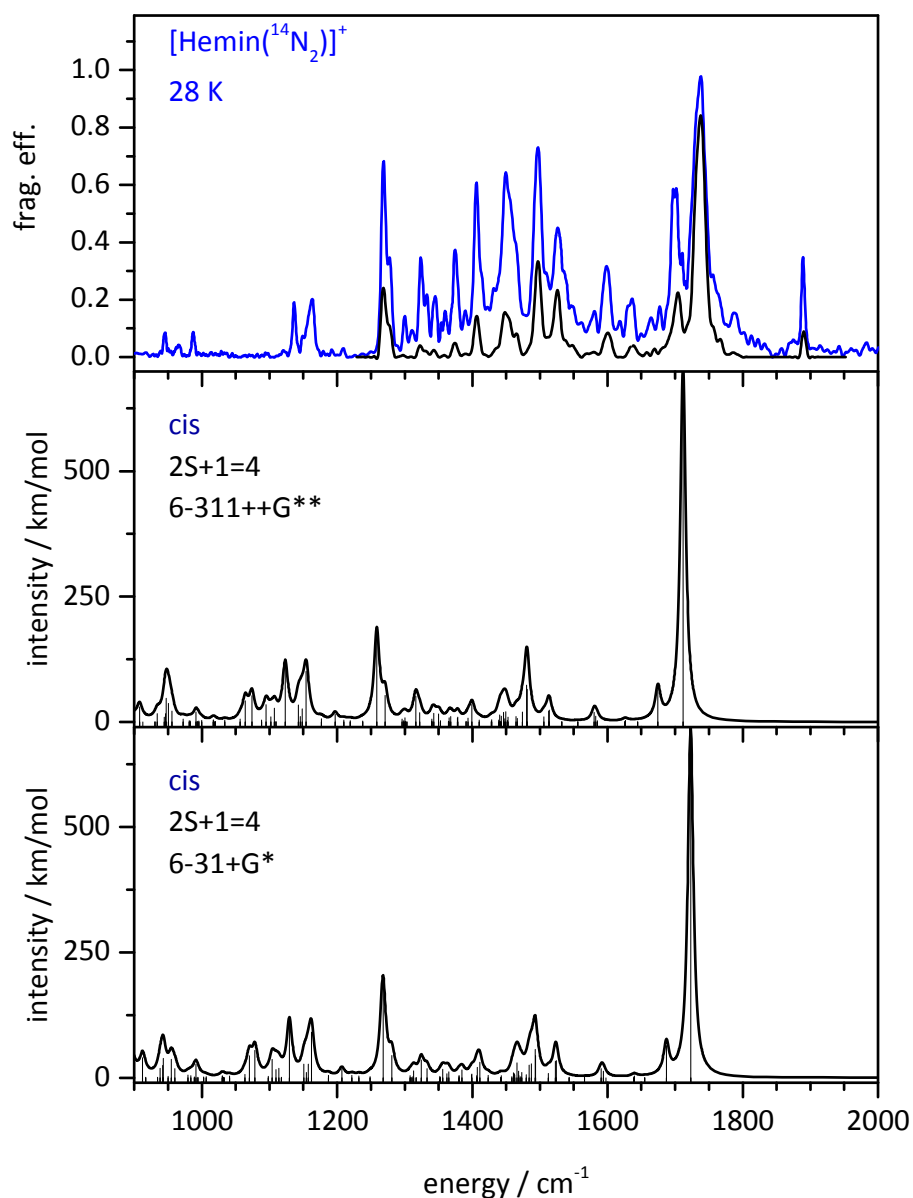


Figure S13. IR-PD spectrum of $[\text{Hemin}({}^{14}\text{N}_2)]^+$ in comparison with DFT calculations with different basis sets of the cis quartet isomer. Calculations were performed at the B3LYP level of theory including the Grimme dispersion correction (GD3) using 6-311++G** and 6-31+G* (C, H, N, O) and Stuttgart RSC 1997 effective core potential (Fe) basis sets. The calculated harmonic vibrations were scaled by a factor of 0.97. The increased basis set does not provide for great improvements in the calculated spectrum.

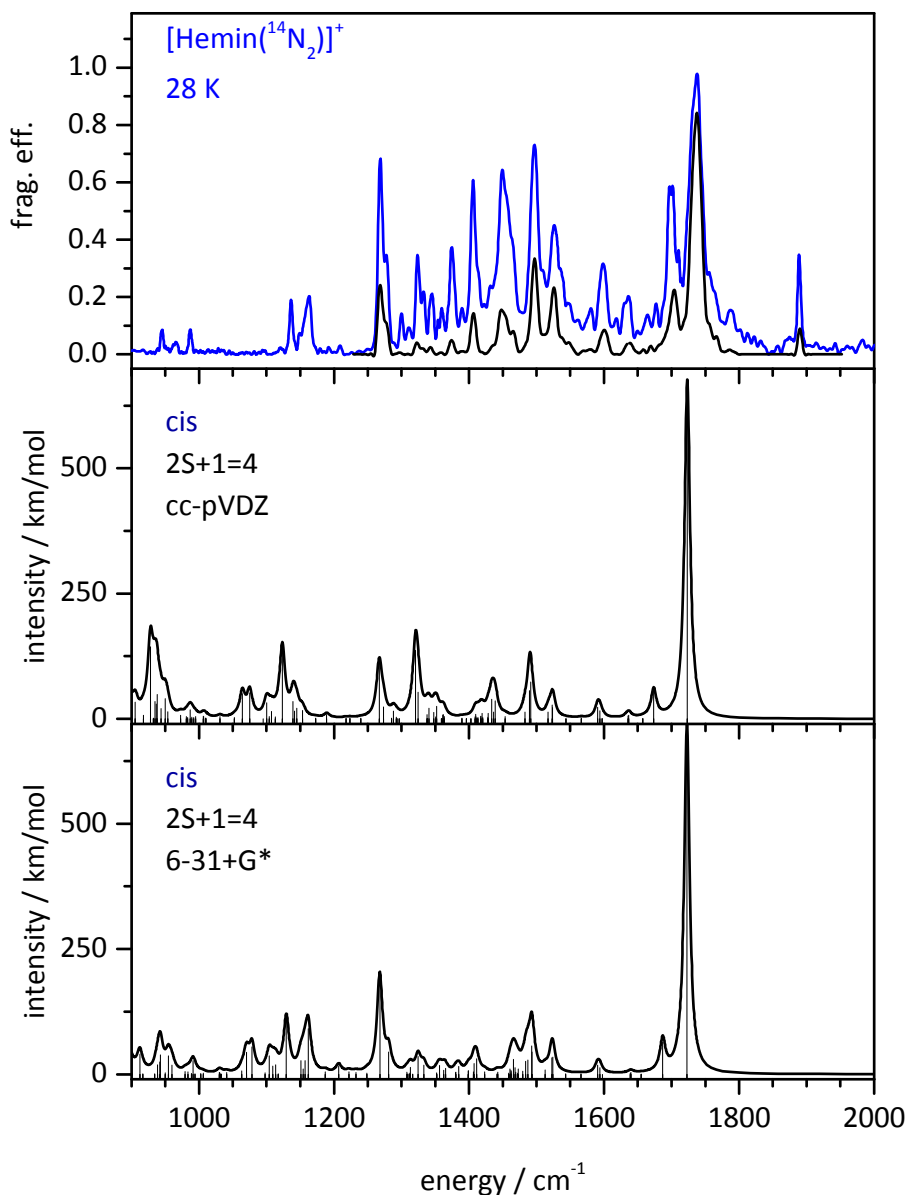


Figure S14. IR-PD spectrum of [Hemin(¹⁴N₂)]⁺ in comparison with DFT calculations with different basis sets of the cis quartet isomer. Calculations were performed at the B3LYP level of theory including the Grimme dispersion correction (GD3) using cc-pVDZ and 6-31+G* (C, H, N, O) and Stuttgart RSC 1997 effective core potential (Fe) basis sets. The calculated harmonic vibrations were scaled by a factor of 0.97. The different basis set does not provide for improvements in the calculated spectrum.

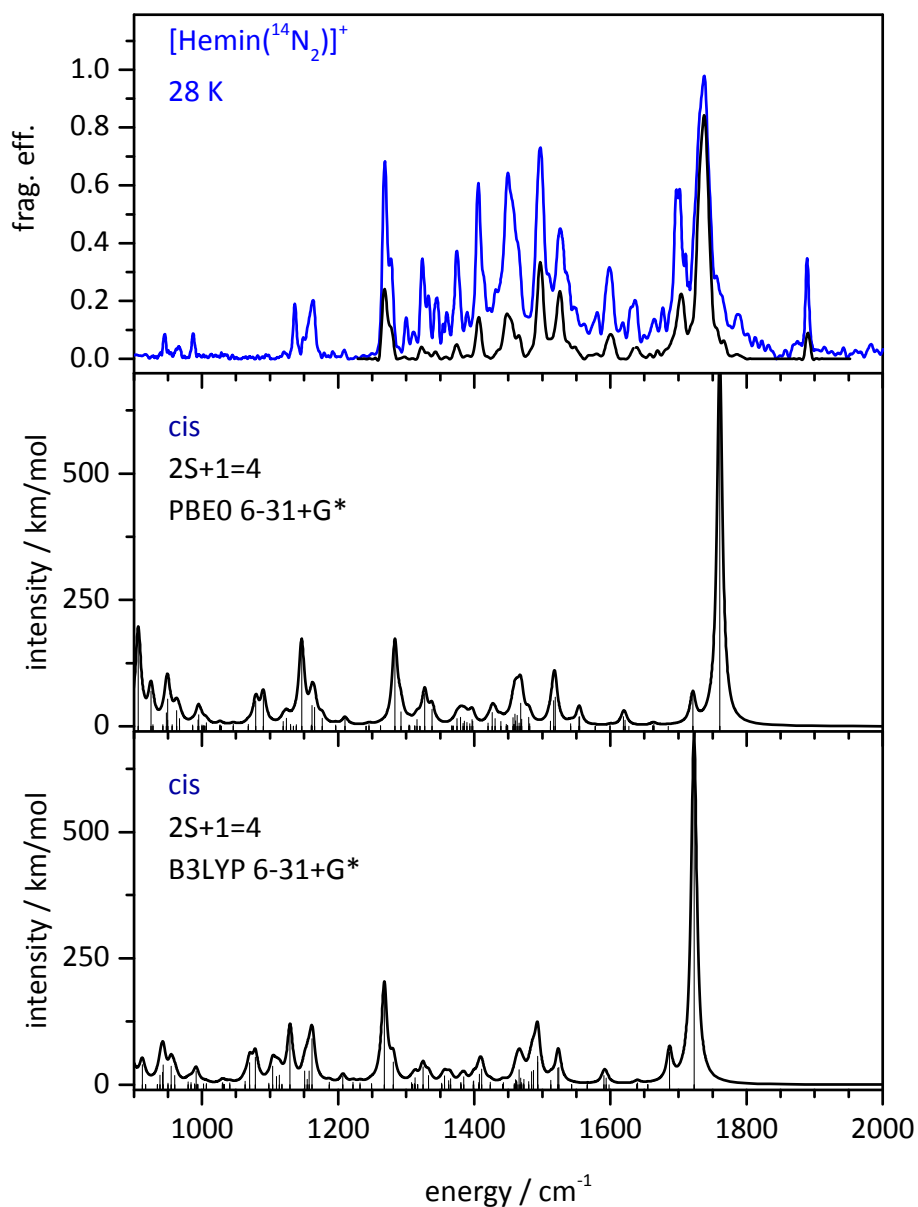


Figure S15. IR-PD spectrum of [Hemin(¹⁴N₂)]⁺ in comparison with DFT calculations with different functionals of the cis quartet isomer. Calculations were performed at the PBE0 and B3LYP level of theory including the Grimme dispersion correction (GD3) using 6-31+G* (C, H, N, O) and Stuttgart RSC 1997 effective core potential (Fe) basis sets. The calculated harmonic vibrations were scaled by a factor of 0.97. The different basis set does not provide for significant improvements in the calculated spectrum.

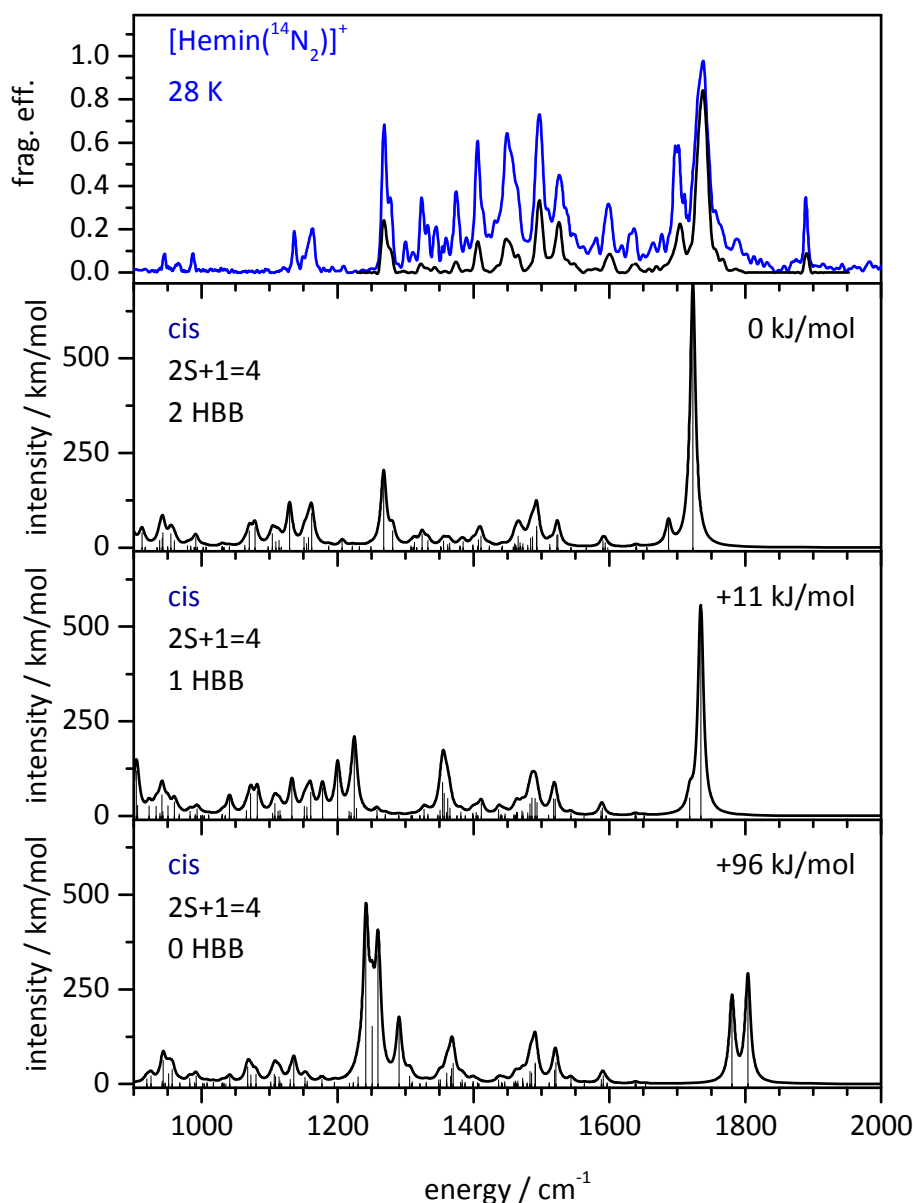


Figure S16. IR-PD spectrum of [Hemin(¹⁴N₂)]⁺ in comparison with DFT calculations of different isomers containing two (top), one (middle) or no (bottom) hydrogen bonds (HBB). Calculations were performed at the B3LYP level of theory including the Grimme dispersion correction (GD3) using 6-31+G* (C, H, N, O) and Stuttgart RSC 1997 effective core potential (Fe) basis sets. The calculated harmonic vibrations were scaled by a factor of 0.97. The spectra of the isomers containing one or no HBB do not provide for a better agreement with the experiment and are higher in energy.

XYZ-Files of Geometry Optimized [Hemin]⁺ Complexes (B3LYP, 6-31+G*, GD3):[Hemin(CO)₁]⁺ (2S+1=4)

Fe	-0.86292	-0.07635	0.08023
C	1.60435	-3.52014	0.50683
C	-4.33032	2.37759	-0.42442
C	-3.37827	3.36686	-0.25298
C	2.56570	-2.54901	0.66417
C	0.34908	-2.83936	0.35432
C	-3.63982	1.12246	-0.30416
C	-2.12301	2.69037	-0.01973
C	1.88562	-1.27782	0.61730
C	-0.85368	-3.49446	0.17402
C	-4.25953	-0.10989	-0.40501
C	-0.92242	3.33841	0.19656
C	2.50208	-0.04576	0.75362
C	-2.07575	-2.87044	0.00264
C	-3.62094	-1.32633	-0.25913
C	0.28504	2.70534	0.42412
C	1.85254	1.17424	0.68246
C	-3.31885	-3.57097	-0.16523
C	-4.29285	-2.60383	-0.33971
C	1.51393	3.41086	0.65453
C	2.49417	2.45903	0.81535
C	4.04197	-2.79968	0.77607
C	3.95245	2.74559	1.02981
C	4.68978	3.15779	-0.28249
C	4.71566	-3.09334	-0.60291
C	4.95002	1.91966	-1.10294
C	4.93435	-1.79672	-1.33879
C	1.78202	-5.00776	0.47094
C	-3.49400	-5.05697	-0.10781
C	-5.73230	-2.76936	-0.52666
C	-6.32606	-3.79021	-1.16742
C	-5.80282	2.54207	-0.64018
C	1.65289	4.90258	0.68649
C	-3.54700	4.81825	-0.25311
H	5.63989	3.63556	-0.03087
H	4.07249	3.85273	-0.85731
H	4.47086	1.89683	1.48831
H	4.04982	3.57309	1.74114
H	5.69202	-3.55555	-0.44231
H	4.08448	-3.76844	-1.18841
H	4.56164	-1.96808	1.26402
H	4.20840	-3.67173	1.41757
H	-6.36549	-1.98825	-0.10841

9. Cryo IR Spectroscopy of [Hemin]⁺ Complexes in Isolation

H	-2.89396	5.37979	0.41358
H	1.40511	5.34687	-0.28602
H	2.67336	5.20526	0.93452
H	0.98519	5.35195	1.43152
H	-6.05796	2.54636	-1.70835
H	-6.37616	1.73810	-0.16829
H	-6.14694	3.49090	-0.21744
H	-5.76258	-4.58563	-1.64600
H	-7.40766	-3.84076	-1.25054
H	-2.76662	-5.52827	0.56023
H	-3.38083	-5.51750	-1.09842
H	-4.49486	-5.30880	0.25652
H	1.48986	-5.42141	-0.50265
H	2.82209	-5.29262	0.64912
H	1.16961	-5.50353	1.23404
H	6.21876	0.49001	-1.25665
H	3.98030	-0.34979	-2.14145
H	-0.83401	-4.57708	0.16079
H	-5.32106	-0.12109	-0.61479
H	-0.92156	4.42108	0.18225
H	3.57277	-0.03560	0.91444
N	0.52186	-1.46254	0.41516
N	0.48931	1.33257	0.44883
N	-2.26129	-1.49340	-0.04457
N	-2.28485	1.31463	-0.05733
O	6.01054	-1.20682	-1.31916
O	3.83528	-1.30927	-1.91249
O	4.09890	1.39316	-1.82002
O	6.15363	1.41023	-0.87748
C	-4.42566	5.50239	-1.00454
H	-5.08019	5.01732	-1.72275
H	-4.49343	6.58406	-0.93562
C	-0.31557	-0.06854	-2.20859
O	0.04785	-0.07217	-3.27974

[Hemin(¹⁴N₂)]⁺ (2S+1=4)

Fe	-0.86244	-0.07579	0.09816
C	1.60515	-3.52040	0.48686
C	-4.31550	2.38063	-0.46671
C	-3.36579	3.36883	-0.27642
C	2.56844	-2.55012	0.63619
C	0.34953	-2.83871	0.34420
C	-3.62810	1.12512	-0.33920
C	-2.11464	2.69129	-0.02799
C	1.88882	-1.27873	0.59642
C	-0.85368	-3.49359	0.17087
C	-4.24857	-0.10569	-0.44662
C	-0.91724	3.33858	0.20366
C	2.50727	-0.04857	0.73457
C	-2.07295	-2.86732	-0.00705
C	-3.61278	-1.32159	-0.29051
C	0.28868	2.70316	0.42907
C	1.85694	1.17081	0.67205
C	-3.31507	-3.56598	-0.18493
C	-4.28533	-2.59801	-0.37462
C	1.51822	3.40712	0.65873
C	2.49925	2.45449	0.80865
C	4.04542	-2.80177	0.73567
C	3.95862	2.74002	1.01708
C	4.68958	3.15903	-0.29664
C	4.70876	-3.08997	-0.64950
C	4.94739	1.92492	-1.12396
C	4.92638	-1.78970	-1.37935
C	1.78136	-5.00806	0.44763
C	-3.49260	-5.05153	-0.12390
C	-5.72259	-2.76218	-0.57870
C	-6.30935	-3.78385	-1.22455
C	-5.78404	2.54733	-0.70626
C	1.65745	4.89862	0.69746
C	-3.53374	4.82021	-0.27291
H	5.64037	3.63641	-0.04682
H	4.06918	3.85606	-0.86556
H	4.47952	1.88916	1.46877
H	4.05908	3.56398	1.73209
H	5.68484	-3.55579	-0.49779
H	4.07171	-3.76004	-1.23442
H	4.56921	-1.97249	1.22319
H	4.21606	-3.67654	1.37231
H	-6.36004	-1.97952	-0.16996
H	-2.88982	5.37844	0.40532
H	1.40867	5.34731	-0.27279
H	2.67831	5.19985	0.94561

9. Cryo IR Spectroscopy of [Hemin]⁺ Complexes in Isolation

H	0.99072	5.34471	1.44532
H	-6.02035	2.56032	-1.77867
H	-6.36595	1.74006	-0.25093
H	-6.13505	3.49301	-0.28207
H	-5.74071	-4.58070	-1.69461
H	-7.38990	-3.83357	-1.32093
H	-2.77604	-5.52030	0.55753
H	-3.36436	-5.51644	-1.11062
H	-4.49920	-5.30081	0.22596
H	1.48361	-5.41974	-0.52511
H	2.82220	-5.29392	0.61955
H	1.17279	-5.50470	1.21322
H	6.21384	0.49424	-1.28624
H	3.97089	-0.33756	-2.17109
H	-0.83580	-4.57621	0.16129
H	-5.30730	-0.11605	-0.66973
H	-0.91625	4.42124	0.19643
H	3.57870	-0.03951	0.89015
N	0.52318	-1.46148	0.40257
N	0.49216	1.32968	0.44492
N	-2.25491	-1.48931	-0.06051
N	-2.27553	1.31499	-0.07365
O	6.00358	-1.20145	-1.36000
O	3.82599	-1.29801	-1.94610
O	4.09525	1.40383	-1.84359
O	6.15020	1.41224	-0.90138
C	-4.40128	5.50827	-1.03364
H	-5.04584	5.02704	-1.76331
H	-4.46915	6.58969	-0.96085
N	0.06050	-0.05051	-3.30524
N	-0.30349	-0.05657	-2.26332

[Hemin(O₂)]⁺ (2S+1=6)

Fe	-0.90549	-0.09299	0.16265
C	1.58021	-3.53448	0.37817
C	-4.34126	2.36461	-0.46625
C	-3.37756	3.35099	-0.34585
C	2.54128	-2.56744	0.56053
C	0.32231	-2.85302	0.26733
C	-3.66372	1.11007	-0.29711
C	-2.12972	2.67377	-0.08515
C	1.85936	-1.29730	0.56042
C	-0.88265	-3.50774	0.11449
C	-4.29817	-0.11681	-0.33641
C	-0.92970	3.31987	0.13134
C	2.47525	-0.07156	0.73693
C	-2.10838	-2.88034	0.00205
C	-3.66023	-1.33172	-0.18906
C	0.26672	2.68243	0.39360
C	1.82420	1.14727	0.68494
C	-3.35591	-3.57682	-0.13306
C	-4.33525	-2.60668	-0.25750
C	1.49459	3.38391	0.63447
C	2.46794	2.42963	0.82142
C	4.01741	-2.82152	0.66802
C	3.92097	2.71379	1.07411
C	4.69257	3.15847	-0.20686
C	4.69837	-3.07754	-0.71456
C	4.96798	1.94303	-1.05546
C	4.93156	-1.75942	-1.40683
C	1.75968	-5.01966	0.29247
C	-3.52977	-5.06349	-0.09851
C	-5.78025	-2.76774	-0.39720
C	-6.39778	-3.78069	-1.02816
C	-5.81302	2.53468	-0.68096
C	1.64109	4.87497	0.65173
C	-3.53209	4.80196	-0.41425
H	5.63735	3.62511	0.08290
H	4.09344	3.87125	-0.77889
H	4.42958	1.85600	1.52654
H	3.99729	3.52488	1.80701
H	5.66991	-3.55219	-0.56142
H	4.06654	-3.72850	-1.32611
H	4.53518	-2.00412	1.18130
H	4.18009	-3.71071	1.28659
H	-6.39688	-1.98961	0.05037
H	-2.86830	5.38917	0.21864
H	1.43849	5.30589	-0.33723
H	2.65185	5.17504	0.93945

9. Cryo IR Spectroscopy of [Hemin]⁺ Complexes in Isolation

H	0.94494	5.33894	1.36068
H	-6.07384	2.49139	-1.74686
H	-6.39195	1.75961	-0.16925
H	-6.14470	3.50574	-0.30111
H	-5.85316	-4.57192	-1.53451
H	-7.48171	-3.82780	-1.07511
H	-2.77429	-5.54927	0.52640
H	-3.46123	-5.50224	-1.10296
H	-4.51393	-5.32250	0.30436
H	1.44909	-5.40277	-0.68777
H	2.80340	-5.30766	0.44132
H	1.16339	-5.54061	1.05165
H	6.22977	0.50988	-1.22377
H	3.98811	-0.28155	-2.16816
H	-0.86243	-4.58960	0.07679
H	-5.36473	-0.12600	-0.51822
H	-0.91995	4.40160	0.09050
H	3.54561	-0.06475	0.89955
N	0.49247	-1.47577	0.36154
N	0.46124	1.30700	0.44082
N	-2.29258	-1.50021	-0.01636
N	-2.30155	1.29657	-0.07345
O	6.01341	-1.18067	-1.36501
O	3.83737	-1.24566	-1.96373
O	4.13350	1.44781	-1.81204
O	6.16022	1.41549	-0.81105
C	-4.40915	5.45742	-1.19278
H	-5.07325	4.94479	-1.88247
H	-4.46479	6.54184	-1.17706
O	1.33225	0.61458	-2.68184
O	0.24586	0.07955	-2.57802

[Hemin(CO)₁]⁺ (2S+1=2)

Fe	-0.88065	-0.07557	0.19580
C	1.63237	-3.55673	0.51356
C	-4.35124	2.41700	-0.40466
C	-3.40684	3.40311	-0.24959
C	2.58450	-2.59092	0.66933
C	0.35978	-2.86247	0.35623
C	-3.63983	1.15099	-0.27649
C	-2.13160	2.71411	-0.01388
C	1.88201	-1.30426	0.61480
C	-0.84645	-3.48977	0.16545
C	-4.26339	-0.11262	-0.37988
C	-0.92360	3.33642	0.18626
C	2.50425	-0.03848	0.74978
C	-2.09996	-2.86357	-0.01981
C	-3.64559	-1.33424	-0.26212
C	0.31902	2.70053	0.40454
C	1.88445	1.18578	0.66806
C	-3.34784	-3.58864	-0.21809
C	-4.32227	-2.63281	-0.38018
C	1.56302	3.43013	0.62252
C	2.53967	2.49080	0.78847
C	4.06338	-2.82693	0.78808
C	3.99919	2.77144	1.00323
C	4.74932	3.16350	-0.30746
C	4.75594	-3.10094	-0.58440
C	4.99090	1.91664	-1.11971
C	4.95636	-1.80192	-1.32151
C	1.80246	-5.04380	0.46954
C	-3.49565	-5.07863	-0.19150
C	-5.75660	-2.79278	-0.59278
C	-6.34139	-3.80075	-1.26311
C	-5.82722	2.56027	-0.61213
C	1.68389	4.92301	0.63262
C	-3.56369	4.85367	-0.26823
H	5.70576	3.62786	-0.05493
H	4.14451	3.86466	-0.88808
H	4.50844	1.92340	1.47439
H	4.09903	3.60617	1.70582
H	5.73937	-3.54603	-0.41891
H	4.14137	-3.78638	-1.17593
H	4.56894	-1.99427	1.29012
H	4.23415	-3.70270	1.42343
H	-6.39556	-2.01691	-0.17275
H	-2.89669	5.41924	0.38150
H	1.41575	5.35194	-0.34176

9. Cryo IR Spectroscopy of [Hemin]⁺ Complexes in Isolation

H	2.70459	5.24106	0.86048
H	1.02218	5.37559	1.38185
H	-6.09887	2.49758	-1.67451
H	-6.38829	1.78211	-0.08366
H	-6.17350	3.52993	-0.24158
H	-5.76954	-4.58533	-1.74961
H	-7.42151	-3.84885	-1.36468
H	-2.80162	-5.54327	0.51688
H	-3.30878	-5.52583	-1.17717
H	-4.51120	-5.35696	0.10684
H	1.53392	-5.44581	-0.51595
H	2.83598	-5.33635	0.67254
H	1.16620	-5.54323	1.21049
H	6.24943	0.48057	-1.29054
H	3.97756	-0.35062	-2.09436
H	-0.83653	-4.57345	0.14159
H	-5.32740	-0.11178	-0.58306
H	-0.91193	4.42001	0.16857
H	3.57517	-0.04019	0.91564
N	0.55713	-1.48813	0.42126
N	0.52293	1.36639	0.43770
N	-2.29148	-1.52319	-0.04392
N	-2.31910	1.34344	-0.04380
O	6.03660	-1.22008	-1.34886
O	3.83574	-1.30568	-1.84424
O	4.12272	1.38812	-1.81405
O	6.19594	1.40227	-0.91322
C	-4.44496	5.53512	-1.02034
H	-5.10852	5.04455	-1.72645
H	-4.50376	6.61811	-0.96576
C	-1.19373	-0.08264	2.05123
O	-1.38322	-0.08601	3.17479
C	-0.56355	-0.06812	-1.66630
O	-0.37328	-0.06477	-2.78885

[Hemin(CO)₁]⁺ (2S+1=4)

Fe	-0.88582	-0.07537	0.20650
C	1.65449	-3.58510	0.52500
C	-4.38455	2.44360	-0.40874
C	-3.43478	3.43342	-0.25013
C	2.61179	-2.61606	0.68333
C	0.37900	-2.89408	0.37506
C	-3.67817	1.17410	-0.28215
C	-2.15833	2.74724	-0.01402
C	1.91371	-1.32640	0.63782
C	-0.84715	-3.50133	0.17140
C	-4.28113	-0.11329	-0.38394
C	-0.92829	3.34922	0.19217
C	2.51760	-0.03632	0.76153
C	-2.12379	-2.89605	-0.02436
C	-3.68146	-1.35653	-0.27091
C	0.33764	2.73408	0.41395
C	1.91531	1.20924	0.68005
C	-3.37268	-3.61756	-0.23201
C	-4.35221	-2.65721	-0.39483
C	1.58566	3.46054	0.62060
C	2.56704	2.51724	0.78726
C	4.09051	-2.85682	0.79436
C	4.02735	2.80345	0.99014
C	4.77082	3.17592	-0.33039
C	4.77896	-3.11760	-0.58298
C	5.01112	1.91612	-1.12229
C	4.97957	-1.81094	-1.30606
C	1.83228	-5.07159	0.47056
C	-3.52820	-5.10721	-0.21523
C	-5.78528	-2.82233	-0.61192
C	-6.37378	-3.84472	-1.25690
C	-5.85924	2.59735	-0.61994
C	1.71461	4.95333	0.61959
C	-3.59556	4.88363	-0.26643
H	5.72772	3.64573	-0.08985
H	4.16175	3.86635	-0.91929
H	4.53909	1.96155	1.47001
H	4.13216	3.64781	1.68036
H	5.76231	-3.56549	-0.42450
H	4.16185	-3.79585	-1.17999
H	4.59809	-2.02843	1.30191
H	4.26400	-3.73842	1.42086
H	-6.42360	-2.03300	-0.21633
H	-2.91138	5.44911	0.36554
H	1.45480	5.37556	-0.36005

9. Cryo IR Spectroscopy of [Hemin]⁺ Complexes in Isolation

H	2.73505	5.26968	0.85136
H	1.05022	5.41542	1.36059
H	-6.12196	2.59742	-1.68642
H	-6.42389	1.78897	-0.14350
H	-6.21095	3.54364	-0.19662
H	-5.80696	-4.64717	-1.71905
H	-7.45382	-3.88761	-1.36148
H	-2.79789	-5.58525	0.44589
H	-3.40156	-5.54300	-1.21545
H	-4.52716	-5.38449	0.13696
H	1.58785	-5.46514	-0.52470
H	2.86198	-5.36315	0.69387
H	1.18177	-5.58105	1.19197
H	6.26659	0.47365	-1.26777
H	4.00494	-0.35631	-2.07897
H	-0.83542	-4.58612	0.14178
H	-5.34648	-0.11325	-0.58671
H	-0.91622	4.43415	0.17555
H	3.59068	-0.03696	0.92190
N	0.59462	-1.52625	0.45344
N	0.55946	1.40595	0.45820
N	-2.33410	-1.56289	-0.04917
N	-2.36432	1.38328	-0.05001
O	6.05811	-1.22491	-1.31907
O	3.86183	-1.31270	-1.83288
O	4.14382	1.37920	-1.81181
O	6.21333	1.40074	-0.90297
C	-4.49520	5.56808	-0.99386
H	-5.17976	5.08142	-1.68213
H	-4.54909	6.65117	-0.93620
C	-1.21488	-0.07733	2.06076
O	-1.41439	-0.07739	3.18151
C	-0.55227	-0.07293	-1.65282
O	-0.35064	-0.07257	-2.77239

[Hemin(CO)₁]⁺ (2S+1=6)

Fe	-0.88705	-0.07111	0.20009
C	1.63019	-3.54752	0.52980
C	-4.36357	2.41134	-0.41572
C	-3.40575	3.40632	-0.24511
C	2.59484	-2.57400	0.69319
C	0.36872	-2.86662	0.38075
C	-3.67681	1.15179	-0.29211
C	-2.14641	2.73040	-0.00588
C	1.91582	-1.29584	0.65437
C	-0.85281	-3.50348	0.17665
C	-4.27705	-0.10336	-0.40044
C	-0.92058	3.35854	0.20930
C	2.51781	-0.04180	0.77930
C	-2.09535	-2.89945	-0.02242
C	-3.65347	-1.34392	-0.28285
C	0.31070	2.74312	0.42736
C	1.88878	1.20157	0.69265
C	-3.33551	-3.59956	-0.23204
C	-4.31655	-2.62822	-0.40456
C	1.55158	3.44780	0.62586
C	2.53485	2.49242	0.79108
C	4.07038	-2.82955	0.79871
C	3.99595	2.78225	0.97781
C	4.71687	3.15935	-0.35443
C	4.73846	-3.12411	-0.58297
C	4.96751	1.89882	-1.14292
C	4.95097	-1.82748	-1.32056
C	1.81564	-5.03329	0.47497
C	-3.51087	-5.08603	-0.21624
C	-5.74841	-2.79634	-0.62404
C	-6.34182	-3.83490	-1.23887
C	-5.83326	2.58461	-0.63977
C	1.70283	4.93827	0.62108
C	-3.57301	4.85518	-0.25350
H	5.66994	3.64365	-0.12755
H	4.09196	3.83826	-0.94004
H	4.51750	1.94172	1.44828
H	4.10693	3.62636	1.66743
H	5.71642	-3.58423	-0.42599
H	4.10581	-3.80091	-1.16481
H	4.59254	-1.99716	1.28302
H	4.23923	-3.70188	1.43953
H	-6.38486	-1.99179	-0.25860
H	-2.86978	5.42055	0.35633
H	1.45777	5.35837	-0.36303

9. Cryo IR Spectroscopy of [Hemin]⁺ Complexes in Isolation

H	2.72470	5.24216	0.86222
H	1.03591	5.41131	1.35223
H	-6.07054	2.68241	-1.70774
H	-6.40752	1.73777	-0.25247
H	-6.19363	3.49059	-0.14158
H	-5.78266	-4.65785	-1.67262
H	-7.42167	-3.87000	-1.34824
H	-2.74771	-5.58054	0.39195
H	-3.45297	-5.51095	-1.22741
H	-4.49082	-5.35293	0.19312
H	1.56289	-5.42876	-0.51737
H	2.84835	-5.32046	0.68923
H	1.17346	-5.54475	1.20236
H	6.22970	0.46004	-1.26560
H	3.99090	-0.38727	-2.13004
H	-0.82979	-4.58692	0.15441
H	-5.33924	-0.11242	-0.61164
H	-0.91638	4.44220	0.19093
H	3.59054	-0.03215	0.93491
N	0.56105	-1.49817	0.45644
N	0.53168	1.37917	0.47362
N	-2.30487	-1.53076	-0.05501
N	-2.32957	1.36361	-0.04533
O	6.02531	-1.23336	-1.30063
O	3.85072	-1.34653	-1.89553
O	4.11083	1.35736	-1.84190
O	6.17006	1.39032	-0.90962
C	-4.49573	5.54350	-0.94872
H	-5.20516	5.06425	-1.61603
H	-4.54305	6.62658	-0.88546
C	-1.30329	-0.09116	2.57553
O	-1.47713	-0.10081	3.69417
C	-0.35188	-0.06100	-2.14705
O	-0.02249	-0.05952	-3.22968

10 Summary and Outlook

This thesis presents research studies on the fundamental interplay of diatomic molecules with transition metal compounds under cryogenic conditions. The FRITZ setup offers a multitude of opportunities to study isolated ions: The ions can either be generated by an ElectroSpray Ionization (ESI) source or a Laser VAPorization (LVAP) cluster ion source. The setup facilitates kinetic investigations of the ions with different reaction gases under well-defined isothermal conditions. Moreover it enables cryo InfraRed (Multiple) Photon Dissociation (IR-(M)PD) spectroscopy in combination with tunable OPO/OPA laser systems. In conjunction with density functional theory (DFT) modelling, the IR(M)-PD spectra allow for an assignment of geometric minimum structures. Furthermore DFT modelling helps to identify possible reaction pathways. Altogether the presented methods allow to gain fundamental insights into molecular structures and reactivity of the investigated systems.

Cobalt: We recorded the IR-PD spectra of the N₂ adsorption on **Co_n⁺** clusters in the size range of $n = 8 - 17$. The spectra exhibit remarkable cluster size dependent features and reveal a head-on μ_1 coordination of the N₂ molecules to the cluster. Preliminary DFT calculations suggest an icosahedral Co₁₃⁺ cluster, yet they fail to predict all observed spectral features. Therefore it is mandatory to spend effort on the theoretical modelling of these systems to gain further insights into the binding motifs of the N₂ and of conceivable activation routes.

Nickel: We elucidated the stepwise N₂ adsorption on size selected **Ni_n⁺** ($n = 5 - 20$) clusters by recording their reaction kinetics and IR-PD spectra at 26 K. We found consecutive adsorption steps by single exponent decays. In all presented cases the stepwise N₂ uptake reaches a strict adsorption limit m_{\max} that scales with cluster size. The IR-PD spectra of all species reveal a head-on μ_1 coordination of the N₂. We investigated the cases of Ni₉⁺ and Ni₁₃⁺ in more detail. They show remarkable differences in adsorption limits, kinetics and IR-PD spectra. The N₂ adsorption to the Ni₉⁺ cluster occurs at individual rates with retardation at an additional adsorption limit. In contrast, the N₂ adsorption to the Ni₁₃⁺ cluster takes place at all equal rates. A corresponding trend is observed in the IR-PD spectra: the IR-PD spectra of the [Ni₁₃(N₂)_m]⁺ species reveal a single dominant band that does not shift upon increasing N₂ adsorption. On the other hand the IR-PD spectra of [Ni₉(N₂)_m]⁺ show significant

shifts of peak positions and splittings by increase of the N₂ coverage. The experimental findings in conjunction with DFT calculations suggest a smooth icosahedral Ni₁₃⁺ cluster, where all surface atoms are equal. In the case of Ni₉⁺ we found a rough cluster surface that possibly isomerizes upon N₂ adsorption.

By recording N₂ adsorption kinetics of the other cationic Ni clusters and the IR-PD spectra of intermittent (n,m_x) and saturated (n,m_{max}) species together with modeled DFT spectra we were able to identify four classes of structure related surface adsorption behavior. The isothermal cryo kinetics on their own allow for a pre-classification into three groups: The clusters Ni₆⁺, Ni₁₃⁺, and Ni₁₉⁺ are highly symmetrical clusters with all smooth surfaces. We observe all even reaction kinetics that point towards all equally coordinated Ni atoms. The clusters Ni₅⁺, and Ni₇₋₁₂⁺ are small clusters with rough surfaces. They show a large variety of stepwise adsorption kinetics that are characteristic for rough cluster morphologies. We likely see a transition from octahedral to icosahedral cluster structures. The clusters Ni₁₄₋₁₈⁺, and Ni₂₀⁺ are large clusters with rough and smooth surface areas. They show initially even kinetics, intermittent limits and some long time kinetics. These indicate partly smooth cluster surfaces with some low coordinated Ni surface atoms that can be explained by a stepwise Ni cluster growth from icosahedron to bi-icosahedron.

In combination with the IR-PD spectroscopy and the DFT modelling, we were able to refine this pre-classification into the final four classes of structure related surface adsorption behavior:

Class (1) of highly symmetrical clusters with all smooth surfaces comprises Ni₆⁺, Ni₁₃⁺, and Ni₁₉⁺, and their N₂ adsorbate complexes up to saturated (n,m_{max}). The IR-PD spectra of the adsorption limits of these clusters are rather simple hinting at an exceptional high symmetry (octahedron, icosahedron, bi-icosahedron). These clusters provide for a smooth cluster core surface of equally coordinated Ni surface atoms.

Class (2) of some highly symmetrical clusters minus one Ni atom comprises Ni₁₂⁺, and Ni₁₈⁺, and their N₂ adsorbate complexes up to saturated (n,m_{max}). The IR-PD spectra suggest that the naked clusters, and those with few N₂ adsorbates, have relaxed into structures with a rather smooth surface. But upon increased N₂ load they reorganize into partially rough surfaces.

Class (3) of small clusters with rough surfaces comprises Ni_5^+ , and Ni_7^+ through Ni_{11}^+ , and their N_2 adsorbate complexes up to saturated ($n_{\text{small}}, m_{\text{max}}$). The IR-PD spectra hint at rough surfaces with one or multiple low coordinated Ni surface atoms. Surface reorganization upon N_2 uptake, namely from rough to rough surface by Ni atom migration are conceivable.

Class (4) of large clusters with rough and smooth surface areas comprises Ni_{14}^+ through Ni_{17}^+ , and Ni_{20}^+ , and their N_2 adsorbate complexes up to saturated ($n_{\text{large}}, m_{\text{max}}$). The IR-PD spectra reveal evidence for smooth surfaces with minor defects such as capping Ni atoms on an icosahedral surface. We see evidence for a stepwise cluster growth on one hemisphere of the initial icosahedron, leaving the other hemisphere largely unaffected.

Iron: We recorded the cryo N_2 adsorption kinetics of size selected Fe_n^+ ($n = 8 - 20$) clusters. We found consecutive adsorption steps by single exponentially decays and by a biexponential decay in the case of Fe_{18}^+ . We see remarkable cluster size dependent adsorption limits that do not allow for a conclusive classification like in the case of the Ni clusters, as of now. We observe the complete unreactivity of Fe_{17}^+ towards N_2 under our experimental conditions. To gain further insight, we recorded the IR-PD spectra of the $[\text{Fe}_n(\text{N}_2)_1]^+$ and $[\text{Fe}_n(\text{N}_2)_2]^+$ species in the N-N stretching region and assigned the observed bands to the μ_1 head-on adsorption of N_2 on the cluster. We do not observe a systematic variation of the band positions following a simple charge dilution model as observed for N_2 Ni clusters. The spectra of $[\text{Fe}_{18}(\text{N}_2)_1]^+$ and $[\text{Fe}_{18}(\text{N}_2)_2]^+$ revealed a far redshifted band that we tentatively assign to a slightly tilted N_2 on the cluster – a possible precursor for the N_2 activation. Preliminary DFT modelling provide for a first understanding of the miraculous unreactivity of Fe_{17}^+ cluster towards N_2 . The calculations found an electronic configuration that should not show a high reactivity towards N_2 . Furthermore it identified two isomers for the Fe_{18}^+ cluster one with a similar electronic configuration as the Fe_{17}^+ cluster explaining the inertness and one reactive isomer.

Ruthenium: We presented the IR-PD spectra of the N_2 , H_2 , and the coadsorption to a Ru_8^+ cluster. The spectra reveal the dissociation of H_2 in all complexes of $[\text{Ru}_8(\text{H}_2)_l]^+$ with $l > 1$ and we postulate a adsorbate induced reorganization after exceeding the intermittent adsorption limit at $l = 6$. In the case of $[\text{Ru}_8(\text{N}_2)_m]^+$ we identified a head-on μ_1 adsorption of the N_2 adsorbates and an intermittent adsorption limit at $m = 5$. Again we speculate about a reorganization beyond this intermittent adsorption limit. We recorded the IR-PD spectra of

the $[\text{Ru}_8(\text{H}_2)_1(\text{N}_2)_4]^+$ and $[\text{Ru}_8(\text{N}_2)_4(\text{H}_2)_1]^+$ species and observed spectral differences depending of the sequence of the reaction gases. DFT modelling helped to interpret this spectral differences in terms of the positioning of the hydrogen atoms on the cluster. The positions of the hydrogen atoms on the cluster depend on their migration possibility which is significantly hindered if the cluster is preloaded with N_2 as confirmed by DFT modelling of migration pathways.

Hemin: The well-resolved gas phase IR-PD spectra of **[Hemin]⁺** complexes identified a negligible spectral effect of single adsorbed molecules. In conjunction with DFT modelling we identified that all single adsorbed species contain a Fe^{3+} in a quartet spin state. In the case of $[\text{Hemin}(\text{O}_2)]^+$ we found an overall sextet spin state as the O_2 retains its triplet state upon adsorption. Furthermore the IR-PD spectra revealed multiple combination bands. A non-classical ($[\text{Hemin}(\text{CO})_1]^+$, blue shifted CO stretching mode) and a classical ($[\text{Hemin}(\text{CO})_2]^+$, red shifted CO stretching mode) carbonyl complex was observed that is accompanied by a quartet and a quenched doublet spin state.

These studies shall help to elucidate crucial elementary steps in catalysis and bio-relevant processes and can be seen as demonstration of the versatile applicability of the utilized methods. Further they shall benchmark current theoretical modelling and help in designing new approaches with predicting power.

Subsequent studies shall further establish the presented coadsorption technique and expand it to other TM clusters or complexes. Furthermore experiments with a two laser scheme would be of great interest. Such experiment could provide for the opportunity to study activated processes of which the activation barrier could be overcome by a laser.

11 Zusammenfassung und Ausblick

Diese Arbeit präsentiert Forschungsstudien zum grundlegenden Zusammenspiel von zweiatomigen Molekülen mit Übergangsmetallverbindungen unter kryogenen Bedingungen. Das FRITZ-Setup bietet eine Vielzahl von Möglichkeiten, isolierte Ionen zu untersuchen: Die Ionen können entweder durch eine ElektroSpray-Ionisation (ESI) Quelle oder eine Laserverdampfungsquelle (LVAP) erzeugt werden. Der Aufbau ermöglicht kinetische Untersuchungen der Ionen mit unterschiedlichen Reaktionsgasen unter wohldefinierten isothermen Bedingungen. Darüber hinaus ermöglicht es die kryo InfraRote (Multi) Photonen Dissoziationsspektroskopie (IR-(M)PD) in Kombination mit durchstimmbaren OPO / OPA Lasersystemen. In Verbindung mit Dichtefunktionaltheorie (DFT) Berechnungen ermöglichen die IR(M)-PD-Spektren eine Zuordnung von Minimumstrukturen. Darüber hinaus hilft die DFT-Modellierung, mögliche Reaktionswege zu identifizieren. Insgesamt lassen sich mit Hilfe der vorgestellten Methoden grundlegende Einblicke in die molekulare Struktur und die Reaktivität der untersuchten Systeme gewinnen.

Kobalt: Wir haben die IR-PD-Spektren der N_2 -Adsorption auf Co_n^+ -Clustern im Größenbereich von $n = 8 - 17$ aufgezeichnet. Die Spektren zeigen bemerkenswerte Clustergrößenabhängigkeiten und zeigen eine *head-on* μ_1 -Koordination der N_2 -Moleküle an den Cluster. Vorläufige DFT-Berechnungen deuten auf einen ikosaedrischen Co_{13}^+ -Cluster hin, doch können sie nicht alle beobachteten Spektralmerkmale reproduzieren. Daher ist es zwingend erforderlich, die theoretische Modellierung dieser Systeme zu verbessern, um weitere Einblicke in die Bindungsmotive der N_2 Moleküle und die möglichen Aktivierungswege zu gewinnen.

Nickel: Wir haben die schrittweise N_2 -Adsorption auf ausgewählten Ni_n^+ ($n = 5 - 20$) Clustern durch Aufzeichnen ihrer Reaktionskinetiken und IR-PD-Spektren bei 26 K untersucht. Wir fanden aufeinanderfolgende Adsorptionsschritte durch einzelne exponentielle Zerfälle. In allen gezeigten Fällen erreicht die schrittweise N_2 -Aufnahme eine strenge Adsorptionsgrenze m_{max} , die mit der Clustergröße skaliert. Die IR-PD-Spektren aller Spezies zeigen eine *head-on* μ_1 -Koordination der N_2 Moleküle. Wir untersuchten die Fälle von Ni_9^+ und Ni_{13}^+ genauer und fanden bemerkenswerte Unterschiede in den Adsorptionsgrenzen, Kinetiken und IR-PD-Spektren. Die N_2 -Adsorption an den Ni_9^+ -Cluster

erfolgt mit individuellen Geschwindigkeitskonstanten und zeigt eine zusätzliche Zwischenadsorptionsgrenze. Im Gegensatz dazu findet die N_2 -Adsorption an den Ni_{13}^+ -Cluster mit gleichen Geschwindigkeitskonstanten statt. In den IR-PD-Spektren wird ein entsprechender Trend beobachtet: Die IR-PD-Spektren der $[Ni_{13}(N_2)_m]^+$ Spezies zeigen eine einzige dominante Bande, die sich mit zunehmender N_2 -Adsorption nicht verschiebt. Auf der anderen Seite zeigen die IR-PD-Spektren der $[Ni_9(N_2)_m]^+$ Spezies signifikante Verschiebungen der Bandenpositionen und Aufspaltungen durch Erhöhung der N_2 -Bedeckung. Die experimentellen Befunde in Verbindung mit DFT-Berechnungen deuten auf einen glatten ikosaedrischen Ni_{13}^+ -Cluster hin, bei dem alle Oberflächenatome gleich sind. Im Falle von Ni_9^+ fanden wir eine raue Clusteroberfläche, die möglicherweise bei N_2 -Adsorption isomerisiert.

Durch die Aufzeichnung der N_2 -Adsorptionskinetiken der anderen kationischen Ni-Cluster und der IR-PD-Spektren von intermittierenden (n,m_x) und gesättigten (n,m_{max}) Spezies zusammen mit DFT-Rechnungen konnten wir vier Klassen des strukturbezogenen Oberflächenadsorptionsverhaltens identifizieren. Die isothermen Kryokinetiken allein ermöglichen eine Vorklassifizierung in drei Gruppen: Die Cluster Ni_6^+ , Ni_{13}^+ und Ni_{19}^+ sind hochsymmetrische Cluster mit glatten Oberflächen. Wir beobachten gleichmäßige Reaktionskinetiken, die auf gleich koordinierte Ni-Atome hinweisen. Die Cluster Ni_5^+ und Ni_{7-12}^+ sind kleine Cluster mit rauen Oberflächen. Sie zeigen Adsorptionsschritte mit unterschiedlichen Geschwindigkeitskonstanten, die für raue Clustermorphologien charakteristisch sind. Wir sehen wahrscheinlich einen Übergang von oktaedrischen zu ikosaedrischen Clusterstrukturen in diesem Größenbereich. Die Cluster Ni_{14-18}^+ und Ni_{20}^+ sind große Cluster mit rauen und glatten Oberflächenanteilen. Sie zeigen zunächst gleichmäßige Kinetiken, Zwischenadsorptionsgrenzen und manche Langzeitkinetiken. Diese Cluster zeigen teilweise glatte Clusteroberflächen mit einigen niedrigkoordinierten Ni-Oberflächenatomen, die durch ein schrittweises Ni-Clusterwachstum von einem Ikosaeder zu einem Bi-Ikosaeder erklärt werden können.

In Kombination mit der IR-PD-Spektroskopie und der DFT-Modellierung konnten wir diese Vorklassifizierung in die vier Klassen des strukturbezogenen Oberflächenadsorptionsverhaltens verfeinern:

Klasse (1) hochsymmetrischer Cluster mit glatten Oberflächen besteht aus Ni_6^+ , Ni_{13}^+ und Ni_{19}^+ und ihren N_2 -Adsorbatkomplexen bis zur Sättigung (n, m_{max}): Die IR-PD-Spektren der Adsorptionsgrenzen dieser Cluster sind einfach und weisen auf eine außergewöhnliche hohe Symmetrie (Oktaeder, Ikosaeder, Bi-Ikosaeder) hin. Diese Cluster besitzen eine glatte Clusteroberfläche mit gleich koordinierten Ni-Oberflächenatomen.

Klasse (2) hochsymmetrischer Cluster abzüglich eines Ni-Atoms besteht aus Ni_{12}^+ und Ni_{18}^+ und deren N_2 -Adsorbatkomplexen bis zur Sättigung (n, m_{max}): Die IR-PD-Spektren deuten darauf hin, dass die nackten Cluster und diejenigen mit wenigen adsorbierten N_2 Molekülen, ein Struktur mit einer ziemlich glatten Oberfläche besitzen. Bei erhöhter N_2 -Beladung reorganisieren sie sich in teilweise raue Oberflächen.

Klasse (3) kleiner Cluster mit rauen Oberflächen besteht aus Ni_5^+ und Ni_7^+ bis Ni_{11}^+ und deren N_2 -Adsorbatkomplexe bis zur Sättigung ($n_{\text{klein}}, m_{\text{max}}$): Die IR-PD-Spektren deuten auf raue Oberflächen mit einem oder mehreren niedrig koordinierten Ni-Oberflächenatomen hin. Eine Oberflächenreorganisation mit steigender N_2 -Adsorption, nämlich von einer rauen zu einer anderen rauen Oberfläche, ist denkbar.

Klasse (4) großer Cluster mit rauen und glatten Oberflächenanteilen besteht aus Ni_{14}^+ bis Ni_{17}^+ und Ni_{20}^+ und deren N_2 -Adsorbatkomplexe bis zur Sättigung ($n_{\text{groß}}, m_{\text{max}}$): Die IR-PD-Spektren zeigen Hinweise auf glatte Oberflächen mit geringfügigen Defekten wie überkappende Ni-Atome auf einer ikosaedrischen Oberfläche. Wir sehen Hinweise für ein schrittweises Clusterwachstum auf einer Halbkugel des anfänglichen Ikosaeders, wobei die andere Hemisphäre weitgehend unberührt bleibt.

Eisen: Wir haben die Kryo- N_2 -Adsorptionskinetiken von gröÙenselektierter Fe_n^+ ($n = 8 - 20$) Cluster aufgezeichnet. Wir fanden aufeinanderfolgende Adsorptionsschritte durch einzelne exponentielle Zerfälle und durch einen biexponentiellen Zerfall im Falle von Fe_{18}^+ . Wir sehen bemerkenswerte clustergrößenabhängige Adsorptionsgrenzen, die eine abschließende Klassifizierung, wie es im Fall der Ni-Cluster möglich war, bis jetzt nicht zulassen. Wir beobachten die vollständige Unreaktivität von Fe_{17}^+ gegenüber N_2 unter unseren experimentellen Bedingungen. Um weitere Einblicke zu gewinnen, haben wir die IR-PD-Spektren der $[\text{Fe}_n(\text{N}_2)_1]^+$ und $[\text{Fe}_n(\text{N}_2)_2]^+$ Spezies im N-N-Streckschwingungsbereich aufgezeichnet und konnten die beobachteten Banden der *head-on* μ_1 Koordination von N_2

auf dem Cluster zuordnen. Die Bandenpositionen zeigen keine systematische Veränderung mit der Clustergröße, welche mit einem einfachen Model, wie dem *charge dilution model*, beschrieben werden können. Die Spektren von $[\text{Fe}_{18}(\text{N}_2)_1]^+$ und $[\text{Fe}_{18}(\text{N}_2)_2]^+$ zeigten eine weit rotverschobene Bande, die wir vorläufig einem leicht gekippten N_2 auf dem Cluster zuordnen, was ein möglicher Vorläufer für eine N_2 -Aktivierung sein könnte. Vorläufige DFT-Modellierung sorgt für ein erstes Verständnis der verwunderlichen Unreaktivität des Fe_{17}^+ -Clusters gegenüber N_2 . Die Berechnungen fanden eine elektronische Konfiguration welche keine zeigt hohe Reaktivität gegenüber N_2 zeigt. Darüber hinaus identifizierten wir zwei Isomere für den Fe_{18}^+ -Cluster, eins mit einer ähnlichen elektronischen Konfiguration wie der Fe_{17}^+ -Cluster, der die Inertheit erklärt, und ein reaktives Isomer erklärt.

Ruthenium: Wir präsentierten die IR-PD-Spektren der N_2 , H_2 und der Koadsorption auf einem Ru_8^+ -Cluster. Die Spektren zeigen die Dissoziation von H_2 in allen Komplexen von $[\text{Ru}_8(\text{H}_2)_l]^+$ mit $l > 1$ und wir postulieren eine adsorbatinduzierte Reorganisation nach Überschreiten der Zwischenadsorptionsgrenze bei $l = 6$. Im Fall von $[\text{Ru}_8(\text{N}_2)_m]^+$ identifizierten wir eine *head-on* μ_1 -Koordinantion der N_2 -Adsorbate auf dem Cluster und eine Zwischenadsorptionsgrenze bei $m = 5$. Dies könnte wieder auf eine Reorganisation jenseits dieser Zwischenadsorptionsgrenze hin deuten. Wir nahmen die IR-PD-Spektren der $[\text{Ru}_8(\text{H}_2)_1(\text{N}_2)_4]^+$ und $[\text{Ru}_8(\text{N}_2)_4(\text{H}_2)_1]^+$ Spezies auf und beobachteten Unterschiede in den Spektren in Abhängigkeit von der Sequenz der Reaktionsgase. DFT-Modellierung half diese Unterschiede über die Positionierung der Wasserstoffatome auf dem Cluster erklären. Die Positionen der Wasserstoffatome auf dem Cluster hängen von ihrer Migrationsmöglichkeit ab, die erheblich behindert wird, wenn der Cluster bereits mit N_2 bedeckt ist. Dies wird auch durch DFT-Modellierungen von Migrationswegen bestätigt.

Hemin: Die gutaufgelösten Gasphasen-IR-PD-Spektren von $[\text{Hemin}]^+$ -Komplexen zeigten einen vernachlässigbaren Effekt einzelner adsorbierter Moleküle. In Verbindung mit DFT-Modellierung haben wir festgestellt, dass alle einzelnen adsorbierten Spezies ein Fe^{3+} in einem Quartett-Spin-Zustand enthalten. Im Fall von $[\text{Hemin}(\text{O}_2)]^+$ fanden wir insgesamt einen Sextett-Spin-Zustand, da das O_2 seinen Triplett-Zustand bei der Adsorption beibehält. Darüber hinaus zeigten die IR-PD-Spektren mehrere Kombinationsschwingungen. Ein nicht-klassischer ($[\text{Hemin}(\text{CO})_1]^+$, blau verschobene CO-Streckschwingung) und ein

klassischer ($[\text{Hemin}(\text{CO})_2]^+$, rotverschobene CO-Streckschwingung) Carbonylkomplex wurde beobachtet, welche in einem Quartett- bzw. einem Doublett-Spin-Zustand vorliegen.

Diese Studien sollen dazu beitragen, entscheidende Elementarschritte in der Katalyse und bio-relevanten Prozessen aufzuklären und können als Beweis für die vielseitige Anwendbarkeit der eingesetzten Methoden angesehen werden. Darüber hinaus sollen sie helfen aktuelle theoretische Modelle zu testen und bei der Entwicklung neuer Ansätze helfen.

Zukünftige Untersuchungen könnten die vorgestellte Koadsorptionstechnik weiter anwenden und auf andere TM-Cluster oder -Komplexe erweitern. Darüber hinaus wären Experimente mit zwei Laser von großem Interesse. Solche Experimente könnten die Möglichkeit bieten, aktivierte Prozesse zu untersuchen, deren Aktivierungsbarriere durch einen Laser überwunden werden kann.

12 Appendix: Further Joint Publications

Content

12.1 Vibrational fingerprints of a tetranuclear cobalt carbonyl cluster within an ion trap

12.2 Vibrational Blue Shift of coordinated N_2 in $[Fe_3O(OAc)_6(N_2)_n]^+$: “Non Classical” Dinitrogen Complexes

12.3 Infrared spectroscopic investigation of structures and N_2 adsorption induced relaxations of isolated Rhodium clusters

12.1 Vibrational fingerprints of a tetranuclear cobalt carbonyl cluster within a cryo tandem ion trap

Jennifer Mohrbach^a, Johannes Lang^a, Sebastian Dillinger^a, Marc H. Prosenc^a,
Pierre Braunstein^b and Gereon Niedner-Schatteburga

a) *Fachbereich Chemie und Forschungszentrum OPTIMAS*
Technische Universität Kaiserslautern
67663 Kaiserslautern, Germany

b) *Laboratoire de Chimie de Coordination, Institut de Chimie,*
Université de Strasbourg,
67081 Strasbourg, France

12.1.1 Preamble

The following chapter is a reprint of a publication in the “Journal of Molecular Spectroscopy”.

The experiments were performed by the experimental team consisting of J. Mohrbach and myself. The data evaluation was done by J. Mohrbach and myself. J. Lang performed the computations. The initial manuscript was written by J. Mohrbach and was revised with the help of G. Niedner-Schatteburg, P. Braunstein, J. Lang and myself.

Full Reference:

Vibrational fingerprints of a tetranuclear cobalt carbonyl cluster within a cryo tandem ion trap

J. Mohrbach, J. Lang, **S. Dillinger**, M. H. Prosenc, P. Braunstein and G. Niedner-Schatteburg, *Journal of Molecular Spectroscopy*, **2017**, 332, 103-108.

<http://dx.doi.org/10.1016/j.jms.2016.11.008>

12.1.2 Reprint

Reprint License

ELSEVIER LICENSE TERMS AND CONDITIONS

Aug 21, 2017

This Agreement between TU Kaiserslautern -- Sebastian Dillinger ("You") and Elsevier ("Elsevier") consists of your license details and the terms and conditions provided by Elsevier and Copyright Clearance Center.

License Number	4173710695920
License date	Aug 21, 2017
Licensed Content Publisher	Elsevier
Licensed Content Publication	Journal of Molecular Spectroscopy
Licensed Content Title	Vibrational fingerprints of a tetranuclear cobalt carbonyl cluster within a cryo tandem ion trap
Licensed Content Author	Jennifer Mohrbach, Johannes Lang, Sebastian Dillinger, Marc Prosenec, Pierre Braunstein, Gereon Niedner-Schatteburg
Licensed Content Date	Feb 1, 2017
Licensed Content Volume	332
Licensed Content Issue	n/a
Licensed Content Pages	6
Start Page	103
End Page	108
Type of Use	reuse in a thesis/dissertation
Portion	full article
Format	both print and electronic
Are you the author of this Elsevier article?	Yes
Will you be translating?	No
Title of your thesis/dissertation	Cryo Spectroscopy and Kinetics of Isolated Transition Metal Clusters and Complexes
Expected completion date	Nov 2017
Estimated size (number of pages)	300
Requestor Location	TU Kaiserslautern Erwin-Schrödinger-Straße 52 Kaiserslautern, 67663 Germany Attn: TU Kaiserslautern
Publisher Tax ID	GB 494 6272 12
Total	0.00 EUR



Contents lists available at ScienceDirect

Journal of Molecular Spectroscopy

journal homepage: www.elsevier.com/locate/jms

Vibrational fingerprints of a tetranuclear cobalt carbonyl cluster within a cryo tandem ion trap



Jennifer Mohrbach^a, Johannes Lang^a, Sebastian Dillinger^a, Marc Prosenc^a, Pierre Braunstein^b, Gereon Niedner-Schatteburg^{a,*}

^aFachbereich Chemie and Forschungszentrum OPTIMAS, Technische Universität Kaiserslautern, 67663 Kaiserslautern, Germany

^bLaboratoire de Chimie de Coordination, Institut de Chimie, UMR 7177 CNRS, Université de Strasbourg, 67081 Strasbourg, France

ARTICLE INFO

Article history:

Received 1 October 2016

In revised form 5 November 2016

Accepted 21 November 2016

Available online 22 November 2016

Keywords:

IR-MPD spectroscopy

Transition metal coordination complexes

DFT modelling

Cryo ion trapping

ABSTRACT

We present well resolved ($\Delta\tilde{\nu} = 3 \text{ cm}^{-1}$) Infrared Multiple Photon Dissociation (IR-MPD) spectra of $[\text{Co}_4(\text{CO})_n(\text{dppa}-\text{H}^+)]^-$ ($n = 3-10$, $\text{dppa} = \text{NH}(\text{PPh}_2)_2$) in the carbonyl stretching range when isolating these species at low temperatures (26 K and below). We utilize IR-MPD in conjunction with DFT calculations to investigate the influence of CO ligands on structure and spin multiplicity of the Co_4 core. The recorded spectra reveal multiple bands of CO stretching vibrations which shift by reduction of CO coverage. This indicates a corresponding change of coordination motifs, and we find a conclusive interpretation of all recorded IR features in the case of the saturated $n = 10$ compound, likely in a singlet state as in solution. We tentatively postulate a singlet/triplet to quintet spin-flip upon removal of the first one or two CO ligands (from $n = 10$ to $n = 9, 8$) as well as a conceivable isomerization at a particular CO coverage ($n = 6$).

© 2016 Elsevier Inc. All rights reserved.

1. Introduction

High resolution mass spectrometry is currently known mostly for its favourable application in analytics, often associated with keywords like genomics, proteomics, metabolomics or petroleomics [1–3]. Other than that, high resolution MS is convenient for the spectroscopic investigation of small to medium sized species ($m/z < 5000 \text{ amu/e}$ and/or up to 200 atoms) when these form individual ions in vacuum. Direct absorption spectroscopy would fail at the number densities of typical ion experiments which do not provide for sufficient optical density. It is of help to invoke instead more elaborate schemes of indirect detection of photonic absorptions, such as so-called consequence or action spectroscopy [4–6]. IR-MPD is one of these advanced techniques [7,8]. It bears the intrinsic risk of power broadening, either by the use of free electron lasers or of table top Optical Parametric Oscillator/Amplifier (OPO/OPA) systems [9–13]. Contemporary IR-action spectroscopy achieves significant advances by so called tagging or messenger techniques where weakly bound, largely inert species (small rare gases and/or H_2) serve to provide for a preferred fragmentation channel, sometimes driven by single photon absorption [14–16]. Somewhat stronger bound messengers (Ar, Kr, Xe,

CO , N_2) often preserve the structures of the hosting species, while their influence onto spectral features allows for additional insights.

Notably, most of the current IR-MPD and messenger/tagging spectroscopic studies take place through single pulse illumination of mass selected ion packages “on the fly” prior to or within Reflectron-Time-Of-Flight (ReTOF) mass spectrometer setups. Only recently, experiments started to combine the advantages of ion trapping and IR-MPD/tagging experiments.

Carbon monoxide is one of the most widely studied ligands in surface and cluster science. Transition Metal (TM) carbonyls are of major significance in organometallic and inorganic chemistry, and they provide classic examples of metal–ligand bonding [17–21]. TM cluster carbonyls act as versatile catalysts [18,22], they serve as model systems for the study of chemisorption on highly curved surfaces [23], and as precursors for the production of nanoparticles [24].

The CO stretching vibration probes the metal–ligand bonding in a sensitive way: its frequency indicates subtle details of the hosts electronic structure, and it helps to elucidate its binding site and the geometric binding arrangement [25–28]. Shifts in CO frequencies are often used for the study of binding sites on TM surfaces, and the CO molecule may be viewed as a classic probe molecule in surface science [23,29]. Vibrational CO shifts are usually discussed in terms of the Dewar–Chatt–Duncanson model, that explains coordinative complexation to single TM centers [30,31], or in terms of the Blyholder model, when interpreting surface

* Corresponding author.

E-mail address: gns@chemie.uni-kl.de (G. Niedner-Schatteburg).

<http://dx.doi.org/10.1016/j.jms.2016.11.008>

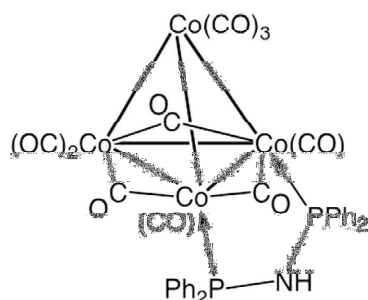
0022-2852/© 2016 Elsevier Inc. All rights reserved.

coordination [32]. Both models describe CO coordination in terms of a donor-acceptor-synergism as follows: The carbonyls C-atom donates electron density from the doubly occupied carbon lone pair σ -orbital along the M–C–O axis into empty TM d orbitals; the coordinating TM center(s) donate(s) back electron density from its (their) occupied d-levels (or d-bands) into one of the antibonding π^* orbitals of the CO. Combined effects of σ donation and π back-bonding most often lead to a weakening of the CO bond and consequently to a lowering or red-shifting of the carbonyl stretch frequency. Most TM carbonyls follow this “classical” behaviour, although examples are known for “non-classical” metal carbonyl complexes, their main feature being a blueshift in CO stretch which is now understood in terms of an interplay between π -back donation and electrostatic effects [33–41]. The study of in situ generated TM clusters helped to elucidate the influence of net charge and oxidation state (+/0/–) onto the single molecule CO adsorption in terms of a charge dilution model [42]. Thermochemical insights – such as Co–CO binding enthalpies and more – arose from a sophisticated combination of ionization and dissociation experiments of atomic cobalt ion carbonyl complexes with *ab initio* calculations [43,44]. The IR-MPD studies of such complexes revealed an induced spin quenching (triplet to singlet) upon an increase of CO coordination ($n = 4$ –5) [36].

The obvious progress in the elucidation of carbonyl complex structure and bonding has brought with it several nomenclatures for the description of the prevailing coordination motifs: Bonding/–coordination of a single CO molecule via its C-terminus to a single metal or TM center – irrespective of the metal coordination to its neighbours if any – has been termed as: terminal, end on, on top, atop, s1, μ_1 , μ^1 , and η_1 – this listing not claiming completeness. For reason of simplicity, we will exclusively utilize the term “terminal” CO and the label CO_{term} in the following. Bonding/coordination of a single CO molecule via its C-terminus to two metal or TM centers has been addressed by: bridging, s2, μ_2 , μ^2 , “in between”. We will exclusively utilize the term μ_2 -CO. The third likely coordination motif of CO involves three metal or TM centers in bonding/–coordination. This motif has been labeled as: capping, on hollow, s3, μ_3 , and μ^3 . We likely do not see this motif in our present study. When appropriate we will discuss it in terms of μ_3 -CO.

In our current ion trapping spectroscopic study, we investigate the tetranuclear cobalt carbonyl complex $[\text{Co}_4(\text{CO})_{10}\text{dppa}]$ [45] which is stabilized by the well-established diphosphine short-bite bridging ligand μ_2 -dppa ($\text{dppa} = \text{NH}(\text{PPh}_2)_2$) [46]. IR spectra of the complex (from KBr plates and in solution) reveal seven bands in the 1930–2070 cm^{-1} range and three bands in 1770–1860 cm^{-1} range, arising from terminal and μ_2 -CO ligands. This is consistent with a C_3 molecular symmetry.

The complex (Scheme 1) finds application in the preparation of TM phosphides, which is generally not easy and otherwise requires



Scheme 1. Molecular structure of the neutral tetranuclear cluster $[\text{Co}_4(\text{CO})_{10}\text{dppa}]$ ($\text{dppa} = \text{NH}(\text{PPh}_2)_2$). The complex consists of a Co_4 core, three μ_2 -CO and seven terminal CO ligands. The dppa ligand bridges two basal cobalt atoms.

the direct combination of elements at high temperature, the reaction of toxic phosphide with metal or metal hydride, or metal organic chemical vapor deposition techniques. Instead, pure cobalt phosphide nanoparticles can be obtained from $[\text{Co}_4(\text{CO})_{10}\text{dppa}]$ by anchoring and thermal treatment [47]. The $[\text{Co}_4(\text{CO})_{10}\text{dppa}]$ complex moreover may serve as a model system for the stepwise regioselective elimination of CO ligands from a metal cluster. The dppa ligand in $[\text{Co}_4(\text{CO})_{10}\text{dppa}]$ stabilizes the Co_4 core and orients further cluster functionalization by selective CO substitution. A second dppa ligand or a N-functionalized dppa ligand would bridge that metal–metal bond which is opposite to that spanned by the first dppa ligand [47]. The regioselective CO elimination would allow e.g. for the specific anchoring of this metal complex within a nanoporous membrane [48].

In this study, we strive for fundamental insight into the stepwise CO elimination from anionic derivatives of the $[\text{Co}_4(\text{CO})_{10}\text{dppa}]$ complex by Collision Induced Dissociation (CID) and by IR-MPD investigations, in conjunction with Density Functional Theory (DFT) to model the anions geometries, spin couplings and force constants. The Co_4 core within these anions might be viewed as a highly curved nano-sized metal surface. Upon adoption of this analogy, it seems appropriate to view the stepwise detachment of CO ligands from the complex as a change in CO surface coverage.

2. Experimental and computational methods

We utilized a customized Fourier Transform Ion Cyclotron Resonance (FT-ICR) mass spectrometer (Apex Ultra, Bruker Daltonics) equipped with an Electrospray Ionization (ESI) source (Apollo 2, Bruker) and a home-built laser vaporization cluster ion source [49,50] (Fig. 1).

The molecular precursor complex $[\text{Co}_4(\text{CO})_{10}\text{dppa}]$ was synthesized from $[\text{Co}_4(\text{CO})_{12}]$ and characterized by its IR (from KBr plates and in solution) and $^1\text{H}/^{31}\text{P}$ NMR spectra [45]. Sample solutions of the $[\text{Co}_4(\text{CO})_{10}\text{dppa}]$ complex in acetonitrile at the concentration of 1×10^{-4} mol/l were used without further purification and continuously infused into the ESI source by a syringe pump at a flow rate of 2 $\mu\text{L min}^{-1}$. The ion source was set to negative electrospray ionization mode. Nitrogen was used as drying gas with a flow rate of 3.0 L min^{-1} at 200 $^\circ\text{C}$. The solutions were electro-sprayed at a nebulizer flow of 1.5 L min^{-1} and the spray shield was held at 3.6 kV. We obtained the deprotonated complex $[\text{Co}_4(\text{CO})_{10}(\text{dppa-H})]^-$, abbreviated $[\text{Co}_4(\text{CO})_{10}\text{L}]^-$ in the following. In the ESI source, the ions may undergo Collision Induced Dissociation (CID) on demand. The successive elimination of up to seven CO ligands is achieved by stepwise increase of the skimmer voltage (at the first ion funnel) from –25 to –95 V (in source CID). Further increase of the funnel voltage did not enhance the elimination beyond seven CO ligands. We mass selected individual members from the resulting series of fragments $[\text{Co}_4(\text{CO})_n\text{L}]^-$ ($n = 3$ –9) and guided those into a 26 K hexapole ion trap. The ion trap is cooled by a closed cycle helium cryostat and held at 26 K for the measurements. Buffer (He) gas was introduced continuously. The pressure is increased from 1.7×10^{-7} mbar up to 3.0×10^{-6} mbar to accomplish efficient trapping and cooling of the ions. The cryo cooled ions are guided by electrostatic lenses into the FT-ICR cell of the so-called “infinity” type [51]. This cell is cooled to a temperature of about 10 K with a closed cycle helium cryostat to prevent heating of the clusters by black body radiation. The ICR cell is used for trapping, isolation and detection of the ions. It is coupled to a tuneable pulsed IR laser ($\Delta\tilde{\nu} = 0.9 \text{ cm}^{-1}$, $\Delta t = 7 \text{ ns}$) to record IR-MPD spectra of isolated $[\text{Co}_4(\text{CO})_n\text{L}]^-$ ($n = 3$ –10) complexes. Fragmentation of the isolated species (CO elimination) indicates the absorption by a resonant vibrational frequency (Fig. 2a). The laser power was attenuated

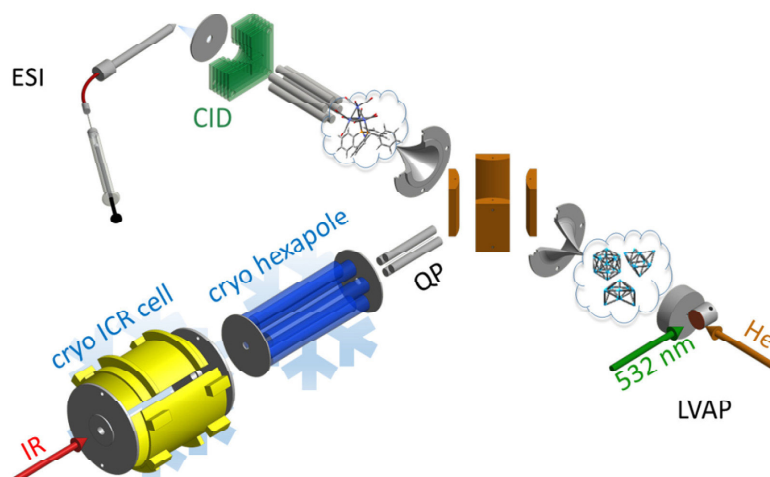


Fig. 1. Schematic drawing of our dual source tandem cryo trap FT-ICR MS setup. Ions are generated either in a Laser VAPorization (LVAP) source or in an Electro Spray Ionization (ESI) source. Either type of ions are injected into the first ion trap (cryo hexapole) via a switchable 90° ion bender and a quadrupole mass filter (QP). Buffer and reaction gases are introduced either pulsed or continuously. The cryo cooled ions and their reaction products are guided into the cryo ICR-cell, where they are isolated, irradiated by IR laser pulses and detected.

for $n = 6$ –10 in the range from 1850 cm^{-1} to 2050 cm^{-1} to prevent excessive fragmentation. In the case of $[\text{Co}_4(\text{CO})_n\text{L}]^-$ ($n = 4$ –10) the only observed fragmentation channel was the loss of CO. In the case of $[\text{Co}_4(\text{CO})_3\text{L}]^-$ the only observed fragment (395 m/z) may be assigned to $[\text{Co}_4(\text{CO})_3\text{NP}_2]^-$ due to the loss of all four phenyl groups from the dppa ligand. Addition of N_2 gas in the cryo hexapole results in N_2 adsorption to coordinatively unsaturated $[\text{Co}_4(\text{CO})_n\text{L}]^-$ ($n = 6, 8$) complexes. These N_2 complexes are isolated in the ICR cell and illuminated by infrared laser pulses. Here, the photo induced loss of N_2 indicates a resonant excitation of the complex (Fig. 2b). Note, that the modest mass difference between CO and N_2 of about 0.01 amu can be accurately resolved with our experimental setup.

The IR laser is a KTP/KTA optical parametric oscillator/amplifier (OPO/A, LaserVision) system pumped by a pulsed 10 Hz injection seeded $\text{Nd}^{3+}:\text{YAG}$ laser (Continuum, Powerlite DLS 8000). In this work we used the difference frequency (DF) between the OPA signal and idler waves generated in a AgGaSe_2 crystal (0.1–1.2 mJ per pulse). We recorded IR-MPD spectra in the range of 1500 – 2300 cm^{-1} . Each trapped and isolated package of ions is irradiated by 15 laser pulses to yield a sufficient amount of fragment ions. The IR spectra were recorded as mass chromatograms while continuously scanning the IR frequency (typically $<0.2\text{ cm}^{-1}/\text{s}$). The IR-MPD signal was evaluated as $\sum_i F_i / (\sum_i F_i + \sum_i P_i)$, where F_i and P_i indicate the fragment and the parent ion signals, respectively. An experimental IR-MPD spectrum arises from a plot of the fragmentation efficiency as a function of laser frequency.

Optimized minimum energy structures and linear IR absorption spectra were calculated at the B3LYP [52,53] and PBE0 [54] level of theory using 6-31++G** basis sets (C, H, N, O, P), and Stuttgart RSC 1997 [55] effective core potential (Co) basis sets, respectively, as implemented in the Gaussian 09 program package [56]. Standard convergence criteria were applied. Full geometry optimization of all nuclear coordinates yields multiple local minimum structures. The lowest energy structure is assumed to represent the most stable isomer. We present singlet as well as quintet spin states. We scaled the calculated harmonic vibrational frequencies by a factor of 0.954 in order to match the calculated highest frequency CO vibration band in $[\text{Co}_4(\text{CO})_{10}\text{L}]^-$ (unscaled at 2143 cm^{-1}) to our experimental value of 2044 cm^{-1} .

3. Results and discussion

3.1. IR-MPD spectra

The IR-MPD spectra of the investigated $[\text{Co}_4(\text{CO})_n\text{L}]^-$ ($n = 3$ –10) complexes (Fig. 3) exhibit several strong bands in the range 1880 – 2050 cm^{-1} , which we assign to the stretching vibrational modes of terminal CO ligands, and weaker bands around 1810 cm^{-1} which we assign to the stretching vibration modes of μ_2 -CO ligands.

There are multiple bands for the terminal CO ligands for all $n = 3$ –10 investigated. All bands are significantly redshifted by 97 – 247 cm^{-1} with respect to the free CO vibration at 2143 cm^{-1} . Judging by the band with highest frequency (indicated by the red line in Fig. 2), all redshifts increase by $\sim 90\text{ cm}^{-1}$ upon decarbonylation (seven fold CO-elimination). The observed redshifts are indicative for a reduction of force constants and weakening of the CO bonds. The likely associated bond lengthening arises through electron density transfer from the tetranuclear cobalt core into antibonding $2\pi^*$ CO acceptor orbitals. As seen before [57] the extent of such electron density shift/charge transfer/electronic transfer does depend on CO coverage. The stepwise decrease of CO coverage reduces the total electron back donation from the Co_4 core to the antibonding CO π^* orbitals, or it enables a higher donation per CO ligand. We assume a combination of both. If so, these arguments fall in line with the observed redshifts of CO_{term} vibrations which increase by decarbonylation/CO elimination.

A conclusive interpretation of all observed CO_{term} bands is not possible at current stage of investigation. DFT modelling helps in the case of $n = 10$ (see subsequent section), and not beyond. Some obvious findings deserve attention: The spectra of $[\text{Co}_4(\text{CO})_n\text{L}]^-$ ($n = 10, 9, 8, 7, 5, 4, 3$) reveal 4, 4, 3, 2, 2, 2 and 2 distinct CO_{term} bands. The level of distinct absorption motifs reduces in parallel to a reduction of the CO coverage. The $n = 6$ case is unique: We find up to 6 partially resolved CO_{term} features. This indicates either a highly specific Co-CO coordination per each CO, or it hints towards an isomeric variation that does not occur in any of the other cases. Isomeric variance may originate from Co_4 core isomers, from variation of CO coordination, or even from a coexistence of complexes in different spin multiplets (singlet/triplet/quintet/...). Naked

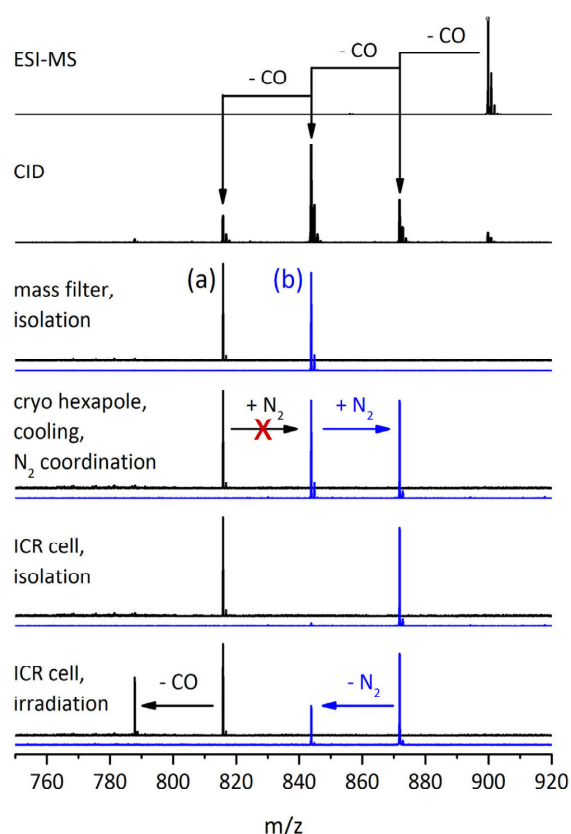


Fig. 2. Mass spectra illustrating the experimental methods. The ESI source delivers $[\text{Co}_4(\text{CO})_{10}\text{L}]^-$ (899 m/z). Subsequent CID yields a series of under-coordinated $[\text{Co}_4(\text{CO})_n\text{L}]^-$ ($n = 3-9$) complexes via successive decarbonylation. After isolation of one of these, the ions of choice are trapped and cryo cooled within the RF hexapole ion trap (a and b). Optional N_2 gas intake may result in the adsorption of one N_2 molecule to distinct complexes, $n = 6, 8$ only (blue spectra, b). Either type of ions (with or without N_2 attached) are guided into a 10 K ICR cell, isolated, irradiated by IR laser pulses, and analyzed for their fragments. (For interpretation of the references to colour in this figure legend, the reader is referred to the web version of this article.)

cobalt clusters are known for their very high spin states [58,59], and an adsorbate induced partial quenching is likely [60]. Further elucidation of such effects remains to be carried out through DFT modelling in the future.

The low energy part of the spectra reveals features typical of μ_2 -CO coordination. Such fingerprints prevail at $n = 5-10$ and vanish at $n = 3, 4$. Other than in the CO_{term} bands, there is no systematic redshift variation as a function of coverage for the μ_2 -CO bands. The magnitude of the μ_2 -CO redshift is large ($\sim 340 \text{ cm}^{-1}$) and in line with numerous previous observations [61,26,19]. In remarkable contrast to the up to six distinct CO_{term} bands, there are just two distinct μ_2 -CO bands at 1790–1810 and 1810–1830 cm^{-1} , respectively. These two bands likely correspond to two species, μ_2^a ($< 1810 \text{ cm}^{-1}$) and μ_2^b ($> 1810 \text{ cm}^{-1}$). The μ_2^a species occurs only at highest coverages $n = 8-10$, and the μ_2^b species occurs only at high coverages $n = 5-10$. At this point the successful DFT modelling of the $n = 10$ case enables a convincing assignment of these two species (see below).

Our investigation did not find evidence for any IR-MPD bands in the range of 1500–1700 cm^{-1} ($n = 6-10$), which allow us to rule out μ_3 -CO coordination in $[\text{Co}_4(\text{CO})_n\text{L}]^-$.

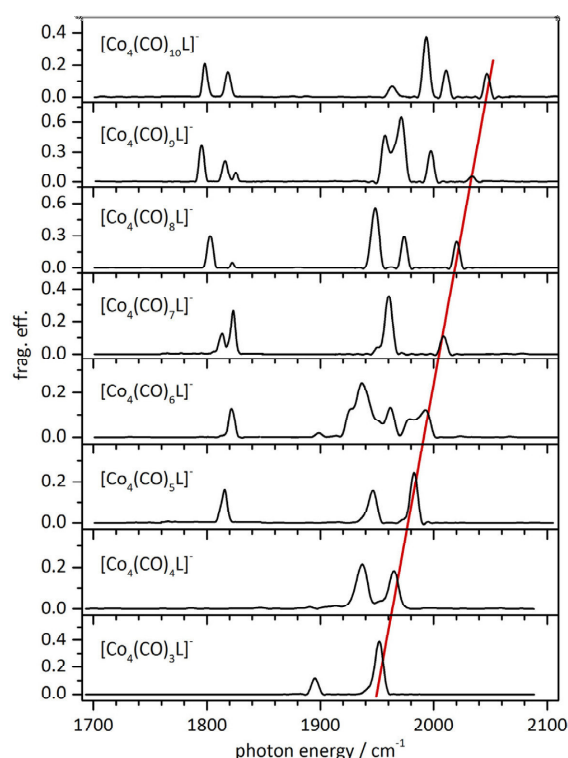


Fig. 3. IR-MPD spectra of $[\text{Co}_4(\text{CO})_n\text{L}]^-$ ($n = 3-10$) complexes at 26 K. The red line serves to guide the eye, emphasizing the redshift of the terminal carbonyl stretches with decarbonylation. (For interpretation of the references to colour in this figure legend, the reader is referred to the web version of this article.)

An interpretation solely in terms of electrostatics and electron density shifts falls short of all prevailing effects. Surely there are coverage dependent steric effects which reflect surface “crowding” by CO adsorbates, and which likely cause concomitant terminal - μ_2 - μ_3 - rearrangements. In parallel, there will be a change in the order of individual $\Delta_{\text{surface}}\text{H}(\mu_x\text{-CO})$ values. Small coverages may go with $\Delta_{\text{surface}}\text{H}(\text{CO}_{\text{term}}) > \Delta_{\text{surface}}\text{H}(\mu_2\text{-CO}) \sim \Delta_{\text{surface}}\text{H}(\mu_3\text{-CO})$ in preference of terminal CO; high coverages may go with $\Delta_{\text{surface}}\text{H}(\mu_2\text{-CO}) \sim \Delta_{\text{surface}}\text{H}(\mu_3\text{-CO}) > \Delta_{\text{surface}}\text{H}(\text{CO}_{\text{term}})$ in preference of $\mu_{2,3}$ -CO. Indeed, our spectra show that CO_{term} prevails at all levels of “coverage” while μ_2 -CO fingerprints diminish upon reduction of CO coverage.

3.2. DFT modelling

We have conducted DFT modelling of the $[\text{Co}_4(\text{CO})_{10}\text{L}]^-$ complex, and we obtained its linear IR absorption spectra in singlet and quintet (+6 kJ/mol) spin states. The calculation of force constants in triplet state did not converge, irrespective of the chosen exchange-correlation functional (B3LYP and PBE0). Geometry optimized calculations of the singlet and triplet state at the somewhat more approximate BP86 level have identified a singlet ground state and a high energy (+46 kJ/mol) triplet state. While we take this finding with a grain of caution, it shall suffice to rule out triplet contributions at the current stage of investigation.

In the following we compare two computed IR spectra (in singlet and quintet state by PBE0) to the experimental IR-MPD spectrum in the CO stretching frequency range (Fig. 4). A B3LYP singlet spectrum is virtually identical to that one by PBE0

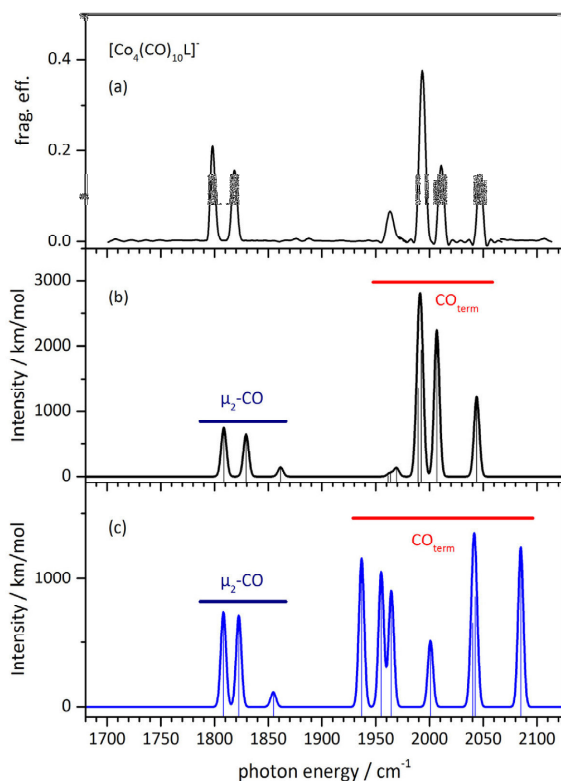


Fig. 4. IR-MPD spectrum of $[\text{Co}_4(\text{CO})_{10}\text{L}]^-$ at 26 K (a) and calculated IR absorption spectra of geometry optimized singlet (b) and quintet (+6 kJ/mol) (c) spin state. The calculations were performed at the Stuttgart 1997 ECP (Co) and PBE0/6-31++G** (H, C, N, O, P) level of theory. The frequencies are scaled with 0.954, and calculated lines were broadened with Gaussians (FWHM = 3 cm^{-1}). The lowest triplet state (+46 kJ/mol) is discussed in the text. For the vector characters of all 10 singlet vibrations refer to Fig. S2 in the supplement.

(cf. Supplement Fig. S1). The DFT computations reveal seven CO_{term} bands and three $\mu_2\text{-CO}$ bands, some of which are almost degenerate. Upon folding in the experimental resolution of 3 cm^{-1} , the DFT modelling predicts four observable CO_{term} bands and three observable $\mu_2\text{-CO}$ bands in the case of a singlet spin state – in agreement with the experimental IR MPD findings. We provide an illustrative visualization of the calculated displacement vectors of these modes in Fig. S2 of the supplement. We assign the two $\mu_2\text{-CO}$ species mentioned above to the one CO ligand that bridges the same cobalt atoms as the dppa ligand (μ_2^3), and to the two CO ligands that bridge one dppa bound Cobalt atom and the third basal Cobalt atom (μ_2^2). We clearly rule out contributions from the calculated quintet state, which would predict six CO_{term} bands across a wider range of frequencies in undisputable disagreement with the experiment.

Unfortunately, our current attempts of further DFT modelling ($n < 10$) have not yet led to converging data and to verifiable conclusions. We are tentatively assuming, that decarbonylation will allow for higher spin states, partially co-existing.

4. Conclusions and outlook

It became possible to record well resolved IR spectra of $[\text{Co}_4(\text{CO})_{10}\text{L}]^-$ ($n = 3\text{--}10$) in the range of CO_{term} and $\mu_2\text{-CO}$ vibrations when isolating these species at low temperatures (26 K and below). We find several bands which shift upon reduction of CO

coverage, indicating a variation of coordination motifs. In conjunction with DFT modelling, we find a conclusive interpretation of all recorded IR features in the case of the saturated $n = 10$ compound, likely in a singlet state similar to solution. We currently fail to achieve such conclusive interpretation in all other cases. We currently speculate about spin switching into higher multiplet states (from singlet into triplet/quintet or even higher) upon stepwise decarbonylation, and about a conceivable isomerization at a particular CO coverage ($n = 6$). The CO coverage dependent redshift of the highest CO_{term} is indicative of the charge dependent $2\pi^*(\text{CO})$ back donation and of its concomitant bond weakening. In contrast, the $\mu_2\text{-CO}$ bands modulate in appearance and intensity upon change of the CO coverage – without shifting significantly.

We are in the process of recording further spectra of Co_4 species with a mixed $\text{N}_2\text{-CO}$ coverage, and we are enforcing further DFT analysis by all means. Once achieved, the then calculated $\Delta_{\text{surface}}\text{H}(\text{CO})$ and $\Delta_{\text{surface}}\text{H}(\text{N}_2)$ values will allow for an elucidation of additional steric effects (“crowding”). We anticipate these effects to modulate the electronics in the known acceptor-donor type Co-CO and Co- N_2 bindings. Such steric effects most likely cause CO_{term} to $\mu_2\text{-CO}$ to $\mu_3\text{-CO}$ rearrangements, and it will be fascinating to compare such findings to the data of CO and N_2 adsorption on flat surfaces.

Acknowledgement

This work was supported by the German research foundation DFG within the transregional collaborative research center SFB/TRR 88 “Cooperative effects in homo- and hetero-metallic complexes” (3MET.de) and by the state research center OPTIMAS.

Appendix A. Supplementary material

Supplementary data associated with this article can be found, in the online version, at <http://dx.doi.org/10.1016/j.jms.2016.11.008>.

References

- [1] G.J. Patti, O. Yanes, G. Siuzdak, Innovation: metabolomics: the apogee of the omics trilogy, *Nat. Rev. Mol. Cell Biol.* 13 (4) (2012) 263–269.
- [2] M. Tyers, M. Mann, From genomics to proteomics, *Nature* 422 (6928) (2003) 193–197.
- [3] A.G. Marshall, R.P. Rodgers, Petroleomics: chemistry of the underworld, *Proc. Natl. Acad. Sci.* 105 (47) (2008) 18090–18095.
- [4] M. Okumura, L.I. Yeh, Y.T. Lee, The vibrational predissociation spectroscopy of hydrogen cluster ions, *J. Chem. Phys.* 83 (7) (1985) 3705–3706.
- [5] R.L. Woodin, D.S. Bomse, J.L. Beauchamp, Multiphoton dissociation of molecules with low power continuous wave infrared laser radiation, *J. Am. Chem. Soc.* 100 (10) (1978) 3248–3250.
- [6] D.S. Bomse, R.L. Woodin, J.L. Beauchamp, Molecular activation with low-intensity CW infrared laser radiation. Multiphoton dissociation of ions derived from diethyl ether, *J. Am. Chem. Soc.* 101 (19) (1979) 5503–5512.
- [7] N.C. Polfer, Infrared multiple photon dissociation spectroscopy of trapped ions, *Chem. Soc. Rev.* 40 (5) (2011) 2211–2221.
- [8] L. MacAleese, P. Maitre, Infrared spectroscopy of organometallic ions in the gas phase: from model to real world complexes, *Mass Spectrom. Rev.* 26 (4) (2007) 583–605.
- [9] J. Oomens, B.G. Sartakov, G. Meijer, G. von Helden, Gas-phase infrared multiple photon dissociation spectroscopy of mass-selected molecular ions, *Int. J. Mass Spectrom.* 254 (1–2) (2006) 1–19.
- [10] J.J. Valle, J.R. Fyler, J. Oomens, D.T. Moore, A.F.C. van der Meer, G. von Helden, G. Meijer, C.L. Hendrickson, A.G. Marshall, G.T. Blakney, Free electron laser-Fourier transform ion cyclotron resonance mass spectrometry facility for obtaining infrared multiphoton dissociation spectra of gaseous ions, *Rev. Sci. Instrum.* 76 (2) (2005) 023103.
- [11] N.R. Walker, R.S. Walters, M.A. Duncan, Frontiers in the infrared spectroscopy of gas phase metal ion complexes, *New J. Chem.* 29 (12) (2005) 1495–1503.
- [12] J. Lang, M. Gaffga, F. Menges, G. Niedner-Schatteburg, Two-color delay dependent IR probing of torsional isomerization in a $[\text{AgL}_2]^+$ complex, *Phys. Chem. Chem. Phys.* 16 (33) (2014) 17417–17421.
- [13] M. Gaffga, I. Munstein, P. Müller, J. Lang, W.R. Thiel, G. Niedner-Schatteburg, Multistate-mediated rearrangements and FeCl_2 elimination in dinuclear FePd complexes, *J. Phys. Chem. A* 119 (51) (2015) 12587–12598.

- [14] A.B. Wolk, C.M. Leavitt, E. Garand, M.A. Johnson, Cryogenic ion chemistry and spectroscopy, *Acc. Chem. Res.* 47 (1) (2014) 202–210.
- [15] J.M. Headrick, J.C. Bopp, M.A. Johnson, Predissociation spectroscopy of the argon-solvated $H_2O_2^+$ “zundel” cation in the 1000–1900 cm^{-1} region, *J. Chem. Phys.* 121 (23) (2004) 11523–11526.
- [16] O. Asvany, S. Brünken, L. Kluge, S. Schlemmer, COLTRAP: a 22-pole ion trapping machine for spectroscopy at 4 K, *Appl. Phys. B* 114 (1–2) (2014) 203–211.
- [17] P. Braunstein, P.R. Raitlby, L.A. Oro, *Metal Clusters in Chemistry*, vols. 1–3, Wiley-VCH, Weinheim, Germany, 1999, p. 1798.
- [18] A.F. Cotton, G. Wilkinson, M. Bochmann, C.A. Murillo, *Advanced Inorganic Chemistry*, Wiley, 1999.
- [19] J.E. Huheey, E.A. Keiter, R.L. Keiter, O.K. Medhi, *Inorganic Chemistry: Principles of Structure and Reactivity*, Pearson Education India, 2006.
- [20] F. Aubke, C. Wang, Carbon monoxide as a σ -donor ligand in coordination chemistry, *Coord. Chem. Rev.* 137 (1994) 483–524.
- [21] J.F. Hartwig, *Organotransition Metal Chemistry: From Bonding to Catalysis*, Univ Science Books, 2010.
- [22] R. Heck, *Organotransition Metal Chemistry A Mechanistic Approach*, Academic Press, 1974.
- [23] G. Somorjai, *Introduction to Surface Science and Catalysis*, Wiley, New York, 1994.
- [24] P. Buchwalter, J. Rosé, P. Braunstein, Multimetallic Catalysis based on Heterometallic Complexes and Clusters, *Chem. Rev.* 115 (1) (2015) 28–126.
- [25] J.E. Huheey, E. Keiter, R. Keiter, *Inorganic Chemistry, Principles of Structure and Bonding*, Harper Collins College Publishers, New York, 1993.
- [26] M. Wrighton, Photochemistry of metal carbonyls, *Chem. Rev.* 74 (4) (1974) 401–430.
- [27] G. Frenking, N. Fröhlich, The nature of the bonding in transition-metal compounds, *Chem. Rev.* 100 (2) (2000) 717–774.
- [28] K. Nakamoto, *Infrared and Raman Spectra of Inorganic and Coordination Compounds*, Wiley Online Library, 1986.
- [29] G. Ertl, *Reactions at Solid Surfaces*, vol. 14, John Wiley & Sons, 2010.
- [30] J. Chatt, L. Duncanson, Olefin co-ordination compounds. Part III. Infra-red spectra and structure: attempted preparation of acetylene complexes, *J. Chem. Soc. (Resumed)* 586 (1953) 2939–2947.
- [31] J. Dewar, A review of the π -complex theory, *Bull. Soc. Chim. Fr.* 18 (3–4) (1951) C71–C79.
- [32] G. Blyholder, Molecular orbital view of chemisorbed carbon monoxide, *J. Phys. Chem.* 68 (10) (1964) 2772–2777.
- [33] A. Fielicke, G. von Helden, G. Meijer, B. Simard, D.M. Rayner, Gold cluster carbonyls: vibrational spectroscopy of the anions and the effects of cluster size, charge, and coverage on the CO stretching frequency, *J. Phys. Chem. B* 109 (50) (2005) 23935–23940.
- [34] D.T. Moore, J. Oomens, J.R. Eyler, G. Meijer, G. von Helden, D.P. Ridge, Gas-phase IR spectroscopy of anionic iron carbonyl clusters, *J. Am. Chem. Soc.* 126 (45) (2004) 14726–14727.
- [35] Z.D. Reed, M.A. Duncan, Infrared spectroscopy and structures of manganese carbonyl cations, *Mn(CO) n^+ (n = 1–9)*, *J. Am. Soc. Mass Spectrom.* 21 (5) (2010) 739–749.
- [36] A.M. Ricks, Z.E. Reed, M.A. Duncan, Infrared spectroscopy of mass-selected metal carbonyl cations, *J. Mol. Spectrosc.* 266 (2) (2011) 63–74.
- [37] J. Velasquez, B. Njagic, M.S. Gordon, M.A. Duncan, IR photodissociation spectroscopy and theory of $Au^+ (CO)_n$ complexes: nonclassical carbonyls in the gas phase, *J. Phys. Chem. A* 112 (9) (2008) 1907–1913.
- [38] A.S. Goldman, K. Krogh-Jespersen, Why do cationic carbon monoxide complexes have high CO stretching force constants and short CO bonds? Electrostatic effects, not σ -bonding, *J. Am. Chem. Soc.* 118 (48) (1996) 12159–12166.
- [39] A.J. Lupinetti, S. Fau, G. Frenking, S.H. Strauss, Theoretical analysis of the bonding between CO and positively charged atoms, *J. Phys. Chem. A* 101 (49) (1997) 9551–9559.
- [40] G. Frenking, U. Pidun, Ab initio studies of transition-metal compounds: the nature of the chemical bond to a transition metal, *J. Chem. Soc. Dalton Trans.* 10 (1997) 1653–1662.
- [41] G. Bistoni, S. Rampino, N. Scafuri, G. Ciancaleoni, D. Zuccaccia, L. Belpassi, F. Tarantelli, How π back donation quantitatively controls the CO stretching response in classical and non-classical metal carbonyl complexes, *Chem. Sci.* 7 (2) (2016) 1174–1184.
- [42] A. Fielicke, G. von Helden, G. Meijer, D.B. Pedersen, B. Simard, D.M. Rayner, Size and charge effects on the binding of CO to late transition metal clusters, *J. Chem. Phys.* 124 (19) (2006), 194305–194305.
- [43] Z. Gengeliczki, B. Sztáray, T. Baer, C. Icmann, P.B. Armentrout, Heats of formation of $Co(CO)_2NOPR_3$, $R = CH_3$ and C_2H_5 , and its ionic fragments, *J. Am. Chem. Soc.* 127 (26) (2005) 9393–9402.
- [44] S. Goebel, C.L. Haynes, F.A. Khan, P.B. Armentrout, Collision-induced dissociation studies of $Co(CO)_x^+$, $x = 1–5$: sequential bond energies and the heat of formation of $Co(CO)_4$, *J. Am. Chem. Soc.* 117 (26) (1995) 6994–7002.
- [45] C. Moreno, M.J. Macazaga, M.L. Marcos, J. González-Velasco, S. Delgado, $[Co_4(CO)_{12}]$ derivatives with bis(diphenylphosphino) amine, an electrochemical study, *J. Organomet. Chem.* 452 (1) (1993) 185–192.
- [46] C. Fliedel, A. Ghisolfi, P. Braunstein, Functional short-bite ligands: synthesis, coordination chemistry, and applications of N-functionalized bis (diaryl/dialkylphosphino) amine-type ligands, *Chem. Rev.* 116 (16) (2016) 9237–9304.
- [47] (a) P. Buchwalter, J. Rosé, B. Lebeau, O. Ersen, M. Girleanu, P. Rabu, P. Braunstein, J.-L. Paillaud, Characterization of cobalt phosphide nanoparticles derived from molecular clusters in mesoporous silica, *J. Nanopart. Res.* 15 (12) (2013) 1–21;
(b) P. Buchwalter, J. Rosé, B. Lebeau, P. Rabu, P. Braunstein, J.-L. Paillaud, Stoichiometric molecular single source precursors to cobalt phosphides, *Inorg. Chim. Acta* 409 (2014) 330–341;
(c) F. Schweyer-Tihay, P. Braunstein, C. Estournes, J. Guille, B. Lebeau, J.-L. Paillaud, M. Richard-Plouet, J. Rosé, Synthesis and characterization of supported Co_2P nanoparticles by grafting of molecular clusters into mesoporous silica matrixes, *Chem. Mater.* 15 (1) (2003) 57–62.
- [48] P. Braunstein, H.-P. Kormann, W. Meyer-Zaika, R. Pugin, G. Schmid, Strategies for the anchoring of metal complexes, clusters, and colloids inside nanoporous alumina membranes, *Chemistry* 6 (24) (2000) 4637–4646.
- [49] S. Maruyama, L.R. Anderson, R.E. Smalley, Direct injection supersonic cluster beam source for FT-ICR studies of clusters, *Rev. Sci. Instrum.* 61 (12) (1990) 3686–3693.
- [50] C. Berg, T. Schindler, G. Niedner-Schatteburg, V.E. Bondybey, Reactions of simple hydrocarbons with Nb^+ : chemisorption and physisorption on ionized niobium clusters, *J. Chem. Phys.* 102 (12) (1995) 4870–4884.
- [51] P. Caravatti, M. Allemann, The ‘infinity cell’: a new trapped-ion cell with radiofrequency covered trapping electrodes for Fourier transform ion cyclotron resonance mass spectrometry, *Org. Mass Spectrom.* 26 (5) (1991) 514–518.
- [52] T.H. Dunning Jr., Gaussian basis sets for use in correlated molecular calculations. I. The atoms boron through neon and hydrogen, *J. Chem. Phys.* 90 (2) (1989) 1007–1023.
- [53] D.E. Woon, T.H. Dunning Jr., Gaussian basis sets for use in correlated molecular calculations. III. The atoms aluminum through argon, *J. Chem. Phys.* 98 (2) (1993) 1358–1371.
- [54] C. Adamo, V. Barone, Toward reliable density functional methods without adjustable parameters: the PBE0 model, *J. Chem. Phys.* 110 (13) (1999) 6158–6170.
- [55] M. Dolg, H. Stoll, H. Preuss, R.M. Pitzer, Relativistic and correlation effects for element 105 (hahnium, Ha): a comparative study of M and MO ($M = Nb, Ta, Ha$) using energy-adjusted ab initio pseudopotentials, *J. Phys. Chem.* 97 (22) (1993) 5852–5859.
- [56] M.J. Frisch, G. Trucks, H. Schlegel, G. Scuseria, M. Robb, J. Cheeseman, A. Scalmani, V. Barone, B. Mennucci, G. Petersson, Gaussian 09, Revision A. 1, Gaussian Inc., Wallingford, CT, 2009.
- [57] F.A. Reboredo, G. Galli, Size and structure dependence of carbon monoxide chemisorption on cobalt clusters, *J. Phys. Chem. B* 110 (15) (2006) 7979–7984.
- [58] S. Dillinger, J. Mohrbach, J. Hower, M. Gaffga, G. Niedner-Schatteburg, Infrared spectroscopy of N_2 adsorption on size selected cobalt cluster cations in isolation, *Phys. Chem. Chem. Phys.* 17 (16) (2015) 10358–10362.
- [59] J. Meyer, M. Tombers, C. van Wüllen, G. Niedner-Schatteburg, S. Peredkov, W. Eberhardt, M. Neeb, S. Palutke, M. Martins, W. Wurth, The spin and orbital contributions to the total magnetic moments of free Fe Co, and Ni clusters, *J. Chem. Phys.* 143 (10) (2015) 104302.
- [60] S.T. Akin, V. Zamudio-Bayer, K. Duanmu, G. Leistner, K. Hirsch, C. Bülow, A. Ławicki, A. Terasaki, B.V. Issendorff, D.G. Truhlar, J.T. Lau, M.A. Duncan, Size-dependent ligand quenching of ferromagnetism in $Co_2(\text{benzene})_n^+$ clusters studied with XMCD spectroscopy, 2016 (in press).
- [61] C. Janiak, H.-J. Meyer, D. Gudat, R. Alsfasser, *Moderne Anorganische Chemie*, Walter de Gruyter, 2012.

12.2 Vibrational Blue Shift of coordinated N₂ in [Fe₃O(OAc)₆(N₂)_n]⁺: “Non Classical” Dinitrogen Complexes

Johannes Lang, Jennifer Mohrbach, Sebastian Dillinger, Joachim M. Hewer,
and Gereon Niedner-Schatteburg

*Fachbereich Chemie und Forschungszentrum OPTIMAS
Technische Universität Kaiserslautern
67663 Kaiserslautern*

12.2.1 Preamble

The following chapter is a reprint of a publication in the journal “Chemical Communications”. The experiments were performed by the experimental team consisting of J. Mohrbach, J. Lang and myself. The data evaluation was done by J. Lang, J. Mohrbach and myself. J. Lang performed the computations. The initial manuscript was written by J. Lang and was revised with the help of G. Niedner-Schatteburg, J. Mohrbach and myself.

Full Reference:

Vibrational blue shift of coordinated N₂ in [Fe₃O(OAc)₆(N₂)_n]⁺: “non-classical” dinitrogen complexes

J. Lang, J. Mohrbach, **S. Dillinger**, J. M. Hewer, and G. Niedner-Schatteburg, *Chemical Communications*, **2017**, 53, 420-423.

<http://dx.doi.org/10.1039/C6CC07481B>

12.2.2 Reprint

Reprint License

Vibrational blue shift of coordinated N₂ in [Fe₃O(OAc)₆(N₂)_n]⁺: “non-classical” dinitrogen complexes

J. Lang, J. Mohrbach, S. Dillinger, J. M. Hower and G. Niedner-Schatteburg, *Chem. Commun.*, 2017, **53**, 420

DOI: 10.1039/C6CC07481B

This article is licensed under a [Creative Commons Attribution-NonCommercial 3.0 Unported Licence](#). Material from this article can be used in other publications provided that the correct acknowledgement is given with the reproduced material and it is not used for commercial purposes.

Reproduced material should be attributed as follows:

- For reproduction of material from NJC:
[Original citation] - Published by The Royal Society of Chemistry (RSC) on behalf of the Centre National de la Recherche Scientifique (CNRS) and the RSC.
- For reproduction of material from PCCP:
[Original citation] - Published by the PCCP Owner Societies.
- For reproduction of material from PPS:
[Original citation] - Published by The Royal Society of Chemistry (RSC) on behalf of the European Society for Photobiology, the European Photochemistry Association, and RSC.
- For reproduction of material from all other RSC journals:
[Original citation] - Published by The Royal Society of Chemistry.

Information about reproducing material from RSC articles with different licences is available on our [Permission Requests page](#).



ChemComm

COMMUNICATION

View Article Online
View Journal | View IssueCite this: *Chem. Commun.*, 2017, 53, 420Received 14th September 2016,
Accepted 2nd December 2016

DOI: 10.1039/c6cc07481b

www.rsc.org/chemcomm

Vibrational blue shift of coordinated N₂ in [Fe₃O(OAc)₆(N₂)_n]⁺: “non-classical” dinitrogen complexes†

Johannes Lang,* Jennifer Mohrbach, Sebastian Dillinger, Joachim M. Hewer and Gereon Niedner-Schatteburg

We present “non-classical” dinitrogen Fe(III) oxo acetate complexes *in vacuo* utilizing Infrared Photodissociation (IR-PD) at cryo temperatures. The IR-PD spectra reveal a blue shift of the N₂ stretching vibration frequencies in the complexes. Density Functional Theory (DFT) calculations confirm the experiments and indicate strengthened N–N bonds due to pronounced σ bonding and a lack of π back donation.

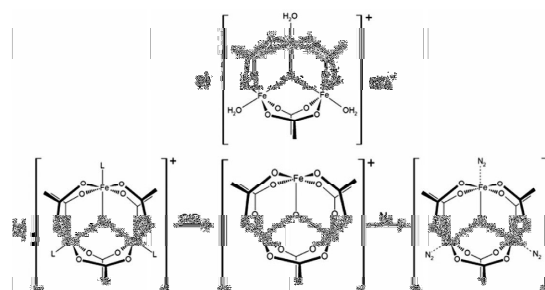
The discovery of transition metal dinitrogen complexes in 1965¹ launched the ever growing research field of N₂ coordination chemistry.^{2,3} One of the main goals is the conversion of N₂ to ammonia under mild conditions⁴ by homogenous catalysis.^{5,6} The basic idea is to weaken N–N bonds upon coordination to enable subsequent functionalization. Precursors to N₂ activation manifest by elongated N–N distances and by red shifting of stretching frequencies^{7,8} with respect to the vibration of the free N₂ molecule. Such bond activation and vibrational red shifts have been interpreted before, *e.g.* in terms of the Dewar–Chatt–Duncanson (DCD) model,⁹ and the Blyholder surface coordination (BSC)¹⁰ model. Theoretical as well as spectroscopic investigations confirmed these interpretations.¹¹ However, FT-IR studies on N₂ coordinated to Lewis acid centers in zeolites¹² and alumina¹³ revealed blue shifted vibrational N₂ stretching frequencies (up to 24 cm⁻¹). This indicates N–N bond strengthening rather than weakening – much beyond these established models. A similar effect has been observed in the case of isoelectronic carbon monoxide: so called “non-classical” metal carbonyl complexes^{14,15} exhibit blue shifted vibrational CO stretching frequencies (up to 138 cm⁻¹).¹⁶ Gas phase studies of isolated non-classical metal carbonyl clusters^{17,18} proved the intrinsic molecular origin of this effect. The cause for the CO blue shift was a topic of debate¹⁹ and is now understood in terms of an interplay between π back donation and electrostatic effects.²⁰ It is paramount to characterize the geometrical and electronic structures of such complexes in

order to acquire a fundamental insight into the prevailing interactions leading to such non-classical behaviour.

The combination of Electrospray Ionization Mass Spectrometry²¹ (ESI-MS) and infrared (IR) laser spectroscopy is suitable for the characterization of isolated coordination complexes with defined stoichiometry. Infrared (Multiple) Photon Dissociation (IR-(M)PD) provides direct access to structural and vibrational information, both under cryogenic conditions^{22,23} and at room temperature.²⁴ The experimental results and dedicated *ab initio* calculations are combined in order to obtain detailed insight into the geometrical structure and intrinsic properties of the isolated molecular ions.

In this work we investigate isolated dinitrogen complexes [Fe₃O(OAc)₆(N₂)_n]⁺ (*n* = 1–3, OAc = CH₃CO₂⁻, *cf.* Scheme 1), which exhibit a significant blue shift (17 cm⁻¹) of N₂ vibrations in the complex with respect to the free N₂ molecule. We examine the N₂ coordination in detail to rationalize the blue shift and N–N bond strengthening. This is, to the best of our knowledge, the first report on the “non-classical” behaviour of isolated N₂ complexes.

We utilize a customized Fourier Transform-Ion Cyclotron Resonance (FT-ICR)-mass spectrometer (Apex Ultra, Bruker Daltonics) equipped with an ESI ion source (Apollo 2, Bruker).



Scheme 1 (a) Molecular structure of the precursor [Fe₃O(OAc)₆(H₂O)₃](ClO₄) salt. In solution the water molecules exchange with solvent molecules (L – *e.g.* acetonitrile). (b) ESI-MS reveals the formation of [Fe₃O(OAc)₆(L)_n]⁺ (*n* = 0, 1, 2, 3). Collision induced dissociation (CID) of L yields the under-coordinated [Fe₃O(OAc)₆]⁺ complex, which binds 1–3 N₂ molecules at 26 K.

Fachbereich Chemie and Forschungszentrum OPTIMAS, Technische Universität Kaiserslautern, 67663 Kaiserslautern, Germany. E-mail: jlang@chemie.uni-kl.de

† Electronic supplementary information (ESI) available. See DOI: 10.1039/c6cc07481b

We coupled the ICR cell with a KTP/KTA optical parametric oscillator/amplifier (OPO/A) IR laser system (LaserVision). Optimized minimum energy structures and linear IR absorption spectra were calculated at the B3LYP²⁵ level of theory using cc-pVTZ basis sets²⁶ and Stuttgart RSC 1997²⁷ effective core potential basis sets (Gaussian 09²⁸). We present calculations with 15 unpaired alpha electrons yielding a spin multiplicity of 16 with other multiplicities (2–18) found to be significantly less stable (*cf.* Fig. S12, ESI[†]). We scale the calculated frequencies with two different scaling factors: one scaling factor (0.951) is specifically designed to elucidate N₂ stretching bands in [Fe₃O(OAc)₆(N₂)_n]⁺. It scales the calculated N₂ stretching frequencies such that a calculated free N₂ stretching vibration frequency matches the experimental value²⁹ of 2330 cm⁻¹. This approach conveniently reveals any effects of Fe–N₂ coordination on N₂ stretching frequencies. A second unspecific scaling factor (0.986) is applied for all other bands below 1800 cm⁻¹. It scales the calculated asymmetric carboxylate stretching vibration frequencies of [Fe₃O(OAc)₆(N₂)_n]⁺ to match our own experimental value of 1587 cm⁻¹. Unscaled spectra are provided in the ESI[†] (*cf.* Fig. S4).

Upon spraying the sample solution and recording mass spectra in the ICR-cell, we observe a series of isotopic peaks matching convincingly with simulated isotopic patterns (*cf.* Fig. S1, ESI[†]). We assign those peaks to [Fe₃O(OAc)₆(L)_n]⁺ (L = H₂O, acetonitrile, acetic acid; *n* = 0, 1, 2, 3). Elimination of L by Collision Induced Dissociation (CID) and subsequent coordination of N₂ in the hexapole at cryo temperatures (26 K) leads to the formation of [Fe₃O(OAc)₆(N₂)_n]⁺ (*cf.* Scheme 1b and Fig. S2, ESI[†]). Note that we observe *n*_{max} = 3, thus “titrating” the three available Fe

coordination sites. The calculated Gibbs energies at various temperatures reveal N₂ binding energies of 11, 9, and 8 kJ mol⁻¹ for the first, second, and third N₂ (26 K; BSSE corrected, *cf.* Fig. S3, ESI[†]). The N₂ binding Gibbs energies diminish with increasing temperature, vanishing above 80 K.

We recorded IR-PD spectra of cryocooled [Fe₃O(OAc)₆(N₂)_n]⁺ (*n* = 1, 2, 3, Fig. 1, black traces) and conducted DFT simulations to obtain their linear IR absorption spectra (Fig. 1, green traces). The DFT calculations reveal optimized minimum structures as depicted in the insets of Fig. 1. We observe several bands between 1300 cm⁻¹ and 1500 cm⁻¹, coinciding with the predicted CH₃ bending modes of the acetate ligands. While the calculated band frequencies around 1423 cm⁻¹ and 1467 cm⁻¹ agree well with the IR-PD spectrum, the calculated intensities differ significantly. Switching the DFT functional from B3LYP to PBE0 yields a much better match of IR intensities but significant deviations of calculated and observed vibrational frequencies (*cf.* Fig. S5, ESI[†]). Neither of these empirical functionals predicts both entities correctly. In the following we utilize the B3LYP results for further discussion.

The amount of N₂ coordination (*n* = 1, 2, 3) has no significant influence on the frequency and intensity of the CH₃ bending bands (neither in the IR-PD experiments nor in the DFT calculations). This finding likely originates from the spatial separation of the affected methyl groups from the Fe–N₂ coordination sites.

We find a strong IR-PD band at 1587, 1590, and 1591 cm⁻¹ in the cases of *n* = 1, 2, 3. We assign this band to carboxylic CO stretching bands of the six coordinated acetate ligands. The *n* = 1 CO stretching band is red shifted by ≈3–4 cm⁻¹ with

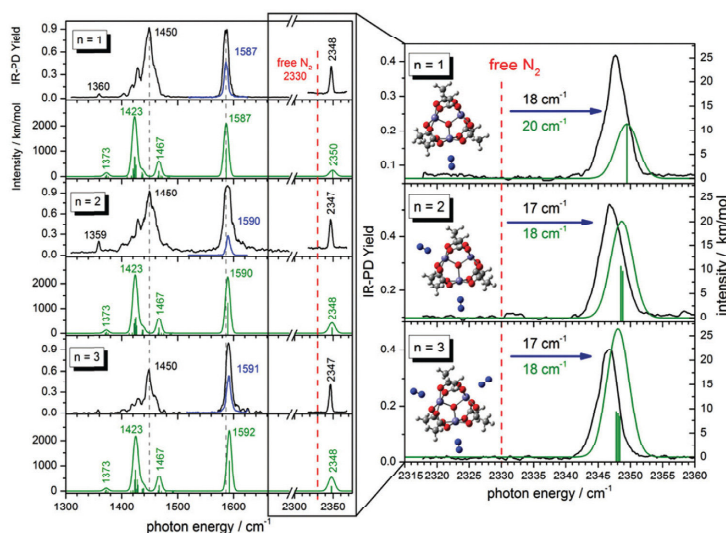


Fig. 1 Left: IR-PD spectra of [Fe₃O(OAc)₆(N₂)_n]⁺ (*n* = 1, 2, 3) at 26 K (black and blue curves) and calculated IR absorption spectra of optimized [Fe₃O(OAc)₆(N₂)_n]⁺ (*n* = 1–3) (green curves) in the range of 1300–2400 cm⁻¹. The blue IR-PD spectrum shows the CO stretching band (recorded with highly attenuated laser power to avoid saturation effects). The calculations were performed at the B3LYP/cc-pVTZ (H,C,N,O) and Stuttgart 1997 ECP (Fe) level of theory. The multiplicity is 16 and frequencies are scaled with 0.951 (0.986) above 2300 cm⁻¹ (below 2300 cm⁻¹). Calculated stick spectra were convoluted with a Gaussian envelope of FWHM = 7 cm⁻¹. Right: A zoom into the N₂ stretching vibration region. Calculated lines were convoluted with a Gaussian envelope of FWHM = 3.5 cm⁻¹. Insets show associated geometry optimized structures.

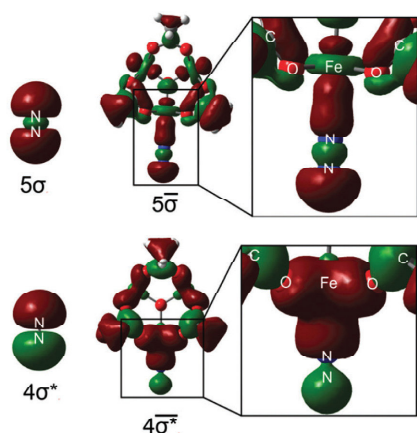


Fig. 3 Left: $4\sigma^*/5\sigma$ molecular orbitals of free N_2 . Right: Selected molecular orbitals of $[Fe_3O(OAc)_6(N_2)_1]^+$ involving the former $4\sigma^*(N_2)$ and $5\sigma(N_2)$ orbitals. $4\sigma^*(N_2)$ electron density delocalizes into the whole complex, thus strengthening the N–N bond.

Fig. S13 for $n = 2, 3, ESI^\dagger$). The electrons of the anti-bonding $4\sigma^*(N_2)$ orbital delocalize into a $4\sigma^*$ MO of the whole complex, whereby the $4\sigma^*(N_2)$ orbital polarizes towards the Fe center. Note that the node plane of $4\sigma^*(N_2)$ (between the N atoms) shifts somewhat towards the Fe center. The depletion of the anti-bonding electron density along the N–N bond increases the net bond order of N_2 and blue shifts the N_2 stretching vibration. The bonding $5\sigma(N_2)$ contributes to a 5σ MO of the complex. This is expected to result in N–N bond weakening counteracting the effect of $4\sigma^*(N_2)$ delocalization. However, $5\sigma(N_2)$ receives a partial $4\sigma^*(N_2)$ character to form the 5σ MO via hybridization. The strengthening effect of $4\sigma^*(N_2)$ electron density delocalization thus seems to be the critical factor for the “non-classical” behavior of $[Fe_3O(OAc)_6(N_2)_n]^+$. The involvement of the $4\sigma^*(N_2)$ orbital in the M– N_2 bonding scheme as well as $4\sigma^*/5\sigma$ hybridization has been suggested in the context of X-ray absorption studies of N_2 adsorbed on metal surfaces.³² Inspection of all other delocalized MOs in the $[Fe_3O(OAc)_6(N_2)_1]^+$ complex reveals a total lack of π back donation from the $[Fe_3O(OAc)_6]^+$ unit to empty $\pi^*(N_2)$ orbitals. Considering the high charge on the Fe center and the long Fe– N_2 distance (see above) this seems reasonable. The N_2 coordination and thus the “non-classical” behavior of $[Fe_3O(OAc)_6(N_2)_n]^+$ originate from σ bonding effects.

Our fundamental insight into the class of “non-classical” N_2 Fe complexes is remarkable in view of the industrial use of bulk iron for N_2 activation and hydrogenation. It might help to advance a general understanding of dinitrogen chemistry beyond established coordination models.

This work was supported by the German Research Foundation DFG within the Transregional Collaborative Research Center

SFB/TRR 88 “Cooperative effects in homo and heterometallic complexes” (3ME1).

Notes and references

- M. D. Fryzuk, *Chem. Commun.*, 2013, **49**, 4866–4868.
- J. L. Crossland and D. R. Tyler, *Coord. Chem. Rev.*, 2010, **254**, 1883–1894.
- N. Khoenkhoen, B. de Bruin, J. N. H. Reek and W. I. Dzik, *Eur. J. Inorg. Chem.*, 2015, 567–598.
- S. F. McWilliams and P. L. Holland, *Acc. Chem. Res.*, 2015, **48**, 2059–2065.
- D. V. Yandulov and R. R. Schrock, *Science*, 2003, **301**, 76–78.
- I. Tanaka, K. Arashiba, S. Kuriyama, A. Sasada, K. Nakajima, K. Yoshizawa and Y. Nishibayashi, *Nat. Commun.*, 2014, **5**, 1–11.
- N. Lehnert and F. Tuczek, *Inorg. Chem.*, 1999, **38**, 1659–1670.
- N. Lehnert and F. Tuczek, *Inorg. Chem.*, 1999, **38**, 1671–1682.
- J. Chatt and L. A. Duncanson, *J. Chem. Soc.*, 1953, 2939–2947.
- G. Blyholder, *J. Phys. Chem.*, 1964, **68**, 2772–2777.
- F. Studt and F. Tuczek, *J. Comput. Chem.*, 2006, **27**, 1278–1291.
- K. Hadjiivanov and H. Knözinger, *Catal. Lett.*, 1999, **58**, 21–26.
- R. Wischert, C. Coperet, F. Delbecq and P. Sautet, *Chem. Commun.*, 2011, **47**, 4890–4892.
- H. Willner and F. Aurbke, *Angew. Chem., Int. Ed.*, 1997, **36**, 2402–2425.
- A. J. Lupinetti, G. Frenking and S. H. Strauss, *Angew. Chem., Int. Ed.*, 1998, **37**, 2113–2116.
- P. K. Hurlburt, J. J. Rack, J. S. Luck, S. F. Dec, J. D. Webb, O. P. Anderson and S. H. Strauss, *J. Am. Chem. Soc.*, 1994, **116**, 10003–10014.
- J. Velasquez, B. Njagic, M. S. Gordon and M. A. Duncan, *J. Phys. Chem. A*, 2008, **112**, 1907–1913.
- A. Fielicke, G. von Helden, G. Meijer, B. Simard and D. M. Rayner, *J. Phys. Chem. B*, 2005, **109**, 23935–23940.
- A. S. Goldman and K. Krogh-Jespersen, *J. Am. Chem. Soc.*, 1996, **118**, 12159–12166.
- G. Bistoni, S. Rampino, N. Scafuri, G. Ciancaleoni, D. Zuccaccia, L. Belpassi and F. Tarantelli, *Chem. Sci.*, 2016, **7**, 1174–1184.
- J. B. Fenn, *Angew. Chem., Int. Ed.*, 2003, **42**, 3871–3894.
- N. Heine and K. R. Asmis, *Int. Rev. Phys. Chem.*, 2014, **34**, 1–34.
- J. Jašík, J. Žabka, J. Roithová and D. Gerlich, *Int. J. Mass Spectrom.*, 2013, 354–355, 204–210.
- J. Lang, M. Gaffga, F. Menges and G. Niedner-Schatteburg, *Phys. Chem. Chem. Phys.*, 2014, **16**, 17417–17421.
- A. D. Becke, *J. Chem. Phys.*, 1993, **98**, 5648–5652.
- T. H. Dunning, *J. Chem. Phys.*, 1989, **90**, 1007–1023.
- M. Dolg, H. Stoll, H. Preuss and R. M. Pitzer, *J. Phys. Chem.*, 1993, **97**, 5852–5859.
- M. J. Frisch, G. W. Trucks, H. B. Schlegel, G. E. Scuseria, M. A. Robb, J. R. Cheeseman, G. Scalmani, V. Barone, B. Mennucci, G. A. Petersson, H. Nakatsuji, M. Caricato, X. Li, H. P. Hratchian, A. F. Izmaylov, J. Bloino, G. Zheng, J. L. Sonnenberg, M. Hada, M. Ehara, K. Toyota, R. Fukuda, J. Hasegawa, M. Ishida, T. Nakajima, Y. Honda, O. Kitao, H. Nakai, T. Vreven, J. A. Montgomery, Jr., J. E. Peralta, F. Ogliaro, M. Bearpark, J. J. Heyd, E. Brodians, K. N. Kudin, V. N. Staroverov, R. Kobayashi, J. Normand, K. Raghavachari, A. Rendell, J. C. Burant, S. S. Iyengar, J. Tomasi, M. Cossi, N. Rega, J. M. Millam, M. Klene, J. E. Knox, J. B. Cross, V. Bakken, C. Adamo, J. Jaramillo, R. Gomperts, R. E. Stratmann, O. Yazyev, A. J. Austin, R. Cammi, C. Pomelli, J. W. Ochterski, R. L. Martin, K. Morokuma, V. G. Zakrzewski, G. A. Voth, P. Salvador, J. J. Dannenberg, S. Dapprich, A. D. Daniels, Ö. Farkas, J. B. Foresman, J. V. Ortiz, J. Cioslowski and D. J. Fox, *Gaussian 09, Revision E.01*, Gaussian, Inc., Wallingford CT, 2009.
- K. P. Huber and G. Herzberg, *Constants of Diatomic Molecules*, Van Nostrand, New York, 1979.
- J. D. Steill and J. Oomens, *J. Phys. Chem. A*, 2009, **113**, 4941–4946.
- A. M. Ricks, J. M. Bakker, G. E. Douberly and M. A. Duncan, *J. Phys. Chem. A*, 2009, **113**, 4701–4708.
- A. Nilsson and L. G. M. Pettersson, *Surf. Sci. Rep.*, 2004, **55**, 49–167.

12.3 Infrared Spectroscopic Investigations of Structures and N₂ Adsorption Induced Relaxations of Isolated Rhodium Clusters

Matthias P. Klein, Amelie A. Ehrhard, Jennifer Mohrbach, Sebastian Dillinger,
and Gereon Niedner-Schatteburg

Fachbereich Chemie und Forschungszentrum OPTIMAS

Technische Universität Kaiserslautern

67663 Kaiserslautern

12.3.1 Preamble

The experiments were performed by an experimental team consisting of M. P. Klein, A. A. Ehrhard, J. Mohrbach, and myself. The data evaluation was done by M. P. Klein. The computations were done by M. P. Klein. The initial manuscript was written by M. P. Klein and revised with the help of G. Niedner-Schatteburg and myself.

This manuscript has been **accepted** for publication in Topics in Catalysis.

Abstract

This paper presents a combined IR photo dissociation (IR-PD) spectroscopic and DFT computational study of cold Rhodium cluster N_2 adsorbate complexes, $[Rh_i(N_2)_m]^+ = (i,m)$, in the ranges of $i = 6, \dots, 15$ and $m = 1, \dots, 16$. DFT modelling of naked Rhodium clusters Rh_i^+ , $i = 6, 7, 9$ reveals high spin states (10tet, 13tet, and 17tet) of octahedral structures ($i = 6, 7$), and a tricapped trigonal prism ($i = 9$). The IR spectra of single N_2 adsorptions red shift in line with the established charge dilution model, and they reveal evidence for structural and/or spin isomers in cases of larger clusters $(i,1)$, $i \geq 12$. The IR spectra of cluster adsorbate complexes at or close to N_2 saturation indicate strong vibrational couplings and likely isomorphism. Together, the IR-PD and DFT spectra of the $[Rh_7(N_2)_{12}]^+ = (7,12)$ complex reveal spin quenching into a triplet state – as compared to the 13tet state of naked Rh_7^+ . This study is the starting point for systematic investigations of Rhodium cluster N_2 adsorbates and of Rhodium Iron hetero cluster N_2 adsorbates, which are work in progress.

Introduction

The study of the physical properties of isolated clusters and of their molecular adsorption kinetics, structures, and vibrational dynamics may enhance our understanding of elementary steps in the early parts of heterogeneous catalytic cycles which are most often based on transition metal compounds. Despite its high price, Rhodium catalysts find widespread applications in many industrial catalytic processes such as cyclopropanation [1,2], hydroformylation [3], and the manufacturing of acetic acid [4]. Nitrogen containing compounds form by Rhodium catalysis in processes such as hydrocyanation, hydroamination, and ammonia oxidation. Rhodium catalysts achieve deoxygenation [5,6] and hydrogenation [7] of nitrogen compounds. Rhodium finds wide spread practical use in car exhaust catalytic converters, where nitrogen oxides are reduced to N_2 [8], and it finds some use in stationary power plant exhaust cleaning [9].

In many cases the active catalyst is nanostructured, and the initial adsorption steps from gas phase are rate limiting – whether recognized or overlooked. It is obviously beneficial to study fundamental processes such as molecular adsorption and desorption, and to characterize suitable model systems such as size selected Rhodium clusters, and their adsorbates and products.

There are numerous studies on Rh gas phase clusters and complexes. Isolated Rh(I) atoms hexacoordinate a first layer of Ar atoms [10]. Numerous diatomic molecules (D_2 , O_2 , CO, and NO) were found to stick readily to Rhodium clusters by room temperature single collisions – except for N_2 , which requires precooling of the clusters (by lq. N_2) [11,12]. An early study found an anticorrelation between D_2 and N_2 reactivity and the Fermi energy of the neutral Rh_n clusters [13].

CO: Mineva et al. found a strong effect of the spin state (and local electronics/NBOs) on vibrational frequencies of $Rh_x(CO)_y$, and a weaker effect of cluster size x [14]. CO proved instrumental to unravel size and charge dependencies in adsorption to Rh cluster cations and anions alike, convincingly concluding in a charge dilution model [15-19]. Subsequent studies identified CO on top and on bridge throughout all Rh clusters studied except for Rh_4 and Rh_{11} where CO on hollow site was observed instead [20]. For larger clusters, Tian et al. found a transition to layered structures in Rh clusters at $n = 11$ to 12 and three types of CO adsorption, not scalable with size: atop, bridge, and face [21]. Non hybrid DFT functional modelling of $Rh_i(CO)_{1+0/-}$ complexes found trigonal prismatic and cubic structural motifs of the cluster core [22] and end on bridging μ_2/μ_3 adsorption motifs of CO on the charged clusters up to $i = 6$ and a end on μ_1 motif for the larger clusters [23].

NO_x: Biexponential kinetics of the initial adsorption step in the $Rh_6^+ + NO$ system suggested the co-existence of stable isomers [24] that quench upon collisional cooling, while the co-existing isomers of Rh_{11}^+ and Rh_{12}^+ persist [25,26]. DFT modelling elucidated the likely structures of the reactive $[Rh_6,NO]^+$ system [27] and of the $[Rh_{3,4,6,13},NO]^{+/-}$ systems [28] in detail. NO adsorption was found with Rhodium clusters of any size, while NO reduction takes clusters Rh_n^+ , $n > 5$ and elevated temperatures ($T > 850$ K) [29]. A series of studies identified nitrogen-bound NO and N_2O on various Rh_n^+ clusters and IR driven or collisional decomposition [30-34]. The Tantalum alloying of Rhodium clusters was found to control NO reduction [35]. Relativistic ZORA level calculations found the N_2O reduction on Rh_6^- and Rh_6^+ sensitive to the cluster charge, rather than to its geometry [36]. The adsorption of a second NO was identified as rate limiting step in CO oxidation on Rh_7^+ by DFT modelling [37], other calculations modelling NO reduction by CO on Rh_4^+ [38].

Hydrocarbon reactions: Rhodium cluster Argon complexes modulate CH_4 activation by the level of Ar coating [10,39]. Benzene adsorption and activation compete on Rh_n^+ clusters for

$n < 19$, the larger ones becoming inert [40] and cluster charge having unexpectedly little effect on the dehydrogenation reactivity [41]. Partial dehydrogenation of small alkanes by Rh_n^+ , $n < 30$ indicated a bi-icosahedral shape of Rh_{19}^+ [42], supported by lack of reactivity with ethane at $n = 17 - 19, 21$ [43]. Azidoacetonitrile ($\text{N}_3\text{CH}_2\text{CN}$) was found to readily release $\text{N}_2 + \text{H}_2$ upon contact to Rh_n^+ generating either interstitial carbides and nitrides, or yielding surface nitriles [44].

Electronics and magnetism: Rhodium cluster geometries by model potentials and magnetism by tight binding have reached limits in simulating magnetic moments of Rhodium clusters [45]. A more recent relativistic modelling study spent high effort on an appropriate description of the electronics of such Rh_n clusters in order to determine the magnetic moments by their spin and orbital contributions. It suffered, however, from little effort on the nuclear coordinates merely assuming fcc lattices of spherical shape without geometric relaxation [46]. DFT modelling of single and multiple charges was found to exert strong influence on the structure and magnetism of Rhodium clusters [47]. Choice of a large basis sets in DFT modelling was found crucial before in order to obtain converged predictions on structures of Rh_n , $n \leq 6$ [48]. Simultaneously performed magnetic and electric deflection measurements of Rhodium clusters (Rh_n , $6 \leq n \leq 40$) reveal ferromagnetism and ferroelectricity at low temperatures neither of which property exists in the bulk metal [49]. Nevertheless, our knowledge of the electronic and magnetic properties of small Rhodium clusters is still limited, and the different structural and spin isomers are very close in energy [50].

A significant advance on the structural elucidation of Rh_n^+ clusters arose through free electron laser and Argon tagging enabled vibrational spectroscopy in conjunction with corresponding DFT modelling (PBE(1)/LanL2DZ) of the obtained spectra [51,26]. The following was found: octahedral structure motifs for the Rh_6^+ and Rh_8^+ cluster, a pentagonal bipyramidal structure for the Rh_7^+ cluster, a trigonal prismatic structure for the Rh_9^+ cluster, and icosahedral structural motif for larger clusters up to Rh_{12}^+ . This as well as another DFT study [52] left some room for improvement in terms of the usage of more advanced basis sets. These investigations are the first to demonstrate the importance of hybrid functionals for the investigation of Rhodium clusters.

Basin hopping DFT calculations predicted various properties of $\text{Rh}_x\text{S}_y^{+/0/-}$ ($x = 1-9$; $y = 0,1$) clusters and emphasized the importance of hybrid_GGA functionals (e.g. PBE0) while questioning the appropriate percentage of exact Hartree–Fock exchange, and concluding on ambiguities in current spin state determination [53].

Prior N_2 vibrations: FT-IR studies of laser ablated Rh atoms in N_2 doped Ar matrix revealed numerous bands in the 600 to 2200 cm^{-1} range which were attributed to $\text{Rh}(\text{N}_2)_{1-4}$ and other small Rh_xN_y products [54]. Investigation of an isolated $\text{Rh}(\text{N}_2)_4^+$ complex by IRMPD spectroscopy obtained an N_2 stretch at 2297 cm^{-1} band [55] which is much less red shifted than in the neutral complexes and close to the free N_2 stretch at 2330 cm^{-1} [56]. This is likely due to less back bonding by cationic Rh.

Our study: We present an IR spectroscopic study of Dinitrogen on cold Rhodium cluster adsorbate complexes with support by some DFT calculations in three cases, Rh_i^+ ($i = 6,7$, and 9), and we chose the experimental and calculated IR spectra of the $[\text{Rh}_7(\text{N}_2)_{12}]^+$ cluster adsorbate complex for an analysis in more detail. Considering conceivable Rh cluster isomerization barriers on the order of N_2 heats of adsorption we expect considerable structural relaxation in the cluster adsorbate complexes as of relevance in the context of catalytically active clusters and nanoparticles in operando.

Experimental and Computational Methods

The experiments were performed by a customized 7 Tesla Fourier Transform-Ion Cyclotron Resonance (FT-ICR)-mass spectrometer (Apex Ultra, Bruker Daltonics). We produced the cluster ions in a home-built laser vaporization source as described before [57-59]. The second harmonic of a Nd:YAG laser is focused on a rotating Rhodium-target (99.8 %, Alfa Aesar, 0.1 mm thick). The resulting plasma is entrained in a helium gas pulse (40 μs , 10-15 bar), which was generated by a homemade piezoelectric valve [60], synchronized to the evaporating laser at 20 Hz. The pressure of the laser vaporization chamber rises from roughly 3.5×10^{-7} to 1.6×10^{-4} mbar during He pulsing. The plasma contains atoms and ions and while they cool down, they aggregate to clusters in the subsequent jet expansion through a 50 mm long channel (2 mm diameter) into vacuum (3×10^{-7} mbar). The cluster beam is skimmed and the cluster ions are accelerated and guided through a 90° static quadrupole ion bender. The required cluster ions are selected by an RF quadrupole mass filter

and stored into a cryogenic hexapole ion trap at 26 K which is held at 3.0×10^{-6} mbar He buffer gas pressure. We achieve Nitrogen attachment by constantly adding $3.0 - 3.8 \times 10^{-7}$ mbar N_2 . Then we use He to increase the pressure in the ion trap to roughly 4.0×10^{-6} mbar. Within ion storage times of up to 2 sec all Rhodium clusters reach adsorbate saturation, and we randomly checked for much longer times no further attachment being observed. Subsequently, all stored ions are gently extracted with as little potential gradient as possible, accelerated, steered and decelerated into the ICR-cell by a high definition electrostatic ion lense setup [61,62]. Transfer and trapping efficiency is about 10%. The ICR-cell of the infinity-type [63] is cooled to 10 K by a closed cycle He cryostat [64,65] in order to prevent activation of the clusters by black body radiation [66,67]. In order to record IR-PD spectra of $[Rh_i(N_2)_m]^+$ cluster adsorbate complexes by their sizes (i,m) we isolate the parent cluster ion of interest by RF exciting and removing all other ions from the cell.

For the acquisition of the IR-PD spectra the FT-ICR cell is coupled to a tunable IR laser ($\delta n = 0.9 \text{ cm}^{-1}$, $\delta t = 7 \text{ ns}$, $E_{\text{puls}} = 0.4 - 1.3 \text{ mJ}$). This laser is a KTP/KTA optical parametric oscillator/amplifier (OPO/A, LaserVision) system which is pumped by a pulsed 10 Hz injection seeded Nd:YAG laser (PL8000, Continuum). The difference frequency (DF) between the OPA signal and idler waves is generated in an AgGaSe₂ crystal. This generates IR radiation in the range of $1000 - 2400 \text{ cm}^{-1}$. Each trapped and isolated package of ions is irradiated by multiple laser pulses (up to 7) in order to accumulate fragment ions. The IR-PD spectra were recorded as ion chromatograms while continuously scanning the IR wavelength. The IR-PD signal was evaluated as $\Sigma_i F_i / (\Sigma_i F_i + \Sigma_i P_i)$, where F_i and P_i indicate fragment and the parent ion signals, respectively. An experimental IR-PD spectrum arises from a plot of the fragmentation efficiency as a function of laser frequency. We employed the IR-PD spectroscopy in the $2140 - 2310 \text{ cm}^{-1}$ range on the $[Rh_i(N_2)_m]^+$ species ($i = 6 - 15$). In this range we expected the N_2 stretching frequencies of the species. For all complexes the loss of the N_2 was the only observed fragmentation channel. Note, that IR-PD spectra of (i,m) species with high m likely originate from single photon absorption, whereas those of low m likely originate from two or even multiple photon absorption – rendering the latter IRMPD spectra.

Density functional modelling was performed by the Gaussian 09 package [68] and with the ECCE interface [69]. We chose the PBE0/ECP(Rh); cc-PVTZ(N) level of theory [70] as proven

suitable before [57,71,72]. We utilize Stuttgart RSC 1997 ECP(Rh) basis sets of double zeta quality throughout [73] which are of significantly higher quality than the often applied basis set LanL2DZ. We did not correct for dispersion effects which we expect small. We do not cover spin orbit coupling which might alter some of our findings. We achieved convergence of our calculation only at the expense of a relaxed convergence criterion of only 10^{-6} , which is well understood in terms of the exceedingly high electronic state density of transition metal clusters [39]. We chose an anharmonic linear scaling factor of 0.9385 to match the calculated free N_2 stretching frequency (2483 cm^{-1}) to the Raman band of free N_2 at 2330 cm^{-1} [56]. We checked the results for spin contamination, and we observed a small rise of the S^2 value merely in cases of the lowest multiplicities and negligible spin state mixing otherwise. We regard our theoretical approach as well gauged by considering our single N_2 adsorption enthalpies of about 50 kJ/mol (lower limit) in comparison to 56 kJ/mol on stepped Rh surfaces as obtained before [74,75].

Results and Discussion

DFT modelling of naked Rh_i^+ clusters ($i = 6, 7,$ and 9)

In order to lay ground for the characterization of N_2 adsorption to the Rh clusters we set off with DFT modelling of the naked Rh clusters in the first place. We focused on Rh_i^+ ($i = 6, 7,$ and 9) in order to identify most stable structures and competing isomers. In particular, we strived to elucidate the prevailing spin states and their interplay with nuclear geometries, and we have investigated Rh_7^+ in depth. We checked the obtained minimum structures for imaginary vibrational frequencies and found all reported isomers to be true minimum structures.

Rh_6^+ : In the case of the Rh_6^+ cluster we started from the three suggested geometries of Harding et al.: a boat like structure (boat), a capped square prism (csp), and an octahedron (oct). We found it appropriate to consider a trigonal prism (tp) as well. Upon investigating these structures, we utilized an extended range of spin multiplicity $2S+1 = 2 - 18$. We found the Rh_6^+ clusters to isomerize significantly upon optimization, in remarkable contrast to the cases of Rh_7^+ and Rh_9^+ clusters, and we provide for a comprehensive overview over the found evolution of starting structures towards optimized structures in the supplementary material (Table S2).

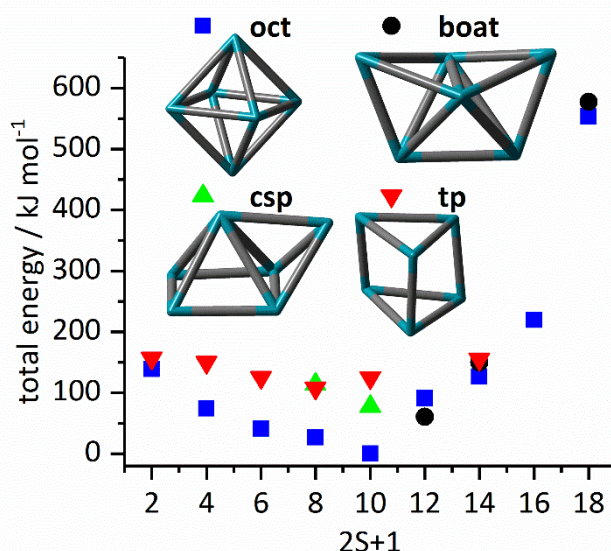


Fig. 1 Total energies of four possible Rh_6^+ cluster structures as a function of the spin multiplicity $2S+1$ in relation to the obtained minimum (oct 10tet). In addition a capped square prism (csp), a trigonal prism (tp), and an octahedron (oct) were considered as starting geometries. The calculated minimum structures for each structural motif are shown as insets. Remarkably, the starting structures are subject to major isomerization. The calculated minimum structure is a distorted octahedron with a 10tet spin state.

The 10tet spin state in octahedral geometry (oct) is the optimum of Rh_6^+ at the level of our DFT calculation (Fig. 1). At all lower spin states down to the doublet the octet minimum structure persists with slight distortions. Increasing total spin beyond 10tet is possible at the expense of reorganization towards a boat like structure. The stability gain by turning two fourfold coordinated Rh atoms into fivefold coordinated ones overcompensates the loss by turning two other fourfold coordinated Rh atoms into threefold coordination. Note, that spin quenching from 10tet to 8tet affords 27 kJ/mol while an isomerization of octet into capped square pyramid (csp) amounts 78 kJ/mol.

The dominance of octahedral cluster structures is in accordance with a previous study that assigned a distorted octahedron with a 10tet electronic state to their experimental spectra of a naked Rh_6^+ cluster [51]. Our present investigation extends that work by covering spins and geometries beyond the predicted optimum. Note, that spin-orbit coupling effects in Rh are on the order of 18 kJ/mol and thus may mediate dynamic spin quenching.

Rh₇⁺: We find a clearly limited variation of spin couplings, while there is a considerable flexibility in nuclear rearrangement: The meridonal square in octahedral geometry (coh) may open into a fivefold ring and convert into pentagonal bipyramid (pbp). In most stable 13tet

spin state this isomerization would take at least ~ 47 kJ/mol, with a possible barrier adding on top. Spin quenching of coh 13tet into 11tet would take only 12 kJ/mol and subsequent isomerizations to a pbp structure are facile.

We optimized possible geometries and spin states of the Rh_7^+ cluster, and we found most stable capped octahedron (coh) in 13tet and 11tet spin states which differ by ~ 12 kJ/mol (Fig. 2). Interestingly, the next stable pentagonal bipyramid structure is almost degenerate in 11tet, 13tet and 15tet states, yet less stable than coh by at least 29 kJ/mol. The pbp structure thus allows for considerable spin variation, while the coh is in favour of a sole spin state. The capped trigonal prism (ctp) is slightly less stable than pbp and considerably less stable than coh. Not that all of this may change through spin orbit coupling effects and / or through antiferromagnetic couplings – both of which are much beyond our current DFT approach.

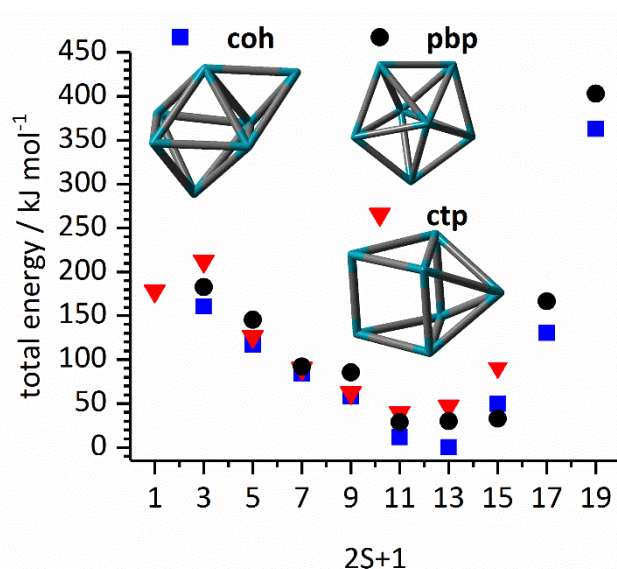


Fig. 2 Total energies of Rh_7^+ cluster structures as a function of the spin multiplicity $2S+1$ relative to the most stable capped 13tet of an octahedron (coh). Other structural motifs are capped trigonal prisms (ctp) and pentagonal bipyramids (pbp) as depicted by the insets.

Harding et al. assigned Rh_7^+ a distorted pbp structure [51], and Hang et al. calculated most stable Rh_7^0 as a distorted pentagonal pyramid and a capped octahedron mere 3.8 kJ/mol less stable [52]. On the other hand, electric deflection studies support the dominance of a capped octahedral structure [76].

We found it appropriate to gauge our computational findings in the case of Rh_7^+ coh 13tet against other studies and species, and we took the Rh-Rh distances as elucidating indicators (see Table 1). Our found coh structure is distorted from C_{3v} symmetry of a perfect capped octahedron, and the interatomic distances deviate. All of the next neighbor distances in Rh_7^+ are considerably longer than in the dimer and somewhat shorter than the solid state values indicating a bond between the next neighbors. The calculated distances in the neutral pbp structure are in the same range.

Table 1 Calculated atomic distances (in Å) for nearest neighbors for the coh Rh_7^+ clusters in comparison with crystal structures, experimental data and calculations on a neutral 14tet pbp structure.

	dimer	Rh_7	Rh_7^+	bulk
Calc.	2.21 ^a	2.61 ^a	2.446 - 2.665 ^{tw}	
	2.27 ^{b1}	2.58 ^{b2}	2.37 - 2.60 ^{b3}	
Exp.	2.3855 ^c			2.69 ^d

a Ref. [77] VASP PW91 GGA / LDA; Rh_7^+ : neutral pbp 14tet

b [78] TZVP, ECP28MWB ; b1: neutral dimer quintet b2: neutral pentagonal bipyramid, 14tet; b3: neutral capped trigonal prism, 12tet

c [79] crystal structure of $[\text{Rh}_2(\text{O}_2\text{CCH}_3)_4(\text{H}_2\text{O})_2]$

d [80] distance of next neighbors in fcc crystal, lattice parameter $a = 3.8032 \text{ \AA}$

tw this work: PBE0, coh 13tet cation

Rh_9^+ : In order to model the Rh_9^+ cluster we have chosen four structural archetypes for optimization: tricapped trigonal prism (tri), capped trigonal antiprismatic structure (trig-ap), double-capped pentagonal bipyramid (dc-pbp), and capped square antiprism (ac-top), and we checked for spin multiplicities $2S+1 = 9, \dots, 21$ (Fig. 3). We find most stable a slightly distorted tricapped trigonal prism (tri, 17tet, D_{3h}), and this motif stays most stable upon total spin variation from 13tet up to 19tet. A previous study concluded in a 15tet tricapped trigonal prism with likely contributions of a dc-pbp like structure to a recorded far IR spectrum [51]. Note, that the neutral Rh_9 cluster seems to persist in a distorted tri structure type geometry in nearly degenerate 12tet and 16tet spin states [52].

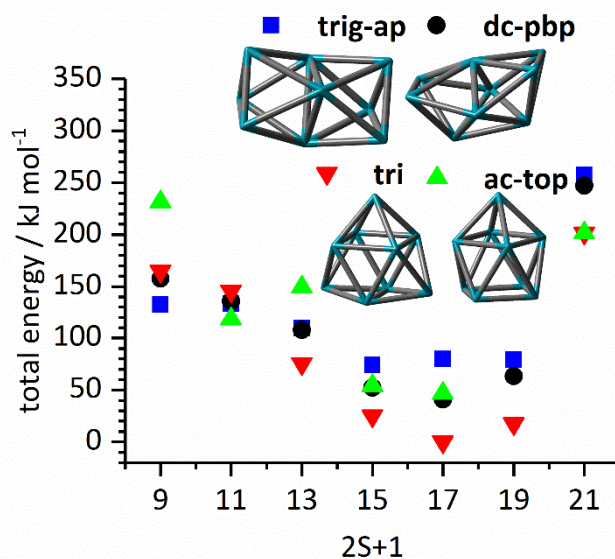


Fig. 3 Total energies of Rh_9^+ cluster structures by their spin multiplicity $2S+1$ relative to the most stable 17tet of a tricapped trigonal prism (tri). Other structural motifs are trigonal antiprisms (trig-ap), double-capped pentagonal bipyramids (dc-pbp), and capped anticubes (ac-top) as depicted by the insets.

IR-PD spectra of single N_2 adsorbates on Rhodium cluster cations

We have recorded IR-PD spectra of $[\text{Rh}_i(\text{N}_2)_m]^+$ cluster adsorbate complexes. Even upon single N_2 adsorption we found a multitude of bands (Fig. 4) which are red shifted by 55 – 120 cm^{-1} with respect to the free N_2 stretching vibration at 2330 cm^{-1} [56]. For ease of reference we will utilize in the following the abbreviating nomenclature $[\text{Rh}_i(\text{N}_2)_m]^+ = (i,m)$. The obtained band positions range from 2210 to 2275 cm^{-1} which is a range similar to the range of observed vibrations of N_2 adsorbates on cobalt clusters [57] as well as to those of nickel and iron clusters [71,81,82]. As for these and Ruthenium clusters [57,71,83], we expect a μ_1 binding motif of N_2 . There are some fluctuations of the exact band positions around the overall trend of red shift with cluster size. There are some additional strong bands ($i = 9, 12, 13, 15$) and some additional weak side bands ($i = 8, 10$ und 11) which are 20 cm^{-1} to the red (marked by red circles). This is reminiscent of similar effects in the previously reported cobalt cluster spectra [57], all of which are non-scalable cluster size effects.

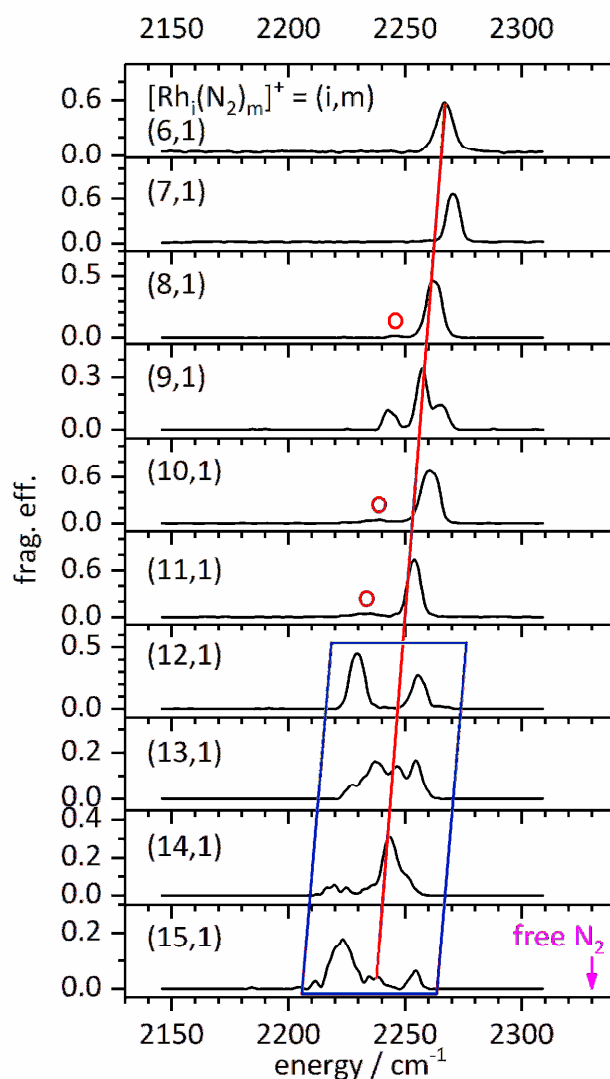


Fig. 4 IR-PD spectra of Rhodium cluster cation single N_2 adsorbate complexes $[\text{Rh}_i(\text{N}_2)_1]^+$, $i = 6 - 15$ as recorded after 26 Kelvin He buffer gas cooling. The red line and the tilted blue box serve to guide the eye indicating the red shift with cluster size i . The red circles mark possible hot bands – or possible isomers (see text for further discussion).

The spectra of (6,1), (7,1), (8,1) (10,1) and (11,1) are dominated by a single strong peak which we assign to the stretching vibration of an N_2 adsorbate end on to the cluster surface. In these cases, we conclude in the absence of geometric isomers of the Rh cluster core, in the dominance of single spin isomers, and in the equivalence of all occupied N_2 binding sites. The additional “red circle” bands might relate to hot bands, which would arise through de-excitation of some soft Rh core vibrations – yet somewhat unlikely in view of the isothermal cryo conditions of our experiment. Other interpretations are conceivable, such as highly coordinated, semi-internal adsorption sites or even some low spin isomers. The latter come

into mind when relating the most stable Rh_6^+ structures of Fig. 1 to the previously found convincing evidence of isomeric reactivity in NO attachment to Rh_6^+ [24]. It is puzzling, however, that the present (6,1) IR-PD spectra of single N_2 attachment do not reveal any evidence of geometric or electronic isomers. It takes further experiments and calculations to resolve this puzzle.

In remarkable contrast the spectra of (9,1), (12,1), (13,1) (14,1) and (15,1) reveal two, three or multiple adsorption bands within the same range. This is clear indication for some kind of isomeric co-existence. Three types of isomers come to our minds: Within the cluster adsorbate complexes there might be structural isomers of the Rh cluster core. There might be coexisting complexes in different spin states. There might be adsorption site isomers. Yet conceivable, we do not find evidence for changes in coordination geometry (μ_1 , μ_2 or μ_3) which would likely lead to much larger jumps of band positions much beyond what we observe. Note, that there is in none of the recorded cases any change of spectral features by the applied laser power (cf. Fig. S2 in the supplement).

The general red shift with respect to the free N_2 vibration is conceivable in terms of the Blyholder model [84]. This model has been developed for the explanation of the IR spectra of CO adsorbed to metal surfaces and may be applied to the isoelectronic N_2 molecule. The synergism of σ -donor und π -acceptor properties of N_2 , similar to the Dewar-Chatt-Duncanson model [85,86], leads to a weakening of the N-N bond and a red shift of the N-N stretching frequency.

There are previous studies on spectral shifts of CO adsorbates on Rhodium clusters which have been interpreted in terms of a charge dilution model [17]. We have utilized this model before in order to explain N_2 red shifts when adsorbed to Cobalt and Nickel clusters [57,71]: An increasing dilution of the positive charge by cluster size leads to a higher electron density at each surface site and thus to an increase of the π backdonation into an antibonding π^* adsorbate orbital which causes red shift of the stretching vibration.

The structure of the Rh cluster core and the occurrence of non-equivalent adsorption sites influence the N_2 vibrations. The Rh surface atoms differ by number and arrangement of next neighbors. *Rough* cluster surfaces originate from a multitude of different adsorption sites, *smooth* cluster surfaces from equivalent ones. The occurrence of internal, inaccessible non

surface atoms sets in at cluster sizes of 13 metal atoms in case of icosahedral Rh structures. Note, that in particular the Rhodium clusters are known for stiff bonds (little bond length variation) in favor of close packing and at the expense of structural ambiguity and co-existing isomers [87]. It thus seems likely that N₂ adsorption may induce cluster surface reorganization to some extent. Our own calculations reveal a strong preference of N₂ adsorbates in an end on μ_1 arrangement (on top). Any of our attempts with μ_2 (bridge) starting geometries swiftly relaxed $\mu_2 \rightarrow \mu_1$. Any adsorption site thus coincides with a single Rh surface atom.

In the light of all of the above we analyze each of the recorded (i,1) IR-PD spectra in the following: The recorded single band of the (6,1) spectrum reveals a single type of adsorption sites as e.g. by an Rh₆⁺ octahedron, in line with present and previous structure calculations [51]. The single N₂ band in the (7,1) spectrum is less red shifted indicating less π back donation as e.g. by the low coordinated Rh capping atom in our calculated octahedron Rh₇⁺ structure, which has merely three next neighbors. This is in contrast to the previous pentagonal bipyramid Rh₇⁺ structure [51] which would not provide for such a low coordinated Rh site. It is conceivable that adsorbates induce structural relaxation. If indeed so, this would imply that π back donation of N₂ makes the difference with respect to Ar which lacks this option/effect – polarizabilities of both being almost identical. Further computations might focus onto this issue. The single strong IR-PD band of (8,1) may originate from either of two conceivable Rh cluster core geometries: a bicapped octahedron or an almost as stable bicapped trigonal prism (+17 kJ/mol) [26,51] with likely swift isomerization into each other, possibly adsorption induced. Marked by a red circle in Fig. 4, this weak band to the red may originate from an N₂ at a higher coordinated Rhodium site. It is the (9,1) cluster N₂ adsorbate complex which reveals a triplet of IR-PD bands which comes as somewhat of a surprise. This work and previous computations [51] agree on Rh₉⁺ in a tricapped trigonal prism geometry [88]. As such structure comes with four- and fivefold coordinated Rh atoms, it provides for two adsorption sites and accordingly, it would explain two N₂ vibrational bands. We take the observation of three N₂ vibrational bands as likely evidence for an adsorption induced relaxation and symmetry reduction of the Rh₉⁺ cluster core in (9,1). In contrast to previous studies on the Rh_i⁺ i = 6 – 8 clusters [24,25] we do not

find any evidence for the existence of multiple isomers in the IR-PD spectra of the correspondent $[\text{Rh}_i(\text{N}_2)_m]^+$, $i = 6 - 8$, $m = 1$, Rhodium cluster single N_2 adsorbate complexes.

The single strong IR-PD band of (10,1) and (11,1) indicates a homogeneous cluster adsorbate ensemble void of N_2 binding site isomers and void of Rh cluster core structural isomers. Due to the reduced red shift of the observed N_2 vibrational bands we tentatively assign these bands to μ_1 adsorbates on top of low coordinated adsorption sites some of which occur in all suggested structures of $\text{Rh}_{10,11}^{-/0/+}$ clusters [51,52]. Initial N_2 adsorption at higher coordinated sites stabilize into the above low coordinated sites via high adsorbate mobility on the surface of the Rh cluster cores. Once more marked by red circles in Fig. 4, these weak bands to the red may originate from N_2 at higher coordinated Rhodium sites.

The two widely split, strong IR-PD bands of (12,1) indicate a transition in the structure of the Rh cluster core and a loss of adsorbate mobility. Note, that the coexistence of cluster adsorbate isomers seems rather unlikely with regard to the considerable heat of N_2 adsorption (56 kJ/mol [74]) which is likely sufficient for annealing of the cluster structure. The predicted layered Rh_{12}^+ structure would provide for two highly coordinated central Rh atoms and ten peripheral low coordinated Rh atoms. We tentatively assign the observed two bands to these adsorption sites, the higher coordinated Rh sites causing the larger red shifts in their N_2 adsorbates. Harding et al. assigned a structure consisting of two centered pentagonal layers [51]. Thus, we can assume the existence of two different adsorption sites reflected in the IR-PD spectra of (12,1).

The multitude of partially resolved IR bands of (13,1), (14,1), and (15,1) ask questions which hardly obtain answers without input from computations. These are not available as of now. We tentatively conclude in the occurrence of several adsorption sites and in reduced N_2 adsorbate mobility. Further insights may arise from future modelling.

IR-PD spectra of multiple N_2 adsorbates on Rhodium cluster cations

The Rhodium clusters Rh_i^+ may adsorb N_2 up to a *maximum adsorption limit*, which is clearly related to the actual cluster structure. It is conceivable, that the $[\text{Rh}_i(\text{N}_2)_m]^+$ reorganize upon stepwise adsorption of further N_2 , and we find clear evidence in at least one case.

In the course of the present study, we recorded IR spectra of the $[\text{Rh}_i(\text{N}_2)_m]^+$ $i = 6 - 11$ cluster adsorbate complexes at or close to N_2 saturation (Fig. 5) in order to augment/complement the IR spectra of single N_2 adsorption discussed before.

All spectra of multiple N_2 adsorptions reveal higher red shifts than those of single N_2 adsorptions. Note, that the Blyholder model would predict the opposite, a reduction of red shift upon N_2 saturation: The more N_2 molecules compete for the electrons of the cluster core, the less electron density is transferred into the π^* orbital of each N_2 molecule. Also, the Rh cluster size dependent charge dilution diminishes upon N_2 saturation, while it is clearly in effect upon attachment of the first N_2 adsorbate.

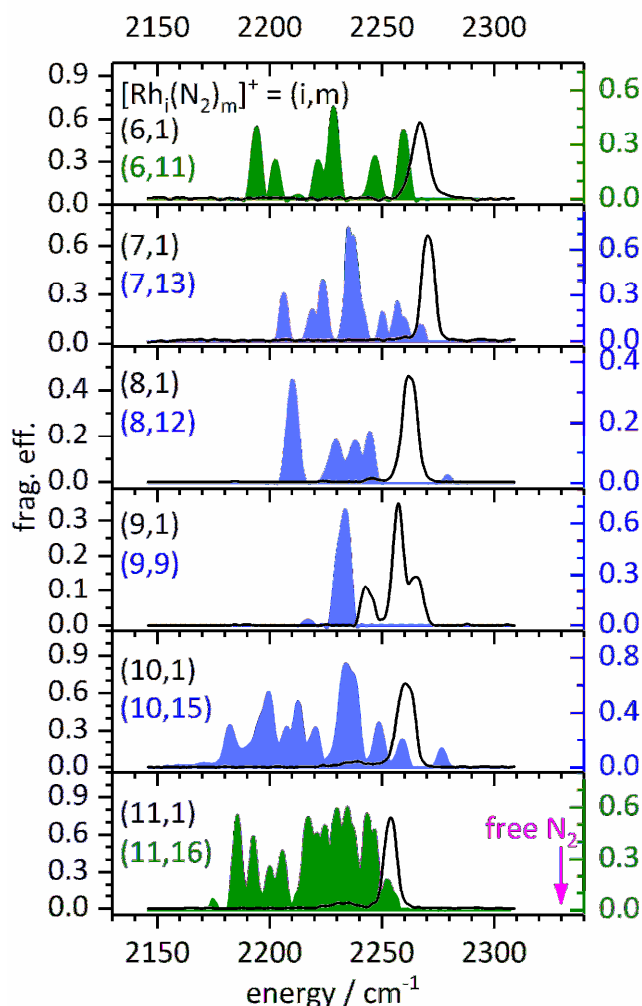


Fig. 5 IR-PD spectra of single (black line) and multiple dinitrogen adsorption on Rhodium clusters at (blue) or close to (green) saturation. The blue areas represent N_2 saturation (at 26 Kelvin), the green areas represent spectra of one N_2 adsorbate less in cases of experimental constraints.

The second finding in all but one of the N₂ saturated IR-PD spectra is a significant *increase* in spectral complexity by multitudes of bands spreading out across up to 110 cm⁻¹, which is not observed upon single adsorptions. The sole exception of (9,9) is to be discussed in the following, where we will discuss the spectral features of each cluster adsorbate complex in detail.

[Rh₆(N₂)₁₁]⁺, [Rh₇(N₂)₁₃]⁺: The IR-PD spectra reveal seven partially resolved bands in the range of 2194 – 2268 cm⁻¹. This multitude of the bands likely indicates the presence of diverse adsorption sites, which is in noteworthy difference to the DFT predictions of naked Rh₆⁺ clusters, and to the IR-PD spectra of single N₂ adsorption, (6,1) and (7,1), see Fig. 4. We take this as a strong indication for N₂ adsorbate induced relaxation of the Rh cluster core geometries, in conjunction with possible spin state quenching. As evidenced before in the case of [Ni₉(N₂)₂]⁺ there are symmetric and asymmetric coupling of stretching modes in adjacent N₂ adsorbates with splittings on the order of 10 cm⁻¹ [71]. We expect such couplings within saturated N₂ layers on Rh cluster surfaces as well. It is hard to conceive, however, that these might make up for all of the observed spread of 70 cm⁻¹.

[Rh₈(N₂)₁₂]⁺: With four bands in the range of 2210 - 2245 cm⁻¹ the spectrum of the (8,12) cluster adsorbate complex reveals less bands than the spectrum of the smaller clusters, likely indicating a high symmetry of the cluster core with less diverse adsorption sites and less or weaker N₂ – N₂ couplings. Other than at i = 6, 7 there is an additional weak band at 2279 cm⁻¹ which we tentatively assign to a stretch – wag combination band.

[Rh₉(N₂)₉]⁺: Remarkably, N₂ saturation arises at mere 1 : 1 stoichiometry in (9,9) while all other studied Rh_i(N₂)_m⁺ clusters saturate at significantly higher N₂ loads close to a 1 : 2 ratio. In the (9,9) cluster adsorbate complex, [Rh₉(N₂)₉]⁺, the small increase in red shift comes with a *reduction* of complexity: Three bands in (9,1) seem to collapse into a single intense band at 2234 cm⁻¹ in (9,9): While single N₂ adsorption reduces symmetry, stoichiometric N₂ saturation seems to recover it. We have assigned a distorted tricapped trigonal prism to the Rh₉ core geometry in (9,1), cf. above, and it may regain full D_{3h} symmetry in (9,9). This implies two types of Rh surface atoms in slightly diverse coordination geometries. If this assumed structure actually prevailed, our spectra would tell that all of the Rh-N₂ pairs are equivalent. Nevertheless, strong electronic Rh-Rh couplings would mediate a coupling between the Rh-N₂ pairs. The weak IR-PD feature at 2217 cm⁻¹ may arise from a hot band.

[Rh₁₀(N₂)₁₅]⁺ and [Rh₁₁(N₂)₁₆]⁺: Similar to the (6,11), (7,13), and the (8,12) cluster adsorbate complexes, the multiple adsorptions of N₂ to the Rh₁₀⁺ and Rh₁₁⁺ clusters reveal a multitude of bands at 2175 - 2277 cm⁻¹, lacking assignments as of now. In principle, they may arise from diverse adsorption sites, from co-existing cluster core or spin isomers, and from vibrational couplings of adjacent N₂ oscillators, likely in conjunction with Rh_i cluster core relaxation upon N₂ adsorption and saturation. As in the spectrum of (8,12) the weak band of (10,15) at 2277 cm⁻¹ may be a stretch-wag combination.

Finally, we review together all of the discussed spectral features upon N₂ saturation (Fig. 5) and upon single N₂ attachment (Fig. 4). This allows to sort the [Rh_i(N₂)_m]⁺ cluster adsorbate complexes into three classes: We label the *i* = 6 - 8, 10, 11 species as *small complexes*, and the *i* = 12 - 15 species as *large complexes* – the latter demarcation based on the spectral complexity of [Rh_i(N₂)₁]⁺ *i* = 12 - 15 complexes (Fig. 4). The sole *i* = 9 complex makes up for its own class of *smooth surface complexes, high symmetry complexes, exceptional complexes*.

Modelling of the vibrational spectrum of the [Rh₇(N₂)₁₂]⁺ cluster adsorbate complex

Up to here, we have presented spectra of single N₂ adsorption and of N₂ saturation. We chose the (7,*m*) complexes for DFT modelling, and we supported this by an additional IR-PD spectrum of (7,12) (Fig. 6). This spectrum reveals a band pattern similar to that of (7,13), with an extra most red shifted strong band at 2192 cm⁻¹. These two findings allow for two interesting conclusions: (1) Spectral complexity does not require a completely saturated N₂ adsorption but sets in earlier. Future studies on IR-PD spectra of intermediate N₂ adsorption levels shall elucidate this aspect further. (2) Even the addition of a single, 13th N₂ does change spectral patterns considerably, indicating strong vibrational and electronic couplings.

With these findings in mind, we spent effort to optimize (7,12) geometries, utilizing as starting geometries the three aforementioned Rh₇⁺ cluster core structures with spin multiplicities $2S + 1 = 1, \dots, 17$ and checking for conceivable N₂ adsorbate distributions. Calculating linear IR absorptions of converged (7,12) structures (Fig. 7 and supplement Fig. S6, Fig. S8, and Fig. S10) and folding with apparatus functions of 5 cm⁻¹ yielded IR spectra to compare with the recorded IR-PD spectrum (Fig. 8, further spectra in supplement Fig. S7 and Fig. S9)

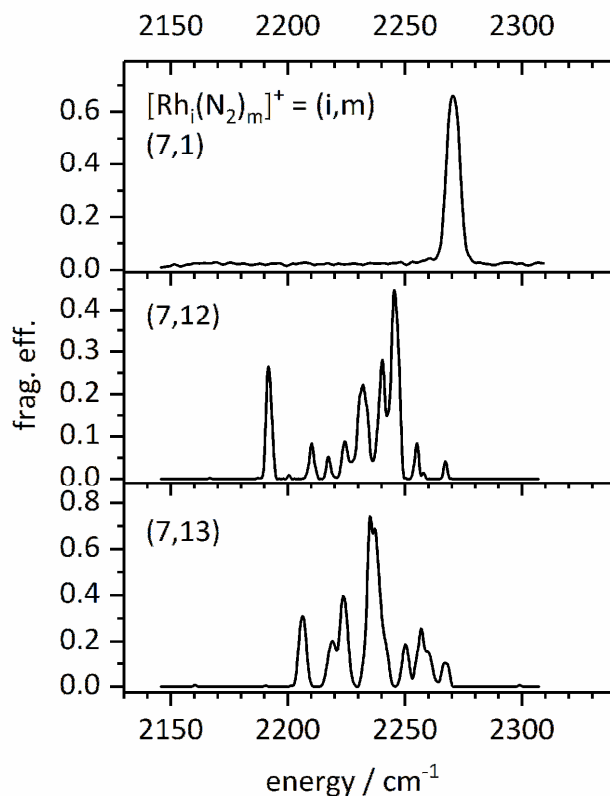


Fig. 6 IR-PD spectra of the $[\text{Rh}_i(\text{N}_2)_m]^+$ cluster for $m = 1, 12,$ and 13 . With an increasing number of N_2 adsorbates there is a spreading out of bands which shift to the red.

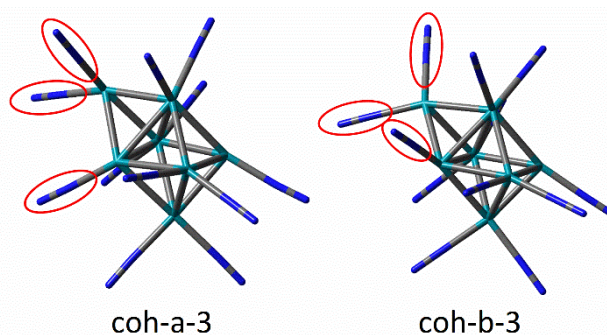


Fig. 7 Two most stable structures of the $(7,12)$ $[\text{Rh}_7(\text{N}_2)_{12}]^+$ cluster adsorbate complexes. Both cluster Rh_7 cores are capped octahedral structures of similar shape; the $[\text{Rh}_7(\text{N}_2)_{12}]^+$ complexes distinguish by the orientations of two adjacent N_2 adsorbates highlighted by red circles.

The calculated spectra of the four lowest energy calculated structures (coh-a-3 and coh-b-3, see supplement) show qualitative agreement to the measured IR-PD spectrum. All of these structures are capped octahedral with either a Rh_7 core distortion or with some torsional polymorphism in the N_2 adsorbate arrangements. All but two Rh atoms accept two

N_2 adsorbates, the remaining two Rh atoms just one N_2 each. The 12 N_2 adsorbates have quenched the 13tet spin state of the naked Rh_7^+ cluster into a mere triplet state of the (7,12) cluster adsorbate complex.

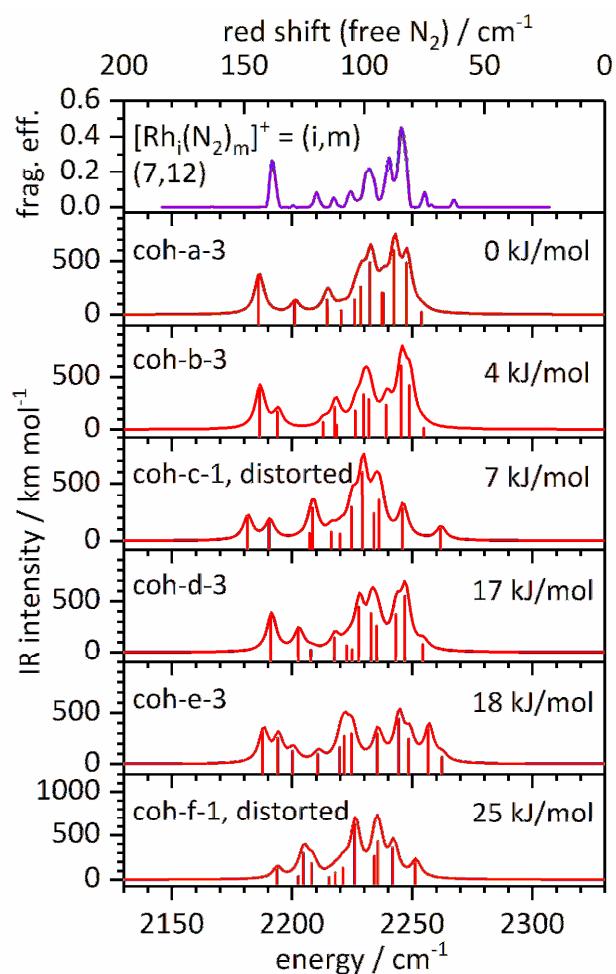


Fig. 8 Experimental IR-PD spectrum of the $[\text{Rh}_7(\text{N}_2)_{12}]^+$ cluster and calculated linear absorption spectra of some isomers (scaled by 0.9385). The calculated spectra represent the six lowest energy structures and the line spectra were convoluted with a 5 cm^{-1} FWHM Gaussian. The three letters indicate the arrangement of the metal atoms in the calculated structures followed by a code for the arrangement of the N_2 molecules and the spin multiplicity. Remarkably all structures have a singlet or triplet multiplicity. The first two calculated spectra satisfactorily resemble the experimental spectrum. The coh-a-3 structure started as a capped trigonal prism and self-optimized into a capped octahedron. The auxiliary axis (on top) indicates the red shift with respect to the IR inactive free N_2 vibration.

Table 2 Calculated vibrational modes of the coh-a-3 cluster in triplet state. The N₂ stretching frequencies are given unscaled and scaled by 0.9385. The Rh atom numbering is provided by Fig. S6 in the supplement. In the case of the stretching vibrations, the position of the oscillators on the cluster is given. The coh-b-3 cluster shows very similar bands.

mode	type / site	frequency / cm ⁻¹	scaled frequency / cm ⁻¹	IR intensity / km mol ⁻¹
N₂ wagging modes				
1-23	wagging	36 - 91		0.0055 – 0.15
Rh skeleton modes				
24-39	cluster core vibrations	101 - 238		0.050 – 2.19
N₂ bending modes				
40-75	N ₂ Bending	247 - 439		0.64 - 18
Single N₂ stretching modes				
76	@ Rh2	2329	2186	375
77	@ Rh6	2345	2201	115
Coupled N₂ stretching modes				
78,79	(asym. coupling @ Rh4) with (asym. @ Rh1) and (asym. @ Rh3)	2360	2215	137, 75
80	asym. @ Rh7	2366	2220	36
81	asym. @ Rh5	2372	2226	138
82	(asym. coupling @ Rh4) with (asym. @ Rh1) and (asym. @ Rh3)	2375	2229	259
83	sym. @ Rh4	2379	2233	485
84	asym. coupling of (sym. @ Rh5) and (sym. @ Rh7)	2384	2237	199
85	sym. @ Rh3	2389	2242	597
86	sym. coupling of (sym. @ Rh5) and (sym. @ Rh7)	2395	2248	483
87	all N ₂ in phase	2402	2254	26

Inspection of all the calculated vibrational mode characteristics reveals categories as listed in Table 2: N₂ wagging modes (36 - 91 cm⁻¹, unscaled), Rh cluster core modes (101 – 238 cm⁻¹), N₂ bending modes (247 – 439 cm⁻¹), and the N₂ stretching modes (2186 – 2254 cm⁻¹, scaled). A closer look on the calculated vibrational modes of the ctp-c-3 cluster supports our assumption that the band at 2267 cm⁻¹ is an N₂ stretch wag combination band.

Based on our prior and present investigation of [Ni_n(N₂)_m]⁺ complexes [71,72] we expect strong couplings amongst geminal N₂ adsorbates on the same Rh site or on neighboring Rh

sites, and no couplings amongst the two lone N_2 adsorbates at the Rh2 and Rh6 sites. Indeed, we assign the two most red shifted bands to the uncoupled lone N_2 molecules. These oscillators do not compete for electron density with another geminal N_2 molecule and they thus achieve higher back donation into their antibonding π^* orbitals, which leads to the observed larger red shifts.

The strong N_2 couplings render an assignment of the stretching bands difficult; yet, there are some recognizable characteristics (listed in Table 3). In particular, we identify symmetric and antisymmetric couplings of geminal and vicinal N_2 oscillators. The single stiffest N_2 stretching mode is delocalized over all N_2 oscillators and an all in phase motion (at 2254 cm^{-1}). By an according analysis, we obtain a similar picture of all the vibrational modes in the coh-b-3 cluster adsorbate complex.

Summary and Conclusions

We have presented the calculated minimum structures of Rh_i^+ ($i = 6, 7,$ and 9) clusters and $[Rh_7(N_2)_{12}]^+$ cluster adsorbate complexes, in conjunction with the recorded IR-PD spectra of $[Rh_i(N_2)_m]^+$ clusters adsorbate complexes (i, m) with a single N_2 ($i = 6 - 15, m = 1$) and with multiple N_2 adsorbates at or close to saturation ($i = 6 - 11$). In particular, we have compared recorded and calculated spectra of $[Rh_7(N_2)_{12}]^+$, and we assign capped octahedral structures of the Rh_7 cores in all $(7, m)$ species. We explain observed red shifts of the various N_2 stretching modes by electronic interactions between adsorbate molecules and cluster cores. For sure, high loads of N_2 adsorbates close to saturation quench high spin states of naked clusters significantly towards much lower multiplicities. Earlier investigations confirmed that assumed isomerization of the cluster cores as well as the spin quenching may be understood as a result of multiple non-reactive collisions [25]. Our cryogenic hexapole ion trap likely provides for effective thermalization, and we may see an enhancement of such effects. Experiments where reactions takes place in the ICR cell with a much lower pressure reveal a variety of isomers [24,25].

The present study is meant to provide first insights into N_2 adsorbate localization at Rhodium cluster surfaces and to elucidate adsorbate induced cluster core relaxation, as evidenced in the case of $(6,11)$ and $(7,13)$.

While the current study is a first step in a larger framework, which is work in progress: It is subject of work in progress to systematically vary the number of N₂ adsorbates, and to study the N₂ stretch couplings and the concomitant stepwise spin quenching in the [Rh_i(N₂)_m]⁺ complexes. Also, work in progress are: the N₂ saturation studies of [Rh_i(N₂)_m]⁺, *i* > 11, the calculation of N₂ adsorbate tilting barriers amongst complex structures of Fig. 7 and their spin state dependencies, the N₂ adsorption kinetics of pure Rh cations and of Fe Rh alloys, and the cryo spectroscopy of the latter.

We emphasize the fundamental value of our above findings for the understanding of the dynamic metal surface adsorbate interplay as of relevance in heterogeneous catalysis with nano-structured surfaces, such as e.g. the annealing of pre-catalyst deposits on substrate surfaces. Able members of the DFT modelling community are invited to join and augment our own efforts.

Acknowledgement

This work was supported by the DFG founded transregional collaborative research center SFB/TRR 88 "3MET.de" and by the state research center OPTIMAS. We thank Thomas Kolling for technical assistance and valuable discussions. We acknowledge valuable comments and suggestions by the reviewers.

References

1. Doyle MP (1986) Electrophilic metal carbenes as reaction intermediates in catalytic reactions. *Accounts of Chemical Research* 19 (11):348-356. doi:10.1021/ar00131a004
2. Werlé C, Goddard R, Philipps P, Farès C, Fürstner A (2016) Structures of Reactive Donor/Acceptor and Donor/Donor Rhodium Carbenes in the Solid State and Their Implications for Catalysis. *J Am Chem Soc* 138 (11):3797-3805. doi:10.1021/jacs.5b13321
3. Rhodium Catalyzed Hydroformylation (2002), vol 22. *Catalysis by Metal Complexes*. doi:10.1007/0-306-46947-2
4. Cheung H, Tanke RS, Torrence GP (2000) Acetic Acid. In: *Ullmann's Encyclopedia of Industrial Chemistry*. Wiley-VCH Verlag GmbH & Co. KGaA. doi:10.1002/14356007.a01_045
5. Kaneda K, Fujita K, Takemoto T, Imanaka T (1991) Selective deoxygenation of various N-O bonds catalyzed by rhodium carbonyl clusters in the presence of H₂O and CO and their heterogenization using amino-substituted polystyrenes. *Bulletin of the Chemical Society of Japan* 64 (2):602-612. doi:10.1246/bcsj.64.602
6. Kaneda K, Takemoto T, Imanaka T (1988) Aminated polystyrene-bound rhodium carbonyl clusters as a catalyst for deoxygenation of various N-O bonds. *Chemistry Letters* (10):1759-1762. doi:10.1246/cl.1988.1759

7. Murahashi S-I, Imada Y, Hirai Y (1987) Rhodium catalyzed hydrogenation of nitrogen heteroaromatics under water gas shift conditions. Selective synthesis of 1,2,3,4-tetrahydroquinolines and -formyl-1,2,3,4-tetrahydroisoquinolines. *Tetrahedron Letters* 28 (1):77-80. doi:10.1016/S0040-4039(00)95653-3
8. Votsmeier M, Kreuzer T, Gieshoff J, Lepperhoff G (2009) Automobile Exhaust Control. In: Ullmann's Encyclopedia of Industrial Chemistry. doi:10.1002/14356007.a03_189.pub2
9. Jung HJ, Becker ER (1987) Emission Control for Gas Turbines. *Platinum Metals Rev* 31 (4):162-170
10. Albert G, Berg C, Beyer M, Achatz U, Joos S, Niedner-Schatteburg G, Bondybey VE (1997) Methane activation by rhodium cluster argon complexes. *Chemical Physics Letters* 268 (3):235-241. doi:10.1016/S0009-2614(97)00202-9
11. Andersson M, Holmgren L, Rosén A (1996) RHODIUM-CLUSTER REACTIVITY: STICKING PROBABILITIES OF SOME DIATOMIC MOLECULES. *Surface Review and Letters* 03 (01):683-686. doi:10.1142/S0218625X96001236
12. Mafuné F, Tawaraya Y, Kudoh S (2016) Nitrogen Molecule Adsorption on Cationic Tantalum Clusters and Rhodium Clusters and Desorption from Their Nitride Clusters Studied by Thermal Desorption Spectrometry. *The Journal of Physical Chemistry A* 120 (24):4089-4095. doi:10.1021/acs.jpca.6b03479
13. Zakin MR, Cox DM, Kaldor A (1988) Gas-phase rhodium cluster chemistry: Influence of adsorbate electronic structure on reaction rate. *The Journal of Chemical Physics* 89 (2):1201-1202. doi:10.1063/1.455234
14. Mineva T, Russo N, Freund H-J (2001) CO Interaction with Small Rhodium Clusters from Density Functional Theory: Spectroscopic Properties and Bonding Analysis. *The Journal of Physical Chemistry A* 105 (47):10723-10730. doi:10.1021/jp0116398
15. Fielicke A, von Helden G, Meijer G, Simard B, Dénommée S, Rayner DM (2003) Vibrational Spectroscopy of CO in Gas-Phase Rhodium Cluster-CO Complexes. *J Am Chem Soc* 125 (37):11184-11185. doi:10.1021/ja036897s
16. Fielicke A, von Helden G, Meijer G, Pedersen DB, Simard B, Rayner DM (2004) Size and Charge Effects on the Binding of CO to Small Isolated Rhodium Clusters. *The Journal of Physical Chemistry B* 108 (38):14591-14598. doi:10.1021/jp049214j
17. Fielicke A, von Helden G, Meijer G, Pedersen DB, Simard B, Rayner DM (2006) Size and charge effects on the binding of CO to late transition metal clusters. *J Chem Phys* 124 (19):194305. doi:10.1063/1.2196887
18. Swart I, de Groot FM, Weckhuysen BM, Rayner DM, Meijer G, Fielicke A (2008) The effect of charge on CO binding in rhodium carbonyls: from bridging to terminal CO. *J Am Chem Soc* 130 (7):2126-2127. doi:10.1021/ja0772795
19. Fielicke A, Gruene P, Meijer G, Rayner DM (2009) The adsorption of CO on transition metal clusters: A case study of cluster surface chemistry. *Surface Science* 603 (10-12):1427-1433. doi:10.1016/j.susc.2008.09.064
20. Shetty S, Strych S, Jansen APJ, van Santen RA (2009) Theoretical investigation of CO adsorption on Rh_n (n = 3-13) clusters. *Canadian Journal of Chemistry* 87 (7):824-831. doi:10.1139/V09-015
21. Tian F-Y, Shen J (2011) Density-functional study of CO adsorbed on Rh_N(N= 2-19) clusters. *Chinese Physics B* 20 (12):123101. doi:10.1088/1674-1056/20/12/123101
22. Dutta A, Mondal P (2016) Structural evolution, electronic and magnetic manners of small rhodium Rh_n^{+/-} (n = 2-8) clusters: a detailed density functional theory study. *RSC Adv* 6 (9):6946-6959. doi:10.1039/c5ra21600a

23. Dutta A, Mondal P (2017) Density Functional Study on Structure and Bonding Nature of CO Adsorbed Rh_n^{+/-} (n = 2–8) Clusters. *Journal of Cluster Science*. doi:10.1007/s10876-017-1241-x
24. Ford MS, Anderson ML, Barrow MP, Woodruff DP, Drewello T, Derrick PJ, Mackenzie SR (2005) Reactions of nitric oxide on Rh₆⁺ clusters: abundant chemistry and evidence of structural isomers. *Physical Chemistry Chemical Physics* 7 (5):975-980. doi:10.1039/b415414b
25. Harding D, Ford MS, Walsh TR, Mackenzie SR (2007) Dramatic size effects and evidence of structural isomers in the reactions of rhodium clusters, Rh_n^{+/-}, with nitrous oxide. *Physical Chemistry Chemical Physics* 9 (17):2130-2136. doi:10.1039/B618299B
26. Harding DJ, Walsh TR, Hamilton SM, Hopkins WS, Mackenzie SR, Gruene P, Haertelt M, Meijer G, Fielicke A (2010) Communications: The structure of Rh(8)⁺ in the gas phase. *J Chem Phys* 132 (1):011101. doi:10.1063/1.3285266
27. Torres MB, Aguilera-Granja F, Balbas LC, Vega A (2011) Ab initio study of the adsorption of NO on the Rh₆⁽⁺⁾ cluster. *J Phys Chem A* 115 (30):8350-8360. doi:10.1021/jp202511w
28. Romo-Avila SL, Guirado-Lopez RA (2012) Adsorption of nitric oxide on small Rh(n)^{+/-} clusters: role of the local atomic environment on the dissociation of the N-O bond. *J Phys Chem A* 116 (3):1059-1068. doi:10.1021/jp208847r
29. Tawaraya Y, Kudoh S, Miyajima K, Mafune F (2015) Thermal Desorption and Reaction of NO Adsorbed on Rhodium Cluster Ions Studied by Thermal Desorption Spectroscopy. *The journal of physical chemistry A* 119 (31):8461-8468. doi:10.1021/acs.jpca.5b04224
30. Anderson ML, Ford MS, Derrick PJ, Drewello T, Woodruff DP, Mackenzie SR (2006) Nitric Oxide Decomposition on Small Rhodium Clusters, Rh_n⁺. *The Journal of Physical Chemistry A* 110 (38):10992-11000. doi:10.1021/jp062178z
31. Hamilton SM, Hopkins WS, Harding DJ, Walsh TR, Gruene P, Haertelt M, Fielicke A, Meijer G, Mackenzie SR (2010) Infrared induced reactivity on the surface of isolated size-selected clusters: dissociation of N₂O on rhodium clusters. *J Am Chem Soc* 132 (5):1448-1449. doi:10.1021/ja907496c
32. Hamilton SM, Hopkins WS, Harding DJ, Walsh TR, Haertelt M, Kerpel C, Gruene P, Meijer G, Fielicke A, Mackenzie SR (2011) Infrared-induced reactivity of N₂O on small gas-phase rhodium clusters. *J Phys Chem A* 115 (12):2489-2497. doi:10.1021/jp201171p
33. Hermes AC, Hamilton SM, Hopkins WS, Harding DJ, Kerpel C, Meijer G, Fielicke A, Mackenzie SR (2011) Effects of Coadsorbed Oxygen on the Infrared Driven Decomposition of N₂O on Isolated Rh₅⁺ Clusters. *The Journal of Physical Chemistry Letters* 2 (24):3053-3057. doi:10.1021/jz2012963
34. Parry IS, Kartouzian A, Hamilton SM, Balaj OP, Beyer MK, Mackenzie SR (2013) Collisional activation of N₂O decomposition and CO oxidation reactions on isolated rhodium clusters. *J Phys Chem A* 117 (36):8855-8863. doi:10.1021/jp405267p
35. Mafuné F, Tawaraya Y, Kudoh S (2016) Reactivity Control of Rhodium Cluster Ions by Alloying with Tantalum Atoms. *The Journal of Physical Chemistry A* 120 (6):861-867. doi:10.1021/acs.jpca.5b11898
36. Francisco H, Bertin V, Soto JR, Castro M (2016) Charge and Geometrical Effects on the Catalytic N₂O Reduction by Rh₆⁻ and Rh₆⁺ Clusters. *The Journal of Physical Chemistry C* 120 (41):23648-23659. doi:10.1021/acs.jpcc.6b08172
37. Xie H, Ren M, Lei Q, Fang W, Ying F (2012) Explore the Catalytic Reaction Mechanism in the Reduction of NO by CO on the Rh₇⁺ Cluster: A Quantum Chemical Study. *The Journal of Physical Chemistry C* 116 (14):7776-7781. doi:10.1021/jp2118357

38. Su B-F, Fu H-Q, Yang H-Q, Hu C-W (2015) Catalytic reduction of NO by CO on Rh₄+clusters: a density functional theory study. *Catal Sci Technol* 5 (6):3203-3215. doi:10.1039/C5CY00119F
39. Niedner-Schatteburg G (2017) Cooperative Effects in Clusters and Oligonuclear Complexes of Transition Metals in Isolation. In: Dehnen S (ed) *Clusters – Contemporary Insight in Structure and Bonding*. Springer International Publishing, Cham, pp 1-40. doi:10.1007/430_2016_11
40. Berg C, Beyer M, Schindler T, Niedner-Schatteburg G, Bondybey VE (1996) Reactions of benzene with rhodium cluster cations: Competition between chemisorption and physisorption. *The Journal of Chemical Physics* 104 (20):7940-7946. doi:10.1063/1.471510
41. Berg C, Beyer M, Achatz U, Joos S, Niedner-Schatteburg G, Bondybey VE (1998) Effect of charge upon metal cluster chemistry: Reactions of Nb_n and Rh_n anions and cations with benzene. *The Journal of Chemical Physics* 108 (13):5398-5403. doi:10.1063/1.475972
42. Adlhart C, Uggerud E (2005) C-H activation of alkanes on Rh⁺_n (n=1-30) clusters: size effects on dehydrogenation. *J Chem Phys* 123 (21):214709. doi:10.1063/1.2131066
43. Balteanu I, Balaj OP, Beyer MK, Bondybey VE (2006) Size-dependent dehydrogenation of ethane by cationic rhodium clusters in the gas phase. *Int J Mass Spectrom* 255-256:71-75. doi:10.1016/j.ijms.2005.08.019
44. Balteanu I, Balaj OP, Fox-Beyer BS, Rodrigues P, Barros MT, Moutinho AMC, Costa ML, Beyer MK, Bondybey VE (2004) Size- and Charge-State-Dependent Reactivity of Azidoacetonitrile with Anionic and Cationic Rhodium Clusters Rh_n[±]. *Organometallics* 23 (9):1978-1985. doi:10.1021/om049946y
45. Aguilera-Granja F, Rodríguez-López JL, Michaelian K, Berlanga-Ramírez EO, Vega A (2002) Structure and magnetism of small rhodium clusters. *Phys Rev B* 66 (22):224410
46. Šipr O, Ebert H, Minár J (2015) Trends in magnetism of free Rh clusters via relativistic ab-initio calculations. *Journal of Physics: Condensed Matter* 27 (5):056004. doi:10.1088/0953-8984/27/5/056004
47. Ahmadi S, Zhang X, Gong Y, Zhu W, Sun CQ (2016) Catalytic and Magnetic Behaviors of Excessively Charged Silver, Copper, Platinum, and Rhodium Atomic Clusters. *The Journal of Physical Chemistry C* 120 (31):17527-17536. doi:10.1021/acs.jpcc.6b05380
48. Chien C-H, Blaisten-Barojas E, Pederson MR (1998) Magnetic and electronic properties of rhodium clusters. *Physical Review A* 58 (3):2196-2202
49. Ma L, Moro R, Bowlan J, Kirilyuk A, de Heer WA (2014) Multiferroic Rhodium Clusters. *Physical Review Letters* 113 (15):157203. doi:10.1103/PhysRevLett.113.157203
50. Sen P (2016) Magnetism in Simple Metal and 4d Transition Metal Clusters. *Journal of Cluster Science* 27 (3):795-815. doi:10.1007/s10876-016-0986-y
51. Harding DJ, Gruene P, Haertelt M, Meijer G, Fielicke A, Hamilton SM, Hopkins WS, Mackenzie SR, Neville SP, Walsh TR (2010) Probing the structures of gas-phase rhodium cluster cations by far-infrared spectroscopy. *J Chem Phys* 133 (21):214304. doi:10.1063/1.3509778
52. Hang TD, Hung HM, Thiem LN, Nguyen HMT (2015) Electronic structure and thermochemical properties of neutral and anionic rhodium clusters Rh_n, n = 2–13. Evolution of structures and stabilities of binary clusters Rh_mM (M = Fe, Co, Ni; m = 1–6). *Computational and Theoretical Chemistry* 1068:30-41. doi:10.1016/j.comptc.2015.06.004

53. Lecours MJ, Chow WCT, Hopkins WS (2014) Density Functional Theory Study of Rh_nSO_x and Rh_{n+10} ($n = 1-9$). *The Journal of Physical Chemistry A* 118 (24):4278-4287. doi:10.1021/jp412457m
54. Citra A, Andrews L (1999) Reactions of Laser Ablated Rhodium Atoms with Nitrogen Atoms and Molecules. Infrared Spectra and Density Functional Calculations on Rhodium Nitrides and Dinitrogen Complexes. *The Journal of Physical Chemistry A* 103 (18):3410-3417. doi:10.1021/jp9846274
55. Brathwaite AD, Abbott-Lyon HL, Duncan MA (2016) Distinctive Coordination of CO vs N₂ to Rhodium Cations: An Infrared and Computational Study. *The Journal of Physical Chemistry A* 120 (39):7659-7670. doi:10.1021/acs.jpca.6b07749
56. Bendtsen J (1974) The rotational and rotation-vibrational Raman spectra of ¹⁴N₂, ¹⁴N¹⁵N and ¹⁵N₂. *Journal of Raman Spectroscopy* 2 (2):133-145. doi:10.1002/jrs.1250020204
57. Dillinger S, Mohrbach J, Hewer J, Gaffga M, Niedner-Schatteburg G (2015) Infrared spectroscopy of N₂ adsorption on size selected cobalt cluster cations in isolation. *Physical Chemistry Chemical Physics* 17 (16):10358-10362. doi:10.1039/C5CP00047E
58. Maruyama S, Anderson LR, Smalley RE (1990) Direct injection supersonic cluster beam source for FT-ICR studies of clusters. *Review of Scientific Instruments* 61 (12):3686-3693. doi:10.1063/1.1141536
59. Berg C, Schindler T, Niedner-Schatteburg G, Bondybey VE (1995) Reactions of simple hydrocarbons with Nb⁺ n: chemisorption and physisorption on ionized niobium clusters. *The Journal of chemical physics* 102 (12):4870-4884
60. Proch D, Trickl T (1989) A high-intensity multi-purpose piezoelectric pulsed molecular beam source. *Review of Scientific Instruments* 60 (4):713-716. doi:10.1063/1.1141006
61. Kofel P, Allemann M, Kellerhals H, Wanczek KP (1985) External generation of ions in ICR spectrometry. *International Journal of Mass Spectrometry and Ion Processes* 65 (1):97-103. doi:10.1016/0168-1176(85)85056-4
62. Kofel P, Allemann M, Kellerhals H, Wanczek KP (1986) Time-of-flight ICR spectrometry. *International Journal of Mass Spectrometry and Ion Processes* 72 (1):53-61. doi:10.1016/0168-1176(86)85033-9
63. Caravatti P, Allemann M (1991) The 'infinity cell': A new trapped-ion cell with radiofrequency covered trapping electrodes for fourier transform ion cyclotron resonance mass spectrometry. *Org Mass Spectrom* 26 (5):514-518. doi:10.1002/oms.1210260527
64. Peredkov S, Savci A, Peters S, Neeb M, Eberhardt W, Kampschulte H, Meyer J, Tombers M, Hofferberth B, Menges F, Niedner-Schatteburg G (2011) X-ray absorption spectroscopy of mass-selected transition metal clusters using a cyclotron ion trap: An experimental setup for measuring XMCD spectra of free clusters. *J Electron Spectrosc* 184 (3-6):113-118. doi:10.1016/j.elspec.2010.12.031
65. Meyer J, Tombers M, van Wüllen C, Niedner-Schatteburg G, Peredkov S, Eberhardt W, Neeb M, Palutke S, Martins M, Wurth W (2015) The spin and orbital contributions to the total magnetic moments of free Fe, Co, and Ni clusters. *The Journal of Chemical Physics* 143 (10):104302. doi:10.1063/1.4929482
66. Schindler T, Berg C, Niedner-Schatteburg G, Bondybey VE (1996) Protonated water clusters and their black body radiation induced fragmentation. *Chemical Physics Letters* 250 (3):301-308. doi:10.1016/0009-2614(96)00002-4

67. Niedner-Schatteburg G, Bondybey VE (2000) FT-ICR Studies of Solvation Effects in Ionic Water Cluster Reactions. *Chemical Reviews* 100 (11):4059-4086. doi:10.1021/cr990065o
68. Frisch MJ, Trucks GW, Schlegel HB, Scuseria GE, Robb MA, Cheeseman JR, Scalmani G, Barone V, Mennucci B, Petersson GA, Nakatsuji H, Caricato M, Li X, Hratchian HP, Izmaylov AF, Bloino J, Zheng G, Sonnenberg JL, Hada M, Ehara M, Toyota K, Fukuda R, Hasegawa J, Ishida M, Nakajima T, Honda Y, Kitao O, Nakai H, Vreven T, Montgomery Jr. JA, Peralta JE, Ogliaro F, Bearpark MJ, Heyd J, Brothers EN, Kudin KN, Staroverov VN, Kobayashi R, Normand J, Raghavachari K, Rendell AP, Burant JC, Iyengar SS, Tomasi J, Cossi M, Rega N, Millam NJ, Klene M, Knox JE, Cross JB, Bakken V, Adamo C, Jaramillo J, Gomperts R, Stratmann RE, Yazyev O, Austin AJ, Cammi R, Pomelli C, Ochterski JW, Martin RL, Morokuma K, Zakrzewski VG, Voth GA, Salvador P, Dannenberg JJ, Dapprich S, Daniels AD, Farkas Ö, Foresman JB, Ortiz JV, Cioslowski J, Fox DJ (2009) Gaussian 09, Revision D.01. Gaussian, Inc., Wallingford, CT, USA
69. Black G, Schuchardt K, Gracio D, Palmer B (2003) The Extensible Computational Chemistry Environment: A Problem Solving Environment for High Performance Theoretical Chemistry. In: Sloat PMA, Abramson D, Bogdanov AV, Gorbachev YE, Dongarra JJ, Zomaya AY (eds) *Computational Science — ICCS 2003: International Conference, Melbourne, Australia and St. Petersburg, Russia, June 2–4, 2003 Proceedings, Part IV*. Springer Berlin Heidelberg, Berlin, Heidelberg, pp 122-131. doi:10.1007/3-540-44864-0_13
70. Adamo C, Barone V (1999) Toward reliable density functional methods without adjustable parameters: The PBE0 model. *The Journal of Chemical Physics* 110 (13):6158-6170. doi:10.1063/1.478522
71. Mohrbach J, Dillinger S, Niedner-Schatteburg G (2017) Cryo Kinetics and Spectroscopy of Cationic Nickel Clusters: Rough and Smooth Surfaces. *The Journal of Physical Chemistry C* 121 (20):10907-10918. doi:10.1021/acs.jpcc.6b12167
72. Dillinger S, Mohrbach J, Niedner-Schatteburg G Probing cluster surface morphology by Cryo spectroscopy of N₂ on Cationic Nickel Clusters. to be submitted
73. Andrae D, Häußermann U, Dolg M, Stoll H, Preuß H (1990) Energy-adjusted ab initio pseudopotentials for the second and third row transition elements. *Theoretica chimica acta* 77 (2):123-141. doi:10.1007/bf01114537
74. Bligaard T, Nørskov JK (2008) Chapter 4 - Heterogeneous Catalysis. In: *Chemical Bonding at Surfaces and Interfaces*. Elsevier, Amsterdam, pp 255-321. doi:10.1016/B978-044452837-7.50005-8
75. Comelli G, Dhanak VR, Kiskinova M, Prince KC, Rosei R (1998) Oxygen and nitrogen interaction with rhodium single crystal surfaces. *Surface Science Reports* 32 (5):165-231. doi:10.1016/s0167-5729(98)00003-x
76. Beyer MK, Knickelbein MB (2007) Electric deflection studies of rhodium clusters. *J Chem Phys* 126 (10):104301. doi:10.1063/1.2698320
77. Mokka JH, Pastor GM (2012) Interplay between Chemical and Magnetic Order in FeRh Clusters. *The Journal of Physical Chemistry C* 116 (32):17228-17238. doi:10.1021/jp3032176
78. Beltran MR, Zamudio FB, Chauhan V, Sen P, Wang H, Ko YJ, Bowen K (2013) Ab initio and anion photoelectron studies of Rh_n (n = 1-9) clusters. *Eur Phys J D* 67 (3):63. doi:10.1140/epjd/e2013-30547-2

79. Cotton FA, DeBoer BG, LaPrade MD, Pipal JR, Ucko DA (1971) The crystal and molecular structures of dichromium tetraacetate dihydrate and dirhodium tetraacetate dihydrate. *Acta Crystallographica Section B* 27 (8):1664-1671. doi:doi:10.1107/S0567740871004527
80. CRC Handbook of Chemistry and Physics (2010). 90 edn. CRC Press, Boca Raton
81. Whetten RL, Cox DM, Trevor DJ, Kaldor A (1985) Free iron clusters react readily with oxygen and hydrogen sulfide, but are inert toward methane. *The Journal of Physical Chemistry* 89 (4):566-569. doi:10.1021/j100250a004
82. Dillinger S, Mohrbach J, Ehrhard A, Klein M, Niedner-Schatteburg G. unpublished data
83. Kerpál C, Harding DJ, Lyon JT, Meijer G, Fielicke A (2013) N₂ Activation by Neutral Ruthenium Clusters. *The Journal of Physical Chemistry C* 117 (23):12153-12158. doi:10.1021/jp401876b
84. Blyholder G (1964) Molecular Orbital View of Chemisorbed Carbon Monoxide. *J Phys Chem-Us* 68 (10):2772-2777. doi:10.1021/J100792a006
85. Dewar JS (1951) A Review of the Pi-Complex Theory. *B Soc Chim Fr* 18 (3-4):C71-C79
86. Chatt J, Duncanson LA (1953) 586. Olefin co-ordination compounds. Part III. Infra-red spectra and structure: attempted preparation of acetylene complexes. *Journal of the Chemical Society (Resumed)* (0):2939-2947. doi:10.1039/JR9530002939
87. Rapps T, Ahlrichs R, Waldt E, Kappes MM, Schooss D (2013) On the structures of 55-atom transition-metal clusters and their relationship to the crystalline bulk. *Angewandte Chemie* 52 (23):6102-6105. doi:10.1002/anie.201302165
88. Robertson BE (1977) Coordination polyhedra with nine and ten atoms. *Inorganic Chemistry* 16 (11):2735-2742. doi:10.1021/ic50177a014

Lebenslauf

Persönliche Daten

Name Sebastian Dillinger
Anschrift: dillinger@chemie.uni-kl.de

Ausbildung

1996 – 2000 Grundschule Rodalben
2000 – 04/2009 Leibniz-Gymnasium Pirmasens
Abschluss: allgemeine Hochschulreife
06/2009 – 02/2010 Zivildienst, Heinrich Kimmle Stiftung Pirmasens
04/2010 – 12/2014 Studium, Technische Universität Kaiserslautern
Fach: Chemie
Studienschwerpunkte: Physikalische Chemie,
AK Niedner-Schatteburg
Abschluss: Diplom
Seit 01/2015 wiss. Mitarbeiter, Technische Universität Kaiserslautern
Fach: Chemie
Schwerpunkte: Physikalische Chemie, AK Niedner-Schatteburg

Weitere Aktivitäten

Seit 01/2015 Sprecher des wissenschaftlichen Nachwuchses des Sonderforschungsbereiches SFB/TRR 88 „3MET.de“

List of Publications

1. *Infrared spectroscopy of N₂ adsorption on size selected cobalt cluster cations in isolation*
S. Dillinger, J. Mohrbach, J. Hewer, M. Gaffga, and G. Niedner-Schatteburg, *Physical Chemistry Chemical Physics*, **2015**, 17, 10358-10362.
<http://dx.doi.org/10.1039/C5CP00047E>
2. *Cryo Kinetics and Spectroscopy of Cationic Nickel Clusters: Rough and Smooth Surfaces*
J. Mohrbach, **S. Dillinger**, and G. Niedner-Schatteburg, *The Journal of Physical Chemistry C*, **2017**, 121, 20, 10907-10918.
<http://dx.doi.org/10.1021/acs.jpcc.6b12167>
3. *Vibrational fingerprints of a tetranuclear cobalt carbonyl cluster within a cryo tandem ion trap*
J. Mohrbach, J. Lang, **S. Dillinger**, M. H. Prosenč, P. Braunstein, and G. Niedner-Schatteburg, *Journal of Molecular Spectroscopy*, **2017**, 332, 103-108.
<http://dx.doi.org/10.1016/j.jms.2016.11.008>
4. *Vibrational blue shift of coordinated N₂ in [Fe₃O(OAc)₆(N₂)_n]⁺: “non-classical” dinitrogen complexes*
J. Lang, J. Mohrbach, **S. Dillinger**, J. M. Hewer, and G. Niedner-Schatteburg, *Chemical Communications*, **2017**, 53, 420-423.
<http://dx.doi.org/10.1039/C6CC07481B>
5. *Cryo IR Spectroscopy of [Hemin]⁺ Complexes in Isolation*
S. Dillinger, J. Lang, and G. Niedner-Schatteburg, *The Journal of Physical Chemistry A*, **2017**, 121, 38, 7191-7196.
<http://dx.doi.org/10.1021/acs.jpca.7b08604>

6. *Probing Cluster Surface Morphology by Cryo Kinetics of N₂ on Cationic Nickel Clusters*
J. Mohrbach, **S. Dillinger**, and G. Niedner-Schatteburg, *The Journal of Chemical Physics*, **accepted**.

7. *Probing Cluster Surface Morphology by Cryo Spectroscopy of N₂ on Cationic Nickel Clusters*
S. Dillinger, J. Mohrbach, and G. Niedner-Schatteburg, *The Journal of Chemical Physics*, **accepted**.

8. *Infrared spectroscopic investigations of structures and N₂ adsorption induced relaxations of isolated Rhodium clusters*
M. P. Klein, A. A. Ehrhard, J. Mohrbach, **S. Dillinger**, and G. Niedner-Schatteburg, *Topics in Catalysis*, **accepted**.

9. *Cryo IR Spectroscopy of N₂ and H₂ on Ru₈⁺: The Effect of N₂ on the H-Migration*
S. Dillinger, M. P. Klein, A. Steiner, D. C. McDonald II, M. A. Duncan, M. M. Kappes, and G. Niedner-Schatteburg, **prepared for submission**.

10. *Cryo IR Spectroscopy and Cryo Kinetics of N₂ on Cationic Iron Clusters*
S. Dillinger, J. Mohrbach, M. H. Prosenc, and G. Niedner-Schatteburg, **prepared for submission**.

Contribution to Conferences

Oral Presentations

Sebastian Dillinger, Jennifer Mohrbach, Annika Steiner, Gereon Niedner-Schatteburg, "Spectroscopy & Kinetics on Metal Cluster Surfaces: The Fe/N₂, Co/N₂ and Ni/N₂ systems", Frühjahrstagung der Deutschen Physikalischen Gesellschaft, Hannover, 29.02.-04.03.2016.

Sebastian Dillinger, "Spektroskopische Untersuchungen von Stickstoff Adsorbaten auf kationischen Cobalt Clustern bei tiefen Temperaturen", Steinhofer Preis 2015, 18.03.2016.

Sebastian Dillinger, Jennifer Mohrbach, Johannes Lang, Pierre Braunstein and Gereon Niedner-Schatteburg, "Cryo IR spectroscopy of a tetranuclear cobalt carbonyl complex in isolation", Frühjahrstagung der Deutschen Physikalischen Gesellschaft 2017, Mainz, 06.-10.03.2017.

Sebastian Dillinger, Jennifer Mohrbach, and Gereon Niedner-Schatteburg, "IR Spectroscopy of Isolated Transition Metal Clusters and Complexes at Cryo Temperatures", 2. Promovierendenseminar des Fachbereichs Chemie, Kaiserslautern, 27.03.2017.

Poster Presentations

Sebastian Dillinger, Jennifer Mohrbach, Maximilian Gaffga, Joachim Hewer, Gereon Niedner-Schatteburg, "Cryo spectroscopy of size selected cobalt clusters", Frühjahrstagung der Deutschen Physikalischen Gesellschaft, Heidelberg, 23-27.03.2015.

Sebastian Dillinger, Jennifer Mohrbach, Maximilian Gaffga, Joachim Hewer, Gereon Niedner-Schatteburg, "Cryo spectroscopy of adsorbed N₂ on size selected transition metal clusters", 594. Wilhelm and Else Heraeus-Seminar "Spectroscopy and applications of cold molecular ions", Bad Honnef, 15.-18.06.2015.

Sebastian Dillinger, Jennifer Mohrbach, Maximilian Gaffga, Joachim Hewer, Gereon Niedner-Schatteburg, "Cryo spectroscopy and kinetics of adsorbed nitrogen on size selected transition metal clusters", 3MET Workshop, Bad Bergzabern, 20.-22.07.2015.

Sebastian Dillinger, Jennifer Mohrbach, Annika Steiner, Gereon Niedner-Schatteburg, "Spectroscopic investigations on nitrogen adsorbed on transition metal cluster cations in isolation", GRS: Molecular and ionic clusters, Ventura, CA, USA, 16.-17.01.2016.

Sebastian Dillinger, Jennifer Mohrbach, Annika Steiner, Gereon Niedner-Schatteburg, "Spectroscopic investigations on nitrogen adsorbed on transition metal cluster cations in isolation", GRC: Molecular and ionic clusters, Ventura, CA, USA, 17.-22.01.2016.

J.M. Hewer, M. Tombers, J.Lang, S. Dillinger, M.H. Prosenc, G. Niedner-Schatteburg, P. Roesky, C. Bülow, T. Lau, "X-ray Magnetic Circular Dichroism, of Heteronuclear Complexes in Isolation", 3rd International Conference on Bimetallic Complexes, Kaiserslautern, 05.-07.10.2016.

Sebastian Dillinger, Jennifer Mohrbach, Gereon Niedner-Schatteburg, "Spectroscopy and Kinetics of N₂ on Transition Metal Cluster Surfaces", 116. Bunsentagung, Kaiserslautern, 25.-27.05.2017.

Danksagung

Ich danke Prof. Dr. Gereon Niedner-Schatteburg für die Betreuung während meiner Promotion, für die gewährten Freiräume und auch für die Bereitschaft das ein oder andere Wochenende zu opfern. Des Weiteren bedanke ich mich für seine Ratschläge und Diskussionsbereitschaft.

Ich danke auch Prof. Dr. Markus Gerhards für die Übernahme des Zweitgutachtens und die netten Gespräche und Diskussion auf dem Flur. Ebenfalls danke ich Prof. Dr. Helmut Sitzmann für die Übernahme des Prüfungsvorsitzes.

Ein großer Dank geht an meine Arbeitskollegen und Freunde: Jennifer Mohrbach, Joachim Hewer, Johannes Lang und Dimitri Ibanmaew. Vielen Dank für die unterhaltsamen Stunden voller Gesang und Tanz sowohl während der Arbeitszeit, als auch danach. Ein zusätzlicher Dank geht an Jennifer Mohrbach für die Einführung (in den AK), die Einarbeitung und tolle gemeinsame Arbeitszeit. Ich werde mich noch in Jahren an unsere stundenlangen tiefgründigen Laborgespräche erinnern („Und jetzt?!“ – „Nein!“).

Ich danke der vorherigen Generation an Doktoranden des AK GNS: Fabian Menges, Lars Barzen, Christine Merkert, Jennifer Meyer, Matthias Tombers und Maximilian Gaffga für die freundliche Aufnahme in den Arbeitskreis und Hilfestellungen jeglicher Art.

Ich danke der neuen Generation des AK GNS: Matthias Klein, Annika Steiner, Björn Kwasigroch und Michael Lembach für ihr engagiertes Arbeiten und für das Weiterführen der Projekte.

Ich danke Meister Kolling für die Hilfe bei allen Problemen, die im Laufe meiner Promotion aufgetaucht sind und dafür, dass er mich jahrelang als Büronachbar ertragen hat.

Ich danke Christoph Riehn für seine Diskussionsbereitschaft und für diverse unterhaltsame Gespräche.

Ich danke Yevgeniy Nosenko für seine Hilfe und seine Geduld.

Ich danke unseren Sekretärinnen Hilde Seelos, Sybille Heieck, Petra Wetzels und Birgit Harrison-Weber für das Erleichtern der Bürokratie.

Ich danke den Mitgliedern der AKs Gerhards, van Wüllen und Patureau für die Ablenkungen und Unterhaltungen während der Arbeitszeit.

Ein besonderer Dank geht an meine Freunde und Familie. Ich bedanke mich für die Unterstützung, den Rückhalt und eure Geduld, auch wenn ich mich eine Weile nicht gemeldet habe.

Eidesstattliche Erklärung

Hiermit bestätige ich, Sebastian Dillinger, dass die vorliegende Arbeit mit dem Titel „*Cryo Spectroscopy and Kinetics of Isolated Transition Metal Clusters and Complexes*“ gemäß der Promotionsordnung des Fachbereichs Chemie der Technischen Universität Kaiserslautern selbstständig und mit keinen anderen als den hier angegebenen Quellen und Hilfsmitteln erstellt wurde.

Kaiserslautern, im September 2017

Sebastian Dillinger